NKS-395
ISBN 978-87-7893-483-3

Scenarios and Phenomena Affecting Risk of Containment Failure and Release Characteristics

Pavel Kudinov[1]
Sergey Galushin[1]
Dmitry Grishchenko[1]
Sergey Yakush[1]
Yvonne Adolfsson[2]
Lisa Ranlöf[2]
Ola Bäckström[2]
Anders Enerholm[2]

[1]Division of Nuclear Power Safety (NPS)
Royal Institute of Technology (KTH)
Sweden

[2]Lloyd's Register Consulting – Energy AB
Sweden

August 2017

Abstract

The report summarizes results achieved within the project NKS-SPARC. The project is motivated by apparently high sensitivity of effectiveness of severe accident management (SAM) strategy in Nordic type BWR to the uncertainties in physical phenomena (deterministic) and accident scenarios (stochastic). We employ ROAAM+ approach in order to address both epistemic and aleatory sources of uncertainty in a consistent manner. The state of the art review of Integrated Deterministic Probabilistic Safety Analyses (IDPSA) is presented. The ROAAM+ framework addressing all stages of the accident progression from initial plant damage states, through core degradation and vessel failure, melt ejection mode to ex-vessel melt-coolant interactions and debris coolability, is discussed in detail along with implementation details of ROAAM+ framework itself. Main findings of the analysis of effectiveness of SAM strategy in Nordic BWRs using ROAAM+ framework and main results are presented using failure domain maps. A conceptual approach for combined use of Probabilistic Safety Assessment (PSA) and Integrated Probabilistic Deterministic Safety Assessment (IDPSA) is illustrated. Methodological enhancements of PSA analysis, based on PSA and DSA integration are proposed. The project outcome will allow the end users to enhance understanding, completeness and consistency of safety analysis dealing with risk analysis in: management of severe accident issues; improved reliability analysis modelling methods for level 2 PSA; presentation of results in level 2 PSA, and related risk criteria; handling of modelling uncertainties.

Key words

ROAAM+, IDPSA, PSA, DSA, BWR, Severe accident, MELCOR, core degradation, steam explosion, debris coolability

NKS-395
ISBN 978-87-7893-483-3
Electronic report, August 2017
NKS Secretariat
P.O. Box 49
DK - 4000 Roskilde, Denmark
Phone +45 4677 4041
www.nks.org
e-mail nks@nks.org

Scenarios and Phenomena Affecting Risk of Containment Failure and Release Characteristics

NKS-R SPARC project

(Contract: NKS_R_2015_114)

Pavel Kudinov[1], Sergey Galushin[1], Dmitry Grishchenko[1], Sergey Yakush[1]
Yvonne Adolfsson[2], Lisa Ranlöf[2], Ola Bäckström[2], Anders Enerholm[2]

[1]Division of Nuclear Power Safety (NPS), Royal Institute of Technology (KTH)
[2]Lloyd's Register Consulting – Energy AB

June 2017

CONTENTS

List of Figures

List of Tables

Chapter 1. **Introduction**

This report summarizes the experience and results achieved within the project NKS-SPARC during 2016. The project is motivated by apparently high sensitivity of effectiveness of severe accident management (SAM) strategy to the uncertainties in physical phenomena (deterministic) and accident scenarios (stochastic). Furthermore, scenarios, including timing of events, and physical phenomena are also important sources of uncertainty for estimation of the consequences of containment failure, i.e. characteristics of the fission product release. Adequate approaches are necessary in order to address both deterministic (epistemic) and stochastic (aleatory) sources of uncertainty for a consistent assessment of the effectiveness of the accident mitigation strategy and environmental impact.

The project aims at integrating probabilistic and deterministic methods to improve risk analyses. Ideally, a risk analysis would at all point consider all challenges that can occur at that particular point in time. The process could be thought of like a dynamic event tree covering all possible failures (aleatory) and uncertainties associated with the lack of knowledge about system response (epistemic uncertainty). As much this is an appealing approach, the state space that would need to be analyzed to cover all possible scenarios and epistemic uncertainties is enormous and it will not be feasible to perform this analysis.

To make it possible to analyze the problem in a PSA-like framework, the problem can be viewed upon from two angles: deterministic and probabilistic viewpoints. From a deterministic analysis point of view a few simultaneous failures are considered during a sequence and the failures may be represented by “super components”. This would allow for a simplified process like the dynamic event tree. The merit would be that the approach would consider all possible effects, known and unknown, of the represented failures. To further limit the state space, consideration needs to be taken to the probability of failures, in such a way that negligible failure combinations are omitted. This approach would hence give a complete picture of the scenarios studied, and not only a few defined scenarios as in the current deterministic calculations.

From a probabilistic point of view all possible failure combinations should be covered by the PSA model. The simplifications therefore need to be regarding grouping of sequences (failure combinations that have similar effect) and simplified treatment of timing of failure combinations. The dynamic approach would give enhanced input about which scenarios that should be studied separately (where epistemic uncertainty can be quantified and eventually reduced), and also information about timing of events of importance. This information is expected especially relevant regarding PSA-L2. The enhanced information requires improvements in the PSA quantification methods to include the information in the PSA model.

The project employs the two above mentioned concepts in order to provide consistent treatment of the uncertainties.

The report is organized as follows: In Chapter 2 the state of the art review of the Probabilistic, Deterministic and Integrated Safety Analyses is presented. We mainly focus on Risk Oriented Accident Methodology (ROAAM+) as a tool for quantifying conditional threats to containment integrity, with emphasis on a Nordic type BWR.
The framework addresses all stages of the accident progression from initial plant damage states (defined in PSA level 1), through core degradation (paragraph 3.3) and

vessel failure (paragraphs 3.4,3.5), melt ejection mode (paragraph 3.6) to ex-vessel melt-coolant interactions (Paragraph 3.8) and debris coolability (Paragraph 3.7), which is presented in Chapter 3, together with implementation details of ROAAM+ framework itself (Paragraphs 3.1,3.2).

In Chapter 4 we present main findings of the analysis of effectiveness of SAM strategy in Nordic BWRs using ROAAM+ framework, considering threats of ex-vessel steam explosion and ex-vessel debris coolability. We present main results as failure domain maps in terms of the most influential parameters (based on full and surrogate model sensitivity analysis results).

In Chapter 5 we outline a conceptual approach for combined use of Probabilistic Safety Assessment (PSA) and Integrated Probabilistic Deterministic Safety Assessment (IDPSA), considering Nordic BWR severe accident issues for illustration. Methodological enhancements of PSA analysis, based on PSA and DSA integration are proposed, in particular – improved sequence definitions for PSA L2 analysis, estimation of probabilities of phenomena and consequences and improved method for integration of timing in the normally static fault tree method.

Main conclusions and suggestions for future research are presented in Chapter 6.
The main benefits of the project are:

- Better understanding of the modelling pre-requisites in current PSA (level 1 input to level 2 and level 2 design).
- New methods for combined deterministic-probabilistic analysis and
- Practical experience in using them in combination with existing PSA models.

The project outcome will allow the end users to enhance understanding, completeness and consistency of safety analysis dealing with risk analysis in:

- management of severe accident issues;
- improved reliability analysis modelling methods for level 2 PSA;
- presentation of results in level 2 PSA, and related risk criteria;
- handling of modelling uncertainties.

Not being the main focus of the proposed project, but the methodology could also be used for (for example): identify safety vulnerabilities (scenarios of safety importance which can threaten safety barriers) in active and passive safety systems.

Experiences from performed studies are summarized in the report as well as suggestions of areas which need further investigations.

Chapter 2. State of the Art Review of the Probabilistic, Deterministic and Integrated Safety Analysis.

Over the past decades, methods of Probabilistic Safety/Risk Analysis (PSA/PRA) have emerged as important tools to examine safety of complex, potentially hazardous, engineered systems such as Nuclear Power Plants (NPP). As safety requirements become increasingly stringent, requirements for quality and completeness of PSA models also increase. However further increase of the PSA models complexity is not necessarily an effective way to increase accuracy of PSA methods.

Deterministic analyses are the basis for construction of a nuclear power plant. The analyses are based on the single failure criterion and a number of conservative assumptions such as loss of offsite power and no credit for non-safety systems. The initiating events considered in the analyses are divided in different event categories, ranging from likely events (once or several times/year) down to residual risks. The more likely the event category is the higher the margins (conservatisms) against core damage must be. Thus, there are already some probabilistic considerations in the deterministic analyses.

The core damage frequency for both existing and advanced future plants is calculated to be in the range from 10^{-5}/reactor year to 10^{-8}/reactor year. However, the plant operation is sometimes hit by “improbable” (defined in PSA as very low probability) events, which can surprise, revealing a potential vulnerability in the complex plant system. We recognize that state of the art PSA methods provide numbers to quantify probability of what is already known as an “issue”, but are not capable of revealing what, and to what extent, is not known (i.e. scenarios that are not prescribed in the PSA input). PSA is based on a set of assumptions about possible accident scenarios believed to be conservative. Such “decomposition” of a complex problem into a set of pre-defined sequences can be prone to false conservatism in the PSA or deterministic analysis, rendering possibility of potentially dangerous scenarios being missed or underestimated.

Standard PSA and deterministic approach has fundamental problems with resolving the dynamic nature of mutual interactions between (i) stochastic disturbances (e.g. failures of the equipment), (ii) deterministic response of the plant (i.e. transients), (iii) control logic and (iv) operator actions. Passive safety systems, severe accident and containment phenomena are examples of the cases when such dependencies of the accident progression on timing and order of events are especially important.

Since the late eighties, realistic deterministic-dynamic models, commonly referred to as best-estimate methods, received recognition as safety analysis tools. However, the best estimate codes are still used in a largely decoupled manner from the PSA. That hinders their application to risk analysis and identification of plant vulnerabilities.

In making predictions regarding the response of a system to disturbances, both the uncertainties arising from the stochastic nature of events (aleatory uncertainties) as well as those arising from lack of knowledge about the processes relevant to the system (epistemic uncertainties) have to be taken into account. Often, it is difficult to distinguish between epistemic and aleatory uncertainties [3]. Dynamic PSA methodologies allow a unified framework to account for the joint effects of both types

of uncertainties simultaneously in predicting the distribution of risk associated with the system response.

Dynamic PSA methodologies can be divided into three main categories [4]: (i) continuous-time methods, (ii) discrete-time methods, and (iii) methods with graphical interfaces. While the methods with graphical interfaces are also either continuous or discrete time methods, they are listed as a separate category because the availability of a graphical interface is usually regarded as rendering them more user friendly. IDPSA tools usually employ (i) system simulation codes and models with explicit consideration of the effect of timing on the interactions between epistemic (modeling) and aleatory (scenario) uncertainties, (ii) a method for exploration of the uncertainty space. A review of the IDPSA methods for nuclear power plant applications can be found in [4, 25]. The inputs for all dynamic methodologies are:

- a time-dependent system model (such as RELAP5 [5] or MELCOR [6] codes),
- possible normal and abnormal system configurations which may need to be determined using a failure-modes-and-effects (FMAE) analysis, and
- transition probabilities (or rates) among these configurations.

2.1.1 IDPSA methods and the decision making process

It was mentioned previously [1] that the readiness of a tool is difficult to determine if there are no clear criteria for success or goal for the analyses. In terms of decision making, quantification of consequences into figures of merit is necessary (i.e. to establish safety goals and success criteria).

IDPSA methods are capable of quantifying aleatory uncertainties in time dependent scenarios. It was emphasized (during the IDPSA meeting 2012 [1]) that this mostly had an effect within the context of academia whereas it did not do much for deployment into the industry. Therefore, focus must be directed towards what the decision makers need and what they regard as important.

Credibility, uncertainty quantification (robustness of decision), comprehensiveness (risk profile instead of one number) and understanding were outlined as important factors in terms of what kind of data to be provided for the decision makers. Consistency was also emphasized as important since different kinds of decisions (e.g. for industry or regulators) put different requirements on the data provided.

2.2 Risk Oriented Accident Analysis Methodology

The Risk Oriented Accident Analysis Methodology (ROAAM) [27], [28] can be considered as an example of a decision support method. The ROAAM marries probabilistic and deterministic approaches. This methodology developed by Professor Theofanous [27] has been applied to successfully resolve different severe accident issues in LWR plants, and severe accident treatments in ALWR designs e.g., [28].

The focus of ROAAM is upon reducing the uncertainty to the extent that a defense-in-depth is considered as achieved. When the whole community of experts in a given problem area is convinced that the demonstration is effected and regarded successful the problem may be considered solved (in a robust and final way). Eventually the complete reaching of all experts is effected by publication in the technical literature, with additional iterations thereof if necessary. ROAAM provides guidelines for development of framework for bounding of epistemic (modelling) and aleatory (scenario)

uncertainties in a transparent and verifiable manner that enables convergence of experts opinions on the outcome of the analysis (not necessarily on the uncertainties in the input information). ROAAM integrates risk assessment (analysis) and risk management (modifications in the design, procedures, etc.) in an effective manner in order to resolve safety issues.

When applied to the Nordic BWR plants, the tight coupling between severe accident threats (steam explosion and basemat melt-through due to debris un-coolability) and high sensitivity of the SAM effectiveness to timing of event (e.g., vessel failure) and characteristics (e.g., melt release conditions) present new challenges in decomposition, analysis and integration.

It is instructive to note that discussion of approaches to risk management regulatory framework has been initiated at US NRC [29]. Risk Management Task Force provided recommendation that NRC should implement a consistent process that includes both deterministic and probabilistic methods. It is acknowledged that Risk assessments provide valuable and realistic insights into potential exposure scenarios. In combination with other technical analyses, risk assessments can inform decisions about appropriate defense-in-depth measures.

ROAAM+ framework employs a two-level coarse-fine iterative analysis. First, fine-resolution but computationally expensive methods are used in order (i) to provide better understanding of key phenomena and their interdependencies, (ii) to identify transitions between qualitatively different regimes and failure modes, and (iii) to generate reference data. The fine-resolution codes are run independently, assuming wider possible ranges of the input parameters. Second, a set of coupled modular frameworks is developed connecting initial plant damage states with respective containment failure modes. Deterministic processes are treated using surrogate models based on the data obtained from the fine-resolution models. The surrogate models are computationally efficient and preserve the importance of scenario and timing. Systematic statistical analysis carried out with the complete frameworks helps to identify risk significant and unimportant regimes and scenarios, as well as ranges of the uncertain parameters where fine-resolution data is missing. This information is used in the next iteration of analysis with fine-resolution models, and then refinement of (i) overall structure of the frameworks, (ii) surrogate models, and (iii) their interconnections. Such iterative approach helps identify areas where additional data may significantly reduce uncertainty in the fine- and coarse-resolution methods, and increase confidence and transparency in the risk assessment results. The overall modular structure of the frameworks and the refinement process are discussed in the paper in detail [25].

2.3 Quantitative Definition of Risk and ROAAM Basics

According to quantitative definition of risk, proposed by Kaplan and Garrick [30], the risk R_i associated with specific scenario s_i can be characterized by its frequency f_i and consequences c_i. Consequences are obtained from predictions that are subject to epistemic uncertainty due to incomplete knowledge. The degree of uncertainty in the prediction of the future course of events can be quantified as "probability" P_i or "likelihood" of c_i. Such probability is evaluated by an expert based on the available evidences (i.e. data and/or experience with similar courses of action in the past). Therefore, two rational beings given the identical evidence must assess the probability identically [30]. "Frequency" is the outcome of an experiment involving repeated trials. Aleatory uncertainty is expressed in terms of frequency.

$$R_i = \{s_i, f_i, P_i(c_i)\} \tag{2.1}$$

Consequences c_i of scenario s_i can be presented as joint probability density function $\mathrm{pdf}_{C_iL_i}(L_i, C_i)$, which accounts for the epistemic uncertainty and possible dependencies between the loads (L_i) on the system in question and its capacity (C_i) to withstand such loads. Thus, failure probability P_{Fi} for scenario s_i can be evaluated as

$$P_{Fi} = P(L_i \geq C_i) = P(C_i - L_i = Z_i \leq 0) = \iint_{Z_i \leq 0} \mathrm{pdf}_{C_iL_i}(c, l)dcdl \tag{2.2}$$

or, in case when load and capacity are independent

$$P_{Fi} = P(L_i \geq C_i) = \int_{-\infty}^{\infty} \int_{-\infty}^{l \geq c} \mathrm{pdf}_{L_i}(l)\, \mathrm{pdf}_{C_i}(c)dc\, dl = \int_{-\infty}^{\infty} \mathrm{CDF}_{C_i}(l)\, \mathrm{pdf}_{L_i}(l)dl \tag{2.3}$$

where CDF_{C_i} is the cumulative probability density function for the capacity. Unacceptability of containment failure is equivalent to requirement that all P_{Fi} should be below "physically unreasonable" level P_S.

The idea of characterizing risk as a set of triplets (scenario, its frequency, and probability of consequences) was further developed and practically applied to assessment of severe accident risks in ROAAM [28]. According to ROAAM, the use of Risk for effective management and regulation of rare, high-consequence hazards requires the simultaneous (coherent) consideration of (i) safety goal, (ii) assessment methodology, and (iii) application specifics. ROAAM provides guidelines for development of frameworks for bounding the epistemic (modeling), and aleatory (scenario) uncertainties in a transparent and verifiable manner that should enable convergence of experts' opinions in the review process.

Important premise of ROAAM is that safety goals can be defined only qualitatively when epistemic uncertainty is significant. The goal should effectively communicate the idea that the perceived hazard is "physically unreasonable" under "any circumstances" leading up to it in a "physically meaningful" context. More specifically, for severe accident analysis the safety goal can be defined as: "containment failure is a physically unreasonable event for any accident sequence that is not remote and speculative" [28].

In order to achieve the transparency and verifiability, ROAAM employs its principal ingredients: (i) identification, separate treatment, and maintenance of separation (to the end results) of aleatory and epistemic uncertainties; (ii) identification and bounding/conservative treatment of uncertainties (in parameters and scenarios, respectively) that are beyond the reach of any reasonably verifiable quantification; and (iii) the use of external experts in a review, rather than in a primary quantification capacity.

Separation of epistemic and aleatory uncertainties stems from the work of Kaplan and Garrick [30]. Separate treatment of screening frequency for aleatory, and the physically unreasonable concept for epistemic uncertainties is a must for clarity and consistency of the ROAAM result.

An arbitrary scale for probability is introduced which defines a physically unreasonable process as one involving the independent combination of an end-of-spectrum with one expected to be outside but cannot be positively excluded [28]:

- 1/10 Behavior is within known trends but obtainable only at the edge-of-spectrum parameters.

- 1/100 Behavior cannot be positively excluded, but it is outside the spectrum of reason.
- 1/1000 Behavior is physically unreasonable and violates well-known reality. Its occurrence can be argued against positively.

The starting point of ROAAM is an interest in the "likelihood" (L_j) of different containment failure modes (hazards H_k) given a set of initial plant damage states ($\{D_j\}$)

$$L_j(H_k) = G(p_1, p_2, \dots, p_l), \quad \text{given } \{D_j\} \tag{2.4}$$

where damage states have frequency higher than selected screening frequency f_s and lower than target frequency f_t achieved as the prevention goal, that is, $f_s < f_j(D_j) < f_t$.

The approach employed in ROAAM is not to realize a defensible approximation to function G, and seeking the likelihood L_j, but to establish that it is (or can be made by appropriate decisions) low enough as to regard the hazard H_k as physically unreasonable, avoiding excess conservatism while still remaining convincing [28].

A separation must be made between the aspects of systems response that can be stated as well-posed physical problems or "causal relations", and other aspects which are subject to inherently variable behavior and called "intangibles". The structure of separation synthesis is called "probabilistic framework". Each framework refers to a particular "scenario" s_i. The art in the decomposition is to envelop the behavior through the coherent use of "intangibles" and respective "scenarios" such that it will be understandable (and scrutable). Each "causal relation" requires an in-depth and demonstrable understanding of the controlling physics; "scenarios" and "intangibles" are to fill in the gaps whenever this is not possible. Uncertainty in causal relations can be reduced. Uncertainty in intangibles can only be qualitatively approached, but it can always be bounded. The adequacy of scenarios can be determined according to the completeness of the logical structures used in deriving them. The process of integration through the probabilistic framework is effected by introducing a scale for the temporary quantification of intangibles, and the results are rendered in qualitative terms by applying this scale in reverse.

The problem is decomposed into framework and stochastic scenarios $\{s_i\}$, such that:

$$L_{ji}(H_k) < P_{ji}(H_k), \quad P_{ji}(H_k) = F(d_1, d_2, \dots, i_1, i_2, \dots) \tag{2.5}$$

where $\{d_i\}$ is a set of "deterministic" parameters, $\{i_i\}$ is a set of "intangible" parameters, $P_{ji}(H_k)$ is based on arbitrary probability scale. The goal of analysis is to show that

$$P_{ji}(H_k) < P_s \text{ given } \{D_j\} \text{ for all } \{s_i\} \tag{2.6}$$

where P_s is the "physically unreasonable" level. The above structure separates out epistemic from aleatory uncertainty which is also motivated by the distinct approaches to judge residual risk: with screening frequency for aleatory, and with physically unreasonable concept for epistemic. Any stochastic behavior not already included in the definition of the severe accident window (the plant damage states to be considered) can be taken up in the definition of scenarios and intangibles, since they would be expected to dominate the uncertainty in any case. If necessary, however, stochastic parameters, or

even processes, can appear explicitly in (2.5). A similar separation can be effected in this case, too, by simply finding the total probability in each frequency range, and applying the same criteria for judging the results – but now these frequencies should be combined with the respective plant damage state frequencies [28].

2.4 Nordic BWR challenges for ROAAM

Severe accident management (SAM) in Nordic boiling water reactors (BWRs) relies on ex-vessel core debris coolability. In the case of core meltdown and vessel failure, melt is poured into a deep pool of water located under the reactor. The melt is expected to fragment, quench, and form a debris bed that is coolable by natural circulation of water. Success of the strategy is contingent upon melt release conditions from the vessel which determine (i) properties of the debris bed and thus if the bed is coolable or not, and (ii) potential for energetic interactions (steam explosion) between hot liquid melt and volatile coolant. Both non-coolable debris bed and steam explosion pose credible threats to containment integrity.

While conceptually simple, this strategy (i) involves extremely complex and often tightly coupled physical phenomena and processes, which are also (ii) sensitive to the conditions of transient accident scenarios. For instance, late recovery actions might affect core degradation and relocation processes, which can change formation of the in-vessel debris bed, reheating and re-melting of multi-component corium debris, thermo-mechanical interactions between melt and vessel structures and penetrations, vessel failure, melt release and jet fragmentation, debris solidification, energetic melt-coolant interactions, two-phase flow in porous media, spreading of debris in the pool, spreading of particulate debris bed, etc. (Figure 2.1). These phenomena have been a subject of extensive investigations in a large-scale research program on Melt-Structure-Water Interactions (MSWI) at the Royal Institute of Technology (KTH) over the past few decades.

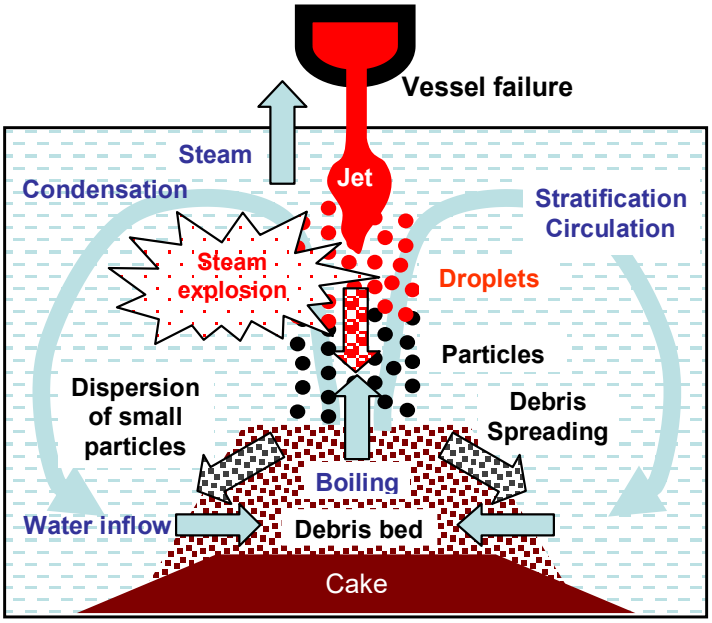

Figure 2.1. Severe accident phenomena in Nordic BWR.

While a significant progress has been made in understanding and predicting MSWI physical phenomena, complex interactions and feedbacks between (i) scenarios of

accident progression, and (ii) phenomenological processes, have hampered a comprehensive assessment of SAM in the Nordic BWRs. Presently, the issues of ex-vessel debris coolability and steam explosion are considered as intractable by only probabilistic or only deterministic approaches.

Information about the initiating events and plant damage states is necessary input information for the IDPSA analysis and it can be provided from the PSA-L1. In Chapter 3 we provide an overview of PSA-L1 results which are used in this work.

Timing of events such as failure and recovery of safety systems determines in-vessel accident progression, core relocation process and properties of the debris in the lower head. The properties and configuration of the debris determine initial conditions for corium-structure interactions, vessel failure and melt release conditions. Therefore core degradation and relocation scenarios have significant impact on the ex-vessel accident progression and risks. For addressing the effect of timing of the events on the in-vessel and ex-vessel accident progression a set of initial plant damage states and possible further failures and recovery actions has to be provided. Such information is available from the PSA-L1. In the following section a discussion of the basic information from PSA-L1 which is necessary for IDPSA analysis and identification of specific topics of interest is provided.

2.4.1 **Phenomenology and Scenarios**

While ROAAM is logically sound and has been successfully applied in several practical cases to resolve severe accident issues, there are some challenges for application of ROAAM to Nordic BWR case. Typical phenomenological stages of severe accident progression in Nordic BWR are shown in Figure 2.2.

The multistage path from the initial plant damage state to the containment threats is an important source of complexity and uncertainty. Phenomena and scenarios including operator actions are tightly coupled in their mutual interactions and eventual impact on the possibility of different containment failure modes. Conditions created at the earlier stages can significantly affect configurations and problem statements at later stages. For instance, if there is no activation of lower drywell flooding, then steam explosion risk is eliminated, but hot corium melt will attack cable penetrations in the containment floor leading to almost immediate containment failure.

Timing of transition between different stages is also important. Different time-dependent trajectories of the accident scenarios with the same logical sequence of the stages can result in different outcomes. For instance, decay heat is decreasing with time providing much better chances for coolability of the debris bed if melt is released from the vessel later [31]. However, if melt is released from the vessel later, it will have higher temperature, which could increase the risk of debris agglomeration [32], [33], [34] hindering coolability of the debris bed [35], and creating a potential for an energetic steam explosion which can threaten containment integrity.

Combination of (at least) two threats (non-coolable debris and steam explosion) is another source of uncertainty. On one hand, there is a possibility that steam explosion might contribute to spreading of the debris over containment floor. On the other hand, even a mild steam explosion might lead to degradation of debris bed cooling function, e.g. by destroying protective covers for cable penetrations in the containment floor and

exposing them to hot debris, or by creating a leak of coolant from the lower drywell, or by activating filtered containment venting, releasing fraction of nitrogen which can potentially lead to drop of containment pressure well below atmospheric level, etc.

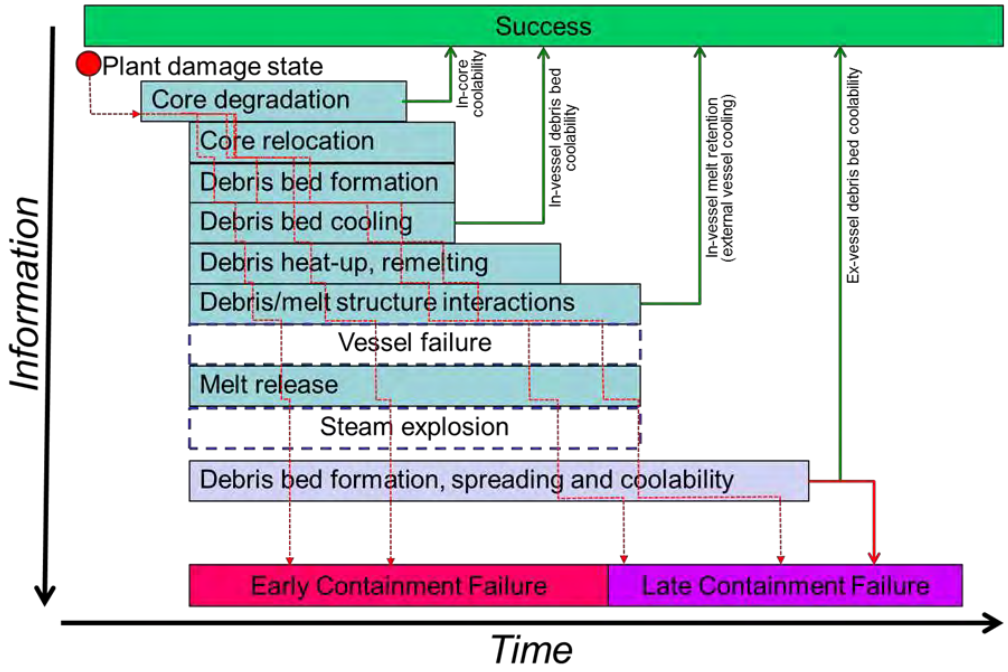

Figure 2.2. Severe accident progression in Nordic BWR.

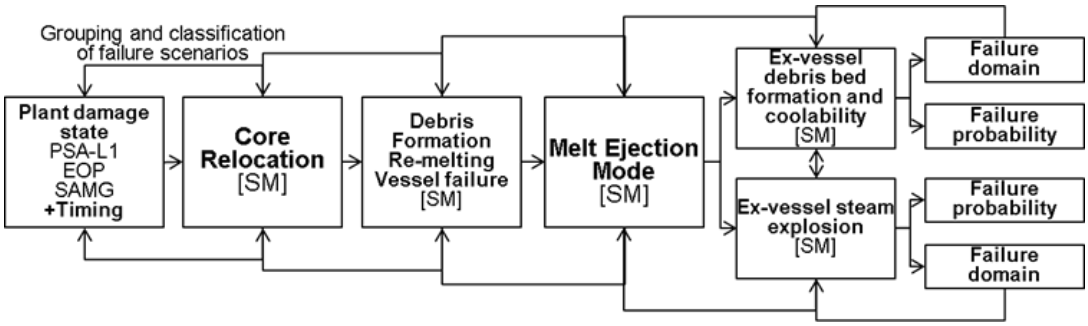

Figure 2.3. ROAAM+ Framework Nordic BWR.

The major challenge for application of ROAAM to Nordic BWR is the complexity of tightly coupled transient phenomena and scenarios which limit the effectiveness of heuristic approaches in (i) problem decomposition and (ii) a priori judgment about importance and impact of coupled and time dependent phenomena and scenarios on the accident progression and outcome.

2.4.2 **Decision Making Context**

Conditional containment failure probability is considered in this work as an indicator of severe accident management effectiveness for Nordic BWR. It is instructive to note that different modes of failure (assumed to be equivalent to loss of containment integrity) can potentially lead to quite different consequences in terms of radioactivity release. At this point we consider any failure mode as unacceptable for the sake of conservatism.

The ultimate goal of ROAAM process is to provide a scrutable background in order to achieve convergence of experts' opinions in decision making on the question: is

containment failure physically unreasonable, given existing SAM and current state-of-the-art knowledge? This question is driven by “concerns”. If inherent safety margins are large, then the answer to the question is positive and can be demonstrated through consistent conservative treatment of uncertainties in risk assessment by improving necessary knowledge and data. Otherwise, improvement of the state-of-the-art knowledge is ineffective. Appropriate modifications of the system (e.g. safety design, SAMGs, etc.) should be undertaken in order to achieve the safety goal.

However, it is not always obvious that existing system cannot meet the safety goal even if further investments in development of new knowledge will be continued. Especially for complex systems, such as SAM of Nordic BWR, uncertainty can create a space for decision makers’ “hope” that the system is safe due to some incompletely understood phenomena or interactions, and thus acquiring further knowledge about the system is justified. As such proposition is driven by the “hope”, it is clear that conservative treatment of uncertainty would not be very helpful. For clarifying if such hope is reasonable, the assessment should be focused on the necessity of containment failure using “optimistic” treatment of uncertainty.

Thus, to be truly useful for decision making on the Nordic BWR SAM case, the risk assessment framework should be capable of providing assessments in support for both possible decisions: (i) current strategy is sufficiently reliable and no changes are necessary; (ii) strategy is not sufficiently reliable and changes are necessary.

A difficulty arises when neither failure nor success can be demonstrated with a sufficient confidence. For instance, bounding (“conservative” or “optimistic”) approaches fail to characterize system risks when failure or success domains are positioned in the middle of the uncertainty space. In other words, only an “optimal” course of events can lead to success or to failure. This is often the case when there are competing phenomena or threats, when positive or negative effect of some parameters or events on the failure possibility changes depending on other parameters or events. For instance, in case of successful attempt of in-vessel debris cooling using control rode guide tube (CRGT) flow, melt release from the vessel can be prevented. However, if corium retention is not successful, CRGT cooling can lead to delay of vessel failure, formation of a larger melt pool with higher superheat. Melt release from the vessel with such conditions can significantly increase potential energetics of steam explosion and the risk of formation of agglomerated, non-coolable debris bed. Feasibility of using “best estimate” or “risk informed” approaches for decision making in this case is contingent on the system, data and knowledge. If dependencies are strong, risk quantification can be polluted with uncertainty to the point where “everything is possible” due to “combinatorial explosion of possibilities”. Using “risk informed” approach in such case with large irreducible uncertainties can be at best inconclusive, and in the worst case misleading. If “everything is possible”, it is a clear sign that the system is complex. In other words, understanding and control of the system is beyond our reach and changes in the system are necessary in order to make its behavior predictable with sufficient confidence.

Eventually decision has to include cost benefit analysis. If potential costs of improving the current state of knowledge are high then the decision to change the system in order to reduce its complexity would be the most reasonable. If the costs of knowledge improvement are acceptable, then extensive sensitivity and uncertainty analysis can be quite useful for identification of priorities for defining research goals and collection of new data. However, quantitative uncertainty in estimations of risks related to potential

losses vs cost of necessary research is usually quite high.

Thus a structured process is needed for coherent (i) development of risk assessment framework, (ii) collection of necessary data, and (iii) development of necessary knowledge. This process should be guided by extensive sensitivity and uncertainty analysis and eventually result in a robust and scrutable assessment of either "possibility" or "necessity" of containment failure in order to support decision making.
The detailed description of the important aspects of development of such process for Nordic BWR SAM can be found in **Error! Reference source not found.**.

2.5 ROAAM+ Probabilistic Framework for Nordic BWR

It is clear that key ingredients of ROAAM such as:

- Separation of aleatory and epistemic uncertainties through
  - Consideration of risk as a set of the triplets (scenario, its frequency, and probability of consequences),
  - Decomposition of the problem into stochastic "scenarios" and deterministic "frameworks",
- Arbitrary scale of probability for epistemic uncertainty,
- Qualitative definition of safety goal,

are critical for consistency of assessment and transparency of review and must be preserved. However, the challenges presented by Nordic BWR SAM strategy require further development of the approach. In this section we discuss the basic ideas and examples of development of such an approach which we call ROAAM+.

The goal of the ROAAM+ approach is to provide sufficient information for a decision to:

I. Keep SAM strategy: "Possibility" of containment failure is low even with "conservative" treatment of uncertainty, thus current strategy is reliable.
II. Modify SAM strategy: "Necessity" of containment failure in the course of accident is high (i.e. "possibility" that containment doesn't fail is low) even with "optimistic" treatment of uncertainty, thus the current strategy is unreliable and changes should be considered.

In order to achieve the goal, ROAAM+ process is developed for construction and adaptive refinement of the risk assessment framework, models, and data. The process is aiming to refine the resolution of the framework in order to bound the influence of the largest contributors to the uncertainty in risk assessment.

2.5.1 Iterative Adaptive Refinement Process for Development of Risk Assessment Framework: Two Level "Coarse-Fine", "Forward" and "Reverse" Analysis.

System complexity can limit effectiveness of heuristic approach (based on expert judgment) to identification of the key physics which drive system behavior. Therefore, there is a need for an iterative research process which can help in identifying and evaluating importance of different factors for the ultimate risk assessment. This implies that at each stage of the process, a framework for risk assessment should exist, providing a means for sensitivity and uncertainty analysis of "possibility" and

"necessity" of containment failure with respect to the uncertain elements of the framework. Such analysis should, in turn, results in activity on improvement of the framework and data to assess the impact of such improvements in the next iteration.

Therefore, in the proposed framework we implement three different types of analysis (i) Conservative assessment of containment failure possibility; (ii) Optimistic assessment of containment failure necessity; and (iii) Sensitivity and uncertainty analysis as an instrument for guiding construction and refinement of the risk assessment framework itself. In practice, different analysis types are implemented through consistent use of assumptions on uncertainty in (i) scenarios and (ii) ranges and probability distributions of the uncertain parameters. Sensitivity and uncertainty analysis is employed for both (i) optimal refinement of the data, knowledge and risk analysis framework, and (ii) optimization and assessment of effectiveness of potential system modifications.

Complex phenomena and feedbacks require adequate complexity of the models. These "full models" (FMs) are usually implemented for each stage of accident progressing in respective multidimensional severe accident, thermal hydraulic, and structural analysis codes. Direct application of such fine-resolution models for extensive sensitivity and especially uncertainty analysis is often unaffordable due to extreme computational costs and difficulties in establishing direct coupling between the codes. Therefore, we employ a two-level coarse-fine modeling approach. At the first (bottom) level we use loosely coupled FMs and available experimental evidences in order to generate relevant data and develop understanding of key physics. The data and knowledge are used to develop and validate coarse-resolution "surrogate models" (SMs). The SMs provide computationally efficient approximations for the most important parameters of the FM solutions. The SMs are used at the second (top) level of the framework for sensitivity, uncertainty analysis and risk quantification. We call this process "forward" analysis.

When complexity is high, it is difficult to identify a priori what is more important and what is missing from our knowledge of each individual stage of the accident progression. Such information can be obtained when all stages are coupled and a connection between uncertainties at each individual stage and resulting uncertainty in containment failure probability can be established. Until such connection is established, it is not possible to assess if FMs and SMs provide sufficient resolution for all important phenomena. In fact, some of the FMs might not be available yet. In such case FMs should be designed according to the requirements which can be inferred from the results of the reverse analysis. Accuracy of the FM should be sufficiently qualified through scaling, calibration, verification, validation and uncertainty quantification process using relevant experimental data. The need for new data stems from the model validation needs. Therefore, there is a need for iterative refinement process of the FMs, SMs, experimental data and structure of the framework. Criteria for the need of refinement can be established based on consideration of the failure domain. Failure domain (FD) is a domain in the space of the uncertain parameters where probability of containment failure is larger than a "physically unreasonable" threshold. The main criteria for the need of the refinement are (i) how large is the uncertainty in resolving the boundaries of the failure domain with existing FM and SM implemented in the framework, and (ii) are there any physical phenomena or scenarios which are not taken into account yet, but can significantly change FD boundaries. Naturally, the FD identification and necessary refinement starts from the last stages of the accident progression analysis and propagates "upstream" to the earlier stages. We call this process "reverse" analysis.

The two-level coarse-fine approach to development and iterative adaptive refinement of the risk assessment frameworks is summarized below:

1) *Development and refinement:* of models, frameworks and data based on the results of the forward and reverse analyses in order to reduce uncertainty in the failure probability and resolution of failure domain boundary.

Experimental evidences and fine-resolution but computationally expensive methods (FMs) are used in order to:

i. Develop hypothesis about key phenomena and provide better understanding of their possible interdependencies,
ii. Identify transitions between qualitatively different regimes and failure modes, and
iii. Generate reference databases for development calibration and verification of coarse-resolution but computationally efficient surrogate models (SMs).

FMs are run in "exploratory" mode, loosely coupled or independently from each other, assuming bounding ranges for model input parameters. Preliminary scaling analysis is carried out for the experimental evidences.

2) *Forward analysis:* quantification of major contributors to the uncertainty in the failure probability at each stage of the modeling of accident progression.

A probabilistic framework is developed based on coupled SMs in order to connect the initial plant damage states with respective containment failure modes.

i. Deterministic processes are treated using the developed and verified SMs preserving importance of scenarios and timing.
ii. Sensitivity and uncertainty analysis is carried out using the framework to:
    a. Identify significant and unimportant parameters, regimes and scenarios.
    b. Quantify the risk and contribution to the overall uncertainty for the most influencing factors.

3) *Reverse analysis:* identification of failure domains and their boundaries at each stage of the modeling of accident progression.

Failure domains and their boundaries are identified in the spaces of uncertain input parameters for each SM (representing different stages of the accident progression) in order to identify the needs for improvement of:

i. Experimental data and scaling.
ii. FMs and their validation matrices.
iii. SMs, calibration and verification databases (based on FMs and experimental data), interconnections and databases of solutions.
iv. Overall structure of the problem decomposition into scenarios and frameworks.

Such iterative process is designed to develop state of the art knowledge, confidence and transparency in the risk assessment results, to the point when convergence of experts' opinion on the possibility or necessity of containment failure can be achieved. Possibility of such convergence is a stopping criterion for the refinement process.

Adaptive decomposition (into scenarios and phenomena) depends largely on the knowledge base (relevant data, code capability, etc.). Employment of the fine resolution FMs in the process of risk quantification and uncertainty reduction is justified when appropriate evidences of the models' validation are provided. Failure domain (reverse) analysis points to the domains of parameters and scenarios where evidences of detailed validation are most needed and improvement of the validation database has the largest impact on the uncertainty reduction. Proper scaling of experimental data is important for establishing consistency between modeling and experimentation in the iterative process of uncertainty reduction. In this light, a list of phenomena and corresponding experiments that can be used for validation of FMs and calibration of SMs should be

provided along with the assessment of the data quality (relevance, scaling, and uncertainty). Such information is a basis for the decisions on decomposition and the needs for improvements of the evidence database.

2.5.2 **Failure Probability**

Quantification of failure probability is the ultimate goal of the analysis. Illustration of the failure probability quantification determined by forward propagation of the uncertainties through a single stage framework is illustrated in Figure 2.4.

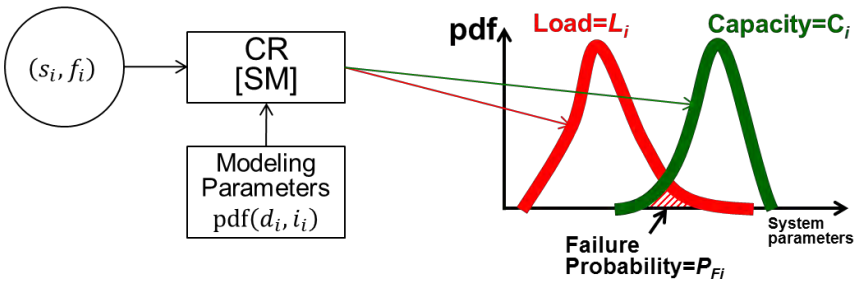

Figure 2.4. Failure probability in a single stage framework.

For each plant damage state $\{D_i\}$ there is a set of respective scenarios $\{s_{ij}\}$, are characterized by frequencies (f_{ij}). For the sake of brevity, in the future we will omit second index when referring to scenarios (s_i) and their probabilities (f_i) considering them as a whole set of all scenarios relevant to all initial damage states. Scenarios (s_i) introduce specific combinations of initial and boundary conditions for causal relationships (CR) and structure of the probabilistic framework. The CR provides "bounding" assessment of the load and the capacity which can provide optimistic and conservative estimates. If bounding assumptions in modeling approaches are not obvious "a priori", sensitivity analysis is required. A set of surrogate models (SM) is used to approximate the CR. Epistemic uncertainty in prediction of the failure probability is introduced by multidimensional probability density function $(\mathrm{pdf}(d_i, i_i))$ of intangible (i_i) and deterministic (d_i) modeling parameters. These distributions determine the probability of the consequences $(P_i(c_i))$ or, more specifically, probability of containment failure (P_{Fi}) of scenario (s_i). It is instructive to note that Figure 2.4 provides a simplified view on the problem, where space of system parameters is generally multidimensional and different types of loads and capacities correspond to different threats and failure modes.

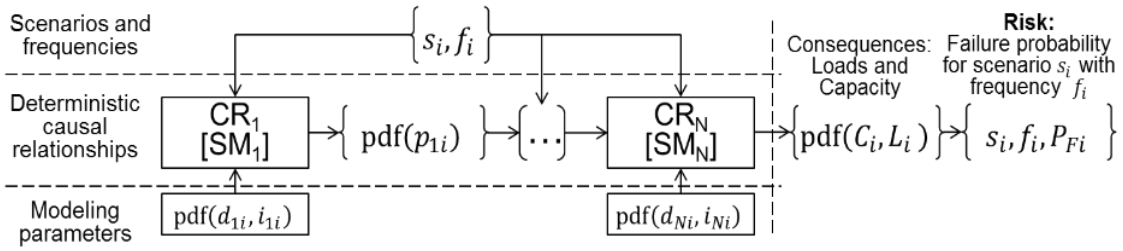

Figure 2.5. Failure probability in a multistage framework.

Similarly to the single stage process, the probability of failure (P_{Fi}) in scenario (s_i) can be introduced for a multistage framework where CR is a set of N models connected through initial conditions (p_{ki}), as illustrated in Figure 2.5. Simulations are carried out

for each individual scenario s_i separately, which enables maintaining of transparent separation of aleatory (characterized by frequency f_i of scenario s_i) and epistemic uncertainties. Note that scenario parameters can affect modeling at any intermediate stage. Respective timing should also be provided as a part of scenario s_i, e.g. timing of activation, failure or recovery of specific safety systems. Different scenarios might require different chains of CRs, or "phenomenological event trees". Splinters should be used to ensure consistent bounding approaches in addressing intangible characteristics of such event trees. Output of CR_k is determined as multidimensional probability density function $\{\mathrm{pdf}(p_{ki})\}$ and provides an initial input conditions for model CR_{k+1}. Timing is explicitly included as one of the p_{ki} parameters.

In the conservative assessment we are seeking for a confirmation that $P_{Fi} < P_S$, or, in other words, that containment failure in scenario s_i can be positively excluded as physically unreasonable according to current state of knowledge. This conclusion would support the proposition that current SAM is reliable and no changes are necessary.

In the optimistic assessment we are looking for confirmation that $P_{Fi} > P_S$ which can be interpreted as: containment failure cannot be excluded as physically unreasonable even with optimistic bounding assumptions and state of the art knowledge. In other words "necessity" of containment failure is unacceptably high and the SAM has to be changed through modifications of the SAMGs or design.

The state of knowledge is expressed in terms of the ranges and probability distributions for the uncertain input parameters. Selection of the models, ranges and distributions is based on evidences (experimental data, scaling, synthesis of fine resolution simulation results, etc.).

Failure probability is used not only as the final results of the assessment, but also as a research instrument in the adaptive process. Sensitivity analysis of P_{Fi} to ranges and distributions of the uncertain parameters is used to identify (i) major sources of the uncertainty and possible unreasonable conservatism in the risk assessment, (ii) the needs for refinement of the evidence database.

Joint consideration of sensitivity of failure probability P_{Fi} to (i) possible improvement of knowledge necessary to reduce conservatism in the framework, and (ii) possible changes in the accident management strategy necessary to decrease failure probability with given state of knowledge, and associated costs for both options can provide a quantitative measure for selection of the most efficient approaches in both (a) risk assessment, and (b) risk management.

In the forward analysis, information is propagated from the initial plant damage state through the sequences of phenomena, determined by specific scenarios, towards the failure probability for each scenario, estimated at the very end. Such process provides limited information for inferring about adequacy of selected framework structure and generated data for the assessment of the failure possibility. Forward propagation of the uncertainties, especially in the multistage modeling framework, often amplifies uncertainties at each stage, unless there are clear limiting physical mechanisms. As a result of such amplification, there is a risk of "phenomenological explosion" (analogous to combinatorial explosion) when epistemic uncertainty becomes so large that success and failures become equally possible and nothing can be positively excluded as physically unreasonable. Therefore, there is a need for another kind of analysis where adequacy and consistency of the modeling framework and data can be evaluated.

2.5.3 **Failure Domain**

The primary goal of failure domain analysis is to identify the conditions and explain the reasons of failure in terms of key physics and scenarios. Identification of the failure domain is a product of the "reverse" analysis which propagates information "backwards" from the end state where failure is determined through the CR to the spaces of input (scenario and modeling) parameters (Figure 2.6). By identifying and grouping scenarios and conditions which lead to failure, we can determine and explain the reasons of failure using compact representation of information, amenable for scrutiny. "Failure Domain" (FD) in the space of scenario parameters $\{s_i\}$ is a subdomain where probability of failure P_F is larger than a "physically unreasonable" level (P_S) of probability ($P_{Fi} \geq P_S$) (Figure 2.6).

$$\{s_i^F | \text{pdf}(d_i\ , i_i\ )\}\text{: } P_F(s_i^F) \geq P_S \tag{2.7}$$

"Failure Domain" (FD) in the space of deterministic modeling parameters $\{d_i\ , i_i\ \}$ is a subdomain where load (L_i) exceeds Capacity (C_i) (Figure 2.6).

$$\{(d_i^F, i_i^F) | s_i\ \}\text{: } Z_i(d_i^F, i_i^F) = C_i - L_i \leq 0 \tag{2.8}$$

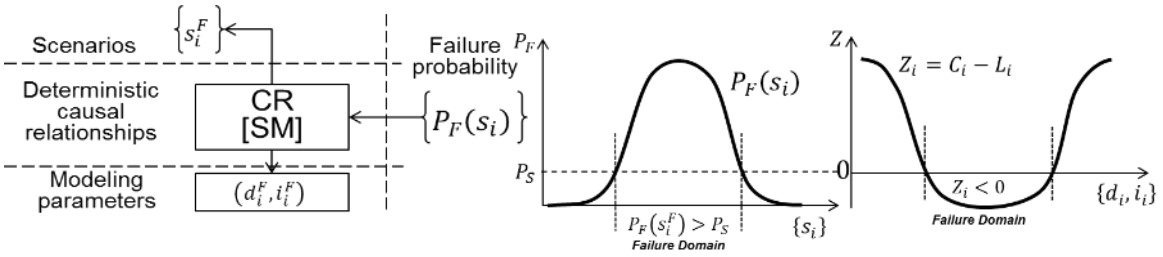

Figure 2.6. Failure probability in a single stage framework.

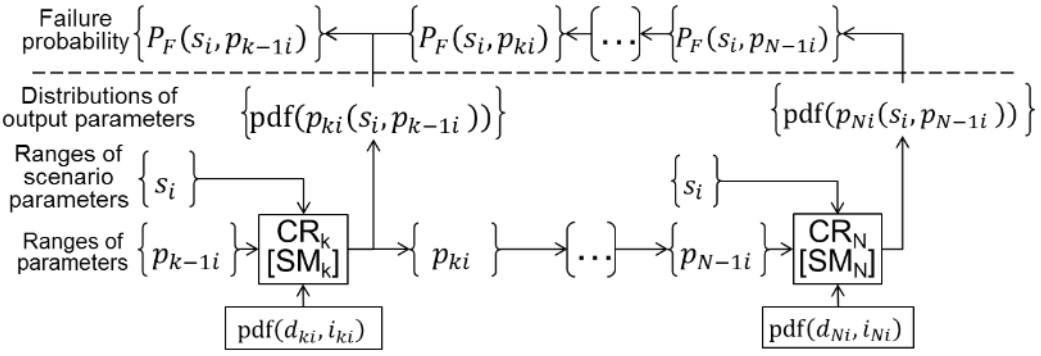

Figure 2.7. Failure probability in a multistage framework.

Failure domain can also be used when CR is presented as a set of models connected through initial conditions. "Reverse" analysis starts from the last stage where information about failure possibility is available and is propagated "upstream" through the previous stages. In this case, the output p_{ki} of any intermediate stage CR_k depends on the input parameters from the previous stage p_{k-1i}, in addition to scenario and modeling parameters, as shown in Figure 2.7. Therefore, characteristics of the failure domain at each stage (k) also include p_{ki} and p_{k-1i}. For instance, failure probability as a function of the output from the previous $(k-1)$ stage $P_F(s_i, p_{k-1i})$ can be calculated

according to (2.9), (2.10) if $P_F(s_i, p_{ki})$ and distribution $\text{pdf}\big(p_{ki}(s_i, p_{k-1i})\big)$ at the current stage (k) are provided.

$$P_F(s_i, p_{N-1i}) = \iint_{Z_i \le 0} \text{pdf}_{Z_i}\big(p_{Ni}(s_i, p_{N-1i})\big) dp_{Ni} \tag{2.9}$$

$$P_F(s_i, p_{k-1i}) = \int_{-\infty}^{\infty} P_F(s_i, p_{ki}) \text{pdf}\big(p_{ki}(s_i, p_{k-1i})\big)\, dp_{ki} \tag{2.10}$$

These formulas can be applied recursively as shown in Figure 2.8 from the very end to the very beginning. The goal of such recursive calculations is to obtain failure characteristics at all intermediate stages.

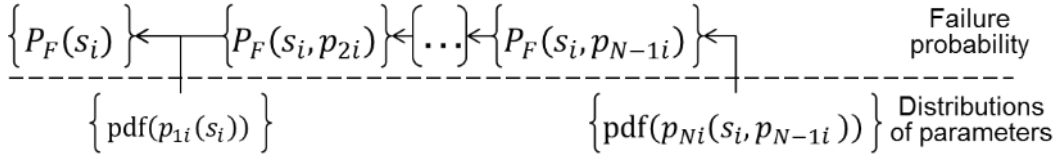

Figure 2.8. Recursive calculations of failure probability in a multistage framework.

At each stage, similarly to the single-stage case, we can determine failure domains in the space of scenarios and model input parameters $(s_i\ , p_{ki})$, and in the space of uncertain modeling parameters (d_{ki}, i_{ki}):

$$\{(s_i^F, p_{ki}^F) | \text{pdf}(d_{ki}, i_{ki})\}: P_F(s_i^F, p_{ki}^F) \ge P_S \tag{2.11}$$

$$\{(d_{ki}^F, i_{ki}^F) | (s_i\ , p_{ki})\}:\ Z_i(d_{ki}^F, i_{ki}^F) = C_i - L_i \le 0 \tag{2.12}$$

Note that $(s_i\ , p_{ki})$ in formula (2.12) is not a distribution but a point selected within the ranges of respective parameters. It is instructive to note that identification of failure domain (s_i^F, p_{ki}^F) can be done even if model CR_k doesn't exist yet. In fact, reverse analysis is an efficient tool for development of requirements (e.g., to resolve boundary of the failure domain (s_i^F, p_{ki}^F)) for the models and new experiments which should be designed and incorporated in the framework.

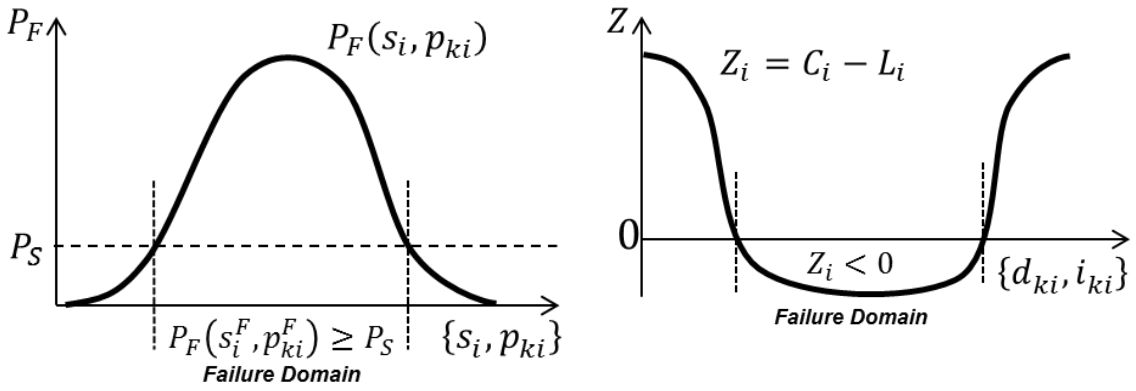

Figure 2.9. Failure domains in a multi-stage framework.

Failure domain boundary (index FB) can be determined in the space of scenario (s_i^{FB}, p_{ki}^{FB}) and modeling parameters $(d_{ki}^{FB}, i_{ki}^{FB})$ using provided formulas (2.11), (2.12) with equality sign. For computationally efficient identification of the failure domain boundaries application of some sort of optimization approach (e.g. such as genetic algorithm) is usually required. Grouping of different scenarios is necessary to present

information in a compact form, especially when different failure modes correspond to multiple failure domains.

In practice, the reverse analysis starts at the end of ROAAM multistage process with SEIM and DECOSIM frameworks. At this stage (Figure 2.10) we identify Failure domain (FD) in the space of model input parameters p_{N-1} as

$$\{(s_i^F, p_{ki}^F)|\text{pdf}(d_{ki}, i_{ki})\}: P_F(s_i^F, p_{ki}^F) \geq P_S \tag{2.13}$$

where P_S is screening frequency.

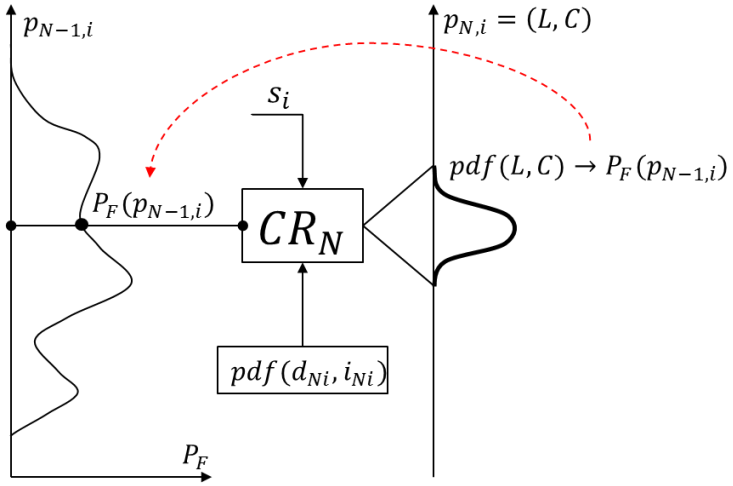

Figure 2.10. Initial stage of the failure domains analysis in a multi-stage ROAAM+ framework.

The Failure domain information is propagated back to identify failure domains at each step of the multistage process as a function of correspondent model input parameters p_k. Different approaches to propagating failure domain can be used (Figure 2.11), for instance:

"Conservative" considers maximum probability value for calculation:

$$P_{F_{MAX}}(s_i, p_{k-1,i}) = \max\left(P_{F_i}(s_i, p_{ki}: p_{ki} \in [p_{ki}(p_{k-1,i})])\right) \tag{2.14}$$

"Optimistic" considers minimum probability value for calculation:

$$P_{F_{MIN}}(s_i, p_{k-1,i}) = \min\left(P_{F_i}(s_i, p_{ki}: p_{ki} \in [p_{ki}(p_{k-1,i})])\right) \tag{2.15}$$

"Best Estimate":

$$P_F(s_i, p_{k-1i}) = \int_{-\infty}^{\infty} P_F(s_i, p_{ki})\text{pdf}(p_{ki}(s_i, p_{k-1i}))\, dp_{ki} \tag{2.16}$$

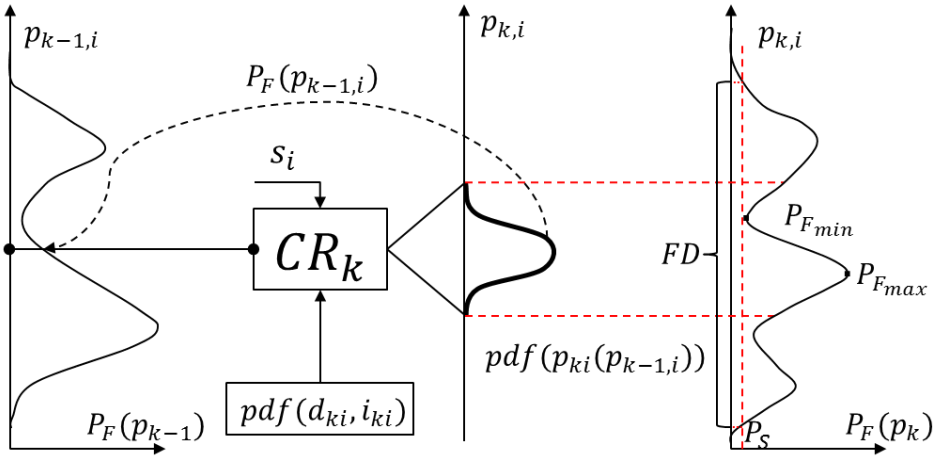

Figure 2.11. Backward propagation of the failure domain in a multi-stage ROAAM+ framework.

Analysis of the failure domain boundary can tell a lot about what is important for transition from "safe" to "failure" to occur. Sensitivity analysis of failure domain boundary is a powerful instrument for identification of the needs for refinement of the data and structure of the risk assessment framework. It points to the key phenomena and data affecting failure probability. Adequacy and consistency between: (i) scenarios, (ii) structure of the framework, (iii) individual physical models, (iv) ranges and distributions of the uncertain modeling parameters, and (v) available experimental data and other evidences, should be carefully evaluated to increase confidence in prediction of the failure domain boundary.

2.5.4 Treatment of the Intangible Uncertain Parameters in Forward and Reverse Analyses

While ranges of the intangible parameters can be always (conservatively) bounded, the knowledge about distributions within the ranges is usually missing. In classical ROAMM, uncertainty in the intangibles can only be qualitatively approached, but it can always be bounded [27]. Such bounding approach is, in fact, similar to the interval analysis [60]. If inherent safety margins are sufficiently large, then bounding approach to the intangibles does not affect conclusions from the risk analysis. For some systems, however, bounding approach to quantification of the influence of intangible parameters might be insufficient. If failure probability P_f is sensitive not only to the ranges but also to the distributions, then uncertainty in prediction of P_f with "conservative" or "optimistic" bounding assumptions might be too large and, therefore, not suitable for a robust decision making process.

In order to assess the importance of the missing information about the distributions we can consider distributions as uncertain parameters. A space of possible probability distributions of the intangible parameters can be introduced. Each randomly selected set of distributions for the intangible parameters will result in a single value of failure probability P_f. Sampling in the space of the distributions for model intangible parameters will result in calculation of different possible values of P_f, including the bounding ones. A cumulative distribution function of $cdf(P_f)$ can be used to characterize confidence in prediction of P_f.

Let's assume that risk acceptance criterion is $P_f < 0.01$. From the interval analysis (resulting P-box shown in Figure 2.12), we can only notice that P_f is between 0 and 1. Such information is not very helpful for making conclusions on the risk acceptance. If we consider cumulative distribution of the confidence in P_f, we can conclude that:

- For green curve: 95% of the cases the value of P_f is in the acceptable region.
  - It is possible to identify a subset of distributions of the model intangible parameters that result in P_f exceeding acceptability value. Once identified, those distributions can be a subject to further research and quantification.
- For red curve: 95% of the cases the value of P_f is in the unacceptable region.
  - This would mean that the system is not safe with most of the distributions belonging to the space of the possible distributions.

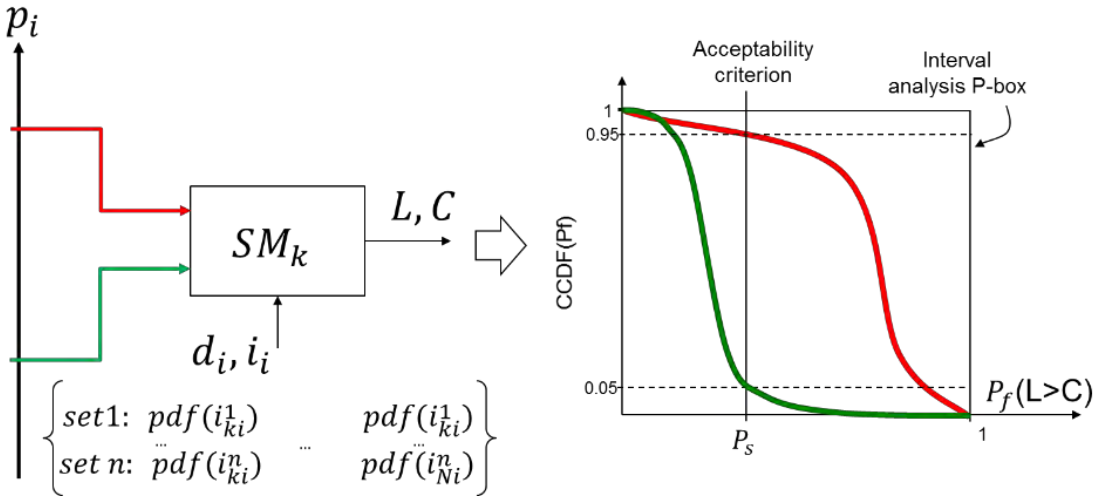

Figure 2.12. The influence of the distributions of intangible parameters on the failure probability.

Mathematical implementation:

Let us assume a model intangible parameter $i_{N,i}$, where we have no knowledge about its probability distribution, but we have knowledge about its range. To evaluate the effect of probability distribution for this parameter the sampling is made in space of possible distributions of this parameter. Each selected distribution out of randomly selected set of distributions will result in a single value of failure probability P_f calculated by

$$P_F(s_i, p_{k-1i}) = \int_{-\infty}^{\infty} P_F(s_i, p_{ki}) \mathrm{pdf}\left(p_{ki}(s_i, p_{k-1i})\right) dp_{ki} \tag{2.17}$$

then, confidence in prediction of P_f or $\overline{CDF}\left(P_F(s_i, p_{N-1,i})\right) = 1 - CDF\left(P_F(s_i, p_{N-1,i})\right)$ can be obtained as follows

$$CDF\left(P_F(s_i, p_{N-1,i})\right) = \int_{-\infty}^{\infty} \left[\int_0^{P_F} pdf\left(P_F(s_i, p_{Ni})\right) \, dP_F\right] pdf\left(p_{Ni}(s_i, p_{N-1i})\right) dp_{Ni} \tag{2.18}$$

where $\mathrm{pdf}\left(P_F(s_i, p_{Ni})\right)$ probability distribution function of P_f is obtained by sampling in space of possible distributions of $i_{N,i}$ and $pdf\left(p_{Ni}(s_i, p_{N-1i})\right)$ – probability distribution function of model output parameters p_{Ni} is obtained by sampling in space of model intangible parameters $i_{N,i}$.

Propagation of the failure domain in ROAAM+ framework reverse analysis:
If we consider multistage framework as in Figure 2.7, the sampling of probability distributions and the calculation of the values of P_F in reverse analysis will be done in similar way as described in chapter 2.5.3, for every selected set of distributions of model intangible parameters for every surrogate model.

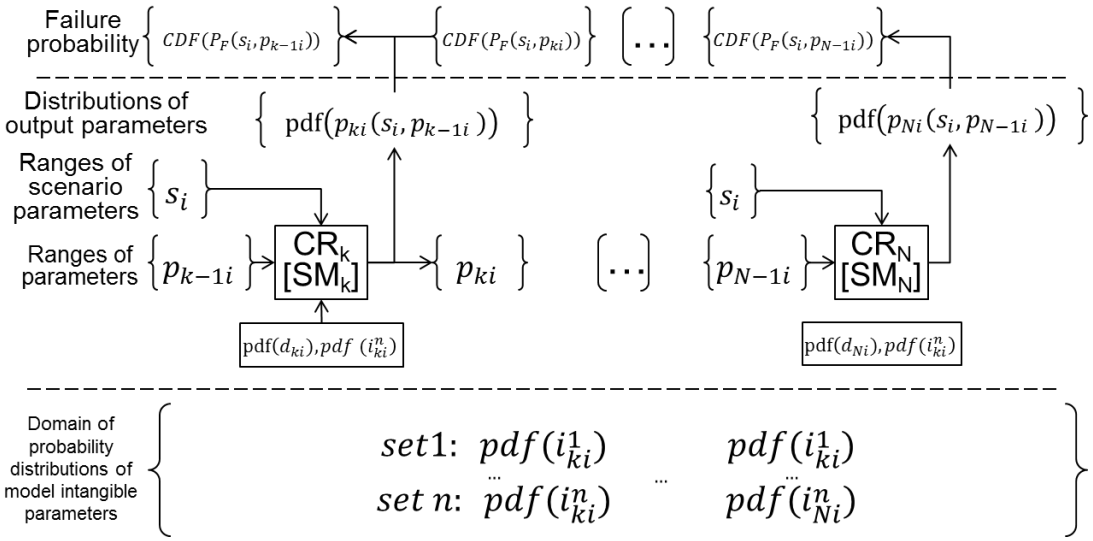

Figure 2.13. Failure probability in a multistage framework taking into account influence of intangible parameters distributions.

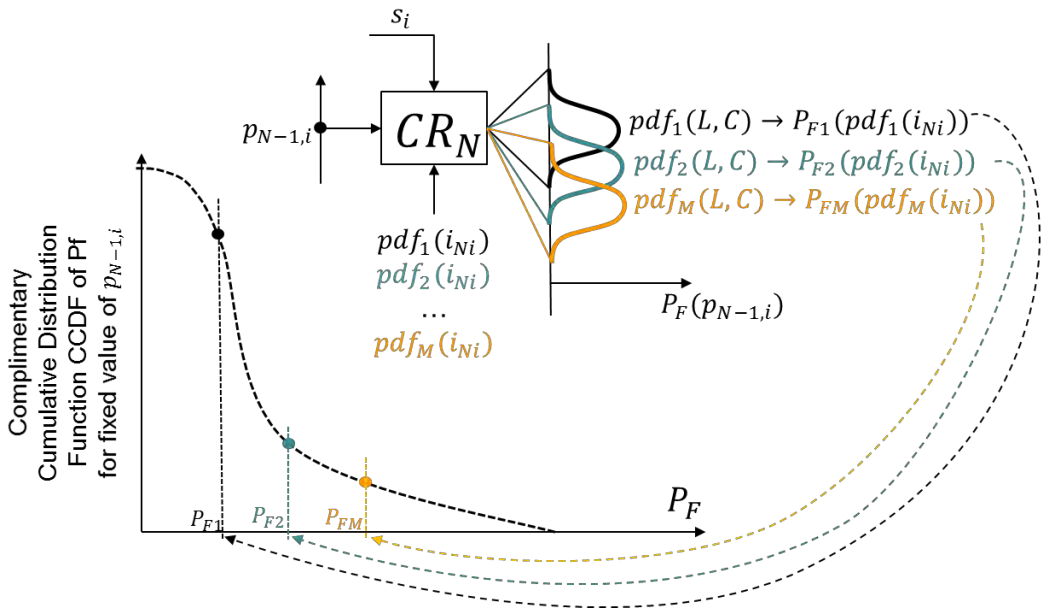

Figure 2.14. Treatment of model intangible parameters in ROAAM+ framework for Nordic BWR.

From the domain of possible distribution of model intangible parameters we select a set of probability distributions calculate the value of P_F for every combination of model input - p_{ki} and scenario parameters -s_i in multistage framework. Repeating this process for every possible set of distributions will yield probability distributions of P_F and $CDF\left(P_F(s_i, p_{k,i})\right)$ in each stage of the framework reverse analysis for every possible combination of model input - p_{ki} and scenario parameters -s_i.

Chapter 3. Development and Implementation of the Framework and Models

3.1 Approach to Development and Refinement of the ROAAM+ Framework, Models and Data for Nordic BWRs

The top layer of the ROAAM+ framework for Nordic BWR (Figure 3.1) decomposes severe accident progression (Figure 2.1) into a set of causal relationships (CR) represented by respective surrogate models (SM) connected through initial conditions. While decomposed, the framework SMs still can be used for an end-to-end transient analysis if necessary.

Computational efficiency of the top layer of the framework allows for extensive sensitivity and uncertainty analysis in the forward and reverse analyses. Forward analysis defines conditional containment failure probability for each scenario $\{s_i\}$. Reverse analysis identifies failure domains in the space of scenarios $\{s_i\}$, and "deterministic" $\{d_i\}$ and "intangible" $\{i_i\}$ parameters specific to each model. Grouping and classification of failure scenarios corresponding to specific initial plant damage states helps to identify plant vulnerabilities and provides insights into possible efficient mitigation actions by operator. Failure domain in the space of deterministic and intangible modeling parameters $\{d_{ki}, i_{ki}\}$ identifies the need for improvement of knowledge, modeling and data.

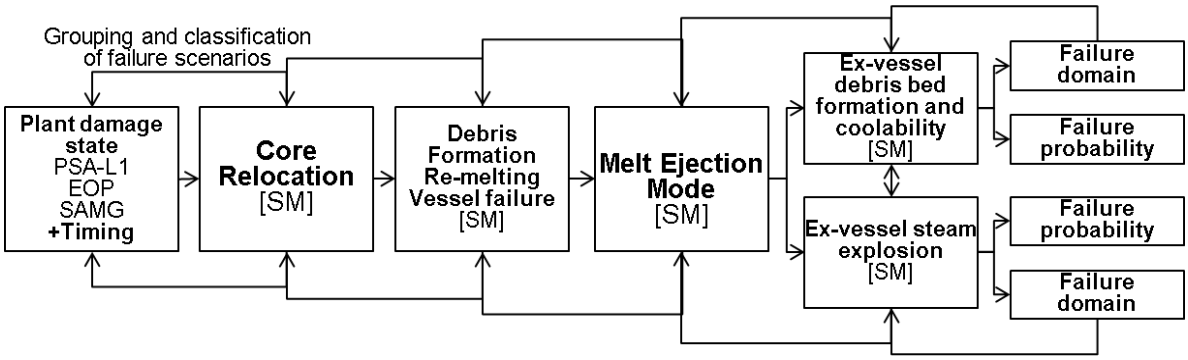

Figure 3.1. ROAAM+ framework for Nordic BWR.

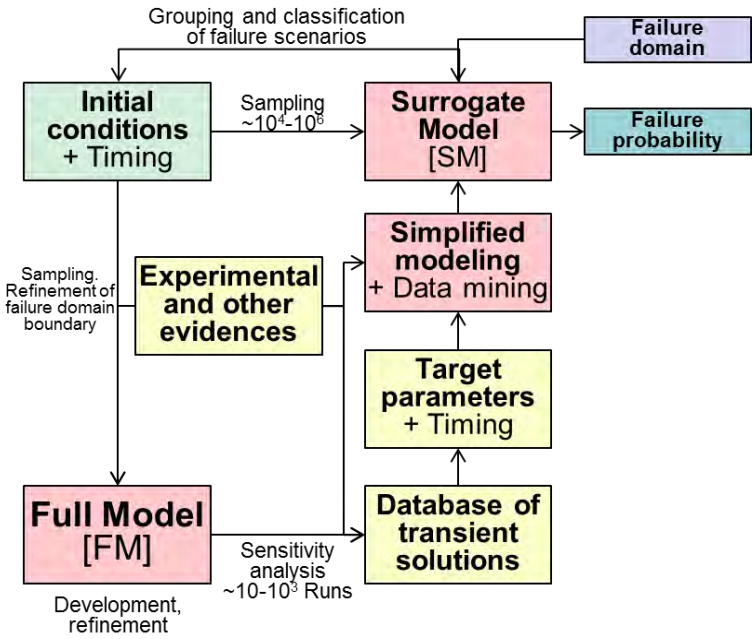

Figure 3.2. Full and Surrogate model development, integration with evidences, refinement, prediction of failure probability and failure domain identification.

The process of development and validation of the individual surrogate models is most important for completeness, consistency, and transparency of the results. General ideas of the process are illustrated in Figure 3.2. Initial conditions come from the SM analysis at the previous stages of the framework. Experimental and other evidences provide a knowledge base for validation of the FMs and calibration of SMs. Full Model (FM) is implemented as detailed fine resolution (computationally expensive) simulation approach. Database of the FM transient solutions is developed in order to provide better understanding of basic physical processes and typical behavior of the target parameters. The target parameters are the input conditions for the next model in the framework. Simplified modeling approaches and data mining techniques are used in order to develop a surrogate model. Surrogate model (SM) is an approximation of the FM model prediction of the target parameters which employ simplified (coarse resolution) physical modeling, calibratable closures, or approximations to the response surface of FM.

3.2 Implementation of ROAAM+ framework architecture

In this section we focus on some implementation aspects of the ROAAM+ framework. The ROAAM+ framework architecture has two levels (Figure 3.1). The first (top) level is based on SMs, all procedures at this level are unified and standardized. The second (bottom) level employs data mining techniques to establish connections between full models, experimental data and evidences, databases of full model solutions and surrogate models (Figure 3.2).

3.2.1 Implementation of ROAAM+ top level framework.

Definition of the initial plant damage states and scenario space.

Initial plant damage states $\{D_j\}$ (determined by availability of safety systems) and their frequencies $\{f_j\}$ are determined based on PSA L1 data. The states are determined aiming at completeness of the analysis.

For each plant damage state, a full set of possible events (such as different recovery and mitigation actions) which can affect further accident progression is considered. The events, their order and timing create a space of scenarios $\{s_i\}$. Timing of events is an important factor. For instance, ECCS failed to start and ECCS failed after 2 hours after an initiating event will result in quite different initial conditions for the further analysis of the accident, e.g. decay heat, water pool level and temperature, etc. Possible ranges for timing of different events are considered based on EOPs and SAMGs.

It is instructive to note that there is a difference between (i) timing of random evens which is a part of scenario description (e.g. recovery of safety systems in MELCOR modeling) and is not predictable by the available deterministic models (aleatory), and (ii) timing of events predicted by the models (epistemic). We treat these two kinds of time differently. Aleatory timing is used in grouping of different scenarios according to their effect (failure domains). Epistemic timing is treated as any other dependent (i.e. obtained in the process of calculations) deterministic modeling parameters (p_{ki}).

The scenarios are used (i) to set specific initial conditions for deterministic analysis of the accident progression and for calculating respective failure probabilities in forward analysis; and (ii) to identify which conditions lead to high probability of containment failure in the reverse analysis. Grouping of scenarios is an iterative process which should aim at adequate resolution of the initial plant damage states which lead to similar consequences with respect to the containment failure.

Specification of the input data and establishing connections between frameworks.

Lists of input/output parameters are determined for each SM:

- Scenario specific data (e.g. water level and temperature in the lower drywell, possible mitigating actions and their timing, etc.).
- Initial conditions (p_{ki}), that connects SMs between each other through SM input/output.
- Deterministic and intangible parameters $\{d_{ki}, i_{ki}\}$ specific to each SM.

Ranges and respective multidimensional probability density functions are determined for all $\{d_{ki}, i_{ki}\}$.

Implementation of the forward and reverse analysis algorithms for the whole framework.

Each framework is implemented as a set of functions in MATLAB, with respective I/O structure for forward and reverse analysis. Implementation of the reverse analysis in ROAAM+ framework for Nordic BWR starts from SEIM and DECO frameworks failure domain analysis, then, information about the failure domain is propagated through their input parameters (output of MEM frameworks) in reverse mode towards the space of scenario parameters.

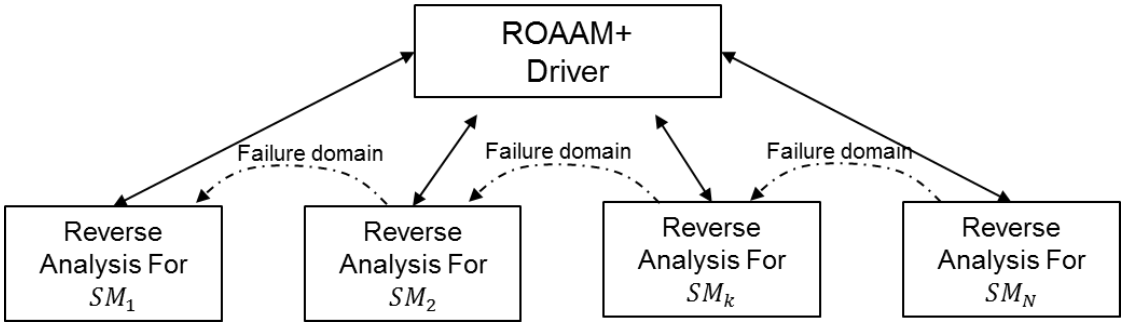

Figure 3.3. ROAAM+ framework reverse analysis implementation

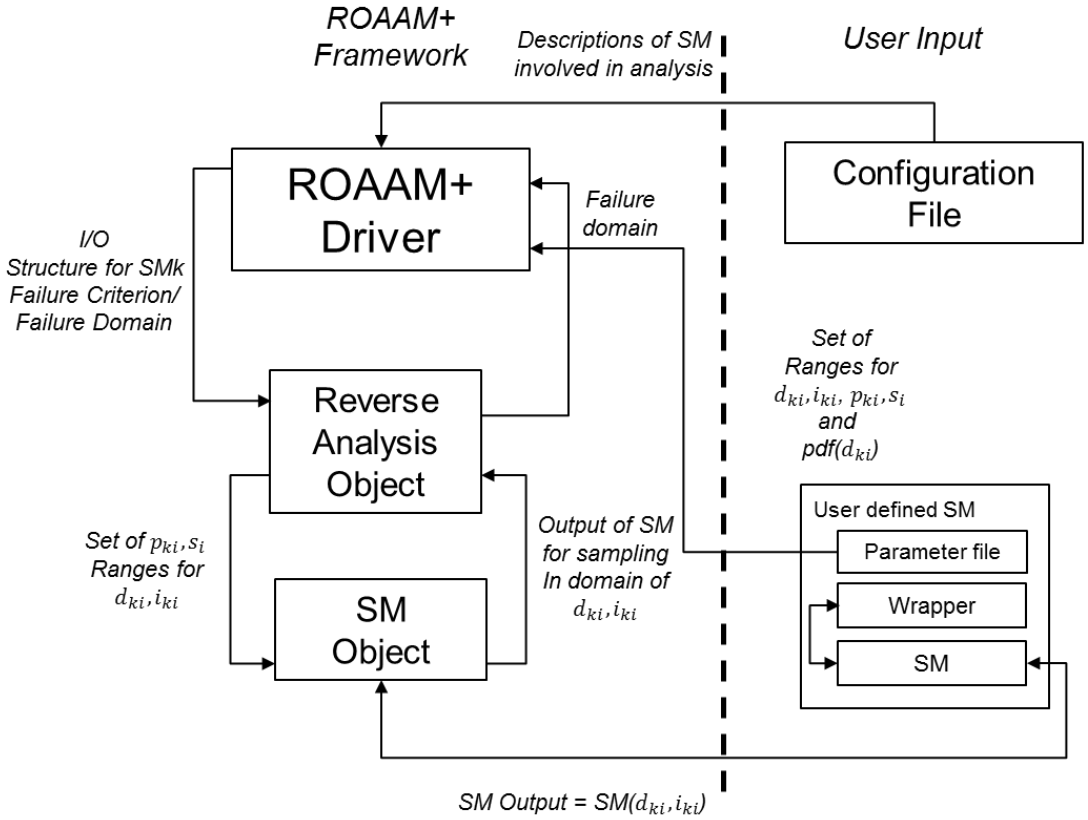

Figure 3.4. ROAAM+ framework reverse analysis implementation

Figure 3.4 represents data flow and connections between different blocks in ROAAM+ reverse analysis. The analysis and the connection between different models in ROAAM+ framework (see Figure 3.1) is driven by ROAAM+ Driver. The main

functions of ROAAM+ Driver is to:

- Establish connections between user defined SM (e.g. failure domain information from SEIM SM will be propagated back to MEM SM).
- Based on connections between SM, establish hierarchy of SM execution (including splinter scenario and different failure modes, for example 3 failure modes in MEM SM (IGT, CRGT, vessel wall) will create three parallel threads of analysis in consequent SMs (SEIM, DECO).
- Provide information about Input/Output structure, ranges and distributions (where applicable) for every surrogate model to Reverse Analysis Object.
- Perform partitioning with n – dimensional grid (binning) of scenario space (scenario space is unique for all surrogate models in the analysis).

Reverse analysis, characterization and propagation of the failure domain is performed by Reverse Analysis Object. Based on the I/O information, ranges of the parameters involved in the analysis Reverse Analysis Object performs:

- Partitioning (binning) of model input - p_{ki} with static/adaptive grid.
- Generation of the sampling set for the analysis in space of model input and scenario parameters.
- For every possible combination Reverse Analysis Object calls SM Object to generate sampling in model deterministic/intangible parameters and calculate SM response for fixed p_{ki} and s_i.
- Calculate probability of failure P_f – for every cell in domain of model input parameters (using equations (2.2), (2.3)).

Partitioning (binning) of the input space is performed with adaptive mesh grid [61], then, the influence of model deterministic and intangible parameters is evaluated using SM Object. The main functions of SM object are:

- Iterative generation of the sampling sets in domains of model deterministic and intangible parameters.
- Generate set of input vectors for SM execution
- Execution of the SM (through the SM wrapper, SM wrapper is a user defined intermediate link between ROAAM+ framework and SM)
- Preliminary analysis of the results for each iteration to establish output convergence.
- Reporting of the results to Reverse Analysis Object for calculation of P_f.

Implementation of sampling in ROAAM+ reverse analysis

The general approach for reverse analysis for failure domain identification in ROAAM+ framework includes:

- Generation of the data base of surrogate model solutions at each step of multistage process, using respective SM, connecting plant damage states to the potential threats for containment integrity.
- Probabilistic evaluation and failure domain analysis, which include
    - Sampling of probability distributions (PDFs)
    - Calculation of probability of failure for selected sets of PDFs.
    - Calculation of cumulative distribution function of probability of failure for selected sets of PDFs.

Generation of the data base of SM solutions involves sampling in domains of:

- Model input parameters $\{p_i\}$
    - Grid based sampling is used in order to get good coverage of the uncertainty space and good knowledge about failure domain location.

- Model deterministic and intangible parameters $\{d_i, i_i\}$
    - Quasi-random Halton sequence is used to generate sampling in multidimensional space of $\{d_i, i_i\}$ parameters.
    - The amount of samples in space of $\{d_i, i_i\}$ parameters depends on the convergence of the SM output between two consecutive generation of samples.

For each combination of parameters $\{p_i\}$ and $\{d_i, i_i\}$ ROAAM+ framework runs SM and stores output in the database of SM solutions for further probabilistic evaluation and failure domain analysis.
Sampling in the space of model input parameters $\{p_i\}$ is performed on the regular (static) grid (in the future Adaptive Mesh Refinement of the boundary of the failure domain will be implemented). Application of grid based sampling techniques, in general, is quite computationally expensive, thus, in order to make failure domain analysis in space of model input parameters feasible, it is necessary to perform model sensitivity analysis with respect to a) Individual models; b) Grouped models.

Model sensitivity analysis is performed for:

- Individual models
    - To identify the most influential parameters with respect to:
        - Model output.
        - Probability of failure (P(L>C)).
- Grouped models:
    - To identify the most influential parameters in the "down-stream" models with respect to
        - Grouped (connected) models output
        - Probability of failure (P(L>C))

Model sensitivity analysis allows to improve our understanding of the impact of each step in multi-stage analysis process on the final outcome and on the probability of failure (e.g. Jet diameter – is the most influential parameter for steam explosion, on the other hand Jet diameter is predicted by Melt-Ejection SM and defined by the properties of relocated debris in LP that depend on the accident scenario and recovery time of safety systems.
Sensitivity analysis of probability of failure currently require an approach that will include parameters that characterize distributions of model intangible parameters, together with model input parameters in the analysis.

Implementation of PDF sampling

In order to assess the importance of the missing information about the distributions we can consider distributions as uncertain parameters (see chapter 2.5.4). A space of possible probability distributions of the intangible parameters can be introduced. Each randomly selected set of distributions for the intangible parameters will result in a single value of failure probability P_f. Sampling in the space of the distributions for model intangible parameters will result in calculation of different possible values of P_f, including the bounding ones. A cumulative distribution function of $cdf(P_f)$ can be used to characterize confidence in prediction of P_f (see Figure 2.12).

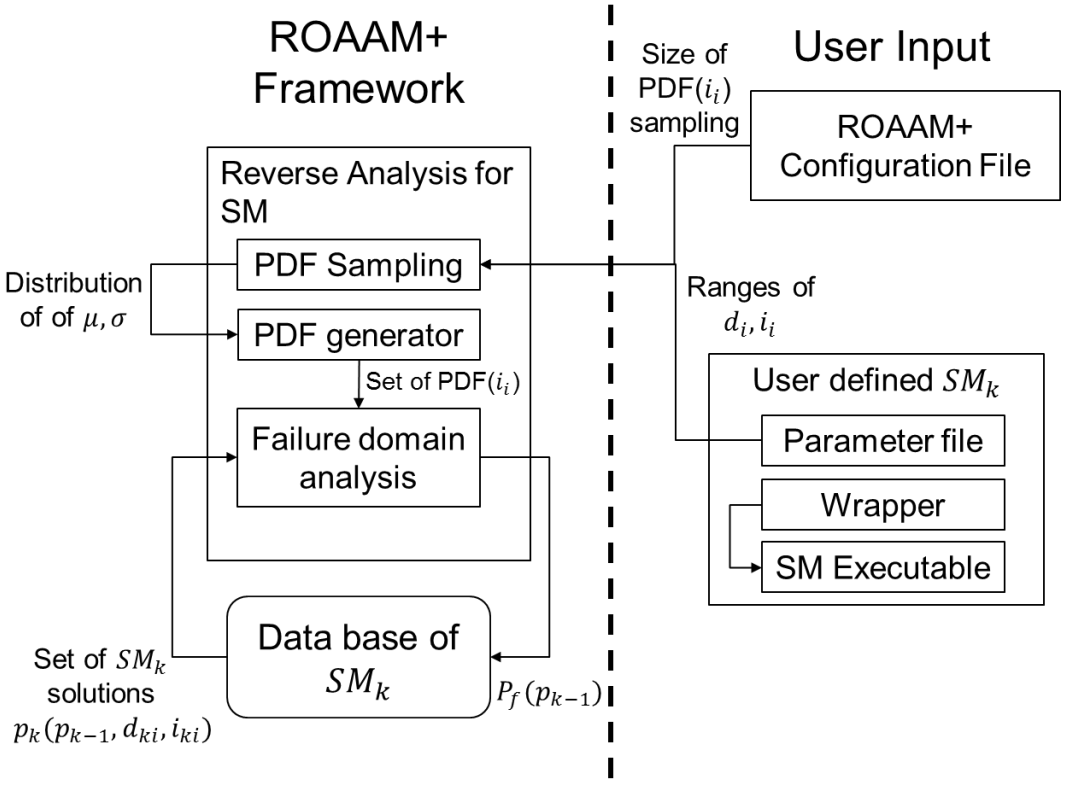

Figure 3.5. Implementation of PDF sampling of intangible parameters in ROAAM+ framework.

Figure 3.5 illustrates algorithmic implementation of PDF sampling of intangible parameters in ROAAM+ framework. The process of PDF sampling is implemented in following steps:

- Based on the user input in ROAAM+ configuration a set of parameters that characterize PDF for every intangible parameter in SM_k is generated (μ, σ – in current implementation we use different variations of normal distributions).
- Function "PDF generator" generates a set of discrete PDFs for every intangible parameter based on the set of μ, σ on the range between [0,1] (see Figure 3.6) and then scales each PDF to specific ranges correspondent to each intangible parameter.

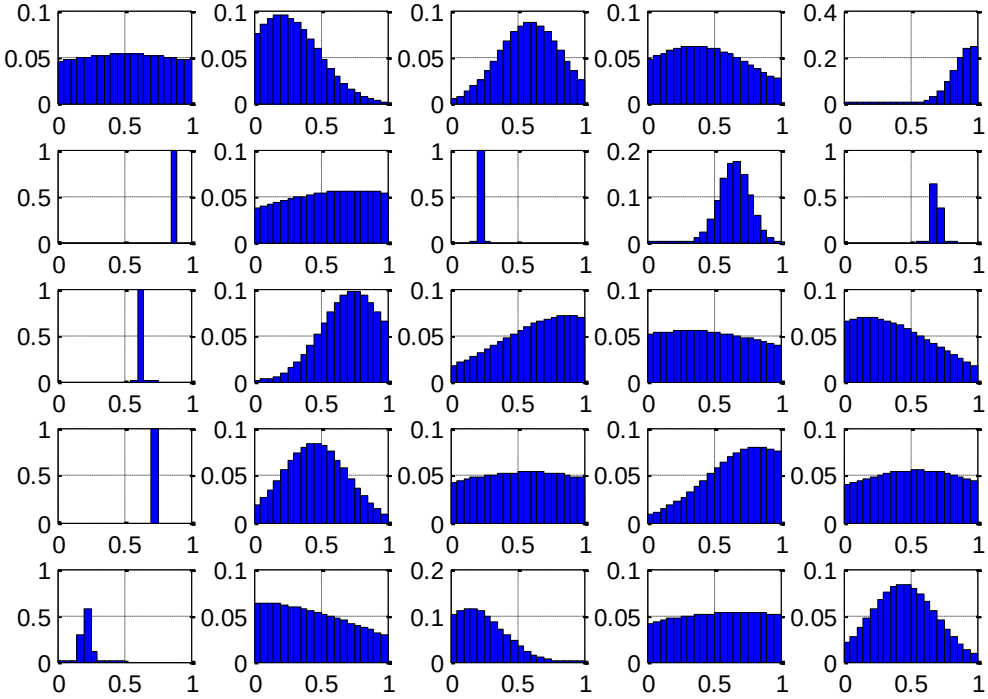

Figure 3.6. Example of randomly generated PDFs for model intangible parameters.

- The value of P_f is calculated for each combination of model input ($p_{k-1,i}$) and selected distribution of d_{ki}, i_{ki} ($pdf(d_{ki}, i_{ki})$.
- For every model input ($p_{k-1,i}$) - $CDF\left(P_F(s_i, p_{k-1,i})\right)$ is obtained using equation (2.18) and can be characterized by exceedance frequency of screening probability P_S.

Figure 3.7 illustrate an example of possible CDFs (or CCDFs) of P_f that can be obtained in ROAAM+ failure domain analysis. These resultant CDFs can be interpreted as follows:

- $CCDF(P_F)$ – where at most 5% of the cases exceed P_S are colored green – it means that with 95% confidence the probability of failure P_F will not exceed selected screening probability P_S. – which is considered as "failure is physically unreasonable".
- $CCDF(P_F)$ – where at least 95% of the cases exceed P_S are colored red – it means that with 95% confidence the probability of failure P_F will exceed selected screening probability P_S. – which is considered as "failure is imminent"
- $CCDF(P_F)$ – where P_F exceed P_S in 5-45% of the cases are colored blue, and – where P_F exceed P_S in 50-95% of the cases are colored purple. These are the cases where we can neither positively exclude failure nor conclude that the failure is imminent at given screening frequency P_S, due to the uncertainties coming from the model deterministic and intangible parameters and their distributions.

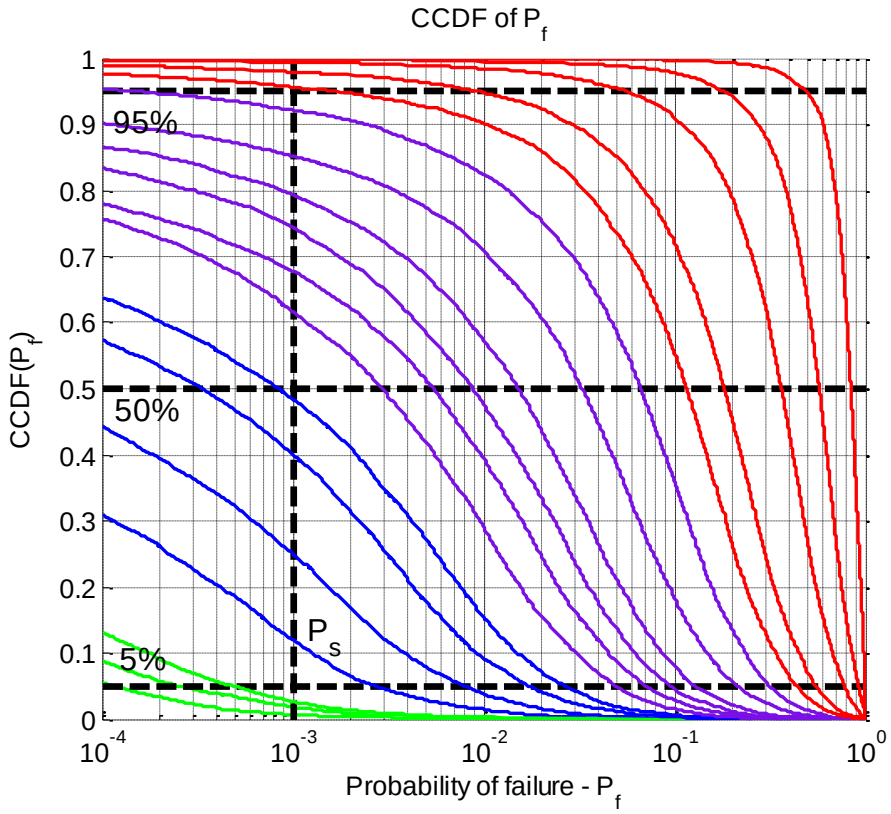

Figure 3.7. Complimentary cumulative distribution function of probability of failure $CCDF(P_f)$

Calculation of probability of failure - P_f

For each cell in space of model input and scenario parameters sampling in space of the model deterministic and intangible parameters d_{ki}, i_{ki} generates a set of points in the load/capacity domain (L,C). Then the values P_f in each cell are calculated using equations (2.2), (2.3).

Numerical implementation of equations (2.2), (2.3) is done by binning in space of Load and Capacity as in Figure 3.8. Then for every cell (i,j) in domain of (L,C) the value of $P_{f(i,j)}$ is obtained by

$$P_{f(i,j)} = \frac{1}{N}\sum_{i,j} p(L > C) \tag{3.1}$$

then the value for the whole domain (L,C) equals

$$P_f = \sum_{\forall i,j} P_{f(i,j)} \tag{3.2}$$

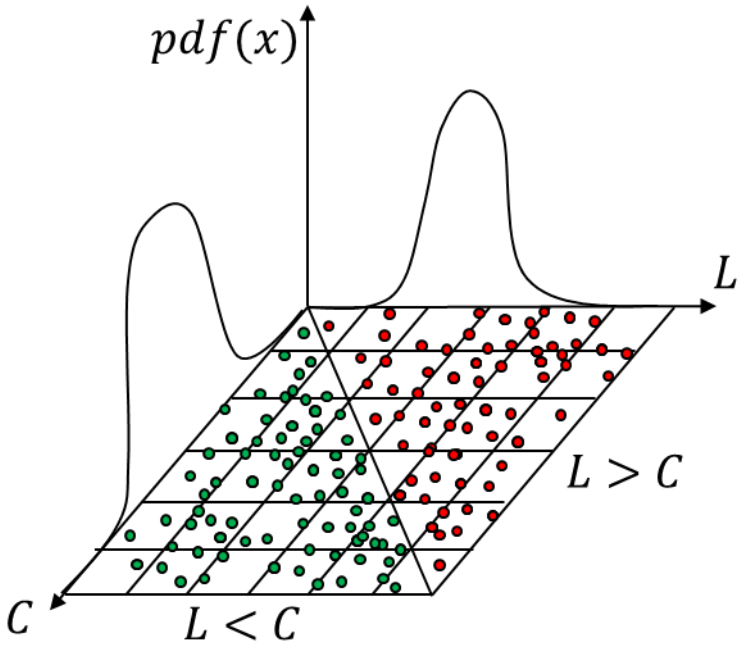

Figure 3.8. Output in Load/Capacity domain.

3.3 Core Relocation

Core relocation in BWR is a complex process. It starts when core melt accumulates on the lower core support plate and drips down to the vessel lower head. Large core relocation seems to occur when the melt accumulation leads to the failure of the lower core support plate and thus discharges large amount of melt resident in the bottom of the core into the lower head. Properties of relocated debris (mass, composition, configuration, etc.) determine the initial conditions for corium-structure interactions, vessel failure and melt release analyses.

Core relocation phenomenon in a reactor can be simulated using severe accident analysis computer codes such as MELCOR, MAAP. However, the calculations using these codes are relatively expensive, while scenario space needed to be sampled is extremely large when taking into account time to event trees in classic probability safety analysis (plant damage states and scenarios of severe accident management). The Core Relocation Surrogate Model (SM) can be constructed based on quite representative database of simulations (e.g. using MELCOR). The SM will provide a much more economical tool to approximately calculate the phenomenon with relatively good accuracy.

3.3.1 Core Relocation Surrogate Model

The work is motivated by the high sensitivity of the vessel failure phenomena to the characteristics of the debris in the lower plenum [65],[66]. The ultimate goal of this work is to develop Core Relocation full and surrogate models that can be used in the ROAAM+ framework [25]for prediction of the effect of core degradation and relocation processes on the debris bed properties in the lower head. General approach to the development of the Core relocation SM is illustrated in Figure 3.9.

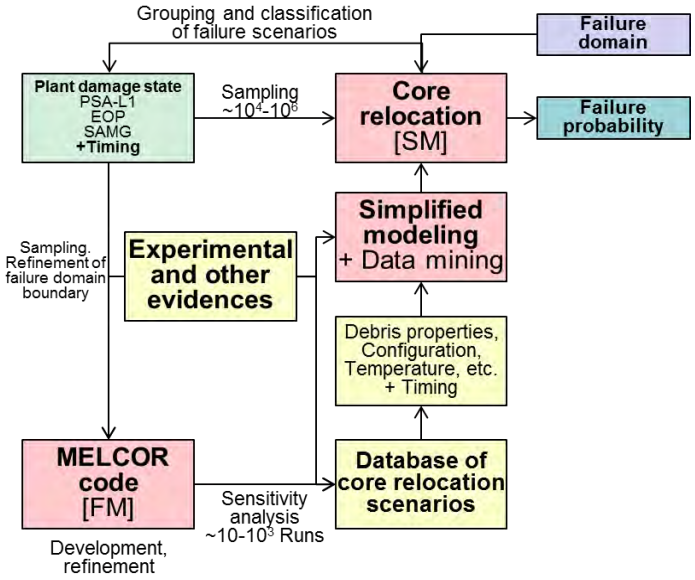

Figure 3.9. Core relocation surrogate model.

3.3.2 Definition of the plant damage states based on PSA-L1 data

This task includes (i) grouping of initial plant damage states based on PSA-L1, EOP and SAMG; (ii) selection of representative plant damage states (based on contribution to total core damage frequency) and scenarios for MELCOR (FM) analysis. It is important to identify (a) possible accident progression scenarios; (b) safety systems that can affect in-vessel/ex-vessel accident progression (e.g. ECCS, RHR, etc.); and (c) conditions for activation of these safety systems (e.g. lower drywell flooding condition – together with ECCS, RHR and depressurization history will identify water pool temperature in the cavity). In PSA L1 for Nordic BWR reference plant design the core damage states are grouped into 4 categories: HS1 (ATWS), HS2 (core damage due to inadequate core cooling), HS3 (core damage due to inadequate residual heat removal) and HS4 (rapid overpressure of the primary system). The categories (HS1, HS2, HS4) correspond to early core damage scenarios, HS3 corresponds to late core damage. In addressing ex-vessel behavior and consequences the following physical phenomena can challenge containment integrity: direct containment heating (DCH), ex-vessel steam explosions (EVE) and basemat penetration (BMP) by non-coolable corium debris. DCH scenario corresponds to high pressure (HP) accident scenario, steam explosion in the containment (EVE) corresponds to low pressure (LP) scenario. Both HP and LP will lead to formation of ex-vessel debris bed and potential corium interaction with containment basemat. The core damage sequences can be grouped together based on the aforementioned challenges to the containment integrity as shown in Figure 3.10. Corresponding frequencies are obtained from PSA L1 data.

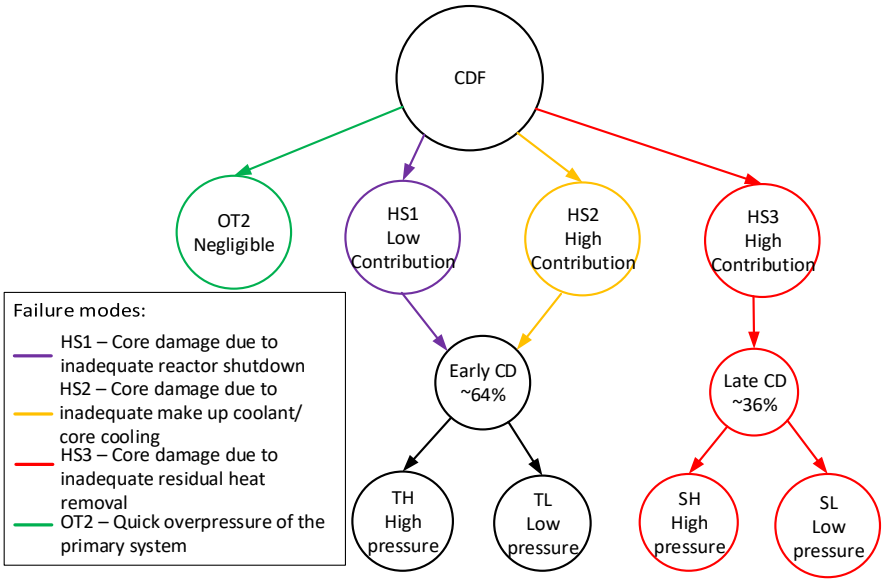

Figure 3.10. Core damage states classification.

Definition of the scenario space with possible recovery and operator actions

In this work we consider station blackout (SBO) scenario with a delayed power recovery. We consider a simultaneous loss of the offsite power (LOOP) and backup diesel generators. This results in the simultaneous loss of all water injection systems, including crud purge flow through the control rod drive tubes. This kind of accident is one of the most challenging accidents scenarios for BWR's as illustrated at Fukushima-Daiichi accident [68] and is among the major contributors to the core damage frequency (CDF) for Nordic BWR according to PSA Level 1 analysis. We consider that the power (external grid or diesel generators) can be recovered after some time delay and emergency core cooling system (ECCS) system can be restarted. According to the considered scenario, the operator can delay activation of the depressurization system to keep coolant in the vessel. Yet, for injection of water with low pressure ECCS, depressurization has to be activated.

The timing of the safety systems recovery is as part of the accident scenario space. For instance, we consider a delay in activation of Reactor Pressure Vessel (RPV) depressurization systems which includes battery-powered ADS-Valves (System 314) and Water-Valves (System VX105, FL314 & FL330). Overpressure protection system (FL314) is spring-operated will open stepwise, starting at slightly above 70 bar and opening completely at 75 bar to protect the RPV from failure. The auxiliary Feedwater System (System 327, FL327) is considered non-functional. Other system like the Control Rod Guide Tube (CRGT) Cooling or the Residual Heat Removal (RHR) Systems are also considered non-functional. The capacity and timing of activation of the Emergency Core Cooling System (ECCS System 323, FL323) is another element of the scenario. Necessary condition for activation of the ECCS is low pressure in the RPV. Mass flow begins at pressure difference of 12.5 bars between down comer (DC) and wet well (WW) and will reach its maximum value at 2 bars above the wetwell pressure.

3.3.3 **Nordic BWR Reference Plant Design**

MELCOR input model for Nordic BWR was originally developed for accidents analysis in the power uprated plants [56]. Current MELCOR input deck has total thermal power

output of 3900 MW. The core consists of 700 fuel assemblies of SVEA-96 Optima2 type – which is divided into five non-uniform radial rings and eight axial levels. The primary coolant system is represented by 27 control volumes (CV), connected with 45 flow paths (FL) and 73 heat structures (HS). The vessel is represented by a 6-ring, 14/19 (for MELCOR 1.86 and 2.1/2.2 correspondingly)-axial level control volume geometry.

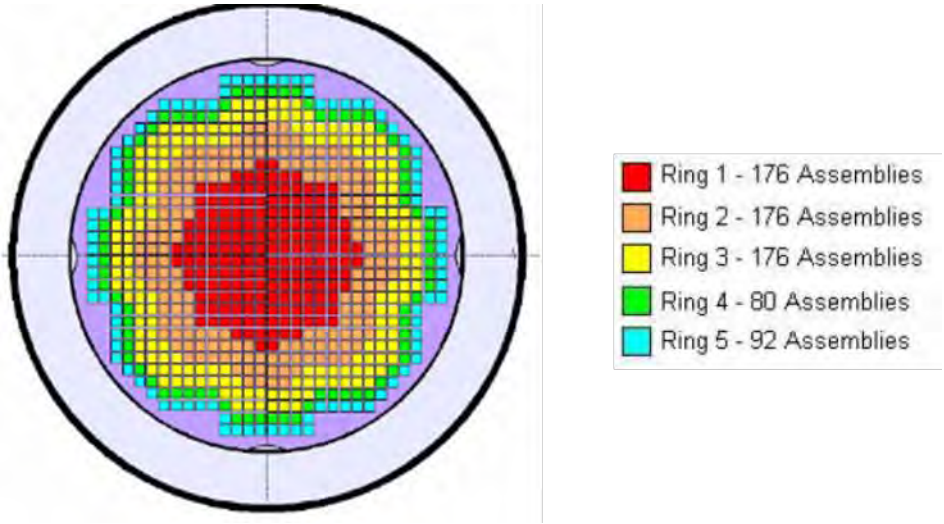

Figure 3.11. Nordic BWR MELCOR Model Core Radial Nodalization (MELCOR 1.86/2.1/2.2)

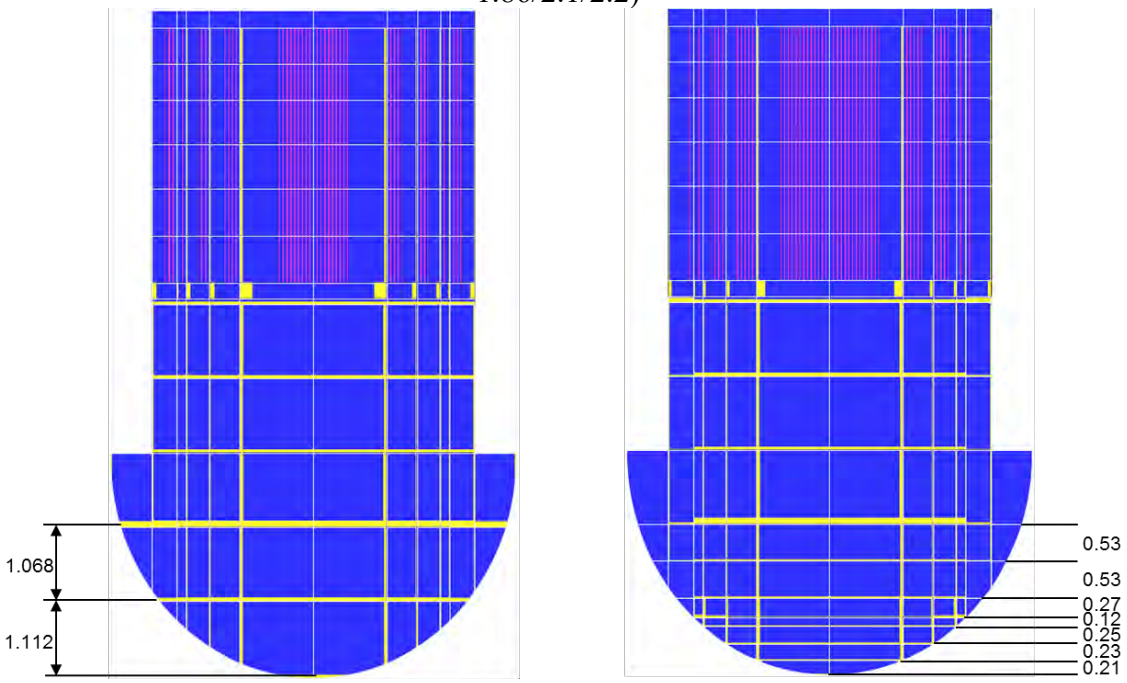

Figure 3.12. Nordic BWR MELCOR Model Core Axial Nodalization (MELCOR 1.86 (LHS) and 2.1/2.2 (RHS))

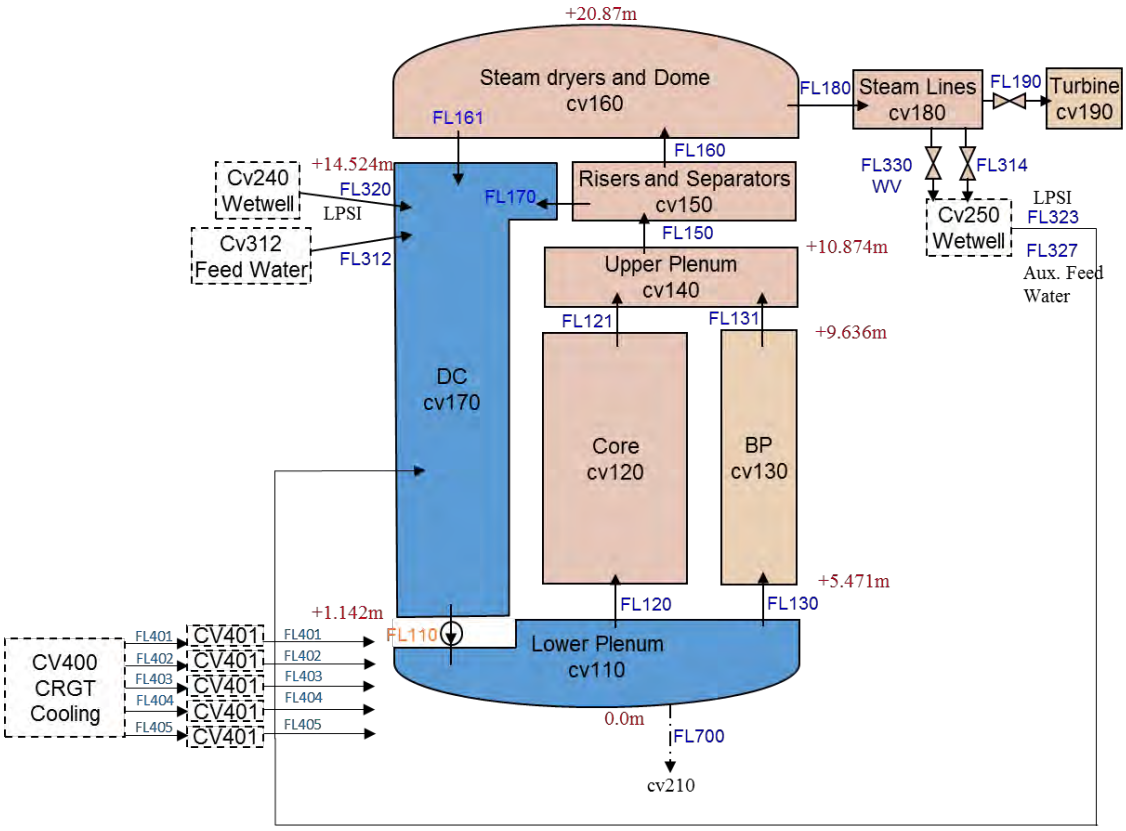

Figure 3.13. Nordic BWR MELCOR Model Vessel Nodalization

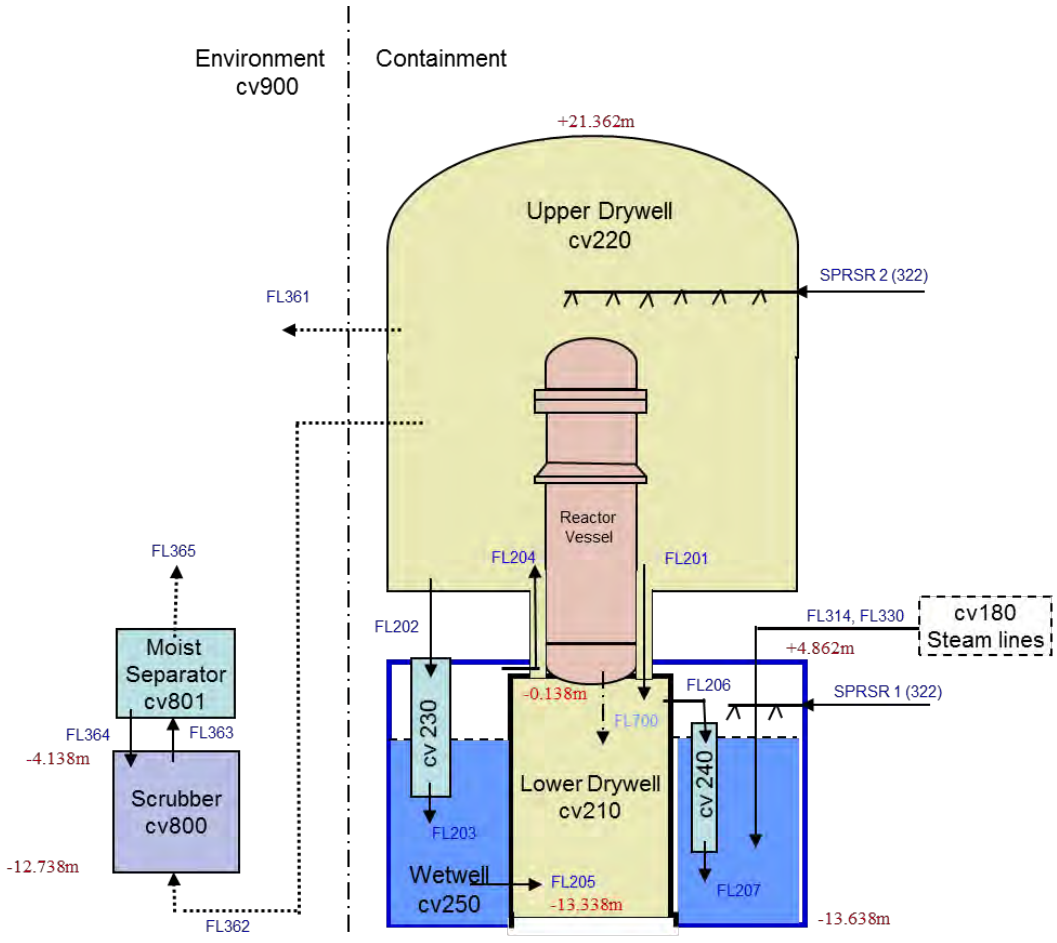

Figure 3.14. Nordic BWR MELCOR Model Containment Nodalization

Description of safety systems used in Analysis:

- System 354: Scram, the hydraulic actuating power shut-off system gives fully insertion of all control rods within a few seconds after initiation. The effect of this system is modeled in MELCOR by fission power decrease (during 3.5 s) according to a tabular function and scram conditions. In this case loss of power, is applied as a control function.
- System 314: Pressure control and relieve system (ADS) has several functionalities and is able to operate with only battery backups:
    - 314 TA Function: The spring-operated part of the overpressure protection system will open valves stepwise, starting at slightly above 70 bar and opening completely at 75 bar, to release steam and protect the Reactor Pressure Vessel (RPV) from a catastrophic failure.
    - 314 TB Function: Activation of 314TB initiates steam discharge into the wet well (WW) on low water level signal L6 (1 m below the core top). The pressure is reduced by ADS to a level sufficient for activation of the low pressure emergency core cooling system (ECCS). At the same time the coolant is lost from the primary system quite rapidly, which leads to core uncover. It is assumed that the actuation of the system can be delayed by the operator.
- System 323: The low pressure coolant injection (LPCI) system is the part of the ECCS, which provides water injection into the downcomer. In station blackout conditions it is not available. The system is activated on L3 level signal (+2m). However, the water injection starts when pressure difference between wet well (WW) and down comer (DC) is below 12.5bar. Maximum injection capacity of ECCS is reached at 2 bar difference between WW and DC and equals to 4 trains x 366 kg/s = 1464 kg/s.
    - It is assumed that the system can activated if power source is recovered after some time delay. Simultaneous recovery of all 4 trains is assumed in this paper. The results for mass flow of 25,50,75% of the designed capacity that corresponds to 1,2,3 injection trains is a subject of the future work.
- System 358: Flooding of LDW from the WW is initiated to provide the water pool for melt fragmentation and debris cooling in case of melt release from the vessel.
- System 361: Non-filtered containment venting system (CVS) is the pressure relief directly to the ambient atmosphere. It is activated when the internal containment pressure reaches to a setpoint that is below containment failure pressure.
- System 362: Filtered containment venting with multi venturi scrubbing system (CVS MVVS) provides pressure relief and scrubbing the radioactive aerosols.

The sampling MELCOR code execution and data extraction processes are driven by a simulation driver, implemented in MATLAB (see Figure 3.15), which performs: i). Sampling generation. (uniform sampling, DAKOTA interface to generate sampling for sensitivity and uncertainty analysis [62]); ii) MELCOR Input file generation; iii)

Execution of the MELCOR code on distributed computing network, which allows performing up to 60 simultaneous threads of calculations. iv). Adaptive refinement of the maximum time step and restarting in case of crashed calculations. v). Extraction of the data to the database of solutions and post-processing of the results.

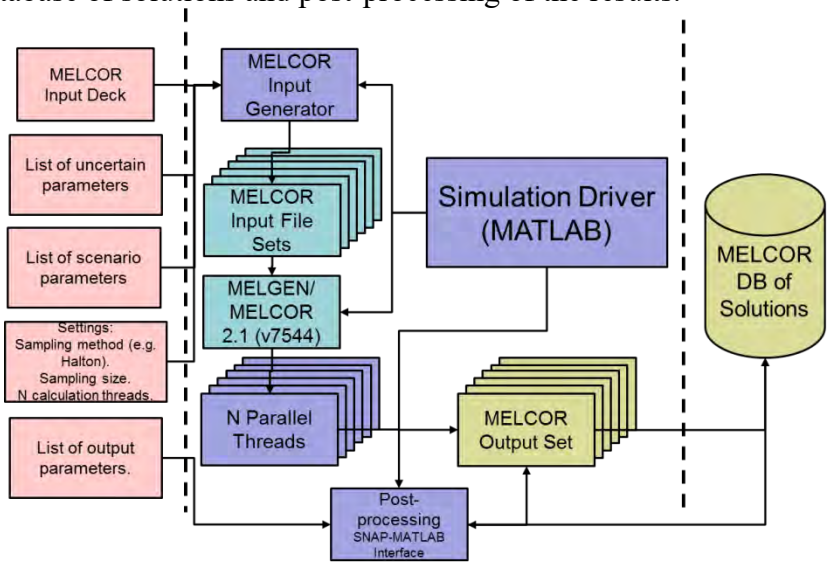

Figure 3.15. Simulation Driver Information Flow

3.3.4 Core Relocation Analysis Results Using MELCOR code

The Effect of Severe Accident Scenario on the Properties of Relocated Debris in LP

The analysis of the effect of severe accident scenario and possible recovery actions using different MELCOR code versions has been performed [64],[69]. A data base of full model solutions has been generated using MELCOR code versions 1.86, 2.2 and 2.2. Summary of the results are presented in Figure 3.16 and 3.17 in form of CCDFs of the most important parameters.

Post-processing of the results has been performed using pattern analysis approach [64]. The results showed that i) the whole scenario domain can be represented by a limited amount of relocation patterns; ii) the most common relocation pattern is a very rapid relocation to LP; iii) the major part of core materials is relocated to LP shortly after initial core support plate failure (within ~30-60mins); iv) delay in activation of ADS can significantly delay massive core relocation to LP, however it results in greater extent of core oxidation; ECCS is effective in preventing massive core relocation only within relatively small time window after activation of ADS; iiv) debris composition (i.e. metallic/oxidic debris fraction) in different layers are highly influenced by severe accident scenario and can be largely classified in limited amount of groups (see Figure 3.18) (Group A – significant metallic fraction – corresponds to early ADS activation, Group B – Significant oxide fraction – corresponds to late ADS activation, Group C – corresponds to the group of scenarios with relocated debris mass within the range of 100 tons.) The oxide fraction of relocated debris in LP in both groups A and B is highly correlated with the hydrogen generated during the course of accident (see Figure 3.18).

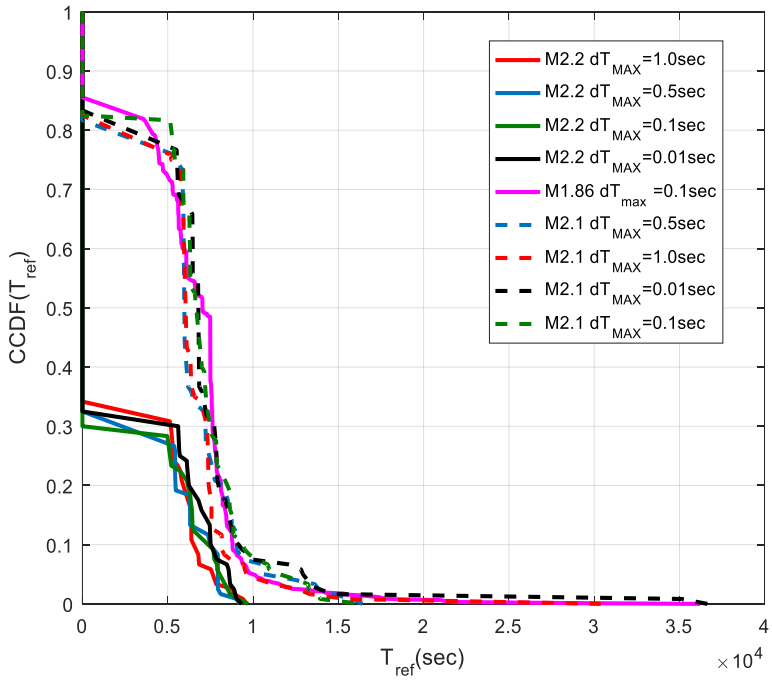

Figure 3.16. Complimentary Cumulative Distribution Function of Tref – Time of the onset of massive core relocation to LP (Time of core support plate failure)

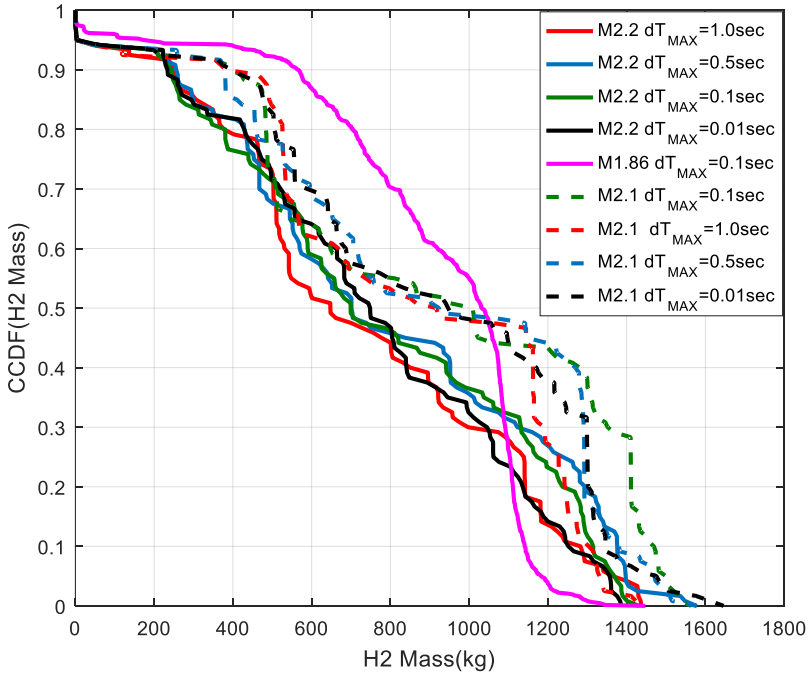

Figure 3.17. Complimentary Cumulative Distribution Function of Hydrogen Mass Generated During the Accident.

From the point of view of vessel failure analysis in ROAAM+ framework, the whole scenario domain can be split into 4 groups:

- Small relocation domain, characterized by small, mostly metallic debris mass (<20 tons).
- Transition domain, characterized by significant range of total debris mass (can range from ~10 to ~200 tons, due to modelling options in MELCOR (e.g. oxidized fuel rod collapse temperature).
- Large relocation domain with small debris oxidation, characteriazed by large debris mass (over 100 tons) and relatively high metallic debris fraction – which is typical for scenarios with early ADS activation.
- Large relocation domain with significant debris oxidation, characterized by large debris mass

(over 100 tons) and relatively small metallic debris fraction – which is typical for scenarios with late ADS activation.

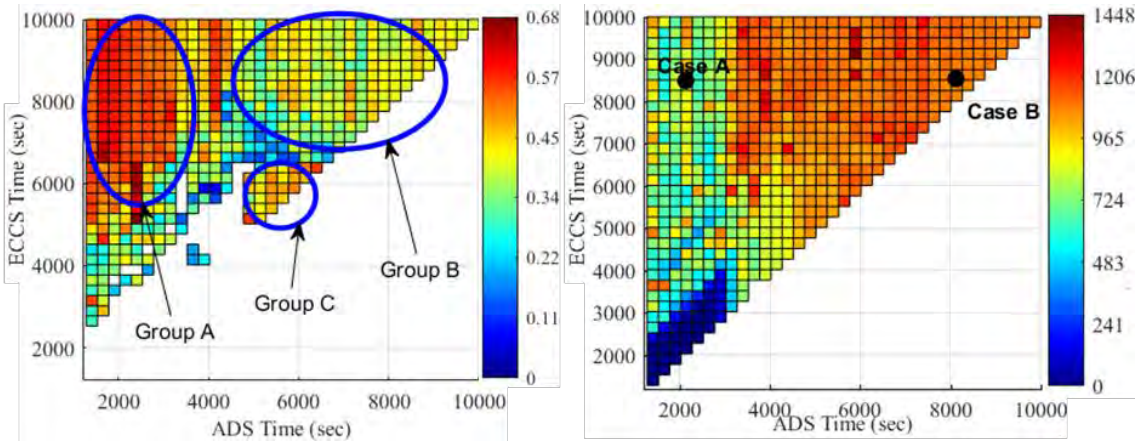

Figure 3.18. Map of metallic debris fraction in the 1st axial level (Left); Hydrogen mass in containment as a function of severe accident scenario (Right)[64].

Moreover, we found that there are some discrepancies in predictions of different code versions [69]. For example, there is major discrepancy in prediction of the total debris mass, time of core support plate failure between MELCOR code versions 1.86/2.1 and 2.2. MELCOR 2.2 predicts that in scenarios with late depressurization (in the range of ~4000-7000 sec.) and reflooding – it is possible to stop accident progression in core region, and prevent massive core relocation to LP. One of the possible explanations for this discrepancy is the change in the process of early core degradation between MELCOR code versions 1.86/2.1 compared to 2.2. In particular, it is assumed in MELCOR 1.86/2.1(rev prior to 7864) that when canister fails and forms PD in a cell and it melts and tries to candle to the cell below where PD may not exist, it will candle onto fuel rods, which freezes metallic Zr onto fuel rods which then oxidizes, failing fuel rods sooner than would be expected. In MELCOR 2.2 (in rev after 7864), it is assumed that it is more physical to candle onto CN (or CB) below, if it exists. Doing this would reduce cliff-edge rod failure when a canister fails and leads to reduced numerical variance in solutions [71][72]. Figure 3.19 shows the difference in the mass of Zr conglomerate on fuel cladding (CL) and canister (CN+CB) as predicted by MELCOR 2.1 rev7544 and MELCOR 2.2 rev9541. Further analysis is necessary to evaluate the effect of these changes between different MELCOR code versions. It is also necessary to evaluate how current Nordic BWR MELCOR model implementation is affected by these changes and introduce necessary modifications to make model and its predictions more realistic (e.g. masses distribution between different components in MELCOR, namely canister (CN), cladding (CL), supporting structures (SS), non-supporting structures (NS)).

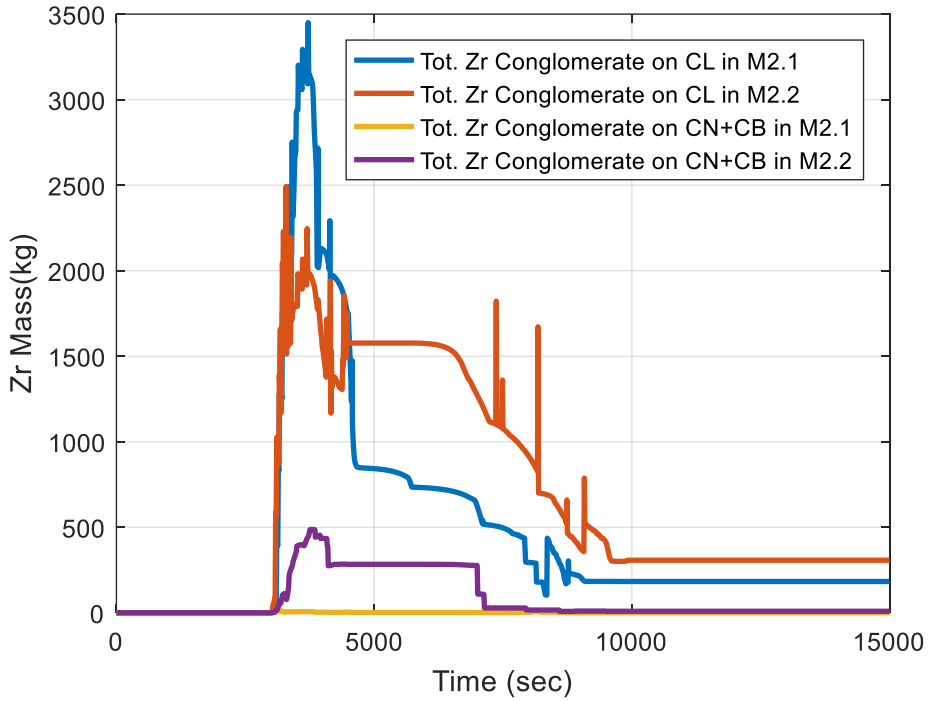

Figure 3.19. Total mass of Zr conglomerate on cladding (CL) and canister (CN+CB) in MELCOR 2.1 (rev7544) and MELCOR 2.2 (rev9541).

We also found differences in prediction of axial debris distribution between code versions 1.86 and 2.1/2.2, which can be due to different values of default and best practices sensitivity coefficients used in the analysis. However, sensitivity study is necessary to confirm this hypothesis.

Nordic BWR Severe Accident Progression and LP Debris Properties Uncertainty Analysis

Sensitivity analysis using Morris method [73] has been performed for a couple of representative cases that represent typical behavior for scenarios with early and late depressurization and late water injection [64][70]. Morris method is a method for global sensitivity analysis. The guiding philosophy of the Morris method [73] is to determine which factors may be considered to have effect, on model outputs, which can be considered as either negligible, linear or non-linear with other factors. The experimental plan proposed by Morris is composed of individually randomized "one-factor-at-a-time" experiments; the impact of changing one factor at a time is evaluated in turn [74] (see references [73],[74] for more details).

Full model sensitivity analysis has been performed for a couple of representative scenarios for large relocation domain with a) small metallic debris fraction (Case B (ADS Time – 8000sec, ECCS Time – 8500sec) – 246 cases have been simulated) b) high metallic debris fraction (Case A (ADS Time – 2500sec, ECCS Time - 8500 sec) – 246 cases have been simulated) (see Figure 3.20, 3.21, 3.22, 3.23 – Pearson and Spearman correlation coefficients, scaled Morris μ - $\bar{\mu}$ and Morris σ - $\bar{\sigma}_i = {}^{\sigma_i}/_{\mu_i}$ [74], and – descriptive statistics in Table 3.2).

Sensitivity Analysis Results with MELCOR 1.86

For the analysis with MELCOR 1.86 we selected 5 parameters that can affect the properties of relocated debris in LP. The list with names and correspondent ranges of the parameters selected for MELCOR sensitivity study is presented in the Table 3.1. Total debris mass, hydrogen mass in containment, metallic fractions in the first and second axial levels and time of onset of massive relocation to LP were taken as response functions in this analysis.

Table 3.1. Selected MELCOR parameters and their ranges.

Parameter name	Range	Units
Maximum Time Step (MTS)	[0.001-2.0]	sec
Particulate Debris Porosity (PDPor)	[0.3-0.5]	-
Velocity of falling debris (VFALL)	[0.01-1.0]	m/s
LP Particulate debris equivalent diameter (DHYPDLP)	[0.002-0.005]	m
Oxidized fuel rod collapse temperature (TRDFAI)	[2500-2650]	K

- Maximum time step (MTS) – specified in executive (EXEC) package, MELCOR calculates its system time step based on directives from the packages, but it cannot take time steps greater than the maximum time and smaller than the minimum time step specified in EXEC package. It has been previously shown in [75],[76], that the MELCOR time step has quite significant effect on the results and lack of time step convergence of the solution with reduction of maximum time step. For the analysis we selected the range [0.001-2.0]sec, however this time step can be reduced by the simulation driver in case of crashed calculations.
- Particulate debris porosity (PDPor) – Porosity of particulate debris for all cells in specified axial level.
- Lower Plenum Particulate debris equivalent diameter (DHYPDLP) - MELCOR idealizes particulate debris beds as fixed-diameter particulate spheres.
  - The extent of debris coolability depends among others on the space between the particles. The porosity of randomly packed spheres is found to be approximately 40 % independent of particle size both by experiments and sophisticated computational methods [79]. The range of entrained particle size is considered to be 1-5 mm based on TMI-2 data [78].
  - Based on [77][80] – the following ranges for porosity of particulate debris [0.3-0.5] and LP particulate debris equivalent diameter [0.002-0.005]m were selected.
- Velocity of falling debris (VFALL) - the debris is assumed to fall with a user-specified velocity. This allows the debris to lose heat to surrounding water in the lower plenum as it falls to the lower head, following failure of the core support plate in each radial ring. Based on [77] and [57][58] the following range for this parameter has been selected – [0.01-1.0](m/s).
- Oxidized fuel rod collapse temperature (TRDFAI) - The temperature at which intact fuel rods are assumed to transition from rod-like geometry to a rubble form can affect the core degradation progression. MELCOR 1.86 default value is 2500K [57][58], which represents the combined effects of eutectic interactions and fractured nature of irradiated fuel pellets. In MELCOR Best Practices as Applied in the State-of-the-Art Reactor Consequence Analyses (SOARCA) Project [[77]] it is suggested to use a new model for time to fuel rod collapse versus cladding oxide temperature, which range from 2500K(time to failure 1 hour) to 2600K(5 min). Within the scope of this work, the following range was used [2500-2650K].

Table 3.2Descriptive statistics for the Case A and B.

	Mean value μ		Standard deviation σ		Min/Max Case A	Min/Max Case B
	Case A	Case B	Case A	Case B		
Debris mass (kg)	212930	134900	20690	36585	155940-264100	18752-215190
Hydrogen mass (kg)	851	1148	217	126	501-1545	969-1649
T_{ref}(sec)	5251	7515	234	2678	4510-5870	0-31000
Metallic debris fraction in 1st axial lvl.	0.48	0.35	0.12	0.12	0.25-0.79	0.13-0.97
Metallic debris fraction in 2nd axial lvl.	0.33	0.25	0.05	0.13	0.19-0.45	0.02-0.99
LDW Pool Temperature (K)	327.1	324	0.47	3.4	326.1-328.1	321-370
Containment Pressure (Bar)	2.6	3.46	0.14	0.25	2.21-3.08	3.17-3.75
LDW Pool Depth (m)	7.71	7.02	0.37	0.1	6.59-8.0	6.56-7.23

Figure 3.20 shows the sensitivity indices of the amount of relocated debris in LP to the modelling parameters in MELCOR. The results indicate that for the Case B, LP debris mass is largely influenced by TRDFAI, where larger values of TRDFAI will yield smaller debris mass (e.g. for TRDFAI = 2650K MELCOR predicts approximately 18 tons of debris in LP, while for TRDFAI = 2500K debris mass can reach 215 tons). Also, judging by Morris $\bar{\sigma}$ and correlation coefficients, there is a linear dependency between TRDFAI and the resultant mass. Debris mass in LP predicted by MELCOR for the Case B ranges from 18 to 215 tons with mean value – 135 tons and standard deviation – 36.5 tons. For the Case A, debris mass in LP is in the range from 155 to 264tons, with mean value – 212.9tons and standard deviation – 20 tons. In case A, according to Morris method sensitivity analysis results, the most influencing parameters are particulate debris porosity (PDPor), falling debris velocity (VFALL) and oxidized fuel rod collapse temperature (TRDFAI), and, judging by $\bar{\sigma}$ values, all involved in non-linear interaction with other parameters.

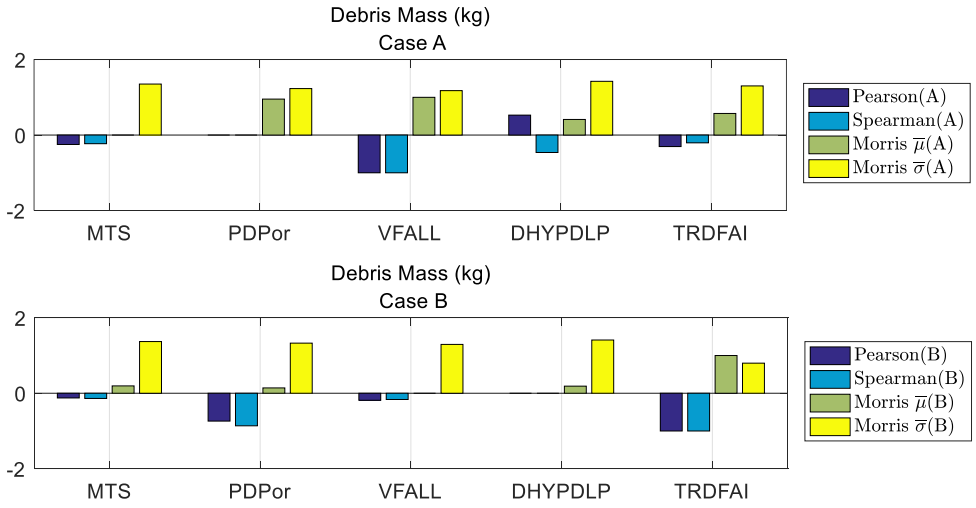

Figure 3.20. Sensitivity of debris mass in LP to modelling parameters in MELCOR.

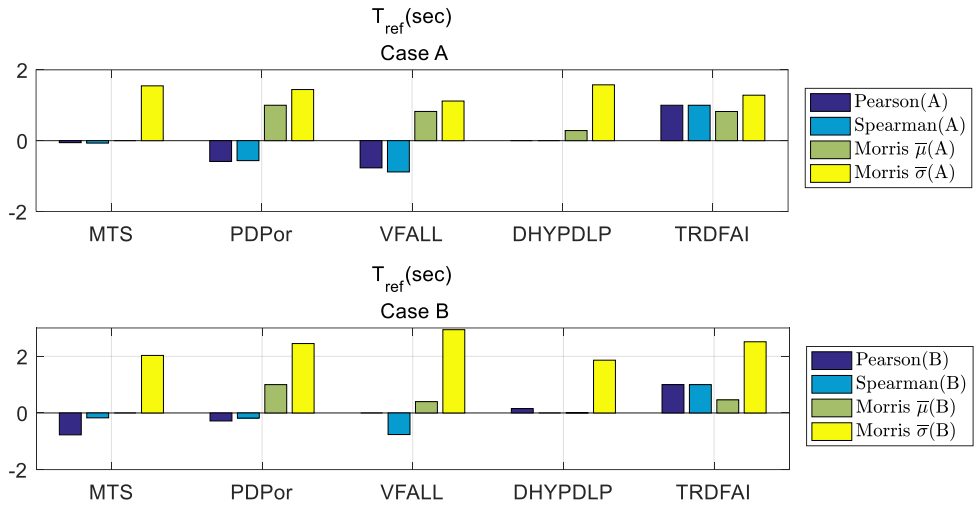

Figure 3.21. Sensitivity of timing of onset of massive core relocation to LP to modelling parameters in MELCOR.

Figure 3.21 shows the sensitivity indices of the time of massive relocation to LP (T_{ref}). For the Case B T_{ref} is largely influenced by particulate debris porosity (PDPor) and oxidized fuel rod collapse temperature (TRDFAI), as well as debris falling velocity (VFALL) – larger values of TRDFAI yield later fuel failure time, thus, delaying massive relocation to LP. It ranges from 0 sec (i.e. no core support plate failure) to 31000sec with mean value of ~7500sec and standard deviation of ~ 2600sec. For the Case A, T_{ref} lies within relatively small time window from 4510 to 5870 sec with mean value of 5251 sec and standard deviation 234 sec. The most contributing factors are PDPor, TRDFAI and VFALL, however the effect of these parameters to the uncertainty in T_{ref} is insignificant.

Figure 3.22 shows the sensitivity indices of the amount of hydrogen produced during the accident to the modelling parameters in MELCOR. In Case B it ranges from 969kg to 1649kg, with mean value of 1148kg and standard deviation 126kg. The most important factors for hydrogen production are particulate debris porosity (PDPor) and debris falling velocity (VFALL). For the Case A, the hydrogen mass ranges from 501 to 1545kg with mean value of 851kg and standard deviation 218kg. The most important factors for hydrogen production in Case A are PDPor, TRDFAI and MTS. The results indicate that there is non-linear interaction between the parameters used in this study.

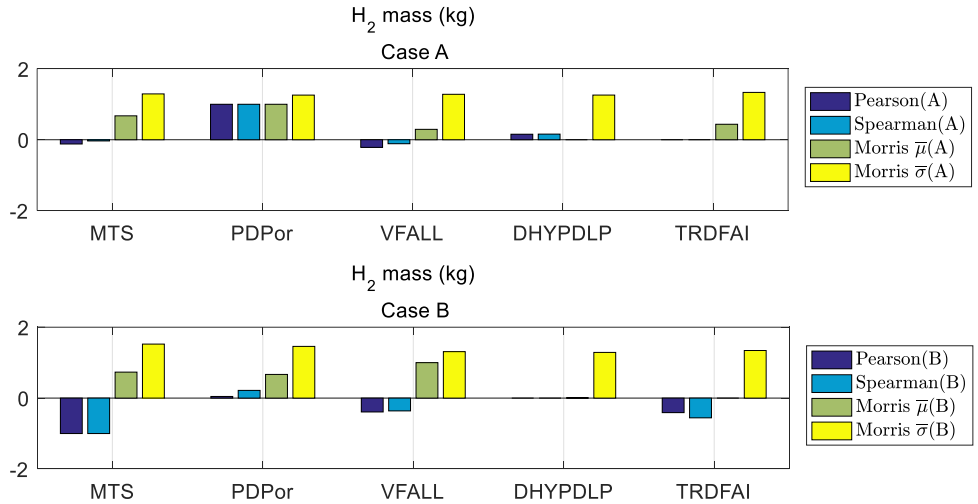

Figure 3.22. Sensitivity of hydrogen mass to modelling parameters in MELCOR.

Figure 3.23 shows sensitivity indices of the metallic debris fraction in the first axial level to the modelling parameters in MELCOR. Metallic debris fraction in the 1st axial level ranges from 0.13-0.97 with mean value 0.35 and standard deviation 0.12 (scenarios with 0.97 metallic debris

fraction corresponds to the cases where MELCOR does not predict core support plate failure and massive relocation to LP), and from 0.26 to 0.79 with mean value 0.48 and standard deviation 0.13 – for the Case B and A correspondingly. The most important factors for metallic debris fraction in the first axial level are VFALL for the Case A and VFALL, PDPor, DHYPDLP for the Case B.

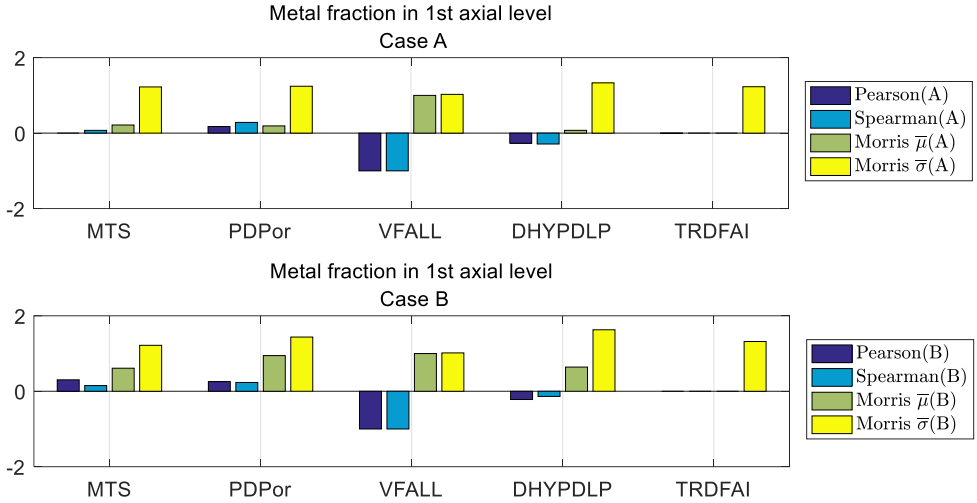

Figure 3.23. Sensitivity of metallic debris fraction in the 1st axial level to modelling parameters in MELCOR.

The results of sensitivity study can be summarized as follows:

- TRDFAI (oxidized fuel rod collapse temperature) – the temperature at which a transition from intact fuel rod geometry to a rubble form is assumed. There is quite significant influence of TRDFAI on the total amount of relocated debris (see Figure 3.20). This influence can be explained by the time (and respective generated heat) that is necessary to reach the fuel failure condition. With increase of TRDFAI it takes more time to heat up the fuel assemblies to the point at which they fail, convert into particulate debris, accumulate and cause support plate failure at certain time T_{ref} (as illustrated by the values of the correlations in Figure 3.20 and 3.21). The difference in relative importance of TRDFAI between Cases A and B (low and high pressure respectively) can be explained by different core heat up rates in these scenarios. The core heat up rate in Case A is higher (because there is no water in the core region) compared to Case B, therefore significance of TRDFAI is lower in Case A compared to Case B. TRDFAI has significant effect on the hydrogen production in Case A and B, where higher values of TRDFAI can result in longer periods of time during which the intact core structures are exposed to oxidation. However, the overall effect on the mass of hydrogen produced (see values of the correlation coefficients in Figure 3.22) is non-monotonic.
- PDPor (particulate debris porosity) – is defined for all cells in specified axial level. When structure failure criteria are reached the structures in the cell are converted into porous debris with the user defined porosity. Particulate debris in MELCOR are represented as spheres with an equivalent diameter. When debris relocates and joins a particulate debris bed in a computational cell, it is assumed that the volume of particulate debris increases and node porosity decreases [58][57]. According to [58], the flow through the core node with particulate debris decreases along with the porosity, however MELCOR never completely blocks the flow. Reduced flow affects both, heat removal from the core and particulate debris by escaping steam, and core\debris oxidation rate (Figure 3.20, 3.21 and 3.22). Figure 3.20 indicates that PDPor has an important non-linear effect on LP debris bed formation, it might be due to: (i) steam flow through the core nodes with increased porosity increase oxidation (see Figure 3.22); (ii) additional steam generation in LP and cooling of outermost rings upon core support plate failure. The difference between Cases A and B can be explained by the effect of depressurization. In Case A, the water level after depressurization drops below the active core region, the uncovered core starts to heat up, eventually reaching the point where

control rods\blades, canisters undergo degradation and relocate downwards to the core plate, where its either rest on top as PD, or refreezes as conglomerate, or flows through the openings into the lower plenum. The variation in PDPor, as a result will affect both, cooling of the core by escaping steam (see Figure 3.20 3.21) and core oxidation (see Figure 3.22). In Case B, the water level in core decreases gradually, so the relative importance of this parameter on steam flow rate through the core is lower, compared to the Case A, which can be observed in (Figure 3.20, 3.21 and 3.22). When it comes to core support plate failure (see Figure 3.21), it seems that larger PDPor values promote core cooling by escaping steam, but, on the other hand, enhance core oxidation and chemical heat production (especially for the Case A, where oxidation starts after water level dropped below active core bottom, so the results in Case A are more sensitive to PDPor compared to the Case B), that may result in earlier degradation of the fuel assemblies and earlier failure of core support plate (T_{ref}), the extent of the effect of this parameter on core cooling\oxidation in different scenarios is also reflected in correlation coefficients in Figure 3.21. The effect of PDPor on the metallic debris fraction (see Figure 3.23) can be explained by the extent of core oxidation, since there is a clear distinction between Case A and Case B, which is quite evident in Table 3.2.

- DHYPD (Lower plenum particulate debris equivalent diameter) – MELCOR uses this parameter to calculate heat transfer surface area of the debris in LP, note that MELCOR equates the oxidation surface area to the heat transfer surface area of the node; so it should have an effect on the debris oxidation and steam generation rate. However, based on the results of sensitivity study the effect of this parameter within considered ranges on debris mass, hydrogen mass, time of core support plate failure was found to be smaller compared to the effect of the other parameters (Figure 3.20, 3.21 and 3.22). On the other hand, it might be involved in interaction with other parameters (e.g. PDPor and VFALL). Further analysis is necessary to determine the effect of particulate debris diameter and heat transfer coefficients in in-vessel debris quench model in MELCOR on the results. The effect of DHYPD on the metallic debris fraction in 1st axial level is yet to be explained.
- VFALL (velocity of falling debris) - MELCOR does not have a mechanistic model for debris dropping into the lower plenum. Instead a number user-specified parameters control the rate at which material relocates into the lower plenum and the effective heat transfer from and associated oxidation of the debris slumping into lower plenum water [58]. The effect of VFALL on the amount of the debris in LP (see Figure 3.20) can be explained by steam generation during core slumping that can affect both: steam cooling of core/core debris and enhanced oxidation. However, based on the results, it seems that the core slumping, together with its modelling parameters (such as VFALL, DHYPDLP and others) has different effect in different severe accident scenarios, e.g. in Case A the core heat up rate in the 1st, 2nd and 3rd radial rings is significantly higher compared to the periphery of the core (rings 4 and 5; ring 5 can also radiate a fraction of its decay heat to the shroud) – see Figure 3.24a, while in Case B, due to gradual coolant evaporation, the core heats up more evenly in all radial rings – see Figure 3.24b. Prior to core plate failure (T_{ref}) there is quite significant difference in fuel temperature in the 4th and 5th radial rings between Cases A and B (see Figure 3.24c, Figure 3.24d). The slumping of the core debris to lower plenum generates steam flow through the core, including outer rings, where it can i) provide steam cooling; ii) cause enhanced oxidation and chemical heat production, if the cladding temperature in the nodes exceeds oxidation cut-off threshold – 1100K. Further analysis of the effect of VFALL, PDPor, DHYPDLP on the flow and hydrogen generation in different radial rings and properties of relocated debris is necessary.

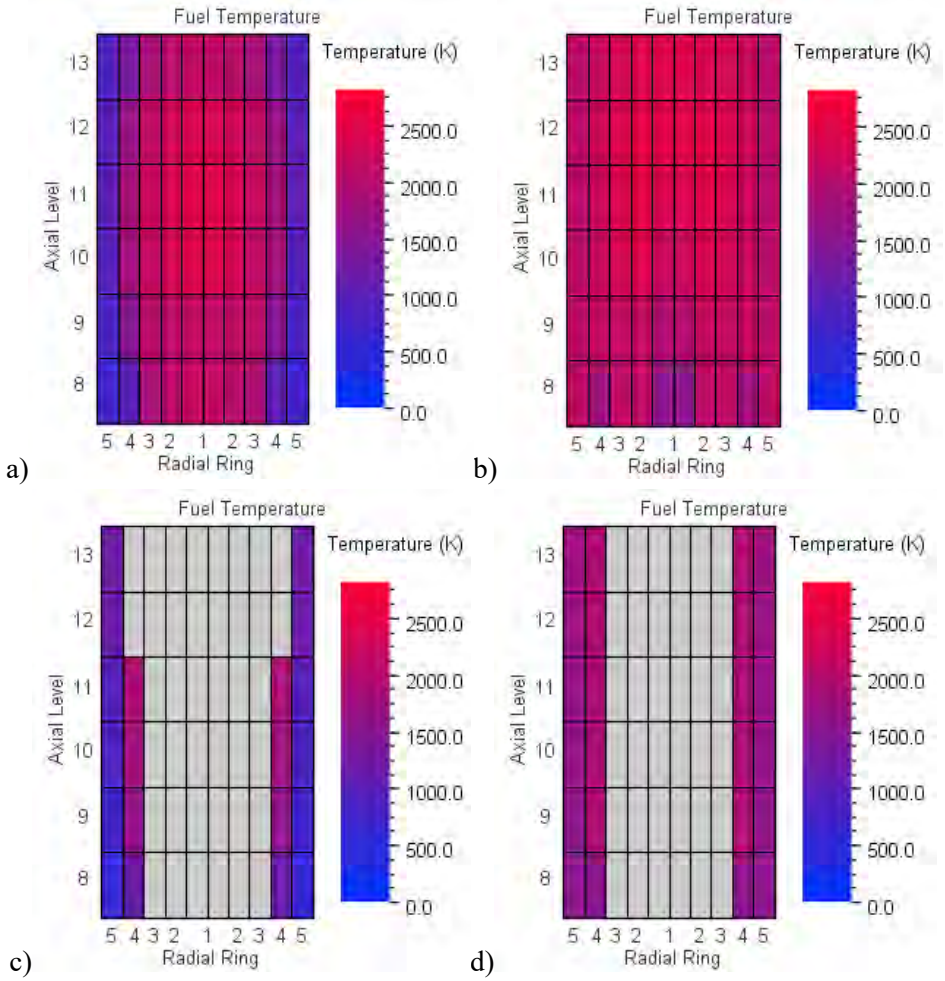

Figure 3.24. Core fuel temperature map prior to: onset of fuel rods failure for a) Case A; b) Case B; core debris slumping to lower plenum (at T_{ref}) for c) Case A; d) Case B.[1]

- MTS (Maximum time step) – based on the results of sensitivity study, MELCOR maximum time step has a very little impact on the mass of relocated debris and the time of core support plate failure, on the other hand, it has some non-negligible effect on the extent of core oxidation, which is linked to the amount of hydrogen produced (see Figure 3.22) and the metallic debris fraction (see Figure 3.23) – which can be caused by the complex non-linear interactions between physical models in MELCOR and their sensitivity to the time step.

Sensitivity Analysis Results with MELCOR 2.1 and 2.2

For the analysis with MELCOR 2.1/2.2 we selected 8 parameters that can affect the properties of relocated debris in LP. The list with names and correspondent ranges of the parameters selected for MELCOR sensitivity study is presented in the Table 3.3. Total debris mass, hydrogen mass in containment, metallic fractions in the different axial levels at the bottom of the vessel and time of onset of massive relocation to LP were taken as response functions in this analysis.

[1] TRDFAI equals to 2500K in these figures.

Table 3.3. Selected MELCOR parameters and their ranges.

Parameter name	Range	Units
Particulate Debris Porosity (PDPor)	[0.3-0.5]	-
Velocity of falling debris (VFALL)	[0.01-1.0]	m/s
LP Particulate debris equivalent diameter (DHYPDLP)	[0.002-0.005]	m
Molten Cladding (pool) drainage rate (SC11412)	[0.1-2.0]	kg/m-s
Molten Zircaloy melt break-through temperature (SC11312)	[2100-2540]	K
Time Constant for radial (solid) debris relocation (SC10201)	[180-720]	sec
Time Constant for radial (liquid) debris relocation (SC10202)	[30-120]	sec
Heat transfer coefficient from in-vessel falling debris to pool (CORCHTP)	[200-2000]	W/m2-K
Oxidized Fuel Rod Collapse Temperature (TRDFAI)	*	*

- Particulate debris porosity (PDPor) – Porosity of particulate debris for all cells in specified axial level.
- Lower Plenum Particulate debris equivalent diameter (DHYPDLP) - MELCOR idealizes particulate debris beds as fixed-diameter particulate spheres.
  - The extent of debris coolability depends among others on the space between the particles. The porosity of randomly packed spheres is found to be approximately 40 % independent of particle size both by experiments and sophisticated computational methods [79]. The range of entrained particle size is considered to be 1-5 mm based on TMI-2 data [78].
  - Based on [77],[80] – the following ranges for porosity of particulate debris [0.3-0.5] and LP particulate debris equivalent diameter [0.002-0.005]m were selected.
- Velocity of falling debris (VFALL) - the debris is assumed to fall with a user-specified velocity. This allows the debris to lose heat to surrounding water in the lower plenum as it falls to the lower head, following failure of the core support plate in each radial ring. Based on [77] and [71],[72] the following range for this parameter has been selected – [0.01-1.0](m/s).
- Heat transfer coefficient from in-vessel falling debris to pool (HDBH2O) – in MELCOR In-Vessel falling debris quench model, it is assumed that the debris fall with a user-specified velocity and heat transfer coefficient. This allows the debris to lose heat to surrounding water in the lower plenum as it falls to the lower head, following failure of the core support plate in each radial ring. Based on [77],[82] and [71],[72] the following range for this parameter has been selected – [200-2000](W/m2-K).
- Molten cladding (pool) drainage rate (SC11312) – used by candling model when molten material has just been released after holdup by an oxide shell or by a flow blockage (crust) [71],[72]. This sensitivity coefficient determine the maximum melt flow rate per unit width after breakthrough. In this study the following range was considered – (0.1-2.0 kg/m-s) [77],[82].
- Molten Zircaloy melt break-through temperature (SC11312) – this sensitivity coefficient is used to define the conditions for which molten material will be held up by an oxide shell. This sensitivity coefficient defined the maximum ZrO_2 temperature permitted to hold up molten Zr in cladding component (CL) in MELCOR code [71],[72]. In this study the following range was considered (2100-2500K) [77],[82].
- Time Constant for radial (solid\liquid) debris relocation (SC10201\SC10202) – Time constant for radial relocation of solid\liquid material.
  - These parameters are responsible for leveling of particular debris and molten pools in Radial Relocation of Solid (SC1020-1) and Molten (SC1020-2) materials. This model intended to simulate the gravitational

leveling between adjacent core rings that tends to equalize the hydrostatic head in a fluid medium [71].

- In this study the following ranges were considered:
  - SC1020-1 - 180-720 sec [71],[72],[82].
  - SC1020-2 - 30-120 sec [71],[72],[82].

Oxidized fuel rod collapse temperature (TRDFAI) – the temperature at which intact fuel rods are assumed to transition from rod-like geometry to a rubble form [[71],[72]]. Results of the previous sensitivity study showed that the properties of relocated debris (total mass, time of the onset of core relocation to LP, etc.) are quite sensitive to the selection of the values of this parameter, especially in the cases with late depressurization [63]. Within this study more advanced "time-at-temperature" fuel rod collapse model has been used. It was developed in SOARCA studies to address cliff-edge behavior in fuel rod collapse that used fixed failure temperature threshold. "Time-at-temperature" model assumes that fuel assemblies collapse when they have been exposed to a temperature for a fixed amount of time. The period of time required to collapse a fuel assembly decreases with increasing temperature [77],[82].

The analysis of the effect of severe accident scenario and possible recovery actions [63],[64],[69] showed that the whole scenario domain consists of scenarios with (i) small relocation (below 20 tons) – characterized by small, mostly metallic debris mass, typically represented by scenarios with ADS activation within ~5000sec after initiating event and ECCS activation within relatively short time window after ADS); (ii) intermediate relocation – debris mass in LP is in the range of 20-100tons; (iii) large debris mass (>100 tons, debris composition and properties are highly influenced by severe accident scenario, typically represented by scenarios with late ECCS activation).
From the point of view of vessel failure mode analysis in ROAAM+ scenarios with large relocation mass contribute the most to the uncertainty in prediction of vessel failure mode [66][65][81]
Full model sensitivity analysis has been performed for a couple of representative scenarios for large relocation domain with a) early ADS (ADS Time – 1500sec) and late ECCS (ECCS Time – 10000sec) activation (Case A) b) late ADS (ADS Time (10000sec) and late ECCS (ECCS Time – 10000sec) activation (Case B). Table 3.4 and 3.5 present descriptive statistics of the results of sensitivity analysis for these representative cases from the large relocation domain with early (Case A) and late (Case B) ADS activation. In the analysis we used MELCOR 2.1 rev7544 (Table 3.4) and MELCOR 2.2 rev9541 (Table 3.5). Figures 3.25, 3.27, 3.29, 3.31 and 3.33 present Pearson and Spearman correlation coefficients, scaled Morris $\bar{\mu}$ (Morris μ values are scaled between 0 and 1, $\bar{\mu}$ – scaled separately for MELCOR 2.1 and 2.2; Figures 3.26, 3.28, 3.30, 3.32 and 3.34 show $\bar{\mu}^*$ - scaled for combined results of MELCOR 2.1 and 2.2 to see relative importance of the parameters between two code versions) and Morris $\bar{\sigma}_i = {}^{\sigma_i}/_{\mu_i}$ [74].

Table 3.4. Descriptive statistics for the Case A and B with MELCOR 2.1.

		Mean value μ Standard deviation σ		**Min Max**		**Skewness Kurtosis**	
		A	**B**	**A**	**B**	**A**	**B**
Debris mass (kg)		209773.36 19220.03	181655.64 37624.16	137373.20 261324.3	80772.82 260196.6	-0.31 4.26	-0.06 2.54
Metallic debris fraction		0.43 0.03	0.36 0.05	0.36 0.5	0.26 0.5	0.01 2.60	0.13 2.29
T_{ref}(sec)		5092.13 559.20	6882.19 905.14	3810.28 6050.1	4285.17 11050.1	-0.74 2.40	0.24 5.05
Hydrogen mass (kg)		583.47 135.83	1184.95 232.54	344.44 1008.1	792.49 1823.0	0.81 3.25	0.29 2.4
Metallic debris fraction in lvl	**1**	0.50 0.32	0.33 0.25	0.07 1.0	0.01 1.0	0.43 1.51	1.21 3.34
	2	0.01 0.02	0.01 0.01	0.00 0.2	0.00 0.1	4.68 33.2	6.65 61.7
	3	0.01 0.03	0.01 0.02	0.00 0.3	0.00 0.2	7.00 62.4	6.06 49.6
	4	0.36 0.12	0.29 0.13	0.11 0.8	0.10 0.8	1.06 4.78	1.14 4.43
	5	0.36 0.10	0.29 0.11	0.08 0.6	0.09 0.7	0.37 3.0	0.62 3.1
	6	0.36 0.10	0.32 0.13	0.12 0.6	0.06 0.7	0.15 2.44	0.37 2.68
	7	0.44 0.13	0.41 0.16	0.12 0.7	0.07 1.0	0.02 2.30	0.31 3.43

Table 3.5. Descriptive statistics for the Case A and B with MELCOR 2.2.

		Mean value μ Standard deviation σ		**Min Max**		**Skewness Kurtosis**	
		A	**B**	**A**	**B**	**A**	**B**
Debris mass (kg)		215722.44 26115.07	189982.17 52635.61	145404.72 278770.2	1171.99 290046.1	-0.25 3.56	-0.90 4.47
Metallic debris fraction		0.43 0.03	0.36 0.05	0.35 0.5	0.22 0.5	-0.08 2.81	0.00 2.50
T_{ref}(sec)		5186.08 797.30	7424.08 1304.18	3735.10 7025.0	0.00 9960.0	0.08 2.04	-2.97 18.44
Hydrogen mass (kg)		602.27 173.03	1231.48 263.86	315.45 1143.9	762.53 2115.4	0.89 3.22	0.28 2.57
Metallic debris fraction in lvl	**1**	0.52 0.32	0.29 0.22	0.0 1.0	0.0 1.0	0.18 1.46	1.40 4.46
	2	0.01 0.02	0.01 0.02	0.00 0.2	0.00 0.2	5.41 38.68	9.26 105.81
	3	0.02 0.04	0.01 0.03	0.00 0.3	0.00 0.3	6.08 45.52	5.77 43.43
	4	0.39 0.15	0.34 0.16	0.04 0.9	0.09 1.0	0.76 3.52	1.13 4.80
	5	0.36 0.10	0.31 0.13	0.14 0.7	0.12 1.0	0.71 4.06	1.81 8.30
	6	0.38 0.10	0.29 0.14	0.18 0.6	0.04 1.0	0.33 2.73	1.90 9.18
	7	0.45 0.13	0.37 0.18	0.18 0.9	0.09 1.0	0.41 2.93	1.12 4.66

Figure 3.25 shows the sensitivity indices of the amount of relocated debris in LP to the modelling parameters in MELCOR (2.1/2.2). Figure 3.26 indicates that relative importance of modelling parameters in MELCOR 2.2 is significantly higher compared to MELCOR 2.1. For example, particulate debris porosity (PDPor), molten zircaloy melt break-through temperature (SC1131-2), LP particulate debris equivalent diameter (DHYPDLP) – have almost twice as large values of $\bar{\mu}^*$ in MELCOR 2.2 compared to 2.1.

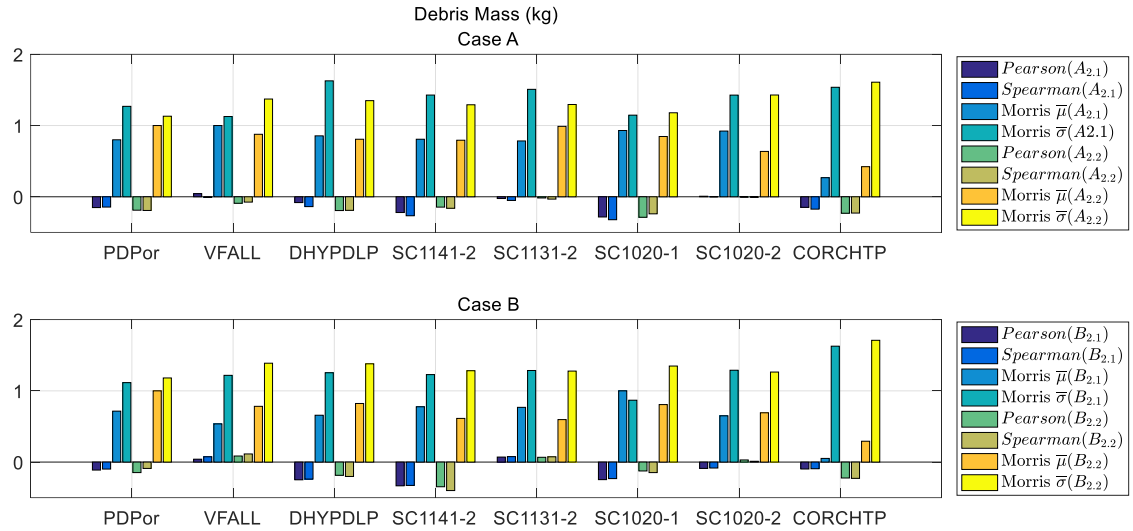

Figure 3.25. Sensitivity of debris mass in LP to modelling parameters in MELCOR (2.1,2.2)

The importance of modelling parameters also depends on severe accident scenario, e.g. in case A (with MELCOR 2.1) the most influential parameters are VFALL, SC1020-1 and SC1020-2, DHYPDLP; in MELCOR 2.2 the most influential parameters are PDPor, SC1131-2, VFALL. In scenario with late depressurization (case A) the parameters that affects LP debris mass are (i) in MELCOR 2.1 – SC1020-1, SC1131-2, SC1141-2; (ii) in MELCOR 2.2 – PDPor, SC1020-1; VFALL and DHYPDLP. In general, the results indicate that for the Case A all MELCOR modelling parameters (both versions 2.1/2.2), with exception to heat transfer coefficient from in-vessel falling debris to pool (CORCHTP), have relatively high values of scaled Morris $\bar{\mu}$, however, judging by standard deviation and kurtosis values (see Table 3.4 and 3.5) overall effect of these parameters on the variance is relatively small. In case B due to variability in MELCOR modelling parameters, the LP debris mass can change in the range 81-260 tons in MELCOR 2.1, and 12-290tons in MELCOR 2.2; both distributions have negative skewness and slight excess kurtosis – which might indicate fatter tails of the distribution.

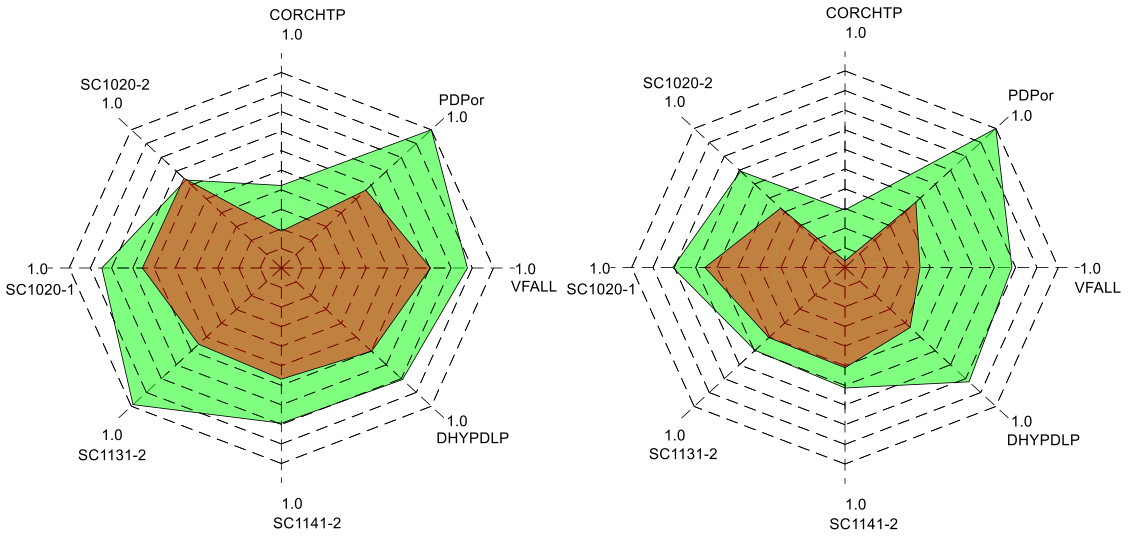

Figure 3.26. Scaled Morris $\bar{\mu}^*$ values for the Debris Mass in LP obtained with MELCOR 2.1(red) and MELCOR 2.2(green) (a) Case A; (b) Case B

Figure 3.27 show the sensitivity indices for the metallic debris fraction in-vessel (core region and lower plenum). In case A and B most of the parameters have relatively high importance according to Morris $\bar{\mu}$ values, except heat transfer coefficient from in-vessel falling debris to pool (CORCHTP). Large Morris $\bar{\sigma}_i$ values indicate that parameters in this study involved in non-linear interactions between each other. It is important to note that in case A the fraction of metallic debris is distributed within relatively narrow range from ~0.35-0.5 for MELCOR 2.1 and 2.2. In case B the fraction of metallic debris is distributed in the range from 0.26-0.5 in MELCOR 2.1 and from 0.22-0.5 in MELCOR 2.2.

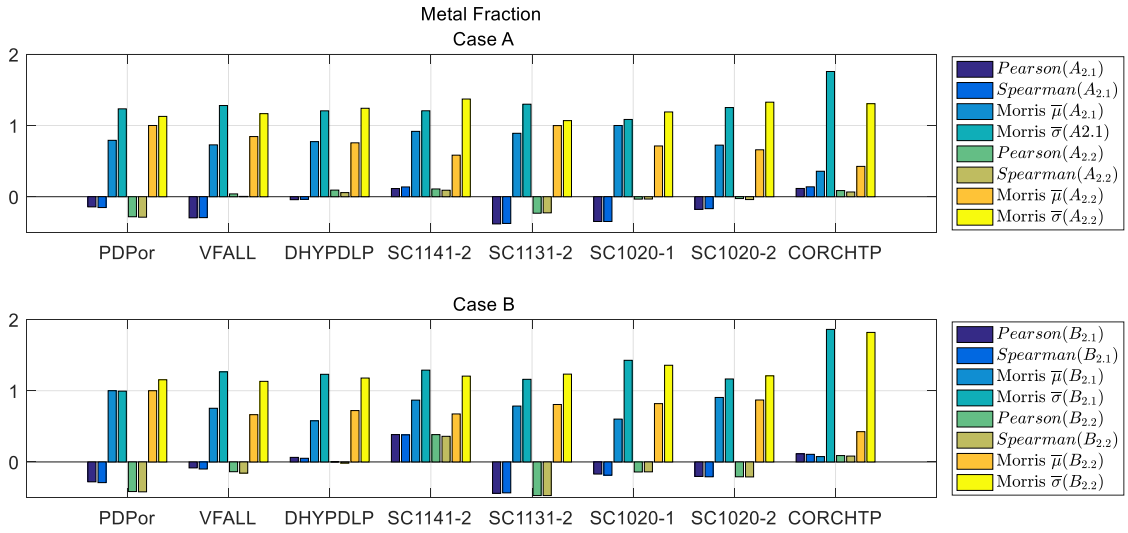

Figure 3.27. Sensitivity Metallic Debris Fraction to modelling parameters in MELCOR (2.1, 2.2)

The relative importance of MELCOR modelling parameters in MELCOR 2.1 and 2.2, according to Figure 3.28, is almost similar, with exception to the effect of PDPor, SC1141-2 and SC1131-2 in scenario with early depressurization.

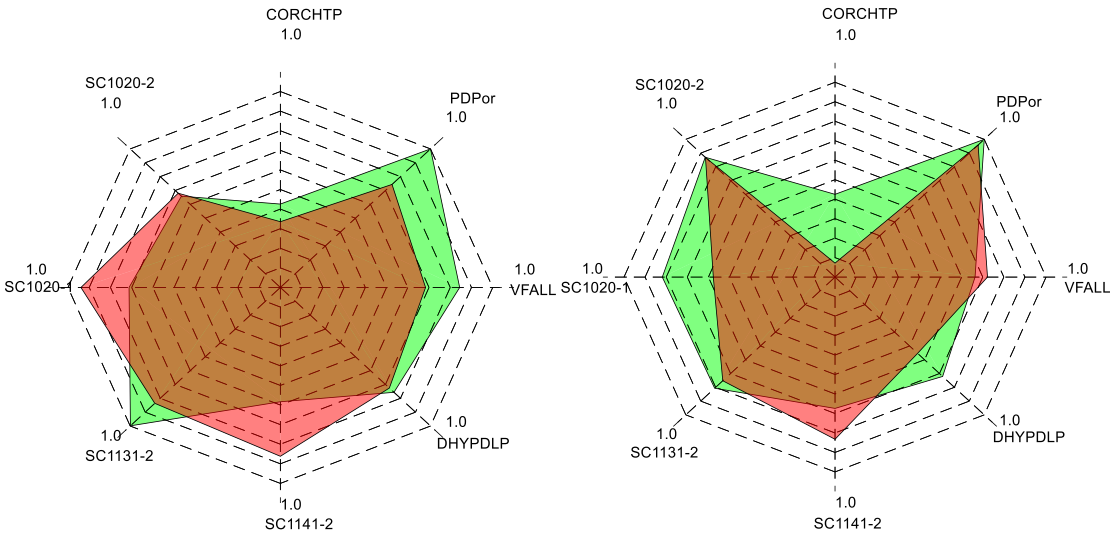

Figure 3.28. Scaled Morris $\bar{\mu}^*$ values for the Metallic Debris Fraction obtained with MELCOR 2.1(red) and MELCOR 2.2(green) (a) Case A; (b) Case B.

Figure 3.29 and 3.30 presents the results of sensitivity of the time of core support plate failure to modelling options in MELCOR. The relative importance of modelling parameters depends on MELCOR code version being used and severe accident scenario. For example, in Case A with MELCOR 2.1 the most influential parameters are SC1141-2, SC1020-1, DHYPDLP; while in MELCOR 2.2 the most influential parameters are PDPor, SC1141-2, SC1131-2 – which is also reflected in Figure 3.30a. In Case B with MELCOR 2.1 – the most influential parameters are PDPor, SC1141-2, SC1131-2; while with MELCOR 2.2 the most influential parameters are DHYPDLP, SC1020-1, PDPor – however the overall impact on the results due to variability of these parameters is significantly higher in MELCOR 2.2 (see Figure 3.30b). Large Morris $\bar{\sigma}_i$ values indicate that parameters in this study involved in non-linear interactions between each other.

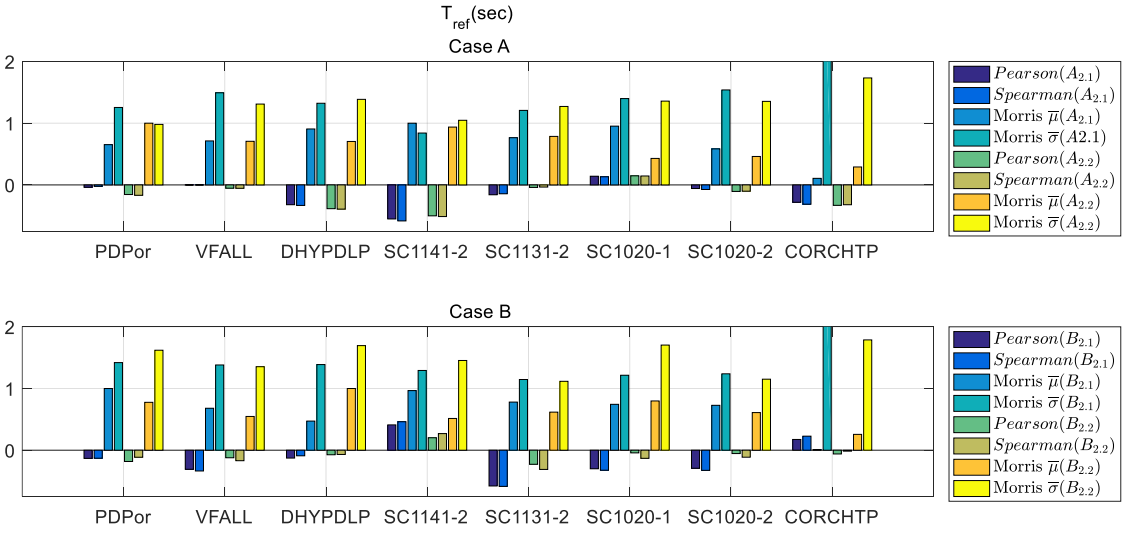

Figure 3.29. Sensitivity of Time of Core Support Plate Failure to modelling parameters in MELCOR (2.1, 2.2)

The time of core support plate failure in case A ranges from ~3700-6000sec and ~3800-7000sec in MELCOR 2.1 and 2.2 correspondingly. In case B it ranges from ~4200-11000sec in MELCOR 2.1 and from 0.0-10000sec (where $T_{ref} = 0$ indicates no core support plate failure, accident stopped in core region). The relative importance of the modelling options is very different in MELCOR 2.1 and 2.2.

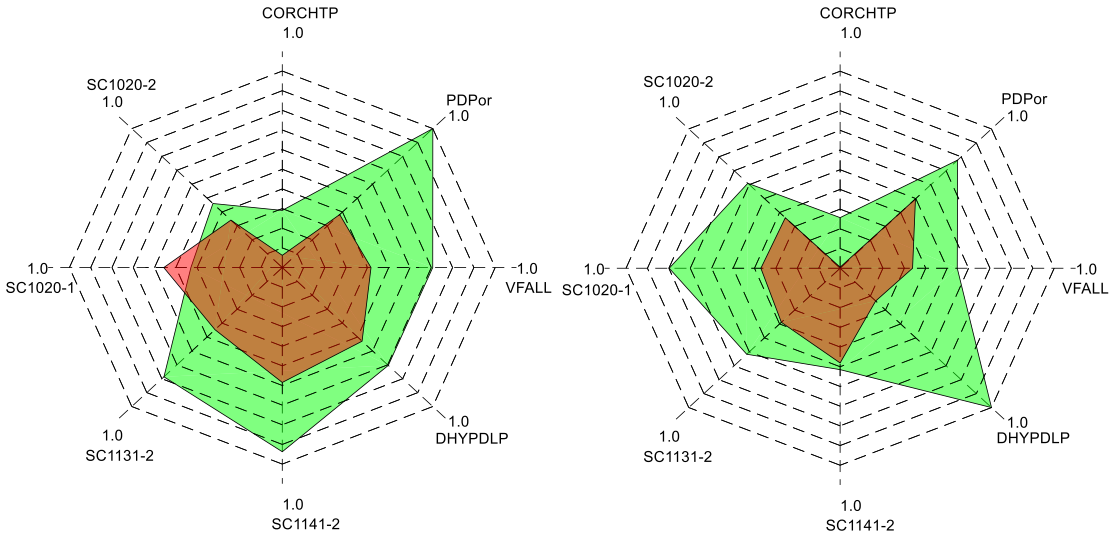

Figure 3.30. Scaled Morris $\bar{\mu}^*$ values for the Time of Core Support Plate Failure obtained with MELCOR 2.1(red) and MELCOR 2.2(green) (a) Case A; (b) Case B

Figure 3.31 show sensitivity indices of Hydrogen generated during the accident to modelling options in MELCOR 2.1/2.2. In case A the hydrogen mass is mostly influenced by PDPor in MELCOR 2.1, while in MELCOR 2.2 – the most influential parameters are SC1141-2, SC1131-2 and PDPor. In case B the most influential parameter is SC1131-2 in MELCOR 2.1 and 2.2 and, judging by Figure 3.32b the relative importance of this parameter in MELCOR 2.1 in slightly higher compared to MELCOR 2.2. The total amount of hydrogen generated during the accident in case A is distributed between ~300-1000kg in MELCOR 2.1 and 2.2; and between ~800-1800/2200kg in MELCOR 2.1/2.2.

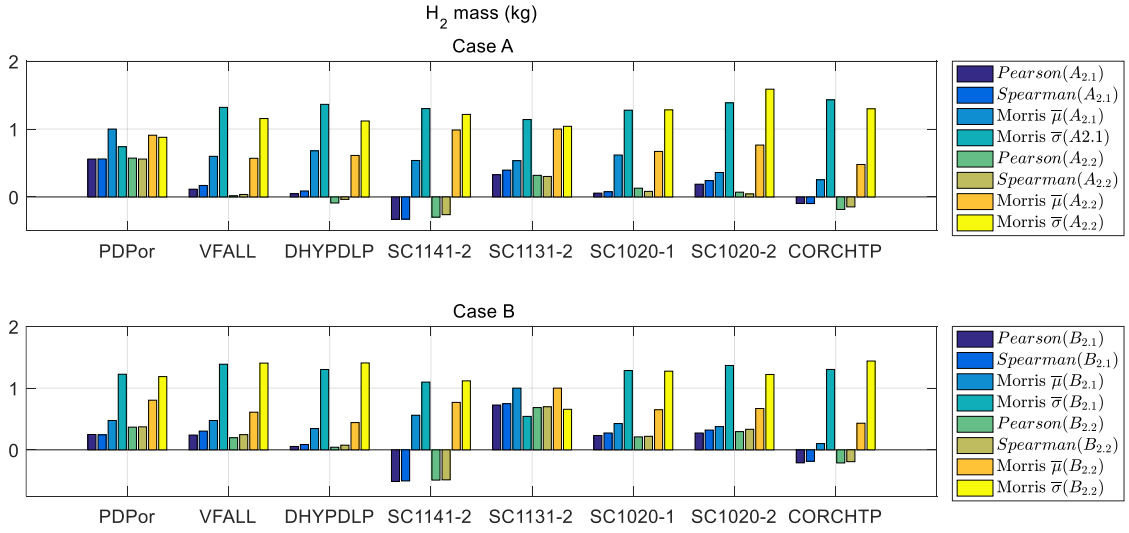

Figure 3.31. Sensitivity of Hydrogen Mass generate during the accident to modelling parameters in MELCOR (2.1, 2.2).

According to Figure 3.32b the relative importance of modelling parameters in MELCOR 2.1 and 2.2 are quite similar between MELCOR versions 2.1 and 2.2, while in case A (see Figure 3.32a) it differs significantly, both the most influential parameters and their contribution to the variance in hydrogen mass generated.

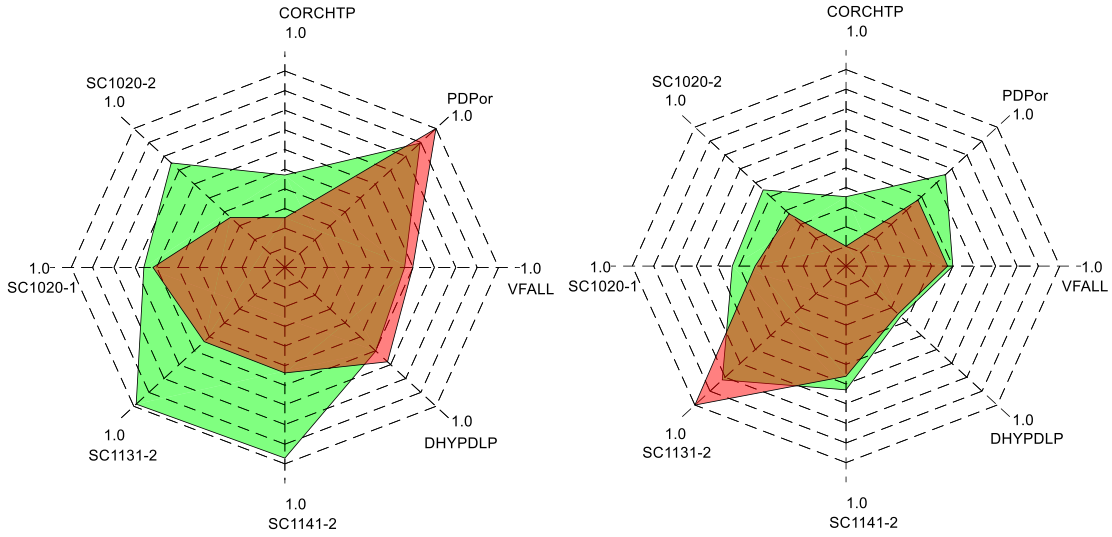

Figure 3.32. Scaled Morris $\bar{\mu}^*$ values for the Hydrogen mass generated obtained with MELCOR 2.1(red) and MELCOR 2.2(green) (a) Case A; (b) Case B

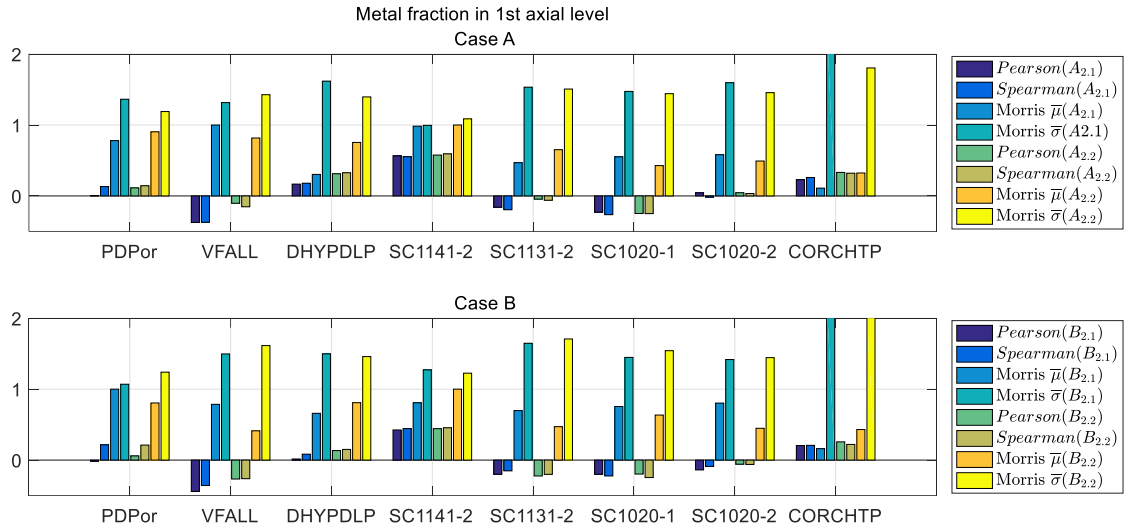

Figure 3.33. Sensitivity of Metallic Debris Fraction in the 1st axial level to modelling parameters in MELCOR (2.1, 2.2)

Figure 3.33 shows the sensitivity indices of Metallic debris fraction at the 1st axial level (approximately 20cm from the bottom of the LP – corresponds to IGT nozzles welding points). In case A the most influential parameters are VFALL and SC1141-2 in MELCOR 2.1, and SC1141-2 and PDPor in MELCOR 2.2. In case B the most influential parameter are PDPor, SC1141-2 and SC1020-2 in MELCOR 2.1, and SC1141-2, DHYPDLP and PDPor in MELCOR 2.2. Metallic debris fraction in the 1st axial level is distributed from ~0.1-1.0 in MELCOR 2.1, and from 0.0-1.0 in MELCOR 2.2 for both cases with early and late depressurization. All distributions have positive skew (left-leaning) and positive excess kurtosis in case B – which might indicate fatter tails of the distribution; and negative excess kurtosis in case A, which indicate that the distribution have several peaks (e.g. beta distribution with $\alpha = \beta = 0.5$, kurtosis ~1.5).

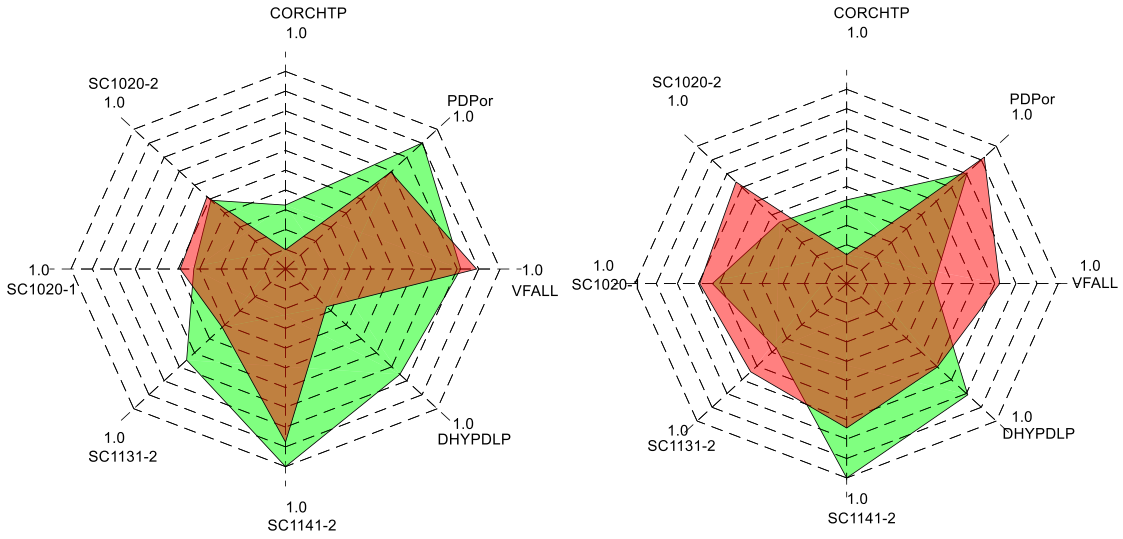

Figure 3.34. Scaled Morris $\bar{\mu}^*$ values for the Metallic Debris Fraction in 1st axial level obtained with MELCOR 2.1(red) and MELCOR 2.2(green) (a) Case A; (b) Case B

Particulate Debris Porosity (PDPor) – is defined for all cells in specified axial level. When structure failure criteria are reached the structures in the cell are converted into porous debris with the user defined porosity. Particulate debris in MELCOR are represented as spheres with an equivalent diameter (DHYPDLP). When debris relocates and joins a particulate debris bed in a computational cell, it is assumed that the volume of particulate debris increases and node porosity decreases [71],[72]. According to [72], the flow through the core node with particulate debris decreases along with the porosity, however MELCOR never completely blocks the flow. Reduced flow affects both, heat removal from the core and particulate debris by escaping steam, and core\debris oxidation rate (see Figure 3.31). It is important to note that MELCOR 2.1 and 2.2 use different default values of SC1505-1 – minimum porosity to be used in calculation the flow resistance in the flow blockage model (0.05 vs 1.e-5 in 2.1/2.2 correspondingly) – which may cause differences between observations in MELCOR 2.1 and 2.2. The difference between cases A and B can be explained by the effect of depressurization. In Case A, the water level after depressurization drops below the active core region, the uncovered core starts to heat up, eventually reaching the point where control rods\blades, canisters undergo degradation and relocate downwards to the core plate, where its either rest on top as PD, or refreezes as conglomerate, or flows through the openings into the lower plenum. The variation in PDPor, as a result will affect both, cooling of the core by escaping steam and core oxidation.

Velocity of falling debris (VFALL) – MELCOR does not have a mechanistic model for debris dropping into the lower plenum. Instead a number user-specified parameters control the rate at which material relocates into the lower plenum and the effective heat transfer (Heat transfer coefficient from in-vessel falling debris to pool (CORCHTP)) from and associated oxidation of the debris slumping into lower plenum water. VFALL has significant effect, judging by Morris $\bar{\mu}$ values on debris mass in LP, metallic debris fraction and metallic debris fraction in the 1st axial level; VFALL has moderate effect on hydrogen mass and timing of core support plate failure. VFALL has also different effect in different severe accident scenarios and MELCOR code version being used. The effect of VFALL together with CORCHTP on the debris mass and other system response quantities can be explained by steam generation during core slumping to LP, that can affect both: core cooling and core oxidation\heat up due to oxidation, especially in the case with early depressurization, where water level dropped below the active core region, due to depressurization, long before the onset of core oxidation; which is also reflected by the difference in sensitivity coefficients between cases A and B. The difference of the effect of VFALL and CORCHTP in different code versions is yet to be explained.

Lower Plenum Particulate Debris Equivalent Diameter (DHYPDLP) – MELCOR uses this parameter to calculate heat transfer surface area of the debris in LP, note that MELCOR equates

the oxidation surface area to the heat transfer surface area of the node; so it should have an effect on the debris oxidation and steam generation rate, however it is not supported by the results (see Figure 3.31). Further analysis is necessary to determine the effect of particulate debris diameter and heat transfer coefficients in in-vessel debris quench model in MELCOR on the results. The effect of DHYPD on the metallic debris fraction in 1st axial level and timing of core support plate failure predicted for case B with MELCOR 2.2 is yet to be explained.

Molten Zircaloy melt break-through temperature (SC1131-2) – defines critical temperature at which molten materials are released from an oxide shell or local blockage (crust). After oxide shell/crust break through MELCOR uses SC1141 array to control candling model, in particular CS1141-2 – Molten Cladding (pool) drainage rate represents a maximum flow rate (per unit surface width) of the molten pool after breakthrough; this coefficient also used to control the time step in candling model, when molten material has just released after hold up by an oxide shell or by a flow blockage (crust) [71],[72]. According the MELCOR manuals description [[71],[72]], these coefficients should have direct effect on the metallic debris fraction at the bottom of the LP, which can be observed in Figure 3.33 and 3.34, i.e. large values of Morris $\bar{\mu}$ and positive correlation coefficients(SC1141-2) in both versions of MELCOR code being used. SC1131-2 has smaller relative importance on the metallic debris fraction in the first axial level, however it is possible that it can be involved in non-linear interaction with other parameters in candling model (including SC1141-2), SC1131-2 has negative correlation coefficients with metallic debris fraction in the 1st axial level – which is opposite to what was initially expected, i.e. larger vales of SC1131-2 would result in larger metallic debris fraction at the bottom of the LP due to higher melt superheat. Sensitivity coefficients SC1141-2, SC1131-2 have significant effect on the processes of core oxidation and hydrogen generation with negative (SC1141-2) and positive (SC1131-2) correlation coefficients, which can be explained by the effect of this parameters to flow blockage formations and structures exposure to oxidation by steam – which is also evident in results for scenario with late depressurization (see Figure 3.31, 3.32b). The effect of these sensitivity coefficients on the amount of relocated debris in LP and timing of core support plate failure is most likely due to the formation of the flow blockages (cooling) and debris interaction with supporting structures (higher metallic debris fraction – higher thermal conductivity of the debris), however, more detailed analysis is necessary to confirm this hypothesis. The results also indicate that these sensitivity coefficients have higher relative importance in MELCOR 2.2 compared to MELCOR 2.1 – which still needs to be explained.

Time constant for radial solid/liquid debris relocation (SC1020-1/SC1020-2) – MELCOR uses particulate debris leveling (SC1020-1) and molten debris leveling (SC1020-2) models for radial relocation of solid and liquid(molten) materials. Sensitivity coefficients SC1020-1/SC1020-2 are used to calculate debris volume relocated during core time step, as follows $V_{rel} = V_{eq}(1 - \exp\left(-\frac{\Delta t_c}{\tau_{spr}}\right))$; where V_{eq} – volume of material that must be moved between the rings to balance the levels, $\frac{\Delta t_c}{\tau_{spr}}$ −COR package time step divided by sensitivity coefficient (SC1020-1/SC1020-2 – for solid/liquid debris correspondingly) [71],[72]. Radial relocation time constants have significant effect on the LP debris mass, metallic debris fraction (in-vessel) and timing of core support plate failure. Negative correlation coefficients in Figure 3.27, suggest that smaller values of sensitivity coefficients will yield larger debris mass in LP – which can be explained by larger debris relocation rate in-between rings in case of core support plate failure, especially in case A, where core support plate failure usually occurs early in one of the central rings (with higher power density) compared to rather gross core support plate failure (failure in several rings) in case B. These parameters have relatively small effect on the hydrogen production and metallic debris fraction in the 1st axial level, and the effect on the timing of core support plate failure and metallic debris fraction (in-vessel) is yet to be explained.

Connection Between Core Relocation and Vessel Failure Analyses

An approach for connection between Core Relocation and In-vessel Debris Bed Coolability and Vessel Failure analyses has been developed [64]. The connection between Core Relocation and Vessel Failure Frameworks (see Figure 3.35) is based on pattern analysis. Coupling between different frameworks within ROAAM+ is established through the one-way connection between the frameworks, providing initial conditions from one model into another. One of the most important features of such approach is its computational efficiency, especially in case of extensive uncertainty (aleatory and epistemic) analyses for failure domain identification and quantification in forward and reverse analyses at each stage of severe accident progression in ROAAM+. The main challenges for such connection between the frameworks is to establish proper timing of transition of data from one model into another. In particular, Core relocation (MELCOR) should provide initial conditions (debris configuration and properties in LP) to Melt-Vessel Interaction/Vessel Failure (ANSYS/PECM) before any significant effect of relocated debris on vessel wall and LH penetrations. On the other hand, the amount of core material held above the core support plate, both debris and partially degraded fuel assemblies) should be small enough, so it does not affect significantly vessel failure analysis results.

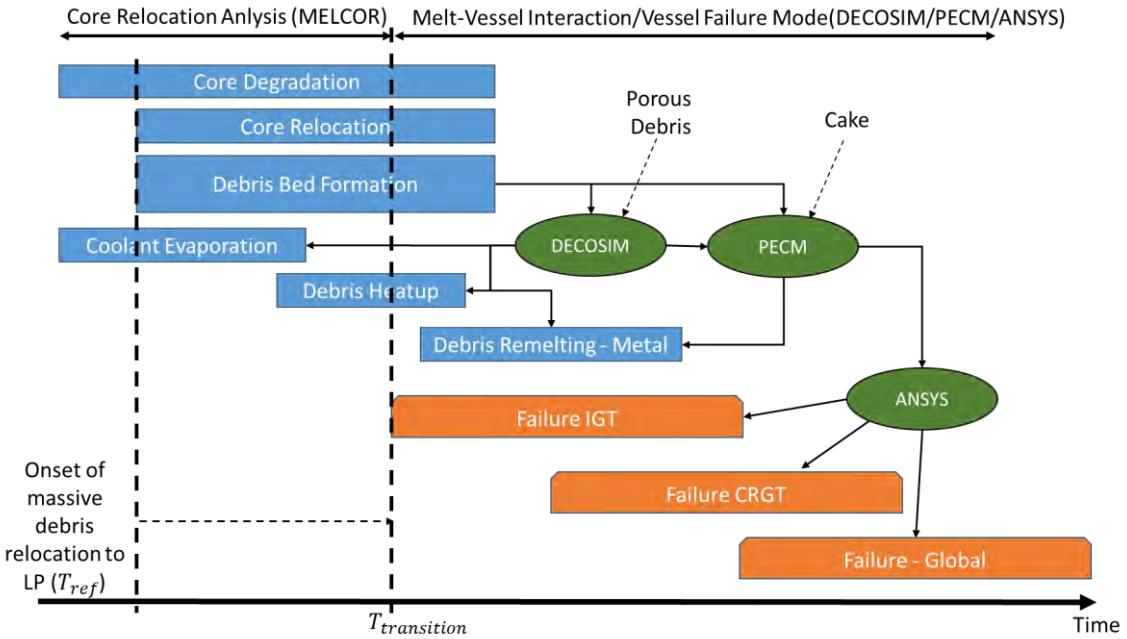

Figure 3.35. Severe Accident progression, connection between Core relocation and Melt-Vessel Interaction/Vessel Failure Frameworks.

In the approach we introduce T_{ref} – *reference time,* the time that characterize onset of massive core relocation to LP. The reference time (T_{ref}) or onset of massive core relocation to LP in most of the cases directly follows the mechanical failure of the core support plate in one of the rings (usually center rings). Using pattern analysis results it has been found that the debris relocate to LP within relatively short time window following mechanical failure of core support plate. The pattern analysis results (see reference [64]) show that the major part of core debris (over 75% of total inventory) relocate to LP within 1800sec after T_{ref}. Based on the results we determine the timing for transition from Core relocation to the Vessel Failure frameworks (Figure 3.35) as T_{ref}+60 min. At this point in time major part of core material is already relocated to LP, but, on the other hand, the thermal load produced by relocated debris is still small.

Core Relocation Surrogate Model

An approach for coupling between core relocation and vessel failure analyses is presented in [64]. The approach is based on pattern analysis and clustering analysis. In this approach typical core relocation transients are identified and grouped into patterns [64]. The effect of timing of scenario events (e.g. ADS, ECCS activation time) on the properties of relocated debris is established using clustering analysis (see [64]). Based on the results of pattern and clustering analyses the surrogate model for prediction of the properties of relocated debris and LDW pool conditions has been developed. The surrogate model is of a "look-up table" type (see Figure 3.36), where major scenario domains have been identified, and the effect of the modelling options in MELCOR has been evaluated. The output of the surrogate model is presented as mean and standard deviation of correspondent distributions of the parameters of interest [63].

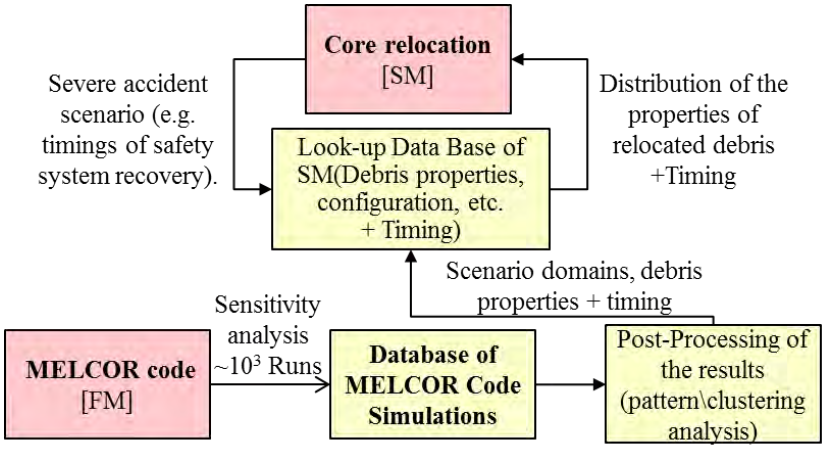

Figure 3.36. Structure of Core relocation SM.[63]

3.4 In-vessel Debris Coolability

3.4.1 DECOSIM Code Overview

The mathematical model implemented in DECOSIM code is based on multifluid equations, it is described in detail in [81], where all governing equations and closures are described. Here, we outline the approach and its numerical implementation, focusing on the specific features necessary to treat in-vessel coolability of porous debris bed. First, we take into account that in the presence of structural elements in the reactor vessel the space accessible by water and corium particles is reduced; therefore, we introduce an effective "porosity" $\varepsilon_c < 1$, assuming that a fraction $1 - \varepsilon_c$ of all volume is unavailable for the flow and debris due to space congestion by the structural elements. The effective "porosity" ε_c enters the phase flow and energy equations together with the "real" porosity ε of debris bed. This approach allows us to consider large-scale flowfields without resolving geometries of each individual CRGTs or IGTs. The volume fraction ε_c is assumed to be constant in time, but it can vary in space according to the availability and size of structural elements in the reactor pressure vessel. This simplification is justified before structural elements lose integrity (i.e., due to melting); we use it throughout the simulation because we are interested here in the conditions developing in the porous debris bed, rather than in detailed description of further melt propagation through the newly opened paths.

By occupying some space in the reactor vessel, the structural elements not only reduce

the volume available to flow, but also change the effective heat capacity and effective conductivity of the medium. It is assumed here that the local temperature of structural elements is the same as that of surrounding porous medium (single-temperature model of solid material). Another simplification often used in the coolability studies is to consider the space above the debris bed as some effective low-drag porous medium (with high porosity and particle diameter), so that the same filtration equations could be applied to obtain the phase velocities in the whole computational domain. Note that in the drag laws, only the "real" porosity ε is taken into account.

Below we summarize the system of equations being solved in DECOSIM; relevant closures and description of numerical implementation can be found in [221]. Note that the same model formulation was applied in [17] to consider in-vessel porous debris bed under continuous water supply conditions. A simpler formulation (with $\varepsilon_c \equiv 1$) was used to model by DECOSIM the post-dryout behavior of ex-vessel debris beds where structural elements are absent [17].

3.4.2 **Governing Equations**

The multifluid three-phase model implemented in DECOSIM includes the mass, momentum, and energy conservation equations for liquid water (index $k = l$), vapor ($k = v$), and solid material (s); for the in-vessel problems we also take into account the congesting structures (index c):

$$\frac{\partial \alpha_k \rho_k \varepsilon \varepsilon_c}{\partial t} + \nabla \varepsilon_c \rho_k \boldsymbol{j}_k = \varepsilon_c \Gamma_k \tag{3.3}$$

$$\nabla P = \rho_k \boldsymbol{g} - \left(\frac{\mu_k}{K K_{rk}} \boldsymbol{j}_k + \frac{\rho_k}{\eta \eta_{rk}} |\boldsymbol{j}_k| \boldsymbol{j}_k \right) + \boldsymbol{F}_k \tag{3.4}$$

$$\alpha_k \rho_k \varepsilon \varepsilon_c \frac{d_k h_k}{dt} = \alpha_k \varepsilon \varepsilon_c \frac{d_k P}{dt} + \nabla(\alpha_k \lambda_k \varepsilon \varepsilon_c \nabla T_k) + \varepsilon_c \Gamma_k (h_k^I - h_k) + \gamma_k \varepsilon_c R_{sk} + \varepsilon_c R_k^I \tag{3.5}$$

$$[\varepsilon_c(1-\varepsilon)\rho_s C_s + (1-\varepsilon_c)(1-\varepsilon_{ci})\rho_c C_c] \frac{\partial T_s}{\partial t} = \nabla(\lambda_{\text{eff}} \nabla T_s) + \varepsilon_c (R_{dh} - R_{sl} - R_{sv}) \tag{3.6}$$

Here, ε is the "real" porosity, the phase volume fractions α_k satisfy the condition $\alpha_l + \alpha_v = 1$; $\boldsymbol{j}_k = \alpha_k \varepsilon \boldsymbol{u}_k$ are superficial phase velocities, $\boldsymbol{u}_k$ are actual phase velocities, the substantial derivatives are $d_i/dt = \partial/\partial t + (\boldsymbol{u}_i \nabla)$, $\boldsymbol{g}$ is the gravity acceleration. Water phase properties (densities ρ_k, specific enthalpies h_k, viscosities μ_k, thermal conductivities λ_k) as functions of pressure P and temperature T_k are approximated by polynomials according to IAPWS-IF97 formulation [222]. In the momentum equation (3.4), K, K_{rk}, η, and η_{rk} are absolute and relative permeabilities and passabilities, $\boldsymbol{F}_k$ is interphase friction force ($\boldsymbol{F}_l = -\boldsymbol{F}_v$), Γ_k is phase change rate ($\Gamma_v = -\Gamma_l$). Equations (3.3)–(3.6) are written in the operator form, with vector quantities typeset in boldface. In the current work, the problem is considered in the axisymmetric framework, with the gradient and divergence operators $\nabla \phi = \left(\frac{\partial \phi}{\partial r}, \frac{\partial \phi}{\partial z} \right)$, $\nabla \cdot \boldsymbol{v} = \frac{1}{r} \frac{\partial r v_r}{\partial r} + \frac{\partial v_z}{\partial z}$, where ϕ is a scalar, $\boldsymbol{v} = (v_r, v_z)$ is a vector quantity, r and z are the radial and vertical coordinate, respectively.

The phase energy equation (3.5) takes into account heat conduction, evaporation, heat exchange with solid particles material (source terms R_{sk} on the right-hand side), and

interphase heat exchange (R_k^I); the superscript I denotes values pertaining to the liquid-vapor interface. In the solid material energy equation (3.6), T_s, ρ_s, and C_s are the temperature, density, and specific heat capacity of corium, ρ_c, and C_c are the density and specific heat capacity of the congesting structures, ε_{ci} is the internal porosity of congesting structures ($\varepsilon_{ci} > 0$ if the structures are not solid, e.g., in hollow pipes). Also, R_{dh} is the decay heat power per unit volume of porous medium, R_{sl} and R_{sv} describe heat exchange with liquid and vapor phases. The effective conductivity in the solid material is evaluated as

$$\lambda_{\text{eff}} = \varepsilon_c(1-\varepsilon)\lambda_s + (1-\varepsilon_c)(1-\varepsilon_{ci})\lambda_c \tag{3.7}$$

In this way, higher heat conductivity in the presence of metal structural elements is taken into account. Also, the properties of corium are taken as weighted between the values for solid (index sol) and molten (index m) states, the weighting factor being the mass fraction of melt χ:

$$\rho_s C_s = (1-\chi)\rho_{sol}C_{sol} + \chi\rho_m C_m, \;\; \lambda_s = (1-\chi)\lambda_{sol} + \chi\lambda_m \tag{3.8}$$

The mass fraction of melt is obtained from energy balance in computational cell, taking into account the fusion heat. Two-phase drag in porous medium is modelled according to [223], with modifications introduced and validated in [224],[118]. Models for source terms are considered in details in [81].

Note finally that all porosities (ε, ε_c, ε_{ci}) and heat conductivities are considered in this work as scalars, i.e., isotropic values being constant for each porous region. More comprehensive treatment of porous media properties taking into account anisotropy due to vertical orientation of structural elements was outside the scope of the current study.

3.4.3 **Implementation in DECOSIM code**

The system of governing equations (3.3)–(3.6) is discretized in axisymmetric geometry on a staggered orthogonal grid in the 2D axisymmetric geometry. The grid was non-uniform in both radial and vertical directions in order to increase spatial resolution in the regions of high gradients. On each time step equation are solved by Newton iterations. On each time step, the momentum equations are solved first to find out the preliminary velocity components of each phase. The velocity corrections are expressed in terms of pressure and volume fraction corrections, with the phase change terms taken into account implicitly. They are then substituted into the phase continuity and energy equation which are solved in a fully coupled manner by an efficient ILUT-preconditioned PGMRES solver. Global iterations are performed on each time step until convergence with prescribed accuracy is reached. The time step is varied adaptively, depending on convergence success or failure [81].

3.4.4 **PARAMETERS**

Vessel and Debris Bed Geometry and Properties

Simulations are performed in the vessel geometry typical of Nordic-type BWRs,

sketched in Figure 3.37a. In the reactor pressure vessel, there is a shroud which limits radial spreading of debris. The congested area containing CRGTs and IGTs is indicated by vertical dashed lines and hatching; in this zone, the structural elements are taken into account, as described above. The effective porosity due to congestion is set to $\varepsilon_c = 0.82$, the internal porosity of structural elements is $\varepsilon_{ci} = 0.02$; details of these can be found in [81]. The levels at which the welding points of CRGTs and IGTs are located (0.4 and 0.17 m above the vessel bottom surface) are shown by the dashed lined. The geometry coincides with that used in our previous works [81], except the vertical extent of computational domain was extended to 6 m, while the initial level of water was set to the height of 4 m, corresponding to the top of computational domain in simulations [81] where continuous water supply was assumed.

Formation of debris bed in severe accident conditions is a complex process, with substantial uncertainties involved with respect to fuel-coolant interaction. In terms of the problem considered, this translates into uncertainties both in properties of debris (porosity, mean particle diameter), debris bed shape (which depends on the formation process, including fuel melt fragmentation, fallout, interaction with boiling water flow in RPV, etc.), as well as the initial state of corium (particle temperature, fraction of quenched material) and water inventory in the reactor vessel. Since no mechanistic model addressing all these issues is available at the moment, we resort to setting the initial conditions *ad hoc*, mostly focusing on revealing the possible outcomes of different scenarios.

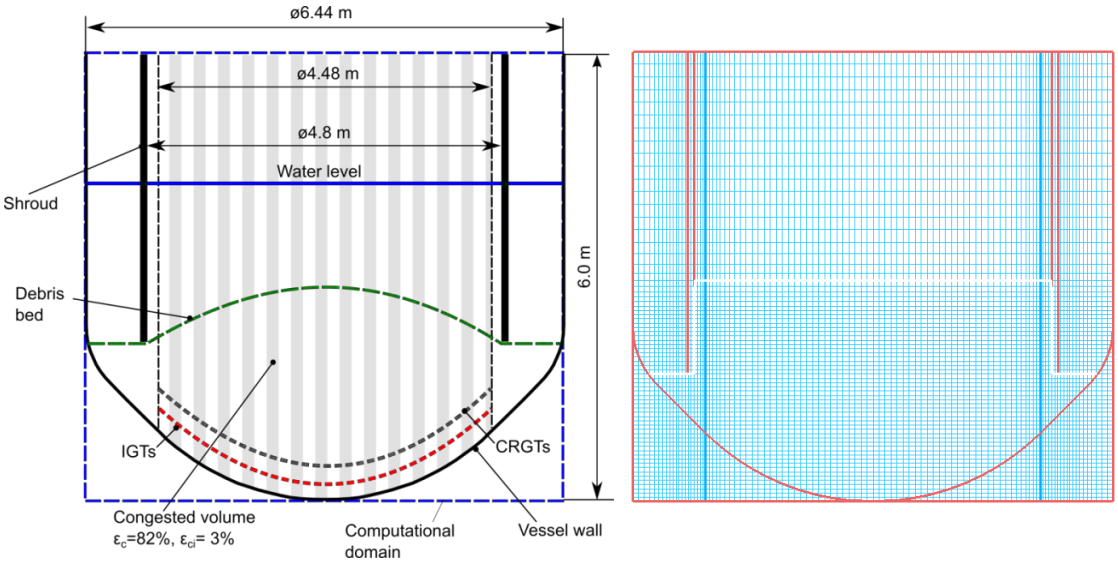

Figure 3.37. Sketch of reactor pressure vessel geometry and computational domain (a), numerical grid (b).

Two debris bed shapes are considered in this work: i) flat-top (corresponding to uniform dripping of core material through the core support plate, or intensive lateral redistribution of corium particles by convective flows); and ii) Gaussian-shaped heap, with the maximum on the axis of symmetry (corresponding to relocation of the large fraction of the core though the central part of the core support plate, e.g. see [64]). Note that some amount of melt can pass through the coolant inlets in the lower part of the shroud (see the horizontal "wings" of the schematic debris bed shape in Figure 3.37). The height of debris bed was determined by its mass M (100, 150, and 200 t), with the porosity taken equal to $\varepsilon = 0.4$. Simulations were performed for particle diameters

d_p = 1.5, 2.0, and 3.0 mm, the specific decay heat power was varying in time, with the core relocation time chosen to be t_r = 1.5 h on the basis of MELCOR simulations for Nordic-type BWRs.

The physical properties of corium were taken from [163]: in the solid state ρ_{sol} = 8285 kg/m^3, λ_{sol} = 1.9 W/m·K, C_{sol} = 566.2 J/kg·K, for melt state ρ_m = 7121.6 kg/m^3, λ_m = 3.6 W/m·K, C_m = 680.7 J/kg·K, the melting temperature is T_m = 2750 K, specific fusion heat is ΔH_m = 428 kJ/kg. The properties of the structural elements were taken constant and characteristic of stainless steel: ρ_c = 7800 kg/m^3, λ_c = 15 W/m·K, C_s = 500 J/kg·K.

Simulations were carried out on a Cartesian grid having 50 × 70 cells in the radial and vertical directions, respectively, see Figure 3.37b. The grid was refined in the debris bed and near the vessel walls and shroud: the minimum and maximum grid cell sizes in the radial direction were 4 and 8 cm, while in the vertical direction the grid cell sizes varied between 5.5 and 17 cm.

3.4.5 **In-vessel Debris Coolability Analysis with DECOSIM**

Next, we present results of DECOSIM Full model calculations. The vessel geometry of a reference design of Nordic-type BWRs is used in simulations (Figure 3.38). A vertical cylindrical shroud is present in RPV which can restrict the lateral spreading of debris in the case of core meltdown and fragmentation. In the bottom part of the shroud, there are windows for coolant inflow. The assumed shape of the top boundary of debris bed repeats the shape of bottom wall of the lower plenum (shown by solid curves in Figure 3.38). The dashed lines (at the heights of 0.17 and 0.4 m above the vessel bottom) indicate positions of IGTs and CRGTs nozzle welding points. Failure of the welds can result in fallout of CRGTs or IGTs leaving paths for melt to escape the reactor vessel possibly before vessel wall loses its integrity [67].

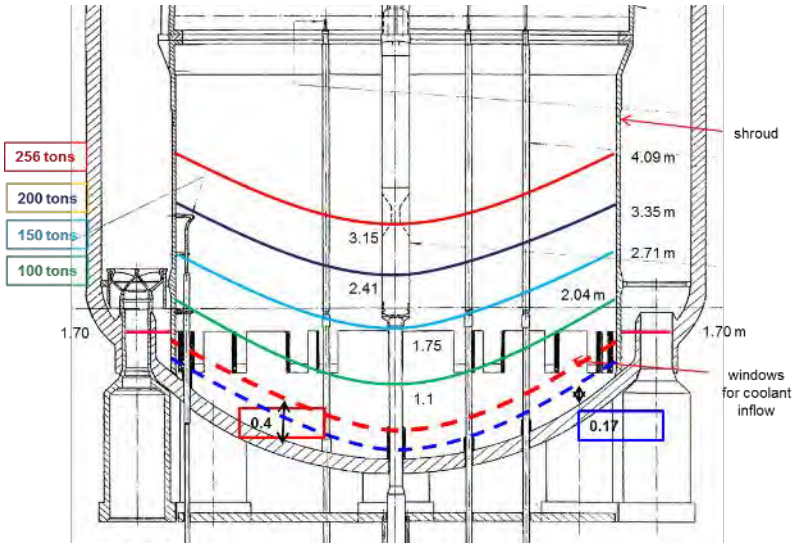

Figure 3.38. Sketch of reactor pressure vessel geometry and assumed debris bed shape.

The following properties of materials were assumed: i) Corium properties in the solid state: density ρ_s = 8285.1 kg/m^3, specific heat capacity C_s = 566.2 J/kg K, heat conductivity λ_s = 1 W/m K; ii) Corium properties in the liquid state: density ρ_s = 7121.6 kg/m^3, specific heat capacity C_s = 680.7 J/kg K, heat conductivity λ_s =

3.6 W/m K; iii) Corium melting temperature: $T_m = 2750$ K, melting heat $\Delta H_m = 4.28 \cdot 10^5$ J/kg; iv) Decay heat specific power was calculated according to ANS 5.1 standard curve, with time after SCRAM equal to the sum of core relocation time t_r and simulation time t; the core relocation time was taken to be $t_r = 1.5$ h and 3 h (based on results of MELCOR simulations for the reference design of Nordic-type BWR); v) Properties of steel: density $\rho_s = 7800$ kg/m^3, specific heat capacity $C_s = 500$ J/kg K, heat conductivity $\lambda_s = 15$ W/m K. Simulations were carried out for the following debris bed properties: i) Particle diameter d = 1 – 3 mm; ii) Porosity $\varepsilon = 40$ %; iii) Total mass of debris bed: $M = 100 - 200$ t. Scenario-dependent parameters: System pressure: 3 bar (was set on the top of the computational domain, 4 m above the RPV bottom point).

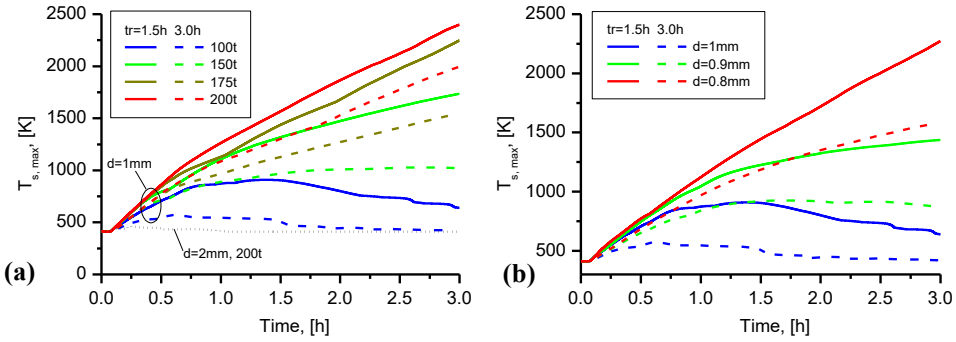

Figure 3.39. Time histories of maximum temperature of solid material in initially quenched debris bed: 1-2 mm particles (a); sub-mm particles (b).

In the initially quenched debris bed case, the initial state of the debris bed was completely filled with water, and the temperature of solid particles was equal to the saturation temperature at the local pressure. Simulations have shown that debris bed coolability is strongly affected by the particle diameter. For 3 mm particles, the debris bed was coolable for all melt masses and relocation times; local dryout did not occur and cooling of the material was provided by water evaporation, the maximum solid particle temperature remained close to the local saturation temperature. For 2 mm particles, local dryout was observed for the largest mass of debris bed $M = 200$ t at the relocation time $t_r = 1.5\,h$, however, in this case the maximum superheat of particles with respect to the saturation temperature was about 50 K, after about 1 hour the dry zone was reflooded again, the solid material temperature remained close to saturation afterwards. For 1 mm particles, debris bed coolability depends on the total mass M and relocation time t_r. Results of simulations are summarized in Figure 3.39 (a) where time histories of the maximum temperature of solid material are shown for 1 mm particles; also, one curve (dotted line) is also shown for 2 mm particles in the above-mentioned case where temporary dryout occurred in the debris bed. Dryout occurs for 1 mm particles in all the cases, however, its consequences depend on the debris bed mass and relocation time. For example, debris bed with $M = 100$t is reflooded after 1.5 hours for $t_r = 3.0\,h$ (i. e., 4.5 hours after SCRAM), while for $t_r = 1.5\,h$ no total reflooding occurs during the whole simulated period (3 h after relocation), however, the maximum temperature remains below 1000K, decreasing gradually after 1.5 h. With the debris bed mass of $M = 150$t, temperature is stabilized at a level of about 1000 K for the relocation time $t_r = 3.0\,h$. All other cases for 1 mm particles are featured by steady temperature escalation, however, none of the cases was featured by oxidic debris material melting during the first three hours after core relocation. Thus, for 1 mm

particles, only for the smallest debris bed mass of $M = 100$t a stable configuration was obtained.

To estimate the margin to the coolability boundary, additional simulations were carried out with two smaller particle diameters, $d = 0.9$ and 0.8 mm (Figure 3.39*b*) for the debris bed mass of 100 t. Particle diameter 0.9 mm represents approximately the boundary between the cases of temperature stabilization and escalation. It should be kept in mind, however, that in the melt-coolant interaction experiments performed at KTH and results with prototypic corium compositions available in the literature (e.g., FARO experiments) such small mean particle diameter was never observed. Therefore, it is reasonable to conclude that fragmented debris beds with mass below 100 t are going to be coolable in the severe accident conditions, provided that sufficient water inventory is maintained in the reactor pressure vessel. The coolability results obtained for initially quenched debris bed are summarized in Figure 3.40 where color coding is use to mark the cases where temperature escalation (red), temperature stabilization (green), or "no dryout" or "dryout followed by reflooding" (blue) was observed within 3 hours after core relocation.

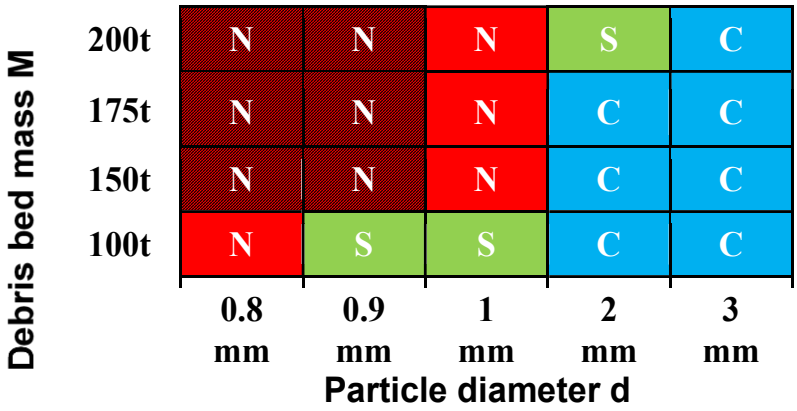

Figure 3.40. Summary of coolability results for initially quenched debris bed. N - non-coolable with temperature escalation, S - dryout with temperature stabilization, C - coolable (no dryout, or dryout followed by reflooding).

To elucidate the development of dry zone in different conditions, spatial distributions of particle temperatures in debris beds are presented in Figure 3.41 for the debris bed masses of 200, 150, and 100 t; the debris bed shape is shown by the white lines. In all cases the particle diameter was $d = 1$ mm, the relocation time for the smallest and largest debris masses was $t_r = 1.5\ h$, while for the intermediate mass of 150 t results are shown in the case of $t_r = 3.0\ h$ (the latter case was chosen because it corresponds to temperature stabilization, see Figure 3.39). It can be seen in Figure 3.41a–c that for the initially quenched debris bed, dryout develops in the upper zone of the debris bed where the vapor flow rate is the highest and, therefore, water penetration into it is more difficult. Water ingress into the debris bed occurs in the bottom part of the debris bed, the vapor flow is directed upwards. Therefore, the water and vapor flows are co-current, rather than counter-current, as is the case in the one-dimensional problem of flat top-flooded debris bed coolability. In the large debris bed (Figure 3.41a) the dry zone extends over the whole top of debris bed. Remelting of the material may occur approximately 4 hours after core relocation (5.5 hours after SCRAM), and a melt pool will be formed in the top part of the debris bed, blocking vapor evacuation and resulting in total dryout. Later on, the molten material can propagate downwards and reach the reactor vessel. In the medium and small-mass debris beds (Figure 3.41b and c) the, occurrence of dryout is also observed near the top boundary of the debris bed. In the

former case, the dryout zone is stabilized by vapor cooling, in the latter case the dryout zone is of small size and is shrinking with time. The decay heat power is gradually decreasing with time, and even when the temperature looks stabilized (namely, the case of 150 t debris bed with 1 mm particles and both cases of 0.9 mm particles in Figure 3.39), it will actually be decreasing slowly later on, and the size of dry zone will be shrinking accordingly.

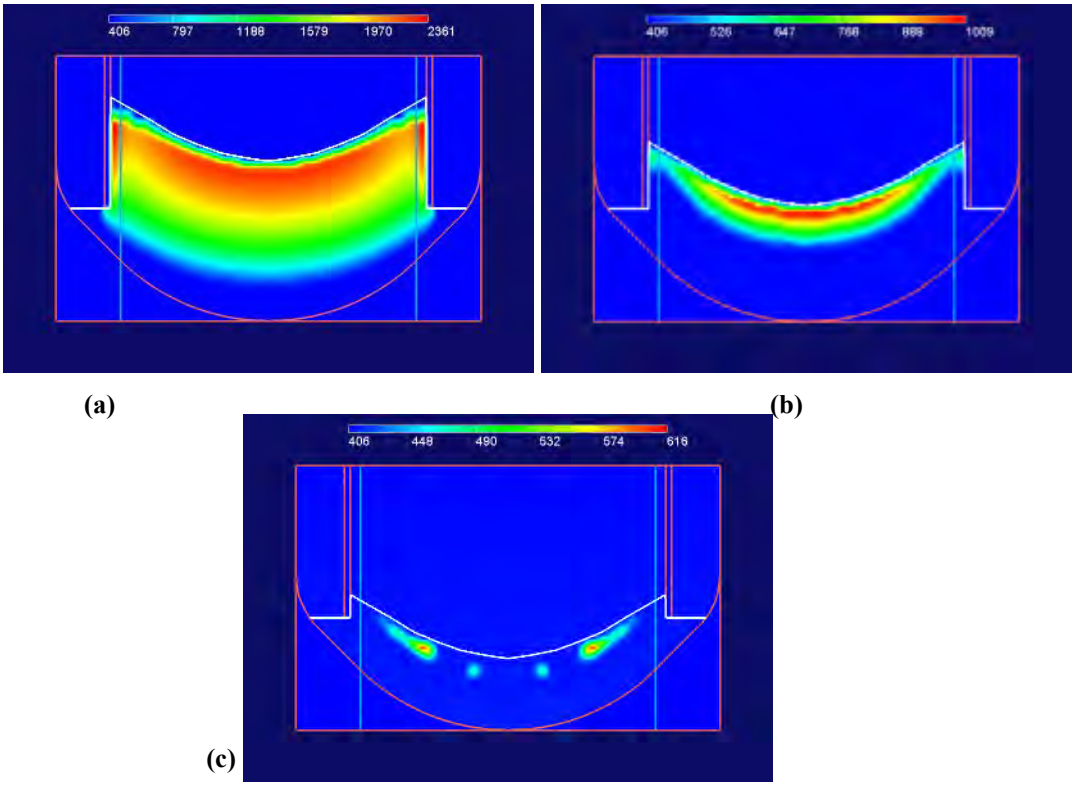

Figure 3.41. Particle temperature in initially quenched debris bed at time t=3 h: (a) $M = 200\ t$, $d = 1\ mm$, $t_r = 1.5\ h$; (b) $M = 150\ t$, $d = 1\ mm$, $t_r = 3.0\ h$; (c): $M = 100\ t$, $d = 1\ mm$, $t_r = 1.5\ h$.

For an initially dry hot debris bed, six cases are considered: debris beds with masses of M = 100 and 150 t and particle diameters of 1 and 2 mm, as well as debris mass M = 200 t and particle diameters 2 and 3 mm; relocation time $t_r = 1.5\ h$. Also, same simulations were repeated for the relocation time $t_r = 3\ h$. The debris bed had initial temperature of 1000K and was initially filled with vapor at the same temperature. The space above the debris bed is filled with saturated water. In these cases, unlike the initially quenched debris bed, the porous material possesses significant initial sensible heat energy which, together with the decay heat, governs the evolution of debris bed. In Figure 3.42, the time histories of maximum temperature of solid material are presented. Initially, the temperature rise rate is the same in all cases, the maximum temperature rise occurring near the shroud. For larger particles, as can be seen from the dashed lines in Figure 3.42, total reflooding of the debris bed occurs after 1–2 hours, and the maximum temperature of solid material falls down to the saturation temperature. For 1 mm particles, as well as for 2 mm particle and corium mass of 200 t, high drag prevents incoming water from reflooding the whole volume of the debris bed, and steady temperature rise can be observed to the levels where remelting of the material can occur. In the case of 200 t – 2 mm debris bed, reflooding occurred for relocation time of 3 h. The time to reach remelting is approximately 2.5 h after core relocation, or 4 h after SCRAM. To demonstrate the process of heatup of an initially dry debris bed, in Figure

3.43–Figure 3.44 the temperature distributions are shown for three of the cases presented in Figure 3.42 in which remelting of porous material occurred. In each case, predicted temperature fields at times 1000 and 10800 s are shown.

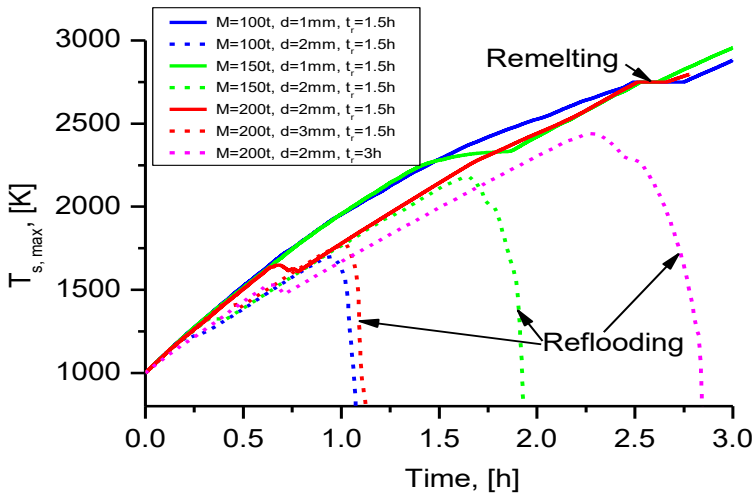

Figure 3.42. Time histories of maximum temperature of solid material in initially dry debris bed with initial temperature 1000 K.

In Figure 3.43, the case of large debris bed ($M = 200\ t$) and moderately small particles ($d = 2\ mm$) is presented. Water ingress occurs along the reactor vessel bottom wall, quenching hot particles and separating the hot debris from the wall, which is important finding for the vessel failure mode. Further ingress of water leads to total detachment of the dry zone from the bottom vessel wall and its shrinking both vertically and horizontally. Eventually, the dry zone becomes localized in the upper part of the debris bed where remelting of the porous material occurs.

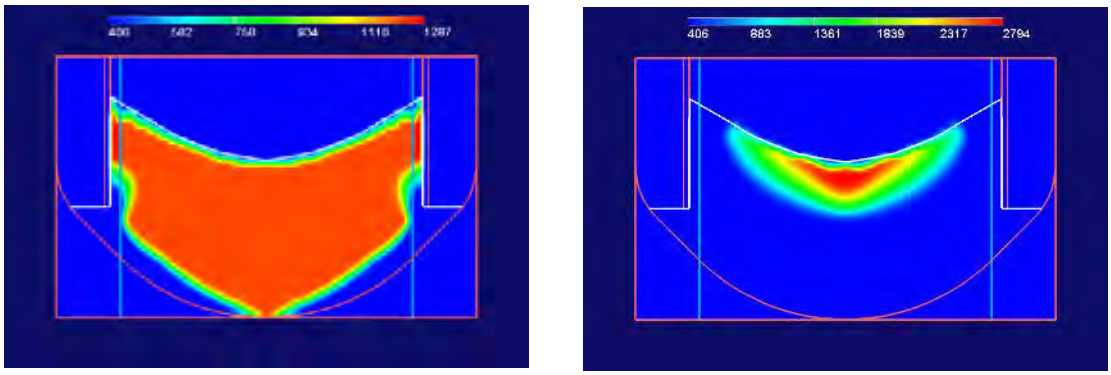

t = 1000 s **t = 10800 s**

Figure 3.43. Particle temperature in initially dry debris bed: $M = 200\ t$, $d = 2\ mm$, $t_r = 1.5\ h$.

For smaller particles ($d = 1\ mm$), high drag in the porous medium significantly hinders water ingress into the debris bed. It can be seen in Figure 3.44 (for debris mass of 100 t) that water front can penetrate along the vessel wall only to approximately half the distance between the windows and axis of symmetry. Also noticeable is water ingress through the upper boundary of the debris bed. For the smallest debris bed mass (Figure 3.44), water front reaches the bottom of reactor vessel by the time 3 h after core relocation. Similar processes are observed for the medium mass (150 t), but the top

water front propagates downwards to about half of debris bed height near the axis. Thus, in all the cases some part of debris remains dry; the temperature in these zones increases and reaches the melting point. To elucidate this, in Figure 3.45 the mass fractions of molten corium are shown at the final instant $t = 3\,h$ (i. e., 4.5 h after SCRAM). Evidently, in the last two cases remelting and high temperatures are reached in the bottom part of the debris bed in the vicinity of the vessel wall.

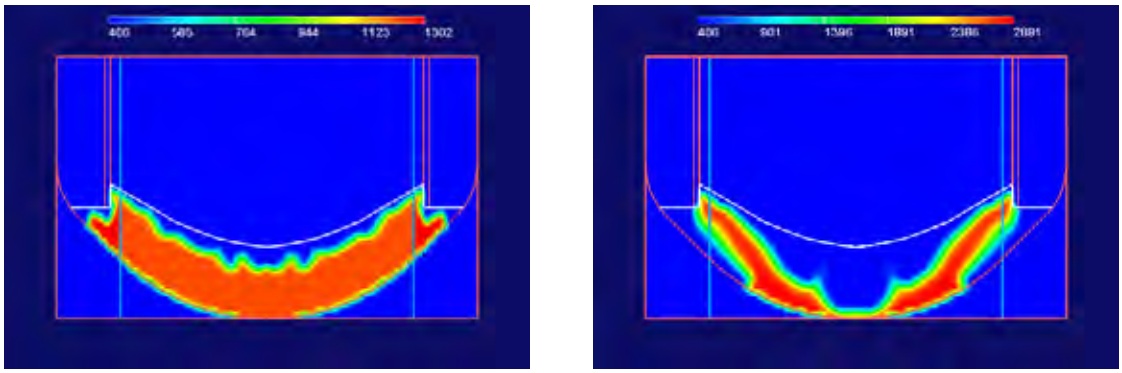

t = 1000 s **t = 10800 s**

Figure 3.44. Particle temperature in initially dry debris bed: $M = 100\,t$, $d = 1\,mm$, $t_r = 1.5\,h$.

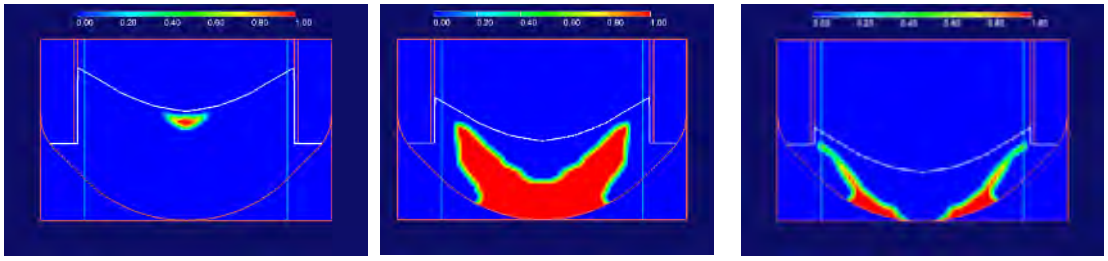

M = 200t, d = 2 mm **M = 150t, d = 1 mm** **M = 100t, d = 1 mm**

Figure 3.45. Melt fraction at time t=3 hours in the initially dry debris bed.

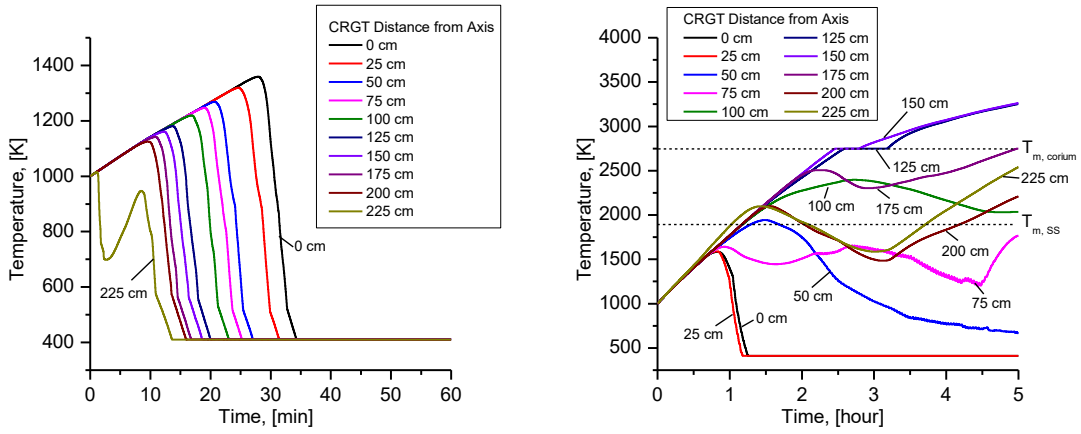

M = 200t, d = 2 mm **M = 100t, d = 1 mm**

Figure 3.46. Time histories of temperatures at CRGT welding points.

In Figure 3.46, the temperatures at the levels of CRGT welding points are shown,

demonstrating rapid quenching of debris bed for M=200 t and d=2mm (the maximum temperature remains below the melting point for stainless steel). However, in the case of small particles (M=100 t, d=1 mm), only the central CGRTs are reflooded completely, while all other CRGTs feature some temporary temperature decrease, turning into secondary reheating because of shrinking of the reflooded zone with time.

Table 3.6 summarizes the coolability of the debris bed and possible model of melt release depending on the initial state of the debris bed. For an initially wet debris bed, it is found to be coolable if the debris mass is less than 100 tons with large particles (>2 mm). On the other hand, if the debris mass is larger and the particle size smaller, a massive melt release is expected. The same scenario is expected for an initially dry debris bed with large mass and large particle sizes. The massive melt release provides conditions for (i) formation of a non-coolable debris bed, and (ii) energetic steam explosion. A dripping melt release is expected for an initially dry debris bed with small mass and small particle sizes. Therefore, the initial conditions of the debris bed are important factor for the melt ejection mode. However, further clarifications are necessary for the core relocation scenarios and possible debris bed sizes.

Table 3.6: Coolability of the debris bed and possible mode of melt release depending on the initial state of the debris bed.

Initial state of debris bed	Debris bed properties	Coolable bed	Dripping melt release	Massive melt release
Wet	Small mass (<100 t) Large particles (>2mm)	**Yes**	-	-
	Large mass (>100 t) Small particles (<1mm)	-	-	**Yes**
Dry	Small Mass (<150t) Small particles (~1mm)	-	**Yes**	-
	Large Mass (>150 t) Large particles (>2mm)	-	-	**Yes**

3.4.6 **Simulation Cases**

Simulations were run for 10,800 sec (3 hours), which, for the chosen relocation time $t_r = 1.5$ h, corresponds to the period from 1.5 to 4.5 hours after SCRAM. During this period, the specific decay heat power drops from $W = 179$ to 132 W/kg. In all cases, the initial temperature of debris bed was $T_s^0 = 1000$ K, the porous medium was filled with single-phase water vapor ar the same temperature. On the top boundary of the computational domain, constant pressure $P_0 = 3$ bar was maintained, the initial temperature of water and gas temperature in the upper space were equal to $T_0 = 405.8$ K, so that the pool is at saturation conditions. Initial water level was set to $H_w = 4.0$ m in all simulations.

In Table 3.7, parameters of all simulations are summarized; also given are the maximum local melt fractions and total masses of melt at the final time, see the three rightmost columns.

Table 3.7: Parameters of simulations and melt masses at time $t = 3$ h

Debris mass M, ton	Initial water mass M_w, ton	Particle diameter d_p, mm	Total evaporation time t_{ev}, h	Max. melt fraction χ, [-]	Mass of melt M_m, ton
Flat Top					
100	55.0	1.5	2h55m	0.19	1.9
		2.0	2h15m	0.38	0.1
150	47.5	1.5	2h50m	0.45	15.8
		2.0	2h10m	0.64	17.3
200	39.1	1.5	2h30m	0.54	43.1
		2.0	2h15m	0.63	37.2
		3.0	1h55m	0.59	29.8
Gaussian-shaped Heap					
100	56.2	1.5	3h10m	0.55	7.2
		2.0	2h40m	0.64	2.3
		3.0	2h10m	0	0
150	47.2	1.5	2h45m	0.40	15.5
		2.0	2h10m	0.62	17.8
		3.0	1h50m	0.65	12.1

3.4.7 **Results**

Reflooding of Debris Bed

Consider first the process of reflooding by water of an initially dry and hot debris bed. In Figure 3.47, void fraction distributions are plotted for the debris bed with $M = 150$ t and $d_p = 2$ mm. One can see that water penetrates into the debris bed along the vessel walls, quenching initially hot debris in the near-wall region. By about $t = 1$ h, the receding water level uncovers the top surface of debris bed, and by about $t = 2$ h, all debris bed becomes dry again. Simulations show that no significant penetration of water through the top surface, as was observed for infinite water supply and smaller debris beds in [221], occurs in this case.

In Figure 3.48, temperature field in the debris bed is shown at times $t = 1$ and 3 h. It can be seen that temperature rises steadily in the top part of debris bed where water cannot penetrate. Accordingly, remelting of the material occurs near the debris bed top surface, while temperature rise near the wall is delayed for the total water evaporation time.

Water ingress in the debris bed depends significantly on the drag determined by the mean particle diameter. To elucidate the differences caused by the drag, in Figure 3.49 void fraction distributions are shown at four consequtive instants for the same debris bed, but with smaller particles ($d_p = 1.5$ mm), while in Figure 3.50 temperature fields are shown at the same time as in Figure 3.48. Evidently, the reflooded near-wall zone is thinner in the case of smaller particles, water penetration proceeds slower, and the size of high-temperature zone is larger.

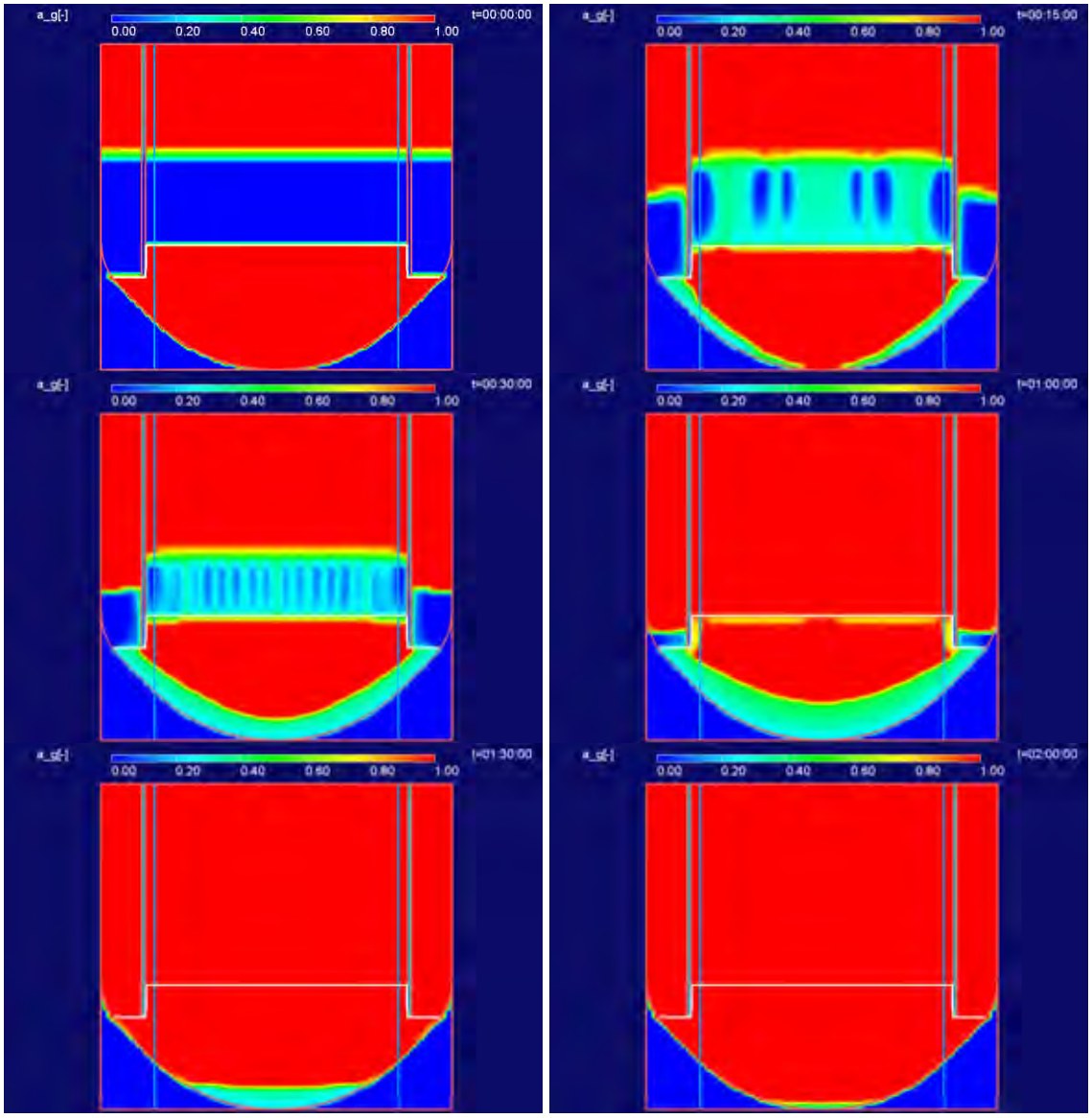

Figure 3.47. Reflooding of initially dry debris bed and subsequent total evaporation of water ($M = 150$ t, $d_p = 2$ mm).

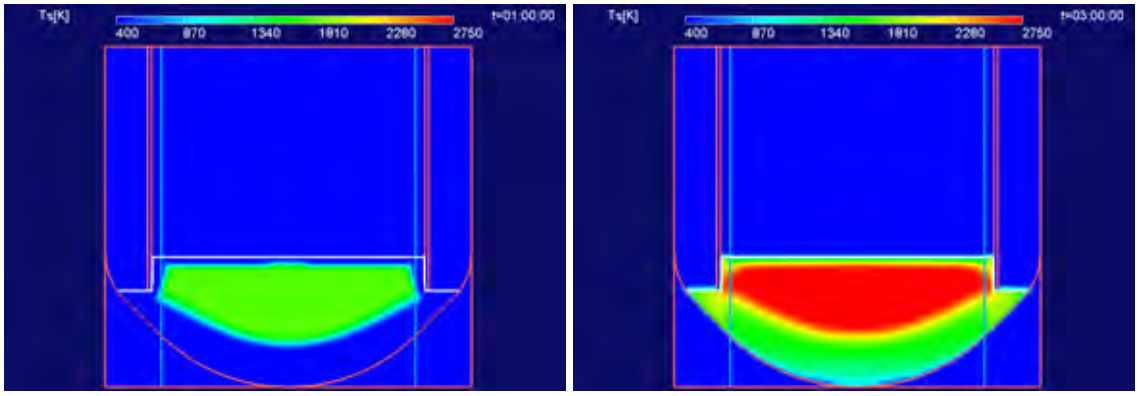

Figure 3.48. Temperature fields in the debris bed ($M = 150$ t, $d_p = 2$ mm).

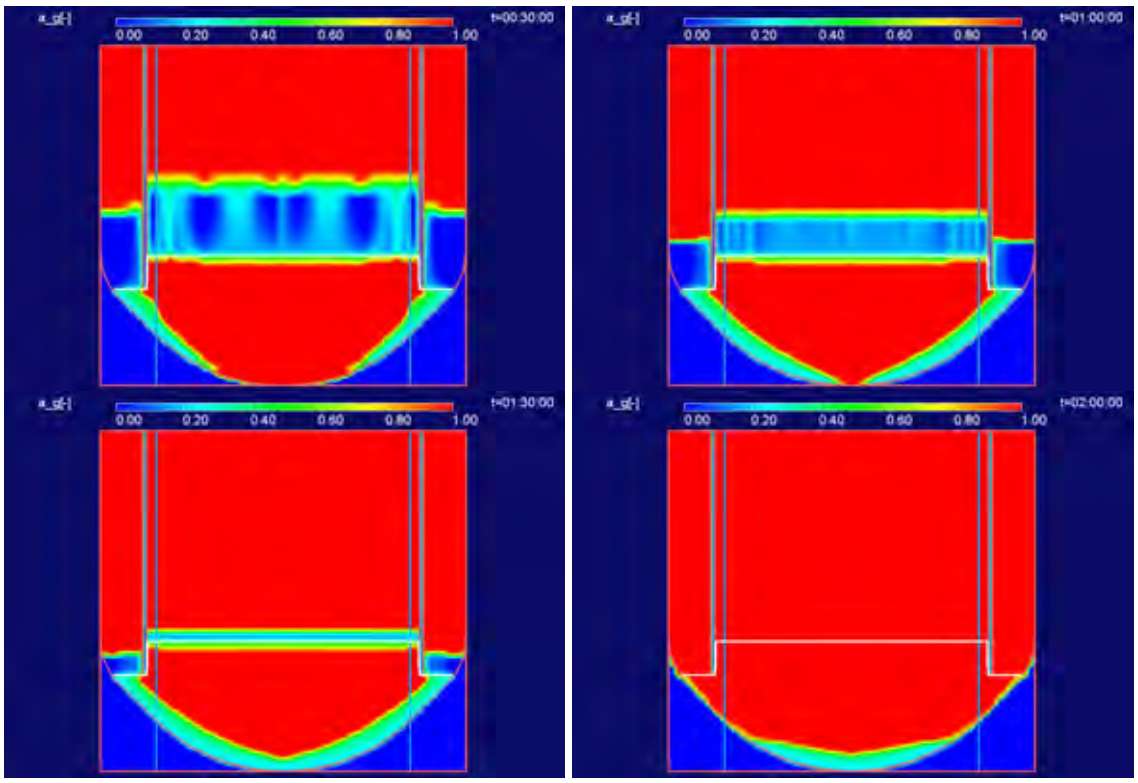

Figure 3.49. Void fraction distributions upon reflooding of initially dry debris bed ($M = 150$ t, $d_p = 1.5$ mm).

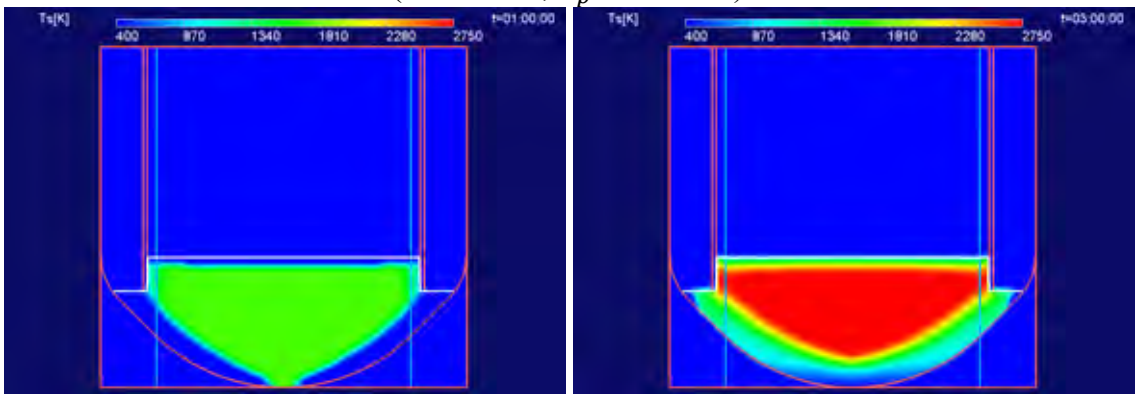

Figure 3.50. Temperature fields in the debris bed ($M = 150$ t, $d_p = 1.5$ mm).

Influence of Debris Bed Shape and Mass on Remelting Patterns

The processes occurring in initially dry debris beds of different shapes and masses are qualitatively similar to those considered previously. Since the amount of water is limited, debris reheating and remelting becomes inevitable after complete water evaporation. However, rewetting of some parts of debris bed proceeds differently, depending on the debris bed shape and size. In this section, we compare the remelting zones developed by the time $t = 3$ h over which simulations were run. Note that in the current DECOSIM model, no melt propagation is accounted for, and the results can be viewed as indication of probable outcome of debris bed reheating, rather than detailed modeling of the remelting stage.

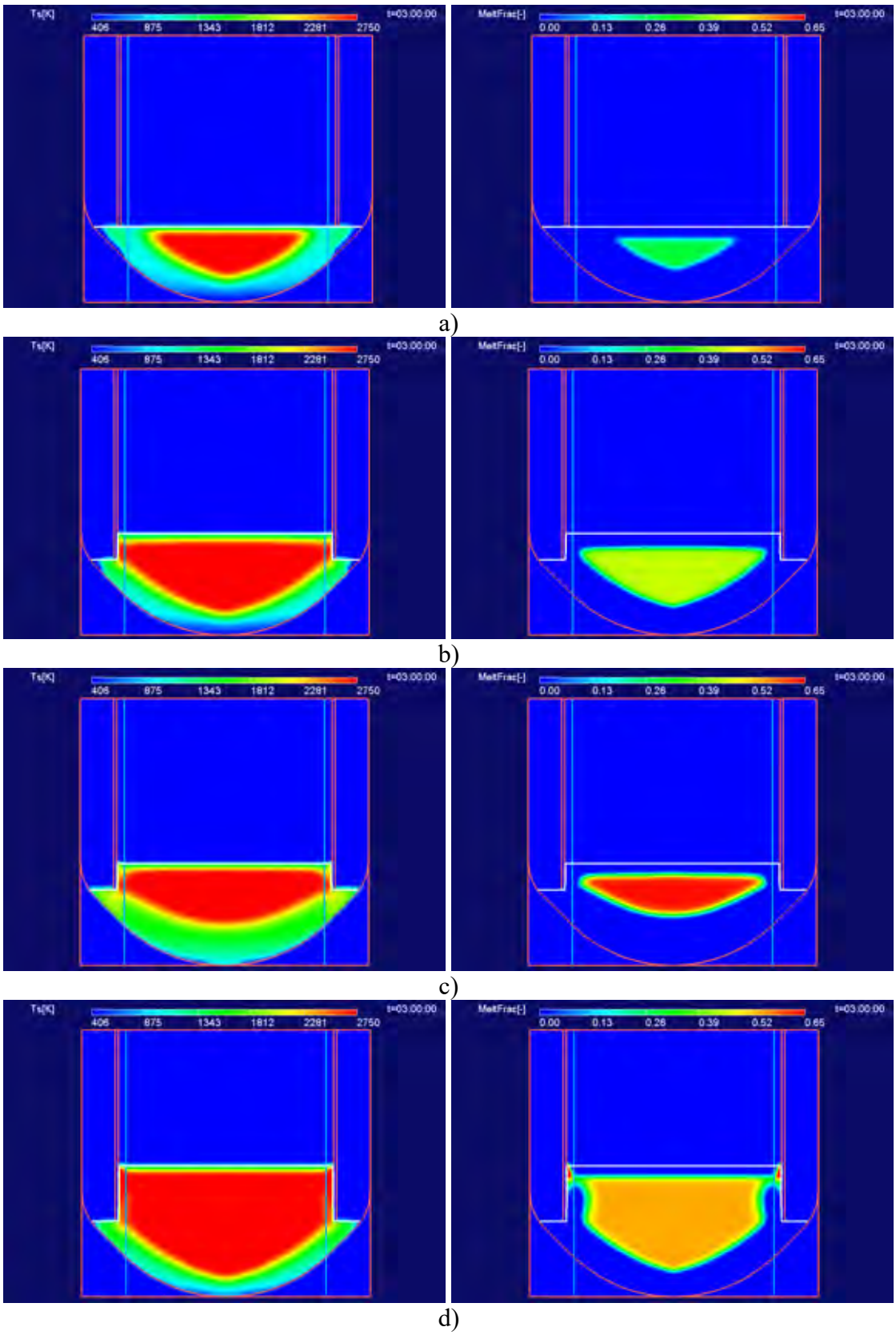

Figure 3.51. Temperature T_s (left) and melt fraction χ (right) in flat-top debris beds at $t = 3$ h after relocation: a) $M = 100$ t, $d_p = 1.5$ mm, b) $M = 150$ t, $d_p = 1.5$ mm, c) $M = 150$ t, $d_p = 2.0$ mm, d) $M = 200$ t, $d_p = 1.5$ mm

In Figure 3.51 distributions of temperature (left column) and melt fraction (right column) are shown for debris beds with flat top, at different debris masses and particle diameters. In Figure 3.52, the same distributions are presented for heap-shaped debris

beds. The masses of melt and maximum melt fraction at the final simulation time $t = 3$ h are listed in the two rightmost columns in Table 3.7. It can be seen that in all cases remelting occurs in the top part of debris bed, while temperature rise in the near-vessel wall region is delayed due to initial water penetration; therefore, the temperature distributions developing in the debris bed are non-uniform.

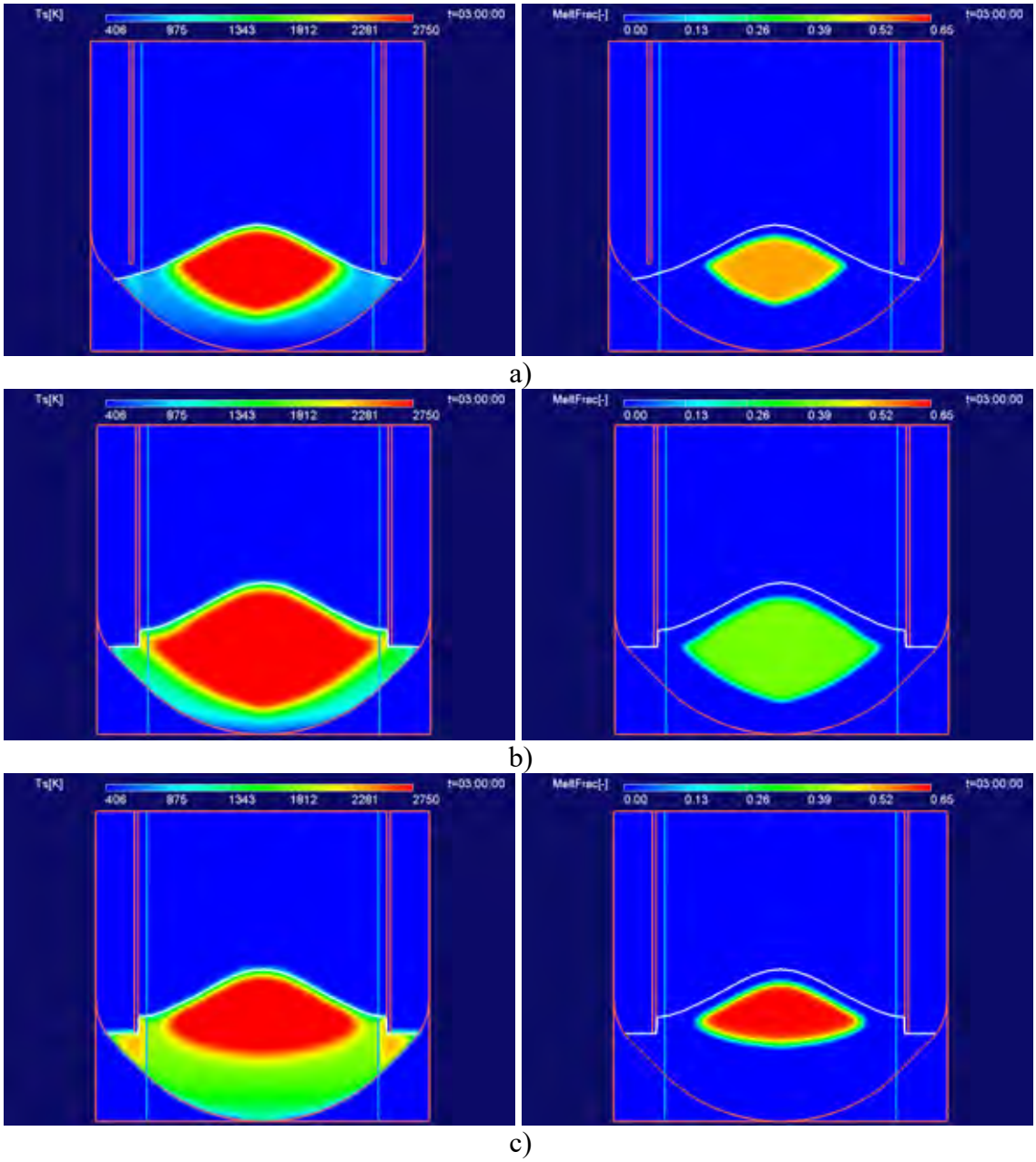

Figure 3.52. Temperature T_s (left) and melt fraction χ (right) in Gaussian heap-top debris beds at $t = 3$ h after relocation: a) $M = 100$ t, $d_p = 1.5$ mm, b) $M = 150$ t, $d_p = 1.5$ mm, c) $M = 150$ t, $d_p = 3.0$ mm

By examining the data in Table 3.7, one can infer that the time to total water evaporation depends significantly on the particle diameter, even though for each particular configuration the decay heat power and initial amount of water remain the same. This dependence is attributed to different rates at which water penetrates into initially dry debris beds with different permeabilities. For larger particle diameters, water penetration is faster, and, therefore, with limited amount of water, total evaporation occurs faster.

Implications for Vessel Failure Mode

From the severe accident analysis point of view, it is important to know not only the integral characteristics of temperature rise and remelting in the dry zone, but also location of hot temperature zones with respect to the vessel wall and structures. In particular, for Nordic-type BWRs having penetrations in the bottom vessel wall for CRGTs and IGTs, one of the possible vessel failure modes is local failure of welding of CRGT and IGT to the penetration nozzles located at elevations of 0.4 and 0.17 m above the vessel wall (see Figure 3.38). Failure of these welding points by remelting can lead to loss of pressure vessel integrity, draining of water, and gradual release of melt in the form of relatively thin jets (as opposed to global vessel failure and melt release in a single large jet).

In Figure 3.53, the time histories of CRGT and IGT temperatures at different radial locations are shown for the $M = 150$ ton heap-shaped debris bed (see Figure 3.52,b-c) with particle diameter $d_p = 1.5$ mm (a) and 3.0 mm (b); these plots are also typical of those obtained for different debris bed configurations.

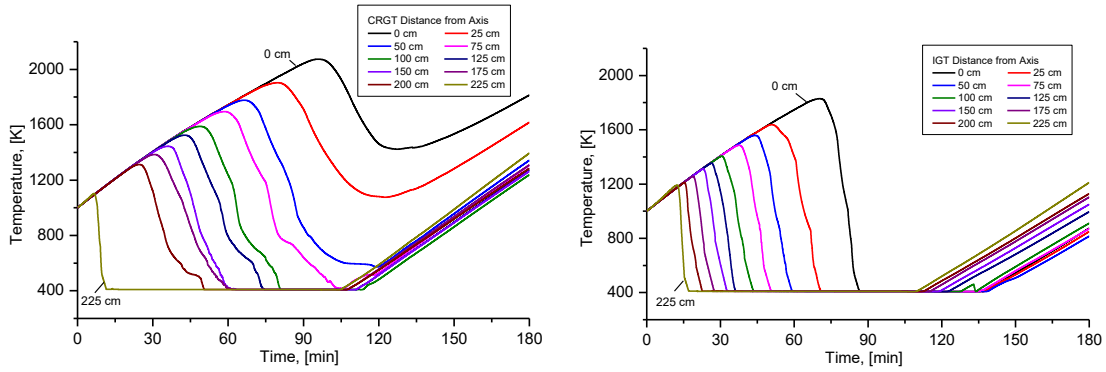

a)

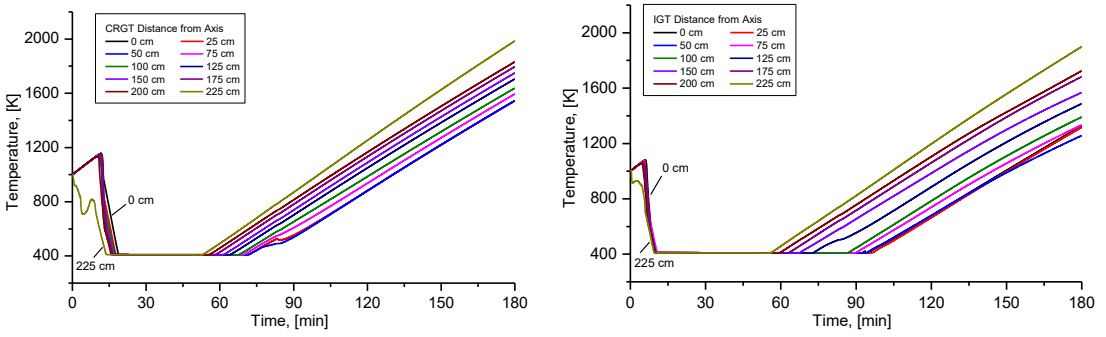

b)

Figure 3.53. Temperature of CRGT (left) and IGT (right) welding points at heights 0.4 and 0.17 m above the bottom vessel wall, respectively, for heap-shaped debris bed with $M = 150$ t; radial positions are indicated in the legends: a) $d_p = 1.5$ mm, b), $d_p = 3.0$ mm.

One can see that the curves consist of two distinct parts: initial temperature rise followed by rapid drop after quenching of near-wall zone by water entering the debris bed along the vessel wall, and steady temperature rise starting with some delay over which water evaporates completely from the debris bed. These two stages are most clearly seen for the larger particles (Figure 3.53,b): the initial quenching occurs over the time of about 15 min, during which the temperature at all positions does not rise by

some 200 K above the initial level of 1000 K. Thus, early failure of CRGTs and IGTs is not expected. The secondary reheating starts with the delay of about 60-90 min, depending on the position; this time is determined by propagation of the receding water level as the amount of liquid in the debris bed is decreased.

For smaller particles, however, water ingress is slower, reflected by longer duration of each stage in Figure 3.53,a. Moreover, for the near-axis CRGTs no complete quenching of the material occurs, so that quite early failure can be expected. The secondary reheating also begins later, reflecting slower water evaporation discussed above.

3.5 Vessel Failure Analysis

3.5.1 Vessel Failure Full Model Results

An important element in the development of the vessel failure SM is the generation of a database of debris reheating, remelting, and melt-interaction with vessel wall and structures. For this purpose, the sufficiently-accurate full models DECOSIM [35] and PECM/ANSYS ([233], [85]) are used. The DECOSIM and PECM/ANSYS codes are complementary approaches which describe two different classes of scenarios with initially (i) porous debris bed and (ii) “solid cake” bed, respectively.

The DECOSIM code that was developed earlier for ex-vessel applications is extended to the in-vessel case by taking into account congestion of lower plenum by structural elements, heat transfer in the vapor phase, as well as remelting of the corium material. Also, the thermal hydraulics module of the code was enhanced to make simulations possible at high temperatures, characteristic of the post-dryout stage of accident progression, including the correlations for boiling heat transfer at different superheats (“boiling curve”) and properties of solid material and water vapor at high temperatures. One of the strengths of the in-vessel DECOSIM is to determine if a porous debris bed is coolable (which then belongs to the non-failure domain) or non-coolable. The non-coolable debris bed requires further assessment (i.e., DECO, SEIM).

The PECM is implemented in the commercial code FLUENT® and simulates the debris bed heatup, remelting, melt pool formation and heat transfer. A coupled thermo-mechanical creep analysis is carried out with ANSYS® code where transient heat transfer characteristics from PECM are used as boundary conditions. The deformation of the vessel wall is assumed to have negligible effect on the melt pool heat transfer, so only one way coupling between PECM and ANSYS is employed.

Vessel Failure Analysis with PECM

Previous PECM-ANSYS calculations [85] were done using a 3D slice model of the lower head (see Figure 3.54b). A more detailed 3D quadrant model of the lower head has also been used but it is computationally expensive. To combine the accuracy of the 3D quadrant model and the efficiency of the 3D slice model, an effective 3D slice model was developed by preserving (i) the cooled surface to heated volume ratio, (ii) surface area (in contact with the debris bed) to volume ratio, and (iii) mechanical load to the vessel wall (due to the penetrations) as in the 3D quadrant model.

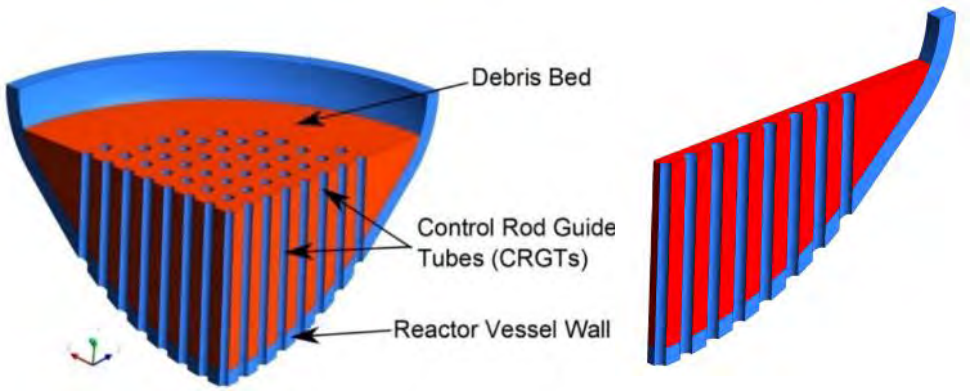

Figure 3.54. Geometry of (a) 3D quadrant and (b) 3D Slice used in PECM.

The debris averaged temperature and melt fraction are presented in Figure 3.55 providing comparison for the (a) 3D quadrant, (b) slice model [85], and (d) effective slice model. Reference time (t = 0) corresponds to the start of PECM simulation, i.e. when core relocation and in-vessel debris bed formation has been finished. This time corresponds to ~2-4 h from SCRAMM, according to MELCOR analyses. The debris averaged temperature and melt mass are in excellent agreement between quadrant and effective slice. The vessel is always depressurized. It has been shown that higher pressure has a small effect on vessel failure timing [66]. Cooling of the CRGTs is considered as possible SAM measure. The debris remelting starts around 2.5 hours, and it intensifies between 2.75 – 3.75 hours; during which more than 50 % (~115 tons of 230) of debris bed becomes molten in all the cases. The vessel wall centerline displacement predicted with the structural analysis is presented in Figure 3.56. It can be seen that displacements in the effective slice model and the 3D quadrant are in excellent agreement until reliably predicted strain is achieved at ~3.7 h. The vessel wall failure time in the effective slice model is ~3 min earlier compared to the 3D quadrant, while the original slice model predicts ~15 min earlier failure.

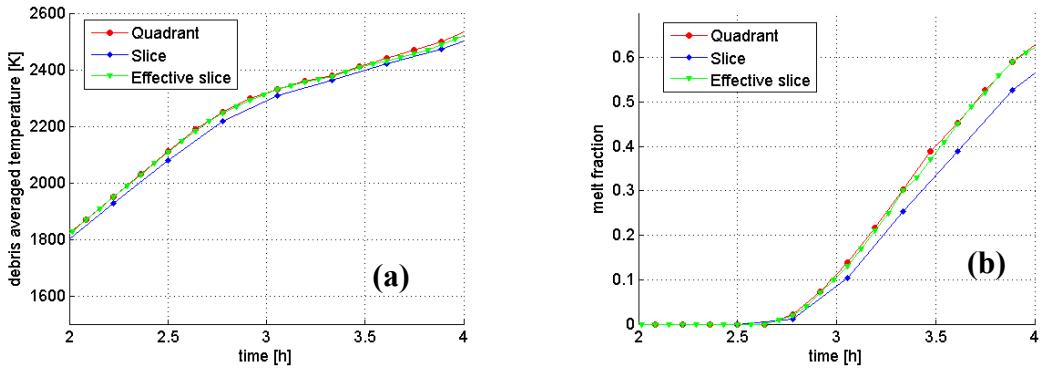

Figure 3.55. (a) Debris averaged temperature and (b) melt fraction as a function of time for both slice and quadrant models.

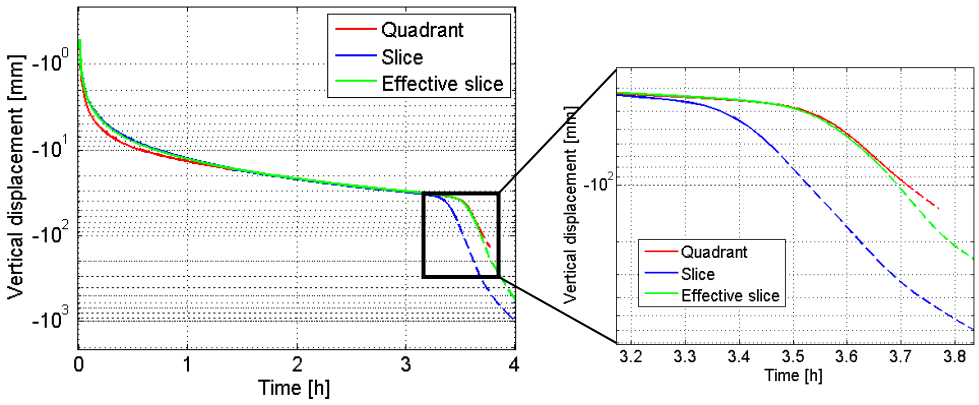

Figure 3.56. Vertical displacement of the vessel bottom centerline for the 3D Quadrant and Effective slice model with axisymmetric 2D mechanical model.

It was also found previously [66] that the thermal conductivity is the most influential parameter for timing of the failure, mass and superheat of liquid melt available for release. Therefore, it is important to consider different configurations and more realistic properties of the debris bed. MELCOR analysis of Core Relocation is used to determine vertical distributions of the debris bed composition and respective properties. Two debris bed configurations are considered (see Figure 3.57): (i) debris bed with horizontal layers; (ii) debris bed with concave layers aligned along the vessel wall. The first configuration can be formed in scenario with melt pool formation in the core region followed by sudden melt drainage to the lower plenum, while the second configuration can be formed in scenario with gradual core melt relocation in dripping mode when lower head is filled with debris layer by layer. Non-homogeneous properties of the debris are obtained using MELCOR analysis. The volumetric decay heat distribution is modeled proportionally to the fraction of total UO_2 mass in each debris bed layer. The major difference between the two configurations is the fact that for concave debris bed the whole vessel surface is uniformly covered with this layer, while for flat configuration layers with high UO2 concentration (and therefore low thermal conductivity, high decay heat) are in direct contact with the vessel wall.

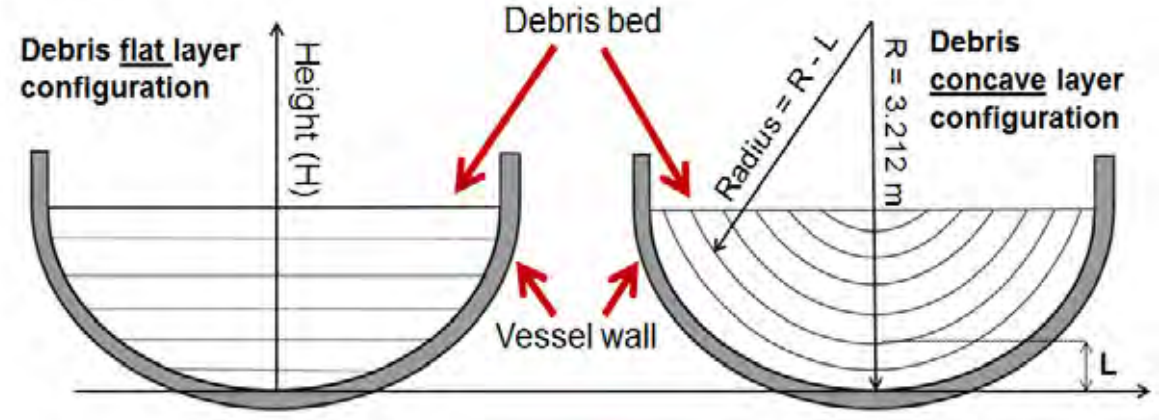

Figure 3.57. Two debris bed models considering different modes of core relocation.

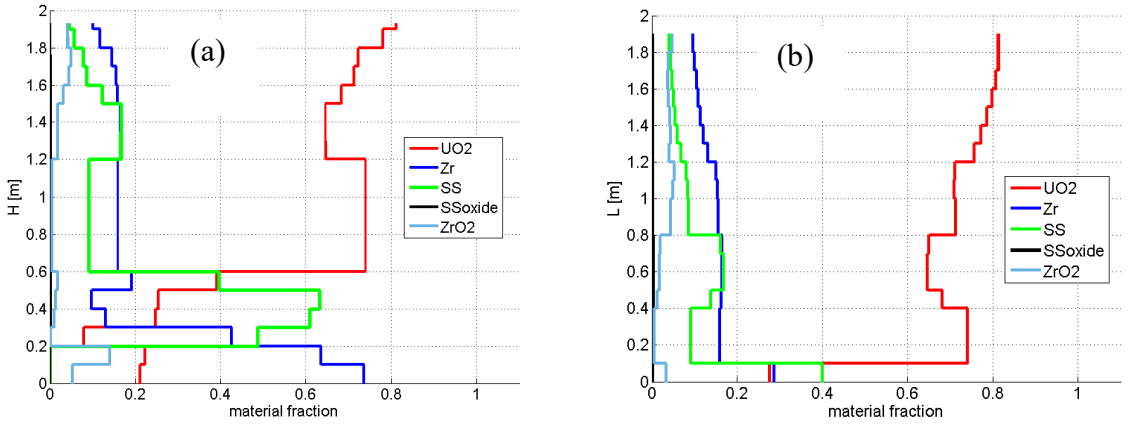

Figure 3.58. Axial composition of debris bed with (a) flat layer and (b) concave configuration at the end of core relocation.

The axial material composition is presented in Figure 3.58 for (a) flat and (b) concave configurations. It should be noted that no activation of ECCS in MELCOR results in low fractions of oxidized steel and zirconium, leading to rather high mass-averaged value of debris solid thermal conductivity. The differences in the material axial profiles between Figure 3.58a and Figure 3.58b are mainly due to the differences between the volume of the layers at different elevations. For example, the volume of the 0.1 m thick layer next to the vessel wall in the concave configuration corresponds to the ~0.6 m layer next to the vessel bottom in the flat configuration (see Figure 3.57).The bottom layers of the debris bed consist mostly of metallic material. The major difference between the two scenarios is that for concave debris bed the vessel surface is uniformly covered with this layer, while for flat configuration, layers with high UO2 concentration (and therefore low thermal conductivity, high decay heat) are also in direct contact with the vessel wall.

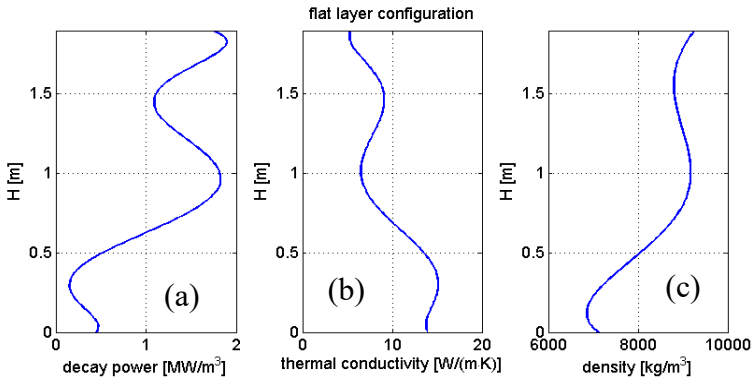

Figure 3.59. (a) Volumetric decay heat, (b) thermal conductivity and (c) density as functions of debris bed height for flat debris bed configuration.

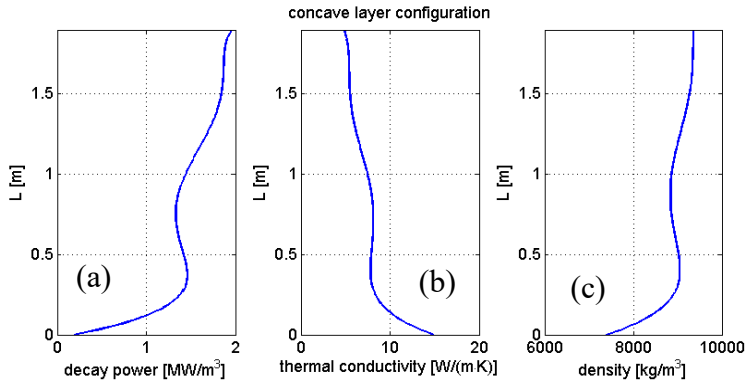

Figure 3.60. (a) Volumetric decay heat, (b) thermal conductivity and (c) density as functions of distance from vessel wall for concave layer configuration.

Based on the material axial distribution, the debris thermal properties are obtained. The thermal conductivity, volumetric decay heat and density are presented as a function of debris bed height in Figure 3.59 for the flat debris bed configuration and as a function of distance from vessel wall in Figure 3.60 for the concave configuration. The UO2 rich regions correspond to locations with highest volumetric decay heat, low thermal conductivity, and maximum density. In Figure 3.61, the thermal conductivities for flat and concave debris configurations are presented. It should be noted that the effective material conductivity is obtained considering a cake-like debris bed with internal porosity and without debris fragmentation, which explains the high values of the thermal parameter.

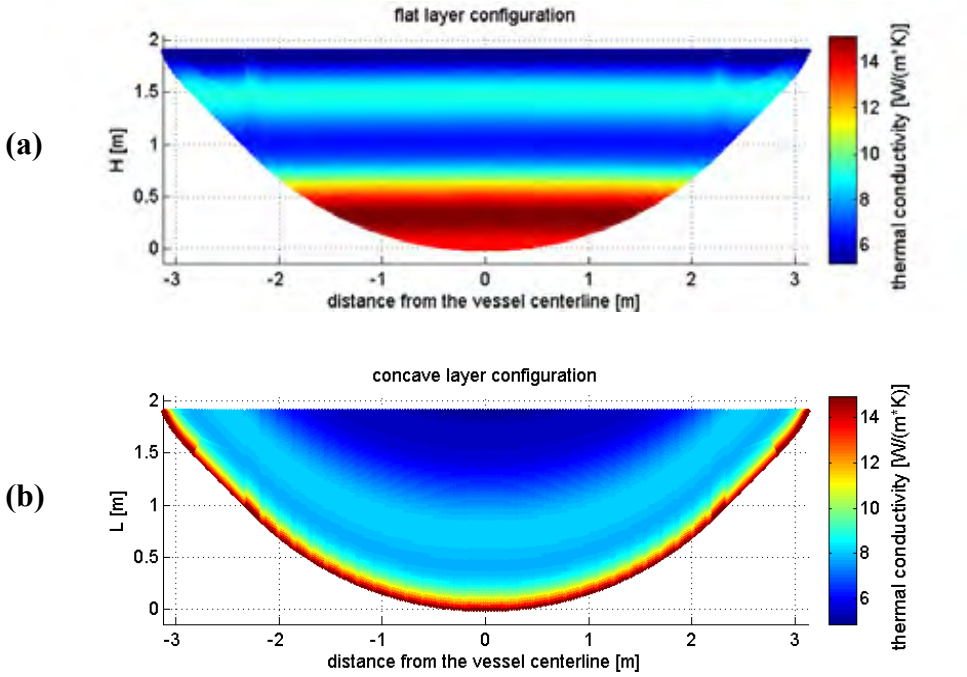

Figure 3.61. Thermal conductivity distribution inside vessel lower head for (a) flat and (b) concave layer debris bed configurations.

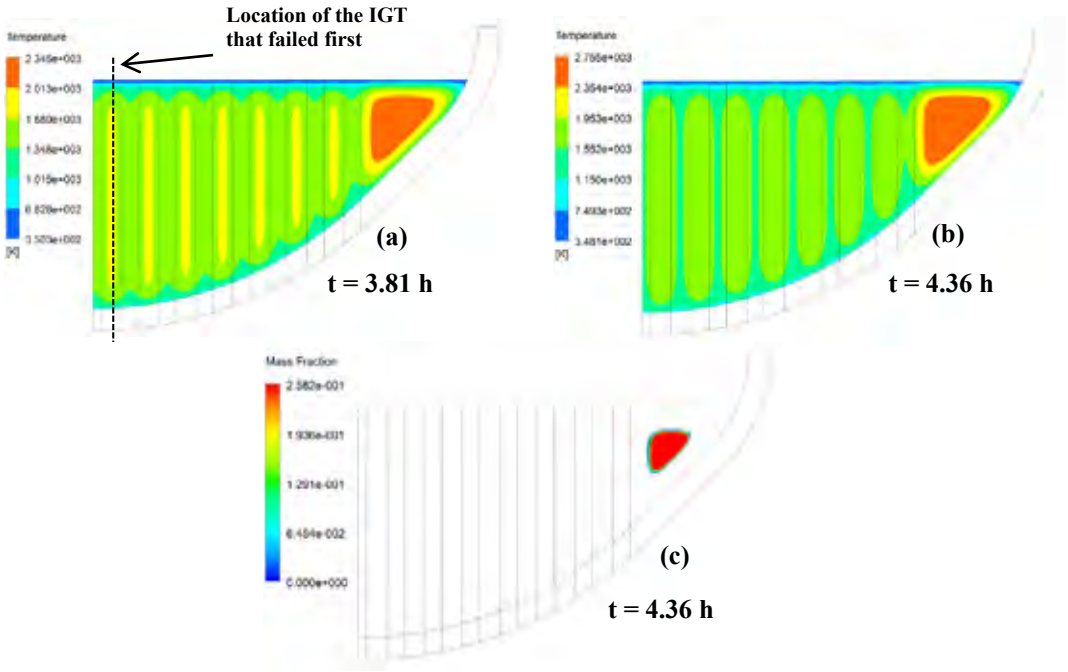

Figure 3.62. Homogeneous debris bed configuration: Temperature profiles between cooled CRGTs at (a) t = 3.81 h, (b) 4.36 h and (c) corresponding amount of liquid melt at 4.36 h.

Temperature profiles for the homogeneous debris bed between cooled CRGTs are presented in Figure 3.62a-b. The failure of an IGT nearest to the vessel centerline is expected at t = 3.83 h (about a minute after snapshot time presented in Figure 3.62a) while failure of other IGTs is expected shortly thereafter (in the order of few minutes). The difference in timing is attributed to the corresponding distances of the IGT nozzles (where failure is assessed) to the inner vessel wall surface. In the BWR design, the IGT nozzles close to the center are farthest away from the inner vessel wall surface compared to the nozzles in the periphery and hence are closer to the bulk of the debris bed having higher temperature than the layers next to the wall (the other nozzles are immersed within the thermal boundary layers). At the time of the first IGT failure the debris bed remains in solid form (see Figure 3.62a where the maximum debris temperature is below debris Tsolidus) and no oxidic melt ejection is expected. The debris bed Tsolidus is reached at 4.22 h, while the location with highest temperature is in the uncooled peripheral debris region. Shortly after that, the vessel wall failure is expected at 4.36 h (see Figure 3.62b). At this time only a minor fraction of debris material has started remelting (1.21 ton with a superheat of 4.9 K) and it is represented as a mushy region in Figure 3.62c.

For a flat layer debris configuration, a different temperature profile was observed (Figure 3.63a-b). The bottom part of the vessel lower head contains mostly metallic material, which produces minor fraction of decay heat and has high thermal conduction. Two pronounced high temperature layers are observed in Figure 3.63a, corresponding to the locations with highest UO2 concentration. These regions are characterized by high volumetric decay heat rate and low thermal conductivity. One of these layers is in direct contact with IGT nozzle weld (IGT located farthest from the vessel centerline) resulting in an early expected failure time at 3.44 h. Similar to the scenario with homogeneous debris bed configuration, there is no oxidic melt at the moment of IGT failure, debris remelting starts at 4.34 h in the uncooled peripheral debris bed region. Shortly after, at 4.51 h, vessel wall failure is expected. At this moment the amount and superheat of the

liquid melt is similar to homogeneous scenario with 0.82 ton at 5 K superheat. The difference in time of vessel wall failure compared to the homogeneous scenario can be explained by the thermal properties profiles (see Figure 3.59a). Two peaks of decay heat, at ~1 m and ~1.8 m, are in the vicinity of cooled region while the layer in-between these peaks (region without CRGT penetrations) contains high metallic material fraction (and thus high thermal conductivity, low decay heat), leading to a lower thermal load to the vessel wall.

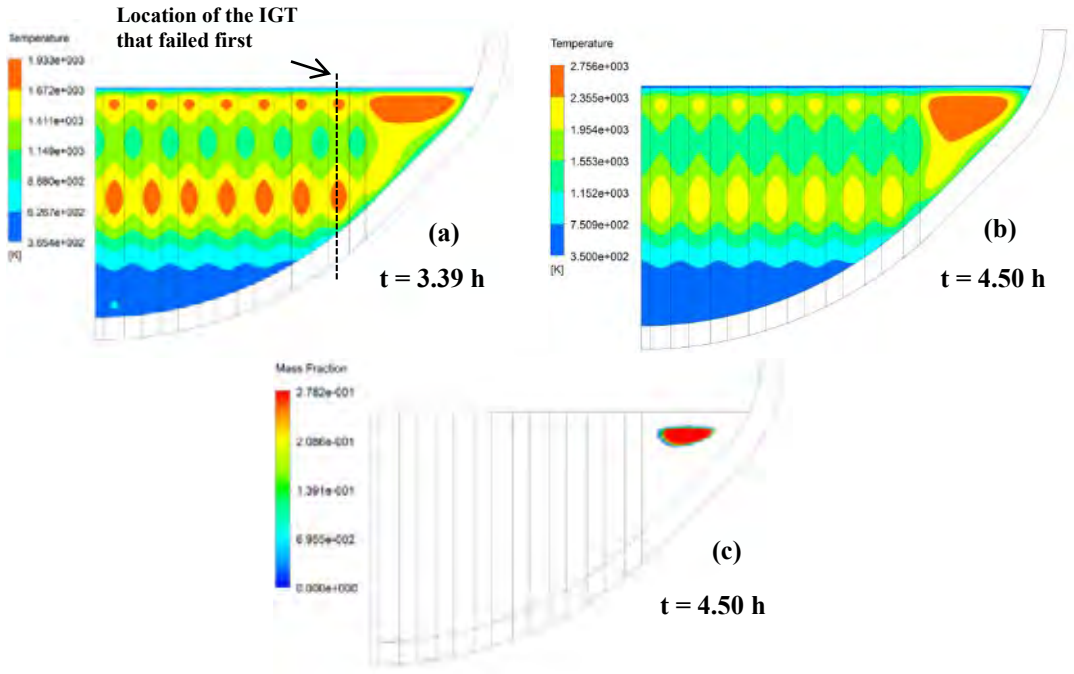

Figure 3.63. Flat debris bed configuration: Temperature profiles of debris bed between cooled CRGTs at (a) t = 3.39 h, (b) 4.50 h and (c) corresponding melt mass fraction at 4.50 h.

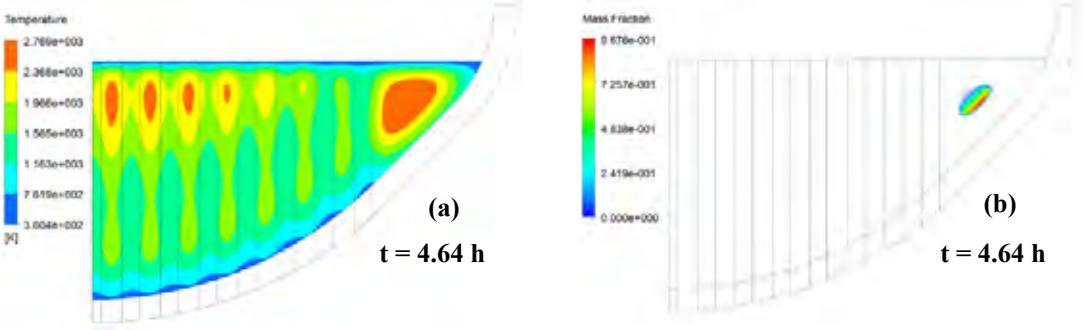

Figure 3.64. Concave debris bed configuration: (a) Temperature profile of debris bed between cooled CRGTs at t = 4.36 h and (b) corresponding melt mass fraction at 4.36 h.

For the concave debris bed configuration, the debris bed temperature profile and amount of liquid melt are presented in Figure 3.64. There was no IGT failure observed in this scenario. This is explained by the mostly metallic layer that covers the vessel wall surface (having low decay heat rate and high thermal conductivity). The temperature gradient in this layer is relatively small. Therefore the IGT nozzles don't reach high

melting temperatures as in the other two cases. The onset of debris remelting is comparable in all cases, from 4.2-4.4 h. At the moment of vessel wall failure at 4.63 h (a moment before the time presented in Figure 3.64b), ~1 ton of liquid melt is formed with 12.6 K superheat and located in the uncooled peripheral debris bed region.

Next, snapshots of the structural analysis of the vessel lower head are presented in Figure 3.65 for the different debris bed configurations. The three simulated scenarios show similar trend, that is, the highest creep strains and deformations are predicted near the debris bed top surface region where there are no CRGT penetrations, while displacements of the bottom part of the vessel are almost uniform. This failure mode is characterized as 'localized creep' as opposed to a ballooning mode for lower melt masses (debris bed with height <1.1 m) [85]. The maximum displacement of the lower head is ~0.09 m for the homogeneous and flat cases, while ~0.07 m for the concave configuration.

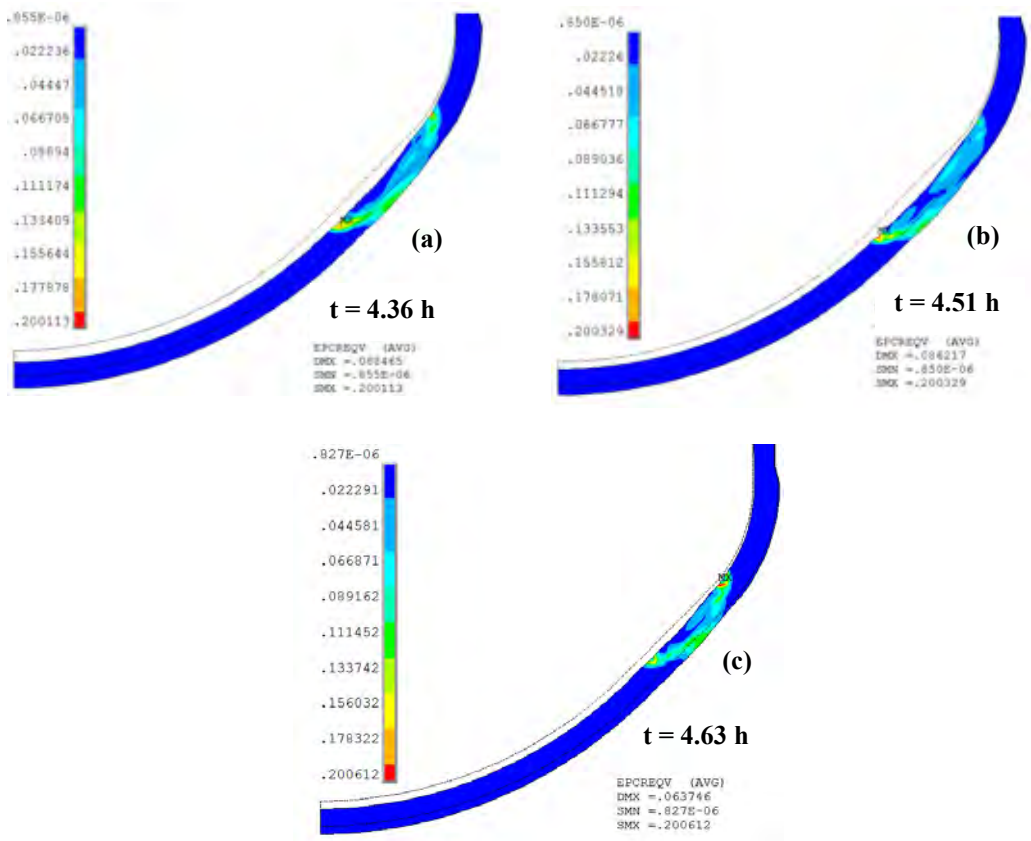

Figure 3.65. Vessel wall deformations and von Mises creep strain for (a) homogeneous, (b) flat and (c) concave debris bed configuration. The original position of the vessel wall is also superimposed.

Similar qualitative behavior was found in terms of debris bed remelting. For all three debris bed configurations, the highest temperature is located in the uncooled debris bed region, where remelting process starts. All the scenarios had similar amount of liquid melt at the time of the vessel wall failure ~1 ton superheated up to ~5 K for homogeneous and flat configuration and up to 12.6 for concave. Low mass of remelted material and presence of IGT penetrations in homogeneous and flat scenario will result in gradual melt release from the vessel wall. In this case development of melt premixing in the water pool is significantly reduced, decreasing the possibility of steam explosion.

In case of concave debris bed configuration there is no IGT failure prior to the vessel wall failure in concave scenario, all the available superheated melt would be ejected at a single instant. This could result in intensive melt-water interaction and energetic steam explosion, posing a threat to containment integrity.

In summary, the debris bed configuration has significant influence on vessel failure mode and timing. However, there are several important phenomena that can affect debris configuration that are not addressed currently:

- Multicomponent reheating and remelting
  - Corium is multicomponent and relocates to the lower head to form a mixture of oxidic and metallic debris.
  - Regions with higher concentration of metallic/oxidic debris can have significantly different thermal properties
    - Different reheating and remelting transient histories.
- Melt and water flow in a porous debris bed
  - Melt pools can form as 'islands' in the debris bed or move in a porous debris bed due to gravity or capillary forces.
  - Water can ingress and enhance cooling of debris and melt pools.
- Debris configuration changes due to
  - Phase changes: Debris can remelt, relocate, and resolidify.
  - Oxidation: Metallic debris can be oxidized at certain conditions.
  - Buoyancy: Melt and debris layers can invert due to density differences.
  - Limited melt release: Changes configuration of the debris bed.
- Melting and collapse of IGT and CRGT pipes are not considered.
  - Cooled CRGTs have a chance to stay intact according to previous analysis.
  - Non-cooled IGT/CRGT pipes will melt and collapse possibly leading to local non-homogenous properties of debris bed (candling).

It is not possible to develop a Full model that can address all of the above in detail due to the extreme complexity of the phenomena. Our approach is then to focus on possible limiting factors in design, scenario, and phenomena that can simplify the analysis but still provide the necessary output for the next SM (Melt Ejection Mode). For example, the effect of the penetration nozzles on the effective properties of the debris bed in the near wall region can be considered. The nozzles take significant fraction of space near the wall, up to ~40cm. Hence, thermal conductivity through the nozzles to the vessel should be considered when estimating thermal conductivity of the debris.

To generate the output for the next SM, we create a database of solutions using the complementary full models (DECOSIM, PECM/ANSYS). From this, we can characterize the data according to:

- Failure mode,
- Failure timing,
- Melt mass available for release,
- Melt superheat, and
- Initial break size,

as functions of initial debris properties.

We are currently in the process of generating this database and characterizing the data. Figure 3.66 shows an example of failure timing of vessel wall plotted with respect to solid debris thermal conductivity (which is one of the most influential parameters) generated from a set of PECM/ANSYS calculations. The plot demonstrates that it is

possible to determine the failure timing given the debris properties from core relocation SM provided that the scenario is within the scenario space considered in the generation of the functional dependency.

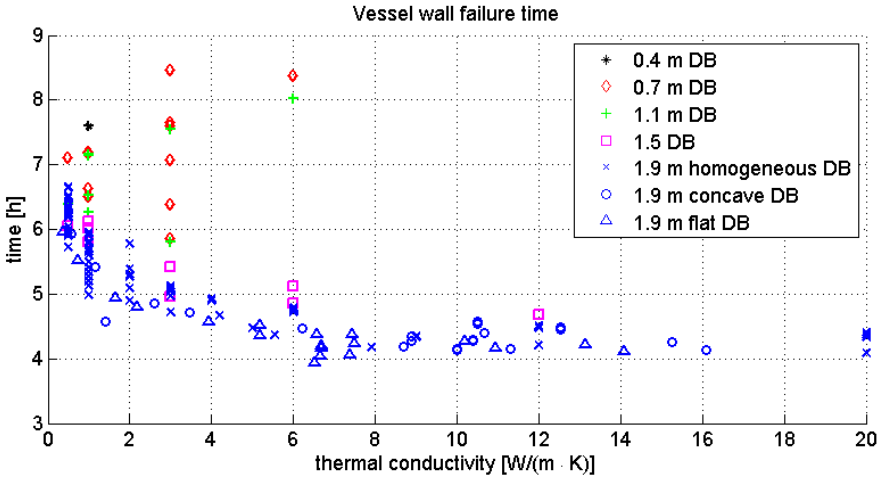

Figure 3.66. The timing of vessel wall failure with respect to thermal conductivity.

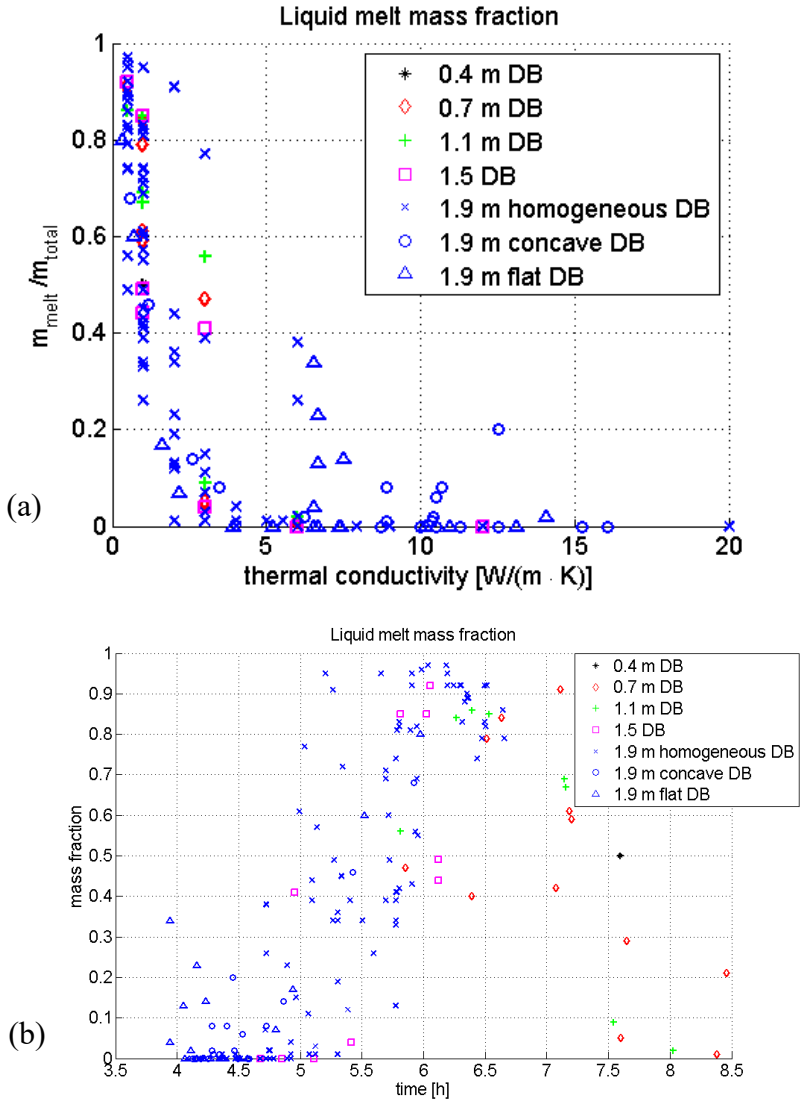

Figure 3.67. Melt mass fraction plotted with respect to (a) thermal conductivity and (b) time of vessel wall failure.

The corresponding melt mass and melt superheat plotted with respect to the thermal conductivity and failure timing of the vessel wall are shown in Figure 3.67 and Figure 3.68. The plots demonstrate that we can connect the debris properties to the melt mass and melt superheat at the time of vessel wall failure. Similar dependencies can be generated for other mode of vessel failures such as IGT and CRGT.

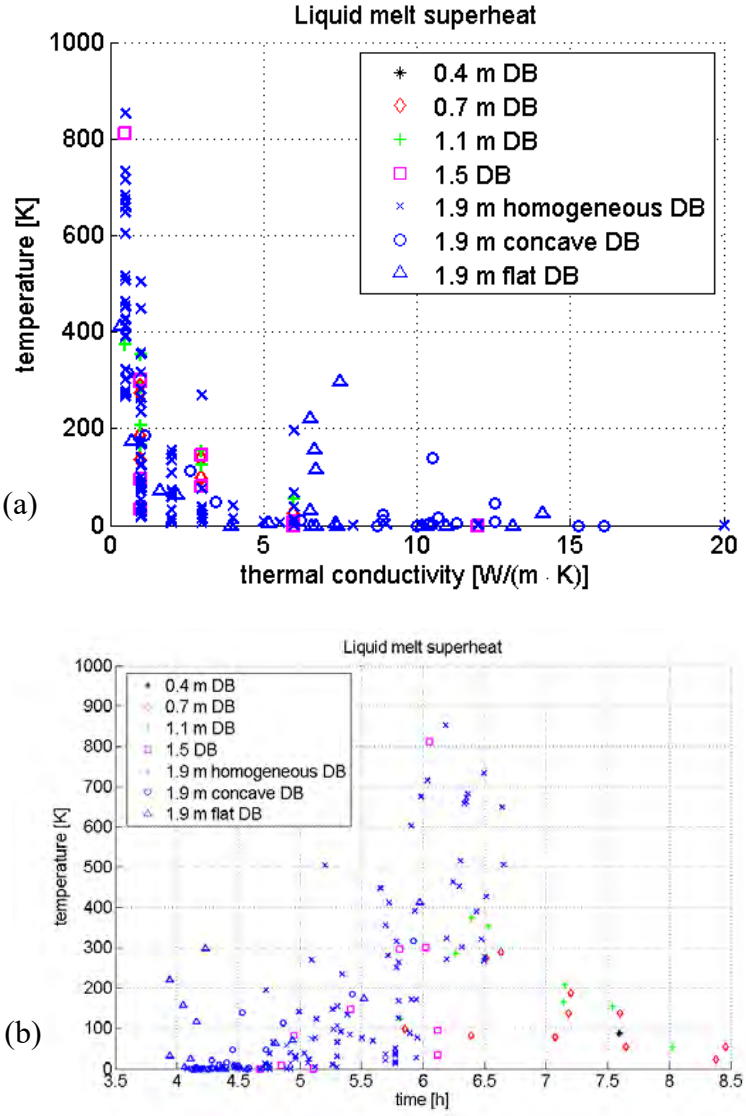

Figure 3.68. Melt superheat plotted with respect to (a) thermal conductivity and (b) time of vessel wall failure.

3.5.2 **Vessel Failure Surrogate Model**

Given the database of PECM (Full Model) results, we can generate surrogate models for prediction of timing, amount, properties, and melt superheat of the melt available for release in different vessel failure modes. Figure 3.69 shows the predictive capability of the generated surrogate models of the timing of the vessel wall failure with different debris bed configurations. Half of the data samples in each corresponding configuration is used for learning and the remaining half is used for testing.

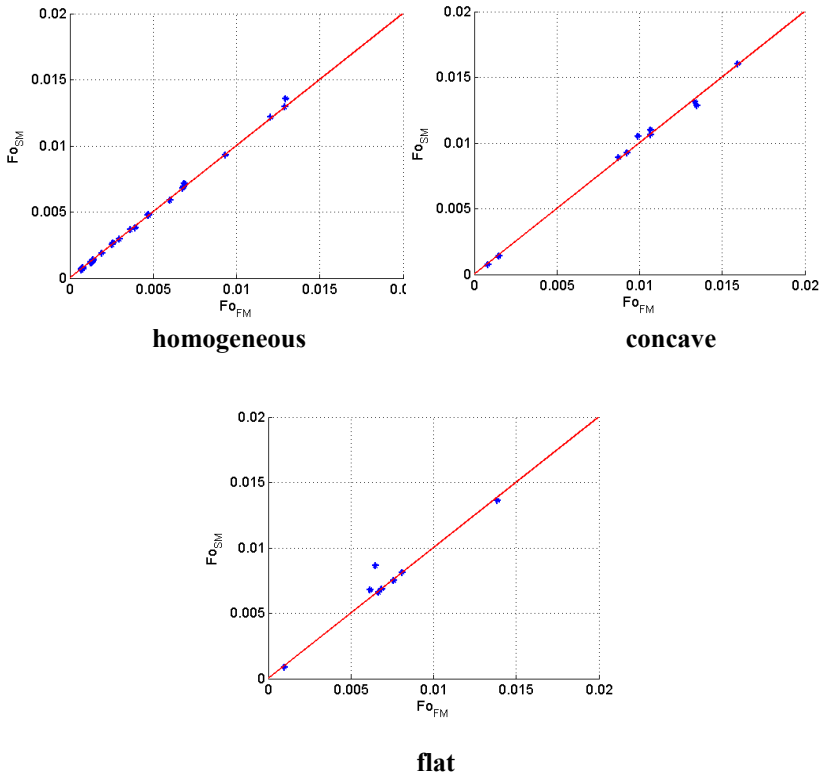

Figure 3.69. Predictive capability of the surrogate models: Timing of the vessel wall failure with different debris bed configurations.

The non-dimensional timing is denoted by $Fo = \frac{t \cdot k_{solid}}{\rho \cdot C_p \cdot L^2}$ where t is the dimensional timing, k_{solid} is the thermal conductivity of the debris bed in its solid form, ρ is the density, C_p is the heat capacity, and L is the debris bed height. Linear and non-linear regression analysis have been implemented relating Fo to the dimensionless input parameters as follows,

$$\mathrm{Pr} = \frac{\nu \cdot \rho \cdot C_p}{k_{solid}}, \text{ Prandtl number,}$$
$$\tilde{T} = \frac{T_{solidus}}{T_{liquidus}},$$
$$\hat{k} = \frac{k_{liquid}}{k_{vessel}},$$
$$\tilde{\beta} = \beta \cdot (T_{liquidus} - T_{solidus}),$$
$$\tilde{Q} = \frac{Q_{latent\ heat} \cdot m}{Q^* \cdot V \cdot t^*}, \text{ and}$$
$$\tilde{k} = \frac{k_{solid} \cdot (T_{solidus} - T_{initial})}{Q^* \cdot L^2}$$

where $\boldsymbol{\nu}$ is the corium kinematic viscosity, $\boldsymbol{\beta}$ is the thermal expansion coefficient, $\boldsymbol{t^*}$ is a time scale (set to 2 h), and $\boldsymbol{m}$ is the debris bed mass. Effective values of the volumetric decay heat, denoted by $\boldsymbol{Q^*}$, is introduced. For the homogeneous debris bed, it is a constant value. For non-homogeneous configurations, it represents the observed behavior in the Full Model solutions. Specifically, we observe that debris properties of the 20 cm thick layer near the vessel wall determine failure time for the concave configuration. Therefore, the volumetric decay heat in this layer is used instead of the volume-averaged decay heat. Similarly, the vessel failure location in the case of flat layer configuration is near the debris bed region with highest fraction of UO_2 (having maximum decay heat and low thermal conductivity). Thus, the volumetric decay heat in

the high UO_2 region is taken as $\boldsymbol{Q}^*$.

A non-linear regression of the form $Fo = Pr^a \cdot \tilde{T}^b \cdot \tilde{k}^c \cdot \tilde{Q}^d \cdot \tilde{\beta}^e \cdot \hat{k}^f$ provided the best result and the coefficients are provided in Table 3.8. The high RMSE for the flat-layered configuration is attributed to the significant influence of the scenario specific location of the UO_2 rich region (having high decay heat and low thermal conductivity on the vessel wall failure).

Table 3.8: Coefficients of the non-linear regression models for different debris configurations.

Configuration	a	b	c	d	e	f	RMSE [min]
Homogeneous	-0.599	0.022	0.041	0.251	0.510	0.262	12.8
Flat-layered	-9.086	6.468	1938.105	-1.757	0.629	0.100	30.6
Concave-layered	-0.022	-0.482	66.202	0.347	-0.188	0.195	14.4

For the melt mass and melt superheat as shown in Figure 3.70, a linear regression of the form $melt\ mass/superheat = a + b \cdot Pr + c \cdot \tilde{T} + d \cdot \tilde{k} + e \cdot \tilde{Q} + f \cdot \tilde{\beta} + g \cdot \hat{k} + h \cdot Fo$ provided the best results and the corresponding coefficients are given in Table 3.9. Further reduction of uncertainty, especially for the melt superheat, is needed. The inclusion of cooling as an input parameter might need to be taken into account.

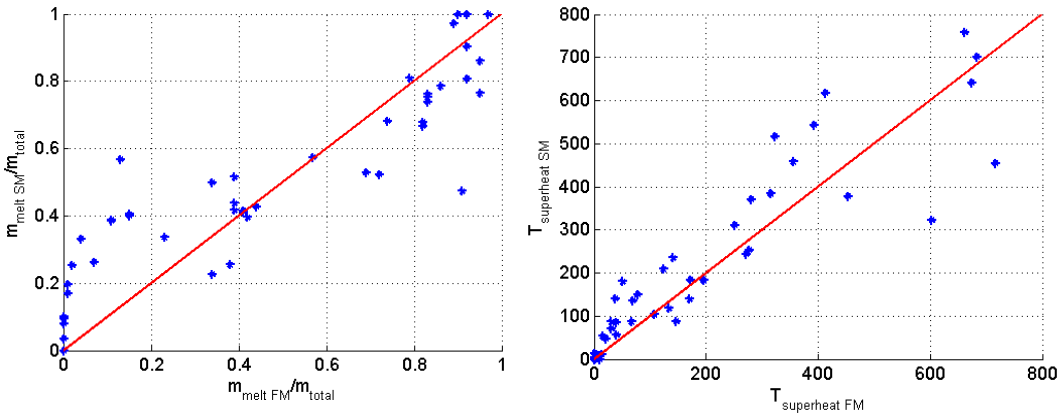

Figure 3.70. Predictive capability of the surrogate models: Melt mass and melt superheat corresponding to the homogeneous debris bed configuration.

Table 3.9: Coefficients of the linear regression models for melt mass and superheat corresponding to the homogeneous debris configuration.

Melt Properties	a	b	c	d	e	f	g	h	RMSE
Mass Fraction	-1.382	0.148	0.001	1.179	17.839	-1.128	1.47e+07	-80.409	0.164
Superheat	591.29	88.67	7.01	-785.3	7853.5	-943.2	6.99e+09	-1.13e+04	322 [K]

Similar surrogate models (timing, melt mass, and melt superheat) will also be obtained for the other modes of failures, specifically IGT and CRGT failures. These surrogate models will then be used in the next SM, Melt Ejection SM, according to the ROAMM+ framework.

3.6 Melt Ejection Mode Analysis

Vessel failure mode provides initial conditions of lower head failure: (i) size of the opening (IGT, CRGT, pump, vessel wall) and (ii) amount, properties and superheat of the available melt. To some extent this data could be used directly in the following steam explosion and debris formation analysis, however, breach size and melt superheat are time dependent parameters and can change during melt release. Quantification of breaching, ablation and plugging of the vessel opening is required to reduce uncertainty in the melt release mode.

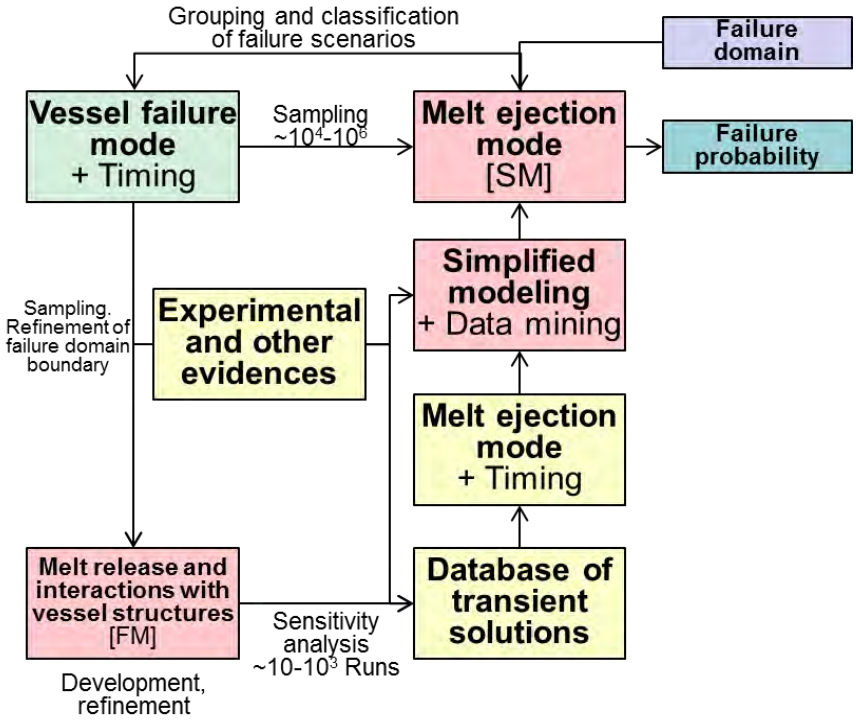

Figure 3.71. Melt ejection mode surrogate model.

There are two constitutive phenomena that should be addressed in the analysis of the melt ejection mode. The first is filtration of liquid melt through the solid porous debris. On one hand it can slow down the release, limiting the effective size of the melt jet; on the other hand it can gradually increase the temperature of the melt jet, for example, in case of liquid metal filtration through decaying oxidic debris bed. The second is ablation / plugging of the initial breach during melt structure interaction. This is the key phenomena that alters jet diameter and therefore its modelling is paramount for ex-vessel scenario progression.

Currently, melt release mode is the least investigated element of the framework that lacks comprehensive modelling of melt structure interaction, melt filtration through porous debris bed and adequate experimental work necessary to collect the relevant evidences.

The goal of this work is to develop the numerical tool that for given initial conditions of

vessel failure can predict transient parameters of melt ejection mode, i.e. jet diameter, melt thermal properties and duration of the release.

3.6.1 **Approach**

The common approach to the development of MEM framework is depicted in the Figure 3.71. It relies on the completeness of the MEM Full Model, which is still under development. Lack of complete FM and consequently a database of FM solutions prevents development of the MEM surrogate model from the MEM FM. In order to make the whole framework operational a temporary fast model for vessel ablation and melt filtration has been implemented. We refer to the temporary fast model as a surrogate model and emphasize that it is not related to the MEM FM and is not intended to reproduce its output.

In the following we, first, describe the status of the Full Model development, second, provide implementation details of the surrogate model (temporary fast model) and some examples of calculation results using SM; and then discuss in details current modelling requirements for MEM FM and development aspects specific to MEM subframework.

3.6.2 **MEM Full Model**

The MEM FM is in general supposed to address two phenomena of melt release. First, phenomena is melt filtration through porous debris bed, this should provide data on the availability of superheated melt for release. And, second, phenomena is breach ablation and plugging. The current FM only addresses the second phenomena.

The FM (or melt / structure interaction model) aims to predict the time evolution of the lower head breach geometry as a function of melt flow rate and melt superheat. The target parameter is the minimum diameter of the breach during transient. The initial parameters are breach geometry, melt temperature and melt mass flow rate.

The full model consist of two domains (see Figure 3.72):

- Lower head domain
  - Represented as an axisymmetric 2D domain with an opening (breach)
  - The 2D domain is subject to Neumann boundary conditions that is:
    - Convective cooling of the lower head
    - Heat flux from the melt
  - Transient temperature profile and ablation are resolved
- Melt domain
  - Represented as a number of 1D transient models that describe melt-crust-metal interface adjacent to the 2D domain
  - Every 1D model is independently coupled to a specific boundary cell in the 2D domain with two parameters used for two-way coupling:
    - Boundary temperature and
    - Heat flux
  - Every 1D model is a subject to specific boundary conditions:
    - Temperature of adjacent (coupled) cell in the 2D domain
    - Local velocity and temperature of the melt
  - Transient thickness of the crust, temperature profile in melt-crust-metal interface and throughout heat flux are resolved

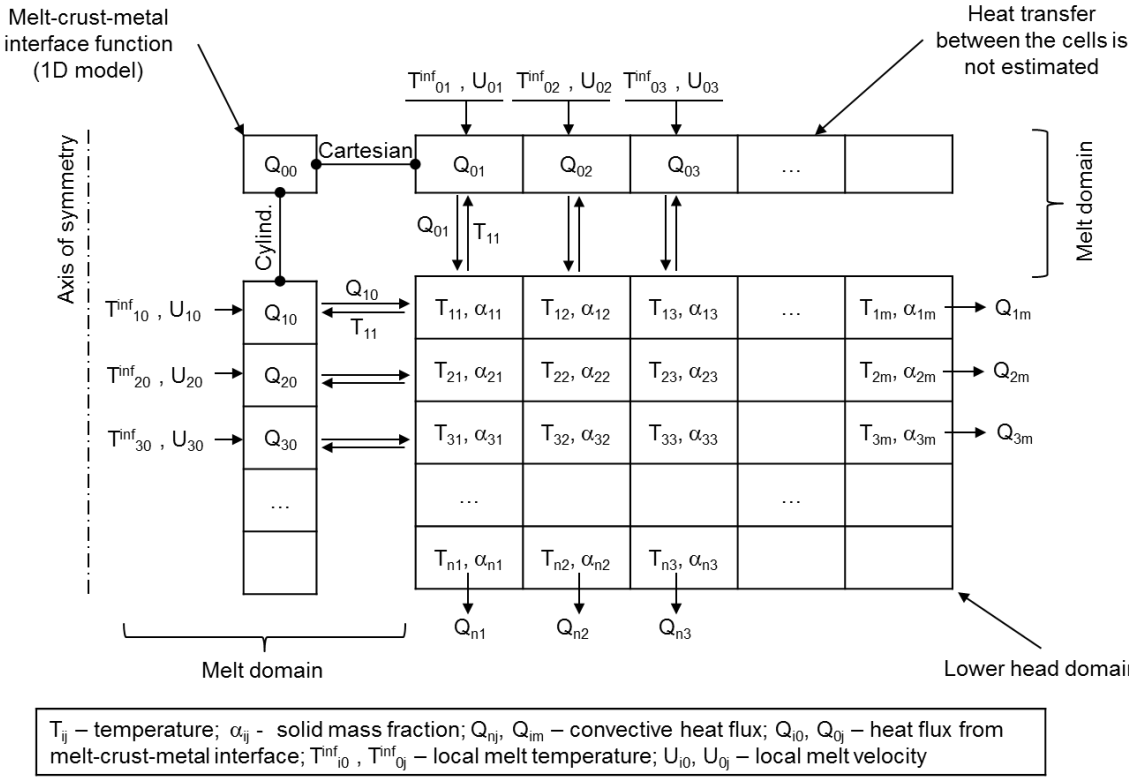

Figure 3.72. Conceptual representation of the melt / structure interaction model

Formulation of the problem in terms of coupled 2D and 1D domains enables to simplify the treatment of the melt / crust interface displacement upon lower head melting. When solid fraction in a coupled cell reaches 0 the cell is removed from calculations and the related 1D models are re-coupled to the adjacent cells. This is done presuming temperature profile and crust thickness in the 1D models but shifting coordinate vector according to the size of the melted cell in the 2D domain. This process is illustrated in the Figure 3.73.

The underlying assumption is that liquid metal formed as result of lower head ablation cannot stay at the interface but is assumed to flow out through the breach. This implies that immediate amount of liquid metal is dependent on the rate of ablation and rate of melt outflow. For simplicity we assume that at any given time there is constant layer of liquid (or, given temperature conditions, solid) metal layer with thickness due to Laplacian radius, that is any melted material above this is excluded from the calculations.

This metal layer (1-2 mm thick) is implemented in the 1D model as a permanent part of 3 layer system: melt, crust, metal. The schematics of the 1D model is detailed in the Figure 3.74. The model estimates the heat transfer through the interface, what defines dynamics of ablation in the 2D domain, and dynamics of the crust growth, i.e. plugging phenomena.

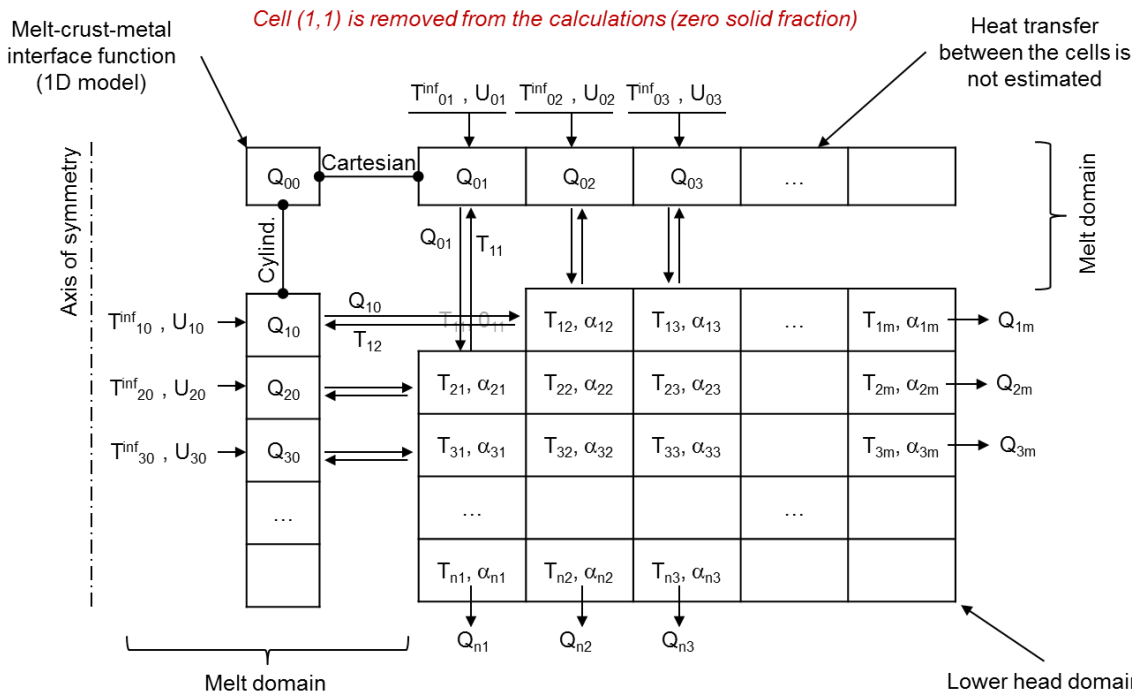

a

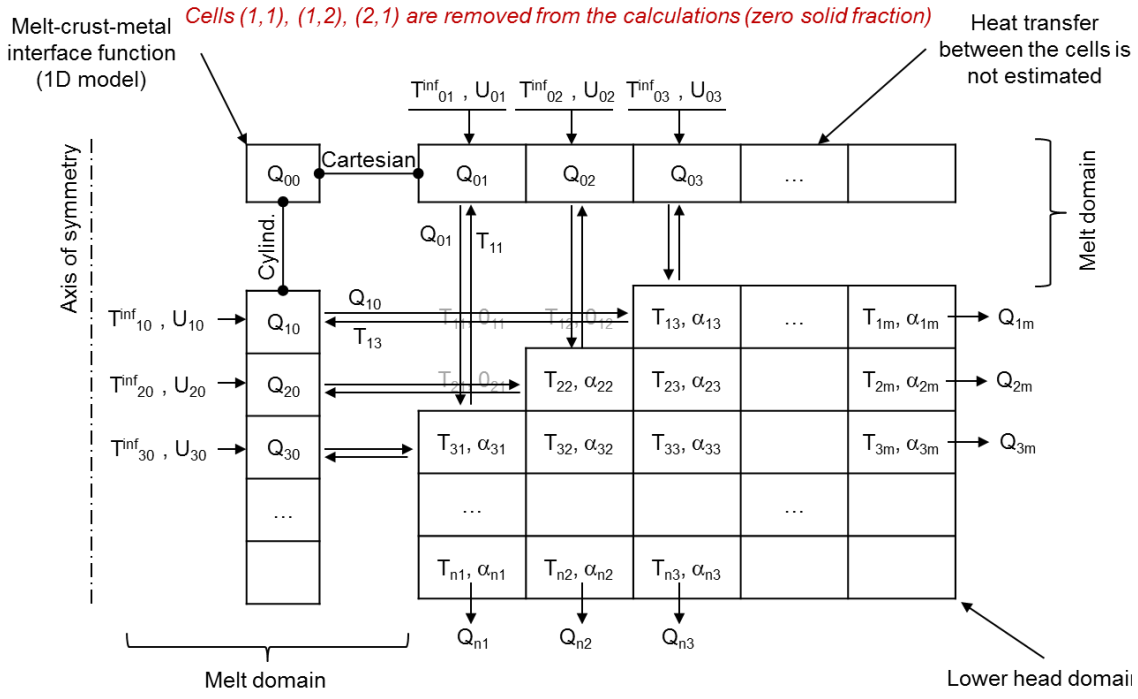

b

Figure 3.73. Modification of the coupling of the 1D models to the 2D domain upon 2D domain melting (a – cell (1,1) is melted; b – cells (1,1), (1,2) and (2,1) are melted)

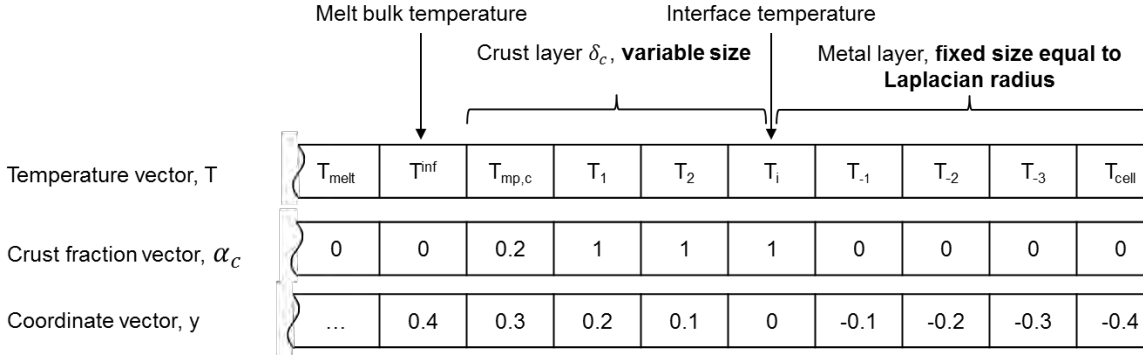

Figure 3.74. Conceptual representation of the melt / crust / metal interface model

Mathematical treatment of the 1D model

The heat transfer through metal and crust sub-domains is estimated using corresponding heat equations:

$$\rho_c C_{p_c} \frac{\partial T_c}{\partial t} = \nabla \cdot \mathrm{k_c} \nabla T_c + \dot{q} \rho_c \tag{3.9}$$

$$\rho_m \bar{C}_{p_m} \frac{\partial T_m}{\partial t} = \nabla \cdot \mathrm{k_m} \nabla T_m \tag{3.10}$$

The thickness of the metal layer is constant and subject to two boundary conditions. First, contact temperature at the metal / crust interface is due to heat balance:

$$k_L \frac{\partial T_L}{\partial y}\bigg|_0 = k_c \frac{\partial T_c}{\partial y}\bigg|_0 \tag{3.11}$$

Second, boundary temperature at the opposite end of the metal layer is equal to the temperature in the 2D domain coupled cell:

$$T_0 = T_{cell}^{2D} \tag{3.12}$$

Since metal layer is subject to melting / solidification a modified expression for metal heat capacity is used that incorporates enthalpy of fusion L_m with a narrow temperature interval δT around metal melting point $T_{mp,m}$:

$$\bar{C}_{p_m} = C_{p_m}(T) + L_m \cdot \frac{1}{\frac{\delta T}{8}\sqrt{2\pi}} e^{-\frac{\left(T - T_{mp,m}\right)^2}{2\left(\frac{\delta T}{8}\right)^2}} \tag{3.13}$$

The temperature at the crust / melt interface is set equal to the crust melting point:

$$T_{m/c} = T_{mp,c} \tag{3.14}$$

Displacement of the melt / crust interface is governed by melting / solidification and expressed as a function of boundary heat fluxes:

$$\rho_c L_m \frac{\partial \delta_c}{\partial \alpha_c} \frac{\partial \alpha_c}{\partial t} = k_c \frac{\partial T_c}{\partial y}\bigg|_{\delta_c} - h_m\left(T_{inf,m} - T_{mp,c}\right) \tag{3.15}$$

In case if crust layer disappears the following equation is used at the melt / metal interface

$$k_m \frac{\partial T_m}{\partial y}\bigg|_0 = h_m\left(T_{inf,m} - T_i\right) \tag{3.16}$$

If resulting interface temperature T_i drops below $T_{mp,c}$ a crust layer is reestablished in the adjacent cell and boundary eq.(3.16) is replaced with eq.(3.11). Amount of generated solid fraction is due to eq.(3.15).

An implicit solver is implemented to compute temperature profile.

Mathematical treatment of the 2D model

The transient temperature profile is estimated in the 2D domain by solving the following heat equation:

$$\rho_m C_{p_m}^{2D} \frac{\partial T_m}{\partial t} = \nabla \cdot \mathrm{k_m} \nabla T_m + Q \tag{3.17}$$

The second term in the rhs of eq.(3.17) is a volumetric heat source that is either due to the heat flux from locally coupled 1D model solution or due to convective cooling of the lower head bottom boundary. The latter is expressed as

$$Q = h_{con}(T - T_{amb}) \tag{3.18}$$

Since melting of the 2D domain is assumed with virtual outflow of the melted mass the equation for the heat capacity is written in the following form:

$$C_{p_m}^{2D} = \begin{cases} \dfrac{\partial T}{\partial t} \geq 0, C_{p_m}(T)\alpha_s + L_m \cdot \dfrac{1}{\frac{\delta T}{8}\sqrt{2\pi}} e^{-\frac{\left(T - T_{mp,m}\right)^2}{2\left(\frac{\delta T}{8}\right)^2}} \\ \dfrac{\partial T}{\partial t} < 0, C_{p_m}(T)\alpha_s \end{cases} \tag{3.19}$$

where α_s is local solid fraction.

Alternating Direct / Implicit (ADI) method is used to solve the above equations.

Coupling approach

The coupling of 1D and 2D domains is demonstrated in the Figure 3.75. It assumes common interface temperature T_{int} between the two domains and common heat flux Q_{int} in accord with the following equations:

$$T_{int} = \frac{T_{01}^{2D} + T_{00}^{2D}}{2}$$
$$T_{int} = \frac{T_1^{1D} + T_0^{1D}}{2} \tag{3.20}$$

$$Q_{int} = \mathrm{k_m} \frac{T_{00}^{2D} - T_{01}^{2D}}{\Delta x^{2D}}$$
$$Q_{int} = \mathrm{k_m} \frac{T_1^{1D} - T_0^{1D}}{\Delta x^{1D}} \tag{3.21}$$

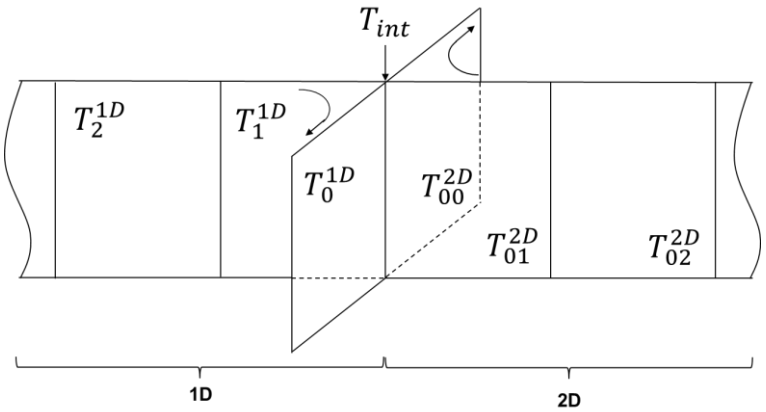

Figure 3.75. Approach to coupling of 1D and 2D domains

3.6.3 **MEM Surrogate model**

Since MEM FM is not yet completed and database of MEM FM solutions is not available, the MEM SM has not been implemented. Instead we have developed a test model that couples MEM/VF models. Refer to chapter 3.6.4 for further details.

3.6.4 **Melt Ejection and Vessel failure surrogate model**

Vessel failure and melt ejection are mutually dependent phenomena:

- release of melt from the vessel is dependent on the timing and location of the failure, rate of breach ablation, amount, composition and availability of melt and rate of melt filtration through the remelting debris bed;
- locatin and timing of vessel wall failure, debris remelting are dependent on the amount and properties of molten debris accumulated in the lower head.

Therefore, robust prediction of melt release conditions requires:

- proper modelling of important relevant phenomena (debris remelting, vessel failure and melt release) and
- establishment of sufficient level of coupling between phenomena related to debris remelting and melt accumulation in the lower head and pehnomena related to melt release and breach ablation and plugging.

In order to identify phenomena important for and to develop requirements to the modelling of the debris remelting, vessel failure and melt release a test surrogate model for melt release and vessel failure has been developed. The model has been implemented in the ROAAM+ framework and used for sensitivity studies, reverse analysis and risk assessments.

MEM/VF SM resolves simultaneously the following phenomena:

- **Debris remelting**:
  - Predicts:
    - Transient temperature of the debris bed
    - Transient masses of solid and molten metallic and oxidic components
  - Uses:
    - 0D model to calculate debris reheating and remelting given net volumetric heat source q and effective heat capacity of the

debris bed Cp_{eff}. Time step dependent temperature change of the debris bed dT_{debris} is estimated using:

$$dT_{debris} = \frac{q\rho V_{tot}}{m_{tot} Cp_{eff}} dt$$

- Effective heat capacity of the debris bed (Cp_{eff}) is taken as a function of the transient debris bed composition (mass fractions of oxidic and metallic debris) and heat of fusion.
- User defined temperature intervals for melting of metallic ΔT_{met} and oxidic debris ΔT_{ox}.

– Remelting model is coupled with melt ejection model.

- **Vessel failure**:
  - Predicts:
    - The time of IGT failure
  - Uses:
    - Failure occurs when debris temperature exceeds a user defined value: T_{vwf}, K
  - Single vessel wall failure is assumed in the model; its geometrical location is not specified; it is assumed that any melt in the lower head can be released through the breach.
- **Melt release:**
  - Predicts:
    - Transient jet diameter and release velocity
    - Transient properties of the released melt
  - Uses:
    - 0D model to estimate ablation rate of the lower head breach:

$$\frac{dD_b}{dt} = \frac{2h_c \cdot (T_M - T_{mp,c})}{\rho_m \cdot (C_{P_m} \cdot (T_{mp,m} - T_v) + L_m)}$$

T_M - melt temperature; $T_{mp,c}$ - melting point of crust; ρ_m - vessel wall density; vessel wall heat capacity; $T_{mp,m}$ - melting point of the vessel wall; T_v - vessel wall temperature; L_m - heat of fusion of the vessel wall material. The above equation implies that there is always crust at the interface between melt and the vessel breach; vessel wall temperature and crust melting temperature are user defined constants; crust melting temperature corresponds to the melting point of steel during release of molten steel and to the melting point of oxides if oxidic components are released.

  – Note: Plugging is not modelled.
- Melt ejection:

  – The heat transfer coefficient for melt / crust interface is estimated proportional to melt release velocity:

$$\mathrm{h_c} = 0.5 \cdot \mathrm{U_{rel}} \cdot C_{p,M} \cdot \rho_M \cdot C_f$$

where $C_f = 0.006$ is the skin-friction coefficient that characterizes roughness of the crust surface; ρ_M is melt density; $C_{p,M}$ is melt heat capacity.

– The melt release velocity U_{rel} is estimated from instantaneous hydrostatic head of liquid melt pool h_{pool} inside the lower and differential pressure ΔP between lower drywell and the pressure vessel:

$$U_{rel}(t) = C_d \sqrt{2 \cdot \frac{\rho_M \cdot g \cdot h_{pool}(t) + \Delta P}{\rho_M}}$$

$$h_{pool}(t) = \frac{M_{melt}(t)}{\rho_m} \cdot \frac{1}{\pi R_{vessel}^2}$$

with discharge coefficient $C_d = 0.67$ (alternatively it can be defined conditionally as a function of breach length to diameter ratio (L/D):

$$C_d = \begin{cases} 0.9, & if\ L \geq D \\ 0.7, & otherwise \end{cases})$$

– Final jet diameter D_{fin} and duration of the release t_{rel} are estimated solving two equations:

$$M_{melt} = \rho_m \frac{\pi}{4} \int_0^{t_{rel}} \left(D_0 + \frac{dD_b}{dt} \cdot t \right)^2 U_{rel}\, dt$$

$$D_{fin} = D_0 + \frac{dD_b}{dt} \cdot t_{rel}$$

The following phenomena were integrated into the modelling in a simplified mechanistic way:

- **Melt absorption** by particulate debris due to interfacial forces:
  - Mass of liquid melt retained (M_{ret}) by particulate debris is proportional to the mass of particulate (solid) debris (M_{sol}) and their (user defined) open porosity (α):

$$M_{ret} = C_{abs} \frac{M_{sol}}{\rho_{sol}} \cdot \frac{\alpha}{1-\alpha} \rho_{liq}$$

  - Upon remelting mass of solid debris decreases reducing total mass of liquid melt that can be retained by interfacial forces.
  - $C_{ret} = [0,\ 1]$ is a user defined parameter, where 0 means no retention and 1 means maximum retention (defined by the free volume of the particulate debris bed)
- **Formation of melt pool**:
  - Release of melt from the lower head is restrained until mass fraction of solid debris (crust) exceeds user defined limit:

$$\frac{M_{sol}}{M_{max}} = \begin{cases} > 1 - C_{pool}, & no\ release \\ \leq 1 - C_{pool}, & release \end{cases}$$

  - Upon remelting mass of solid debris (crust) decreases, once it becomes less than C_{pool} melt release starts.
  - $C_{pool} = [0,\ 1]$ is a user defined parameter: zero means all melt is immediately available for release, 1 means that until complete melting of the debris bed no melt is available for release; any intermediate values are equivalent to the mass fraction of the accumulated molten debris at which melt release starts.
  - M_{max} is the total mass of debris relocated into the lower head.
- **Melt filtration** through particulate debris:

$$\tilde{U}_{rel} = U_{rel} \cdot c_{filt}$$

– $C_{filt} = (0, 1]$ is a user defined parameter that characterizes the effect of melt filtration through the debris bed and nozzle on the melt release rate.

The MEM/VF SM predicts as a function of time instantaneous values of: jet diameter, release velocity, melt thermal properties, superheat and others. However, to simplify the connection of the MEM/VF with the subsequent models in the framework, the MEM/VF surrogate model estimates mass averaged characteristics of melt release:

- Effective jet diameter
- Effective melt release velocity
- Effective melt properties:
  - Superheat
  - Heat capacity
  - Latent heat
  - Thermal conductivit

Each (mass averaged) effective parameter is estimated using the general equation:

$$P_{eff} = \frac{1}{\int \dot{M}(t)dt} \int_0^{t_{rel}} P(t)\dot{M}(t)dt$$

where $\dot{M}(t)$ is rate of melt release, [kg/sec].

A complete list of model input parameters and their ranges is provided in the Table 3.10

Table 3.10: List of MEM/VF input parameters

#	Parameter	Units	Min	Max	Comments
1	Mox_sol	kg	20000	200000	Initial mass of oxidic debris
2	Mmet_sol	k	0	150000	Initial mass of metallic debris
3	Hmet	J/kg	250000	300000	Heat of fusion of metallic debris
4	Hox	J/kg	300000	400000	Heat of fusion of oxidic debris
5	Tmp_met	K	1600	1700	Melting point of metallic debris
6	Tmp_ox	K	2.80E+03	2.90E+03	Melting point of oxidic debris
7	Cpox_sol	J/kg·K	4.90E+02	6.50E+02	Heat capacity of solid oxidic debris
8	Cpox_liq	J/kg·K	4.90E+02	6.50E+02	Heat capacity of molten oxidic debris
9	Cpmet_sol	J/kg·K	3.50E+02	4.90E+02	Heat capacity of solid metallic debris
10	Cpmet_liq	J/kg·K	3.50E+02	4.90E+02	Heat capacity of molten metallic debris
11	rho_ox_sol	kg/m3	7.90E+03	8.50E+03	Density of solid oxidic debris
12	rho_ox_liq	kg/m3	7.90E+03	8.50E+03	Density of liquid oxidic debris
13	unused	-	0	0	-
14	rho_met_so	kg/m3	7.50E+0	7.90E+0	Density of solid metallic

	l		3	3	debris
15	rho_met_liq	kg/m3	7.50E+03	7.90E+03	Density of liquid metallic debris
16	Td	K	1100	1100	Initial debris temperature
17	Tv	K	5.00E+02	1.30E+03	Vessel wall temperature
18	rhov	kg/m3	7.20E+03	7.20E+03	Vessel wall density
19	Cpv	J/kg·K	4.00E+02	4.00E+02	Vessel wall heat capacity
20	Tmpv	K	1.70E+03	1.70E+03	Vessel wall melting point
21	Hfv	J/kg	250000	250000	Vessel wall heat of fusion
22	Cf	-	0.005	0.007	Coefficeint for heat transfer estimation
23	Tvwf	K	1550	1700	Temperature of the vessel wall failure
24	Dvwf	m	0.07	0.07	initial diameter of the vessel wall breach
25	C1	-	1	1	Melt filtration coefficient
26	por	-	0.1	0.4	Debris bed open porosity
27	dP	Pa	0	300000	Differential pressure
28	C2	-	1	1	Melt pool coefficient
29	C3	-	0	1	Melt absorption coefficient
30	dTmet	K	30	30	Temperature interval for melting of metallic debris
31	dTox	K	30	30	Temperature interval for melting of oxidic debris
32	Qdox	W/kg	50	150	Decay heat per unit mass of oxidic debris
33	Qdmet	W/kg	10	30	Decay heat per unit mass of metallic debris
34	TAS	sec	3600	9600	Time after SCRAM

In the following we demonstrate results of sensitivity study performed towards two output function:

- Jet radius, m (see Figure 3.76a)
- Rate of enthalpy release, W (see Figure 3.76b)

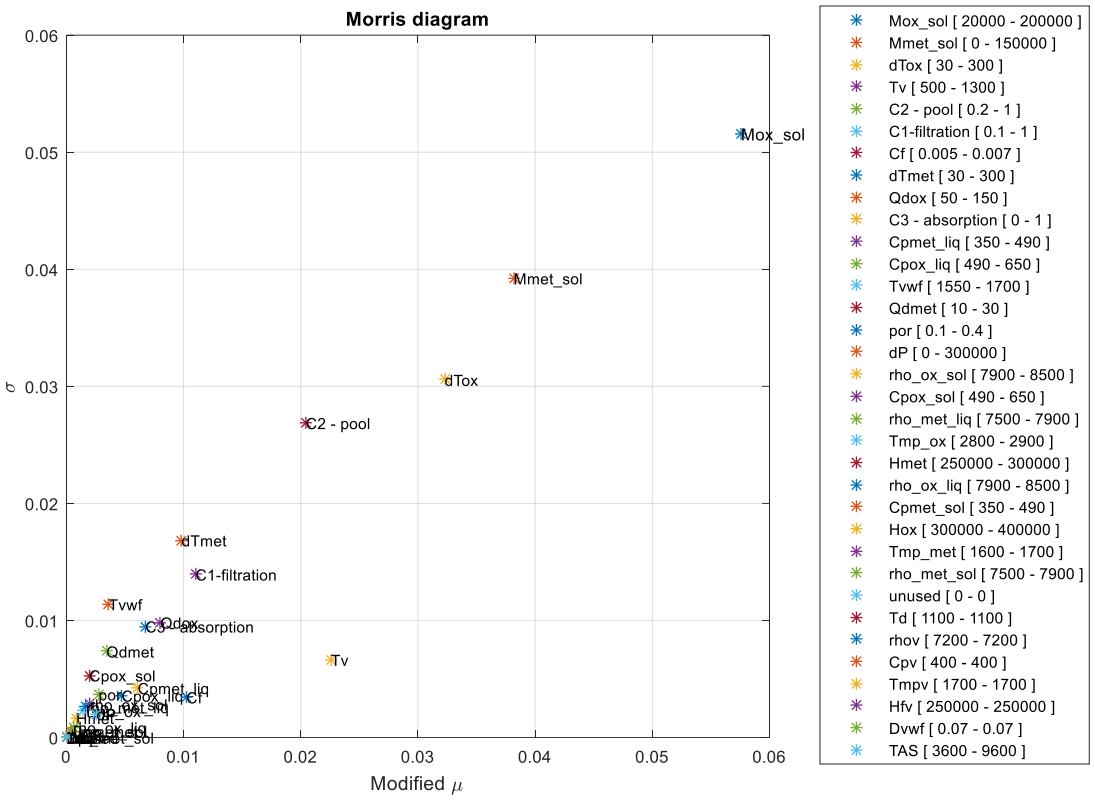

a

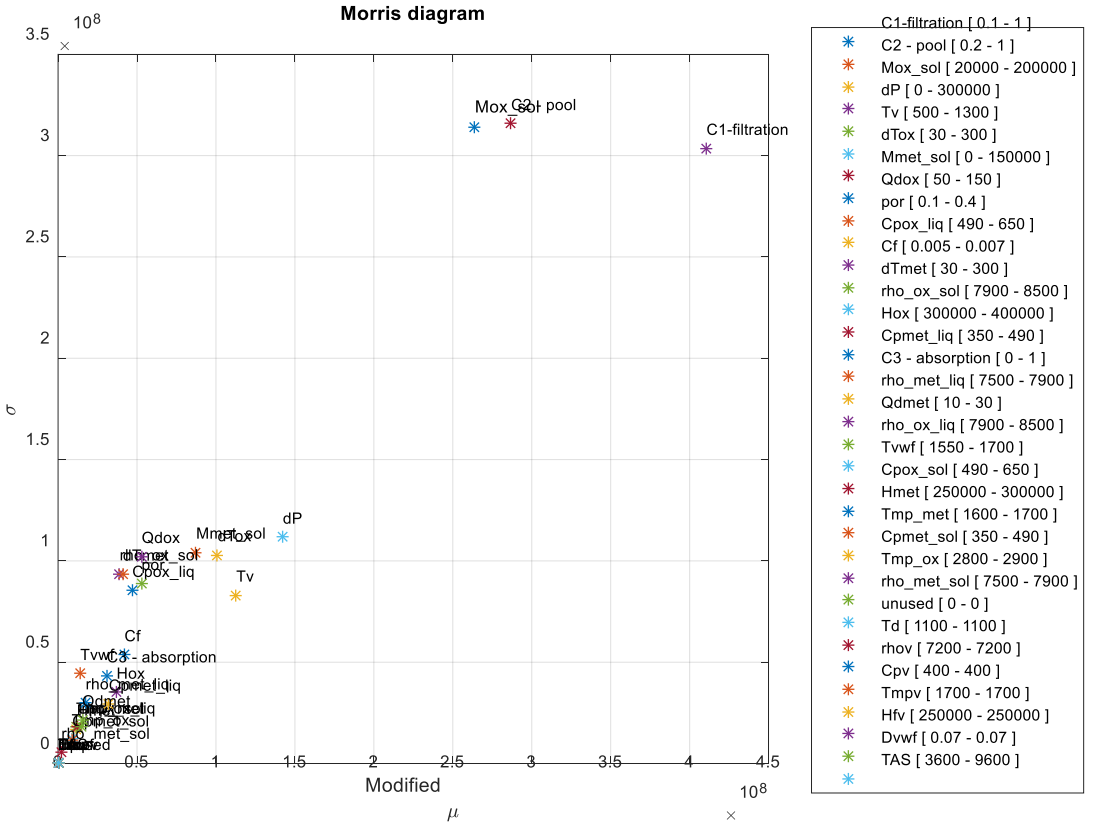

b

Figure 3.76: MEM/FM sensitivity study
(a – rate of enthalpy release; b – jet radius)

Jet radius was previously demonstrated as one of the most influential parameters for modelling of ex-vessel accident progression. The rate of enthalpy release, i.e. the product of melt release mass rate and specific enthalpy, was found to be in linear correlation with steam explosion impulse.

Results suggest that with respect to jet size the most influential parameters of MEM/VF SM are

- Total mass of relocated debris in the lower head (Mox_sol + Mmet_sol).
- Vessel temperature (Tv) - parameter effecting the rate of vessel wall ablation.
- Melt pool coefficient (C1-pool) and melting interval of oxidic phase (dTox), which define melt acumulation and superheat before the start of melt release.

With respect to the rate of enthalpy release the most influential parameters are:

- Coefficients of melt filtration (C1-filtration) and melt pool fomration (C2-pool), which define rate of melt supply to the vessel breach and melt pool accumulation in the debris bed before the release.
- Total mass of relocated oxidic debris.

The results suggest that proper modelling of debris remelting is paramount for the reliable prediction of the conditions of melt release. The key phenomena in the model of the debris remelting is melt filtration. It defines availability of melt for release considering location of the vessel breach, rate of melt supply to the breach, possibility of melt accumulation after the vessel breach is established.

3.6.5 **Discussions**

The complexity of the MEM/VF framework stems from the complexity of involved phenomena and importantly from the high level of their mutual dependency. While development of melt filtration / remelting model, vessel breach ablation / plugging model and vessel failure model is straightforward, their integration into the framework is complicated by the necessity to establish feedbacks. Specifically, modelling of debris remelting and vessel wall failure is dependent on the characteristics of melt release and vice versa modelling of melt release (i.e. ablation / plugging) is dependent on the transient characteristics of the debris bed.
There are two limiting cases of melt filtration. In the first case, it may be assumed that upon remelting all superheated melt is immediately available for the release at any identified location of the lower head breach and at the rate defined by unconstrained melt filtration through porous debris bed (see Figure 3.77b). In the second cases it is assumed that no superheated melt is available for the release until the melt pool reaches the location of the vessel wall failure (see Figure 3.77a).

The case depicted in the Figure 3.77a is expected to be the most conservative in terms of predicted melt release diameters and rate of enthalpy release. The truth is expected to be somewhere in between and can be captured if modelling of the melt filtration (including solidification and remelting) is implemented.
The considered logic for calculation of the melt release mode and coupling of respective models is provided in the Figure 3.79. It is based on three models that may be developed independently.

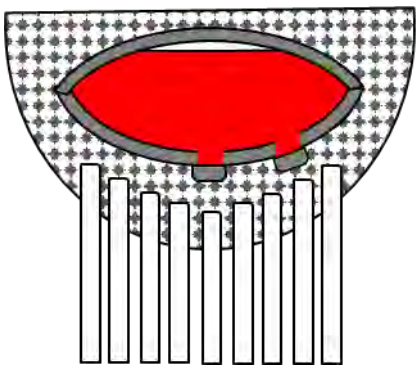

Melt is not available for release due to no or limited filtration through the debris bed

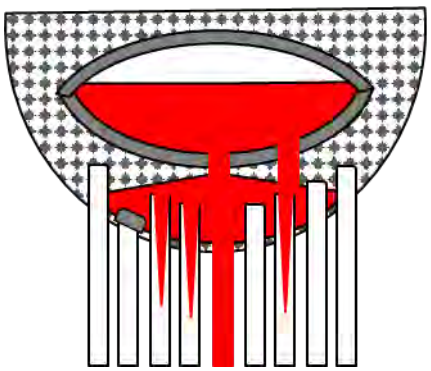

All melt is available for release due to unconstrained melt filtration through the debris bed

a b

Figure 3.77. Two limiting cases of melt filtration through the porous debris bed

(a – no melt filtration through the debris bed; b – unconstrained melt filtration)

First model is the model of debris remelting. Based on the properties of the debris bed predicted by the core relocation SM the debris remelting model is supposed to provide snapshots of transient solutions that include:

- Mass and thermal properties of liquid melt available for release at potential locations of vessel breach
- Rate of melt delivery to potential locations of vessel failure
- Vessel wall temperature

The second model is model of the lower head failure. In case if superheated melt can reach the potential location of the lower head breach at the rate sufficient for melt release, the model of lower must assess the likelihood of such failure. In case if failure does not occur, the model of the debris remelting is supposed to provide the snapshot of the transient solutions. Otherwise, the data on the size of the vessel wall breach and characteristics of melt available for the release must be provided to the Model of melt ejection.

The Model of melt ejection is supposed to estimate the conditions of melt release and in case of continuous release provide feedback to the transient configuration of the debris bed, or in case of dripping and plugging provide no modification to the transient solution of debris remelting Figure 3.78.

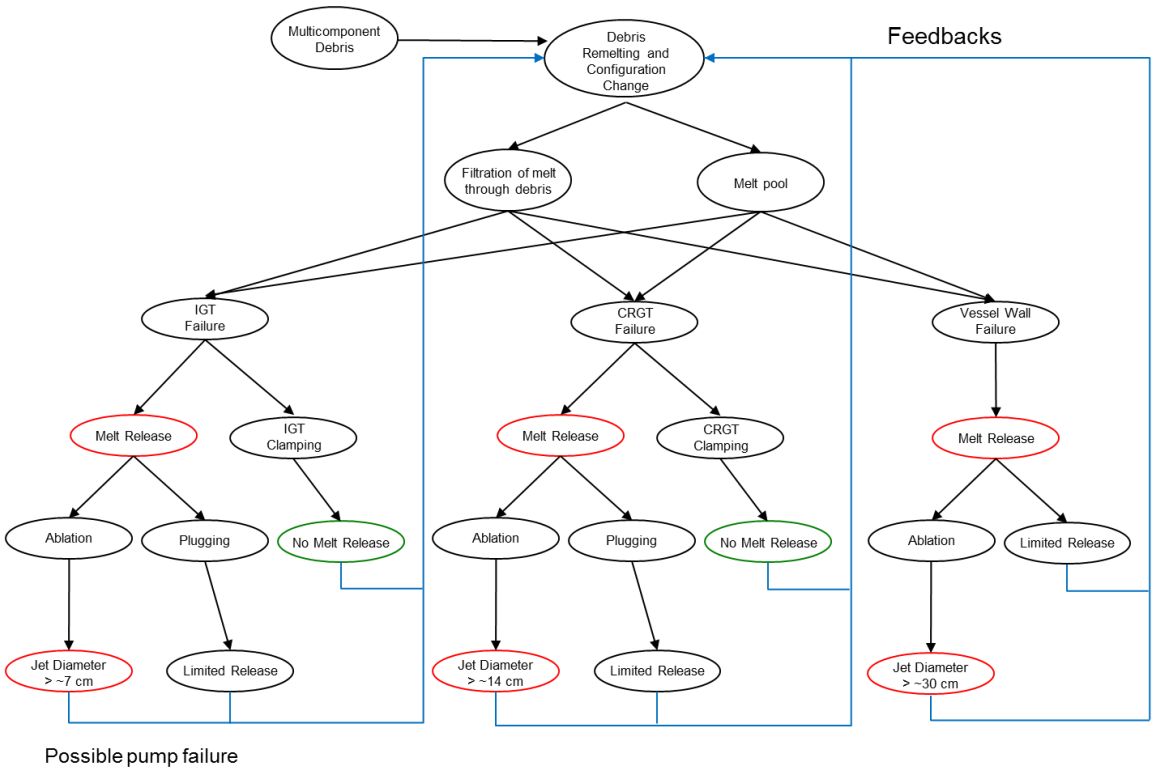

Figure 3.78. Scenarios and feedbacks in melt release mode.

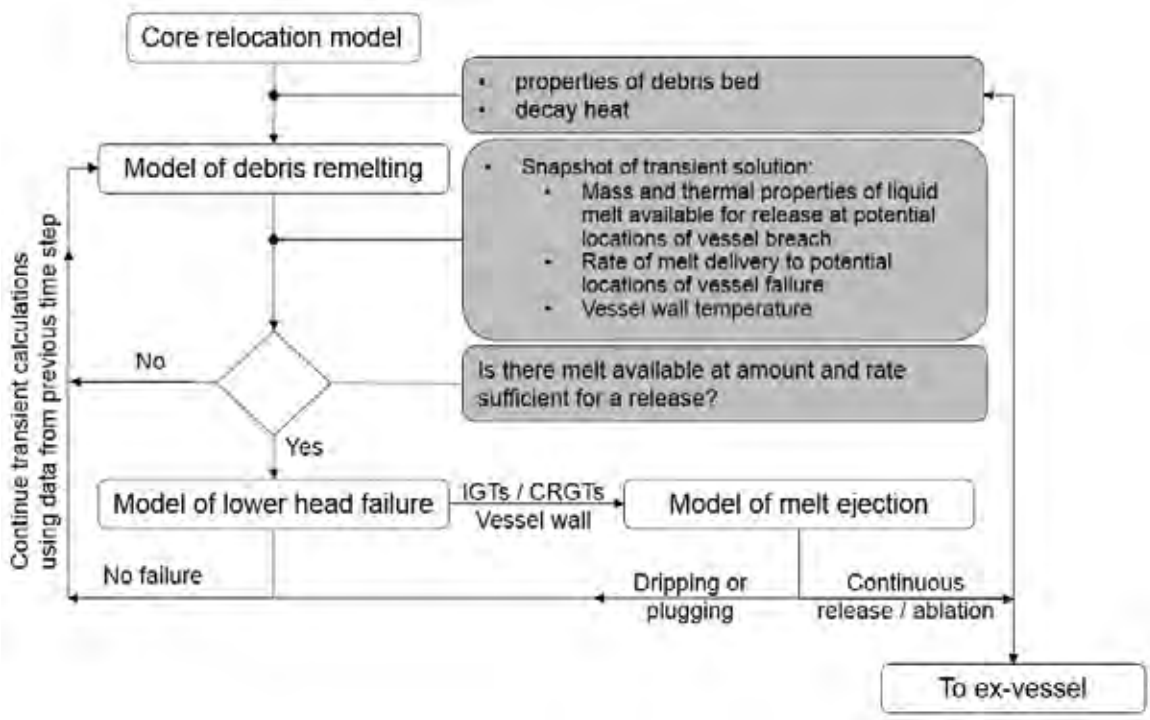

Figure 3.79. “Brute force” logic for the modelling of melt release.

Regardless of the actual implementation of the framework logic, it still lacks comprehensive modelling of the melt filtration through the porous debris bed. Development of such modelling is paramount for the success of the project.
Development and validation of melt filtration model lacks the necessary experimental data. In order to provide such data we are currently developing an experimental program that will address relevant phenomena of debris remelting and melt filtration and focus

on the effect of the interfacial forces and melt solidification dynamics upon filtration. Details of this work are beyond the scope of the current report.

3.6.6 Conclusion and outlook

Currently MEM/VF SM is the least developed part of the framework. The model is based on 0D modelling approach suggested in the MVI project and complemented with simplified modelling of debris remelting and melt filtration. The MEM/VF SM does not model plugging. The MEM/VF SM was implemented with mechanistic modelling of debris bed remelting, melt filtration, absorption and accumulation in form of the pool. Sensitivity study has revealed importance of melt accumulation and filtration for the modelling in-vessel accident progression and prediction of melt release conditions for ex-vessel accident analysis.

Experimental evidences are required to develop models of debris remelting. An experimental program for investigation of debris remelting is currently under development. Conceptual design of the experimental setup and the experimental test matrix has been prepared and the facility is currently at the stage of purchase of equipment and facility assembly.

3.7 Ex-Vessel Debris Coolability

Phenomenology of ex-vessel debris bed formation and coolability is quite complex, it includes (i) jet breakup, (ii) melt droplet sedimentation and interaction with water pool; (iii) debris agglomeration; (iv) particle spreading by pool flows; (v) debris bed self-levelling by vapor flows; (vi) debris bed coolability; (vii) post-dryout behavior with possible remelting, etc. The physical phenomena involved are closely coupled and interconnected. Debris bed cooling is provided by heat transfer to the water that enters the porous bed interior by filtration from the pool. Steam generated inside the debris bed is escaping predominantly upwards, generating two-phase convection flows in the pool and changing conditions for FCI. In turn, FCI phenomena affect particle properties (size distribution and morphology). Particle properties, packing, agglomeration and lateral redistribution affect the debris bed coolability phenomena. The large-scale circulation in the pool can spread effectively the falling corium particles over the basemat floor, distributing the sedimentation flux beyond the projection area of particle source (e.g., size of reactor vessel). Debris is gradually spread under the influence of steam production in the bed, resulting in self-leveling of the settled portion of the debris and changing the shape of debris bed with time. This can serve as an additional physical mechanism that prevents formation of tall non-coolable debris bed.

Relevant phenomena have been extensively studied in the past. Experiments (Figure 3-80) on debris bed and particle properties (DEFOR-S) [46] debris agglomeration (DEFOR-A) [32], porous media coolability (POMECO) [47], particulate debris spreading (PDS) [48] have been carried out. A set of full and surrogate model has been developed and validated against produced experimental data for the debris formation [49], agglomeration ([50], [34]), coolability ([31]) and spreading [51] of the debris (Figure 3-80).

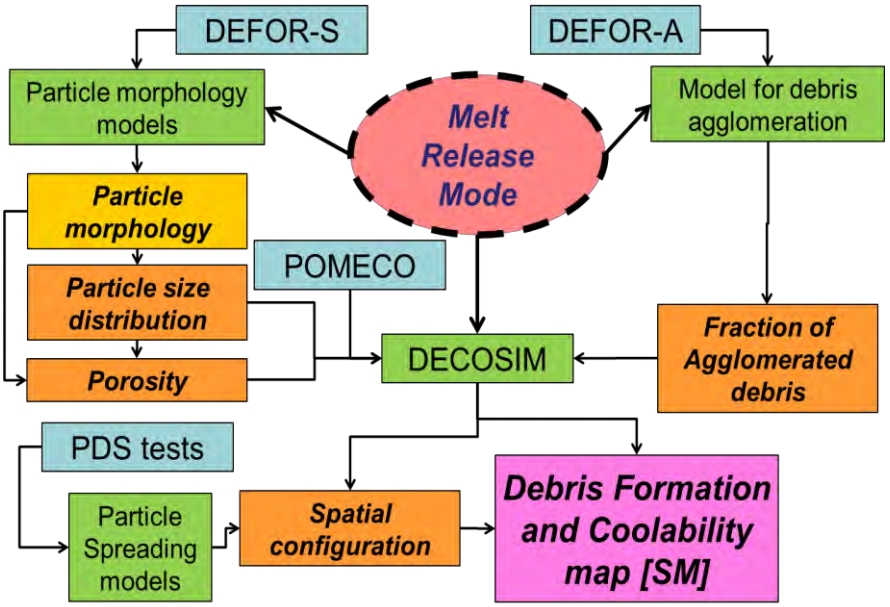

Figure 3-80. Ex-vessel debris bed formation and coolability phenomenology, experiments and code development.

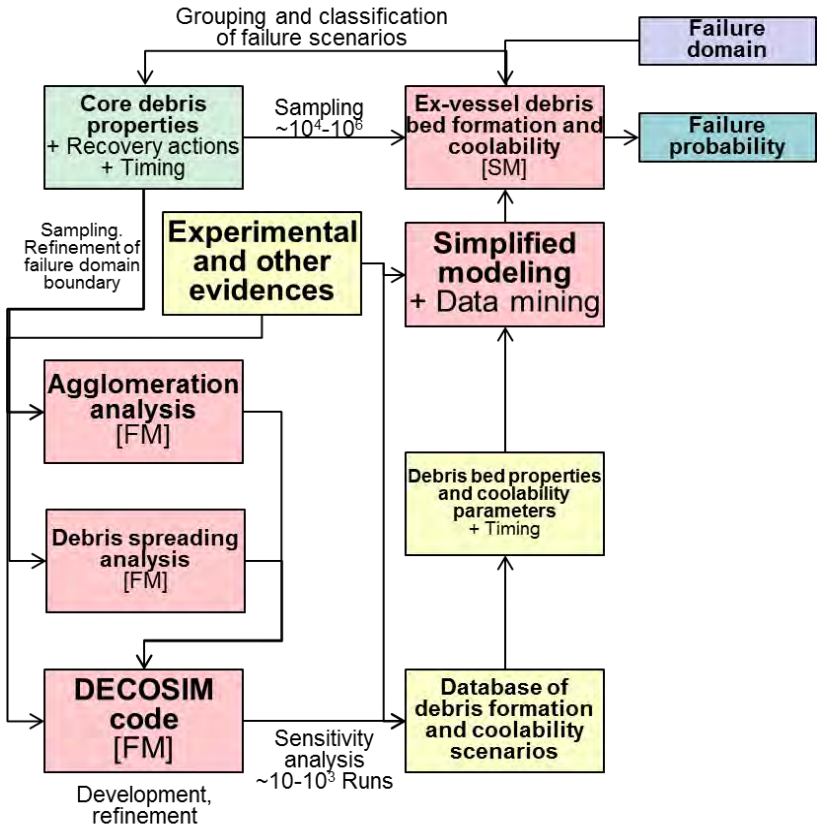

Figure 3.81. Ex-vessel debris bed formation and coolability surrogate model.

Influence of severe accident scenarios is very important for the debris bed coolability. The most important factors for coolability are scenarios of:

- Melt ejection mode (MEM):
  - Total melt mass,
  - Timing of vessel failure,
  - Duration of melt release,

  - Melt composition,
  - Melt superheat,
  - Melt jet diameter,
- Pool conditions during melt release (dependent on the operator actions):
  - Pool depth (water inventory) at time of melt release,
  - Lower drywell pool initial temperature,
  - Pool temperature in the wetwell,
  - Connection between lower drywell and wetwell.

Melt ejection mode and pool state determine the properties of the debris bed:

  - Porosity,
  - Particle size distribution,
  - Mass fraction of agglomerated debris,
  - Spatial configuration of the bed.

All parameters can be assessed based on deterministic models and experimental evidences for specific melt pouring conditions.

Debris particle formation determines particle morphology (porosity) and size distribution. Both factors are very important for coolability. Debris particle formation has been addressed in DEFOR-S experiment and analytical models have been developed for prediction of particle morphology. Confirmatory tests with other binary-oxidic simulant materials also have been carried out to confirm how sensitive experimental results are to the material properties. Data produced in the DEFOR tests can be used for validation of the models and extrapolation of the results to plant conditions.

The influence of the reference plant design specific condition (e.g. melt free fall height) on the size of the debris has to be further investigated. E.g. high speed of the melt jet at the entrance to the pool can decrease size of the debris and thus negatively affect coolability. Experiments with higher initial velocity of the jet have been carried out in DEFOR facility to clarify these concerns. No significant effect of the initial jet velocity (starting from few meters per second) was found. Therefore, no need for further development of jet breakup modeling approaches was identified.

Debris bed formation phenomena include particle packing, avalanching, and agglomeration, which, together with the distribution of mass flux of particles falling onto the pool basemat determine the shape of debris bed, an important factor for coolability. DECOSIM code has been developed for analysis of debris spreading by large scale recirculation flows in the pool and debris bed formation in the case of gradual melt release. Systematic parametric studies are necessary to build a debris bed shape map. Another factor that affects debris bed shape is “self-leveling” (self-spreading) of the debris under the influence of steam escaping the debris bed. PDS (particulate debris spreading) experimental and analytical activities are ongoing, with the aim to quantify the time scale of debris bed self-spreading and to compare it with the characteristic times for reaching dryout, temperature escalation and, possibly, remelting of the debris in the cases where vapor cooling is insufficient to stabilize the dry zone temperature.

Agglomeration of the debris has been demonstrated in analysis and experiments as a negative factor for coolability. Confirmatory DEFOR-A tests with different simulant materials have been carried out for validation of methods and tools developed for prediction of agglomeration.

Prediction of the debris bed coolability is the ultimate goal. Experimental data has been produced for validation of the codes and models against following phenomena: (i) effect of the debris bed spatial configuration on the debris bed coolability; (ii) effect of the prototypical debris bed morphology and size distribution on the pressure drop and dryout heat flux. DECOSIM code is used to quantify debris bed coolability in different debris bed configurations and scenarios, and to create a surrogate model for the bed coolability map, taking into account uncertainties in: (i) properties of the debris bed; (ii) modeling uncertainties in the porous media flow models [21].

3.7.1 **Debris Agglomeration Full and Surrogate Model**

Severe accident (SA) mitigation strategy in Nordic BWRs employs ex-vessel debris bed coolability. Core melt released from the vessel is expected to fragment and quench in a deep pool of water. Decay heat should be removed by natural circulation of coolant through the porous debris bed. Hydraulic resistance is a limiting factor that determines maximum decay heat that can be removed from the bed. If decay heat exceeds this maximum value, it will lead to the bed dryout, reheating and remelting of the debris. Melt attack on the containment basemat presents a credible threat to containment integrity.

This work is a part of DEFOR (Debris Bed Formation) research program [46], [86], [88], [89], [32], [18], [91], [92], [93], [94], [52], [96], [98], [97], which aim is to develop experimental and analytical tools for prediction of the debris bed properties, such as particle size, porosity, shape of the bed, decay heat, etc. which determine its coolability [35], [101], [122]. The properties of the bed are determined by molten fuel-coolant interactions (FCI) and debris bed formation phenomena. Vessel failure mode, timing [85], [123], [66] determine scenarios of melt release and conditions for the debris bed formation and coolability. If melt is not completely solidified prior to settlement on top of the debris bed, agglomeration of the debris and even “cake” formation is possible [124], [125], [88], [86], [89], [32], [126], [91].

Formation of agglomerated debris can significantly increase hydraulic resistance and reduce maximum decay heat which can be removed without reaching dryout of the debris bed. Thus agglomeration is important factor which can inhibit effectiveness of ex-vessel debris coolability [35]. Although agglomeration of the debris and “cake” formation have been observed in previous fuel-coolant interaction (FCI) experiments with prototypic corium mixtures (e.g. in FARO [124], CWTI and CCM [125] tests) and with corium simulant materials (e.g. in DEFOR-E [86] and DEFOR-S [88] tests), the first systematic experimental data was provided in DEFOR-A [89], [32], [126], [91] experiments.

The data obtained in DEFOR-A tests was used for development and validation of modeling approaches for prediction of agglomerated debris in various scenarios of melt ejection [92], [93], [52], [96], [98], [97]. Proposed model for agglomeration is implemented in deterministic code VAPEX-P [127], [117] originally developed at Electrogorsk Research & Engineering Center of NPP Safety (Russia). The VAPEX-P code simulates Fuel-Coolant-Interaction (FCI) phenomena including melt jet breakup, formation of liquid droplets, heat transfer between melt and coolant, sedimentation and solidification of the particles. In the VAPEX-P code, three phases are considered: the liquid water, the vapor (it may be a mixture of steam and hydrogen), and the melt.

Eulerian approach is used for water and vapor dynamics and heat transfer, while Lagrangian approach is used for the melt dynamics and cooling.

Computational costs of running a multidimensional FCI code (such as VAPEX-P) are quite large, especially when parametric sensitivity and uncertainty (S&U) analysis is necessary in order to quantify the influence of the scenarios of melt release from the vessel. The goal of this work is to develop and validate a simplified, physics based, surrogate model (SM) for prediction of mass fraction of agglomerated debris. The model should be (i) computationally affordable in extensive sensitivity/uncertainty analysis, and (ii) sufficiently accurate in reproducing results of the original full model, which has been extensively validated.

Development of Physics Based Surrogate Model

Surrogate Model (SM) approach is necessary when application of original complex model is prohibitively computationally expensive, e.g. in sensitivity and uncertainty analysis, and for identification of failure domain characteristics in multi-parameter space [128], [121], [129]. The goal of the SM is to reproduce results of the original, more complicated, full model (FM) with superior computational efficiency and acceptable accuracy. The process of development of SM benefits from the data produced by the FM as described below [128]:

(i) Full model is used to generate a database of solutions.
(ii) SM is developed using insights from the database.
(iii) The database of full model solutions is used:
    a. to calibrate SM closures;
    b. to verify predictions of the SM.
(iv) Calibrated and verified SM is used instead of full model for S&U analysis, etc.

Usually different data sets are used to calibrate and to verify the SM. Surrogate modeling is often implemented as an advanced mathematical approximation (e.g. using Neural Networks) of a complex function represented by a database of full model solutions. In this case, there is no physics modeling involved in the SM itself, and the process of SM development is essentially a data fitting process. While such approach is quite universal in the sense that it can be applied in principle to any type of problem, there are a few practical limitations. First of all, it usually requires quite large number of points calculated with the original FM (e.g. see [131]). If such calculations are time consuming the overall gain in computational efficiency of the SM development and application process might diminish. Second problem is that surrogate models based on pure interpolation are generally not reliable outside of the domains of parameters covered in the original database of full model solutions.

In this work we pursue a middle ground approach, where most important physical phenomena are modeled explicitly in the SM itself (e.g. see [121]). In such physics based surrogate modeling approach, computational efficiency and numerical stability are achieved by (i) considering only most important physical phenomena, and (ii) by decomposing tightly coupled problem into a set of loosely coupled ones with information exchange through initial and boundary conditions. We apply process of calibration only to those parameters which are responsible for the other physical interactions, which are not modeled directly in the SM. With such approach one can:

- Significantly reduce the number of parameters which have to be calibrated (approximated) in the SM, and thus dramatically reduce the number of the full model runs which are necessary for the calibration process.
- Expand the domain of robust application of the SM beyond the domain covered with the original model, given that important physical phenomena are properly resolved in the SM and in the calibrated relations between SM and full model parameters.

Extrapolation of the applicability domain can be achieved even more reliably if proper scaling is applied in the development of a SM [121].

In this work we use the following general approach to development of the surrogate model:

1) Selection of parameter(s) to be predicted by SM. It is important to emphasize that the only purpose of SM is to predict this parameter(s), not to reproduce all details of the FM solution.
2) Decomposition of tightly coupled model into a set of loosely coupled ones (separate effects) and selection of physical processes, which will be
   i. modeled directly in the SM (phenomena that can be solved with high computational efficiency and sufficient accuracy);
   ii. "approximated" using data from the FM (e.g. phenomena and complex feedbacks, that can be considered in SM as "closures").
3) Implementation of the SM and data structure.
4) Post-processing of the FM data (e.g. averaging of certain values, etc.) in order to establish relations between parameters of the selected closures.
5) Calibration of the SM closures. Here we use the freedom in the "closures" to match results of the SM to the FM. Advanced approaches (such as Artificial Neural Networks, multi-objective optimization, etc.) can be applied to calibration of the SM closures if necessary.
6) Verification of the model on different sets of FM solutions to check possibilities to extrapolate solution of the SM to the areas where FM data was not provided in the calibration process. This might be possible if key physics is properly captured by the SM and calibrated closures.
7) Validation of the SM to shows discrepancy between SM and physical reality. Validation also can be useful for calibration if experimental data is abundant and easier to obtain than FM predictions. In some cases FM might be completely replaced with experimental data and adequate scaling considerations.
8) Application of SM in sensitivity/uncertainty analysis. It is the ultimate goal of the SM development.

Selection of the SM Output Parameters

Agglomeration of debris and "cake" formation can occur if significant fraction of the melt is in liquid state when it reaches the floor of the lower drywell. Formation of agglomerated debris and "cake" regions, which increase hydraulic resistance of the bed, can negatively affect coolability of the bed [35]. Thus we select the mass fraction of agglomerated debris as the main parameter to be predicted by the SM.

Problem Decomposition

Prediction of the fraction of agglomerated debris can be split into two main tasks. The

first one is prediction of the fraction of liquid particles at specific depth of the pool. If such fraction is known then second task is to predict the fraction of agglomerates, e.g. using approach developed and validated in [92], [93], [52], [96], [98], [97]. Thus the primary goal for surrogate model development in this work is prediction of mass fraction of liquid particles as a function of the pool depth. Following key physical phenomena and parameters are paramount for accurate assessment of agglomeration fraction (Figure 2.2):

(i) Jet breakup and penetration depth into a pool of coolant.
(ii) Fragmentation of liquid melt which determines size distribution of the droplets.
(iii) Sedimentation, cooling and solidification of the melt droplets. These phenomena eventually determine fraction of liquid melt and thus mass fraction of agglomerated debris at the top of the debris bed.

The interactions between the models, which describe the phenomena listed above, can be introduced through the model input/output parameters. Thus all models can be implemented and used independently from each other. For instance, as the dynamics of the droplet is considered independently from the jet breakup phenomena, it is possible to create a database of solutions for different conditions of a single melt droplet falling and cooling in a pool of water, e.g.:

$$Particle\left(T_{average},\ T_{surface},\ \delta_{crust},\ \ldots\right) = F(L_s,\ T_{init}) \tag{3.22}$$

where L_s is particle sedimentation length in the pool.

Particle parameters at certain pool depth in a given melt release conditions can be determined from the database by determining

$$L_s = H_{pool} - L_{brk} \tag{3.23}$$

where L_{brk} is jet breakup length.

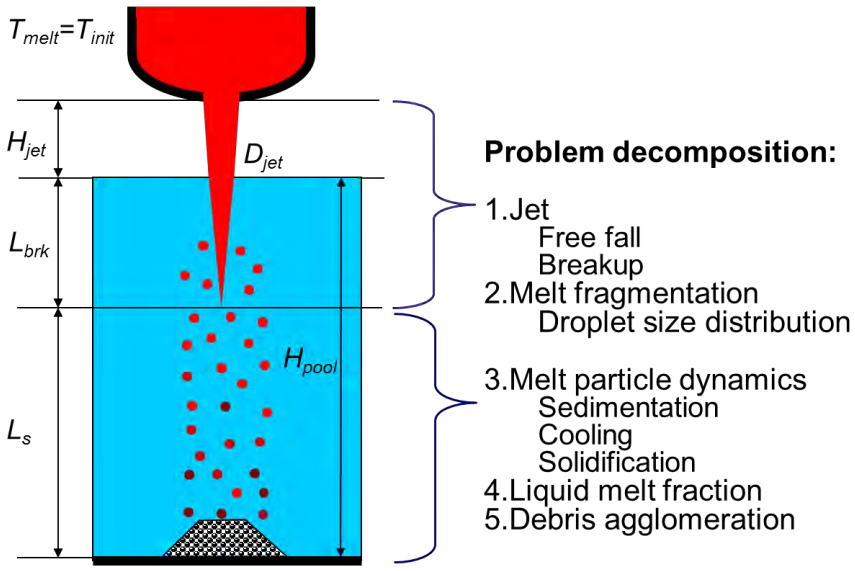

Figure 3.82. Problem decomposition for development of surrogate model of prediction of debris agglomeration.

Physical Processes Simulated Directly in SM

The most important phenomena are simulated explicitly in the proposed SM using respective physical models described in this section. Only mutual feedbacks between different phenomena are resolved using closures, which were produced using FM data analysis.

3.7.1.1.1 Jet free fall

Melt jet is characterized by its initial velocity and diameter. Jet accelerates as it is falling in the gas space above the pool (Figure 3.82). Jet diameter at the free surface will be determined by the mass conservation equation

$$A_{jet}^{0} U_{jet}^{0} = A_{jet} U_{jet} \tag{3.24}$$

where A_{jet}^{0}, U_{jet}^{0} and A_{jet}, U_{jet} are jet cross section areas and velocities initial and at the impact on the pool surface respectively. Thus jet diameter at the free surface can be calculated as

$$D_{jet} = 2\sqrt{\frac{A_{jet}^{0} U_{jet}^{0}}{\pi U_{jet}}} = D_0 \sqrt{\frac{U_{jet}^{0}}{U_{jet}}} \tag{3.25}$$

Velocity of the jet at impact on the free surface can be obtained (neglecting by the aerodynamic drag in gas phase)

$$U_{jet} = \sqrt{\left(U_{jet}^{0}\right)^2 + 2gH_{jet}} \tag{3.26}$$

where H_{jet} – distance between vessel bottom and pool surface (Figure 3.82).

3.7.1.1.2 Jet breakup

Despite significant research efforts in the past, considerable scatter in available experimental data yields no real consensus on best approach to modeling of jet breakup [103], [104], [105], [132], [133]. Several correlations exist for prediction of dimensionless jet breakup length L/D where $L \equiv L_{brk}$ is jet breakup length, and $D \equiv D_{jet}$ is diameter of the jet at the entrance point to the pool (Figure 3.82). Taylor [134] proposed a correlation:

$$L/D = \frac{1}{E_0}\sqrt{\frac{\rho_m}{\rho_w}} = 5.3\sqrt{\frac{\rho_m}{\rho_w}} \tag{3.27}$$

where ρ_m is density of the melt, ρ_w is density of the coolant, and E_0 is a proportionality factor which can be considered also as an entrainment coefficient [105]. The proportionality factor was determined by Taylor, based on the data from experiments with jets in non-boiling (liquid-gas and liquid-liquid) contact mode. Taylor correlation (3.27) provides a lower bound [105] for the experimental data obtained in different tests on jet breakup.

In a boiling contact mode, experimentally obtained [135], [136], [112] non-dimensional jet breakup length was found in correlation with the Froude number $Fr = U^2/gD$, where U is jet velocity at the entrance point to the coolant and g is gravitational acceleration. However, in some corium-water experiments carried out at ANL, dimensionless breakup length was reported to be similar to those observed in liquid–liquid contact mode and not sensitive to the Froude number. In this work we use correlation (3.28) proposed by Saito et al. [135]

$$L/D = 2.1\sqrt{Fr}\sqrt{\frac{\rho_m}{\rho_w}} \tag{3.28}$$

for conservative assessment of the jet breakup length. This correlation generally provides longer jet breakup length, than Taylor correlation (3.27), except for the cases with very low velocity of jet entrance into the pool.

3.7.1.1.3 Particle sedimentation and cooling

Particle sedimentation and cooling dynamics is determined by a set of ordinary differential equations with necessary closures (see also Figure 3.83, Figure 3.84).

$$\frac{d\bar{r}}{dt} = \bar{U}_f; \quad \rho_f \frac{d\bar{U}_f}{dt} = -\bar{F}_{drag} - \bar{g}\left(\rho_f - \rho_a\right) \tag{3.29}$$

$$\rho_f c_f \frac{dT_f}{dt} = -(\alpha_c + \alpha_r)\frac{6}{d_f}\left(T_{fs} - T_a\right) \tag{3.30}$$

where $\boldsymbol{r}$ and $\boldsymbol{U_f}$ are position vector and velocity of melt particle, $\boldsymbol{d_f}$, $\boldsymbol{\rho_f}$, $\boldsymbol{c_f}$, $\boldsymbol{T_f}$ and $\boldsymbol{T_{fs}}$ are particle diameter, density, specific heat, average and surface temperature, $\boldsymbol{\rho_a} = (\boldsymbol{1} - \boldsymbol{\varphi})\boldsymbol{\rho_w} + \boldsymbol{\varphi}\boldsymbol{\rho_v}$ and $\boldsymbol{T_a}$ are coolant density and temperature, $\boldsymbol{\rho_w}$ and $\boldsymbol{\rho_v}$ are densities of liquid and gas phases of coolant, $\boldsymbol{\varphi}$ is volumetric void fraction, $\boldsymbol{g}$ is acceleration of gravity. The drag force $\boldsymbol{F_{drag}}$ is determined as 3.31

$$\begin{aligned} \bar{F}_{drag} &= \frac{3}{4}C_d\rho_a\frac{1}{d_f}\left(\bar{U}_f - \bar{U}_a\right)^2 \\ C_d &= \frac{24}{Re_f} + \frac{4}{\sqrt{Re_f}} + 0.4 \end{aligned} \tag{3.32}$$

where U_a is coolant velocity and Re_f is the particle Reynolds number. The film boiling coefficient α_c and radiation heat transfer coefficient α_r are defined as

$$\begin{aligned} \alpha_c &= 2.98\left\{\frac{\rho_v\lambda_v\left[h_{ev} + 0.68c_{pv}\left(T_{fs} - T_a\right)\right]}{d_f\left(T_{fs} - T_a\right)}\left|\bar{U}_f - \bar{U}_a\right|\right\}^{1/2} \\ \alpha_r &= \sigma_{SB}\varepsilon_f\frac{T_{fs}^4 - T_a^4}{T_{fs} - T_a} \end{aligned} \tag{3.33}$$

where ρ_v is steam density, λ_v is steam thermal conductivity, c_{pv} is steam specific heat at constant pressure, h_{ev} is heat of evaporation, σ_{SB} is the Stefan-Boltzmann constant, ε_f is melt emissivity. In the full model initial temperature and velocity of a droplet are

determined by the local temperature and velocity of the jet.

Particle cooling and solidification is described in three stages. First stage is initial cooling. At this stage droplet is liquid and isothermal:

$$T(r,t) = T_f(t) \tag{3.34}$$

where r is radial coordinate counted from the center of the droplet.

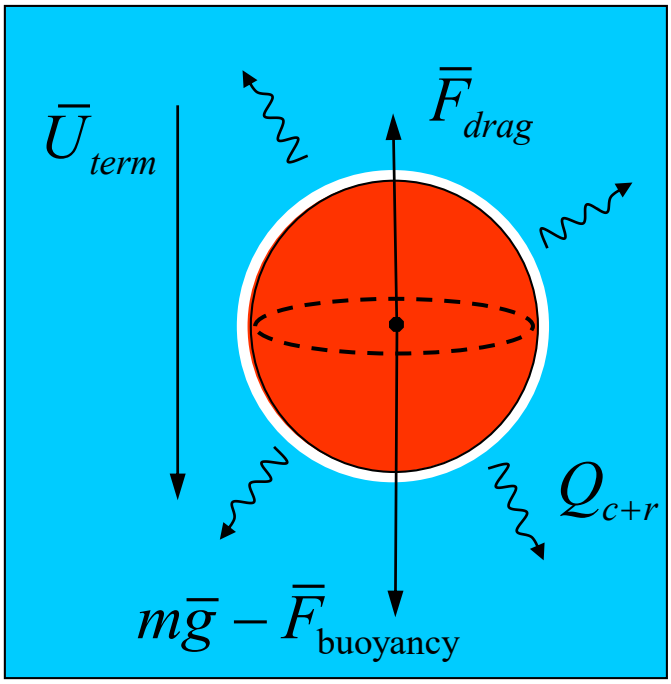

Figure 3.83. Physical phenomena and parameters for single droplet sedimentation and cooling.

Second stage is solidification. It begins at the moment when droplet temperature reaches the melting point. During this stage particle has a liquid core and a solid layer (crust) at the surface. At this stage temperature profile inside solidifying particle can be approximated as [137]:

$$T(r,t) = T_m - \left[T_m - T_{fs}(t)\right]\frac{r - r_i}{R - r_i}\theta(r - r_i) \tag{3.35}$$

where $R = d_f/2$ is outer radius of the particle, $T_{fs}(t) = T(R,t)$ is surface temperature of the particle, T_m is corium melting temperature, r_i is current radius of the crystallization front inside the particle, $\theta(x)$ is Heaviside step function.

Using temperature profile (3.35) in equations for transient heat conduction problem for opaque spherical particle during the particle solidification the following coupled ordinary differential equations with initial conditions can be obtained [137], [117]:

$$\begin{aligned}\left[\left(T_m - T_{fs}\right)\frac{1 + 2\hat{r}_i + 3\hat{r}_i^2}{4} + 3\frac{L_f\hat{r}_i^2}{c_f}\right]\frac{d\hat{r}_i}{dt} + + \frac{3 - \hat{r}_i - \hat{r}_i^2 - \hat{r}_i^3}{4}\frac{dT_{fs}}{dt} \\ = -\frac{3}{\rho_f c_f R}(\alpha_c + \alpha_r)\left(T_{fs} - T_a\right)\end{aligned} \tag{3.36}$$

$$\left[\frac{\lambda_f}{R} + (1-\hat{r}_i)(\alpha_c+\alpha_r)\right]\frac{dT_{fs}}{dt} = (\alpha_c+\alpha_r)(T_{fs}-T_a)\frac{d\hat{r}_i}{dt} - (1-\hat{r}_i)\left[(T_{fs}-T_a)\left(\frac{d\alpha_c}{dt}+\frac{d\alpha_r}{dt}\right) - (\alpha_c+\alpha_r)\frac{dT_a}{dt}\right]$$

$$\hat{r}_i(0) = 1; \quad T_{fs}(0) = T_m$$

where $\hat{r}_i = r_i/R$, and λ_f is corium thermal conductivity.

The problem (3.36) is solved from $t = 0$ to $t = t_{sol}$ when complete solidification is achieved, which is defined by equation $\hat{r}_i(t_{sol}) = 0$. During solidification stage the crust thickness is calculated as $\delta = R - r_i$ (see Figure 3.84).

Third final stage is cooling of the solid particle. It is characterized by parabolic temperature profiles typical for quasi-steady cooling regime with no phase change:

$$T(r,t) = T_c(t) - \left[T_c(t) - T_{fs}(t)\right]\left(\frac{r}{R}\right)^2 \tag{3.37}$$

where T_c is temperature of the particle center.

At the beginning of this stage it is assumed that surface temperature T_{fs} is equal to $T_{fs}(t_{sol})$ taken from the solution presented above. A relation between average and surface temperatures can be obtained as solution of equations for transient heat conduction problem for an opaque spherical solid particle using temperature profile (3.37):

$$T_f = T_{fs} + 0.2\frac{R}{\lambda_f}(\alpha_c+\alpha_r)(T_{fs}-T_a) \tag{3.38}$$

Average temperature T_f is calculated from the energy balance equation (3.30). Then the surface temperature is obtained from equation (3.38).

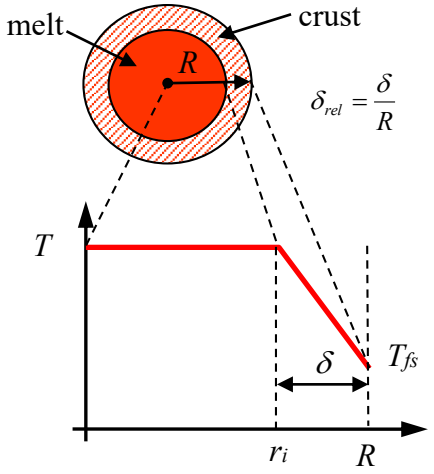

Figure 3.84. Particle solidification parameters.

Described model has two main advantages in comparison to the isothermal particle

model. The first obvious benefit is that calculations of heat transfer between the corium and water based on the particle surface temperature are more accurate. However, the most important for prediction of agglomeration is that the dynamics of crust solidification on the corium particle surface is explicitly resolved. The crust layer on the surface of solidifying particles should be taken into account in the estimates of possible further fragmentation and agglomeration of the melt particles.

Significant improvement of the computational efficiency can be achieved if each droplet cooling transient is calculated only once and used then as a lookup table to determine particle parameters at certain depth. Therefore a database of pre-calculated solutions for particles of different diameters is generated using described above modeling assumptions, and wide ranges of initial and boundary conditions.

The database of pre-calculated solutions of particle dynamics and heat transfer for all possible combinations of particle initial velocities and temperatures would be an enormous task. If coolant velocity is constant, particle velocity with respect to the coolant relatively quickly approaches to the terminal velocity that can be calculated according to the formula:

$$U_\tau = \sqrt{\frac{4g(\rho_f - \rho_a)d_f}{3\rho_a C_d}} \tag{3.39}$$

Therefore we use following approach to reduce the size of the database of single particle sedimentation and cooling histories:

- Individual histories are calculated for each selected particle diameter and coolant void fraction (e.g. void fraction in the range from 0 to 1 with a step 0.1 and particle diameters from ~0.1 to 12mm).
- Terminal velocity and a high (~1000K) melt superheat above liquidus point (to cover possible ranges of possible initial melt superheats in practical application of the SM) are used as initial conditions for simulation of the histories.
- Convective heat transfer between particle and coolant is determined using terminal velocity.
- Parameters of the particles are calculated as functions of so called “sedimentation lengths” L_s – the trajectory length of the particle moving with terminal velocity in the frame of reference attached to the coolant. The effects of coolant velocity (vertical and horizontal component), the difference between initial droplet velocity and terminal velocity, etc. can be taken into account through so called “effective sedimentation length” L_s^{eff}. L_s^{eff} is determined such that L_s^{eff}/U_τ is equal to the time of the particle residence in the coolant during which it travels distance L_s.

Initial velocity U_0 of the droplet created in the process of jet breakup is considered to be equal to the jet velocity, which in general case, is different from the terminal velocity. Except for the case of large void fraction in the FCI zone, initial velocity of the droplet is larger than terminal velocity, which increases effective sedimentation length. Time t^* necessary for reaching $U^* = 1{,}001 \cdot U_\tau$ can be estimated by integrating equation equations of particle motion (3.29) in the following form

$$\frac{dU_f}{dt} = \frac{3}{4} C_D \frac{\rho_a}{\rho_f} \frac{1}{d_f} \left(U_\tau^2 - U_f^2\right) \tag{3.40}$$

where U_0 is used as initial fuel droplet velocity:

$$t^* = \frac{2}{3}\frac{d_f}{C_D}\frac{\rho_f}{\rho_a}\frac{1}{U_\tau}\left(\ln\left|\frac{U_0 - U_\tau}{U_0 + U_\tau}\right| - \ln\left|\frac{U^* - U_\tau}{U^* + U_\tau}\right|\right) \tag{3.41}$$

The distance that particle will travel during t^* also can be calculated:

$$L^* = \frac{2}{3}\frac{d_f}{C_D}\frac{\rho_f}{\rho_a}(\ln|U_0^2 - U_\tau^2| - \ln|U^{*2} - U_\tau^2|) \tag{3.42}$$

If $L^* \leq L_s$, then effective sedimentation length is calculated as follows

$$L_s^{eff} = L_s - L^* + U_\tau t^* \tag{3.43}$$

If $L^* > L_s$ then t^* is calculated from equation (3.41) where U^* is calculated from (3.42) by substituting $L^* = L_s$. Then effective sedimentation length is determined as

$$L_s^{eff} = U_\tau t^* \tag{3.44}$$

If an average coolant velocity in the FCI zone has a non-zero vertical component U_a^v then a cinematic Galilean transformation (3.45) is used

$$L_s^{eff} = L_s \frac{U_\tau}{(U_a^v + U_\tau)} \tag{3.45}$$

The effect of the coolant lateral velocity in the FCI zone is more complex. In order to take it into account we use a simplified approach for correction of L_s^{eff}

$$L_s^{eff} = L_s \frac{\sqrt{U_\tau^2 + U_a^{l2}}}{U_\tau} \tag{3.46}$$

Any combination of the corrections to L_s^{eff} can be applied by consecutive application of respective equations (3.43) or (3.44) and (3.45), (3.46).

Physical Effects and Feedbacks Approximated from FM and Available Experimental Data

Most of the physical phenomena are modeled in the proposed SM explicitly. However, mutual feedbacks between such parameters as jet breakup length and coolant void fraction are not modeled directly in the SM. Nevertheless, SM can take these effects into account if such relations are provided as external closures, e.g.

$$\begin{gathered} L_{brk} = L_{brk}\left(D_{jet}, \varphi, \ldots\right) \\ \varphi = \varphi\left(D_{jet}, C_{FCI}, \ldots\right) \end{gathered} \tag{3.47}$$

We use “calibration” of the SM to determine such relations using data from the FM analysis.

3.7.1.1.4 Particle fragmentation

Particle size distribution is one of the most influential parameters for the debris

spreading and porous bed coolability [101], [122]. It can be predicted based on the models which take into account local parameters of the melt-coolant interactions and liquid melt breakup phenomena. Alternatively, it can be determined based on the available data from the corresponding experiments. There is are different models proposed for melt fragmentation. However, there is a lack of consensus about a best universal approach. On the other hand, as it was shown in [126] [91], comparison of data from different FCI tests with simulants and prototypical corium mixtures suggests that the ranges of particle size distributions for binary oxides of heavy metals are quite close to each other despite sometimes significant differences in the experimental conditions (such as initial melt temperatures, pool size, jet diameter, free fall height etc.) Therefore, in order to avoid uncertainties associated with the droplet fragmentation models, in this work we use fixed size distribution obtained in the DEFOR-A experiments [126], [91] which also agrees well with the data from FARO tests with prototypic corium mixtures [124].

3.7.1.1.5 Coolant void fraction generated in FCI zone

In case of a steady state complete jet fragmentation in a pool

$$G_{frag} = G_{in} = \frac{\pi}{4} D_{jet}^2 U_{jet} \rho_f, \tag{3.48}$$

where G_{in}, G_{frag} are mass flow rates of the melt at the jet orifice and fragmented melt respectively, D_{jet}, U_{jet} are diameter and velocity of the jet at the coolant free surface and ρ_f is melt density. Energy rate introduced along with the melt is

$$Q_{in} = G_{in}\left(c_m T_{in} + h_{fus}\right) \tag{3.49}$$

where c_f is specific heat capacity, T_{in} is initial temperature, h_{fus} is latent heat of fusion.

At the same time, energy rate of melt droplets leaving FCI zone is

$$Q_{out} = G_{in} \sum_{i=1}^{n} f_m^i \left\{ c_f T_{out}^i + h_{fus} \theta\left(T_{out}^i - T_{sol}\right) \right\} \tag{3.50}$$

where f_m^i is mass fraction of i^{th} group of droplets (determined by the droplets size), T_{out}^i is temperature of the i^{th} droplets when they are leaving FCI zone, T_{sol} is melt solidification temperature, $\theta(x)$ is Heaviside step function.

Assuming that all heat transferred from the melt to the liquid coolant contributes to evaporation of the coolant, the steam mass generation rate can be expressed as

$$\begin{aligned} \dot{M}_{in} &= (1-\varphi)\frac{Q_{in} - Q_{out}}{h_{ev}} \\ &= (1 \\ &- \varphi)\frac{\pi D_{jet}^2 U_{jet} \rho_f}{4 h_{ev}} \sum_{i=1}^{n} f_m^i \left(c_f\left(T_{in} - T_{out}^i\right) + h_{fus}\theta\left(T_{out}^i - T_{sol}\right)\right) \\ &= \end{aligned} \tag{3.51}$$

$$= (1-\varphi)\frac{\pi D_{jet}^2 U_{jet}\rho_f}{4h_{ev}}\sum_{i=1}^{n} f_m^i\,\Delta h^i$$

where φ is volumetric void fraction, h_{ev} is latent heat of evaporation, Δh^i is specific enthalpy change of i^{th} droplets group during sedimentation.

Generated steam is leaving FCI zone at the top boundary. Mass flow rate of the steam outflow can be estimated as

$$\dot{M}_{out} = \varphi A_{FCI} U_v \rho_v \tag{3.52}$$

where $A_{FCI} = \frac{\pi D_{FCI}^2}{4}$ is cross-section area of FCI zone, D_{FCI} is characteristic diameter of FCI zone, U_v is vapor velocity at the top of the FCI zone, and ρ_v is vapor density.

Maximum possible vertical velocity of the vapor at the top boundary can be assessed using Archimedes buoyancy force

$$U_{v,max} = \sqrt{2g\frac{(\rho_w - \rho_v)}{\rho_v}H^*} \tag{3.53}$$

where ρ_w is density of liquid coolant and H^* is characteristic length for vapor acceleration. Note that real vapor velocity can be much smaller than $U_{v,max}$ due to the drag in the two-phase flow. We define height of the FCI zone as H^* (the distance from the leading edge of the jet to the bottom of the pool). This height is considered as the particle sedimentation length L_s in the SM.

$$H^* = L_s = H_{pool} - L_{brk} \tag{3.54}$$

We introduce a closure C_{FCI} parameter as a product of the two ratios (i) area or FCI zone to the area of jet, and (ii) actual steam velocity to maximum steam velocity at the top of the FCI zone.

$$C_{FCI} = \frac{D_{FCI}^2}{D_{jet}^2}\,\frac{U_v}{U_{v,max}} \tag{3.55}$$

C_{FCI} also can be interpreted as a normalized non-dimensional steam flow rate at the top of the FCI zone. This parameter is not modeled in the SM and is subject to calibration (see next section).

In a steady state steam generation and evacuation rates are equal to each other. Substituting (3.53), (3.54) and (3.55) into (3.51) and (3.52), one can obtain

$$(1-\varphi)\frac{U_{jet}\rho_f}{h_{ev}}\sum_{i=1}^{n} f_m^i \Delta h^i = \varphi C_{FCI}\rho_v\sqrt{2g\frac{(\rho_w-\rho_v)}{\rho_v}\left(H_{pool}-L_{brk}\right)} \tag{3.56}$$

From equation (3.56) the vapor volume fraction can be obtained

$$\varphi = 1 - \frac{1}{\left(1 + \frac{U_{jet}\rho_f \sum_i^n f_m^i \Delta h^i}{C_{FCI}\rho_v h_{ev}\sqrt{2g\frac{(\rho_w - \rho_v)}{\rho_v}(H_{pool} - L_{brk})}}\right)} \quad (3.57)$$

3.7.1.1.6 Coolant vertical velocity in FCI zone

Mass flow rate of melt particles sedimentation to the bottom of the pool can be expressed as

$$G_{sed} = f\frac{\pi}{4}D_{FCI}^2\hat{U}_{sed}\rho_f \quad (3.58)$$

where f $\hat{\mathrm{V}}_{\mathrm{sed}}$ is volume fraction of the melt, $\hat{U}_{sed}$ is averaged particle sedimentation velocity. In steady state mass flow rate of particle generation and sedimentation are equal. Using equations (3.48) and (3.58) one can obtain expression for volume fraction of the melt in the FCI zone.

$$f = \frac{D_{jet}^2 U_{jet}}{D_{FCI}^2 \hat{U}_{sed}} \quad (3.59)$$

It is instructive to note that at relatively high melt fraction, group effects can affect particle dynamic such that motion of individual particles is not independent any more. Such conditions are beyond the scope of this paper.

Residence time of each portion of the particles in the FCI zone can be estimated as

$$t_{sed} = \frac{H^*}{\hat{U}_{sed}} \quad (3.60)$$

where H^* characteristic height of the FCI zone.

Coolant in the FCI zone is accelerated due to the drag force F_{drag} between the particles and the coolant. Assuming that coolant velocity is proportional to drag force

$$U_a^v \sim f F_{drag} t_{sed} \sim f\frac{\hat{U}_{sed}^2}{\hat{d}_f}\frac{H^*}{\hat{U}_{sed}} \quad (3.61)$$

we introduce following closure for the coolant vertical velocity in the SM model:

$$U_a^v = C_v\frac{U_{jet}H^*}{\hat{d}_f} + B_v \quad (3.62)$$

where $\hat{d}_f$ is an averaged particle diameter, C_v $\mathrm{C_m}$, $\mathrm{C_v}$ and B_v are the closure parameters. C_v includes a ratio of the areas of the jet cross section to FCI zone cross section, and an coefficient of proportionality. The values of C_v and B_v are calibrated using FM data. Average particle diameter is calculated in SM according to the particle size distribution.

3.7.1.1.7 Coolant lateral velocity in FCI zone

In the framework of the SM 3D flow effects (such as lateral component of coolant velocity) are not modelled in SM. In order to provide a closure for taking into account such effects we use an approximation of the FM solution.

Implementation of the SM for prediction of debris agglomeration

The developed surrogate model for prediction of agglomeration fraction consists of the following main steps:

1. Determination of parameters of the melt release scenario such as:
    a. Melt thermo-physical properties such as density, solidus, liquidus and initial temperatures, etc.
    b. Melt release conditions, i.e. melt flow rate (initial melt velocity), initial jet diameter, jet free fall height, pool depth, etc.
2. Creation of a database of cooling histories for single droplets of different diameters using models for:
    a. drag of a spherical particle,
    b. film boiling and radiation heat transfer,
    c. particle temperature profile,
    d. crust formation.
3. Assessment of the parameters of corium jet at water pool surface according to the jet free fall model.
4. Calculation of jet breakup (jet penetration) length using respective correlations.
5. Determination of melt droplet size distribution.
6. Prediction of the fraction of liquid droplets at certain pool depth using the database for single droplet cooling histories and melt release scenario parameters.
    a. Particle sedimentation length is determined using scenario data (pool depth), the jet breakup length and some other task parameters (jet velocity, coolant motion).
    b. Fraction of liquid particles is obtained from pre-calculated database.
    c. Liquid droplets are determined as particles which have crust thickness less than certain value at given pool depth.
    d. Mass faction of liquid droplets at certain depth is determined taking into account particle size distribution.
7. To calculate mass fraction of agglomerated debris using the correlation for agglomeration coefficient and predicted mass fraction of liquid droplets.

When surrogate model is applied, first, effective particle sedimentation length L_s^{eff} is determined using scenario data and the jet dynamics.

The database of the particles sedimentation, cooling and solidification histories is searched to find state of the individual particles at given L_s^{eff} and other parameters of the scenario such as water temperature, melt superheat, void fraction etc. The search process is iterative because determination of void fraction in the FCI zone requires knowledge of integral heat loss from the particles which in turn depends on the void fraction.

Fraction of liquid particles is obtained from pre-calculated database. Liquid droplets are determined as particles which have crust thickness less than certain value at given pool depth. In this analysis the selected crust thickness fraction threshold was 0.1 for the sake of conservatism. Mass faction of liquid droplets is determined taking into account

particle size distribution.

Finally mass fraction of agglomerated debris is determined using model proposed and validated in [92], [93], [52], [96], [98], [97]

$$m_{aggl} = \alpha(m_{liq}) \cdot m_{liq}, \tag{3.63}$$

where m_{aggl} is the mass fraction of agglomerated debris, m_{liq} is the mass fraction of of "liquid particles" which have relative crust thickness (crust thickness divided by particle radius) smaller than certain value (e.g. 0.1 in this work) and $\alpha(m_{liq})$ is a coefficient of agglomeration, which is a function of mass fraction of the liquid particles

$$\alpha(m_{liq}) = \begin{cases} 4 \cdot m_{liq}, & m_{liq} \leq 0.5 \\ 1/m_{liq}, & m_{liq} \geq 0.5 \end{cases} \tag{3.64}$$

Post-processing of the FM data

Proposed SM was calibrated and verified using FM data for different scenarios of melt ejection from the vessel into a flooded drywell of a Nordic BWR. The goal of such FM calculations was to obtain mass fraction of agglomerated debris at the bottom of the pool as a function of melt release scenario parameters. Most important parameters of the scenarios are presented in Table 3.11. Main variable parameters are pool depth, jet diameter and melt superheat.

Table 3.11. Melt release scenario conditions

Parameter	Value
Pool parameters	
Diameter, m	9
Depth, m	7-12
Initial pressure, bar	1
Water temperature, K	373
Melt parameters	
Composition	Eutectic corium, steel
Total mass, t	180
Initial met superheat, K	200-1000
Jet diameter, mm	50-360
Jet release height above water surface, m	1-6

FM resolves temporal and spatial distribution of thermal hydraulic parameters [127], [117] while SM is a combination of steady 0D and 1D models. In order to use FM data for calibration of SM closures the data has to be averaged in space and time. VAPEX-P saves thermal hydraulic data on the computation grid for continuous and disperse phases (volume fractions, velocities, temperatures, etc.) with certain time interval (e.g. 0.1 seconds). A separate post-processor code averages data over a selected sub-domain in space and time for: volume factions of coolant and particles, water velocity, steam velocity, It is instructive to note that averaged parameters are necessary to identify conditions which would be most representative for a particle sedimentation and cooling history in the FCI one. Therefore each parameter y is averaged with respect to corium

volume fraction in addition to averaging in space and time

$$\hat{y} = \frac{\sum(\tau v_i f_i y_i)}{t_\Sigma V_\Sigma \sum(f_i)} \tag{3.65}$$

where τ is interval for saving the data, v_i is volume of the grid cell, f_i is volume fraction of corium in the grid cell, y_i is the value of the averaged parameter in the cell, t_Σ is time averaging interval, V_Σ is volume of the averaging sub-domain. All parameter are averaged independently from each other.

One of the important problems for proper averaging of the FM data is selection of the averaging sub-domain. Small size particles can spread by convective flows in the pool. This might lead to overestimation of the contribution to the averaged parameters of the cells with small fractions of the particles. Analysis of the FM data suggested that the zone with non-negligible fraction of particles has quite well defined boundaries, beyond which the amount of particles drops by an order of magnitude or more. This zone is used as averaging sub-domain. In each FM analysis the size of the zone is different. An example of the averaging domain is shown in Figure 3.85 (width of about ~1.8m, height from the bottom of the pool to the leading edge of the jet). The grid is 5x13 cells, each cell is 0.9 m wide in radial direction and 1.0m tall.

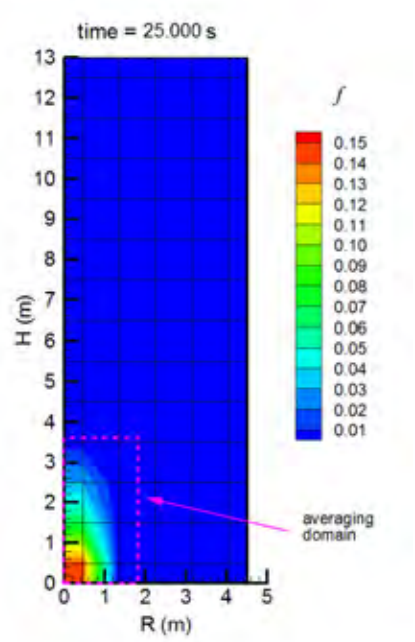

Figure 3.85. An example of FM parameter averaging domain.

Calibration and Verification of the Surrogate Model Closures

First a confirmation of adequacy of proposed physical models was carried out by comparison of SM and FM predictions with all closure parameters fixed to the averaged values obtained from the FM data analysis. The purpose of the analysis is to demonstrate that physical models, which constitute the SM, can reproduce FM solution with reasonable accuracy if adequate closures will be provided. An example of comparison of the FM and SM results is presented in Figure 3.86. The results are obtained for metallic melt properties, superheat of 1000 K, and different jet diameters

and pool depths. Values of the jet breakup length L_{brk}, vapor volume fraction φ, vertical U_a^v and lateral U_a^l components of water velocity in the FCI zone were fixed to the averaged values obtained in the respective FM calculations. Analysis of the data suggested that the difference in the predicted by FM and SM jet dimeters at which fraction of agglomeration reaches 0.1 does not exceed 7-9%, which is considered as acceptable accuracy, given other sources of uncertainties in severe accident analysis.

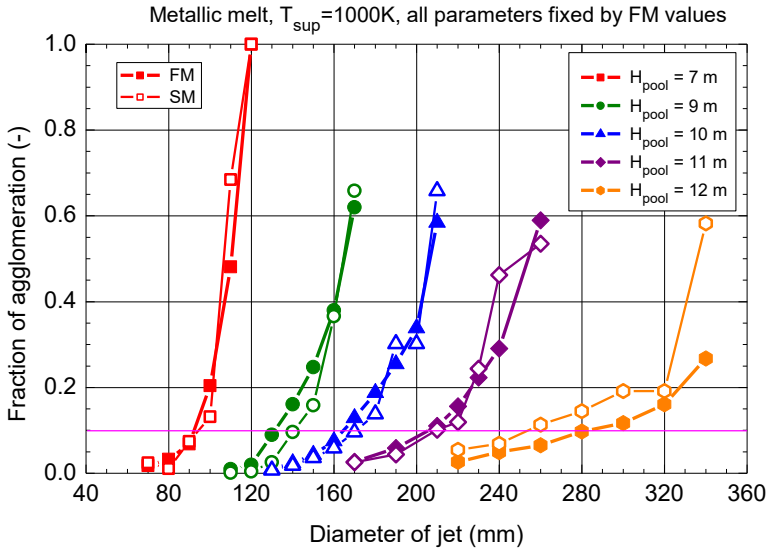

Figure 3.86. Comparison of predictions of mass fraction of agglomerated debris with FM and SM with closures parameters determined by averaging of the FM data. Solid symbols – FM, hollow ones – SM.

Correlation between Jet Breakup Length in Surrogate and Full models

The difference in prediction of the jet breakup length with Saito correlation (3.28) and FM is shown in Figure 3.87 for the case with metallic melt at superheat of 1000 K. The data demonstrates the effect of the feedbacks and phenomena of the jet – coolant interactions, which are not modeled directly in the SM. The most significant difference is observed for shallower pools. In order to minimize the difference between jet breakup length predicted by SM and FM, we introduce a correction factor L_{corr}

$$L_{brk} = L_{brk}^S - L_{corr} \tag{3.66}$$

where L_{brk}^S is predicted with Saito correlation (7). Main factor which affects jet breakup length is drag force F_{drag} between melt jet and coolant. Therefore it is assumed that

$$L_{corr} \sim F_{drag} t_{brk}^2 \sim \frac{U_{jet}^2}{D_{jet}} \frac{L_{brk}^2}{U_{jet}^2} = C_L \frac{L_{brk}^2}{D_{jet}} + B_L \tag{3.67}$$

where t_{brk} $\tilde{\mathrm{V}}_{\mathrm{sed}}$ is characteristic time of fragmentation of a portion of the melt, C_L and B_L are closure parameters. In the process of calibration following expressions for of C_L and B_L were obtained

$$C_L = \frac{0{,}004}{\sqrt{D_{jet}}}, \qquad B_L = 0.01 \tag{3.68}$$

In Figure 3.88 the difference between prediction of the FM and calibrated SM model is presented. Reasonable agreement between the data is achieved.

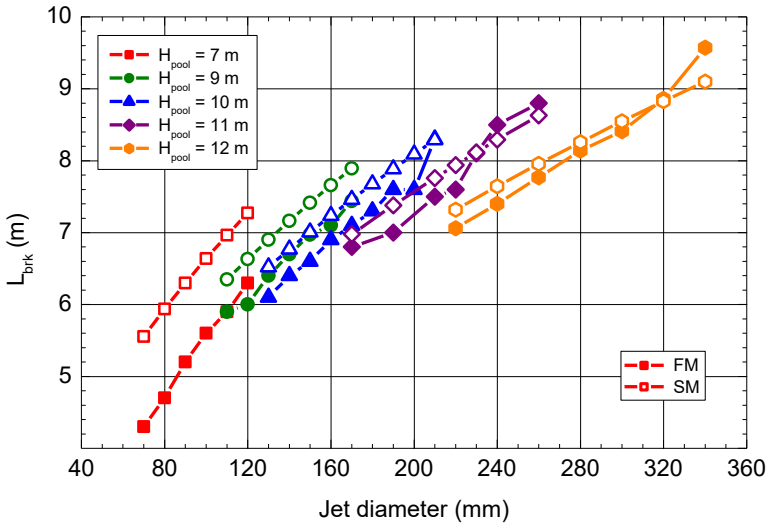

Figure 3.87. Comparison between jet breakup lengths predicted with Saito (3.28) and FM.

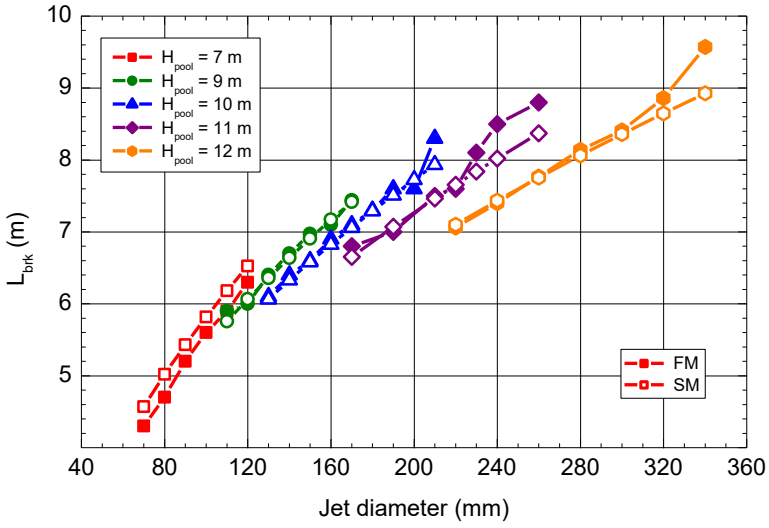

Figure 3.88. The difference between jet breakup lengths predicted by FM and SM after correction.

In Figure 3.89 a comparison of the FM and SM predictions of agglomerated debris fraction is presented for metallic melt properties and superheat of 1000 K. SM results are obtained with L_{brk} predicted with the closure (3.66)-(3.68). The other closure parameters are fixed to the averaged values obtained from FM data. Comparison of Figure 3.86 and Figure 3.89 demonstrates the effect of the closure of the jet breakup length on the fraction of agglomerates. A reasonable agreement between FM and SM data is observed.

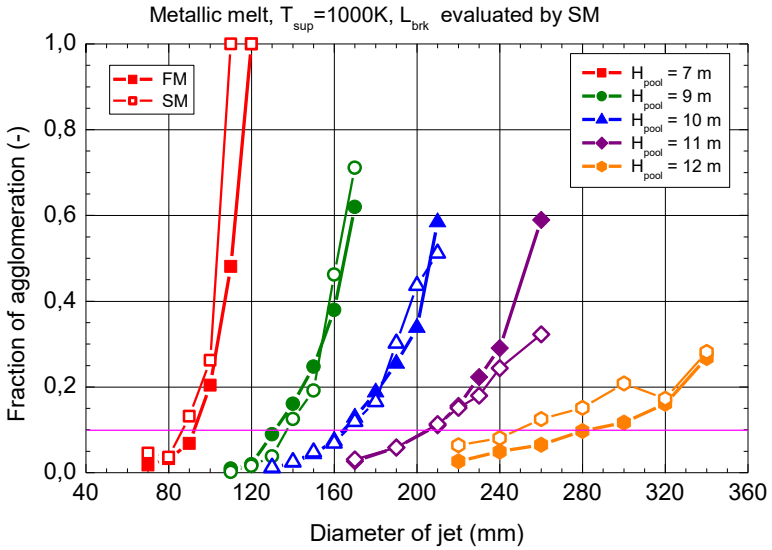

Figure 3.89. Comparison of predictions of mass fraction of agglomerated debris with FM and SM with jet breakup length predicted by SM and the other closures parameters fixed to those obtained from averaging of the FM data.

Calibration of the Model for Void Fraction in the FCI zone

Another uncertain parameter in the framework of the SM is C_{FCI} in the model for estimation of void fraction in FCI zone. This parameter is also be calibrated using the data from the FM. The closure was calibrated in order to minimize the difference between predicted void fraction with FM and SM. All other closures were fixed to the data obtained in the FM.

$$C_{FCI} = 42 + \frac{26}{D_{jet}} + \frac{4}{D_{jet}^2} \tag{3.69}$$

In Figure 3.90 we present void fraction in the FCI zone obtained for different scenarios of melt release using equation (3.57) with closure (3.69). In Figure 3.91 a comparison of the FM and SM prediction of the fraction of agglomerates is presented for metallic melt release with 1000 K superheat. Void fraction in the FCI zone was obtained using the calibrated SM closure and other closure parameters fixed according to the data obtained from FM. A reasonable agreement suggest that the model for the FCI zone voiding provides a reasonable closure for the SM.

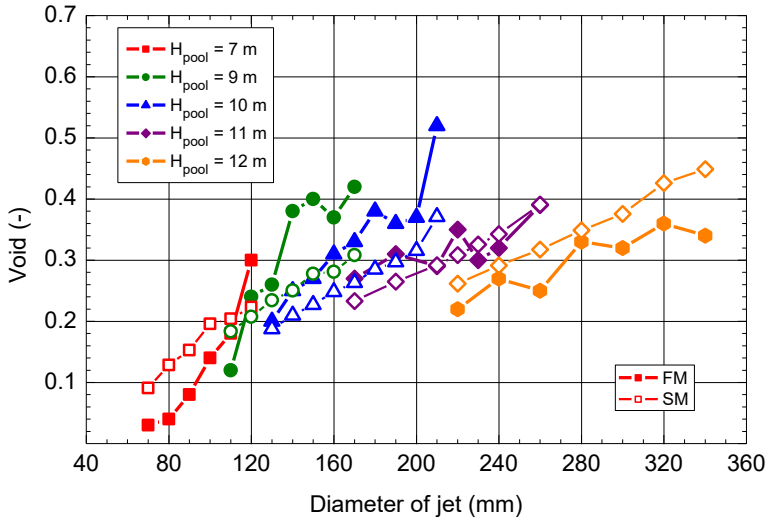

Figure 3.90. Comparison of void fraction predicted by SM and FM.

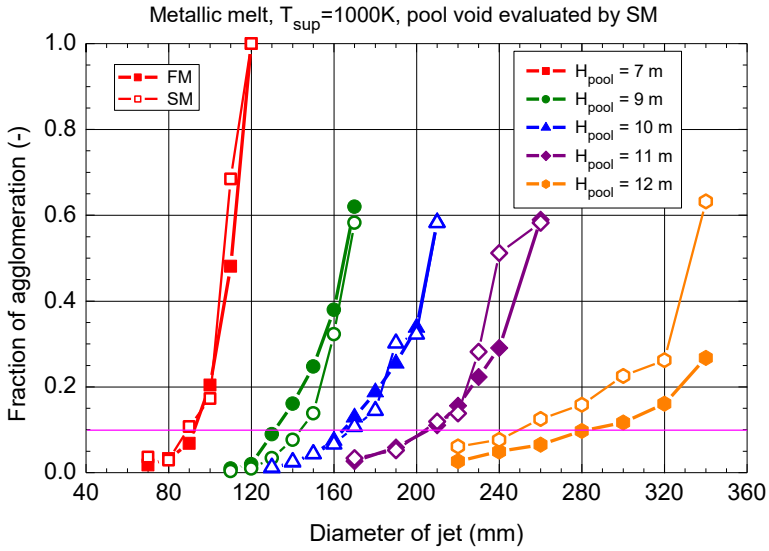

Figure 3.91. Comparison of predictions of mass fraction of agglomerated debris with FM and SM with void fraction predicted by SM and the other closures parameters fixed to those obtained by averaging of the FM data.

Calibration of coolant vertical velocity model

Calibration of the closure parameters C_v and B_v from the model for vertical component of coolant velocity provided following expressions

$$C_v = \frac{0.023 D_{jet}^2}{4 + 12 D_{jet} + 9 D_{jet}^2}, \qquad B_v = -0.3 \tag{3.70}$$

Figure 3.92 presents results for coolant vertical velocity in the FCI zone obtained for different scenarios of melt release using equation (3.62) with closure (3.70). As in previous cases a reasonable agreement was achieved. In Figure 3.93 a reasonable agreement between FM and SM predictions for the fraction of agglomerated debris is

presented for the case of metallic melt release at 1000 K superheat. Vertical component of the coolant velocity was estimated using obtained closure and the other closure parameters were fixed according to the FM data.

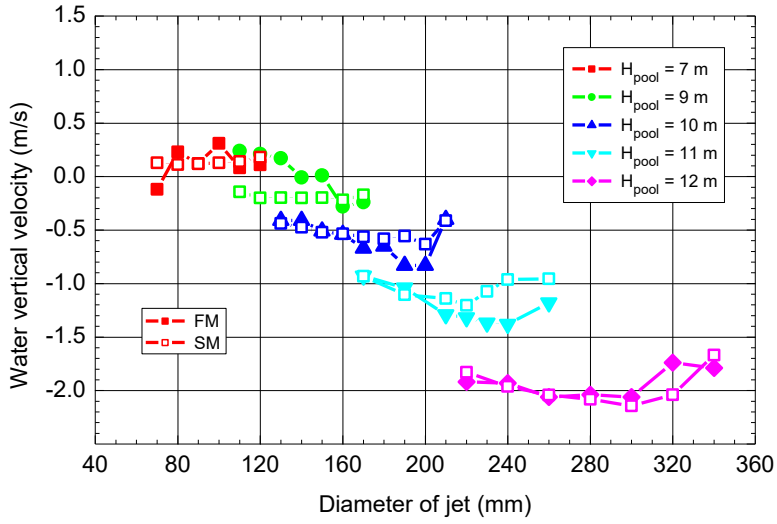

Figure 3.92. Comparison of water vertical velocity by SM and FM.

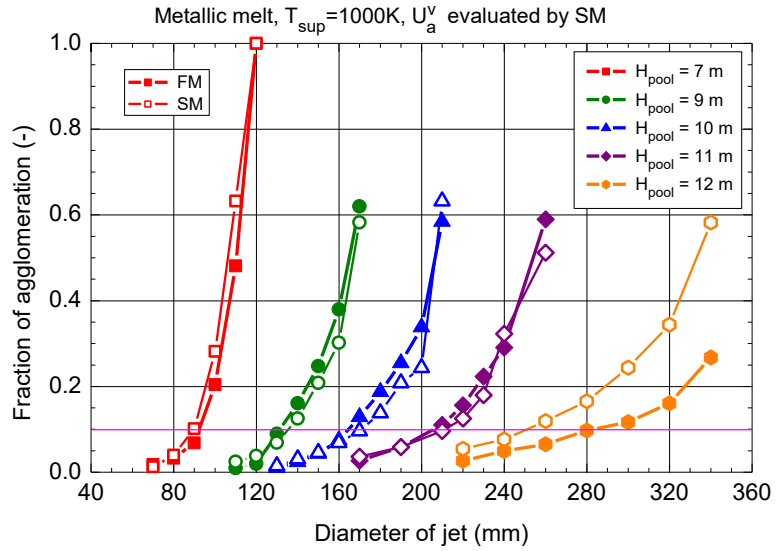

Figure 3.93. Comparison of predictions of mass fraction of agglomerated debris with FM and SM with coolant vertical velocity predicted by SM and the other closures parameters fixed to those obtained by averaging of the FM data.

Calibration of coolant lateral velocity model

Due to the inherent limitations of the 0D approach it was not possible to propose a physics based closure for assessing lateral component of coolant velocity. Therefore this parameter is was obtained directly from calibration process as a function of the jet diameter $U_a^l = f(D_{jet})$

$$U_a^l = \begin{cases} 0.05, & if\ D_{jet} \leq 0.15 \\ 10D_{jet}^2 - 0.5D_{jet} - 0.1, & if\ D_{jet} > 0.15 \end{cases} \quad (3.71)$$

In Figure 3.94 lateral component of coolant velocity obtained with FM and with the closure (3.71) are compared. Fractions of agglomerated debris predicted with FM and SM are compared in Figure 3.95. As in the previous cases we show data for metallic melt release with melt superheat 1000 K. Lateral coolant velocity in the FCI zone was obtained in SM using (3.71) and the other parameters where fixed according to the averaged data from FM solutions.

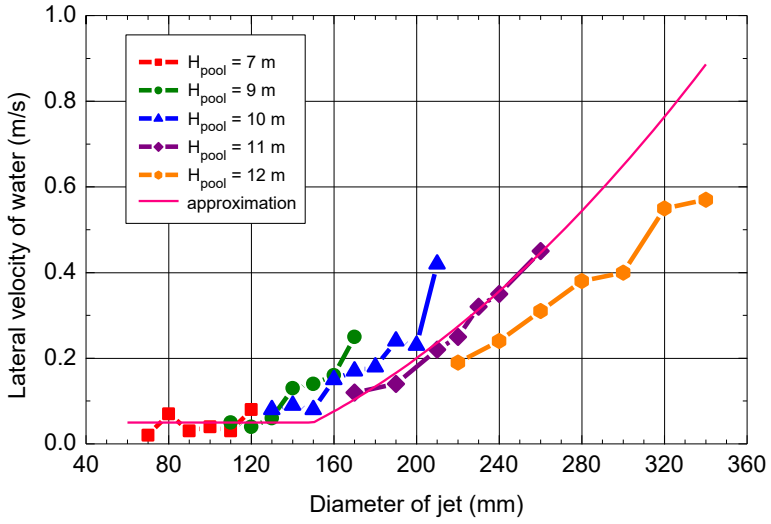

Figure 3.94. Comparison of water lateral velocity predicted by SM and FM.

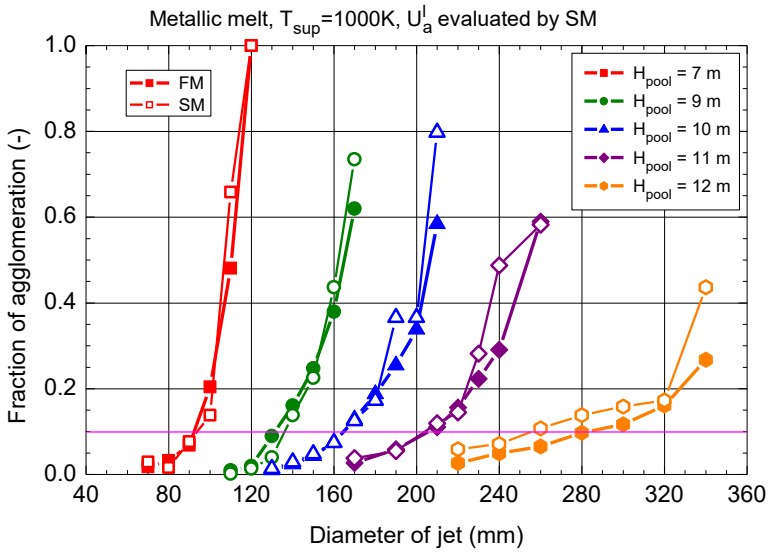

Figure 3.95. Comparison of predictions of mass fraction of agglomerated debris with FM and SM with coolant lateral velocity predicted by SM and the other closures parameters fixed to those obtained by averaging of the FM data

Validation of SM

While verification shows some discrepancies between FM and SM, validation can reveal discrepancy between SM and physical reality. In order to validate developed SM the model was applied to predict DEFOR-A2 test results [126], where significant influence of the coolant flow was observed [97]. Figure 3.97 presents a comparison between experimental data on mass fraction of agglomerated debris measured at 4 different elevations and SM model prediction. Input parameters were determined according to the experimental conditions. Analysis was done using all SM models and closures described in the previous sections. No model further calibration of the SM closures was used. The only difference was that instead of the conservative approach a best estimate model suggested in [97] was used for prediction of the fraction of agglomerates as a function of the mass fraction of liquid droplets. Good agreement with experimental data suggest that the model is capturing the key physics and can be applied at different scales.

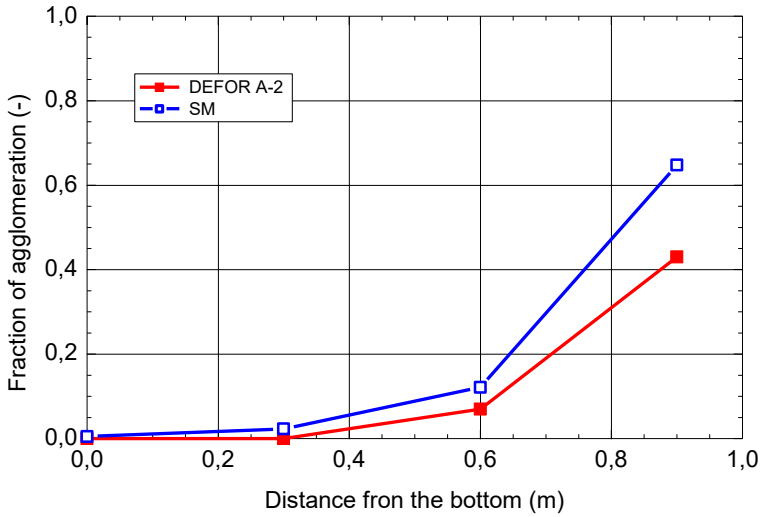

Figure 3.96. Comparison of mass fraction of agglomerated debris obtained in DEFOR-A2 test and SM calculation.

Application of Developed SM to Plant Scale Analysis and Computational Efficiency

In Figure 3.97 results obtained with SM and FM for metallic melt at 1000 K superheat are presented. Other important parameters of considered scenarios are presented in Table 3-12. Analysis was done with FM and SM for each combination of jet diameter and water pool depth. Comparison of results suggests that calibrated SM can reproduce mass fraction of agglomerated debris predicted by full model for the considered ranges of jet diameters and pool depth with sufficient accuracy. The difference between SM and FM in predicted jet diameters corresponding to agglomeration fractions 10%, which can negatively affect coolability [35], does not exceed 9%.

Table 3-12 Debris catchers

Parameter	Value
Pool parameters	
Diameter, m	9
Depth, m	7-12
Initial pressure, bar	1
Water temperature, K	373
Melt parameters	
Composition	Eutectic corium, steel
Total mass, t	180
Initial met superheat, K	200-1000
Jet diameter, mm	50-360
Jet release height above water surface, m	1-6

It is instructive to note that FM single calculation for one point in Figure 3.97 (one combination of jet size and pool depth) can take between 24 to 168 hours of computational time. While obtaining complete set of the data (all curves in Figure 3.97) using SM on the same computer takes less than half an hour (with post processing of the results). This is a significant improvement in computation efficiency. However, it might be still insufficient for extensive uncertainty analysis and risk assessment [128]. Nevertheless, such physics based surrogate model can be used for generation of sufficiently large database of solutions for training of an Artificial Neural Network.

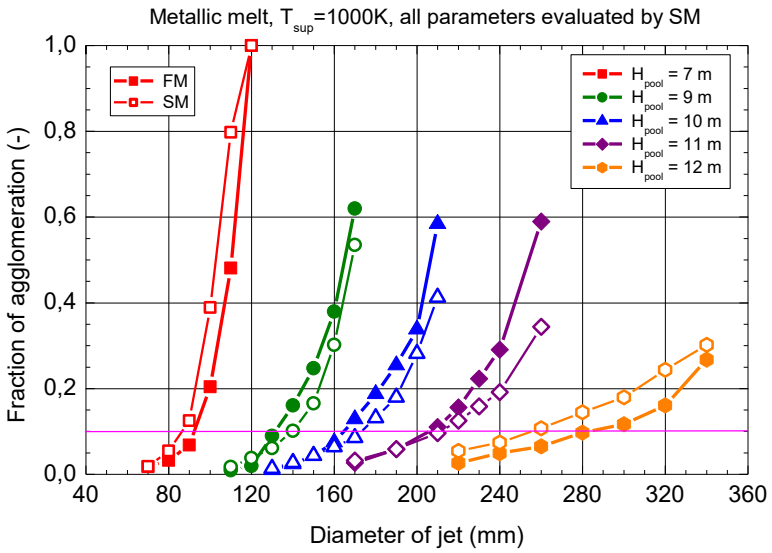

Figure 3.97. Comparison of predicted mass fraction of agglomerated debris with FM and SM (all closure parameters calculated by SM).

Summary and Conclusions

Physics based surrogate modeling (SM) approach is proposed for prediction of mass fraction of agglomerated debris in case of corium melt release into a pool of water. The

SM aim is to reproduce results of the full model (FM) fuel coolant interaction code VAPEX-P. The SM is based on decomposition of initial tightly coupled problem into a set of loosely coupled ones, i.e. (i) jet breakup; (ii) particle sedimentation, cooling and solidification; (iii) agglomeration of incompletely solidified debris. These problems can be linked together through initial and boundary conditions. Due to the loose coupling, it is possible to pre-calculate a set of solutions in order to increase the computational efficiency of the whole model. Specifically, cooling and sedimentation histories of individual particles of different diameters are pre-calculated and used as lookup tables.

Four SM model parameters are obtained using analytical closures and data from the full model in order to take into account phenomena and feedbacks, which are not modeled explicitly in the SM itself, but still have important effect on the results of the prediction. Namely, closures are proposed for correction of the jet breakup lengths, void fraction, vertical and lateral velocities of the coolant in the FCI zone.

The SM is validated against DEFOR-A experimental data. A good agreement is reported between measured predicted by SM fractions of agglomerated debris. Comparison of the results predicted with the FM and calibrated SM for plant scale analysis suggest that SM provides acceptable accuracy obtained with about hundred times smaller computational effort.

In the future more work would be necessary on validation of the SM against other experiments, on development of the database of the SM results that can be used in sensitivity, uncertainty and risk analysis.

Sensitivity Analysis and Debris Agglomeration SM

Global sensitivity analysis was carried out using Morris method [73] and physics based SM described in the previous section in order to identify the most influential parameters for debris agglomeration. The experimental plan proposed by Morris is composed of individually randomized “one-factor-at-a-time” experiments; the impact of changing one factor at a time is evaluated in turn (see references [73],[74] for more details). In the analysis we considered both parameters of the melt release scenario and calibrated coefficients used in the SM closure parameters.

Figure 3.98 illustrates details of computational debris agglomeration analysis. The execution of the model is performed in two steps: (i) calculation of the data base of cooling histories of a single spherical particle falling through a fluid (VAPEX-SD), given properties of the melt, particles sizes and other parameters that can affect particle interaction with a fluid (see Table 3.13); (ii) calculation of the fraction of agglomerated debris, given single particle cooling histories, particle size distribution, jet properties (jet size, jet release velocity), pool conditions and closure parameters ranges, which based on the results of models calibration (see Table 3.14).

Figure 3.99 presents the results of Morris sensitivity analysis. The results show that the fraction of agglomerated debris is mostly influenced by the parameters of the melt release scenarios DPARN (jet diameter), UPIN (initial melt release velocity) and XPW (pool depth). This is because the jet break up length, which is one of the most important factors for debris bed agglomeration, is mostly influenced by DPARN, UPIN, XPW and closure coefficient CBR, however, the relative importance of CBR and XPW is significantly smaller compared to DPARN and UPIN for the selected ranges of the parameters. Further analysis is necessary, to determine the relative importance of jet

break up model parameters on the results. This concerns mainly relatively small jet diameters (e.g. IGT failure), where uncertainty in the results due modelling parameters might be more important.

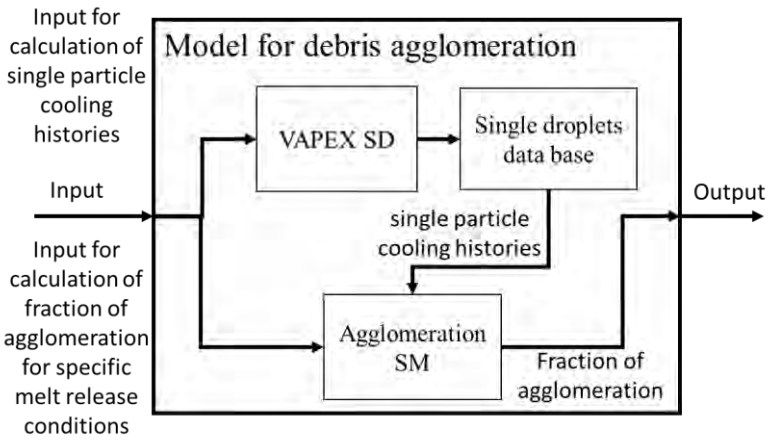

Figure 3.98. Physics based (SM) model for debris agglomeration, organization structure.

Table 3.13. VAPEX SD model input parameters

Variable Name	Description	Units	Range
RHOP	Fuel density	kg/m3	[7500 ; 8500]
PHEAT	Fuel latent heat	J/kg	[2.6e5 ; 4.0e5]
CP	Fuel heat capacity	J/kg*K	[350 ; 650]
KFUEL	Fuel thermal conductivity	W/m*K	[2 ; 42]
Em	Emissivity	-	[0.1 ; 1.0]
TLIQSOL	Liquidus\Solidus Temperature	K	[1600 ; 2800]
po	Containment pressure	Pa	[1e5 ; 4e5]
tlo	Water pool temperature	K	[288 ; 368]

Table 3.14. Agglomeration SM Model input parameters

Variable Name	Description	Units	Range
DPARN	Jet diameter	m	[0.07 ; 0.6]
UPIN	Melt release velocity(initial)	m/s	[1 ; 8]
TSH	Melt superheat	K	[10 ; 1000]
xpw	Pool depth	m	[5 ; 9]
CBR = C_{brk}	Jet break up correlation coefficients		[0.0002 ; 0.001]
BBR = B_L			[0.0 ; 0.01]
AFCI = A_{FCI}	Pool void model;		[5 ; 15]
BFCI = B_{FCI}			[0.5 ; 3]
AVW = A_{vw}	Pool vertical velocity model;		[19.78 ; 19.78]
BVW = B_{vw}			[13.19 ; 19.78]
CVW = C_{vw}			[-0.35 ; -0.25]
AUW = A_{uw}	Pool lateral velocity model;		[10 ; 14]
BUW = B_{uw}			[-1.5 ; -0.5]
CUW = C_{uw}			[-0.1 ; -0.05]
UMIN = U_{min}			[0.0 ; 0.05]

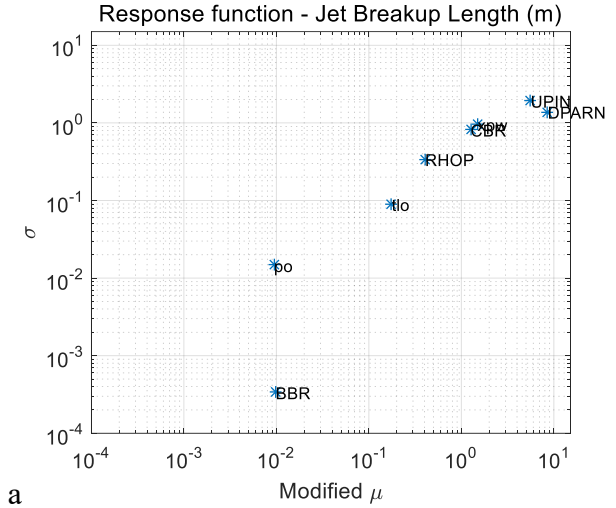

a

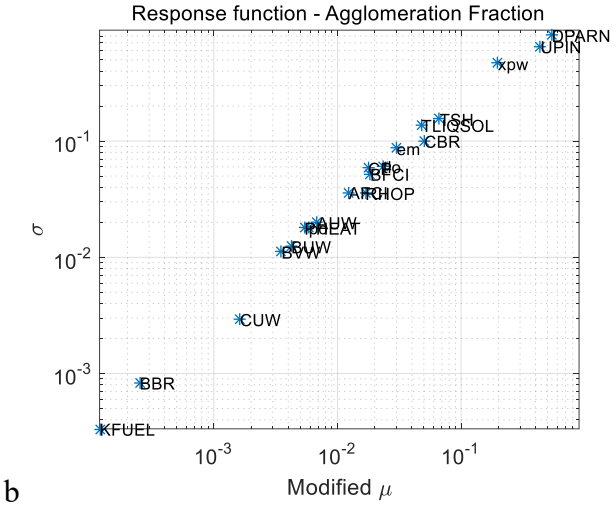

b

Figure 3.99. Morris Sensitivity Analysis results for: a. Jet Breakup Length(m); b. Debris agglomeration fraction;

3.7.2 Particulate Debris Bed Spreading Experiments and Modeling

In order to prevent containment basemat penetration after melt release from the vessel in a hypothetical severe accident (SA) in Nordic type BWR reactors, the lower drywell is flooded with water. When released from the reactor vessel (RV) into a several meters deep water pool, molten corium is expected to fragment, be quenched and form a porous debris bed. In order to avoid corium debris bed dryout and re-melting, the decay heat should be removed by evaporation of water driven by the natural circulation of coolant through the bed. The properties of the debris bed (particles size, bed porosity, bed geometry, etc.) and SA scenario conditions (e.g. system pressure) can affect coolability of the bed. Analytical and experimental studies [138], [35], [139] suggested that geometrical configuration of the debris bed is one of the main factors influencing the bed coolability. A tall debris bed can hardly be coolable and, in contrast, the same mass of the corium material can be cooled easily if the debris is spread uniformly over the whole available basemat area [138].

The shape of the debris bed is affected by debris particle transport:

i. after settlement on the debris bed (by self-leveling);
ii. in the water pool above the bed (by turbulent two-phase flows).

The corresponding test series or modeling of (i) self-leveling is referred as PDS-C (Particulate Debris Spreading - Closures), whereas (ii) particles spreading in the pool is named as PDS-P (Particulate Debris Spreading in the Pool). Each of above listed transport we investigate in our separate-effect studies. Such separation allows us to perform physical effect-focused experiments, generalize the observed results and, finally, build and validate a proper full model of the phenomenon. The development of the surrogate model is possible when further simplification and generalization of the full model is performed.

Both full and surrogate models have been developed within PDS-C sub-framework, whereas PDS-P is at the stage of scaling model development and full model validation. Nevertheless, the main results and achievements from both, experiments theoretical elaborations in PDS are provided in the following sections.

PDS experiments

3.7.2.1.1 PDS-P experiments

The large-scale turbulent two-phase flows (as illustrated in Figure 3.100a) may affect the particle lateral spreading over the basemat [35], preventing formation of a tall debris bed. Smaller particles are more effectively transported by the flow. In Figure 3.100(b-c) from [35], the flow field (white lines on the left), void fraction distribution (color map), particle trajectories (yellow lines) and bed shape (dashed line) are presented for simulation times of 30 minutes and 4 hours. The debris bed is spread over the bottom of the pool, despite the fact that all particles are released from a relatively small source near the axis.

It should be noted that in some accident scenarios the pool can be initially subcooled. In this case, boiling in the pool can start when the hot water plume stemming from the debris bed approaches the surface and its temperature exceeds the local saturation temperature corresponding to the local hydrostatic pressure head. This effect was demonstrated in [141]. In recent studies [140], the influence of two-phase flow on sedimentation of the different in size particles has been investigated experimentally. Numerical approaches employing discrete element analysis for particle spreading are also under development [142], [143].

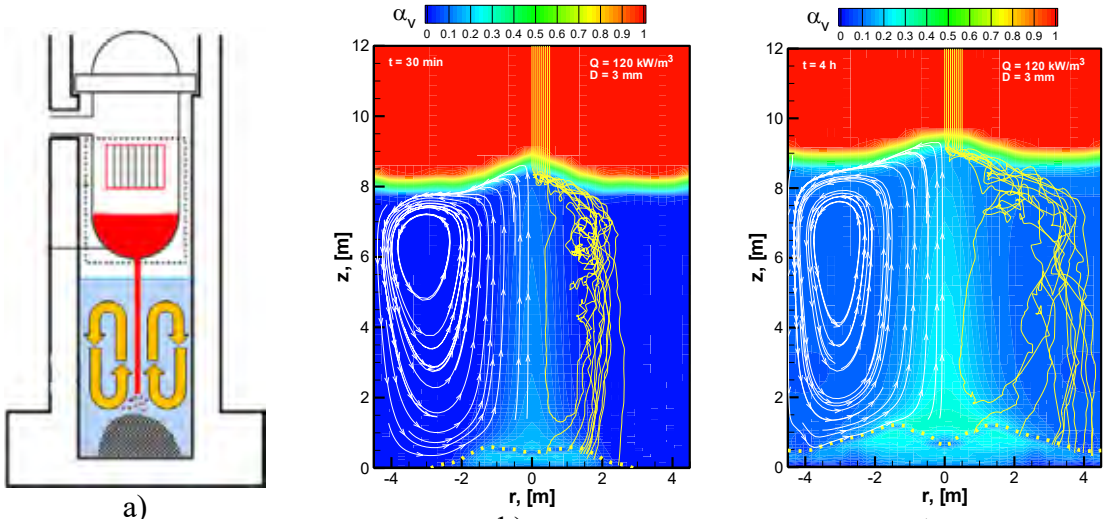

Figure 3.100: Illustration of the large-scale turbulent currents during corium debris release in RV cavity under SA conditions (a) and simulation of particle trajectories affected by the circulation in the saturated pool at 30 min (b) and 4h (c) [35].

The main goal of PDS-P work is to provide data for code validation. Therefore, selection of experimental parameters is based not only on consideration of severe accident (SA) conditions, but on the merits of experimental data for validation of different models. The general aim of the tests is to cover possible ranges of different regimes and parameters in order to provide data for understanding of importance of separate effects.

In the experiments, we quantify the distribution of particles along the pool bottom as a function of gas injection parameters. The technique is similar to that used in the studies on self-leveling and spreading of the particulate debris bed in PDS-C facilities reported in [144] and [145]. A detailed description of the measurement techniques is reported in [146]. The test conditions and measured parameters for the new series of the tests are given below.

The PDS-P facility consists of the following main parts: the particle delivery system, main water tank, the particle collection system, gas supply and flow rate measurement system [146]. The general view of the facility is illustrated in Figure 3.101(a). A snapshot of facility operation is given in Figure 3.101(b). The tests reported herein were performed with the following variable and fixed parameters (see Figure 3.101 for definition of some parameters): the depth of water pool, H_{pool}, was either: 0.5, 0.7, or 0.9 m; the pool length, L_{pool}, was either: ~0.5; ~0.9[2] or 1.5 m; the tank width was fixed to 72 mm. These dimensions were chosen in order to preserve close to 2D geometry for the turbulent currents and particles spreading, i.e. the pool width was much smaller than the length and height of the pool. On the other hand, the pool width was much larger than the characteristic particle size in order to minimize the influence of particle-wall interaction. The water tank is made of 20 mm thick acrylic material. Several pairs of rigid bars are installed (as shown in Figure 3.101) to minimize vibrations and bulging of the tank walls during air injection. The water temperature was kept within 15-18°C.

[2] The exact value of 0.894 m is rounded in the legends of the plots to 0.89 m or 0.9 m for the sake of brevity.

The gas injection chamber was a rectangular box with the height 60mm, length 200mm, and width 70mm. The air injecting holes in perforated top plate were 1mm in diameter, the pitch size of the holes was 10mm in both directions. The air mass flow rate, Q_g, is adjustable and provides uniform gas injection within the range of 2.2-14.5 g/s. The top limit of the range was selected in order to be able to achieve fluidization of settled debris bed at the highest values of Q_g.

Particles were delivered from the top boundary of the facility at the fixed height of 1.61m above the top of the particle catchers through a funnel equipped with Archimedes screw as shown in Figure 3.101(a) and schematically in Figure 3.115. The particle delivery rate was varied in the range between 1 and 5 g/s in order to minimize particle-particle interactions and the effect of the particles on the flow field. Few tests were performed in the same pool flow conditions, but with the particle delivery rate increased ten times. The ultimate particle spreading patterns obtained in all tests were similar, suggesting that there were no "collective" effects due to particle-particle and particle-flow interactions. The following particles were used in the experiments:

- Stainless steel spheres 3 mm in diameter (SSs_S3) with density $\rho_{p,SS3} \cong 7.8\ \mathrm{g/cm^3}$;
- Glass spheres 3 mm in diameter (GLs_S3) with density $\rho_{p,GL3} \cong 2.6\ \mathrm{g/cm^3}$;
- Stainless steel spheres 1.5 mm in diameter (SSs_S1.5) with density $\rho_{p,SS1.5} \cong 7.8\ \mathrm{g/cm^3}$.

Particles reaching the pool bottom were collected by several catchers. The catchers were designed to be accessible from the outside of the tank. A single catcher consists of i) catcher wall separator, ii) small funnel (Figure 3.101b), iii) quick coupler (black components attached to the tank bottom in Figure 3.101a), and iv) 50 mm diameter hose in which the particles are accumulated. The longest hoses (0.5 m) were positioned near the gas injection chamber where the largest mass fraction of the particle material was expected. The distance between the catcher walls was 10 cm. The first catcher (Figure 3.101a) also collected particles which fell on the gas injection plate and, thus, it has the effective length of 30 cm.

Note that the main goal of the work is to provide data for code validation, therefore, selection of particle size and density was based not only on consideration of possible values in prototypic severe accident (SA) conditions, but on the merits of experimental data for validation of different models and for understanding of the effects of separate parameters. For instance, particle parameters were chosen to provide non-trivial particle spreading patterns, given the geometry of the facility and gas flowrates, and to provide data necessary to clarify the effects of particle size and density. For particles of 1.5mm and 3mm diameters (also expected as a mean sizes of the particles resulting from corium fragmentation in water), it was found that particle-flow interaction is sufficiently strong, so that significant particle spreading occurs, but, on the other hand, such particles are not suspended in the flow (as would be the case for sub-mm particles). The particle supply rates were maintained low in order to decrease the effect of particle-particle and particle-flow interactions in order to produce data for separate effect code validation.

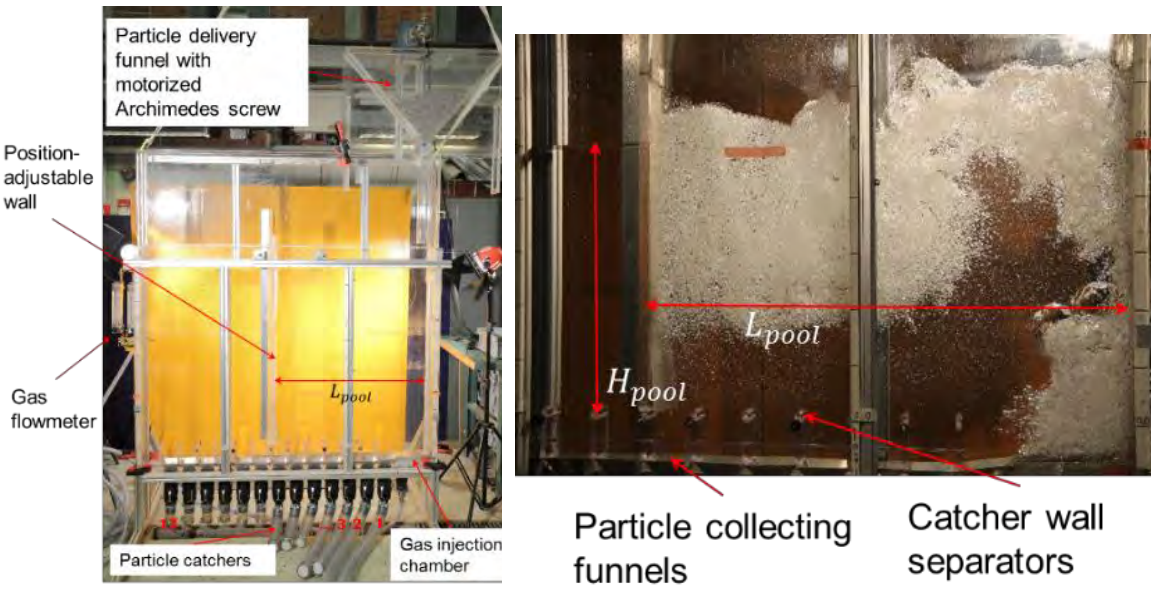

a) b)

Figure 3.101: PDS-P facility: general view (a) and test section in operation (b). The pool depth $\boldsymbol{H_{pool}}$ (b) is measured from the upper tip of the walls separating particles catchers.

3.7.2.1.2 PDS-C experiments

Debris bed self-leveling occurs due to the mechanical energy of two phase flow in the porous bed. Pioneering experiments conducted with metallic powders showed that, indeed, coolant boiling promotes debris self-leveling, influences the horizontal velocity of vertically falling particles, affecting thus the repose angle of the bed [147]. The effectiveness of particulate debris bed spreading has been considered in the experimental and theoretical studies [148], [149], [150], [144], [145], [51], [151]. As was shown in the experiments, debris self-leveling occurs due to particle motion in the top layer of the debris bed [144].

In our previous work [144] several PDS facilities were used with gas injection provided at the bottom of the debris bed in order to study spreading phenomena at prototypic gas velocities and different length scales and spatial configurations. The most important observations from the earlier PDS tests [144] are:

1. Local slope angle of the debris bed depends on local gas velocity. For instance, Figure 3.102 shows debris bed shape after gas injection was provided in the central section (indicated by two vertical dashed lines). Remarkably, the slope angle changed only in this middle section, while initial slope angle remained unchanged in the other parts of the bed.
2. The bulk volume of the debris bed is immovable. The particles are moving only in the topmost layer of the bed. Video recording of the debris bed spreading process demonstrated that the thickness of the moving layer is of the order of few particle diameters.
3. The presence of two different regimes of particle spreading: rapid and slow particle spreading. The former occurs at the initial instant of the experiment where large masses of particles are moving simultaneously in an avalanche regime. The latter is a slow process driven by the stochastic interactions of the rising bubbles with individual particles at the bed top surface. The avalanche regime stops when the bed reaches a new stable angle of repose. The slow spreading regime can continue in-principle until a flat debris bed configuration is reached. However, the time which would be necessary for reaching a flat configuration can be very large.

Observed behavior was insensitive to the scale and spatial configuration of the facility, mass of the debris, and gas flux until debris bed fluidization limit is reached. The fact that local gas-coolant-particle interactions in the thin top layer of particles are responsible for spreading suggests that experiments in reduced size laboratory facilities (such as PDS-C) can be used to capture the key relevant physical phenomena. Experimental closures for particle mass flow rate per unit width of the bed (referred as “particulate flow rate” for the sake of brevity) as a function of local slope angle and gas velocity have been obtained at different test conditions and for different particle types [145], [144]. Using such closures an approach for predicting spreading dynamics of a debris bed with arbitrary initial shape was proposed [144]. However, if the data produced in such tests is expressed in the dimensional form, it can be directly applicable to estimation of the particle spreading flow rate in accident conditions only if the properties of the particles and coolant (such as particle size distribution, morphology, density, coolant density, viscosity, etc.) are the same as the prototypic ones. Also, for each new type of particles and gas flow conditions, a separate set of experiments is necessary in order to provide data on the dimensional particle flow rate.

The goal of this work is to develop a scaling approach to generalize the experimental

data for prediction of the particle flow rate for different kinds of particles and gas flow conditions.

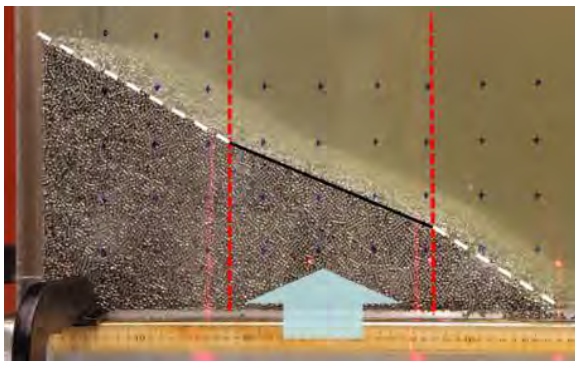

Figure 3.102. The slope angle of the heap is changed only above the section where gas injection was provided (between the two vertical dashed lines).

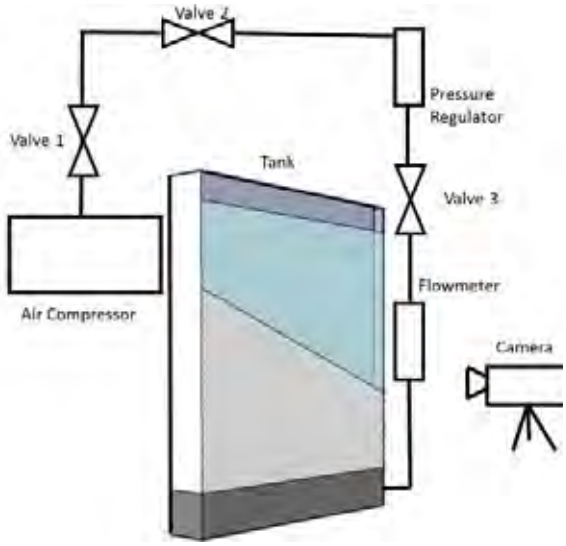

Figure 3.103: Schematic diagram of the PDS-C facility.

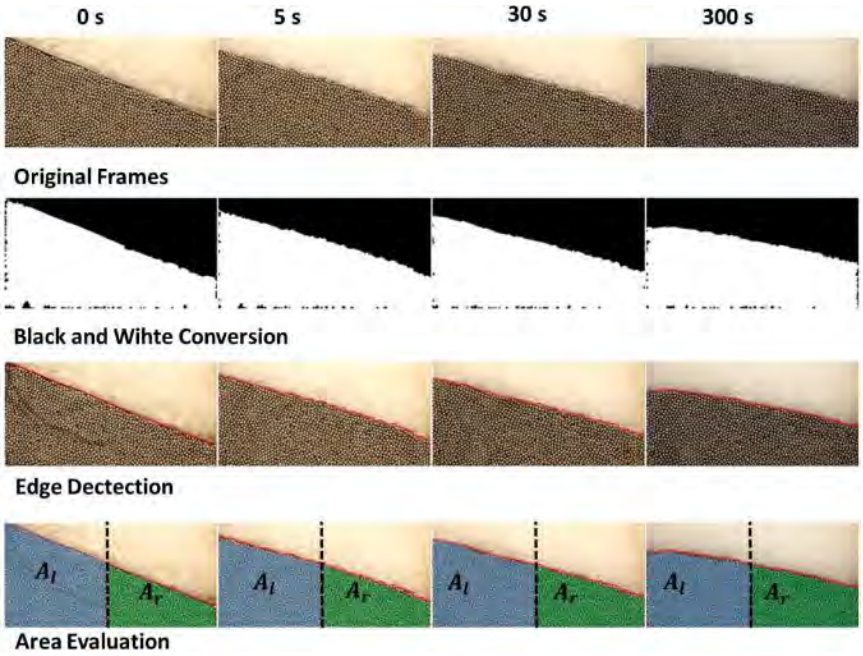

Figure 3.104: Stages of the video image post-processing technique employed for estimation of the particle flow rate (PDS-C8 test).

Particulate Debris Spreading Closures (PDS-C) experimental facility is designed to study phenomena of particulate debris spreading caused by upward two phase (water and gas) flow. The facility is composed of a vertical rectangular open on top test section, made of acrylic glass with internal dimensions as length L=405 mm, width W=72 mm, height H=915 mm. Gas injection chamber (with dimensions 405x72 mm) is installed at the bottom of the test section and connected to the constant 8 bar pressure compressed air supply system, the schematic shown in Figure 3.103. A camera is used to record evolution of the heap shape in each experiment. The compressed air at pressure up to 2 bar (set by the pressure regulator) is supplied through the injection

chamber. The top plate of the chamber is a perforated with 287 (7x41) cylindrical orifices 1.5 mm in diameter positioned as a quadratic grid with 10 mm pitch. The plate can provide uniform and constant in time air injection with up to 70 L/s total flow rate, which corresponds to gas superficial velocity of 2.4 m/s. The gas flow rate is regulated by valve-3 and measured by an in-line flow meter Omega FL-505.
The total volume of particulate debris bed typically used in each test is about 8.5 liters. Different types of particles were used in the test series: stainless steel (SS) cylinders: 3 mm in diameter and 3 mm long; 3 mm in diameter and 6 mm long; SS spheres: 1.5 mm, 3 mm, and 6.0 mm in diameter; and different mixtures of these particles, i.e. a mixture of SS 1.5 mm spheres and SS 3x3 mm cylinders; and a mixture of SS 3 mm spheres and SS 6.0 mm. The properties of the particles are summarized in
Table 3.15.
Experimental procedure for a typical PDS-C test consists of the following steps:

1. Particles are loaded into the facility test section.
2. The test section is filled with water up to the level of 550 mm from the top of the air injection plate.
3. The particles bed is shaped as a heap with a slope angle close to the critical angle of repose θ_{rep}^{0} i.e. the steepest angle achievable without causing avalanches.
4. The debris bed is held in its initial shape using a stiff stainless steel net when gas injection is activated in order to avoid a "water piston" effect. The effect (also noticed by Cheng et al. in [152]) is observed at the start of gas injection when liquid (which initially fills the pores in the bed and the gas chamber) is pushed as a "piston" by the gas injected at high velocity causing rapid motion of the whole debris bed.
5. Gas injection flow rate is gradually adjusted to reach the desired superficial air velocity.
6. Then the net is quickly removed in upward direction allowing particles to start the spreading process.

The runtime of experiments can vary from tens of seconds up to 5 minutes. The entire test is recorded by a video camera. Individual frames are extracted and analyzed later on, using following image processing technics. First, the noise reduction algorithm is applied and frames are converted to black-white images. The Sobel edge detection algorithm is applied in order to detect the top edge of the bed. The image of the bed is split into two parts (left and right) by a centerline. The areas of the left and right parts of the bed (A_l and A_r respectively) under the edge are calculated (Figure 3.104).

Table 3.15: Properties of the particles used in PDS-C tests.

Particle	**Equivolume sphere diameter (d_p) [mm]**	**Material density (ρ_p) [kg/m^3]**	**Angle of repose at $U_g = 0$ (θ_{rep}^{0}) [degree]**	**Minimum fluidization velocity (U_{mf}) [m/s]**	**Sphericity (Φ) [-]**	**Porosity (ε) [-]**
SS cylinders 3 by 3 mm	3.4	7800	33.0	2.44	0.87	0.35
SS cylinders 3 by 6 mm	4.3	7800	36.5	2.79	0.83	0.36
SS spheres	1.5	7800	22.0	1.43	1.0	0.40
SS spheres	3.0	7800	22.0	2.27	1.0	0.40
SS spheres	6.0	7800	22.8	3.34	1.0	0.40
Mixture 1[a]	2.6	7800	29.5	2.07	0.97	0.33
Mixture 2[b]	2.1	7800	24.5	1.80	0.98	0.34
Mixture 3[c]	4.0	7800	24.0	2.68	1.0	0.36

[a] is composed by SS spheres 1.5 mm (volume fraction 0.25, mass fraction 0.23) and by SS cylinders 3 by 3 mm (volume fraction 0.75, mass fraction 0.77)

[b] is composed by SS spheres 1.5 mm (volume fraction 0.5, mass fraction 0.48) and by SS cylinders 3 by 3 mm (volume fraction 0.5, mass fraction 0.52)
[c] is composed by SS spheres 3.0 mm (volume fraction 0.5, mass fraction 0.5) and by SS spheres 6 mm (volume fraction 0.5, mass fraction 0.5)

Post-test analyses

3.7.2.1.3 PDS-P results and analysis

In this work, we report 34 two-phase flow tests performed without particles, and 63 tests performed with particles delivered at a low rate In our previous work, the gas injector was positioned symmetrically between the pool walls [146]. In this work, given that the number of tests was limited and the number of other free parameters was significant, it was decided to place the gas injection near one of the side walls. This resulted in a more stable (not subject to meandering and splashing) bubble plume than in the case of central injection, which is advantageous in view of providing numerical code validation data. Also, the plane pool with side injection can be considered as "one half" of a pool with enforced symmetric conditions. Conditions of all tests are provided in Table I, Table II and Table III in [146].

3.7.2.1.4 Tests without particles

The comparison of the tests performed without particles and with gas injection in the center and near the side wall is shown in Figure 3.105. We followed image processing technique developed in [146] to determine the total void fraction α as an average from five snapshot images of the pool. Namely, each test has been recorded as a video clip. Video frames are randomly selected and analyzed by image processing. The void fraction from each frame is calculated based on the excess of the area occupied by the two-phase mixture with respect to the original water level. If the water surface edge is blurred then a middle curve is used to approximate the edge. Resulting data is shown in Figure 3.105. Note that relatively large error bars in Figure 3.105 can be attributed to the oscillations of the instantaneous void fraction in time. It is instructive to note that air injection near the side wall resulted in a more stable at macroscopic level (less subject to meandering and splashing) bubble plume than in the case of central injection, which is advantageous in view of providing numerical code validation data.

We found that the total void fraction in the pool is different for the tests where ratio H_{pool}/L_{pool} (ranging from 0.31 to 1.81, see Table II in [153]) is the same but the H_{pool} and L_{pool} values are different, e.g. $H_{pool}/L_{pool} = 0.5/0.497 \approx 0.9/0.894 \approx 1.01$. Therefore, we approximate the total void fraction by the following formula where both dimensions of the pool are considered as separate variables:

$$\alpha = a \cdot L_{pool}^{b} \cdot H_{pool}^{c} \cdot Q_g^{d}, \tag{3.72}$$

$$a = 0.052, b = -0.818, c = -0.197, d = 0.474,$$

where $a \ldots d$ are fit constants, Q_g is expressed in g/s and pool dimension are in meters. The coefficient a has dimensionality of $\mathrm{m}^{-(b+c)} \cdot (\mathrm{g/s})^{-d}$. The quality of this fit is illustrated in Figure 3.106. As can be seen, the maximum deviation from the experimental values is below 10% of measured void fraction. The gas mass flow rate exponent d is comparable to the value of 0.5 determined previously [138] for the

symmetric pool-centered gas injection.

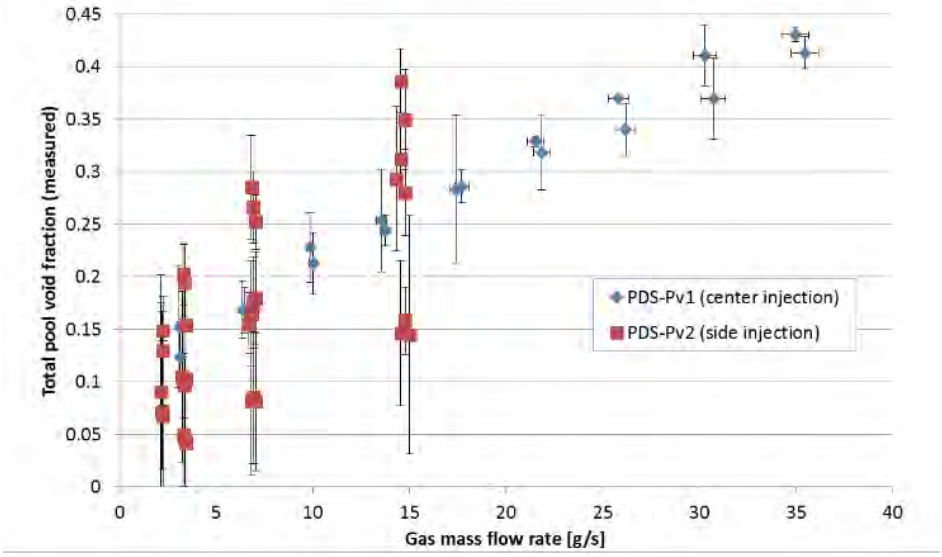

Figure 3.105: Measured total void fraction in the pool for tests without particles (two-phase flow). The measurement error of the gas flow rate does not exceeds 2%.

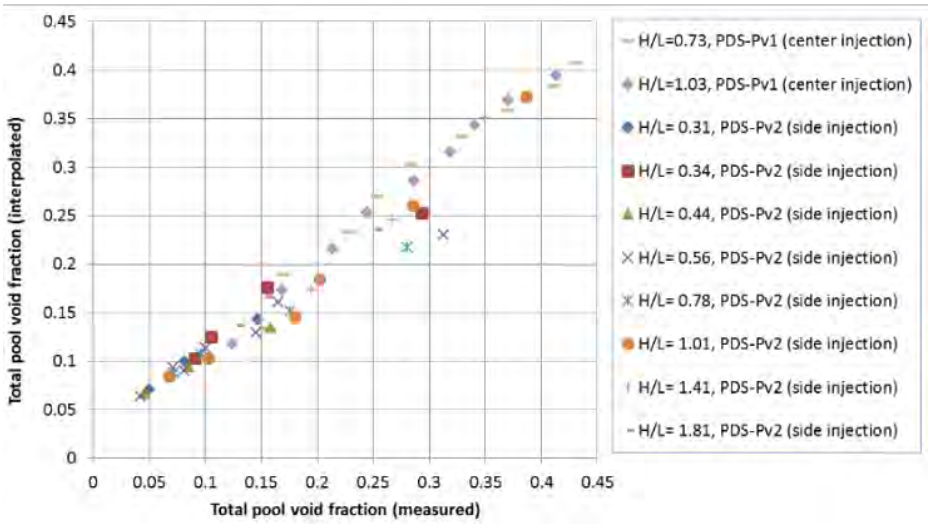

Figure 3.106: Approximate dependency for average void fraction Eq. (3.72) versus experimentally measured values. $\boldsymbol{H/L}$ is the ratio of the pool depth to its length $\boldsymbol{H_{pool}/L_{pool}}$.

The estimated total void fraction α is an integral quantity characterizing the turbulent two-phase flow in the pool. Another characteristics which can be easily estimated is an effective void fraction α_{eff}. It is defined as the average void fraction within the active pool zone where two-phase flow (bubbles) is visually observed. Typically it is the upper half and right side (above the injection plate) of the pool as shown in Figure 3.101(b). The same image processing procedure (as for the determination of the total void fraction) has been applied to estimate the area of the active zone. The comparison of the α_{eff} versus experimentally measured values of α is shown for all side-injection experiments in Figure 3.107. As is seen from the graph, the effective void fraction can be about10% higher than the total one in the pool. The highest values are observed for the lowest pool aspect ratio H_{pool}/L_{pool}. On the other hand, high gas flow rate causes $\alpha_{eff} \to \alpha$ i.e. void is present almost everywhere in the pool.

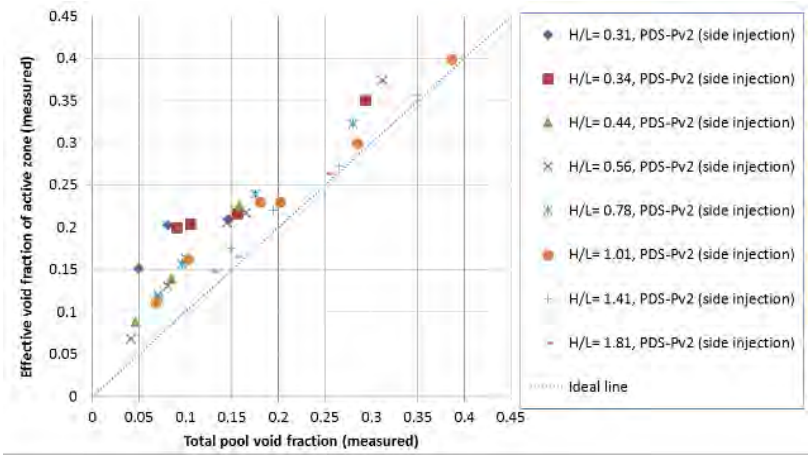

Figure 3.107: Comparison of the measured total versus effective void fractions in the pool.

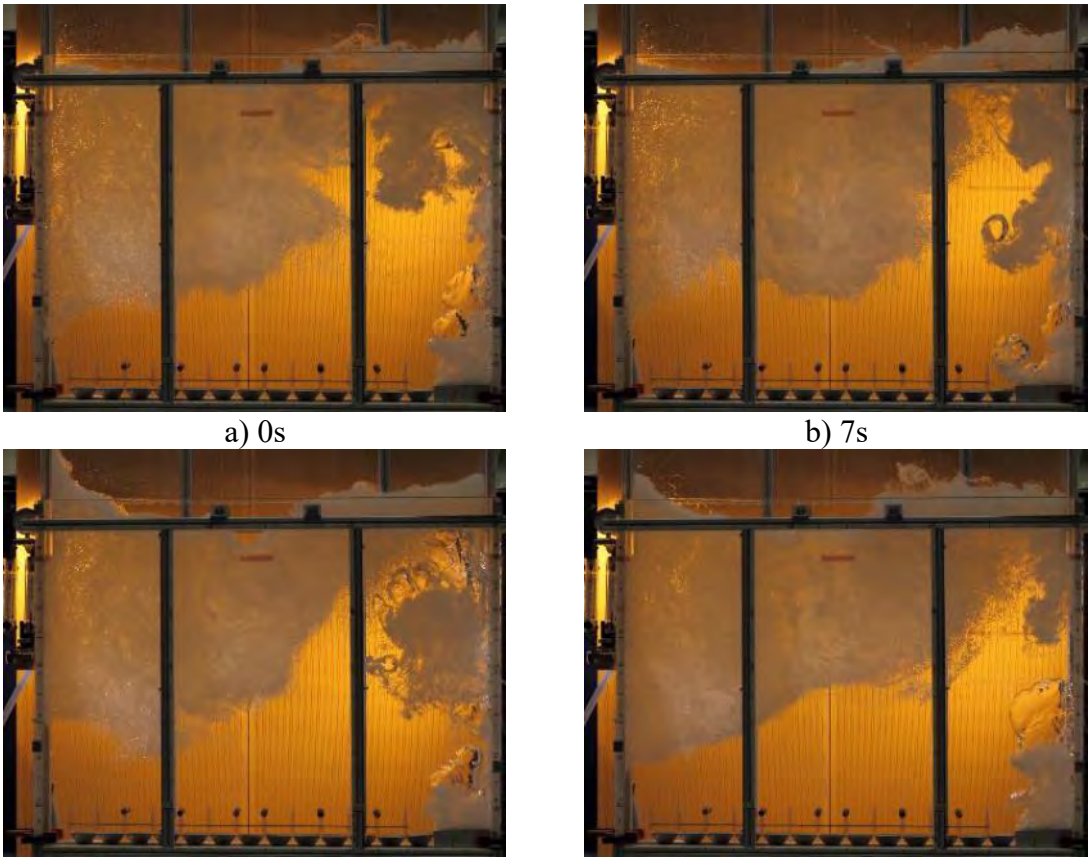

a) 0s b) 7s

c) 14s d) 22s

Figure 3.108: Snapshots of the test NOPs-28 with highest air flow rate of 15 g/s, $\boldsymbol{H_{pool} = 0.9}$ m pool depth and $\boldsymbol{L_{pool} = 1.6}$ m pool length. The relative to the first image (a) time offset in seconds for each snapshot is indicated below each figure.

Another remarkable feature of the flow is that at low gas injection rate a quasi-steady flow pattern and void distribution is observed whereas at high injection rates the pattern can change dynamically producing a quasi-periodic large scale void structures as shown in Figure 3.108. Large waves created by the large void structures disturb the water surface, and the flow in the pool experience erratic oscillations. Large regions with high void fraction above the injection chamber (Figure 3.108d) and regions with low void fraction can be formed for short periods of time. Such behavior is difficult to quantify in the experiment.

3.7.2.1.5 Tests with particles

In this work, we consider the effects (Figure 3.109 through Figure 3.111) of (i) gas injection flow rate, (ii) particle diameter: 3 or 1.5 mm; (iii) particle density: glass or stainless steel; on particle spreading. Conditions of the tests were changed one parameter at a time in order to analyze separate effects. The legend of the tests includes particle material ("NOP" – no particles; "SS" – stainless steel; "GL" – glass), location of the gas injection ("c" – injection in the center; "s" – gas injection at the side), particle shape and size (e.g. "SSs_S3" – stainless steel sphere 3 mm in diameter, side injection), test number, height and length of the pool and gas injection flow rate. On the horizontal axis the particle catcher position r_i is normalized to the total length of the pool as r_i/L_{pool}. The non-dimensional mass fraction per catcher area on the vertical axis is defined as:

$$\tilde{m}_i = \left(\frac{m_i}{M_{tot}}\right) / \left(\frac{A_i}{A_{tot}}\right), \text{ where } M_{tot} = \sum_i m_i\,,\ A_{tot} = \sum_i A_i, \tag{3.73}$$

where the i^{th} catcher has the area A_i, the particle mass is m_i. As is seen from the figures, small 1.5 mm (Figure 3.111) or light glass (Figure 3.110) particles are spread more effectively to farther locations than the largest 3 mm stainless steel particles (Figure 3.109).

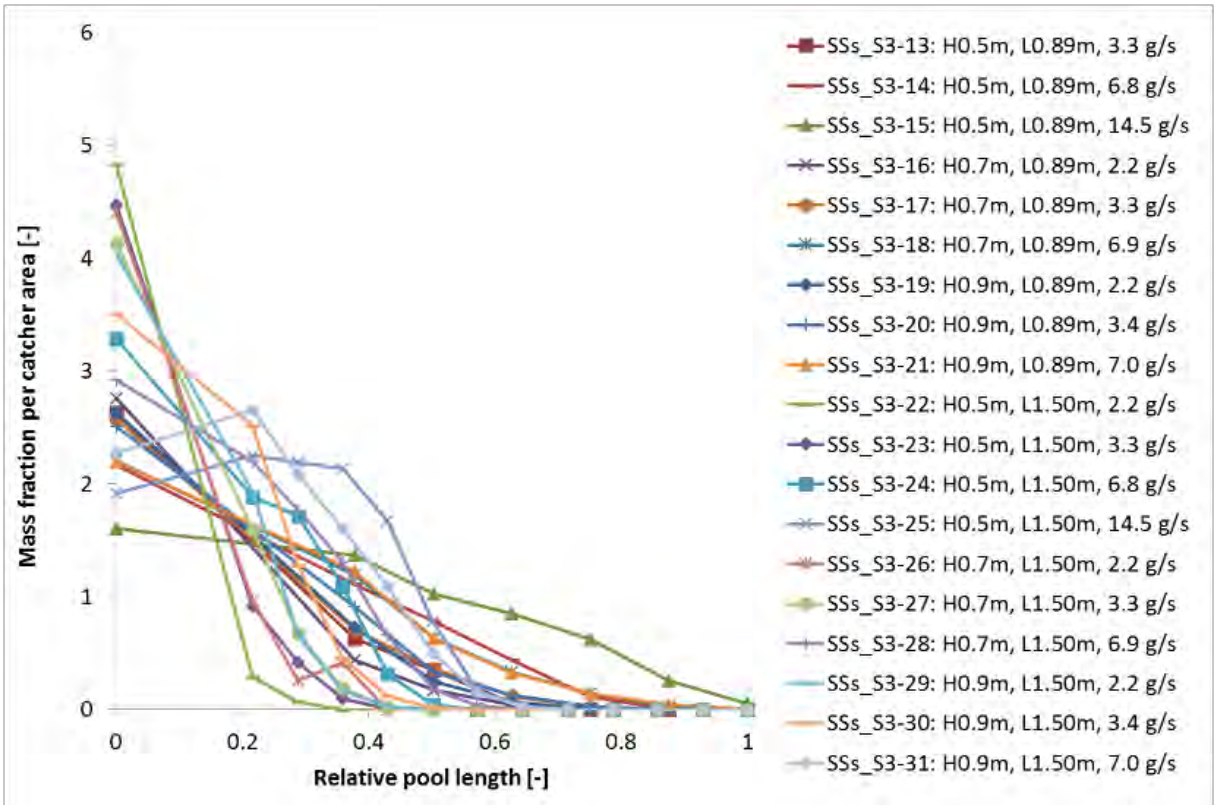

Figure 3.109: Spatial distribution of normalized particle mass fraction: 3 mm stainless steel particles.

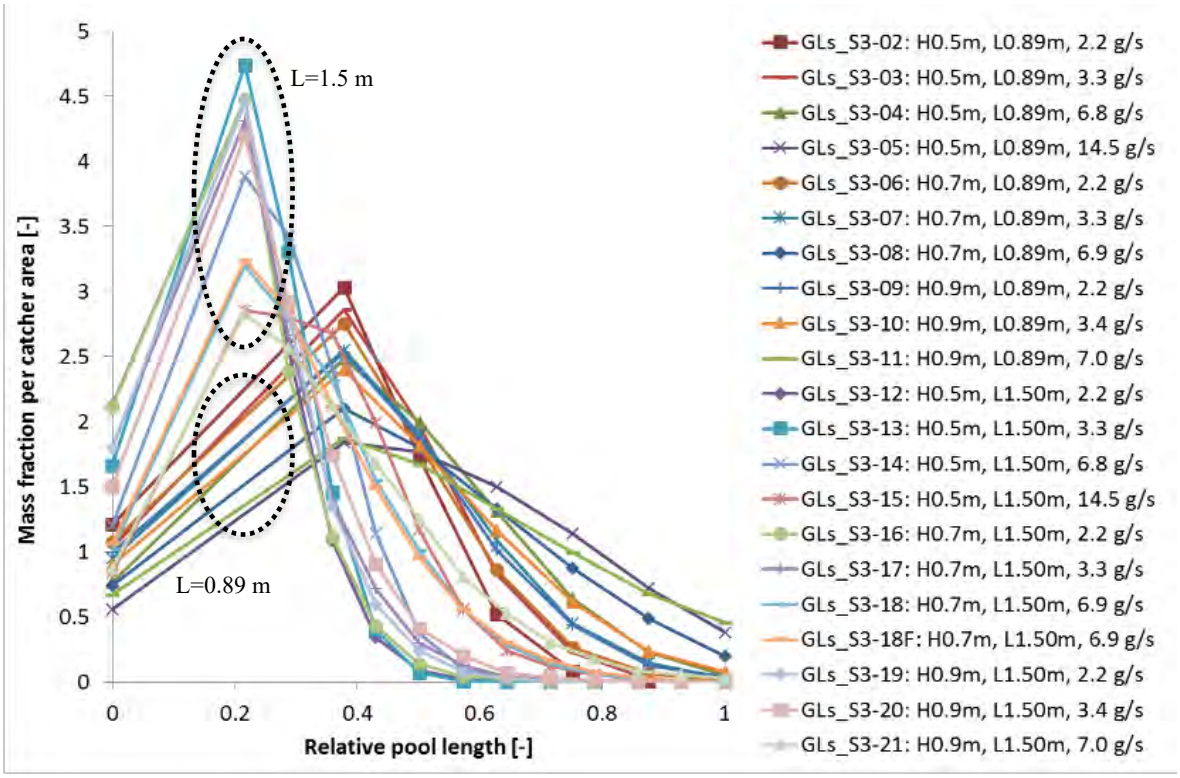

Figure 3.110: Spatial distribution of normalized particle mass fraction: 3 mm glass particles.

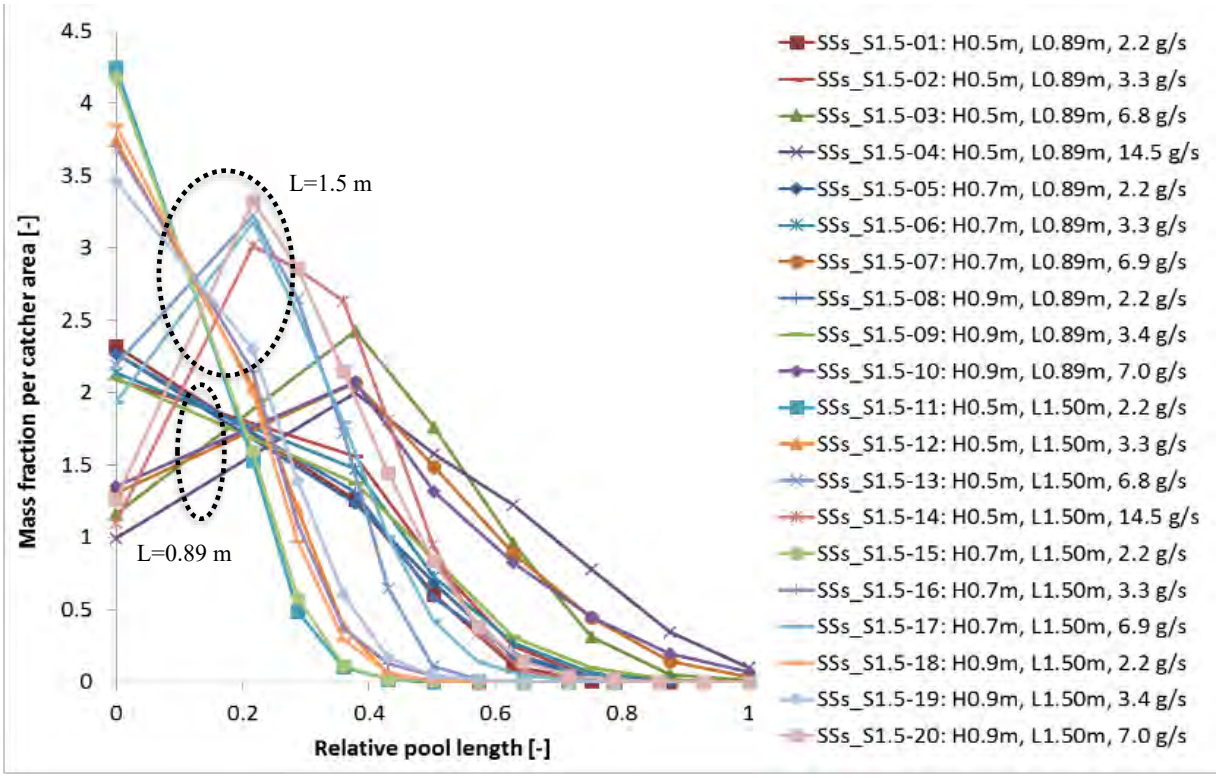

Figure 3.111: Spatial distribution of normalized particle mass fraction: 1.5 mm stainless steel particles.

Figure 3.112 illustrates the influence of the gas flow rate for fixed dimensions of the pool and particles of different diameters and materials. It is clear that lighter and smaller particles are spread more efficiently. However, at higher flow rates, the difference

between the shapes of the beds becomes less significant (Figure 3.112c).

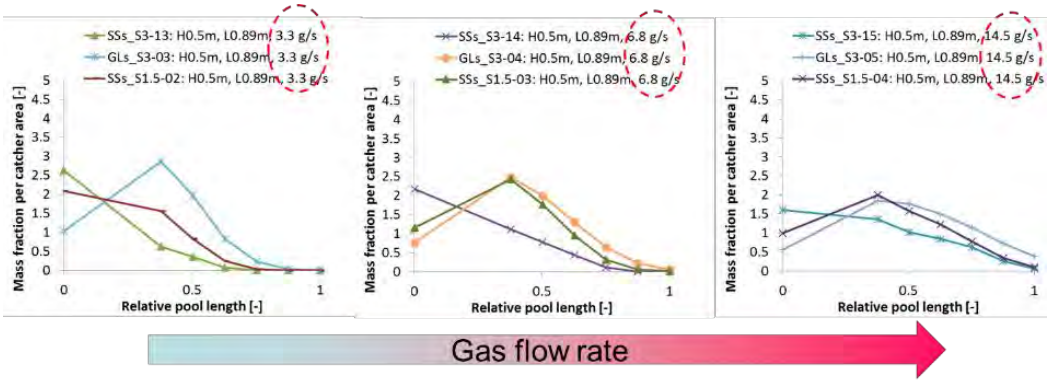

a) b) c)

Figure 3.112: Spatial distribution of normalized particle mass fraction obtained at different gas flow rates.

3.7.2.1.6 PDS-C results and analysis

The A_l and A_r areas obtained from the frames of the recorded video data, are used to calculate the particle mass flow (Q_p) at given local angle of the heap slope (α) and experimental conditions (gas superficial velocity, particle properties, etc.):

$$Q_p^n = \rho_p \cdot (1-\varepsilon) \cdot \frac{A_n^{t1} - A_n^{t2}}{(t2-t1)}, \tag{3.74}$$

$$\alpha = \frac{1}{2}\text{atan}\left(\frac{A_l^{t1} - A_r^{t1}}{\left(\frac{L}{2}\right)^2}\right) + \frac{1}{2}\text{atan}\left(\frac{A_l^{t2} - A_r^{t2}}{\left(\frac{L}{2}\right)^2}\right) \cdot, \tag{3.75}$$

where n indicates the heap side : $n = l, r$, ρ_p is the particle material density, ε is the porosity of the bed and L the facility length.

The areas calculated from each frame are averaged with 1 second interval in order to reduce the noise in the data due to possible random errors in the edge detection for each individual frame. Then, time intervals $[t1, t2]$ are selected automatically to ensure that statistically significant number of particles moves across the centerline during each time interval. We found that ~5 particles crossing the centerline during the time interval is necessary in order to obtain a monotonic dependency of the particle flow on the local slope angle.

The experimental error in the particle mass flow can be estimated as:

$$Q_p^{err} = Q_p^l + Q_p^r, \tag{3.76}$$

When superficial air velocity reaches minimum fluidization velocity (U_{mf}) the force exerted on the bed by the flowing media is sufficient to fluidize the entire bed. Minimum fluidization velocity for 3-phase flow can be calculated by Eq. (3.77), where Re_{gmf} is the so called "gas particle" Reynolds number obtained according to the

empirical correlation proposed by Lucas et al. [115] for round particles, since all our particles have a sphericity between 0.8< Φ <1 and reported in Eq. (3.78).

$$U_{mf} = \frac{\mu_g \cdot Re_{gmf}}{\rho_g \cdot d_p} \tag{3.77}$$

$$Re_{gmf} = \sqrt{29.5^2 + 0.0357 \cdot Ar_{lg}} - 29.5 \tag{3.78}$$

In Eq. (3.78) we use the gas phase Archimedes number with liquid-buoyed solids (Ar_{lg}) (Eq. (3.79)) in order to take in account the effect of the liquid phase, as it is proposed by Zhang et al. (1998).

$$Ar_{lg} = \rho_g \cdot (\rho_p - \rho_l) \cdot g \cdot d_p^3/\mu_g^2 \tag{3.79}$$

where μ_g and ρ_g are gas dynamic viscosity and density respectively; ρ_l is the liquid density; d_p is equivolume sphere diameter. In the experiments with mixtures of different particles, d_p was assumed to be equal to the mean reciprocal diameter as it is suggested by Wen-Ching Yang in [154]:

$$d_p = \frac{1}{\sum_{i=1}^{N}(v_i/d_{p_i})} \tag{3.80}$$

where v is the volume fraction of respective particles in the solid mixture.

The gas injection normalized velocity (Q_g) is defined as a ratio of the gas superficial velocity (U_g) to the minimum fluidization velocity (U_{mf}):

$$Q_g = \frac{U_g}{U_{mf}} \tag{3.81}$$

The experimental matrix is provided in Table 3.16. For each test condition 2 or 3 tests were carried out to ensure repeatability. The particulate flow rate as function of the slope angle was obtained using Eq. (3.74) and Eq. (3.75) for each experiment performed at fixed gas flow rate. An example of such dependency is shown in Figure 3.113, while in Figure 3.114 the complete set of the experimental results are reported. Figure 3.114 shows the spread of the data due to different test conditions, particle properties as well as experimental error (Eq. (3.76)). Experimental observations suggest that spreading is much faster (especially at high air superficial velocity) at the initial stage of the test, when slope angle is large and avalanches are observed. Similar observations also have been made by Cheng et al. [155].

Table 3.16: Experimental matrix

Particle type	U_g [m/s]	Q_g [-]	Experiment
SS cylinders 3x3 mm	0.34	0.14	PDS-C01
	0.52	0.21	PDS-C02
	0.86	0.35	PDS-C03
	1.38	0.56	PDS-C04
	1.91	0.78	PDS-C05
SS cylinders 3x6 mm	0.17	0.06	PDS-C06
	0.34	0.12	PDS-C07
	0.52	0.18	PDS-C08
	0.69	0.24	PDS-C09
	0.86	0.31	PDS-C10
SS spheres 1.5 mm	0.17	0.12	PDS-C11
	0.34	0.24	PDS-C12
	0.86	0.60	PDS-C13
	1.04	0.72	PDS-C14
SS spheres 3.0 mm	0.17	0.07	PDS-C15
	0.34	0.15	PDS-C16
	0.69	0.30	PDS-C17
	1.56	0.68	PDS-C18
SS Spheres 6.0 mm	0.17	0.05	PDS-C19
	0.52	0.15	PDS-C20
	0.86	0.26	PDS-C21
	1.04	0.31	PDS-C22
	1.21	0.36	PDS-C23
	1.56	0.46	PDS-C24
	1.73	0.52	PDS-C25
Mixture 1	0.69	0.33	PDS-C26
	1.04	0.50	PDS-C27
Mixture 2	0.34	0.19	PDS-C28
	0.69	0.38	PDS-C29
	1.04	0.57	PDS-C30
Mixture 3	0.17	0.06	PDS-C31
	0.34	0.13	PDS-C32
	0.52	0.19	PDS-C33
	0.86	0.32	PDS-C34
	1.21	0.45	PDS-C35
	1.38	0.51	PDS-C36
	1.56	0.58	PDS-C37
	1.73	0.64	PDS-C38

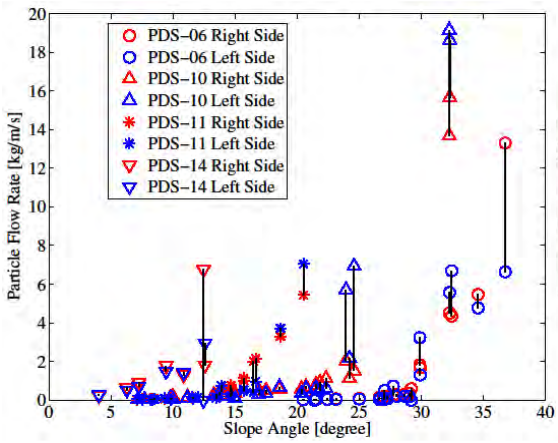

Figure 3.113: Particulate flow rate per unit width as function of heap slope angle obtained (PDS-C06, PDS-C10, PDS-C11, PDS-C14).

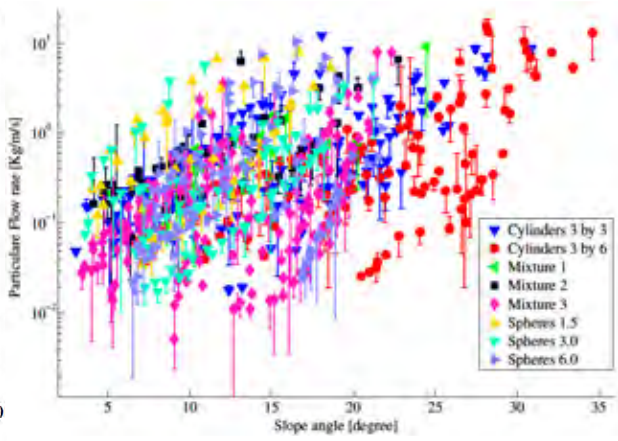

Figure 3.114: Particle flow rate as a function of slope angle for all the PDS-C experiments (Table 3.16)

Modeling and scaling approach

In this section the latest results on generalization of experimental data is presented. This concerns both, elaboration of the closure-based scaling approach in self-leveling (PDS-C) and development of the first scaling approach of the particles spreading in the pool (PDS-P). Each of them is discussed separately.

3.7.2.1.7 PDS-P: preliminary scaling approach

In order to characterize effectiveness of particle spreading we introduce the tangent of characteristic spreading angle $\tan\phi$ (see Figure 3.115)

$$\tan\phi = \frac{R_c}{H_{pool}} \tag{3.82}$$

where R_c is an average spreading distance defined as the distance from the axis of the particle source (funnel) to the center of mass of the debris collected in all catchers:

$$R_c = \frac{\sum_i m_i \cdot r_i}{\sum_i m_i}. \tag{3.83}$$

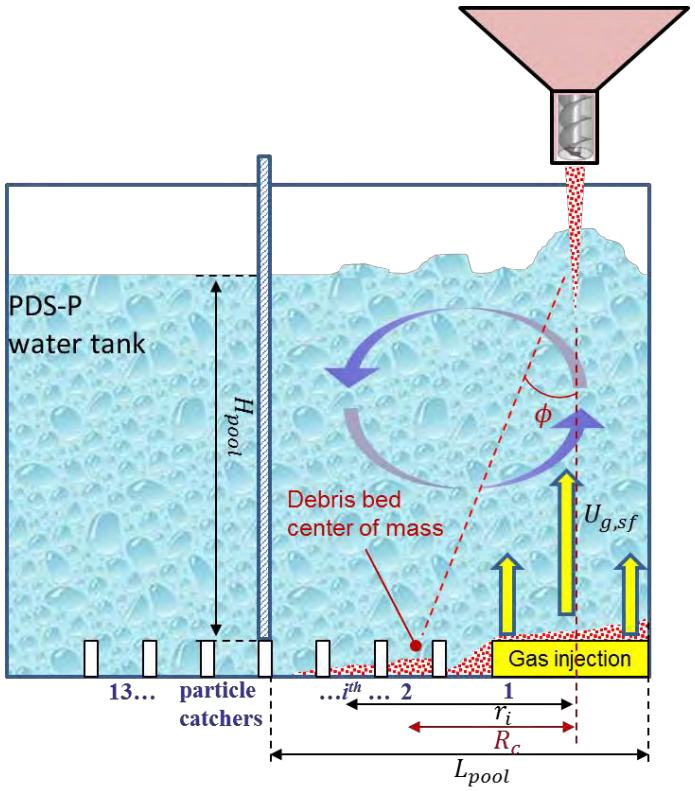

Figure 3.115: Schematics of the particle spreading in the PDS-P pool and definition of characteristic spreading angle $\boldsymbol{\phi = \tan^{-1}\frac{R_c}{H_{pool}}}$.

In Figure 3.116, tests with the 3 mm in diameter glass and stainless steel particles are compared to show the effect of particle material density. The effect of particle size is illustrated in Figure 3.117. At low gas flow rates (few points lying near the diagonal at $\tan\phi \cong 0.21..0.25$ in Figure 3.117) the effect of changing particle size from 1.5 to 3 mm becomes small. This can be explained by the fact that at low gas flow rate gravity force has dominant effect on spreading. At high gas flow rates (upper right part of the plots in Figure 3.116 and Figure 3.117) all experimental points start to gravitate toward the diagonal again, indicating diminishing effects of the size and density on the mass averaged spreading distance (see also Figure 3.112). This can be considered as an indication of the increasing dominance of large scale two-phase circulation flow structure and geometrical configuration of the facility. Comparing Figure 3.116 and Figure 3.117 one can conclude that particle density has stronger influence on particle spreading than particle size for the selected ranges of sizes and densities. The complete tests matrix with main test conditions and resulting R_c are given in Table III of the APPENDIX A in [153].

In order to describe spreading of non-interacting particles by large scale turbulent two-phase flows in the pool, we propose a semi-empirical scaling approach. Consider a particle of diameter d_p falling in the water pool of depth H_p. The terminal velocity of falling particle U_t is evaluated from the balance of gravity and drag forces:

$$U_t = \sqrt{\frac{4}{3C_d}\frac{\rho_p - \acute{\rho}_c}{\acute{\rho}_c} g d_p}, \tag{3.84}$$

where ρ_p is particle density, $\acute{\rho}_c$ is modified coolant density $\acute{\rho}_c = (1-\alpha)\rho_c + \alpha\rho_g \approx (1-\alpha)\rho_c$ and the drag coefficient C_d is a function of particle Reynolds number Re_p. The void fraction α is determined from the analysis of the tests without particles

depending on pool dimensions and gas flow rate (3.72). For high particle Reynolds numbers it can be assumed that $C_d \approx 0.45$ (e.g. see Eq. (2.69) in [156] for $Re_p > 1000$ in the limit of small volume fractions of solid phase). The Reynolds number based on the terminal velocity in single phase water was estimated in the range from 830 to 2300 for the tests conditions. The particle-water interaction time in the pool is then proportional to $t_{int} \propto H_p/U_t$. For a plane pool, the characteristic flow circulation time t_{circ} can be estimated as the ratio of the flow path (perimeter) to gas superficial velocity $U_{g,sf}$:

$$t_{circ} \propto \frac{2\left(L_p + H_p\right)}{U_{g,sf}} = \frac{H_p}{U_{g,sf}}\left(1 + \frac{L_p}{H_p}\right). \tag{3.85}$$

On the other hand, the characteristic horizontal velocity of the flow is

$$v_{hor} \propto \frac{L_p}{t_{circ}}. \tag{3.86}$$

It can be assumed that the average horizontal distance R_{spr} by which a falling particle will be transported by the circulation flow is proportional to:

$$R_{spr} \propto v_{hor} \cdot t_{int} \propto U_{g,sf} \cdot \frac{L_p}{L_p + H_p} \cdot \frac{H_p}{U_t} = \left(\frac{U_{g,sf}}{U_t}\right) \cdot \frac{L_p H_p}{L_p + H_p} \tag{3.87}$$

or, the average tangent of the "spreading cone" angle ϕ (see Figure 3.115) is:

$$\tan\phi = \frac{R_{spr}}{H_p} \propto \frac{U_{g,sf}}{U_t} \cdot \frac{L_p}{L_p + H_p} = \left(\frac{U_{g,sf}}{U_t}\right) \cdot \frac{1}{1 + \chi}\ , \tag{3.88}$$

where $\chi = H_p/L_p$ is the ratio of the pool dimensions. We use the following regression formula

$$\tan\phi = F\left(\frac{U_{g,sf}}{U_t}\right) \cdot G\left(\frac{1}{1+\chi}\right), \tag{3.89}$$

where, for the sake of simplicity, we choose both unknown functions $F()$ and $G()$ to follow the power law with proportionality constant c_1 and exponents c_2, c_3:

$$\tan\phi = c_1 \cdot \left(\frac{U_{g,sf}}{U_t}\right)^{c_2} \cdot \left(\frac{1}{1+\chi}\right)^{c_3}. \tag{3.90}$$

To validate the approach given by Eq. (3.90), we analyzed the experimental data and assumed that the center of mass of the debris bed (3.83) can be used as the average lateral particle spreading distance (3.87), i.e. $R_{spr} = R_c$. By performing the regression analysis, we determined the unknown fit coefficients used in (3.90):

$$c_1 = 1.0000,\ c_2 = 0.4814,\ c_3 = 0.8537. \tag{3.91}$$

Remarkably, the exponent c_2 of the velocities ratio is close to the exponent of the gas flow rate in the empirical expression for the total void fraction of the pool (3.72), both values being very close to 0.5. The scaling expression (3.90) with the determined fit

coefficients (3.91) is tested for prediction of the effects of particle density and size (see Figure 3.116 and Figure 3.117 solid and dashed lines). It is in reasonable agreement with the available experimental data, though for larger values of $\tan\phi > 0.8$ (i.e. high gas flowrates in a pool having the depth relatively small with respect to the spreading distance) further experiments are necessary to evaluate the scaling formula performance.

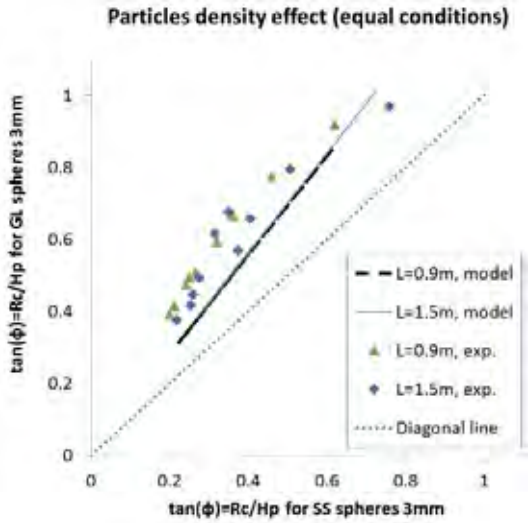

Figure 3.116: Particle density effect: comparison of the average spreading angle of the corresponding experiments (symbols) performed at equal test conditions except for the density of the particles (glass versus stainless steel). The modelling data (lines) are also provided for comparison.

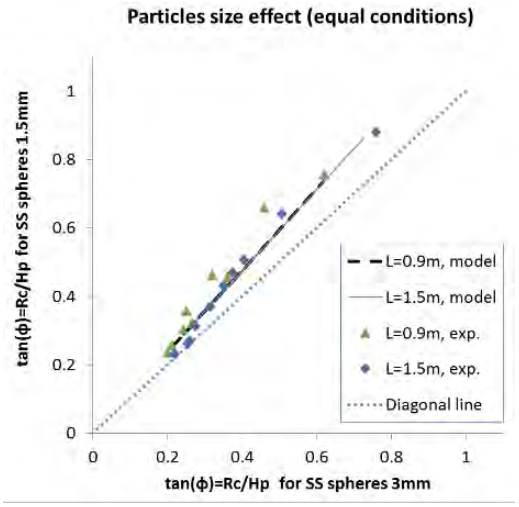

Figure 3.117: Particle size effect: comparison of the average spreading angle of the corresponding experiments (symbols) performed at equal test conditions except for the size of the particles (1.5 mm versus 3 mm). The modelling data (lines) are also provided for comparison.

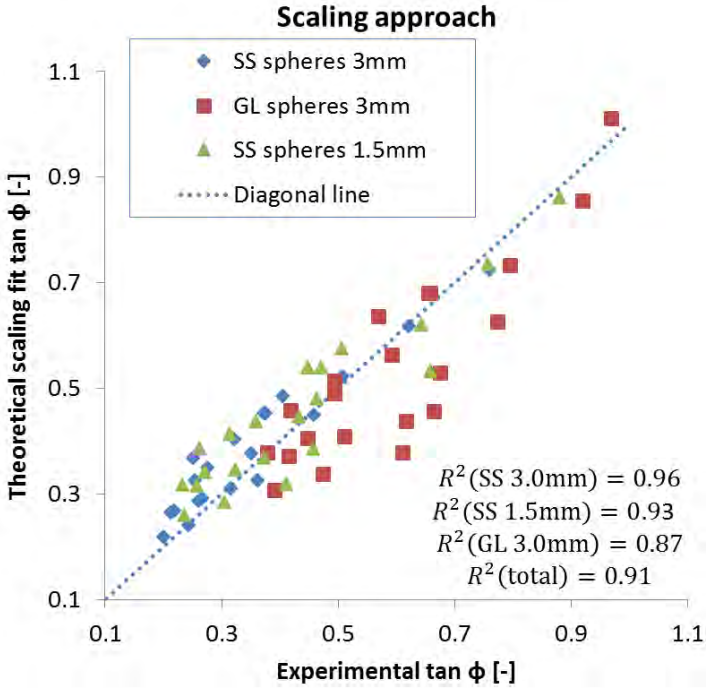

Figure 3.118: Validation of the scaling fit against experimental data.

The results of the regression analysis are shown in Figure 3.118. The average spreading of the stainless steel particles having 1.5 and 3 mm diameter is predicted reasonably well by (3.90), with coefficient of determination $R^2_{SS1.5} = 0.93$ and $R^2_{SS3.0} = 0.96$. However, for the glass particles (red squares in Figure 3.118) the resulting coefficient of determination is lower, $R^2_{GL3.0} = 0.87$. This type of particles is spread on average better than Eq. (3.90) predicts. We observed in the experiments that glass particles residing in the pool can be entrained by the turbulent flow for a long time ranging from tens of seconds up to few minutes after particles delivery is stopped. Further analysis and tests are necessary in order to clarify this effect as well as to improve the proposed semi-empirical model.
Experimental data on particulate debris spreading driven by large scale turbulent flow in the pool are reported. The work is motivated by the need to provide separate effect validation data for the models which can assess effectiveness of the spreading of fragmented corium debris over the pool basemat in prototypic severe accident conditions.
Post-test analysis of the experimental data suggests that the gas injection rate, pool dimensions, and particle properties have strong influence on debris bed formation. A semi-empirical scaling for the generalization of the data has been proposed demonstrating fairly good agreement with experimental data.
Further experimental work is required in order to develop a database of particle spreading in the pool with wider ranges of pool configuration, particle properties and debris release conditions. Improved scaling, such as inclusion of bubble-particle, turbulence-particle, particle-particle interactions into the scaling expression, might be helpful for further generalization of the data.

3.7.2.1.8 PDS-C: Scaling approach of self-leveling

In this work, our aim is to develop a universal scaling approach for generalizing empirical data on particle spreading rate at different gas injection conditions. Obtained non-dimensional closures for particle spreading rate should be valid for different particle properties.

The self-leveling phenomenon is a particular case of a more general problem of three phase gas–liquid–particle flow. In Figure 3.119 the main forces acting on the particles are shown schematically: (i) buoyancy (F_B), (ii) aerodynamic drag (F_D), (iii) gravity (F_G), and (iv) inter-particle friction (F_{Fr}). Given that average particle spreading velocity is relatively slow we neglect inertia forces. We also do not consider capillary and cohesion forces, which can become important for very small particles. The two-phase coolant flow drag counteracts with gravity and friction forces leading to spreading and reduction of the repose angle, as shown by Eames and Gilbertson [157]. At some point drag can overcome gravity force leading to fluidization of the bed.

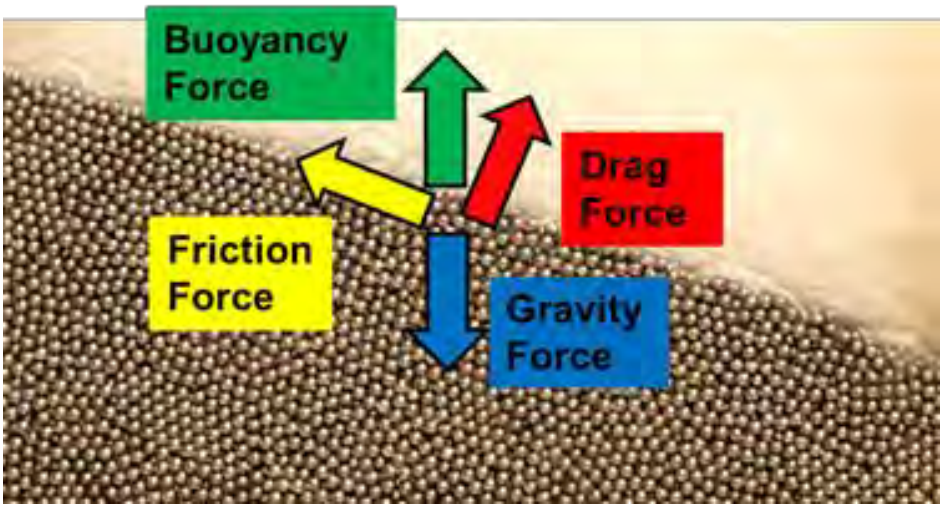

Figure 3.119: Schematic of the balance between main forces acting on a particle in the debris bed.

The particle flow rate should be a function of the main forces:

$$Q_p = f(F_D, F_B, F_{Fr}, F_G), \tag{3.92}$$

or, equivalently, a function of the parameters which can affect the forces:

$$Q_p = f\left(d_p, U_g, \rho_p, \rho_l, \rho_g, \mu_g, \mu_l, \sigma, g, \alpha, k_{Fr}\right), \tag{3.93}$$

where α is a local slope angle; $k_{Fr} = \tan\theta_{rep}(Q_g)$ is friction coefficient which is a function of gas flow rate and for the coarse, cohesion-less materials is equal to the tangent of the repose angle as shown in Eames and Gilbertson [157], where Eq. (3.94) was obtained and validated.

$$\theta_{rep}(Q_g) = \theta^0_{rep} - arcsin\left(\frac{C_d(Re)\cdot Q_g|Q_g|}{C_d(Re_{gmf})} sin(\theta^0_{rep})\right) \tag{3.94}$$

where $\boldsymbol{Q_g}$ is the gas injection normalized velocity (Eq. (3.81)); $\boldsymbol{\theta^0_{rep} = \theta_{rep}(0)}$ is critical repose angle of a particle heap [158] at $\boldsymbol{Q_g = 0}$ (see Table 3.15); C_d is the aerodynamic drag coefficient; Re and Re_{gmf} are respectively the particle Reynolds number at U_g and at U_{mf}. Eq. (3.93) can be represented with five independent non-dimensional combinations of the parameters

$$F\left(\frac{Q_p}{(\rho_p-\rho_l)\cdot\sigma/\mu_l\cdot d_p}, Q_g, Ar_{lg}, \frac{tan\,\theta_{rep}(Q_g)}{tan\,\theta^0_{rep}}, \frac{tan\,\alpha}{tan\theta_{rep}(Q_g)}\right)=0 \tag{3.95}$$

In this work we use following expression for the normalized non-dimensional particle spreading rate Q^*_p

$$Q^*_p = \frac{Q_p}{(\rho_p - \rho_l)\sigma/\mu_l \cdot d_p} = K \cdot {Q_g}^a \cdot {Ar_{lg}}^b \cdot \gamma^c \cdot \beta^d \tag{3.96}$$

where

$$\gamma = \frac{tan\,\theta_{rep}(Q_g)}{tan\,\theta^0_{rep}} \tag{3.97}$$

$$\beta = \frac{tan\,\alpha}{tan\,\theta_{rep}(Q_g)} \tag{3.98}$$

are normalized friction force (γ) and normalized slope angle (β). In eq. (3.96) the Ar_{lg} represents the effect of gravitational and buoyancy forces, Q_g the effect of aerodynamic drag and finally γ and β describe friction forces. Larger particles made of denser material will resist to the spreading according to the effect of the Archimedes number in Eq. (3.96) and as it was observed by Cheng et al. [150].

Dimensional analysis of Q_p [kg/s/m] suggests it has to be normalized by the product of: (i) density scale, (ii) length scale and (iii) characteristic velocity. In this work $(\rho_p - \rho_l)$ and d_p have been selected as scales for density and length respectively. Different combinations of the influential parameters have been tested as the characteristic velocity term: (i)$\sqrt{gd_p}$, (ii) U_g, (iii) terminal particle velocity V_t; and (iv) ratio of surface tension to dynamic viscosity σ/μ. The last one has allowed to obtain the best fit in the regression analysis of the experimental data produced in this work. The ratio of surface tension to viscosity in normalization of velocities has been used to characterize the suspension of solid particles in three phase columns, a phenomenon determined by similar set of forces as the self-leveling phenomenon. For instance Koide et al. [159], [160] and more recently some studies on self-leveling [150] use a dimensionless parameter in the form $(\mu \cdot V_t)/\sigma$. It is instructive to note that $(\mu \cdot V_t)/\sigma$ has been used for successful generalization of the experimental data from the tests on fluidization of three-phase columns with different fluids (pure water and mixtures of water with glycerol or ethylene) [159], [160]. In this work, however, σ/μ is a constant since we do not vary the liquid in our experiments. Thus the extrapolation of the model to other coolant properties is a subject for future work.

Based on the PDS-C experimental data, the constants K, a, b, c and d are evaluated by performing regression analysis (RA). Two separate RAs were necessary in order to represent different regimes of particle spreading: rapid avalanche and slow particle spreading (see Table 3.17).

Table 3.17: Empirical constants in Eq. (3.96)

Q_p^*	K	a	b	c	d
<0.0024	3.356	1.089	-0.325	2.628	4.306
>0.0024	0.159	0.432	-0.162	1.366	0.876

The dimensionless Eq. (3.96) reflects importance of different forces, which can be expressed as

$$Q_p \sim \frac{F_D \cdot F_B}{F_{Fr} \cdot F_G}. \tag{3.99}$$

I.e. the larger gravity and friction forces (larger Ar_{lg} and smaller β in Eq. (3.96)) will reduce particle flow rate, and vice versa, higher drag force and buoyancy (larger U_g and

smaller Ar_{lg} in Eq. (3.96)) will increase particulate flow rate.
Finally the obtained expression is used to verify its capability to predict correctly the dynamics of the heap slope angle. Parameter $R(t)$ is introduced and defined as ratio between heap slope angle at time t and the repose angle at zero gas velocity Eq. (3.100) :

$$R(t) = \frac{\alpha(t)}{\theta^0_{rep}} \tag{3.100}$$

The predicted R(t) is calculated by finding the corresponding $\alpha(t)$ after implementing the proposed closure in the mass balance equation in order to obtain the local bed height h:

$$\frac{\partial h(x,t)}{\partial t} + \frac{1}{\rho_b}\frac{\partial}{\partial x}\left(Q_p\left(Q_g(h), \frac{\partial h}{\partial x}, p\right)\right) = 0 \tag{3.101}$$

Where ρ_b is the bulk density of the heap, x represents the planar coordinate, p is the set of properties of particles and fluids. A detailed formulation of this approach can be found in [145].

Parity plot of predicted and experimental $R(t)$ is presented in Figure 3.120, here $R(t)$ is shown illustratively at 5% 10% 20% 50% 80% of the total spreading time in the experiment. The data points from all experiments with different particles and particle mixtures are clustered along the diagonal of the plot, suggesting that proposed scaling approach captures most important physical phenomena and can predict the debris bed self-leveling behavior. The greater difference is observed for larger particles. Further experimental studies of the effects of the particle density, particle size and surface tension on Q_p would be necessary to clarify the reasons. For instance, different ratios between the gravity, drag, fraction and surface tension forces can be studied by using particles of the same dimensions but different densities and morphologies.
Obtained correlation has been used to predict evolution of the debris bed shape in time for reactor accident conditions. A comprehensive sensitivity and uncertainty analyses of the spreading efficiency are given in [145].

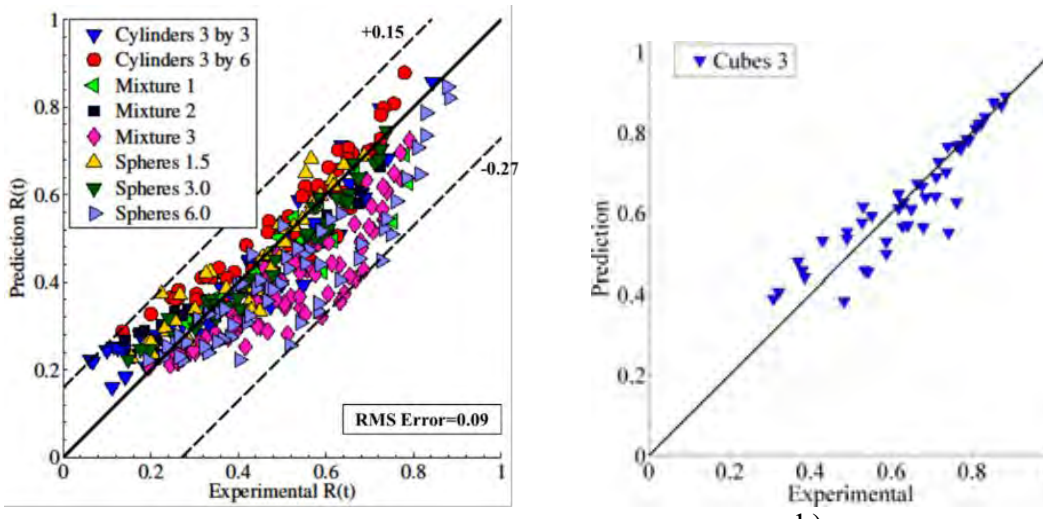

a) b)

Figure 3.120: Comparison between predicted and experimental R(t) in the PDS-C experiments. R(t) is calculated at 5%, 10%, 20%, 50% and 80% of the total

experimental time. Root mean square (RMS) error is equal to 0.09.

A set of PDS-C experiments has been carried out with different types of stainless steel particles and their mixtures in order to quantify particle flow rate in debris bed self-leveling phenomenon.

A scaling approach has been proposed for generalization of the experimental data on the non-dimensional particulate debris spreading rate. Application of proposed scaling approach to different PDS-C tests results in dense clustering of the data from different tests suggesting that the most important physical phenomena are captured properly.

Despite some remaining uncertainties, developed scaling method provides a viable approach to development of experimental closures universal for different types of particles, gas and coolant properties and flow characteristics.

More tests will be carried out in the future with particles made of different materials, mixtures of particles with different sizes and irregular shapes, etc. and with different liquid properties in order to extend the database for validation of the proposed closures and scaling approaches.

Modeling results

3.7.2.1.9 PDS-P: Preliminary results on modeling of experiments

The particular debris spreading in the pool has been implemented in DECOSIM code. An important task is to simulate particle spreading in the pool numerically with the goal to validate following models implemented in DECOSIM:

- Two-phase convection in the pool,
- Particle spreading by convective flows.

Preliminary simulations have been carried out with the following parameters:

- Pool length: 0.9 m,
- Pool depth: 0.6 m (taking into account that pool depth in PDS-P experiments was 0.7 m, but lower 0.1 m are taken by particle catchers),
- Water/air two-phase flow at 20 degrees,
- Superficial air velocity at the gas injector: 0.2 m/s.

Target parameters:

- Average void fraction in the pool,
- Particle distributions over the catchers,
- Mean spreading angle.

The simulation snapshots where turbulence dynamics and vortex formation can be seen are shown in Figure 3.121. The selected simulations of spreading of the particles 1.5 and 3 mm are compared versus experimental data. As seen (Table 3.18) the predicted spreading distances and angles are within 10% of the PDS-P experimental data. As seen from the particle mass flux as function of distance along the pool (Figure 3.122) the smaller particles are distributed more efficiently. Further DECOSIM validation against PDS-P experiments are ongoing.

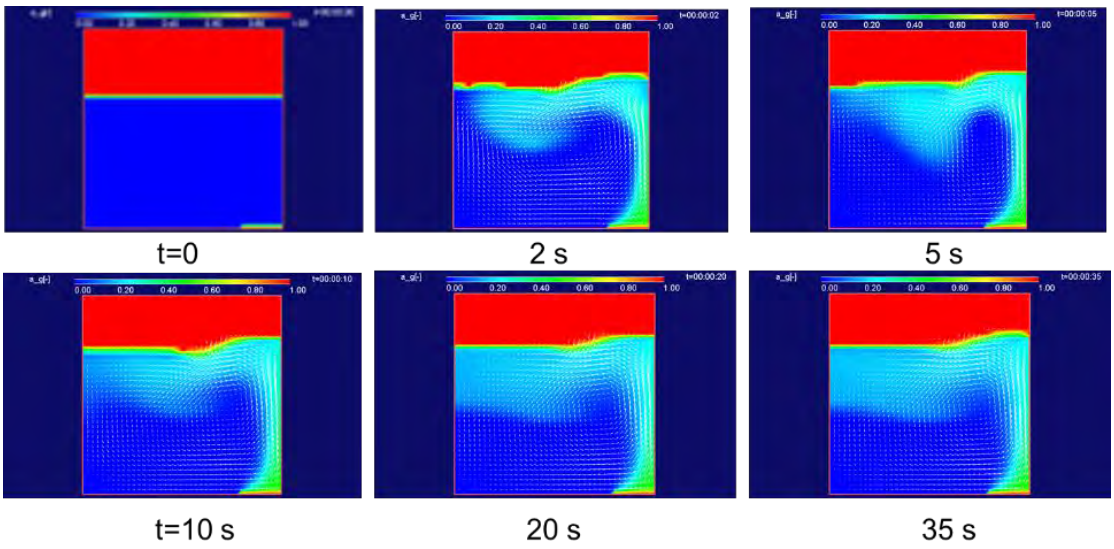

Figure 3.121: Vortex flow develops in the pool due to gas injection.

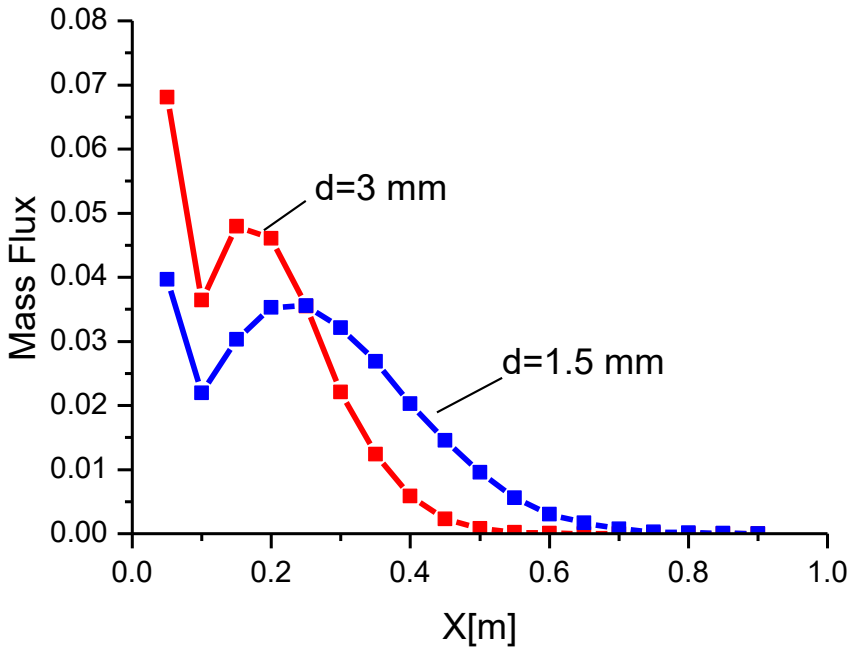

Figure 3.122: Example of DECOSIM simulation of PDS-P experiments.

Table 3.18: Spreading efficacy (comparison) obtained with DECOSIM and PDS-P selected tests.

Particle diameter	**Distance to center of mass [m]**		**Tangent of spreading angle**	
	PDS-P	DECOSIM	PDS-P	DECOSIM
3 mm	0.19	0.17	0.266	0.242
1.5 mm	0.23	0.25	0.322	0.360

PDS-C: sensitivity analysis of the coupled closures-based FM and coolability SM

Coupled code

Two models, the debris bed self-leveling FM and coolability SM (described in [121]),

have been coupled in order to estimate the time to reach a coolable configuration t_c in the scenarios associated with the formation of a conical (or conical + cylindrical base) porous bed over the basemat. The debris bed heat flux Q_{HF}=$\rho_b Wh$ calculated at the maximum local height $h = h_{max}$ is compared at each time step to the dryout heat flux (DHF). The debris bed is considered coolable if the decay heat released in the material is lower than the ability to remove this heat by water evaporation without local dryout. In the analytical form this condition can be represented as:

$$Q_{HF}(h_{max}) \leq DHF \tag{3.102}$$

Note, that the implementation of the coupled code does not take into account the case when the water penetration into the bed is blocked by the high steam flow rate at $Q_{HF} > DHF$.

3.7.2.1.10 Factor Screening and identification of important factors

The extended Morris method [161], [73], [74]has been applied to the coupled code in order to rank the relative importance of the parameters affecting the debris bed coolability. This methodology is a one-at-a-time global sensitivity analysis based on assessing the output of trajectories within the input parameters space of the numerical model.
In [161] it has been demonstrated that the modified mean index obtained from the extended Morris method is a good proxy for the total effect sensitivity index, i.e. the overall influence of a parameter. The final goal of such analysis is to rank the input parameters according to their influence on output variance. By gathering this information is then possible to assign constant values to the less influential parameters without losing a significant information on the system behavior in subsequent simulations.

The quantity t_c, and thus, the time when eq.(3.102) is satisfied, has been chosen as a target function of the analysis

The ranges of the uncertain model input parameters are selected in order to conservatively cover uncertainties in the complex phenomena involved in the debris bed formation process, the plant design, the SA conditions, the properties of the debris bed and the available experimental data. The list and the ranges of input parameters for modeling of the debris bed coolability are given in Table 3.19.

Table 3.19: Input parameters with corresponding uncertainty ranges.

Input parameter	Uncertainty range	
	Lower boundary	**Upper boundary**
Scenario-related conditions		
Drywell radius [m]	Fixed to 6	
Total Debris mass [tons]	10	250
Containment Pressure [Bar]	1	4
Effective operation Time [days]	365	1095
Time from scram [hours]	2.5	5.25
Reactor Thermal Power [GW]	1.4	3.9
Initial angle factor [-]	0.1	1
Physical properties		
Material density [kg/m^3]	7500	9000
Debris Bed Porosity [-]	0.3	0.6
Effective Particle diameter [mm]	1.0	6.0
Critical angle of repose at zero gas flow [degree]	22º	35º
Modeling parameters		
Closures uncertainty	-0.25	0.27
Number of cells [-]	50	
Time step	Adaptive: between 10 msec and 10 sec	
Output parameter		
Analyzed function for sensitivity:	Time since relocation to reach a coolable configuration (t_c)	

A uniform probability distribution function is used for all uncertain parameters by recourse to the Laplacian concept of insufficient reason [162], i.e. a uniform distribution should be used to describe the uncertainty when only the set of possible values can be identified due to the lack of information to substantiate a more definite choice.
A description of the ranges and parameters considered in the analysis is presented hereafter:

- Total debris mass. It indicates the total relocated corium in the lower drywell and it affects the total volume of the debris, thus the initial maximum height. The range is set to cover the values between small relocations (10 tons) and large relocations (250 tons).
- Pressure in the reactor cavity. It depends on the accident scenario and can be affected by the effectiveness of the containment pressure suppression function and venting systems. The initial containment pressure (1 bar) and the set point for activation of filtered containment venting system (4 bar) are chosen as range bounds. The pressure value affects the steam properties, calculated according to IAPWS IF-97 (IAPWS, 2007);
- Density of the corium debris particles. It has been selected to vary between 7500 and 9000 kg/m^3, which is slightly larger than the range of 8200-8700 covering UO_2-ZrO_2 proportion from 70:30 to 80:20 [163], in order to cover possible ranges of different corium compositions with different content of oxidic and metallic components. It affects the total volume of the debris bed, thus the initial maximum height, and the particle flow rate in the equation (3.96);
- Effective operation time of the reactor. The range [365;1095] days, has be assumed by considering the refueling of one third of the core each 12/18 months. This parameters affects the amount of fission products contained in the corium and thus the W_{decay} ,see the equation (3.103;

- Time from SCRAM. The range [2.5; 5.25] hours has been chosen according to the calculations performed with MELCOR [64][165] and MAAP [164][165] on reactor vessel failure time for Nordic BWR. It affects the W_{decay} ,see the equation (3.103;
- Porosity of the debris bed. The range [0.3; 0.6] is based on the available experimental data about packing of irregular particles and from the DEFOR-S experiments [88] on debris bed formation in the process of melt-coolant interactions. It affects the estimation of DHF, and the total volume of the debris bed, thus the initial maximum height;
- Effective particle diameter. It is calculated as the reciprocal mean diameter [154]. The range [1; 6] mm is set according to DEFOR [88] and FARO experiments. It affects the particle flow rate in equation (3.96) and the estimation of DHF.
- Reactor thermal power. The range [1.375; 3.9] GW is selected according to the existing Nordic BWRs. It affects the W_{decay} ,see equation (3.103;
- Critical angle of repose at zero flow. It represents the maximum angle before particle avalanching starts in no gas flow conditions. The range [22; 35] degrees is chosen according to values observed in experiments [166], [158]. It affects the initial maximum height, the particle flow rate in equation (3.96) and the estimation of initial DHF.
- Initial angle factor. It affects the initial slope configuration of the bed, which is calculated as the product of the initial angle factor with the critical angle of repose at zero flow. The range covers the interval between 0.1 and 1. The lower boundary corresponds to assumingly good pre-spreading of the falling debris particles by large turbulent flows in the pool [35], [167], while the implication of the upper boundary assumes nearly no convective spreading;
- Closure uncertainty. The range [-0.25; 0.27] derives from the analysis of the experimental data [166].

The lower drywell radius is considered as a design specific parameter in all the calculations and fixed to 6 meters.

Specific power of decay heat W_{decay} is calculated using

$$W_{decay}(T_{scram}, T_{oper}) = \frac{RP}{M_0} \cdot \frac{p_r(T_{scram}, T_{oper})}{100\%} \tag{3.103}$$

where T_{scram} and $T_{oper}$are the times from the scram and the equivalent operation time respectively; RP is the reactor thermal power; and M_0 is the maximum total mass of corium taken as 256 tons; p_r is relative power (in percent) obtained from the American Nuclear Society (ANS) 5.1 standard tables.

A total of 200 trajectories, corresponding to 2400 model runs, are evaluated. The Morris indexes of the elemental effects are estimated and plotted in **Figure 3.123** with the modified mean shown on the x-axis and the standard deviation shown on the y-axis. Observing that all the parameters have the standard deviation much larger that the modified mean, we can infer that all the parameters show to have a strong coupling or higher-order interaction with other parameters.
Moreover it is instructive to compare these results with the sensitivity study conducted exclusively on the self-leveling phenomenon and reported in our recent work [168]. In **Figure 3.124** the Morris indexes for the maximum debris height after 2 hours are

plotted. A clear difference is that all the input parameters exhibit mostly a linear influence on the output. In contrast, once it is coupled to the SM for predicting the debris bed dryout the resulting code demonstrates to have a strong interplay between parameters as seen in **Figure 3.123**. This behavior is ascribable to the fact that the dryout condition, equation (3.102), applied at each time step is strongly affected by parameters interactions.

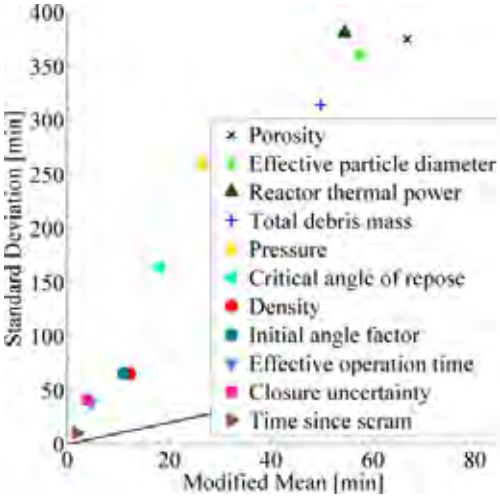

Figure 3.123 Modified mean and standard deviation of the time to reach a coolable configuration analyzed with Morris sensitivity method. The dashed line represents the first quadrant diagonal.

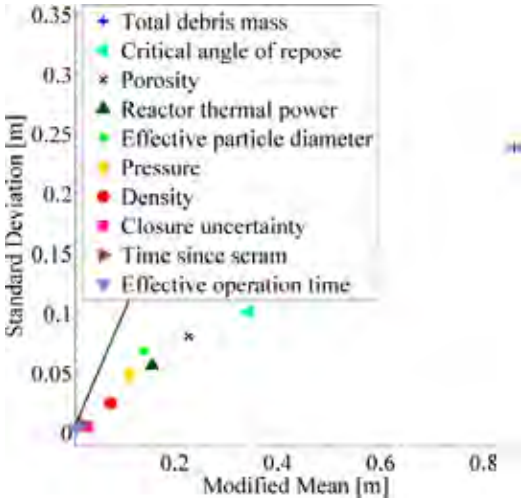

Figure 3.124 Modified mean and standard deviation of the maximal bed height analyzed with Morris sensitivity method at time 2 hours. The dashed line represents the first quadrant diagonal.

Table 3.20 reports the input parameter rankings based on the normalized modified mean values listed in columns three to four. A similar ranking would be reached with a sensitivity metric considering the distance-to-origin.

According to the evaluated rank **(**Table 3.20**)** we conclude to keep the parameters that contribute to 95% or more of the sensitivity influence on the model output. The others parameters have been screened out due to their not-significant influence on the output variance and a constant value provided in **Table 3.21** has been assigned. This factor fixing strategy is highly recommended in order to follow the concept of parsimony and simplicity involved in modelling activity [74] and to possibly decrease the computational cost during future analyses.

Table 3.20: Model input parameters ranked using the Morris modified-mean index.

Ranking	Parameter	Normalized modified mean **[%]**	Cumulated Statistic **[%]**
1	Porosity	0.22	0.22
2	Effective Particle Diameter	0.19	0.41
3	Reactor Thermal Power	0.18	0.59
4	Total Debris Mass	0.16	0.75
5	Pressure	0.08	0.83
6	Critical Angle of Repose	0.06	0.89
7	Density	0.04	0.93
8	Initial Angle Factor	0.03	0.96
9	Effective Operation Time	0.01	0.98
10	Closure Uncertainty	0.01	0.99
11	Time since Scram	0.01	1.0

Table 3.21: List of the parameters screened out and assigned constant values.

Parameter	Assigned constant value
Effective Operation Time [days]	400
Closure Uncertainty [-]	0
Time since Scram [hours]	3

3.7.2.1.11 Coolability time in the input domain

In the context of the coolability issue it is important to evaluate whether the time to reach a coolable configuration of the debris bed is lower than the debris bed re-melting time.

A first step is to provide data on the relative frequencies of the time to reach a coolable configuration. Thus a Monte-Carlo experiment has been conducted by using a Halton sampling method [169] to generate ~10.5 millions of input sets in the eight dimensional space given by the significant parameters reported in Table 3.20. The generated input sequences are evaluated computing the coolability time t_c. The relative frequencies of the outcome results are then summarized in Figure 3.125 and Figure 3.126. The former plot shows the results classified between the accident cases where the debris bed is initially coolable and the cases where it is not. Only a small fraction, ~3%, of the total runs appear to be non-initially coolable, i.e. expression (3.102) is not valid at the initial debris heap conditions. In the latter plot only the realizations of the model with a non-initially coolable debris configuration are considered and the relative frequencies of discrete intervals are reported. By interpreting the results in Figure 3.126 n combination with Figure 3.125 we can estimate that less than the 1.5% of the all possible cases will result in a non-coolable configuration at time 30 minutes from the relocation.

Parallel coordinates [170] is another method to visualize the outcomes of our Monte-Carlo experiment. In this graphical technique each polyline in the used 2D coordinate system corresponds to a single point in the high-dimensional input space.

Representation of the higher dimensions is possible when coordinate axes are arranged in parallel rather than orthogonal to each other. The results for $t_c > 0$ are plotted in such parallel coordinates system as shown in **Figure 3.127**. The vertical scales (set of parallel axes) for the studied parameters (horizontal axis) have been normalized as percentage, with the highest value at the top (100%) and the lowest at the bottom (0%). The resulting time to reach a coolable configuration varies between 0 sec and more than 183 hours. From the plot in **Figure 3.127** it is evident, for instance, that the specific cases having a porosity smaller than 0.35 are the ones with a larger time to reach a coolable configuration.

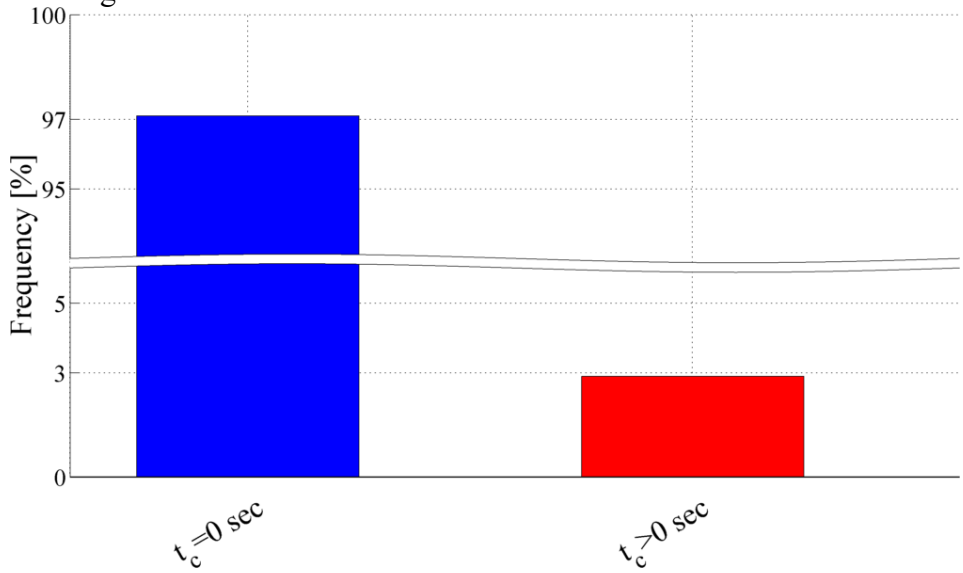

Figure 3.125 Relative frequencies plot of the model results for the time to reach a coolable configuration. The results are split between time equals to zero and time greater than zero.

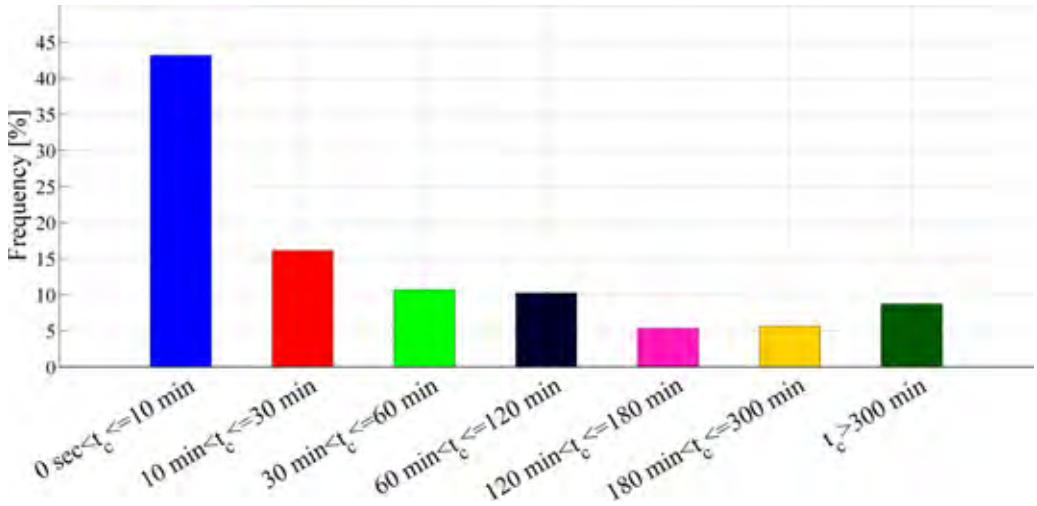

Figure 3.126 Relative frequencies plot of the model results for the time to reach a coolable configuration. Results are filtered to consider exclusively time greater than zero and successively split between time intervals.

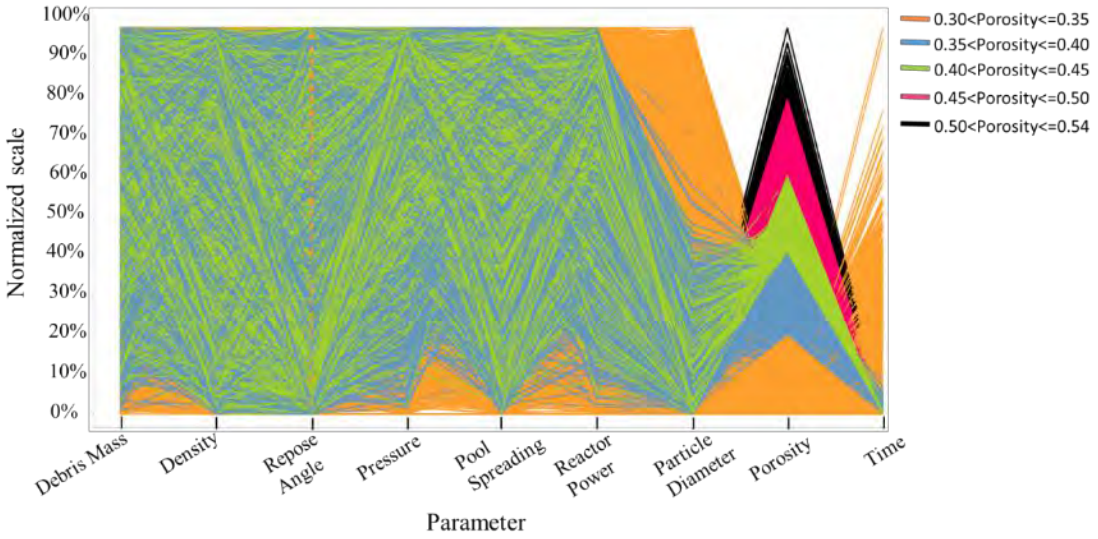

Figure 3.127 Parallel coordinates plot of the modeling results for coolability time greater than zero.

Finally by filtering the entire database of simulations has been possible to obtain important information on how specific combinations of inputs resolve in the output domain. Table 3.22 and Table 3.23 report the values of other parameters that combined singularly with the variable filtered (second column in the tables) allows to reach a coolable configuration before the threshold time is reached (see first column in the tables). We have reported only the filtering results for the porosity (**Table 3.22**) and the effective particle diameter (Table 3.23) since they are the ones exhibiting the greatest effect.

The data in the two tables provide insights to obtain a rough upper estimation for the time to reach a coolable configuration for any set of input parameters. For instance by assuming the bed porosity greater than 0.40 we would be able to infer a coolability time smaller than 30 minutes in the cases where either (i) the total debris mass is less than 50 tons or (ii) the effective particle diameter is greater than 1.72 mm or (iii) the pressure is greater than 3.94 bar or (iv) the reactor power is less than 2.1 GW or (v) the initial angle factor is less than 0.11.

It is worth to note that for the cases where porosity is higher than 0.539 the debris bed is immediately coolable regardless of the other parameters values. The porosity is the only one to show a similar characteristic, meaning that the other parameters do not have any value in the considered ranges where independently from other inputs we obtain zero as coolability time.

Given the large amount (~10.5 millions) of available data in the input domain space, each limit presented in the two table has a good level of accuracy. In particular we can estimate that there is a probability of 99.9% with a confidence level of ~100% that the limit will not be exceeded. This assessment has been obtained by applying the one-sided tolerance Wilks' formula (Wilks, 1941, 1942):

$$1 - a^n \geq b \qquad (3.104)$$

Where $b \cdot 100$ is the confidence level (%) that the maximum coolability time will not be exceeded with the probability of $a \cdot 100$ (%) of the relative output distribution and n is the number of performed calculation.

Table 3.22 Analysis of the results filtered for the value of the porosity.

Threshold Time [min]	Bed Porosity [-]	Debris Mass [tons]	Particle Density [kg/m^3]	Effective Diameter [mm]	Pressure [bar]	Reactor Power [GW]	Repose Angle [degree]	Initial angle factor [-]
=0	Whole interval[a]	---	---	---	---	---	---	---
	>0.35	---	---	>5.75	---	---	---	---
	>0.40	---	---	>3.51	---	---	---	<0.11
	>0.45	<36	---	>2.01	---	<2.2	---	<0.317
	>0.50	<136	---	>1.45	>2.06	<3.00	<23	<0.587
<=10	Whole interval[b]	---	---	--	---	---	---	---
	>0.35	<15	---	>3.55	---	---	---	---
	>0.40	<43	---	>2.22	---	<1.8	---	<0.11
	>0.45	<138	---	>1.35	>2.28	<2.9	<26.32	<0.53
<=30	Whole interval[c]	---	---	>5.13	---	---	---	---
	>0.35	<16	---	>3.2	---	<1.43	---	---
	>0.40	<50	---	>1.72	>3.94	<2.10	---	<0.11
	>0.45	<172	<7900	>1.07	>1.22	<3.3	<30.36	<0.66
<=60	Whole interval[d]	---	---	>4.25	---	---	---	---
	>0.35	<27	---	>2.35	---	<1.46	---	---
	>0.40	<74	---	>1.59	>3.2	<2.29	---	<0.11
	>0.45	<225	<9000	>1.001	>1.1	<3.80	<33.8	<0.80
<=120	Whole interval[e]	<11	---	>3.3	---	---	---	---
	>0.35	<34	---	>2.15	---	<1.73	---	---
	>0.40	<109	---	>1.36	>2.1	<2.74	---	<0.11
<=180	Whole interval[e]	<11	---	>2.95	---	---	---	---
	>0.35	<38	---	>2.00	---	<1.79	---	---
	>0.40	<137	---	>1.19	>1.67	<3.05	<24.88	<0.15
<=300	Whole interval[f]	<17	---	>2.71	---	---	---	---
	>0.35	<72	---	>1.7	>3.9	<1.95	---	---
	>0.40	<208	<7746	>1.07	>1.3	<3.13	<28.64	<0.51

a: For the selected time threshold the debris bed is coolable before the threshold in any scenarios where the porosity is >0.539;
b: For the selected time threshold the debris bed is coolable before the threshold in any scenarios where the porosity is >0.48
c: For the selected time threshold the debris bed is coolable before the threshold in any scenarios where the porosity is >0.465
d: For the selected time threshold the debris bed is coolable before the threshold in any scenarios where the porosity is >0.460
e: For the selected time threshold the debris bed is coolable before the threshold in any scenarios where the porosity is >0.44
f: For the selected time threshold the debris bed is coolable before the threshold in any scenarios where the porosity is >0.415

Table 3.23: Analysis of the results filtered for the value of the effective particle diameter.

Threshold Time [min]	Effective Diameter [mm]	Debris Mass [tons]	Particle Density [kg/m^3]	Bed Porosity [-]	Pressure [bar]	Reactor Power [GW]	Repose Angle [degree]	Initial angle factor [-]
=0	Whole interval	---	---	>0.539	---	---	---	---
	>1.2	---	---	>0.52	---	---	---	---
	>1.5	---	---	>0.49	---	---	---	---
	>2	<11.5	---	>0.47	---	---	---	<0.12
	>3	<27	---	>0.41	---	<1.5	---	<0.34
<=10	Whole interval	---	---	>0.48	---	---	---	---
	>1.2	---	---	>0.48	---	---	---	---
	>1.5	<19	---	>0.43	---	---	---	---
	>2	<30	---	>0.41	---	<1.57	---	<0.12
	>3	<75	---	>0.36	>3.9	<2.2	---	<0.34
<=30	Whole interval[a]	---	---	>0.465	---	---	---	---
	>1.2	<11	---	>0.44	---	---	---	---
	>1.5	<21	---	>0.419	---	---	---	---
	>2	<55	---	>0.39	---	<1.8	---	<0.12
	>3	<109	---	>0.35	>3.7	<2.55	---	<0.34
<=60	Whole interval[b]	---	---	>0.46	---	---	---	---
	>1.2	<11	---	>0.43	---	---	---	---
	>1.5	<23	---	>0.402	---	<1.45	---	---
	>2	<55	---	>0.37	---	<1.84	---	<0.12
	>3	<152	---	>0.33	>2.2	<3.12	<26	<0.35
<=120	Whole interval[c]	<11	---	>0.44	---	---	---	---
	>1.2	<19	---	>0.41	---	---	---	---
	>1.5	<36	---	>0.39	---	<1.65	---	---
	>2	<84	---	>0.35	>3.8	<2.32	---	<0.15
	>3	<189	<8400	>0.31	>1.2	<3.59	<31	<0.57
<=180	Whole interval[d]	<11	---	>0.44	---	---	---	---
	>1.2	<19	---	>0.4	---	<1.485	---	---
	>1.5	<53	---	>0.37	---	<1.65	---	---
	>2	<84	---	>0.34	>3.6	<2.4	---	<0.25
<=300	Whole interval[e]	<17	---	>0.41	---	---	---	---
	>1.2	<28	---	>0.4	---	<1.5	---	---
	>1.5	<54	---	>0.36	---	<1.99	---	---
	>2	<132	---	>0.33	>2.0	<3.15	---	<0.25

a:For the selected time threshold the debris bed is coolable before the threshold in any scenarios where the diameter is >5.1 mm;
b: For the selected time threshold the debris bed is coolable before the threshold in any scenarios where the diameter is >4.2mm
c: For the selected time threshold the debris bed is coolable before the threshold in any scenarios where the diameter is >3.3 mm
d: For the selected time threshold the debris bed is coolable before the threshold in any scenarios where the diameter is >2.95 mm
e: For the selected time threshold the debris bed is coolable before the threshold in any scenarios where the diameter is >2.71 mm

3.7.2.1.12 Summary from performed sensitivity analysis of the coupled code

A coupled code between a model for particulate debris spreading and a surrogate model for the determination of the coolability has been implemented. It allows to predict the time to reach a coolable configuration for a conical (or conical + cylindrical base) porous debris bed after relocation in the hypothetical case of SA in Nordic BWR.

The sensitivity analysis has been carried out using the extended Morris method. It allowed to rank the influence of the parameters on the time to reach a coolable configuration as following: (i) porosity, (ii) effective particle diameter, (iii) reactor thermal power, (iv) debris total mass, (v) pressure, (vi) repose angle, (vii) particle density and (viii) initial angle factor. Moreover, the three parameters effective operation time, closure uncertainty and time since scram have been screened out by assigning them a constant value since they have shown to have least influential effect on the variance of the model output.

A Monte-Carlo experiment was performed executing more than ten millions calculations using the multi-dimensional Halton sampling method to generate the inputs in the eight dimensional space. The outcomes of the analysis suggest that barely 3% of all the possible scenarios in the considered inputs domain will result in a non-initially coolable configuration and less than 1.5% will exhibit a greater than 30 minutes time to reach a coolable configuration . It has been possible to identify the most important input regions where a finite upper-limit of the response can be used as a rough estimator of the time to reach a coolable configuration for the inputs combination.

These findings are important for the debris bed coolability and it will be possible to use the obtained data for the development and implementation of computationally inexpensive methods such as classification tree or artificial neural network. This would effectively replace the coupled system.

3.7.3 Debris Bed Formation and Coolability Full (DECOSIM) Model Analysis

DECOSIM Code

The mathematical models implemented in DECOSIM code are based on multifluid formulation, they include a number of submodels describing two-phase pool flows, disperse particle sedimentation, as well as flows in heat-releasing porous media related to debris bed coolability in in-vessel and ex-vessel configurations. In this work, we concentrate on validation of the models relevant to modeling natural convection flows in the pool, spreading of particles and their fallout onto the bottom surface of the pool [231].

3.7.3.1.1 Governing Equations

Isothermal air-water flow in the pool is described by the mass and momentum, and energy conservation equations for liquid water (index $\boldsymbol{k = l}$) and gas ($\boldsymbol{k = g}$); turbulence is taken into account only in continuous liquid and described by the $\boldsymbol{k-\varepsilon}$ model with additional terms for turbulence generation due to relative motion of liquid and gas phases:

$$\frac{\partial \alpha_k \rho_k}{\partial t} + \nabla \alpha_k \rho_k \boldsymbol{u}_k = 0 \tag{3.105}$$

$$\alpha_k \rho_k \left(\frac{\partial \boldsymbol{u}_k}{\partial t} + (\boldsymbol{u}_k \cdot \nabla)\boldsymbol{u}_k \right) = -\alpha_k \nabla P + \alpha_k \nabla \boldsymbol{\tau}_k + \alpha_k \rho_k \boldsymbol{g} + \boldsymbol{F}_{kl} \tag{3.106}$$

$$\boldsymbol{\tau}_l = \mu \left(\nabla \boldsymbol{u}_l + \nabla \boldsymbol{u}_l^T - \frac{2}{3}\delta(\nabla \cdot \boldsymbol{u}_l) \right), \quad \boldsymbol{\tau}_g = 0 \tag{3.107}$$

$$\frac{\partial \alpha_l \rho_l k_t}{\partial t} + \nabla \alpha_l \rho_l \boldsymbol{u}_l k_t = \nabla \left(\alpha_l \frac{\mu}{\sigma_k} \nabla k_t \right) + \alpha_l \left(G - \varepsilon + G_g \right) \tag{3.108}$$

$$\frac{\partial \alpha_l \rho_l \varepsilon_t}{\partial t} + \nabla \alpha_l \rho_l \boldsymbol{u}_l \varepsilon_t = \nabla \left(\alpha_l \frac{\mu}{\sigma_\varepsilon} \nabla \varepsilon_t \right) + \alpha_l \frac{\varepsilon_t}{k_t} \left(C_1 G - C_2 \varepsilon + C_3 G_g \right) \tag{3.109}$$

$$G = \mu_t \left(\frac{1}{2} |\nabla \boldsymbol{u}_l + \nabla \boldsymbol{u}_l^T|^2 - \frac{2}{3}(\nabla \cdot \boldsymbol{u}_l)^2 \right) - \frac{2}{3}\rho_l k_t (\nabla \cdot \boldsymbol{u}_l) \tag{3.110}$$

$$G_g = C_p \alpha_g \frac{\left| \boldsymbol{u}_l - \boldsymbol{u}_g \right|^3}{D_b}, \mu = \mu_l + \mu_t, \quad \mu_t = C_\mu \rho_l \frac{k_t^2}{\varepsilon_t} \tag{3.111}$$

In this formulation, water is assumed to be the continuous phase where turbulent stresses are taken into account, no account for turbulence in the gas phase is taken. Turbulent water flow is described by the Reynolds-averaged Navier-Stokes equations, with the stress tensor $\boldsymbol{\tau}_l$ (see Eq. (3.107)) in the liquid momentum equation (3.106) related to the average velocity gradient via the effective viscosity[156], the latter is the sum of laminar and turbulent contributions. Equations (3.6) and (3.109) correspond to the $k-\varepsilon$ turbulence model [225], modified by the volume fraction α_l; also, additional generation term G_g due to the presence of gas phase is taken into account [226]. The constants for the model are $C_\mu = 0.09$, $C_1 = 1.44$, $C_2 = 1.92$, $\sigma_k = 1.0$, $\sigma_\varepsilon = 1.3$, $C_3 = 1.4$. Validity of $k-\varepsilon$ turbulence model in the context of two-fluid model has been addressed previously [156],[47][226][227].

The drag force on the dispersed phase, d, surrounded by the continuous phase, c, is

$$\boldsymbol{F}_{dc} = \alpha_d \frac{3}{4}\frac{\rho_c}{D_d} C_D^{dc} |\boldsymbol{u}_c - \boldsymbol{u}_d| (\boldsymbol{u}_c - \boldsymbol{u}_d) \tag{3.112}$$

where the drag coefficient C_D^{dc} depends on the flow regime determined by the local void fraction α_g, according to correlations[156], [228]. For churn turbulent flow $(0.3 < \alpha_g < 0.7)$

$$d = g, \qquad c = l, \qquad C_D^{dc} = \frac{8}{3}(1-\alpha_g)^2, \quad D_d = 4\left(\frac{g(\rho_l - \rho_g)}{\sigma}\right)^{-1/2} \tag{3.113}$$

while for dispersed flow (bubbly and droplet flow regimes)

$$C_D^{dc} = \frac{2}{3} D_d \left(\frac{g(\rho_l - \rho_g)}{\sigma}\right)^{1/2} \left(\frac{1 + 17.67 f^{6/7}}{18.67 f}\right)^2 \tag{3.114}$$

where for bubbly flow $(\alpha_g \le 0.3)$ $d = g$, $c = l$, $f = (1-\alpha_g)^{3/2}$, for droplet flow $(\alpha_g \ge 0.7)$ $d = l$, $c = g$, $f = \alpha_g^3$. To take into account the turbulent dispersion of bubbles, a term proportional to the gradient of void fraction is added to the drag force (3.112) [229].

Water phase properties (densities ρ_k, specific enthalpies h_k, viscosities μ_k, thermal conductivities λ_k) as functions of pressure P and temperature T_k are approximated by polynomials according to IAPWS-IF97 formulation [222], air is described by the ideal gas equation of state.

3.7.3.1.2 Model for Particles

Lagrangian model is used for particles falling into the pool from a prescribed height. Flow-particle interaction due to drag depends on the diameter of the particle, relative velocity and phase composition of the ambient two-phase mixture. Each particle is characterized by its diameter D_p, position vector, $\boldsymbol{r}^k$, and velocity, $\boldsymbol{u}_p^k$ (the superscript k denotes the particle index). The equations for the position vector and momentum are:

$$\frac{d\boldsymbol{r}^k}{dt} = \boldsymbol{u}_p^k, \qquad \rho_p \frac{d\boldsymbol{u}_p^k}{dt} = \boldsymbol{F}_{pl} + \boldsymbol{F}_{pg} + (\rho_p - \rho_a)\boldsymbol{g} \tag{3.115}$$

where $\rho_a = (1-\alpha_g)\rho_l + \alpha_g \rho_g$ is the void fraction-weighted ambient density. The drag forces due to particle interaction with k-th phase ($k = l, g$) are

$$\boldsymbol{F}_{pk} = \alpha_k \frac{3}{4}\frac{\rho_k}{D_p} C_{D,k} |\hat{\boldsymbol{u}}_k - \boldsymbol{u}_p| (\hat{\boldsymbol{u}}_k - \boldsymbol{u}_p) \tag{3.116}$$

where $\hat{\boldsymbol{u}}_k$ is the effective velocity of k-th phase. The drag coefficient $C_{D,k}$ is calculated as a function of particle Reynolds number with respect to k-th phase, $\mathrm{Re}_{p,k} = \rho_k D_p |\hat{\boldsymbol{u}}_k - \boldsymbol{u}_p| / \mu_k$:

$$C_{D,k} = \frac{24}{\mathrm{Re}_{p,k}} + \frac{4}{\sqrt{\mathrm{Re}_{p,k}}} + 0.4 \tag{3.117}$$

To account for turbulent dispersion of particles, the random walk model is applied. The effects of turbulence on particle dispersion are modeled by adding a fluctuating

component to the liquid phase velocity: $\widehat{\boldsymbol{u}}_l = \boldsymbol{u}_l + \boldsymbol{u}_l'$, where the fluctuating component $\boldsymbol{u}_l'$ is modeled by a random vector with uniform angular distribution; each of its three components has Gaussian probability distribution with zero mean value and variance $2k_t/3$. Particle interacts with an eddy for a time interval $\min(t_e, t_t)$, where t_e is the characteristic eddy lifetime, and t_t is the time over which particle traverses the eddy; after that a new random vector is picked up for $\boldsymbol{u}_l'$. The characteristic eddy size is evaluated as $L_e = C_\mu^{3/4} k_t^{3/2}/\varepsilon_t$, the mean eddy lifetime is picked up randomly as $t_e = -0.15 k_t/\varepsilon_t \log r$ (where r is a random number distributed uniformly on the interval $(0,1]$; the particle traversal time is evaluated from the eddy size and relative velocity, taking into account particle deceleration due to drag: $t_t = -\tau_p \log\left(1 - L_e/\left|\boldsymbol{u}_r^p\right|\tau_p\right)$, where the characteristic drag time is $\tau_p = \frac{3}{4}\frac{\rho_k}{\rho_p D_p} C_{D,k}\left|\boldsymbol{u}_r^p\right|$, see Eq. (3.116); $\boldsymbol{u}_r^p = \boldsymbol{u}_p - \widehat{\boldsymbol{u}}_l$ is the current relative velocity of particle with respect to liquid.

Note that in the current DECOSIM implementation, the coupling between particles and two-phase flow is "one-way", i. e., particle effect on the flow is neglected. This is because the primary target of DECOSIM development was to study the gradual melt release in severe accidents in Nordic-type BWRs, where melt can escape from the reactor pressure vessel in the "dripping" mode through numerous vessel penetrations in a form of small jets, rather than as a single coherent jet. Estimates of the conditions under which "collective effects" are negligible and particle drag acting on two-phase flow is much less than the buoyancy force were made in [230]. In particular, it was shown that in the scenario where $M = 200$ tons of corium melt are released over the time 4 hours from an area of diameter 1 m (multiple small openings in the reactor vessel), the maximum volume fraction of 3 mm particles in the pool is as low as 0.25%, while the buoyancy force acting on two-phase flow exceeds the drag exerted by particles provided that the void fraction in the bubble plume exceeds some 2%, a condition well satisfied in most dripping mode scenarios of interest. Note that PDS-P experiments [146][153] were specifically designed to ensure that particle interaction and effect on the flow was negligible; therefore, their results are adequate for validation of the current DECOSIM model. Studies of high-concentration particle releases would require both different experimental conditions and model implementation with "two-way" particle-flow coupling; which is beyond the scope of the present work.

3.7.3.1.3 Numerical Implementation

The system of governing equations (3.3)–(3.111) is discretized in 2D planar geometry on a staggered orthogonal grid; on each time step equation are solved by Newton iterations. On each time step, the momentum equations are solved first to find out the preliminary velocity components of each phase. The velocity corrections are expressed in terms of pressure and volume fraction corrections, with the phase change terms taken into account implicitly. They are then substituted into the phase continuity and energy equation which are solved in a fully coupled manner by an efficient ILUT-preconditioned PGMRES solver. Global iterations are performed on each time step until convergence with prescribed accuracy is reached. The time step is varied adaptively to control convergence process. The particle momentum equation (3.115) is integrated by one-step implicit scheme, after which the particle position is updated. In the 2D formulation, the liquid phase velocity $\boldsymbol{u}_l$ calculated from the momentum equation (3.106) contains only two components, those in the horizontal direction X and vertical direction Z. The third component of $\boldsymbol{u}_l$ in the normal-to-the-pool direction Y is zero because flow across the pool is not modeled. However, the fluctuation of liquid

phase velocity, $\boldsymbol{u}_l'$, is picked up randomly with all three components present, accordingly, particles interact with three-dimensional velocity $\widehat{\boldsymbol{u}}_l = \boldsymbol{u}_l + \boldsymbol{u}_l'$, and particle velocities $\boldsymbol{u}_p$ obtained from equation (3.115) are also three-dimensional. Accordingly, the particle position vector $\boldsymbol{r}^k$ updated by $\boldsymbol{u}_p$ contains all three coordinates of which only those in X and Z directions are relevant and determine the particle trajectories in the planar pool.

3.7.3.1.4 Parameters

Detailed description of PDS-P facility, experimental procedure and processing of results obtained can be found in recent publications [146][153]. Here, we overview in short the geometry, gas injection parameters, and particle feeding and collection, relevant to DECOSIM validation purposes.

The PDS-P (Particulate Debris Spreading in the Pool) facility consists of the particle delivery system, main water tank, particle collection system, gas supply and flow rate measurement systems [146][153]. The water tank planar pool with 20 mm thick transparent acrylic walls was of adjustable horizontal dimension, allowing experiments to be carried out in pools of length $L_P = 0.9$ and 1.5 m. Water pool depth above the particle catchers was set at $H_P = 0.5$, 0.7, and 0.9 m. The width of test section was fixed at 72 mm, which resulted in essentially 2D planar flow structure.

Air was injected at the bottom of the test section, near one of its side walls, the gas injection chamber was a rectangular box with the height 60 mm, length 200 mm, and width 70 mm. Air injection holes were 1 mm in diameter, the pitch size of the holes was 10 mm in both directions. The air mass flow rate was varied in the range $Q_g = 2.2 - 14.5$ g/s, corresponding to the superficial gas velocity at the injector in the range $V_g = 0.12 - 0.69$ m/s.

Spherical stainless steel particles of diameters $d_p = 1.5$ and 3 mm (particle density $\rho_p = 7.8 \cdot 10^3$ kg/m^3), and glass particles with $d_p = 3$ mm ($\rho_p = 2.6 \cdot 10^3$ kg/m^3) were delivered from the top boundary of the facility at the fixed height of $H_p^0 = 1.61$ m above the top of the particle catchers through a funnel equipped with Archimedes screw. The particle supply rate was low enough to avoid "collective effects", so that each particle can be considered as falling separately from the others.

In DECOSIM simulations, the horizontal size of computational domain was taken of the same length as the corresponding pool (0.9 or1.5 m), while the vertical size was taken equal to $H_0 = 1.5$ m. The computational mesh was uniform and had square cells of 2 cm size in each direction. For each combination of pool length L_P, water depth H_P, and superficial velocity V_g, simulations were first run for 60 seconds which was sufficient to establish steady-state convection in the pool. After that, particles were released. For each particle sort (i.e., material and diameter), total of $N_p = 5 \cdot 10^4$ particles were used, which was sufficient to generate statistically meaningful distributions (the increase of particle number to 10^5 altered the mass fractions of particles collected in catchers by less than 1%). The initial horizontal position of each particle was picked randomly on the interval [0.065,0.075] m, reproducing the particle delivery funnel which was located in the experiments at a distance 7 cm from the side wall (particles were released above the gas injector). The initial vertical position of all particles was set equal to the upper boundary of computational domain (1.5 m). Since this height is smaller than the above-mentioned experimental particle release height, the

vertical velocity of each particle was assigned the initial value of $\sqrt{2g\left(H_p^0 - H_0\right)} = 1.47$ m/s.

For each particle, trajectory in the two-phase pool flow was traced; it was assumed that particles reaching the pool bottom remain stuck at the bottom. Particles were collected on a pool bottom mesh with 10 cm long cells, imitating the particle catchers used in PDS-P experiments. As a result, particle mass distributions over the pool bottom were obtained for each pool geometry, injection rate, and particle properties. These mass distributions were compared with the experimental results, in terms of local distribution functions, and integral quantities characterizing particle spreading: the mean spreading distance defined by the horizontal coordinate of the center of mass of collected particles. For each particle the trajectory length was calculated, which allowed us to evaluate the mean trajectory length and its standard deviation. Particle trajectory densities were also obtained by registering the normalized number of particles crossing each computational cell.

DECOSIM simulations were carried out in order to investigate post-dryout debris bed. The studies extended the results obtained earlier in [31] to wider ranges of debris bed parameters (particle diameters and porosities), as well as to more debris bed shapes (Gaussian shape was studies in addition to conical and mound shapes). Also, longer transients were simulated in order to obtain the stabilized temperatures after occurrence of dryout. The main target quantities were the maximum temperature of solid particles in the dry zone, as well as the top and bottom boundaries of the dry zone from which the relative size of dry zone was evaluated. The results obtained were applied to the development of a surrogate model capable of predicting the dry zone characteristics, these results are considered in Section 0 (see Figure 3.141 and Figure 3.142).

Results

3.7.3.1.5 Two-phase Flow Field in the Pool

Gas injection near the pool side wall results in the development of natural convection flow with a bubble plume rising along the side wall, causing water circulation in the pool. In Figure 3.128, typical steady-state void fraction distributions are shown at $t = 60$ s; the velocity field in water is drawn by arrows (for clarity, only every other vector is shown). The void fraction distributions and shapes of pool surface agree qualitatively with the experimental observations [146][153]. In particular, a “dome” is visible on the pool surface above the gas injector, where the plume reaches the surface and then turns sideways, creating the principal vortex. For higher injection rates (see Figure 3.128 d–f), a “dent” is visible on the pool surface, marking the end of the “dome” and separation between the principal vortex attached to the plume, and large-scale circulatory flow spanning to the rightmost wall of the tank. Another characteristic feature of the flow, also observed experimentally, is that the two-phase water-gas plume is compacted horizontally by the water flow towards the pool wall, so that its thickness in the pool is smaller than the length of gas injector (20 cm in the PDS-P facility).

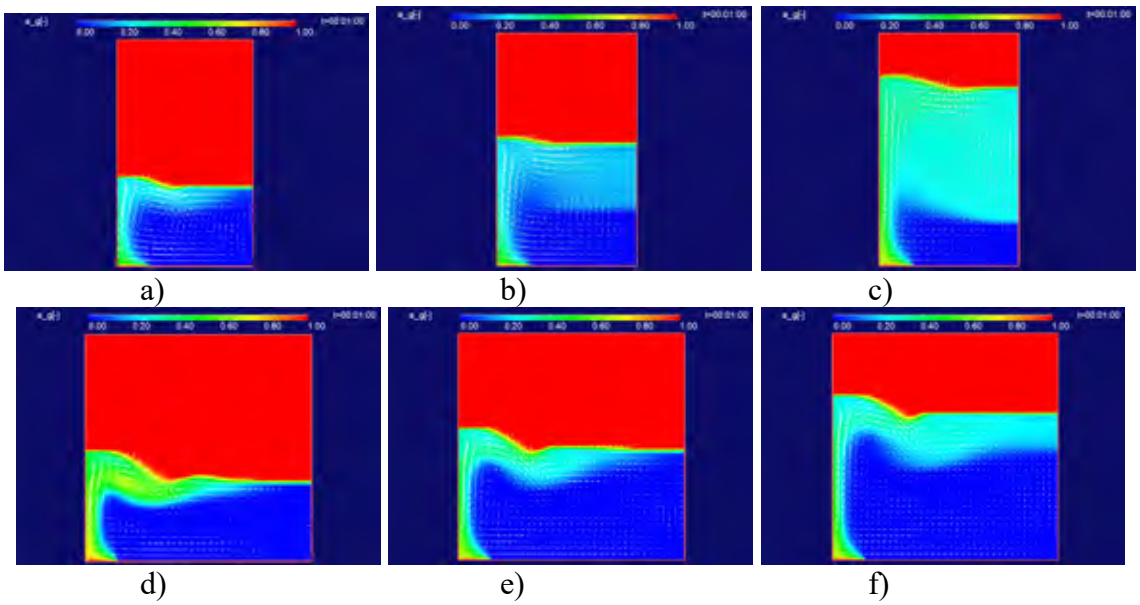

Figure 3.128 Void fraction distributions in water pool: a) $H_P = 0.5$ m, $V_g = 0.17$ m/s; b) $H_P = 0.7$ m, $V_g = 0.17$ m/s; c) $H_P = 0.9$ m, $V_g = 0.17$ m/s; d) $H_P = 0.5$ m, $V_g = 0.69$ m/s; e) $H_P = 0.7$ m, $V_g = 0.35$ m/s; f) $H_P = 0.9$ m, $V_g = 0.35$ m/s. Pool length is $L_P = 0.9$ m (a–c) and 1.5 m (d–f).

3.7.3.1.6 Particle-Flow Interaction in the Pool

Consider the simulation results demonstrating particle interaction with two-phase flow. As an example, the case is chosen in which $L_P = 0.9$ m, H_P=0.7 m. In Figure 3.129 a–c, flow patterns are presented for three superficial gas injection velocities $V_g = 0.12, 0.17,$ and 0.35 m/s. In the leftmost column, void fraction distributions and water velocities in the pool are shown. The second-to-fourth columns demonstrate the particle trajectory densities for different particles, denoted as SS for stainless steel and GL for glass. The particle trajectory density is defined as the total number of times that a particular mesh cell was crossed by a particle of each sort, normalized by the total number of particles of this sort, N_p. Thus, unity particle trajectory density means that the mesh cell was traversed once by each particle, or the total number of such particles was less than N_p, but some particle crossed the cell several times.

A common feature of the particle trajectory density distributions shown in Figure 3.129a–c is the presence of high trajectory density spots where the particles falling in the air (see the straight vertical stripe beginning on the top boundary of the domain) plunge in water. In these regions, particles are decelerated, losing their initial vertical momentum due to high drag, which increases their residence time. Particle trajectories there are quite tortuous due to turbulent fluctuations of water velocity, so that multiple crossing of mesh cells occur. Another stagnant zone is observed near the wall where the main flow, deviating horizontally towards the top of two-phase plume, forms a kind of lower-velocity “funnel” where particles reside for longer time. Turbulence intensity is lower near the wall, which also contributes to longer residence times in the near-wall region. Such particle behavior was indeed visible in the experiments, although, no detailed measurements which could be used to quantify the stagnation zones were done.

With time, the mean vortex flow entrains particles. They move from stagnation spot along trajectories bended around the main vortex and eventually reach to the bottom of

the pool. Notably, larger-diameter SS particles ($d_p = 3$ mm) can fall "through" the vortex, whereas smaller SS particles ($d_p = 1.5$ mm) and lighter glass particles ($d_p = 3$ mm) mostly travel around it. Note also the vertical stripe along the vertical wall, spanning from the stagnation region to the gas injector; this stripe, particularly visible for lower gas injection velocity in Figure 3.129a, corresponds to particles falling in the near-wall boundary layer, where the vertical liquid velocity and turbulence intensity are lower than in the main part of the plume.

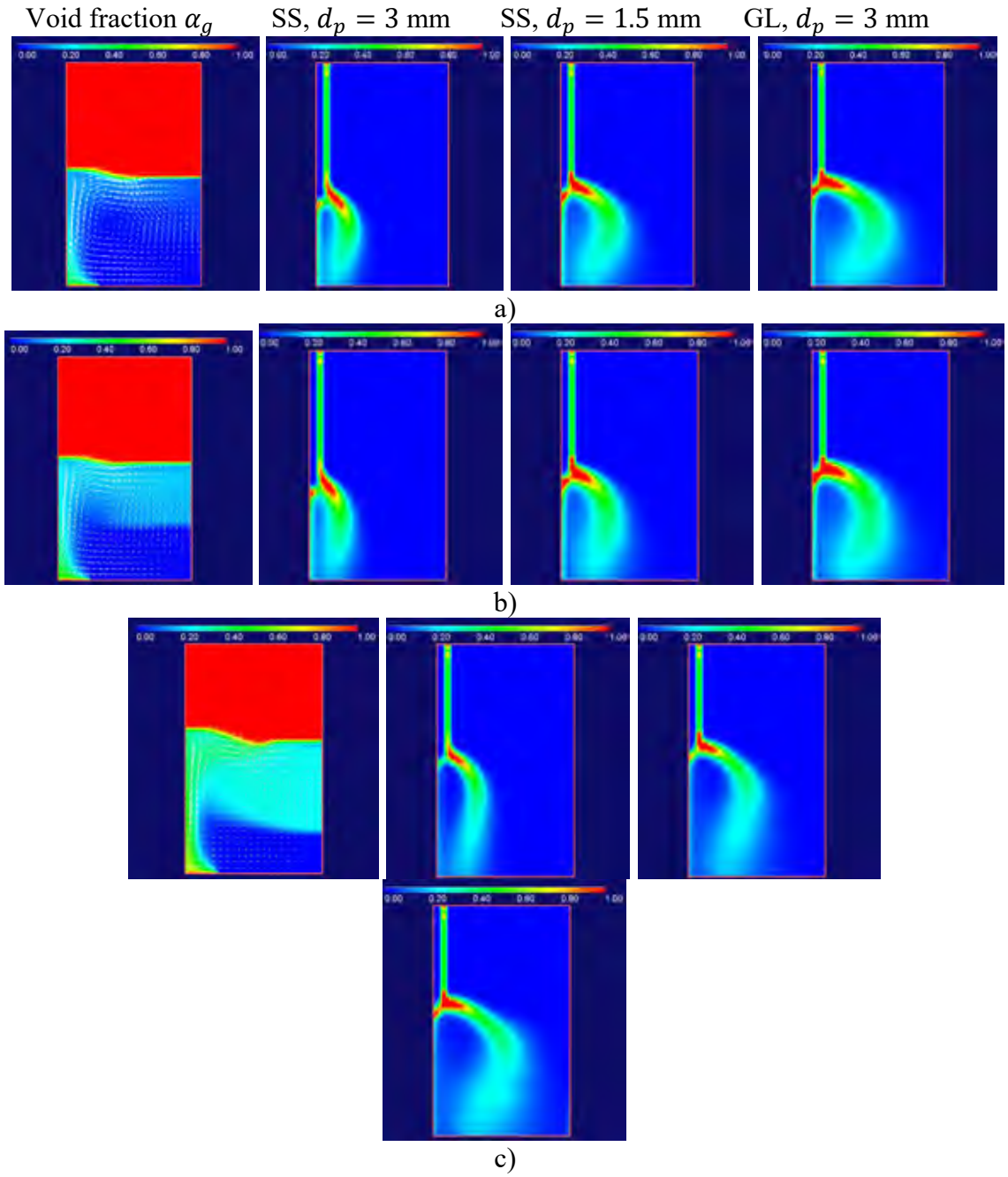

Figure 3.129 Particle sedimentation in pool with $L_P = 0.9$ m and $H_P = 0.7$ m: a) $V_g = 0.12$ m/s; b) $V_g = 0.17$ m/s; c) $V_g = 0.35$ m/s.

3.7.3.1.7 Comparison of Predicted and Experimental Particle Fallout Distributions

In the experiments [146][153] carried out on PDS-P facility, particles were collected by catchers spanning the pool bottom between the gas injection plate (of length 20 cm) and far side wall of the pool, with the length of each catcher equal to 10 cm. The injection plate had small inclination towards the first catcher in order to avoid particle accumulation on the injector plate. According to the experimental procedure adopted in [146][153], after the end of each experiments all particles remaining on the injector plate were also swiped into the first catcher. Therefore, when using the data reported in [146][153] for validation, it should be kept in mind that the particle masses reported for the first catcher (spanning the interval from 20 to 30 cm along the pool bottom) were, in fact, collected on a longer interval (from 0 to 30 cm), and no details of how the particle flux was distributed on this interval can be inferred.

In DECOSIM simulations, catchers were imitated by introducing a 1D mesh of 10 cm long cells on the bottom boundary of computational domain. As soon as some particle reached the bottom surface, a boundary cell was determined, and particle mass was added to the corresponding element of caught mass array. Note that in simulations the actual masses caught by the first catcher cells were obtained, without lumping particles into a single catcher. Also, perfect catching efficiency was assumed, i.e., trajectory of any particle reaching the pool bottom was immediately terminated and its mass considered as caught.

3.7.3.1.8 Mean spreading distance

The main output of each simulation was the distribution of mass fraction of particles χ_i and the mean spreading distance R_c defined as the horizontal coordinate of center of mass of particles:

$$\chi_i = \frac{m_i}{\sum_{i=1}^{N_c} m_i}, \quad R_c = \sum_{i=1}^{N_c} \chi_i R_i, \quad R_i = \left(i - \frac{1}{2}\right) L_c, \quad N_c = L_P / L_c \tag{118}$$

where $L_c = 0.1$ m is the catcher length, N_c is the number of catchers, R_i is the coordinate of i-th catcher center measured from the wall abutting the gas injector, m_i is the mass collected by i-th catcher center. DECOSIM validation was carried out by comparing the predicted values with those measured in PDS-P experiments.

In Figure 3.130a,b the parity plots are presented for both pool lengths $L_P = 0.9$ and 1.5 m, respectively, with abscissa of each point equal to the measured coordinate R_c and ordinate equal to the predicted coordinate in the same conditions. Parameters of simulations are shown in the graph legends; for most simulations there shown three points, obtained for the superficial gas injection velocities $V_g = 0.12$, 0.17, and 0.35 m/s, except the pool depth $H_P = 0.5$ m/s where results for $V_g = 0.69$ m/s are also presented (for 3 mm SS particles experiments were not performed for the lowest injection velocity). One can see that, generally, simulation results agree with PDS-P measurements, the point are scattered on both sides of the diagonal (corresponding to perfect matching). For the shallowest pool ($H_P = 0.5$ m), the spreading distances predicted by DECOSIM are systematically smaller than measured ones, especially for large SS particles. Predictions for $H_P = 0.7$ and 0.9 m agree with experiments better,

both for the narrow ($L_P = 0.9$ m) and wide ($L_P = 1.5$ m) pools. In the latter case, it can be seen that points corresponding to the two lower gas velocities (i.e., 0.12, 0.17 m/s, or the two leftmost points in each group of points) in many cases lie above the diagonal, whereas the point for the highest gas velocity (the rightmost point) underestimates spreading distance (points lie below the diagonal).

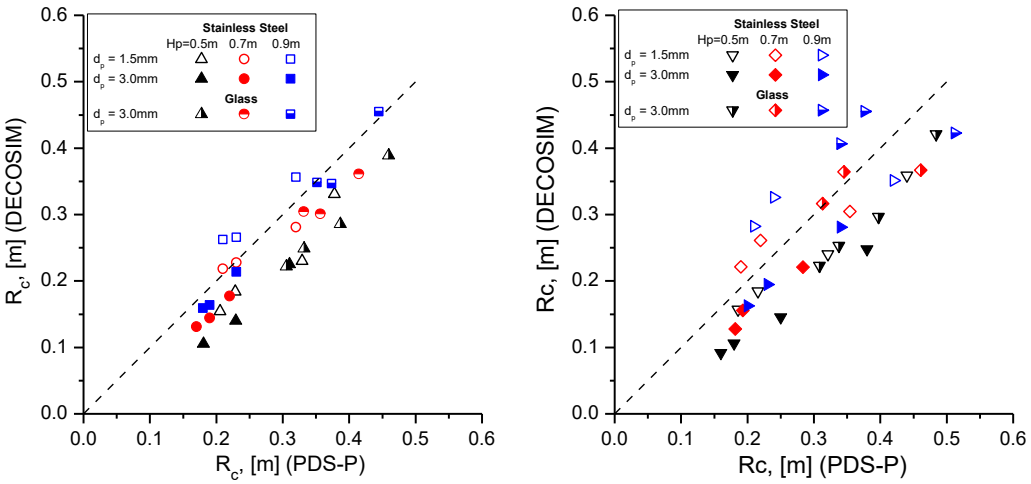

a) b)

Figure 3.130 Comparison of DECOSIM predictions for center-of-mass coordinate R_c with PDS-P experiments: a) pool length $L_p = 0.9$ m, b) $L_p = 1.5$ m.

3.7.3.1.9 Particle fallout distributions

More detailed comparison can be performed by considering distribution of particle mass fraction in catchers along the pool bottom obtained in simulations and experiments. In Figure 3.131, 3.132, 3.133, the distributions calculated for the narrower pool and different water depths are plotted together with corresponding experimental data denoted in the legend according to [153]. In Figure 3.134, 3.135, 3.136, similar graphs are plotted for the wider pool. Note that in some cases where experiments gave very high fraction in the first catcher (corresponding to the third catcher in simulations), experimental mass fraction is presented as distributed evenly over the first three points. The reasons for the experimental uncertainty related to the gas injection plate have been discussed in Section 4.3.1, this uncertainty will be reduced in the future experiments. In this work, therefore, we are mainly focusing our attention on the particle distributions away from the gas injector plate, i.e., at $X \geq 0.3$.

Generally, the graphs exhibit good agreement between the simulations and experiments. For steel particles, agreement is better for 0.7 and 0.9 m deep pools, whereas steel particle spreading in the shallow (0.5 m deep) pool is underpredicted, especially for 3 mm particles. An interesting feature observed in the experiments but not reproduced numerically is that the fallout distributions of 1.5 and 3 mm particles in the case $L_P = 1.5$ m and $H_P = 0.9$ m practically coincide (see the top row graphs in Figure 3.136); simulations predict more effective spreading of smaller particles, as in all other cases.

Another interesting feature is that fallout of lighter glass particles is predicted better at high gas injection velocity ($V_g = 0.35$ and 0.69 m/s), while for lower V_g experiments show particle fallout closer to the injector, while simulations predict substantial particle spreading (see bottom row graphs in Figure 3.135 and 3.136). The reasons behind there

discrepancies are not clear at the moment, they deserve special studies. Particularly, it is possible that the assumption of immediate catching of particle upon reaching the pool bottom need to be revised. Indeed, the catchers used in the PDS-P experiments could perturb the near-bottom flow, so that there was a chance that some particles could be carried by turbulent vortices back into the main flow. The discrepancies also can be caused by an interplay between modeling of the flow structures and particle drag in the two-phase turbulent flow. More precise flowfield registration is necessary in order to check these hypotheses. This would provide the necessary basis for model improvement, for example, by introduction of particle catching efficiency at the bottom surface.

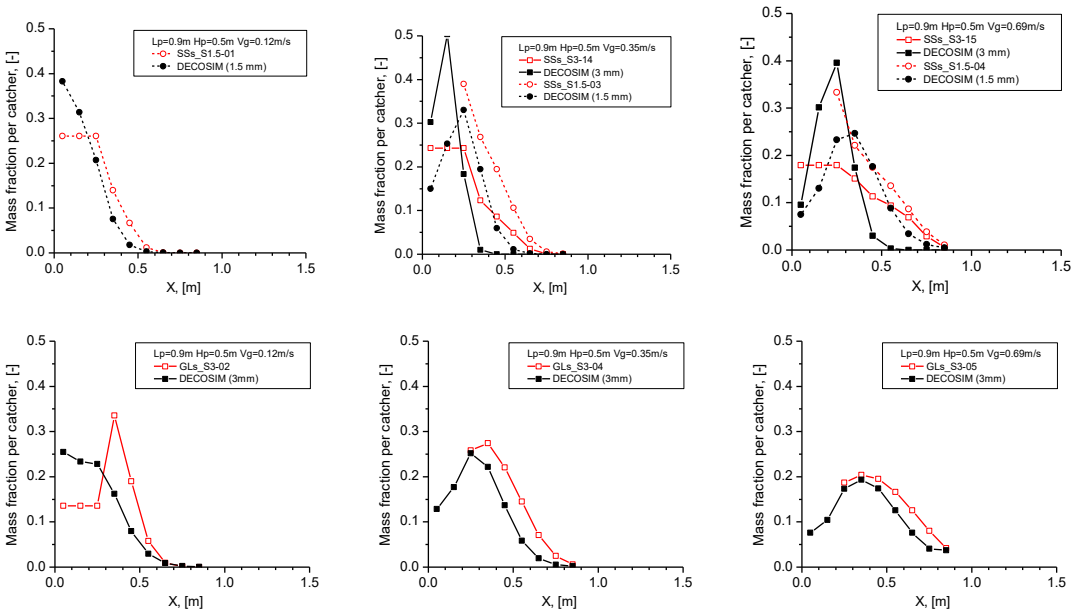

Figure 3.131 Fallout of SS (top row) and GL (bottom row) particles for $L_P = 0.9$ m, $H_P = 0.5$ m.

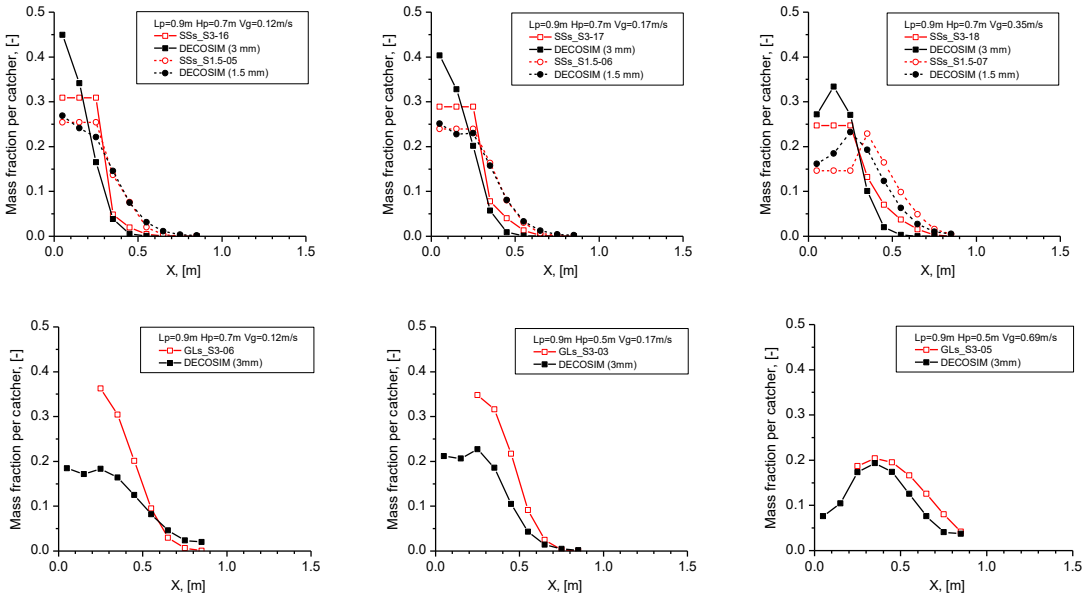

Figure 3.132 Fallout of SS (top row) and GL (bottom row) particles for $L_P = 0.9$ m, $H_P = 0.7$ m.

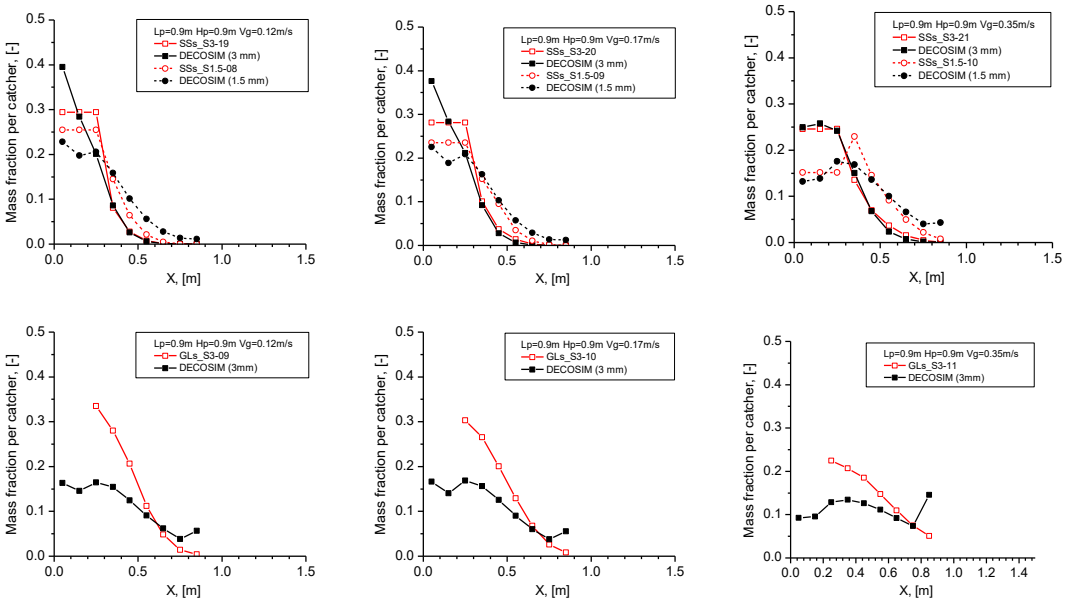

Figure 3.133 Fallout of SS (top row) and GL (bottom row) particles for $L_P = 0.9$ m, $H_P = 0.9$ m.

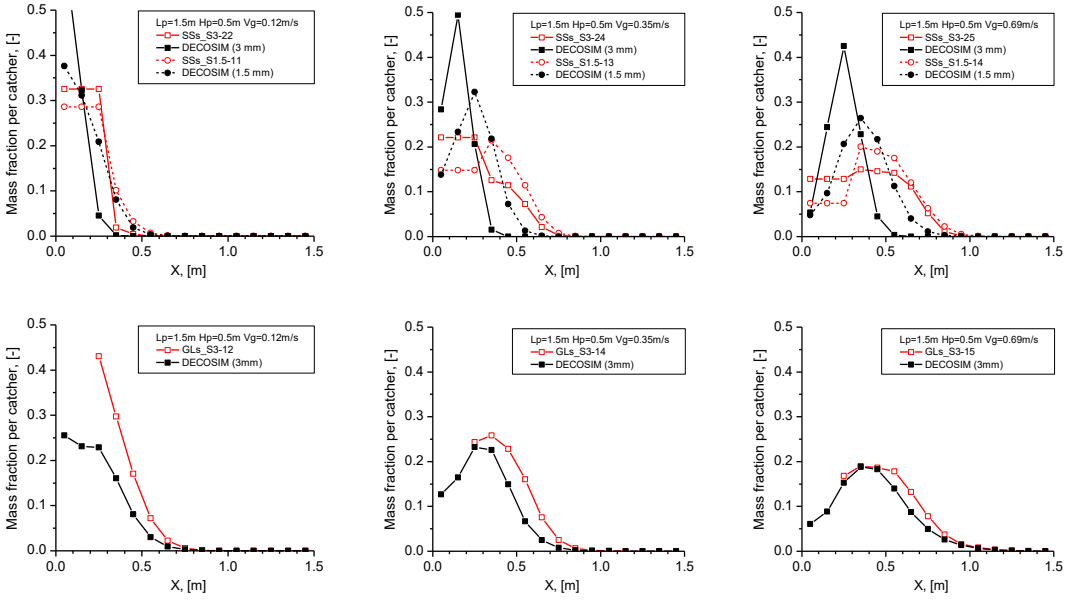

Figure 3.134 Fallout of SS (top row) and GL (bottom row) particles for $L_P = 1.5$ m, $H_P = 0.5$ m.

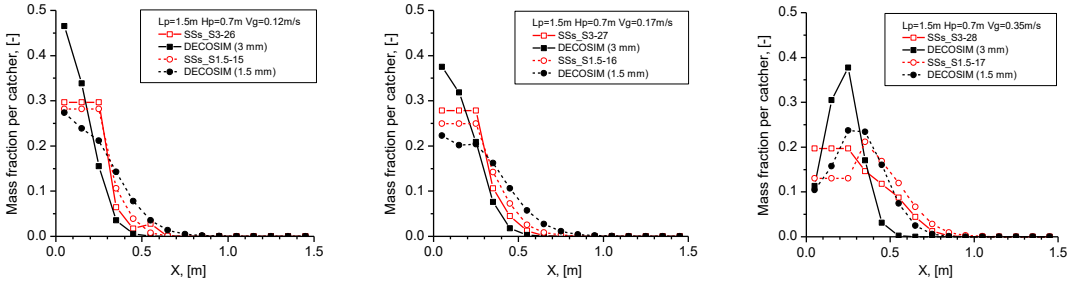

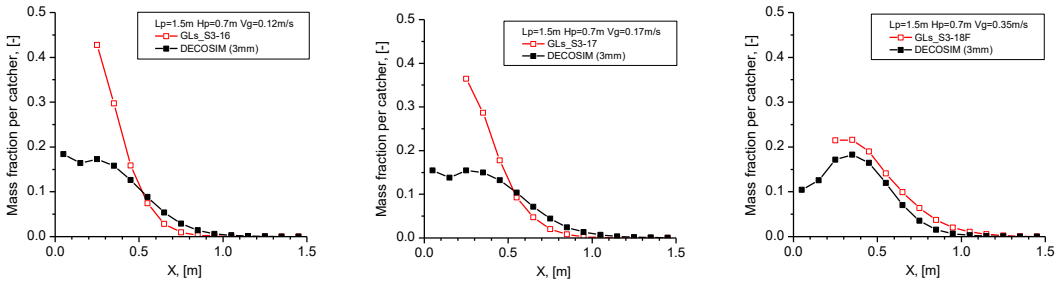

Figure 3.135 Fallout of SS (top row) and GL (bottom row) particles for $L_P = 1.5$ m, $H_P = 0.7$ m.

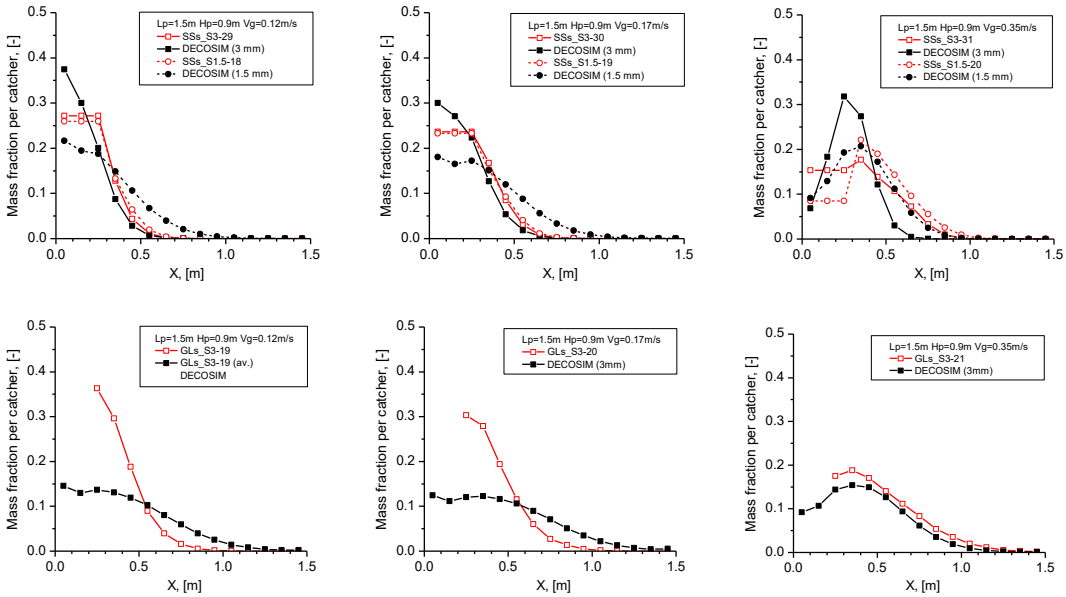

Figure 3.136 Fallout of SS (top row) and GL (bottom row) particles for $L_P = 1.5$ m, $H_P = 0.9$ m.

Also, DECOSIM simulations were carried out in order to study the coupled debris bed spreading by self-levelling and coolability. , a set of simulations was performed

- Initial debris bed height: 2 m;
- Slope angle equal to avalanche angle of 30 degrees;
- Particle size: 1, 1.5 and 2 mm;
- Relocation time: 1.5 and 3 hours (used to evaluate the decay heat power according to ANS5.1 standard curve);
- Transient duration: 2 hours.

The results of DECOSIM predictions for debris bed height are compared with those obtained from a simple model in which the superficial gas velocity is evaluated from the heat released in the debris layer of local debris bed height [51]. Also, post-dryout stage is considered at which the maximum temperatures reached in the debris bed are compared with those calculated without particle spreading taken into account (fixed-shaped debris bed).

In **Table 3.24**, all simulation cases are presented, with their outcomes indicated. Generally, three main outcomes were observed: i) a coolable debris bed without dryout occurrence; ii) dryout in the top part of debris bed persisting for some time, followed by reflooding and quenching of the dry zone, and iii) dryout with steady temperature escalation. All these cases are discussed in detail from the debris bed shape and

coolability points of view in the following two sections.

Table 3.24: Simulations of debris bed self-leveling and coolability

Particle diameter d_p, [m]	Relocation time t_r, [hours]	Bed height after 1 h (DECOSIM)	Bed height after 1 h (Model [12])	Coolability
1.0	1.5	1.55	1.63	Dryout
	3.0	1.55	1.66	Dryout
1.5	1.5	1.61	1.67	Dryout/Refloodin g
	3.0	1.67	1.70	Dryout/Refloodin g
2.0	1.5	1.65	1.68	No Dryout

An important finding of the analysis was that in the case of dryout the self-levelling mechanism remains effective, i.e., reduction in the debris bed height with time is not deteriorated. This also allows one to apply the simple model [51] for evaluation of debris bed self-levelling and coolability in order to obtain conservative estimates of the time after which the debris bed becomes coolable.

Figure 3.137 summarizes the predicted time histories of solid particle maximum temperatures in the simulations where dryout occurred (simulations with particle diameter of 2 mm resulted in no dryout, therefore, temperatures were near the saturation point and are not shown due to triviality). One can see that debris beds with 1 mm particles are non-coolable, regardless of whether particle spreading is taken into account or not; these are featured by steady temperature escalation.

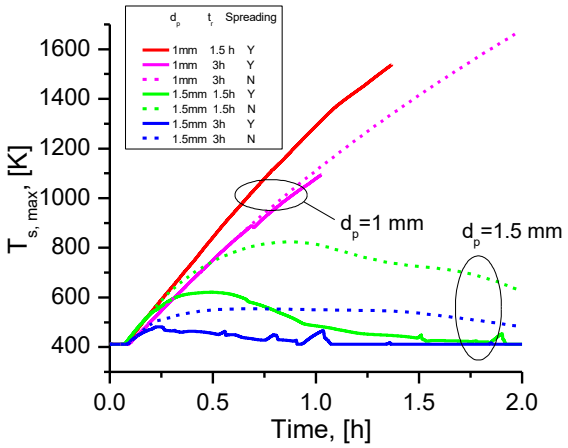

Figure 3.137. Maximum temperatures of solid particles in simulations with (Y) and without (N) particle spreading.

On the other hand, debris beds with particle diameter of 1.5 mm are featured by dryout, however, temperature is stabilized due to vapor cooling, and even in the case of fixed-shape debris bed it gradually decreases due to decrease in the decay heat power with time. If particle spreading is active, slumping of the debris bed results in its faster reflooding (compare the solid lines with corresponding dashed lines in Figure 3.137).

In Figure 3.138, the case of debris bed with 1 mm particles is demonstrated (the initial shape of debris bed is shown by white lines). The relocation time for this case was $t_r = 3$ h, the distributions are shown at time 1 h after relocation, i.e., 4 h after SCRAM.

One can see that significant part of debris bed (roughly, upper half of its height) is dry; slumping of the debris bed due to particle spreading reduces somewhat the size of high-temperature zone, but effect of the slumping is insufficient to prevent material reheating.

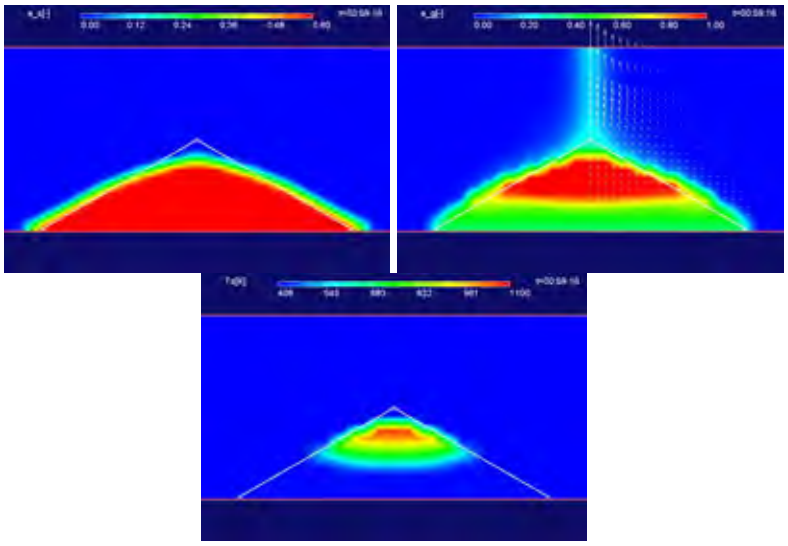

particle spreading

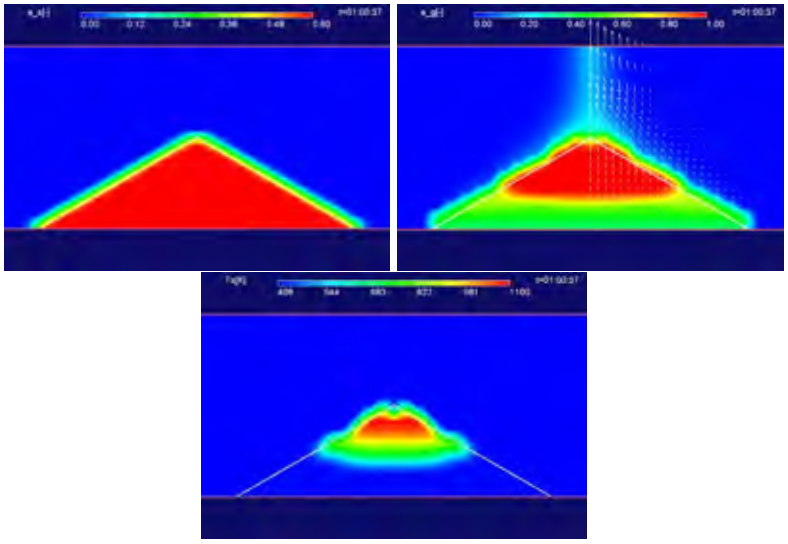

Without particle spreading

Figure 3.138. Volume fraction of particles (left), void fraction (middle) and particle temperature (right) in the debris bed with 1 mm particles at time 1h after relocation.

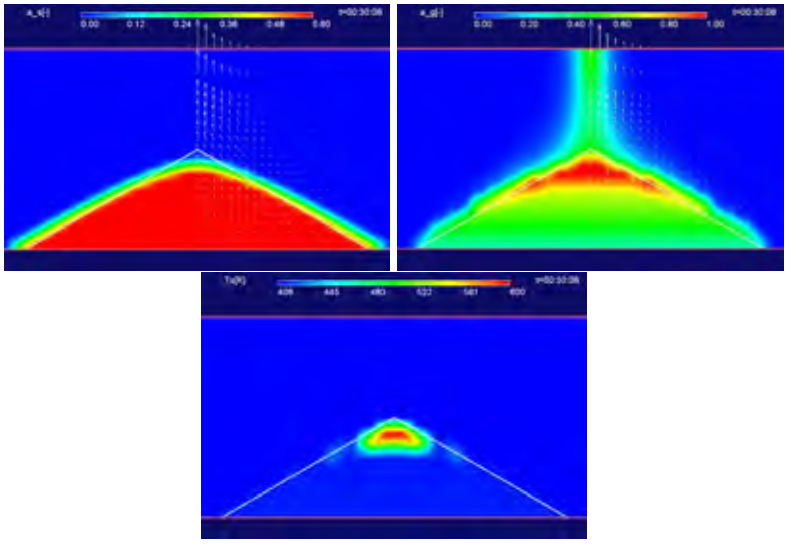

Time: 30 min

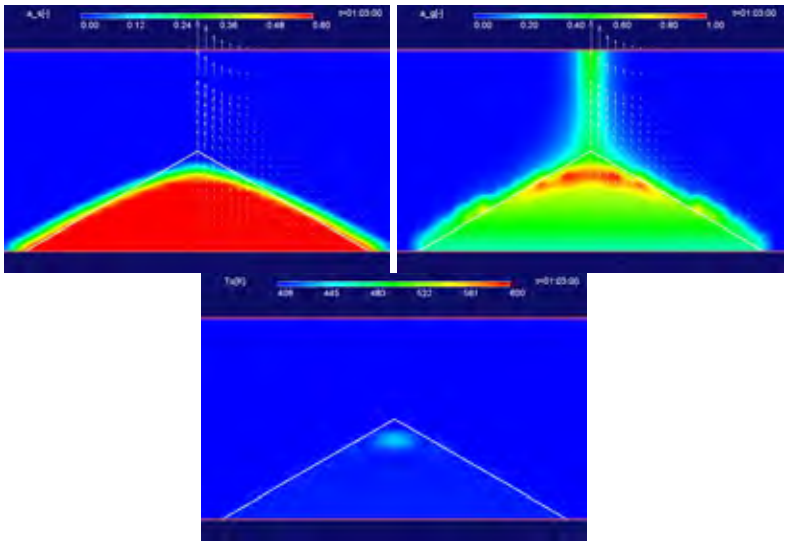

Time: 1 h

Figure 3.139. Volume fraction of particles (left), void fraction (middle) and particle temperature (right) in the debris bed with 1.5 mm particles at times 30 min (top row) and 1h (bottom row) after relocation.

In Figure 3.142, the case where debris bed reflooding occurs is presented (particle diameter 1.5 mm, relocation time $t_r = 1.5$ h, the distributions are shown at times 30 min and 1 h after relocation, i.e., 2 and 2.5 h after SCRAM). The dry zone is limited in size, the temperature in the dry zone is stabilized by vapor flow and then returns to saturation as material rewetting proceeds due to combined effect of debris bed slumping and gradual decrease in the decay heat power.

Physical mechanisms considered decrease the possibility that a tall non-coolable ex-vessel debris bed can be formed in the course of severe accident where deep enough water pool is available. Among the important findings of this work is the development of a correlation for particle spreading in a saturated water pool, and demonstration that self-leveling of debris bed is not deteriorated if dryout occurs in the bed. Taking into account these mechanisms will be important in safety and risk analysis because they

change the failure domain related to ex-vessel debris bed coolability.

These mechanisms, though, have their own efficiency limits which have to be taken into consideration. For example, particle spreading in the pool due to natural circulation flows only becomes efficient after boil-up of water (even partial), therefore, some delay is expected if water subcooling is high. Particle spreading due to partial fluidization of the top layer of the debris bed (self-leveling) possesses its own time scales and may be insufficient for temperature stabilization, even though debris bed slumping proceeds. Also, if the pool depth is smaller than the melt jet breakup length, a solidified "cake" can be formed in the top part of debris bed. In this latter case, evidently, the particle spreading mechanism is not effective. Debris agglomeration is not only a problem for spreading, but it also significantly deteriorate debris bed coolability due to increased resistance for the coolant flow through the porous media [35]. Therefore, further comprehensive research is necessary in order to put these phenomena in the time frame of severe accident scenarios.

Debris Bed Formation and Coolability Surrogate Models

Full model (DECOSIM) simulation results were used as the basis for development of computationally efficient surrogate models for debris bed formation and coolability [171].

Surrogate model for debris bed formation

In the case of gradual melt release into a deep saturated water pool the interaction of falling particles with the flow results in spreading of melt over the pool basemat, the smaller the particles and higher the decay heat power, the more effective is the spreading. In order to estimate the efficiency of particle spreading, a simple empirical model can be developed which generalizes the results of simulations [167]. Consider a droplet of diameter d_p falling in the water pool of depth H_P. The terminal velocity of falling droplet V_p is evaluated from the balance of gravity and drag forces:

$$V_p = \left(\frac{4 g d_p}{3 C_d} \frac{\rho_p - \rho_l}{\rho_l} \right)^{1/2} \tag{3.119}$$

where the drag coefficient C_d is a function of particle Reynolds number, but for heavy particles it can be assumed that Newton regime is reached in which $C_d \approx 0.45$. The particle-water interaction time in the pool is then proportional to $t_{int} \propto H_P / V_p$. Convection in the pool is governed by vapor release in the debris bed, and the characteristic superficial velocity of vapor on the top surface of debris bed can be evaluated as $V_g = \Gamma \cdot H_b = \rho_p (1-\varepsilon) W H_b / \rho_g \Delta H_{ev}$, where Γ is the volumetric evaporation rate, ε is debris bed porosity, W is the specific decay heat power per unit mass of corium, H_b is the maximum debris bed height, ΔH_{ev} is the latent heat of evaporation. Assuming that characteristic horizontal velocity (responsible for particle spreading) is proportional to V_g, we can write that the characteristic width of debris bed is proportional to $R_b \propto V_g t_{int} \propto \rho_p (1-\varepsilon) W H_b / \rho_g \Delta H_{ev} \cdot \left(H_P / V_p \right)$. Therefore, the tangent of slope angle, $\tan\phi \propto H_b / R_b$, is expected to depend on a non-dimensional parameter χ:

$$\tan\phi = f(\chi), \qquad \chi = \frac{\Delta H_{ev}\rho_g}{\rho_p(1-\varepsilon)WH_P}\left(\frac{4gd_p}{3C_d}\frac{\rho_p-\rho_l}{\rho_l}\right)^{1/2} \tag{3.120}$$

the vapor density must be evaluated at the pressure near the pool bottom, i.e., with the hydrostatic head taken into account: $\rho_g = \rho_g\left(P_{sys} + \rho_l g H_P\right)$, with P_{sys} being the system pressure in the gas space above the pool level.

The tangent of debris bed slope angle $\tan\phi$ must be an increasing function of χ : the higher the value of χ , the weaker the interaction of particles and convective flow. The above formula is qualitatively correct because it predicts more efficient spreading (smaller χ) due to the following factors:

- Lower system pressure: lower vapor density ρ_g means larger vapor volume and more intensive convection in the pool;
- Larger pool depth H_P (vapor density is increasing in the nominator, but the denominator overweighs it, and χ is a decreasing function of H_P);
- Smaller particle diameter d_p ;
- Higher specific decay heat power W ;

The function $\tan\phi = f(\chi)$ must be obtained from numerical simulations. A tentative form may be proposed as $\tan\phi = A\cdot\chi^B$ satisfying the condition $\tan\phi|_{\chi=0} = 0$ ("infinitely efficient" spreading results in a flat debris bed).
Results of six numerical simulations [167] were processed, each performed for saturated pool of 8 m depth, with the system pressure of 1 bar. The main variable parameters were the decay heat power ($W = 25$ and 62.5 W/kg) and particle size ($d_p = 3$, 5, and 10 mm). For each simulation, the final shape of debris bed was processed, and the characteristic tangent of slope angle determined. The data obtained are presented in Fig. 1 by the points. The solid line shows the best fit to the data, with $A = 0.1076$ and $B = 1.86$. By the horizontal dashed line, the tangent of typical avalanche angle $\theta^0_{rep} = 35^o$ is plotted, indicating that the fit obtained describes the whole interval of interest.

Having in hand the approximation (Figure 3.140), it is easy to show that for prototypic conditions relevant to severe accidents at Nordic-type BWRs particle spreading in the saturated pool is an effective mechanism for reducing the height of debris bed. Since it takes few hours after SCRAM for reactor pressure vessel to fail and gradual melt release to begin, the decay heat power can be expected to be in the range 100–150 W/kg. The largest mean particle diameter, as is suggested by available melt-coolant interaction experiments, can be expected in the range of 1–5 mm. From the particle spreading point of view, the largest slope angle expected can be about 8 degrees maximum, reached for the largest particle diameter and lowest decay heat power. Smaller particles are distributed almost evenly over the pool basemat. Thus, we can conclude that if the pool is at saturated conditions, particle spreading by natural convection flows is an effective physical mechanism preventing formation of tall debris beds which can prove non-coolable in the case of gradual melt release.

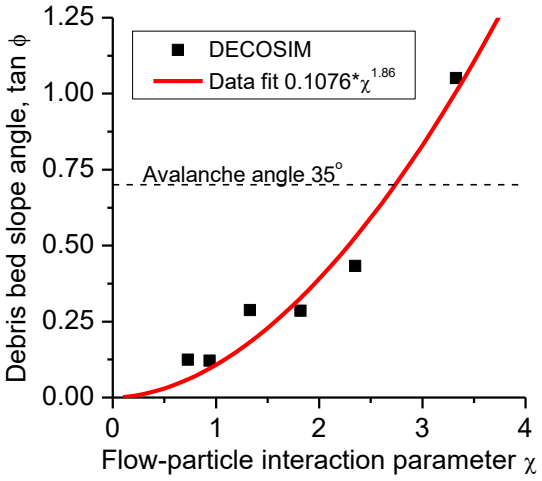

Figure 3.140. Debris bed slope angle for gradual formation of debris bed in saturated water pool.

If the pool is subcooled, vapor released by the debris bed condenses above it, so that the pool remains single-phase beyond the debris bed for a substantial period (the case of gradual melt release is considered here). Simulations of debris bed formation in a subcooled pool performed in [141] showed that temperature differences arising in the pool cause some natural circulation, but it is much weaker than that in a saturated pool and, therefore, the shape of debris bed at the initial stage is governed by particle avalanching only. However, gradual increase in the pool temperature due to latent and fusion heat transferred from hot melt particles, as well as decay heat released in corium results in boil-up of the pool after some delay time. The boil-up starts at the top layer of the pool where hot water plume from the debris bed reaches saturation conditions, while the rest of the pool remains subcooled. After the onset of boil-up, intensive convection starts in the pool, so that the remaining part of melt interacts with the circulatory flow in the pool and is dispersed efficiently over the pool basemat. Thus the debris bed grows upwards mainly at the pre-boiling stage, while afterwards it mostly grows laterally, with the particle sedimentation flux distributed evenly over the pool bottom. This simple scheme can be used to set up the intermediate or final shape of the debris bed.

The time to boil-up of a pool having initial subcooling $\Delta T_w^0 = T_{sat}^0 - T_w^0$ (T_{sat}^0 is the saturation temperature at the pool pressure, T_w^0 is the initial water temperature) can be evaluated from a simple energy balance model offered in [141]. Consider the total mass of melt M_w supplied to the water pool over the period t_0 (gradual melt release mode). The specific heat (per unit mass of melt) transferred to water is $q = c_{m.l}\left(T_m^0 - T_m^M\right) + \Delta H_f + c_{m,s}\left(T_m^M - T_{sat}^0\right)$, where $c_{m,l}$ and $c_{m,s}$ are specific heat capacities of liquid and solid corium, ΔH_f is the fusion heat, T_m^0 is the initial melt temperature, T_m^M is the melting temperature of corium,. Introduce the non-dimensional time of pool boil-up, $\tau = t_{boil}/t_0$ where t_{boil} is the time after which the pool temperature is increased by ΔT_w^0 and the pool becomes saturated. It is shown in [141] that

$$\tau = \frac{\sqrt{2B\xi + 1} - 1}{\xi}, \qquad B = \frac{M_w c_w \Delta T_w^0}{M_m q}, \qquad \xi = \frac{W t_0}{q} \tag{3.121}$$

where B is the ratio of energy necessary to bring the pool to saturation and the total latent and fusion energy of melt, ξ is the ratio of decay and latent heats.

If we assume that at the pre-boiling stage the growing debris bed has conical shape with the slope angle equal to the repose angle, then the debris bed height at the time of boil-up is given by

$$H_{DB}(\tau) = \left(\frac{3 V_B^{\max} \tan^2 \theta_{rep}^0}{\pi} \right)^{1/3} \left(\frac{t}{t_0} \right)^{1/3}, \quad t \le t_{boil} \tag{3.122}$$

where $V_{DB}^{\max} = M_m / \rho_p (1 - \varepsilon)$ is the total volume of porous debris bed. After the boil-up, it can be assumed that the remaining volume of debris, $V_{DB}^{\max}(1 - \tau)$, is distributed evenly over the pool bottom, adding to the debris bed a layer of height $4 V_{DB}^{\max}(1 - \tau) / \pi D_P^2$. This simple geometry approximation is confirmed by numerical simulations at different subcoolings in [141].

Surrogate model for post-dryout debris bed properties

The numerical results obtained by DECOSIM indicate that in the cases where dryout occurs in the debris bed

- Dryout zone is located in the top part of the debris bed;
- Vapor flows through the dry zone vertically upwards;
- Temperatures of solid particles and vapor increase in the vertical direction almost linearly, the difference between them being few degrees;
- Maximum temperatures of solid particles and vapor are attained in the top part of the dry zone;
- Vapor cooling is capable of stabilizing the solid material temperature, provided that its flowrate through the dry zone is sufficient.

These observations allowed an analytical model for the maximum temperature in the dry zone to be developed, laying the basis for post-dryout debris bed surrogate model [31]. The model was confirmed by further numerical simulations carried out by DECOSIM. In Figure 3.141, the maximum temperature of solid particles in the dry zone, $T_{s,max}$, is presented as a function of relative size of the dry zone with respect to debris bed height, ξ. The solid line corresponds to the analytical formula [31]

$T_{s,max} = T_{sat} + \frac{\Lambda}{C_P} \frac{\xi}{1 - \xi}$ Λ is the heat of evaporation, C_P is the heat capacity of vapor.

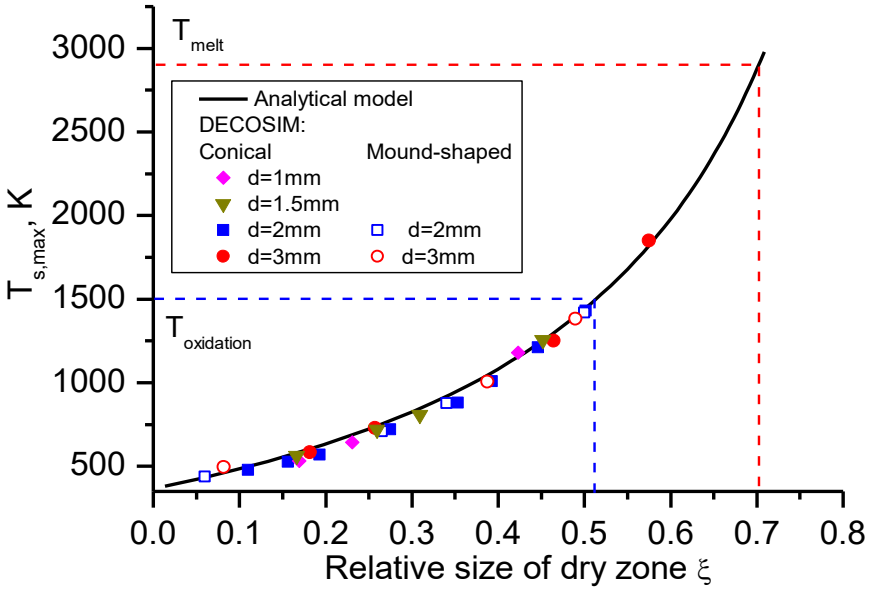

Figure 3.141. Dependence of the maximum particle temperature on the relative size of dry zone.

order to apply the above formula in a surrogate model, it is necessary to relate the relative size of dry zone ξ to other problem parameters. of DECOSIM simulations on post-dryout debris beds were processed in order to obtain a unified relationship for the dry zone size. It was shown that linear dependence exists between the dry zone size and the overheating parameter $\psi = (W - W_0)/W_0$, where W_0 as the dryout decay heat power. This is illustrated in Figure 3.142 where results of DECOSIM simulations are given in the "raw" form (a), as well as in the non-dimensional form (b).

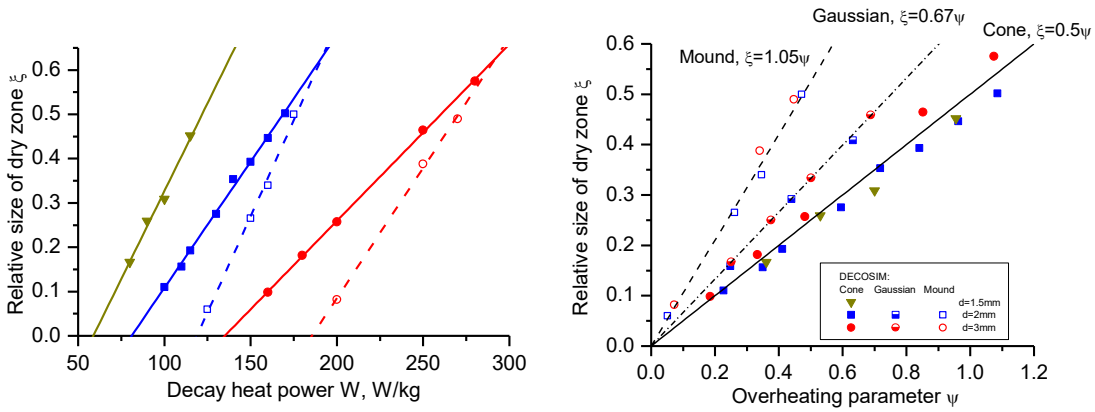

(*a*) (*b*)

Figure 3.142. Dependence of the relative size of dry zone on decay heat power W (*a*) and overheating parameter ψ (*b*). The legend applies to both Figures.

The tentative form of the surrogate model for the relative size of the dry zone in a post-dryout debris bed is

$$\xi(\Pi_{prop}, \Pi_{sys}, \Pi_{shape}) = b(\Pi_{shape}) \cdot \psi(\Pi_{prop}, \Pi_{sys}, \Pi_{shape}) = b(\Pi_{shape}) \cdot \left(\frac{HF}{DHF(\Pi_{prop}, \Pi_{sys}, \Pi_{shape})} - 1 \right) \quad (3.123)$$

Π_{prop}, Π_{sys}, and Π_{shape} denote the sets of parameters characterizing the debris bed properties (particle size and porosity), system conditions (system pressure, pool depth), and debris bed shape (geometry, aspect ratio, etc.) respectively. Notably, the model contains one shape-dependent parameter $b(\Pi_{shape})$ for which further research is needed, while the heat flux HF and dryout heat flux DHF in the parentheses can be taken from previous coolability studies and surrogate models developed therein. Current results suggest that $b(\Pi_{shape})$ lies in the range between 0.5 and 1.05, see Figure 3.142 (b).

ANN-based surrogate model

Quantification of uncertainties involves a vast number of models evaluations. Due to large number of calculations, the models used for the analysis must be computationally efficient, otherwise the total computational time and cost would become unfeasible. For this reason a surrogate model has been developed in the form of an artificial neural network (ANN) to proxy the coupled code in the risk analysis.

The structure of the neural network consists of parallel computing elements, called neurons. Each neuron performs some operations and transmits the results to the neighboring elements through links having their own weight. During the training procedure the weights are optimized to achieve the best possible match between the obtained output from the ANN and the target output without incurring in over-fitting. Several types of ANNs are available to forecast models output, a complete review can be found in the broad literature on the topic [172], [173].

In our approach a multilayer perceptron network has been designed by means of the Matlab-Neural Network Toolbox™ [174]. The network has been trained using the second order method of Levenberg-Marquardt (p. 180 [173]). The general practice during the design of a multilayer neural network is to split the dataset in three different subsets: (i) the training set, used to update network weights and biases; (ii) the validation set, used to avoid over-fitting by means of early stopping strategy (p.197 [173]) and (iii) the testing set, used exclusively at the end of the training phase to compare different networks implementations and assess the generalization capability of the ANN. The typical fractions for these three subsets are 0.5, 0.25 and 0.25 (p.67 [172]) since, typically, a whole dataset consist of few thousands cases. In our study, given the relative great size of the dataset ($\sim 10^7$), the ratios for training, validation and testing capable to give satisfactory results have been found to be 0.039, 0.017 and 0.944 respectively. The only condition for the applicability of these ratios was to guarantee that one half of the cases in the training and validation subsets had an output t_c greater than zero. This condition guarantees to have a sufficient number of calculations required to train the network. This is because among the whole dataset there are barely 3% of the samples having $t_c > 0$.

The optimized ANN structure consists of two hidden layers formed by 9 sigmoid neurons and 5 sigmoid neurons respectively, followed by a single linear output layer. The results for the all three subsets together with the whole set fitting are shown in Figure 3.143. As seen, the applied ANN-based SM gives very satisfactory results in terms of the coefficients of determination $R^2 \rightarrow 1$ values. The main advantage of using ANN-based surrogate modeling is indeed a tremendous win in computation time without introduction of significant uncertainties into the output. In our particular case

the performance win factor is about 10^7.

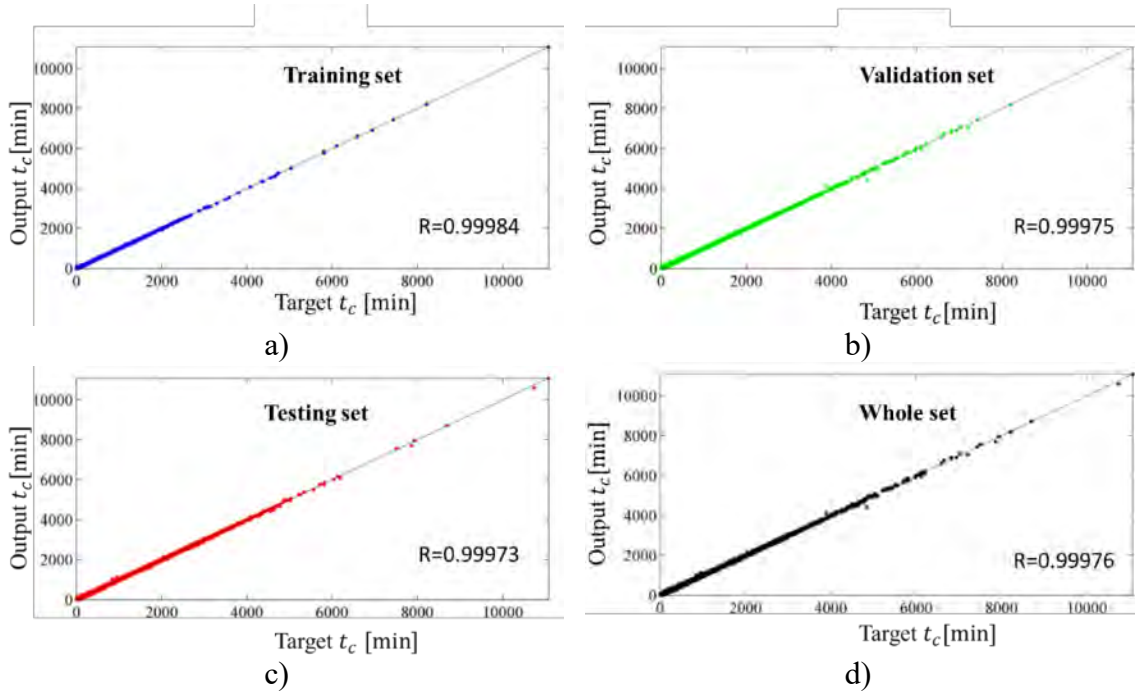

Figure 3.143 ANN-based SM parity plot for: (a) training set, (b) validation set, (c) testing set, (d) whole set.

This is because the ANN-based SM provides us with computationally fast and accurate enough modeling result though the intermediate iteration steps such as time resolved evolution of the system of course are not available.

3.7.3.1.10 Failure Criteria

In order to estimate the probability of failure of the system, a necessary step is to define the failure criteria. In the plant design considered in this work, the flooding of the lower drywell is used as a SA mitigation strategy. In the considered design the failure of the containment integrity after the vessel failure can occur due to three main issues: (i) non-coolable debris bed, (ii) steam explosion or (iii) re-criticality. The present paper examines exclusively the coolability issue, with further assumption of non-agglomerated debris i.e. without formation of the corium cakes.

The failure of the containment is assumed to occur once the debris bed (or a part of it) reaches 2800 K the onset temperature of re-melting. Thus, a particular model input causes the failure of the containment if the t_c is greater than the re-melting time t_{rm}.

3.7.3.1.11 Debris Bed Re-melting Time

The quantification of t_{rm} is made on the assumption that if the model input does not give an immediate coolable debris bed (i.e. $t_c = 0$), the temperature of the established dry-zone will start to raise with a certain heat-up rate $\dot{T}_{rate}$.
Since the heat transfer is not resolved in the model, the parameter $\dot{T}_{rate}$ has to be assumed. Three hypothetical cases are considered:

- $\dot{T}_{rate} = 0.2$ K/s, the average rate obtained in [175] study, where the jet breakup and particle settling JEMI model [176]has been coupled to the debris cooling MEWA model [177];

- $\dot{T}_{rate} = 1.0$ K/s, approximately the rate obtainable if the whole decay in the dry zone heats-up the debris (no steam cooling);
- $\dot{T}_{rate} = 10$ K/s, a pessimistic assumption implying, for example, a possible fast zirconium oxidation. This value is particularly high and more typical during core degradation phenomena [178].

The initial temperature T_{ini} of the settled particles is considered to be varied along possible values: 400 K , 600 K, 900 K, 1200 and 1700 K (maximum settling temperature predicted by JEMI). Assessed t_{rm} for all combinations of the considered cases is provided in Table 3.25. As seen, the resulting values of t_{rm} are ranging slightly wider than two orders of magnitude.

Table 3.25 Time (in seconds) for onset of re-melting for different conditions of initial bed temperature and heat-up rate.

	$\dot{T}_{rate}$=0.2 K/s	$\dot{T}_{rate}$=1 K/s	$\dot{T}_{rate}$=10 K/s
T_{ini}= 400 K	12000	2400	240
T_{ini}= 600 K	11000	2200	220
T_{ini}= 900 K	9500	1900	190
T_{ini}= 1200 K	8000	1600	160
T_{ini}= 1700 K	5000	1000	100

3.7.3.1.12 Uncertainty quantification

There are two types of uncertainties which are usually treated in the analysis of models: aleatory and epistemic uncertainties. The aleatory type of uncertainty [179], [180], [181] describes the uncertainty that results from inherent randomness in the system behavior. It is also known as stochastic uncertainty, type A uncertainty or the irreducible uncertainty. The epistemic uncertainty [179], [180], [181] is referred as the uncertainty due to the lack-of or incomplete knowledge about physical system properties or modeling characteristics. Uncertainty of this type indicates a variable has a real single value, but lacking information about its location with preciseness. It is also known as subjective uncertainty, type B uncertainty or the reducible uncertainty.
From the risk analysis prospective it is important that the method, used to treat both types of uncertainties, is able to propagate their effects parted in the final results. This allows the analyst to determine the feasibility of an uncertainty reduction in the output. In other words, if the output uncertainty is mainly due to epistemic uncertainties, a desired reduction in the output uncertainty can be possible by collecting more information about the inputs. On the other hand, if the output uncertainty is mainly due to aleatory uncertainties a desired reduction can be achieved only by modifying the system. This implies that risk analysis where epistemic and aleatory are parted can provide vital information in terms of safety improvement and risk-informed decisions in general.

The risk analysis approach followed in this work is schematically shown in Figure 3.144. A detailed description is provided in the next sections.

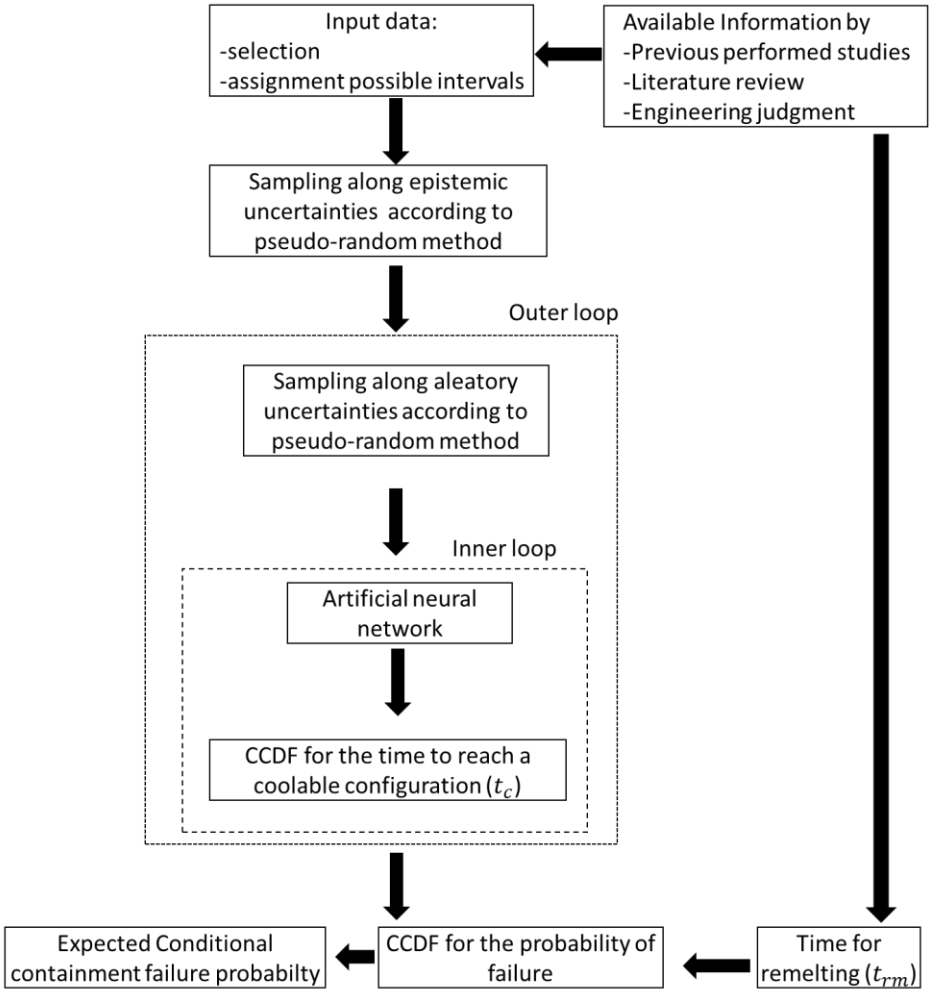

Figure 3.144 Schematic diagram of the methodology followed in this work.

3.7.3.1.13 Probability Theory

Several mathematical approaches are available to represent uncertainties: (i) probability theory [182], (ii) evidence theory [183], [190] [184], (iii) possibility theory [185], [186] and (iv) interval analysis [187], [188].

In the present study the probability framework is employed since it is traditionally used to treat uncertainties in risk analysis [189], [191], [192]. Its first application in the safety analysis of NPPs dates back to 1975 [193]. Application of this approach implies that both, the aleatory and epistemic uncertainties are kept parted and the final results are represented as probabilities of frequencies [194], [30].

The probabilistic framework requires the definition of the probability space $(X_p, \mathbb{X}_P, m_{px})$ where $X_p$is the set of all possible values, $\mathbb{X}_P$is the convenient set of subsets of $X_p$and m_{px} is the probability factor that defines the probability for the individual elements of $\mathbb{X}_P$ [60], [197].

The developed ANN-based SM describes a phenomenon where all input variables can vary stochastically because they are determined by the accident conditions which occur with certain relative frequencies. This means that the probability space $(X_p, \mathbb{X}_P, m_{px})$ can be represented by the joint probability density function (PDF) D_{joint} of the PDFs

characterizing aleatory uncertainties.

The selection of the PDFs is not straightforward without using bounding assumptions. In the probabilistic approach the epistemic uncertainty is used to describe the true value of a relative frequency, i.e. the unknown values of the distribution parameters describing aleatory uncertainties.

Table 3.26 Input parameters with corresponding uncertainty ranges. Each PDF of an aleatory uncertainty is assumed to be a beta distribution with unknown shape parameters represented by epistemic uncertainties.

Input parameters subjected to aleatory uncertainty	**Aleatory uncertainty range**	**Epistemic uncertainty ranges for the shape parameters used in the beta distribution**	
		$\boldsymbol{\alpha}$	$\boldsymbol{\beta}$
Total debris mass [tons]	10-250	0.01-100	0.01-100
Containment pressure [Bar]	1-4	0.01-100	0.01-100
Initial angle factor [-]	0.1-1.0	0.01-100	0.01-100
Particle density [kg/m^3]	7500-9000	0.01-100	0.01-100
Debris bed porosity [-]	0.3-0.6	0.01-100	0.01-100
Effective particle diameter [mm]	1.0-6.0	0.01-100	0.01-100
Critical angle of repose at zero gas flow [degree]	22-35	0.01-100	0.01-100

In this study the normalized beta distribution is used to represent the PDF of the each aleatory uncertainty given the wide variety of possible shapes it can take by varying its two shape parameters α and β.

α and β are the epistemic uncertainties ($E_{j,\alpha}, E_{j,\beta}$) sampled from an uniform distribution ranging between 0.01 and 100 for each j^{th} aleatory uncertainty:

$$e_i \begin{cases} E_{1,\alpha}, E_{j,\alpha}, \cdots, E_{7,\alpha} \\ E_{1,\beta},, E_{j,\beta}, \cdots, E_{7,\beta} \end{cases} \qquad (3.124)$$

The e_i in (3.124) indicates the i^{th} vector of epistemic uncertainties values.

3.7.3.1.14 Propagation of uncertainties

The uncertainties propagation is carried out by a second order probabilistic analysis, also called “two dimensional Monte Carlo analysis” [198], [199], [60], [197]. Monte Carlo sampling method consists in drawing random samples of the uncertain input parameters values from their PDFs and evaluating the model output for each set of sampled values. In order to propagate epistemic uncertainties, a pseudo-random sample of e_i of size $n_{SE} = 10000$ is generated assigning a uniform distribution to each element $E_{j,\alpha}$and $E_{j,\beta}$ within the intervals specified in Table 3.26.

The aleatory uncertainties can be propagated by generating a pseudo-random sample of size $n_{SA} = 2 \cdot 10^7$ conditional on the elements of the first sampled e_i. At last, the model output is evaluated for each set of the sampled values.

The failure probability conditional on each e_i is obtained by binning the input space as following approximation:

$$\begin{aligned} &Prob(\widetilde{t_c} > t_{rm}|e_i) \\ &\quad = \int_{V\in \mathrm{ID}} \delta_{t_c}\big(f(a_k|e_i)\big)\, D_{joint} dV_{\mathrm{ID}} \\ &\quad \cong \frac{1}{nA}\sum_{k=1}^{nA} \delta_{t_c}\big(f(a_k|e_i)\big) \end{aligned} \qquad (3.125)$$

and

$$\delta_{t_c}\big(f(a_k|e_i)\big) = \begin{cases} 1, & \text{if } f(a_k|e_i) > t_{rm} \\ 0, & \text{otherwise} \end{cases} \qquad (3.126)$$

$$a_k = [D(A_1)_k, D(A_j)_k, \dots, D(A_7)_k] \qquad (3.127)$$

Where $D(A_j)$ is the PDF associated with j^{th} input parameter; $a_k$is the k^{th} vector of the aleatory uncertainty; $f(a_k|e_i)$ is the model function affected by epistemic and aleatory uncertainties; $\delta_{t_c}$is an indicator function which is equal to either 1 if the vector of the input parameters belong to the failure domain, i.e. $t_c > t_{rm}$ or to the value of 0 otherwise; ID indicated the input parameters domain.

In summary, our iteration algorithm is implemented with the help of two nested loops: the outer-loop where the distribution parameters are pseudo-randomly generated and an inner-loop where these parameters are fixed and pseudo-random sampling is used to create distributions.
All the PDFs parameters are assumed to be independent both internally (within distribution) and externally (across distributions). Therefore, the D_{joint} is directly computable as product of PDFs:

$$D_{joint} = \prod_{j=1}^{7} D(A_j) \qquad (3.128)$$

3.7.3.1.15 Results

The resulting sets of failure probabilities, $Prob(\widetilde{t_c} > t_{rm}|e_i)$, are reported as complementary cumulative density functions (CCDFs) in Figure 3.145, Figure 3.146 and Figure 3.147 for all the considered values of t_{rm} listed in **Table 3.25**. The representation through CCDFs allows to keep parted aleatory from the epistemic uncertainties: the former determining horizontal (x-axis) values, while the latter is affecting the vertical (y-axis) values and indicating the degree of belief of the failure probabilities $(t_c > t_{rm})$. As seen from these plots, the influence of the initial temperature diminishes as $\dot{T}_{rate}$ increase, i.e. all the curves are gradually collapsing into a single curve.

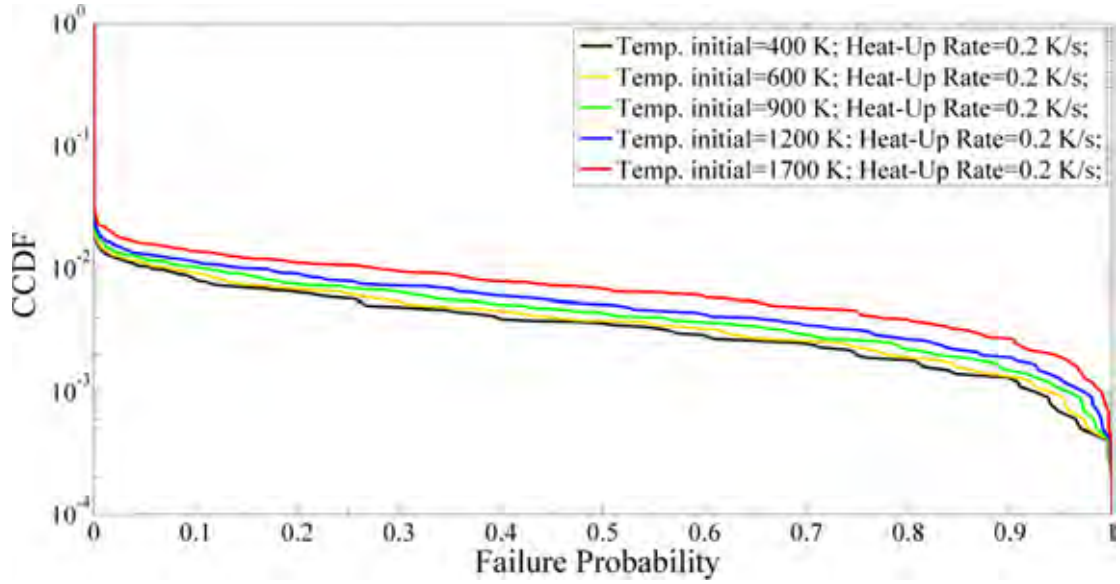

Figure 3.145 Failure Probability CCDFs for heat-up rate value of 0.2 K/s

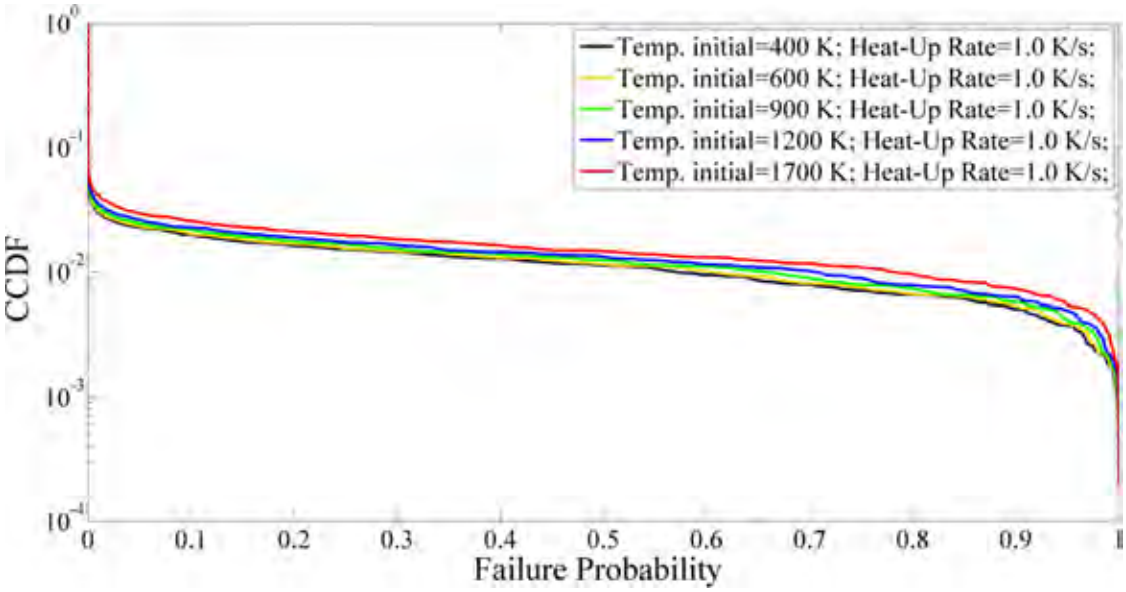

Figure 3.146 Failure Probability CCDFs for heat-up rate value of 1.0 K/s

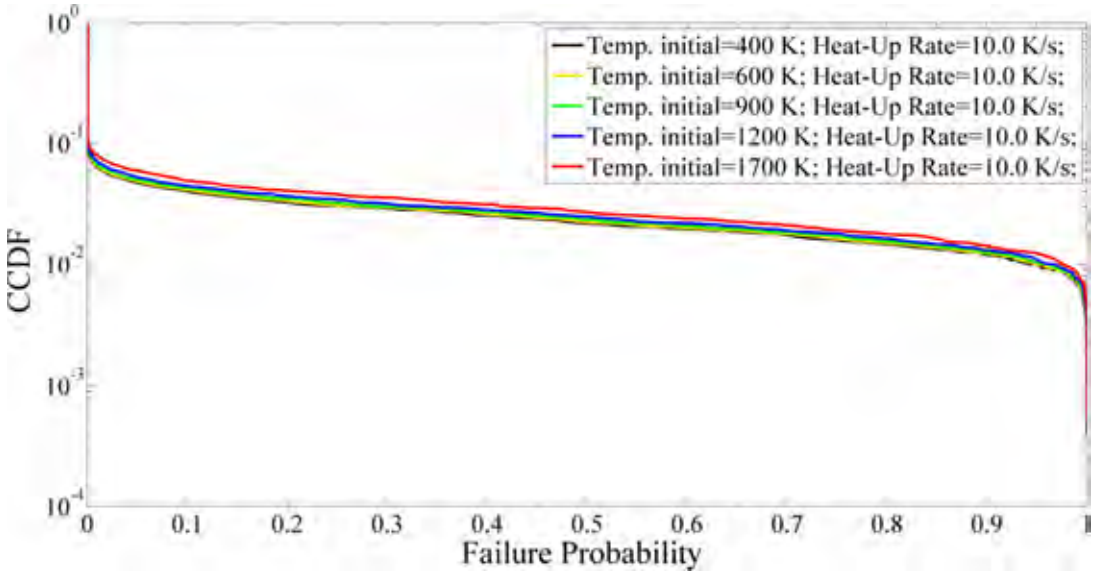

Figure 3.147 Failure Probability CCDFs for heat-up rate value of 10 K/s

The obtained results have to be examined and compared with numerical safety criteria, safety goals or benchmark values in order to evaluate the effectiveness of the designed SA mitigation strategy.

For new or advanced NPPs the US NRC has developed a safety goal for the conditional containment failure probability (CCFP) stating that the expected value for CCFP given the occurrence of a severe accident has to be less than 0.1 [196].

The contribution to the total expected CCFP of debris bed re-melting threat for the Nordic BWR is provided in Table 3.27 for all the considered cases. It corresponds to the expected value calculated from CCDFs in **Figure 3.145**, **Figure 3.146** and **Figure 3.147**.

Table 3.27: Expected value of CCFP due to debris bed remelting threat for Nordic BWR.

	$\dot{T}_{rate}$=0.2 K/s	$\dot{T}_{rate}$=1 K/s	$\dot{T}_{rate}$=10 K/s
T_{ini}= 400 K	0.0041	0.0118	0.0245
T_{ini}= 600 K	0.0045	0.0122	0.0250
T_{ini}= 900 K	0.0051	0.0130	0.0260
T_{ini}= 1200 K	0.0059	0.0138	0.0272
T_{ini}= 1700 K	0.0077	0.0157	0.0301

Finally as noted by Helton and Breeding [200] it is important to admit that safety goals based on expected values lead to a loss of information since an entire distribution is reduced to a single number. Therefore, they should be used cautiously since they may undermine the objectives of a risk-informed decision process. Similar concerns are also expressed in the report on the Quantification of Margins and Uncertainties by the National Academy of Science and the National Research Council [195].

3.7.3.1.16 Conclusions

A probabilistic risk analysis has been performed to examine and quantify uncertainties involved in the debris bed coolability issue, a matter especially relevant for Nordic BWRs. The input domain is considered to be affected by aleatory uncertainties where input values are distributed according to a certain density functions. These distributions are unknowns given the lack of available data at the present time. The characterizing parameters of the distributions are treated therefore as epistemic uncertainties.

Both uncertainties have been propagated using the pseudo-random sampling in a nested iteration. Assumptions about the ranges for the input parameters were made using engineering judgments based on information on the possible accident progression. In this study we assume that each input variable is independent from the others due to difficulties to determine any correlations. Therefore, further comprehensive analysis of scenarios is necessary to determine dependencies (if any) between the inputs and evaluate more complex joint PDFs. The Risk-Oriented Accident Analysis Methodology Plus (ROAAM+) [128], evolution of the ROAAM originally developed by Theofanus [27], [28], has the objective to solve this challenge. Given its capability to obtain input

domain PDFs conditional to specific scenarios occurring with certain frequencies, it may allow more accurate estimation of the value for the CCFP due to non-coolable debris in Nordic BWRs.

3.8 Ex-Vessel Steam Explosion

The ex-vessel steam explosion framework connects melt ejection mode with steam explosion loads on the containment structures to estimate containment failure probability. Development of the SM relies on a database of solutions generated by a 1D FCI code.

Multidimensional fuel-coolant-interaction (FCI) codes can help to identify information which is missing in 1D FCI codes. However, 2D/3D FCI codes are too computationally expensive to provide even sensitivity analysis, given large number of uncertain scenario and modeling parameters. Application of 1D code requires an additional method for calculating loads on containment structures. There is a need to resolve the link between ex-vessel coolability and steam explosion. Even a mild steam explosion might lead to degradation of debris bed cooling function. However, small size particles generated in steam explosion have little chance to settle on the bed as long as there is intensive coolant circulation in the pool.

Steam Explosion Impact Map probabilistic framework is demonstrated in the Figure 3.148. Melt Ejection Mode is defined as a number of vessel failure scenarios each characterized by a specific set of modelled and stochastic parameters. Pool Characteristics are determined by the accident scenario progression and plant damage state Pdfs. Steam Explosion Load analysis is performed with NRC approved 1D code TEXAS-V and complemented by MC3D 2D calculations for resolving spatial effects that are not captured by 1D code but required as an input and for cross-code comparison. Cumulative density function cdf3.2 requires both (i) addressing bounding failure criteria and (ii) deterministic analysis of failure mechanisms.

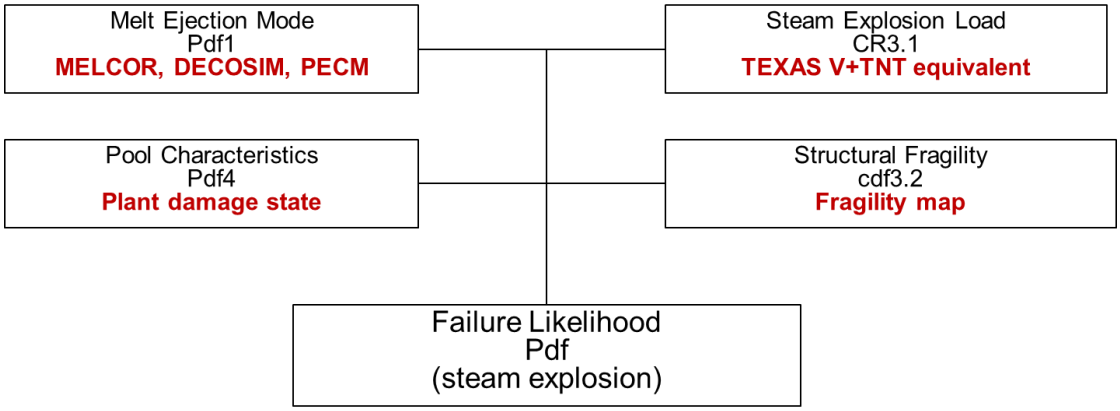

Figure 3.148. SEIM framework

3.8.1 **Approach**

The employed here process of development and validation of a surrogate model is illustrated in Figure 3.149. Initial conditions come from the analysis at the previous stages of the deterministic framework (details of which are beyond the scope of this paper). Experimental and other evidences provide a knowledge base for calibration and validation of the models. Full Model (FM) is used to provide a database of solutions and better understanding of basic physical processes and typical behavior of the target parameters. Simplified modeling approaches and data mining techniques are used in order to develop a surrogate model. Surrogate model (SM) is an approximation of the FM model prediction of the target parameters. SM employs simplified physical modeling, calibratable closures, or approximations to the response surface of FM.

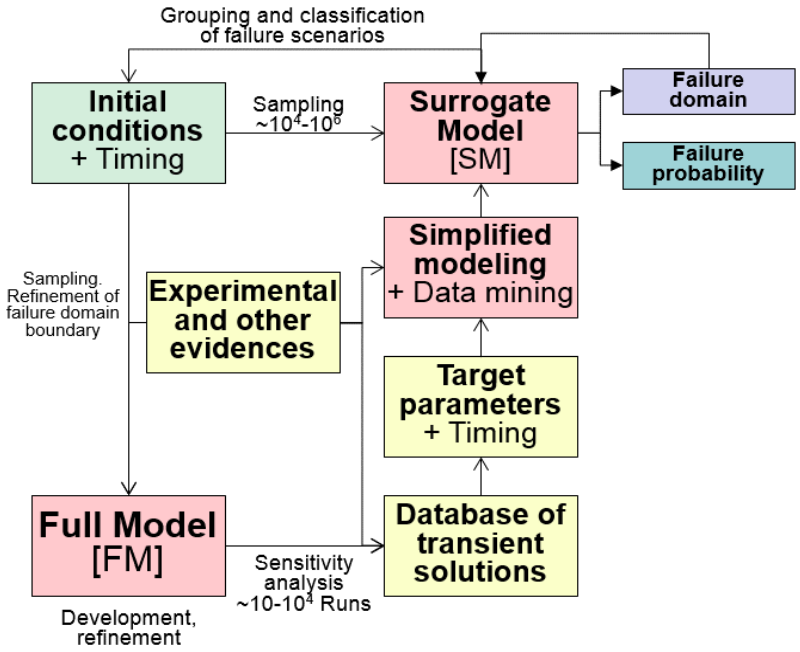

Figure 3.149. Full and Surrogate model development, integration with evidences, refinement, prediction of failure probability and failure domain identification.

In Section 3.8.2 we start with choice of the Fuel Coolant Interaction (FCI) code and detailed review of the modeling approaches in order to (i) select the most suited modeling options provided by the code for the calculation of premixing and steam explosion and (ii) define the list of relevant input and output model parameters. Implementation of the Full Model is detailed in the second paragraph of the Section 3.8.2 and followed by the definition of the relevant target functions, introduction of a simplified method for impulse propagation and approach for statistical treatment of the triggering time. A comprehensive sensitivity study to screen out non-influential parameters from the FM input is carried out in last paragraph of the Section 3.8.2. Development of the database of the FM solutions and its verification is undertaken in Section 3.8.3. Section 3.8.4 provide details on the development of the SM and comprehensive comparison of different characteristics of the full and surrogate models.

3.8.2 **Steam Explosion Full Model**

Review of TEXAS-V

TEXAS-V was chosen as a physics model to calculate premixing and steam explosion in Nordic type BWRs [201]. The choice was motivated by (i) TEXAS-V relatively high computational efficiency, (ii) extensive validation database.

Texas-V is a 1D 3-field transient code with Eulerian fields for gas and liquid and a Lagrangian field for fuel particles. It is comprised of two modules for calculation of premixing and steam explosion.

The premixing model is based on (i) two constitutive relations: the *fragmentation model for mixing* and the *phase change model;* (ii) two alternative modes of melt release: in the form of a coherent jet and in the form of discreet master particles; and (iii) two alternative mechanistic approaches for jet front breakup: *leading edge* and *trailing edge*.

The *fragmentation model for mixing* is comprised of three mechanisms: Kelvin-Helmholtz instability, boundary layer stripping and Rayleigh-Taylor instability. The former two are considered to have minor effect with vapor film present and are reduced rapidly with rise of void fraction. The Rayleigh-Tailor instability is thus the key mechanism describing fuel fragmentation in TEXAS. The model considers the fuel particles to be deformed and dynamically fragmented into a discrete number of particles from its initial diameter to smaller size [202], [203]:

$$D_f^{n+1} = D_f^n \cdot \left[1 - C_0 \Delta T^+ \cdot \left(\frac{\rho_c U_{rel}^2 D_f^n}{\sigma_f}\right)^{0.25}\right] \quad (3.129)$$

$$\Delta T^+ = \frac{U_{rel} \cdot (t^{n+1} - t^n)}{D_f^n} \cdot \left(\frac{\rho_c}{\rho_f}\right)^{0.5} \quad (3.130)$$

$$C_0 = 0.1093 - 0.0785 \cdot \left(\rho_c/\rho_f\right)^{0.5} \quad (3.131)$$

where $n, n+1$ designate old and new time step values; D_f is fuel particle diameter; ΔT^+ is a dimensionless time step; C_0 is the constant; U_{rel} is relative velocity; t is time; σ_f is fuel surface tension; ρ_f, ρ_c are densities of fuel and coolant respectively.

Therefore, the primary breakup is dominated by the existence of the jet front, the moment the jet front reaches the bottom of the domain primary breakup sharply reduces. It is further assumed that coherent fuel jet will not breakup until the fuel particle at the leading edge, exposed to the oncoming coolant, is fragmented (and swept away from the interface). This means that only master particles included in the leading edge of the jet can be subject to fragmentation.

The onset of master particle fragmentation is driven by one of the mechanistic approaches for jet front breakup. The *trailing edge* algorithm forces the leading master particle to fragment at the tail of the fragmented debris, i.e. at the beginning of the premixing region. The *leading edge* algorithm implies the start of the leading master particle fragmentation at the leading front of the fragmented debris, i.e. at the end of the premixing region.

The phase change model (in continuous liquid field) is comprised of two primary equations that define:

1. Heat loss from fuel particles $\dot{q}_{fuel}$:

$$-\dot{q}_{fuel} = \pi D_f^2 h_{film}\left(T_f - T_{sat}\right) + \pi D_f^2 \sigma F\left(T_f^4 - T_{sat}^4\right), \qquad (3.132)$$

where the first term on r.h.s. describes convection heat transfer rate from the fuel particle to the liquid vapor interface, and the second term is the radiation heat transfer rate from the fuel particle to the saturated liquid-vapor interface; T_f and T_{sat} are fuel and saturation temperatures respectively; h_{film} is convection heat transfer coefficient; σ is Stefan-Boltzmann constant and F is the view factor between fuel particle surface and liquid-vapor interface. The temperature profile inside a particle is assumed constant in the bulk and linearly decreasing within a thin thermal layer δ.

The corresponding steam generation rate $\dot{\mathrm{M}}_{\mathrm{s,p}}$ is than derived from:

$$-\dot{q}_{fuel} = \pi\left(D_f + 2\delta_{film}\right)^2 h_{lg}\left(T_f - T_{sat}\right) + C_{rad}\pi D_f^2 \sigma F\left(T_f^4 - T_{sat}^4\right) + \dot{\mathrm{M}}_{\mathrm{s,p}} h_{fg}, \qquad (3.133)$$

where the first term on the r.h.s. is convection heat transfer rate from the liquid-vapor interface around the fuel particle to bulk liquid field and the second term is the fraction C_{rad} of radiation heat flux that is absorbed in the subcooled liquid; h_{fg} is the latent heat of evaporation; δ_{film} is the thickness of the steam film surrounding the fuel particle; $\dot{\mathrm{M}}_{\mathrm{s,p}}$ is ; h_{lg} is heat transfer coefficient from vapor to bulk liquid.

2. Heat flux balance around steam bubbles and resulting steam generation rate $\dot{\mathrm{M}}_{\mathrm{s,b}}$:

$$A_{gL} K_g \frac{\left(T_g - T_{sat}\right)}{\delta_g} = A_{gL} h_{L.sL}\left(T_{sat} - T_L\right) + \dot{\mathrm{M}}_{\mathrm{s,b}} h_{fg} \qquad (3.134)$$

where the term on the l.h.s. is the vapor bubble-side heat transfer rate; the first term on the r.h.s. is the bulk liquid-side heat transfer rate; A_{gL} is the surface area of the interface between the liquid field and the vapor field as determined from the vapor bubble radius and the flow regime; K_g is effective thermal conductivity of the vapor film; δ_g is the vapor thermal thickness in the vapor bubble (taken in the range from 1 to 20% of the bubble size); $h_{L.sL}$ is heat transfer coefficient in the bulk liquid; T_L is liquid temperature; T_g is the temperature of the vapor bubble.

The net rate of steam generation $\dot{m}_s$ per unit volume is thus expressed in terms of the net heat flux $\dot{q}_{net,f}$

$$\dot{m}_s = \frac{\dot{q}_{net,f}}{h_{fg} V_{cell}} \qquad (3.135)$$
$$\dot{q}_{net,f} = \dot{q}_{fuel} - \dot{q}_l - \dot{q}_v$$

where $\dot{q}_l$ and $\dot{q}_v$ are the heat received by coolant liquid and coolant vapor respectively, which becomes the internal energy of the coolant; and V_{cell} is cell volume.

The **fine fuel fragmentation** (upon steam explosion) is a computed using Tang and Corradini model [207] which is based on the original Kim's work [208]. It takes into account a combination of thermal and hydrodynamic fragmentation phenomena:

1. Film boiling around a molten fuel particle.
2. Film collapse by external pressure pulse.

3. Coolant micro-jets impingement on the surface of fuel droplet.
4. Rapid coolant expansion and fragmentation of the fuel into droplets.

The model is implemented in TEXAS with a semi-empirical equation where fine fragmentation rate $\dot{m}_f$ is expressed as:

$$\dot{m}_f = Cm_p \cdot \left(\frac{P - P_{th}}{\rho_c R_p^2}\right)^{0.5} F(\alpha) g(\tau) \tag{3.136}$$

where m_p is mass of the initial particle; R_p is radius of the initial particle; P_{th} is the threshold pressure necessary to cause film collapse; P is ambient pressure; $F(\alpha)$ is the compensation factor for coolant void fraction; and $g(\tau)$ is the factor for available fragmentation time.

The factor $F(\alpha)$ decrease from 1 to 0 at $\alpha = 0.5$ in order to take into account that coolant jet impingement become less likely to occur as vapor fraction increases. In the TEXAS input file this limit is named ALPHAS.

The threshold pressure P_{th} is evaluated based on theoretical work by Kim and experimental data. At ambient pressure 1 Bar the threshold pressure is in the range from 2 to 4 Bars. As the ambient pressure increases the threshold pressure also increases, however no quantitative values are suggested in the code manual. In the TEXAS input file this parameter is designated as POLD.

The integral fragmentation mass depends on the duration of the fragmentation process. The factor $g(\tau)$ is introduced as an empirical approach to account for the characteristic fragmentation time τ during which the above mechanism is considered to be active. The factor $g(\tau)$ decreases from 1 to 0 as this characteristic time is exceeded. At ambient pressure (1 Bar) the recommended value for it is 1-4 ms [203]. It is indicated that as ambient pressure increases the fragmentation limit time decreases.

The heat generated due to dynamic fine fragmentation is expressed in TEXAS as:

$$\dot{q}_{frag} = \dot{m}_f \cdot (C_{pf} \cdot (T_f - T_{sat}) + i_f) \tag{3.137}$$

where i_f is fuel latent heat; T_f is fuel temperature; C_{pf} is specific heat for the fuel. Due to extremely fine fragmentation of the fuel the rate of heat transfer is very fast. It is assumed that steam generation rate $\dot{m}_s$ per unit volume can be estimated as:

$$\dot{m}_s = \frac{\dot{q}_{net,f} + \dot{q}_{frag}}{h_{fg} V_{cell}} \tag{3.138}$$

Further details on the implemented models in TEXAS-V can be found in the thesis by Chu [203] for premixing model, by Tang [207] for propagation model and by Murphy for hydrogen generation [209], or in the TEXAS-V manual [206].

Modelling of steam explosion in Nordic type BWRs with TEXAS-V

The height of the computational domain, from the point of melt release to the bottom of the water pool, is set to 13.0 m in accord with design of Nordic type BWRs. The computational domain is divided onto 26 cells, each 0.5 m high with the same cross

section area A_{cell}.

The study of the effect of the mesh cell height on TEXAS-V calculations suggests that with the decrease of the cell height from 0.4 to 0.2 m explosion impulses get weaker and the number of failed calculations increases; explosion impulses and statistics of numerically failed calculations were not sensitive to the variation of cell height in the range from 0.4 to 0.6 m.

The mesh cell cross-section area A_{cell} appeared to have a profound effect on the dynamic pressure and consequently on the explosion pressure impulse I_p:

$$\frac{\Delta I_p}{I_p} \cong \frac{A_{cell}}{\Delta A_{cell}} \tag{3.139}$$

We found that for chosen ranges of input parameters the product of the pressure impulse [Pa·s] and the cell cross section area [m^2] (a measure of the total released energy) remains practically independent from the mesh cell cross-section area (see Figure 3.150). Therefore we set the ratio of the jet radius (R_{jet}) to cell radius (R_{cell}) approximately the same as in KROTOS experiments (against which the TEXAS-V code was extensively validated). In this work the following relation has been used:

$$R_{cell} = 11.0 \cdot R_{jet} \tag{3.140}$$

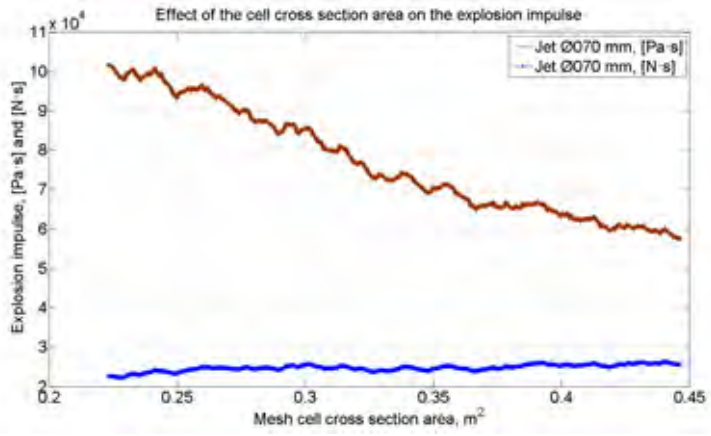

Figure 3.150. Effect of the mesh cell cross section area on the explosion impulse (blue) and the explosion pressure impulse (brown)

Reduced time steps were chosen to decrease the number of failed calculations (crashed due to problems with achieving numerical convergence), specifically, the maximum time step for premixing calculations was set to 10^{-6} s and the maximum time step for explosion was $0.5 \cdot 10^{-6}$ s.

The threshold pressure for film collapse in eq.(3.136) was set to be twice the system pressure: $P_{th} = 2 \cdot P$. The alternative formulation $P_{th} = P + 1Bar$ resulted in twice larger number of failed calculations.

A comparative calculation using trailing edge and leading edge algorithms (see Figure 3.151) suggests that the trailing edge algorithm provides slower jet propagation in water, enhanced primary breakup and higher steam generation rates. Supposedly, it is intended to reproduce fragmentation of small jets, i.e. jets prone to sinusoidal instability.

Given characteristic scales of melt release in the reactor case and by comparison with the jet front propagation velocity in water predicted using MC3D [210] we have chosen the leading edge algorithm for modelling of jet fragmentation.

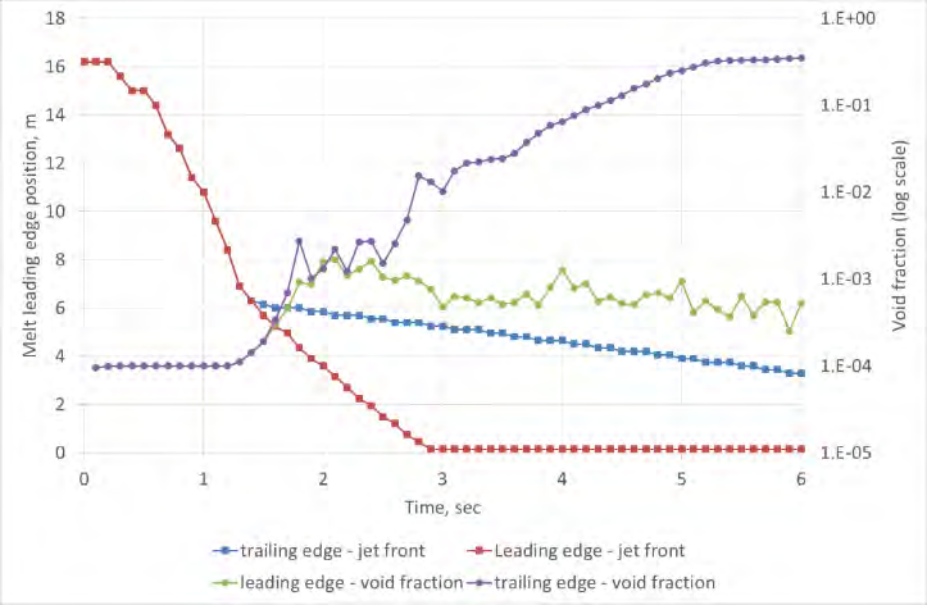

Figure 3.151. Trailing edge breakup vs leading edge breakup mechanisms.

Two more assumptions were made: (i) the model for hydrogen generation was not used and (ii) effects of the crust on explosion propagation were not modelled.

Processing of the Full Model output

3.8.2.1.1 Output functions

Two functions were derived to characterize a single TEXAS-V calculation: one for the characterization of the steam explosion energetics, i.e. explosion impulse (F_{expl}); and one for the characterization of the potential explosivity of premixture, i.e. total surface area of liquid melt droplets in water (F_{prmx}). Note that in TEXAS-V the rate of fine fragmentation, as defined in eq.(3.136), is proportional to the surface area of liquid melt. This means that F_{prmx} characterizes amount of melt available for explosion.

Explosion impulse was integrated from the dynamic pressure history for every cell separately; the maximum impulse was then taken:

$$F_{expl} = \max\left(\sum_i (P_{ij} - P_{0j})\delta t_i\right) \cdot A_{cell},\ [N \cdot s] \tag{3.141}$$

where P_{ij} is pressure in the cell j at the time instance i; P_{0j} is pressure in the cell j at time 0; δt_i is the time step at the time instance i, A_{cell} – mesh cell cross section area.

The total surface area of liquid melt droplets in water was approximated as:

$$F_{prmx} = 4\pi \sum_k \begin{cases} n_k R_k^2, & [Vs_{i(k)} < 0.5,\ T_k > T_{melt}] \\ 0, & otherwise \end{cases},\ [m^2] \tag{3.142}$$

where k is Lagrangian particle group number; R_k is particle radius in the k particle group; n_k is the number of particles in the k particle group; T_k is particle bulk temperature in the k particle group; T_{melt} is melting temperature of the fuel; $Vs_{i(k)}$ is steam fraction in the cell i where k particle group is located.

3.8.2.1.2 Impulse propagation

The explosion impulse in eq. (3.141) is a result of 1D solution taken from a single cell. It can be considered as a point like source. In order to estimate the explosion impulse at different locations in the containment an appropriate impulse propagation method must be used. For demonstration purposes it is assumed that explosion pressure impulse I [Pa·s] (similar to pressure distribution in a propagating spherical shock wave) is a decaying function of the distance r from the center of the explosion:

$$I = \tilde{c} \cdot r^{\nu}, \nu \cong -1, \tilde{c} = const \tag{3.143}$$

The constant $\tilde{c}$ in eq.(3.143) is estimated assuming (i) explosion impulse F_{expl} to be distributed over the complete area of the containment base A_b and (ii) the point source of the explosion to be located in the center of the corresponding cell in TEXAS:

$$I_b = F_{expl}/A_b \tag{3.144}$$

$$I_b = \frac{2}{r_b^2}\int_0^{r_b} \frac{\tilde{c}}{(h_c^2 + r^2)^{0.5}} \cdot r dr \tag{3.145}$$

$$I(r) = I_b \cdot \frac{r_b^2}{2 \cdot ((r_b^2 + h_c^2)^{0.5} - h_c)} \cdot \frac{1}{r} \tag{3.146}$$

where r_b is the radius of the containment; h_c is elevation of the computational cell above the bottom of the domain.

The impulse at the center of the containment floor is estimated substituting in eq.(3.146) $r = h_c$; the impulse at the wall of the containment is estimated assuming melt jet release at the side of the lower head, i.e. $r = 3\ m$ away from the wall.

3.8.2.1.3 Probabilistic treatment of the triggering time

During melt water interaction premixing conditions may vary rapidly in time [211]. This makes energetics of steam explosion sensitive to the triggering time.

To address the importance of this phenomena the dependence of normalized F_{prmx} and F_{expl} functions on the triggering time was investigated [131]. The data was obtained in two steps. First, premixing was calculated starting from melt release till the jet front arrival to the bottom of the domain and instantaneous premixing configurations were saved with 1 ms time step. Second, steam explosion calculations were carried out for every instantaneous premixing configuration. According to the Figure 3.152 during melt water interaction (t > 1.4 s) the normalized F_{prmx} and F_{expl} functions demonstrate quasi periodic and apparently correlated behavior. However, the correlation between the functions is not strong enough to use F_{prmx} for prediction of potential premixture explosivity: in the considered case the largest impulse is obtained at only about 40% of the maximum values of F_{prmx}.

The results in the Figure 3.152 indicate that *small variations in the triggering time may lead to large changes in the explosion energetics*: for example, between 1.90 and 2.01 s,

i.e. within 110 ms time window, the explosion impulse changes almost 50 times from 377 kPa·s to 8 kPa·s.

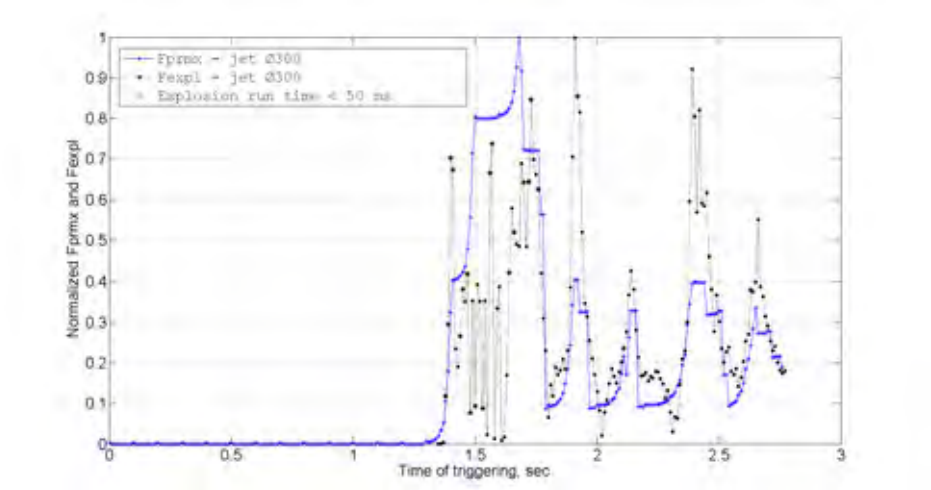

Figure 3.152. The dependence of normalized premixing F_{prmx} and explosion F_{expl} functions on the triggering time (release of oxidic corium melt with jet Ø300 mm into a 7 m deep water pool)

The high sensitivity of the explosion impulse to the triggering time is an intrinsic characteristic of the steam explosion.

In FCI calculations, the chaotic behavior of the steam explosion impulse with respect to the discreet triggering time makes the problem of prediction of steam explosion impulse ill-posed and, consequently, interpretation of FCI codes results highly uncertain. This is one of the main reasons for the large spread of (i) predictions with different FCI codes, and (ii) predictions with the same FCI code obtained by different users (see, for example, SERENA-II benchmark exercise [214] and [213], [212] for SERENA-I results). It is instructive to note that previous studies with the TEXAS code [215], [216], [217] or other codes were not able to identify and address the effect of the triggering time and resulting ill-posedness of the problem due the limited number of computations. The most robust approach to the treatment was attempted in [218], [219]. From risk perspective, the choice of the triggering time can change prediction of containment failure from physically unreasonable (at ~8 kPa·s) to unavoidable (at ~377 of kPa·s). Therefore we advocate statistical treatment of the triggering time effect in both cross code comparisons and risk analysis.

In FCI experiments, the chaotic nature of steam explosion is expected to manifest itself through stochastic variations of explosion characteristics due to aleatory variability of (i) the triggering time and (ii) melt release conditions. Considering possible variation of the impulse (e.g. see Figure 3.153), the effect of the triggering time on the measurement of steam explosion energetics may exceed the effect of the other experimental parameters. Thus only statistical treatment using data from many repeatability tests can be used to reveal the influence of different factors.

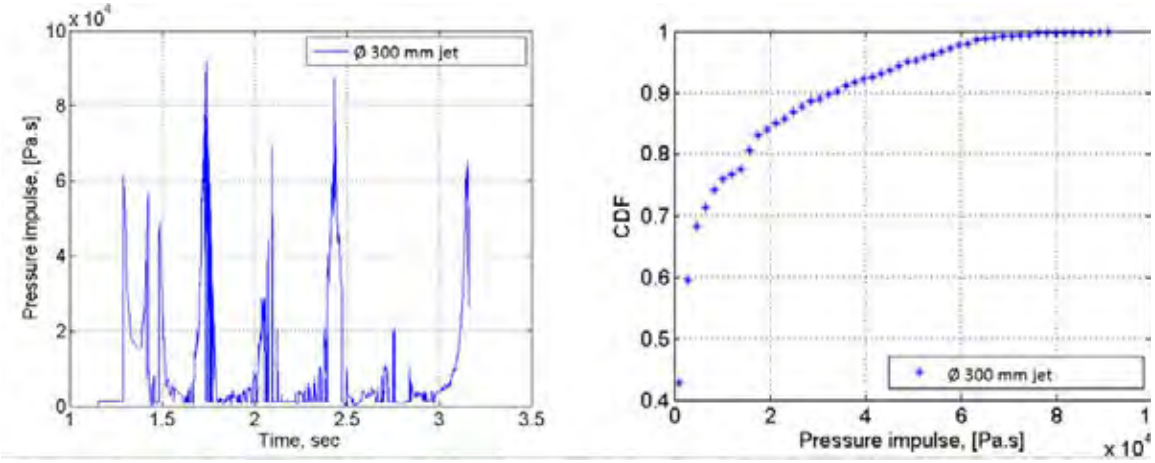

a b

Figure 3.153. Evolution of the explosion pressure impulse at pedestal wall as a function of triggering time (a) and resulting distribution of the explosion pressure impulse (b)

The ill-posedness and resulting chaotic behavior of the explosion impulse can be also addressed by considering statistical distributions of the impulses obtained at all the same conditions except for the triggering time. For example, evolution of the explosion impulse in Figure 3.153a can be characterized by a cumulative density function (CDF) of the predicted impulses as shown in Figure 3.153b. According to the data in the Figure 3.153b the percentile of explosion impulses that do not exceed, say, 80 kPa·s is 99.75%.

In order to make model output well-posed and independent from the choice of the triggering time we introduced statistical treatment of explosion impulse. For every melt release scenario, we estimate the values of the impulses that correspond to 50, 75, 95, 99 and 100 percentiles of the CDF. For example, for the cumulative distribution function (CDF) reported in Figure 3.153b, we can infer that for 95% of all possible triggering times the explosion impulse at the pedestal wall (plotted in Figure 3.153a) will not exceed 50 kPa·s.

Choice of important input parameters

Out of about 160 TEXAS-V input parameters 23 were selected for further analysis. The complete list is provided in Table 3.28. Ranges of parameters used in the sensitivity study were defined for typical scenario of oxidic melt release in Nordic BWR [220], [131]. Parameters not mentioned in the Table 3.28 were set in accord with default values defined in the TEXAS-V manual [206].

Table 3.28: Selected TEXAS-V parameters and their ranges

Parameter	**Units**	**Range**	**Description**
PO	**Bar**	**1÷4**	**Initial pressure**
TLO	**K**	**288-366**	**Water temperature**
XPW	**m**	**3.2-8.2**	**Water level in the containment**
TGO	K	TLO	Cover gas temperature
TWO	K	TLO	Wall temperature
RPARN	m	0.07	Fuel injection radius
		0.15	
CP	**J/kg·K**	**400÷570**	**Fuel capacity**
RHOP	**kg/m3**	**7600-8600**	**Fuel density**
PHEAT	**kJ/kg**	**260÷360**	**Fuel latent heat**
TMELT	K	2850	Fuel melting temperature

TPIN	**K**	**2850÷3150**	**Fuel injection temperature**
UPIN	**m/sec**	**1.5÷2.5**	**Fuel injection velocity**
KFUEL	**W/m·K**	**2÷11**	**Fuel thermal conductivity**
C(32)	**J/m^2**	**0.4÷0.6**	**Fuel surface tension**
C(18)	**-**	**0.6÷0.9**	**Fuel emissivity**
DXI	m	0.5	Cell height
ARIY	**m^2**	**0.7÷1.8**	**Cell cross-section area**
		3.8÷8	
TMAX	sec	-	Premixing time
CFR	**-**	**2.0÷2.7 E-03**	**Proportionality constant for the rate of fuel fine fragmentation**
RFRAG	**m**	**8÷1.2 E-05**	**Initial size of fragmented particles**
POLD	Pa	2×PO	Threshold pressure for film collapse
TFRAGLIMT	**s**	**0.0005÷0.0030**	**Fuel fragmentation time interval**
PTRIG	Bar	3	Trigger pressure

The sensitivity study used extended Morris method [73][74][161] and addressed 16 independent input parameters (printed in bold in the Table 3.28). The mean pressure impulse ($\bar{F}_{expl}/A_{cell}$, [Pa·s]) has been used as the response function. The results in Figure 3.154 are provided for the scenario with 140 mm jet diameter. The elements in the legend are sorted in descending order of Morris modified mean μ^* value. The spread of the results established in 3 consecutive sensitivity studies that used different number of trajectories is also illustrated in the figure. Two input parameters were screened out: RFRAG and C(18).

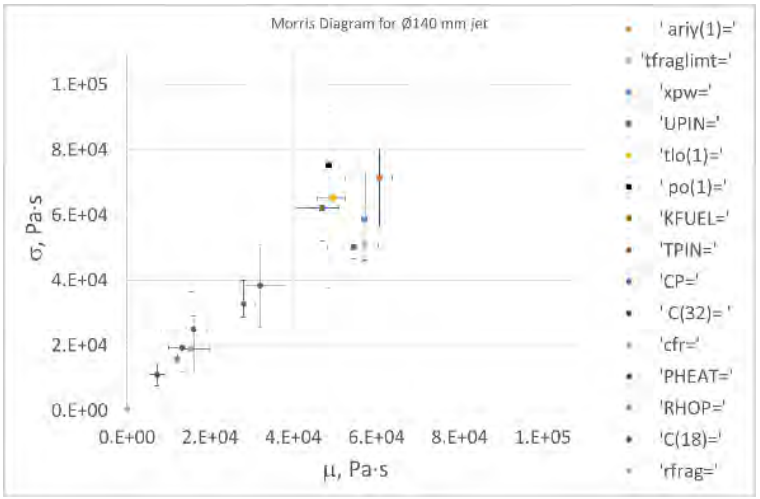

Figure 3.154. Morris diagram for mean pressure impulse

3.8.3 **Database of full model solutions**

Database generation approach

The database consists of 1500 premixing sets and 455,386 explosion calculations. The list of input parameters and respective ranges is provided in the Table 3.29. Note that the ranges were extended compared to those used in the sensitivity study to include scenarios of metallic melt releases.

Table 3.29: Ranges of input parameters used for generation of the database of FM solutions

#	Parameter	Units	Range		Explanation
			min	max	
1	XPW	M	5	9	Water level
2	PO	Bar	1	4	System pressure
3	TLO	K	288	368	Water temperature
4	RPARN	m	0.035	0.3	Initial jet radius
5	CP	J/kg·K	350	650	Fuel heat capacity
6	RHOP	kg/m3	7500	8500	Fuel density
7	PHEAT	J/kg	260 000	400 000	Fuel heat capacity
8	TMELT	K	1600	2800	Fuel melting point
9	TPIN	K	1620	3150	Melt superheat
10	UPIN	m/s	-8	-1	Melt release velocity
11	KFUEL	W/m·K	2	42	Fuel thermal conductivity
12	CFR	-	0.002	0.0027	Proportionality constant for the rate of fuel fine fragmentation
13	TFRAGLIMT	ms	0.5	2.5	Fragmentation time

Parameters were considered as independent, except for TPIN > TMELT. Halton method [169] was used for the generation of the input. Explosion calculations were performed with 4 ms time step starting from melt contact with water and till melt contact with the bottom of the water pool.

Database verification and filtering of numerically failed cases

In order to verify the physical consistency of the database and address effects of crashed calculations, sensitivity and parametric studies have been performed. Three response functions were considered:

- For numerical stability: Explosion runtime (*ER*, s)
- For premixing: surface area of liquid melt in the regions with void fraction below 0.5(*LMSA*, m^2)
- For explosion: mean pressure impulse at the wall (*Impulse*, Pa·s)

Three sensitivity indices have been estimated from the database of the model solutions:

- Pearson correlation coefficient
- Spearman rank coefficient
- Normalized of Morris modified $\tilde{\mu}$ and $\tilde{\sigma}$

Normalization was done in the following manner:

$$\tilde{\mu}_i = \frac{\mu_i - \mu_{min}}{\mu_{max} - \mu_{min}} \quad (3.147)$$

$$\tilde{\sigma}_i = \frac{\sigma_i}{\mu_i} \quad (3.148)$$

where μ_i and σ_i are Morris modified mean and standard deviation for parameter i; μ_{min} and μ_{max} are minimum and maximum values of μ_i. Note that when $\tilde{\sigma}_i < 1$ than the corresponding parameter is expected to have dominantly linear contribution to the output.

Morris sensitivity indices were used to evaluate relative importance of input parameters and non-linearity. Spearman and Pearson coefficients were used to clarify whether an input parameter is positively or negatively correlated with a given response function.

3.8.3.1.1 Identification and filtering of failed calculations

Premixing calculations had very few if any failed cases. On contrary, (Figure 3.155), less than 73% of the explosion calculations succeeded to complete analysis for 50 ms of explosion propagation time (ER = 0.05 s, which was defined in the code input), and almost 10% of cases have failed during the first 10 ms. Inclusion of such numerically failed cases into the FM database has to be avoided in order to obtain physically sound predictions with the SM.

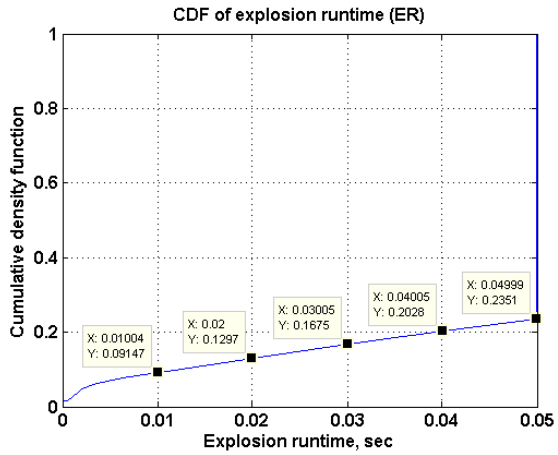

Figure 3.155. CDF of explosion runtime

The sensitivity indices of the explosion run time to the input parameters are plotted in Figure 3.156. The results suggest that failure of the explosion calculations is strongly dependent on the development of the premixing (LMSA), with most influential input parameters being: melt superheat (TPIN-TMELT), jet radius (RPARN), and melt release velocity (UPIN). Dependence of the explosion runtime on these parameters and LMSA is demonstrated in the Figure 3.157.

The results suggest that explosion calculations have high failure frequency for premixing cases with combinations of high-melt superheat, high release velocity and large jets. Jet radius (RPARN) has a non-monotonic influence on ER.

In order to filter failed explosion calculations we applied the following two step approach:

1. A set of explosion cases that correspond to the same melt release conditions (premixing set) and differ only in the triggering time is removed from the

database if the number of cases with runtime below 35 ms exceeds 20% of the set.

2. Estimation of the mean and standard deviation of the explosion impulse from the remaining premixing sets is performed excluding those cases that have explosion runtime below 10 ms. These cases, most often produce zero or close to zero impulses before crashing.

About 32% of computed premixing sets (482 out of 1500) were removed from the database in step 1. The frequency of failed calculations grows with potential "explosivity" of the premixture. Therefore, such filtering might be biased towards premixing sets with potentially high energetics of the explosion.

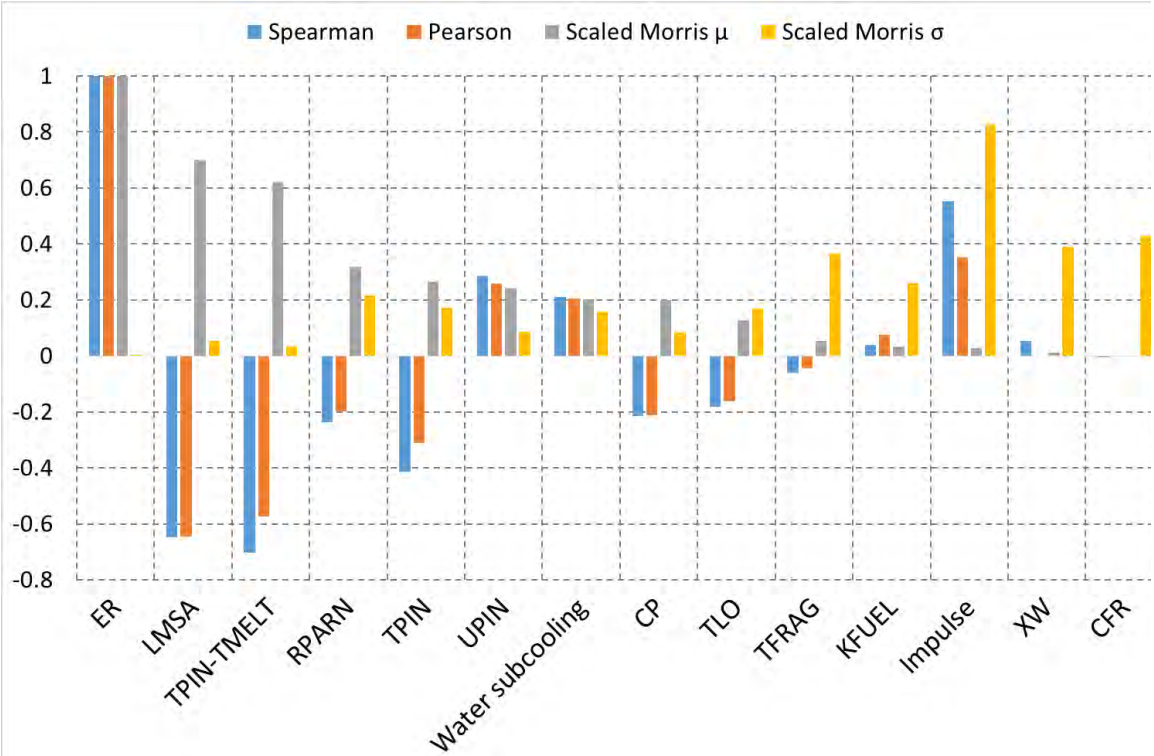

Figure 3.156. Sensitivity of explosion runtime (ER) to the model parameters (parameters are arranged from left to right in descending order of importance)

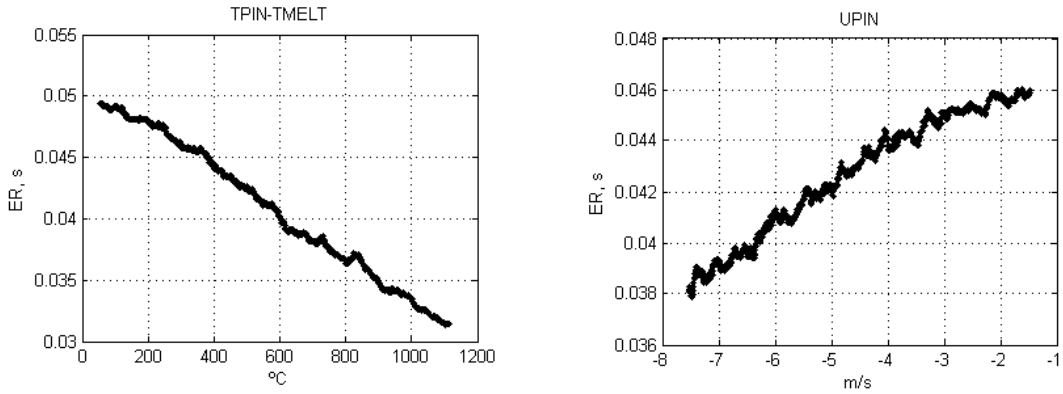

a b

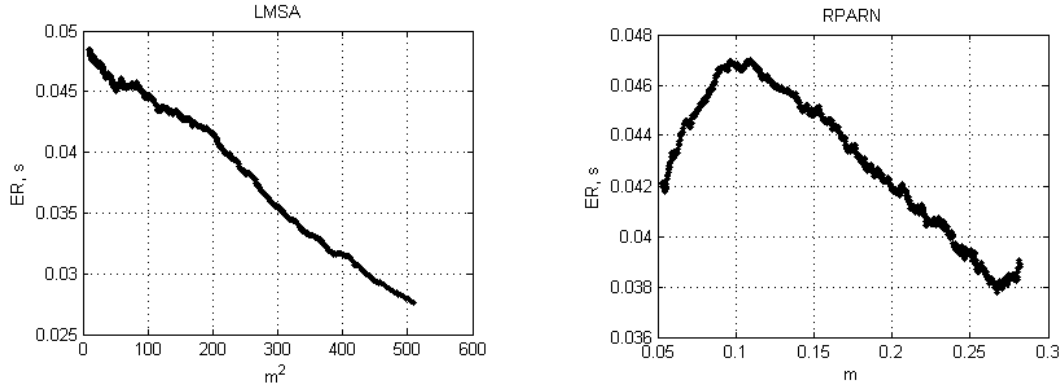

Figure 3.157. Moving average for explosion runtime as a function of melt superheat (a), melt release velocity (b), liquid melt surface area (c) and jet diameter (d).

3.8.3.1.2 Effect of input parameters on development of premixing

Liquid melt surface area in water regions with void fraction below 0.5 (LMSA) indicates the effectiveness of melt fragmentation and was found to be well correlated with the explosion energetics (Figure 3.158).

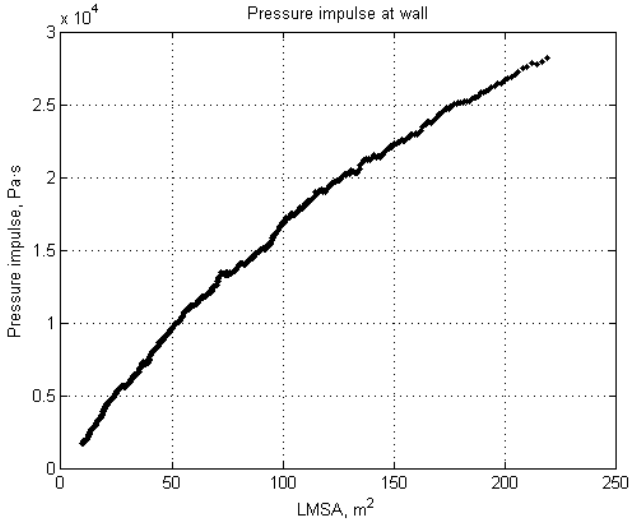

Figure 3.158. Moving average for mean pressure impulse at the pedestal wall vs LMSA
Sensitivity of the LMSA to the model parameters is demonstrated in the Figure 3.159.

The most influential parameters are jet diameter (RPARN), melt superheat (TPIN-TMELT), melt release velocity (UPIN) and water subcooling. Dependence of the LMSA on these parameters is provided in Figure 3.160. The effect of the jet diameter is trivial. Growth of LMSA with melt release velocity is consistent with the assumption that increase in melt release velocity should enhance fragmentation. The decrease of LMSA with decrease of melt superheat and increase of water subcooling could be attributed to the increased rate of melt solidification. In general, the effect of input parameters on the premixing conditions is considered as physically sensible.

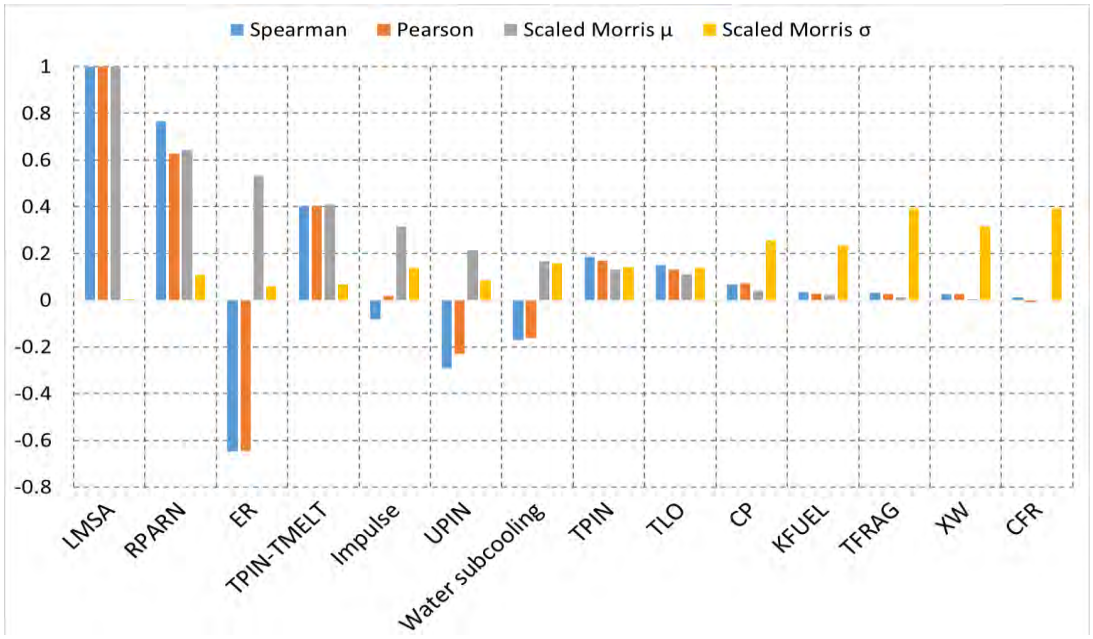

Figure 3.159. Sensitivity of liquid melt surface area (LMSA) to the model parameters (parameters are arranged from left to right in descending order of importance)

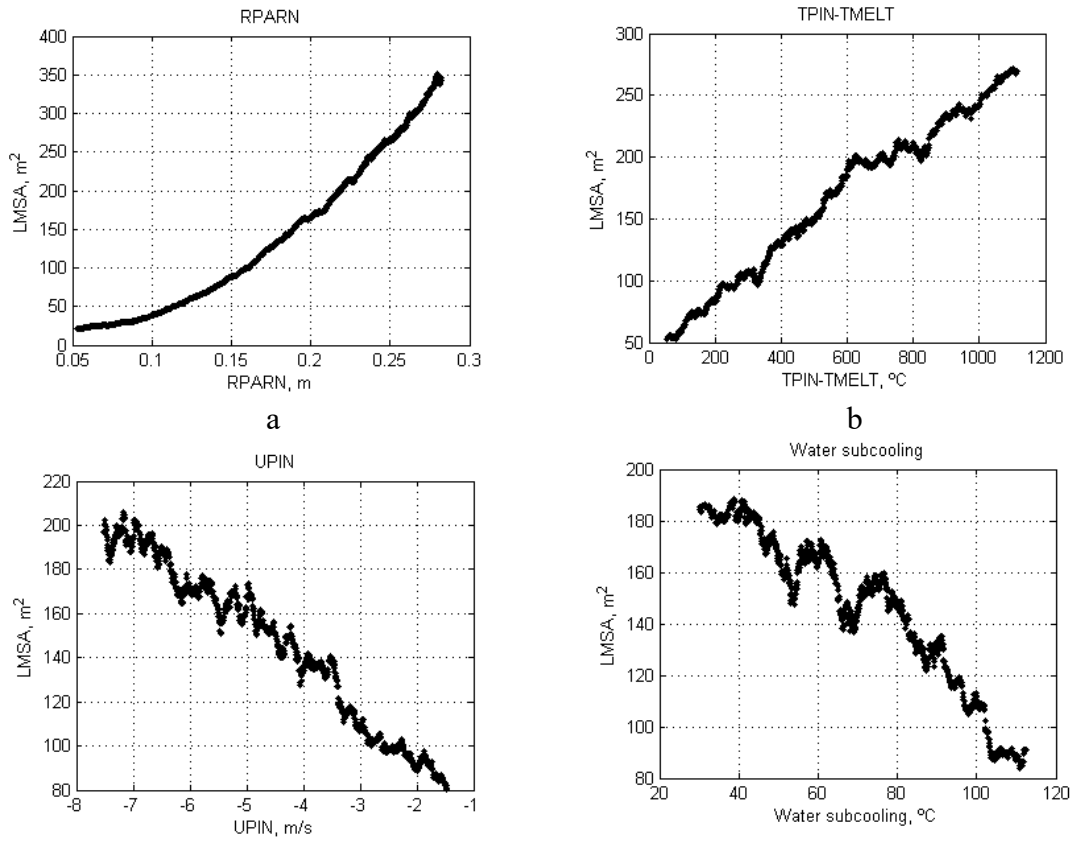

Figure 3.160. Moving average for liquid melt surface area as a function of jet diameter (a), melt superheat (b), jet release velocity (c) and water subcooling (d).

3.8.3.1.3 Effect of input parameters on explosion energetics

The sensitivity indices were calculated for the explosion impulse at the wall using filtered database. The results are provided in Figure 3.161. The dependence of the

pressure impulse on the most influential parameters (jet diameter, melt superheat, melt release velocity and fragmentation time) is shown in Figure 3.162. The results demonstrate physically sensible behavior with only one exception: melt superheat. Up to about 400ºC of the melt superheat the explosion impulse keeps slowly growing as expected, but rapidly decreases afterwards. The sudden decrease is an artifact caused by the correlation between the distributions of the input parameters introduced in the filtering process. The correlation between average melt superheat and average jet diameter is shown in the Figure 3.163. It is clear that in the filtered data the number of cases with simultaneously large jets and large melt superheats is much smaller than in the original sample. This correlation affected the moving average of the impulse with respect to the melt superheat presented in Figure 3.162b.

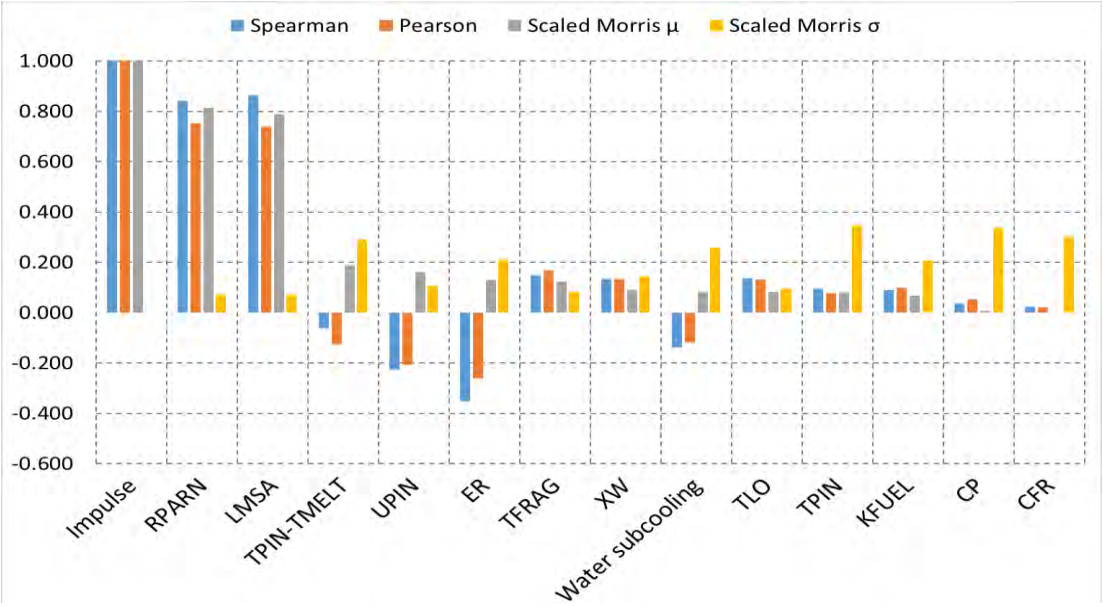

Figure 3.161. Sensitivity of explosion pressure impulse at wall to the model parameters (parameters are arranged from left to right in descending order of importance)

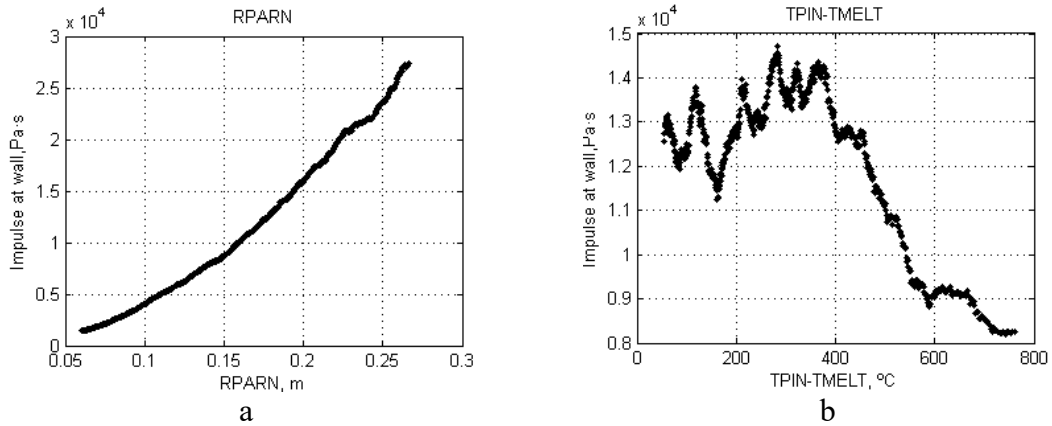

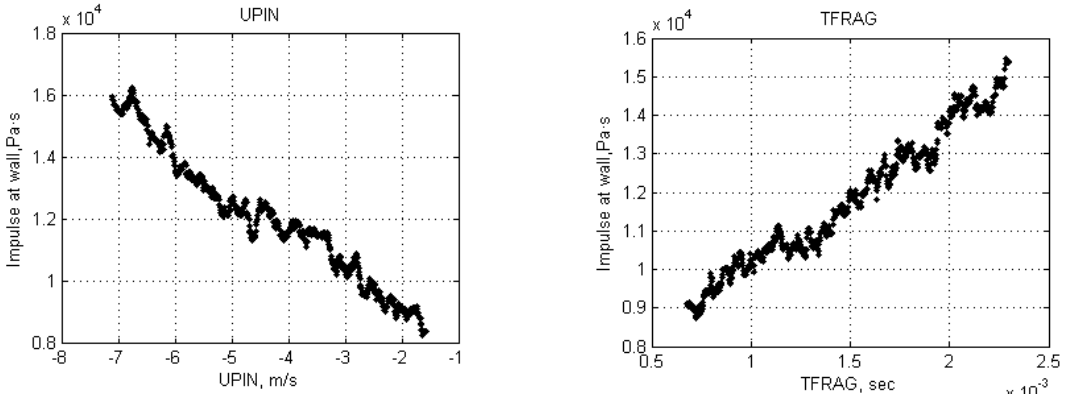

c d

Figure 3.162. Moving average for explosion pressure impulse at wall as a function of jet diameter (a), melt superheat (b), jet release velocity (c) and fragmentation time (d).

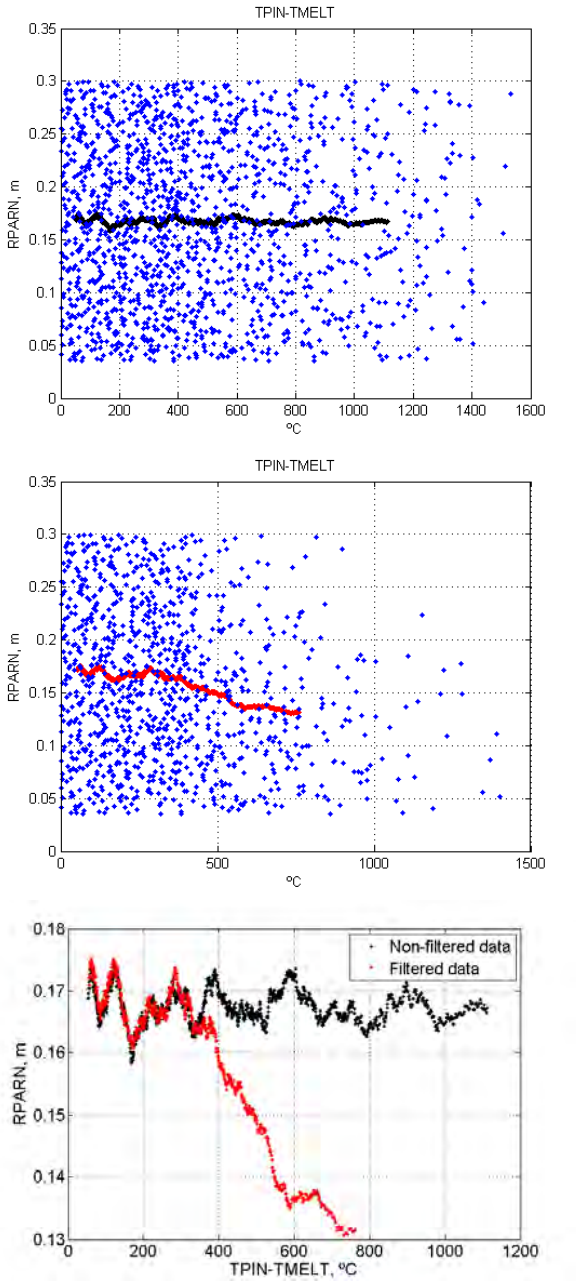

Figure 3.163. Moving average for jet diameter as a function of the melt superheat for non-filtered (black) and filtered (red) data. Original data is shown with blue dots.

3.8.4 **Steam explosion Surrogate Model**

Implementation of the Surrogate Model

The surrogate model has been developed using Artificial Neural Networks (ANNs). In this work a feedforward neural network with Bayesian regularization and backpropagation was implemented. The ANN structure obtained after training consists of two hidden layers formed by 3 sigmoid neurons and 5 sigmoid neuron respectively, followed by the output layer with 4 linear neurons (see Figure 3.164).

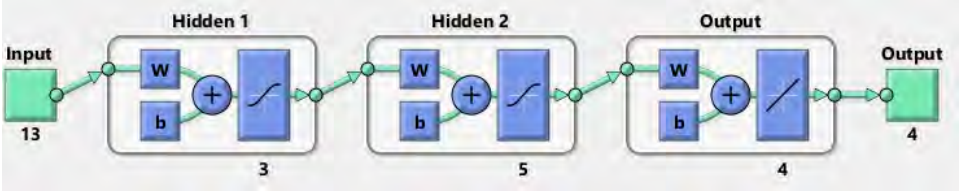

Figure 3.164. ANN structure

The network is trained according to Levenberg-Marquardt optimization algorithm, applying internally Bayesian regularization. The filtered database (see Chapter 3.8.3.1.1) was used for the training of the ANN.

The ANN predicts the mean and standard deviation of the impulse $\bar{I}_0$ at the center of the containment floor and at the wall (4 outputs) given 13 TEXAS-V parameters in the input: XPW, PO, TLO, RPARN, CP, RHOP, PHEAT, TMELT, TPIN, UPIN, KFUEL, CFR, and TFRAGLIMT.

Verification

The parity plots for all predicted percentiles of explosion impulses were plotted and demonstrated good agreement between SEIM FM and SEIM SM. In the Figure 3.165 we demonstrate the parity plots for 95% of the explosion impulse, as an example. The linear correlations coefficients (R^2) for the 95% of the pressure impulse at the wall training and testing data sets are 0.921 and 0.921 respectively.

Training data set

Testing data set

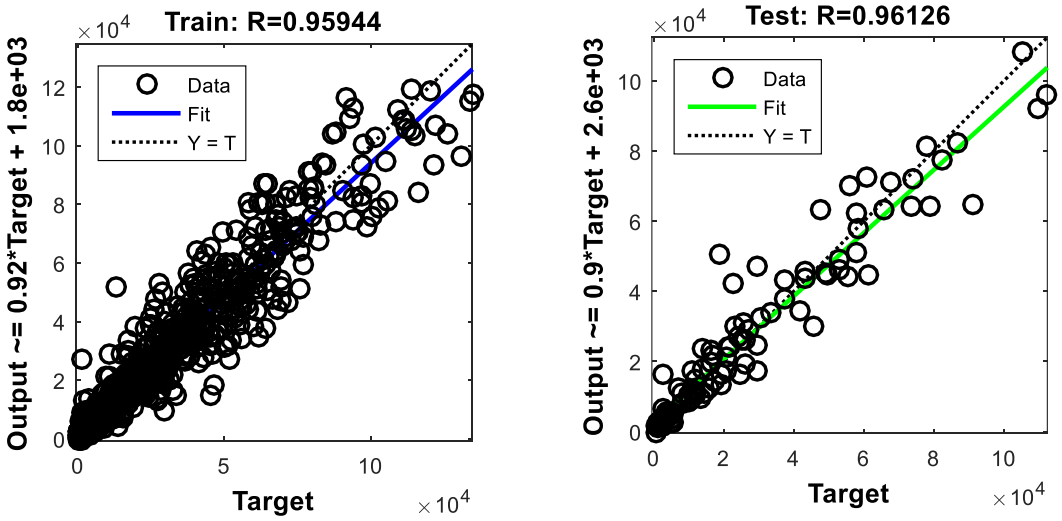

Figure 3.165. Parity plots for the 95% of the explosion impulse at the center of the drywell base

The model output distribution for different percentiles of the explosion impulse is demonstrated in the Figure 3.166. The data is obtained assuming uniform distribution for all input parameters. Explosion impulses at the containment base are generally higher than those at the pedestal wall. The reason is that the distance from the epicenter of the explosion to the side walls is generally larger than to the pool bottom.

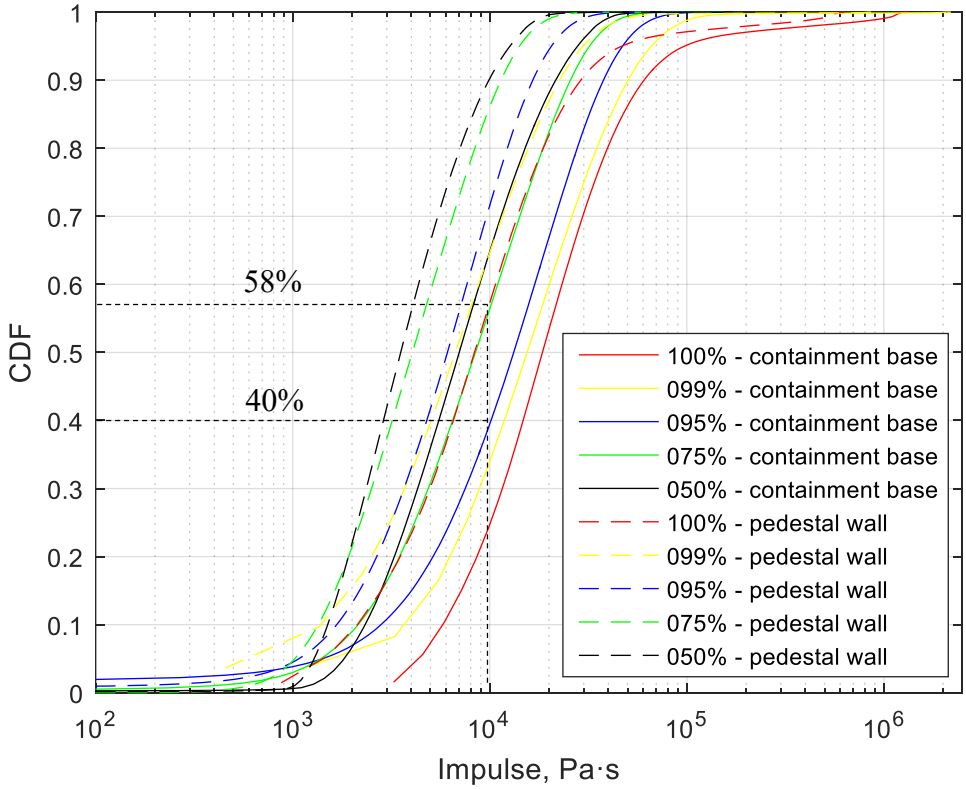

Figure 3.166. Distribution of the explosion impulse at the containment base and pedestal wall predicted by the surrogate model.

In the further analysis we consider 95% of the CDF of explosion impulses at the pedestal wall and containment base for risk assessment. Higher/lower values of the percentile can be considered, depending on the decision making criteria. As an example, the data in the Figure 3.166 can be interpreted in the following way:

1. At least 5% of the impulses at the pedestal wall will exceed 10 kPa·s in 58% of all possible melt release scenarios.
2. At least 5% of the impulses at the containment base will exceed 10 kPa·s in 40% of all possible melt release scenarios.

If all scenarios leading to steam explosion are equiprobable, then the plots in Figure 3.166 can be used to assess the conditional containment failure probability. For example, if fragility of the pedestal wall is 50 kPa·s, then conditional failure probability is $(1-0.9998)\cdot(1-0.95) = 10^{-4}$ for 95% percentile and $(1-0.8953)\cdot(1-0.99) = 10^{-3}$ for 99% percentile. For 80 kPa·s fragility limit the respective conditional failure probabilities are $(1-0.9960)\cdot(1-0.95) = 2.0\cdot10^{-4}$ and $(1-0.9725)\cdot(1-0.99) = 2.75\cdot10^{-4}$. These numbers are similar to 10^{-3} value that was estimated in the APRI-4 report for Swedish BWRs.

Comparison of SM and FM

Comparison of CDFs of explosion impulse at the pedestal wall and at the base of the

containment for two inputs: (i) training set, filtered from numerically failed cases, and (ii) prediction set obtained with random sampling are shown in the Figure 3.167. There is a good agreement between TEXAS and SM for the same training input dataset. However, for a randomly generated input data the SM predicts on average higher impulses. This is attributed to the combined effect of slightly larger mean values of the three most influential parameters in the random dataset: jet radius, melt superheat and melt release velocity (see Table 3.30).

In order to further verify that developed SM has properly captured physical behavior of the full model we provide a comparison of dependences of predicted impulses on separate parameters (Figure 3.168). The SM demonstrates a physically sensible response to the changes in the input parameters. Remarkably, the SM has captured the expected dependence between melt superheat (TPIN-TMELT) and explosion impulse in the ranges of parameters which were only sparsely covered in the filtered training data set.

Table 3.30: Mean values of input parameters in different input datasets

Parameter	**Units**	**Training dataset**		**Random**
		before filtering	**after filtering**	
RPARN	m	167.4	157.9	167.5
TPIN-TMELT	ºC	475.1	343.1	475.5
UPIN	m/s	4.498	4.183	4.496

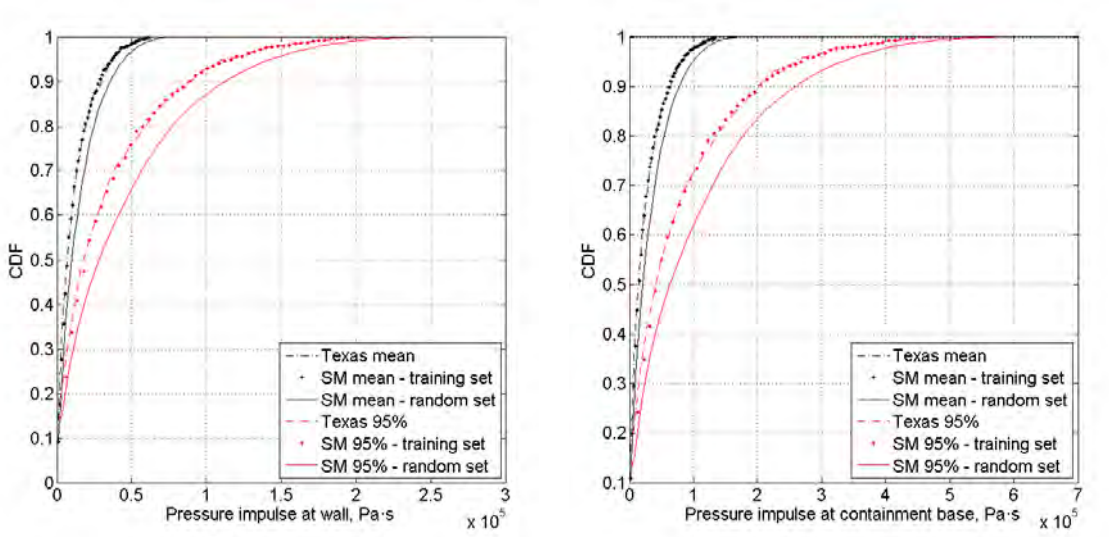

a b

Figure 3.167. CDFs of explosion pressure impulse at pedestal wall (a) and at containment base (b) by TEXAS, SM with the training input and SM with a random input

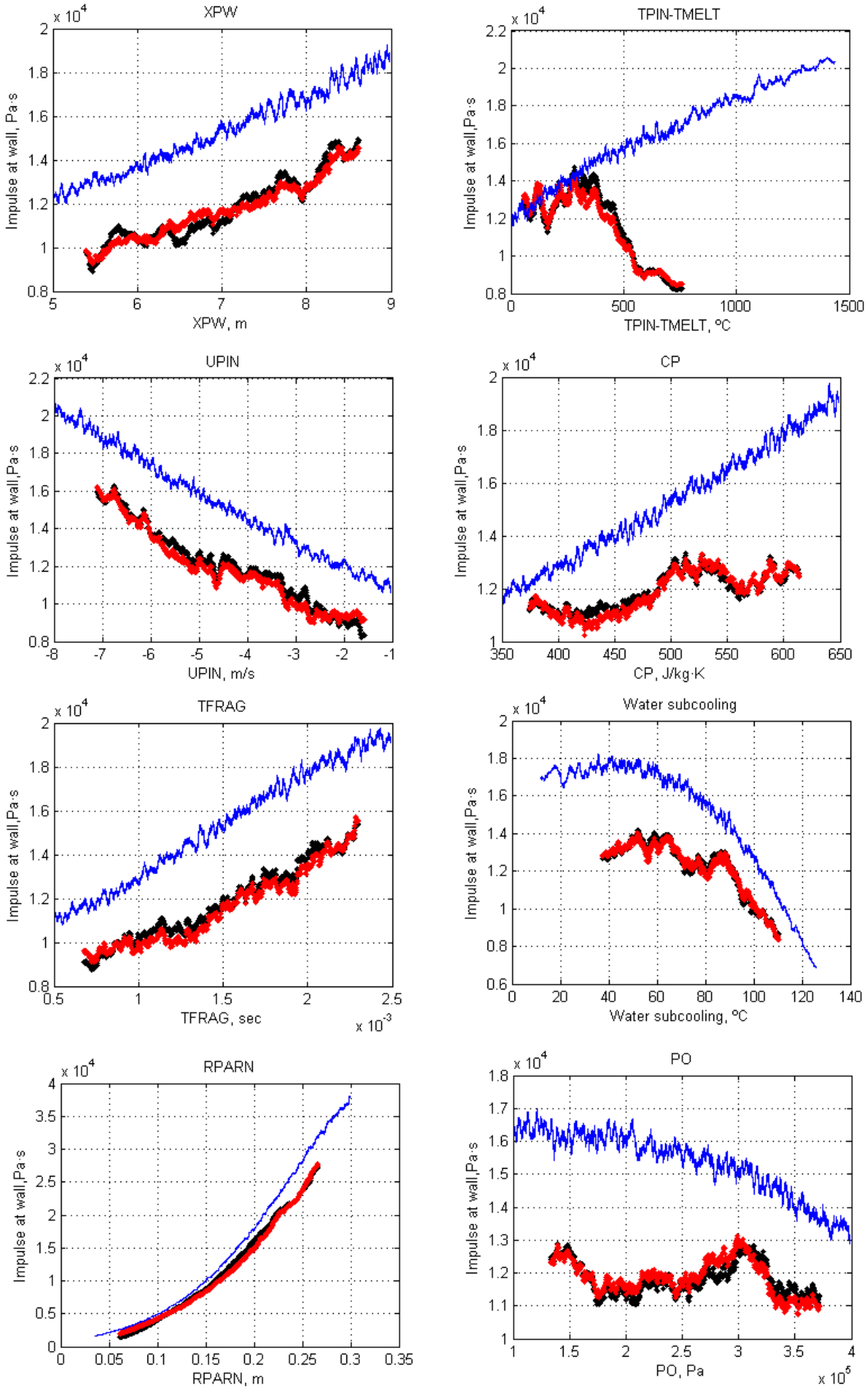

Figure 3.168. Comparison of SM and FM predicted impulses at the pedestal wall (blue – SM with random input; red – SM with training input; black – TEXAS with training input)

3.8.5 **Example application of SEIM SM**

As an example of the application of the steam explosion surrogate model we consider SERENA-2 BWR benchmark exercise. The values of the model input parameters are provided in Table 3.31. Parameters selected as aleatory (such as jet diameter, melt superheat, melt release velocity, density etc.) are varied by ±5%. Deterministic and intangible parameters (cfr and tfraglimt) are varied within their full ranges. For the uncertainty propagation we use uniform distribution for all input parameters, random sampling assuming independency of the parameters within their ranges.

Results of uncertainty propagation are presented (Figure 3.169) in the form of P-boxes. Each P-box is defined by a pair of bounding distributions. The overall slant of P-box characterizes the effect of aleatory uncertainties. The horizontal distance between the distributions characterizes the effect of epistemic uncertainty. Considering that fragility of the pedestal wall is on the order of 6 kPa·s due to failure of non-reinforced hatch door, regardless of the influence of epistemic modelling uncertainty the containment is expected to fail. On the other hand, if the hatch doors leading to the containment will be reinforced to the level of 50 kPa·s, no damage to the containment wall is expected, again regardless of the modelling uncertainty.

The maximum impulse at the containment base is ~70 kPa·s which provides a ~10 kPa·s margin for assumed fragility of the containment base on the order of 80 kPa·s. It is instructive to note that code to code comparison performed in SERENA-2 was done without quantification of the aleatory and epistemic uncertainties that for our model can lead to variation of the output in the range of 20 and 45 kPa·s respectively.

Table 3.31: Input parameters and their ranges for SERENA-2 BWR exercise calculations.

Input parameters	BWR SERENA	BWR TEXAS	Range (±5%)		Parameter type
		average	min	max	
Scenario parameters					
Melt properties					
Density liquid [kg/m^3]	8000	8000	7600	8400	aleatory
Thermal conductivity [W/m/K]	2.88	2.88	2.74	3.02	aleatory
Cp – liquid [J/kg/K]	510	510	485	535	aleatory
Cp – solid [J/kg/K]	450	-	-	-	aleatory
Latent heat [J/kg]	320000	320000	304000	336000	aleatory
Tsolidus [K]	2840	2840	-	-	aleatory
Tliquidus [K]	2870	-	-	-	aleatory
Surface tension [N/m]	0.45	0.5	-	-	-
Emissivity [-]	0.79	0.78	-	-	-
Dynamic viscosity [Pa/s]	0.008	-	-	-	-
Melt release conditions					
Initial Melt temperature [K]	80 K superheat	80	76	84	aleatory
Melt jet diameter [m]	0.30	0.30	0.285	0.315	aleatory
Melt mass [kg]	40 000	-	-	-	
Containment conditions					
Initial pressure [MPa]	0.3	0.3	0.285	0.315	aleatory

Initial gas temperature [K]	363 (90°C)	333	316	350	aleatory
Initial water pool temperature [K]	333 (60°C)	333	316	350	aleatory
Water pool depth [m]	7.2	7.2	6.84	7.56	aleatory
Free fall height of jet in atmosphere [m]	9.0	5.8	5.44	6.16	aleatory
Triggering [on centreline]	Not applicable	-	-	-	
Melt release velocity (UPIN), [m/s]	-	-4	-4.20	-3.80	aleatory
Intangible and deterministic parameters					
tfraglimt, [ms]	ms	0.5÷2.5			epistemic
cfr	-	0.002÷0.0025			epistemic

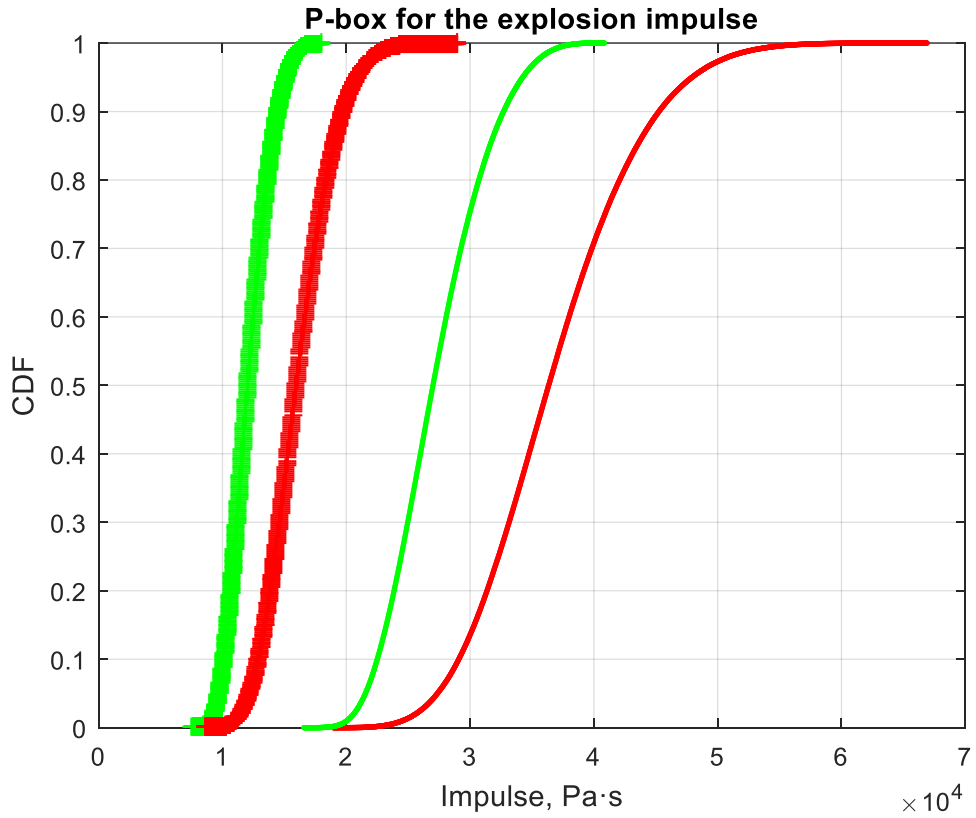

Figure 3.169: P-boxes for the explosion impulse at the containment base (right pair of lines) and pedestal wall (left pair of lines). Green – lower bound CDF, red – upper bound CDF.

3.8.6 **Summary and conclusions**

The goal of this work was development of a fast numerical tool (surrogate model) that can be used for the assessment of the risk of containment failure in Nordic type BWR due to steam explosion. Three primary tasks have been accomplished: (i) development of the Full Model, (ii) generation of the Full Model solution database, and (iii) development of the surrogate model.

We utilized TEXAS-V to build the Full Model (FM) for the assessment of the steam explosion energetics in Nordic type BWRs and combine it with a simplified impulse propagation approach.

Extensive simulations using the TEXAS-V revealed that explosion impulse is a chaotic

function of the triggering time – phenomena that has an important impact on both risk analysis and interpretation of experimental results. Specifically, it was found that explosion impulse can change 50 times within just a 110 ms time window. It is instructive to note that in the steam explosion experiments the aleatory uncertainty due to the influence of the triggering time is also expected to be significant. Proper statistical treatment with multiple repletion of the tests at the same melt release conditions is necessary in order to measure the effects of the other experimental parameters.

We have further, implemented an approach to encompass the chaotic nature of the explosion impulse by characterizing its statistical distribution. The objective is double fold, first it imposes well-posedness on the response function and second allows characterization of the explosion impulse in terms of confidence intervals and confidence levels – approach highly beneficial for risk assessment.

After ensuring model physical well-posedness we proceed with detailed sensitivity study followed by parameter screening leaving 13 most important parameters. The model was then sampled to generate a large database of solutions (1500 premixing sets comprised of 455K of premixing/explosion calculations). Numerically failed calculations were filtered from the database. Physical sensibility of the FM model response to variation of the input parameters was verified in a statistical sense. The database was used for the development of the surrogate model. The surrogate model was implemented using ANN. SM and FM were then systematically compared and results were found to be in a satisfactory agreement.

There are several issues that still should be addressed:

1. Melt releases with multiple jets.
2. Multiple consecutive steam explosions.
3. Effect of crust formation around melt particles on the energetics of the steam explosions.
4. Generation of non-condensable gases during premixing.
5. Validation of the explosion propagation model.

Chapter 4. Risk Analysis Results using ROAAM+ Framework

4.1 Results using ROAAM+ Framework

The goal of this section is to illustrate comprehensive uncertainty analysis for identification and clarification of (i) main contributors to the uncertainty and risk; (ii) importance of the dependencies between different accident stages in different accident progression scenarios; (iii) the needs for further refinement of the knowledge and tools (models, experimental data, etc.)

We discuss key elements of the reverse analysis with the failure domain (FD) identification and forward analysis with estimation of failure probability (FP) for ex-vessel steam explosion and coolability.

4.1.1 Description of the framework

The surrogate models implemented in the framework (see Figure 2.3) and their role is detailed in the Table 4.1. Four techniques were used for implementation of the SMs: (i) mapping (based on mapping of the FM solution to a grid in the space of the input parameters); (ii) polynomial (scaling analysis and data fitting); (iii) physics based uses simplified modelling of the phenomena; (iv) Artificial Neural Networks (ANN is based on complex regression analysis). Failure criteria are determined for SEIM and DECO.

Table 4.1: Surrogate models of the ROAAM+ framework

SM	Type	Role
CORE	Mapping	Given timings of ADS and ECCS recovery provides time, composition and mass of core relocation and conditions in the lower drywall: pressure, pool temperature and depth
Vessel failure	Polynomial	Given mass and composition of the debris in the lower head computes timings of the IGT, CRGT and vessel failures and corresponding mass and composition of liquid melt available for release
Melt release	Physics based	Given timings and mode of lower head failure computes conditions of melt release, i.e. ablation of the breach, rate and duration of the release, thermal properties of the melt
SEIM	ANN	Given conditions of melt release and LDW characteristics, returns three explosion impulses and three values of containment capacity
DECO	Physics based	Given conditions of melt release and LDW characteristics, returns dryout heat flux and max debris bed heat flux

At given melt release conditions SEIM surrogate model estimates characterizes loads by mean and standard deviation of the explosion impulses predicted by TEXAS-V for different triggering times. The SEIM failure domain is determined for three fragility

limits: 6, 50 and 80 kPa·s. These roughly correspond to the order of magnitudes of fragility limits for non-reinforced hatch door, reinforced hatch door and reactor vessel pedestal respectively.

Current implementation of DECO is a combination of two surrogate models: (i) spreading of particles during sedimentation in the pool which estimates the slope angle of the formed debris bed; (ii) debris bed coolability (returning actual and critical heat flux for given debris bed configuration).

Forward and reverse analysis (see Figure 2.3, Chapter 2.2) is currently performed by considering two distributions (optimistic and pessimistic) for the intangible parameters. Optimistic distribution is determined such that it decreases the probability of high loads. Pessimistic distribution decreases probability of low loads.

The failure domain is constructed in the space of the input parameters (input space) partitioned into a finite number of cells. Every cell is characterized by a unique combination of the input parameters ranges. The output of the SM is sampled in each cell (by varying deterministic and intangible parameters). The framework compares loads against capacity and renders every computed case to a failure or success. The number of "fail" and "success" cases is counted in each cell, weighted by corresponding probability density functions of deterministic and intangible parameters and normalized to provide conditional failure probability which is compared to the screening probability. The cells where conditional failure probability exceed screening level are grouped into a "failure domain" indicating conditions at which the mitigation strategy fails. For visualization we introduce four-colored failure domain map (see Figure 4.1) where color-code is defined as in Table 4.2

Table 4.2: Definition of failure domains

Failure domain map	Definition	Comments
Red	$CCDF(P_f > 10^{-3}) > 95\%$	Failure probability is larger than 10^{-3} for 95% of possible distributions of the intangible parameters.
Green	$CCDF(P_f > 10^{-3}) < 5\%$	Failure probability is larger than 10^{-3} for only 5% of possible distributions of the intangible parameters.
Blue	$5 \leq CCDF(P_f > 10^{-3}) < 50\%$	Failure probability is larger than 10^{-3} in 5-50% of possible distributions of the intangible parameters.
Purple	$50 \leq CCDF(P_f > 10^{-3}) \leq 95\%$	Failure probability is larger than 10^{-3} in 50-95% of possible distributions of the intangible parameters.

The greed domain represent the area where SAM is successful and containment failure (due to ex-vessel steam explosion or ex-vessel debris coolability) is physically

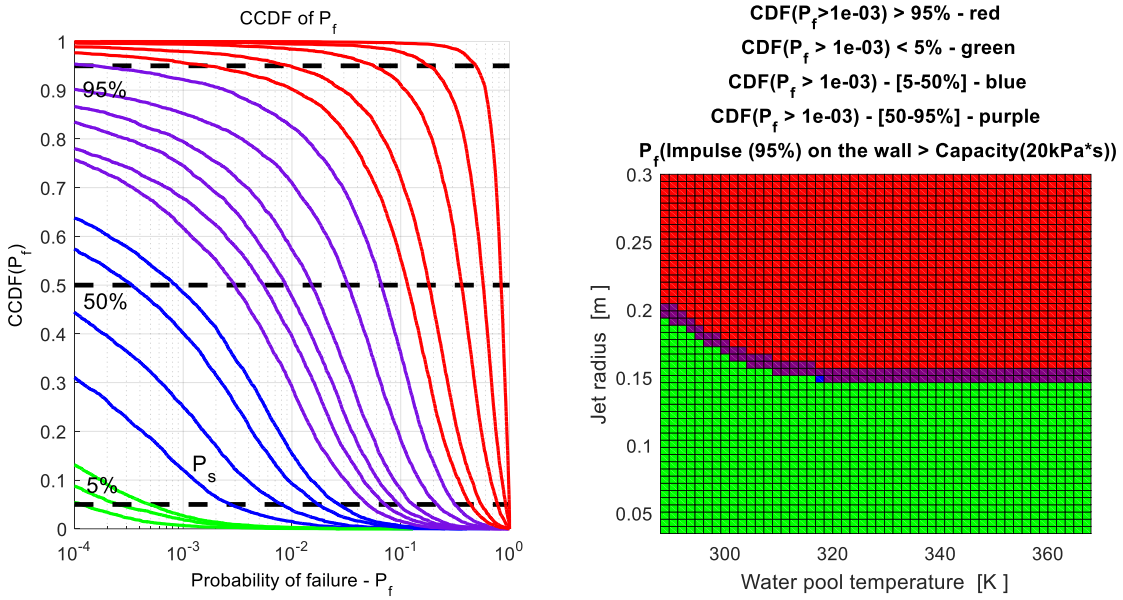

a b

Figure 4.1: Example of the CCDFs of failure probability (a) taken from the first vertical line in failure domain map (b).

unreasonable [27] with 95% confidence level, the red domain represents the area where within 95% confidence level the failure imminent (i.e. failure probability exceed physically unreasonable threshold). The domains colored purple and blue represent the area of scenario space where the outcome depends on uncertainty coming from model deterministic and intangible parameters and their distributions.

4.2 Reverse Analysis for Steam Explosion using SEIM Surrogate Model

Different scenarios of melt release have been considered in the analysis. The failure domain is determined in the space of the SEIM input parameters: XPW – water pool depth, UPIN – melt jet release velocity; RPARN – Jet radius.

Results suggest that in case of non-reinforced hatch door (fagility limit 6 kPa·s), the failure of the containment is imminent (red domain) for most of possible combinations of scenario parameters (RPARN, XPW and UPIN). If the hatch door is reinforced (50 kPa·s) there is no risk of containment failure (see Figure 4.2b,d,e and Figure 4.3b,d,e). Note that the jet diameter is limited to Ø300 mm in this analysis. For larger size jets, the risk of containment failure will be larger.

For assessment of the risk of containment failure in Swedish type BWRs we employ failure domains approach. Two scenarios of melt release are considered: release of oxidic or metallic melt. Release of metallic melt was further split into two subcases: Case 01 with up to 1150 K melt superheat and Case 02 with maximum melt superheat of 300 K (the same as for oxidic melt).

Classification of the parameters and their ranges are provided in the Table 4.3. Estimated failure domain maps are given in the Figure 4.2 and Figure 4.3. The maps were estimated taking 95% of the explosion impulse, 0.001 as the screening probability. The color map used in the failure domain maps is explained in the Figure 4.1.

Table 4.3: Classification and ranges of model input parameters used for estimation of failure domain maps

#	Parameter	Units	Oxydic		Metallic (Case 01 / Case 02)	
Name	Meaning		min	Max	min	max
Scenario parameters						
RPARN	Initial jet radius	m	0.035	0.150	0.035	0.150
UPIN	Melt release velocity	m/s	-8	-1	-8	-1
XPW	Water level	m	5	9	5	9
Deterministic and intangible parameters						
PO	System pressure	Bar	100000	400000	100000	400000
CP	Fuel heat capacity	J/kg·K	490	650	350	490
RHOP	Fuel density	kg/m3	7900	8500	7500	7900
PHEAT	Fuel heat capacity	J/kg	300000	400000	250000	300000
TMELT	Fuel melting point	K	2800	2800	1650	1650
TPIN	Melt temperature	K	2810	3150	1660	2800 / 1966
TLO	Water temperature	K	288	368	288	368
KFUEL	Fuel thermal conductivity	W/m·K	2	6	6	32
CFR	Proportionality constant for the rate of fuel fine fragmentation	-	0.00200	0.00270	0.00200	0.00270
TFRAGLIMT	Fragmentation time	ms	0.00050	0.00250	0.00050	0.00250

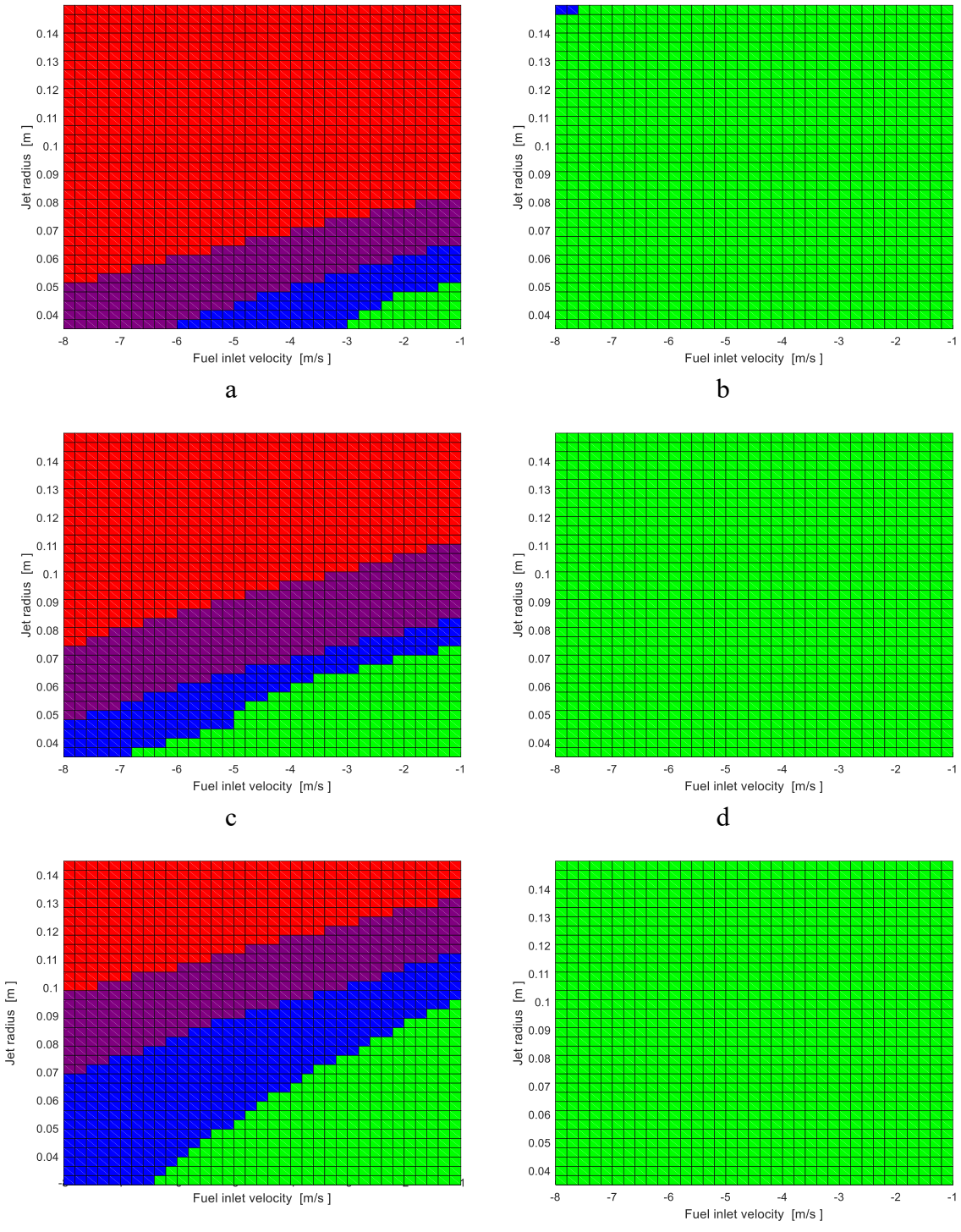

Figure 4.2: Failure domain maps in terms of melt release velocity and jet radius (a and b – scenario of oxidic melt release for 6 kPa·s and 50 kPa·s fragility limit; c and d – scenario of metallic melt release Case 01 for 6 kPa·s and 50 kPa·s fragility limit; e and f – scenario of metallic melt release Case 02 for 6 kPa·s and 50 kPa·s fragility limit)

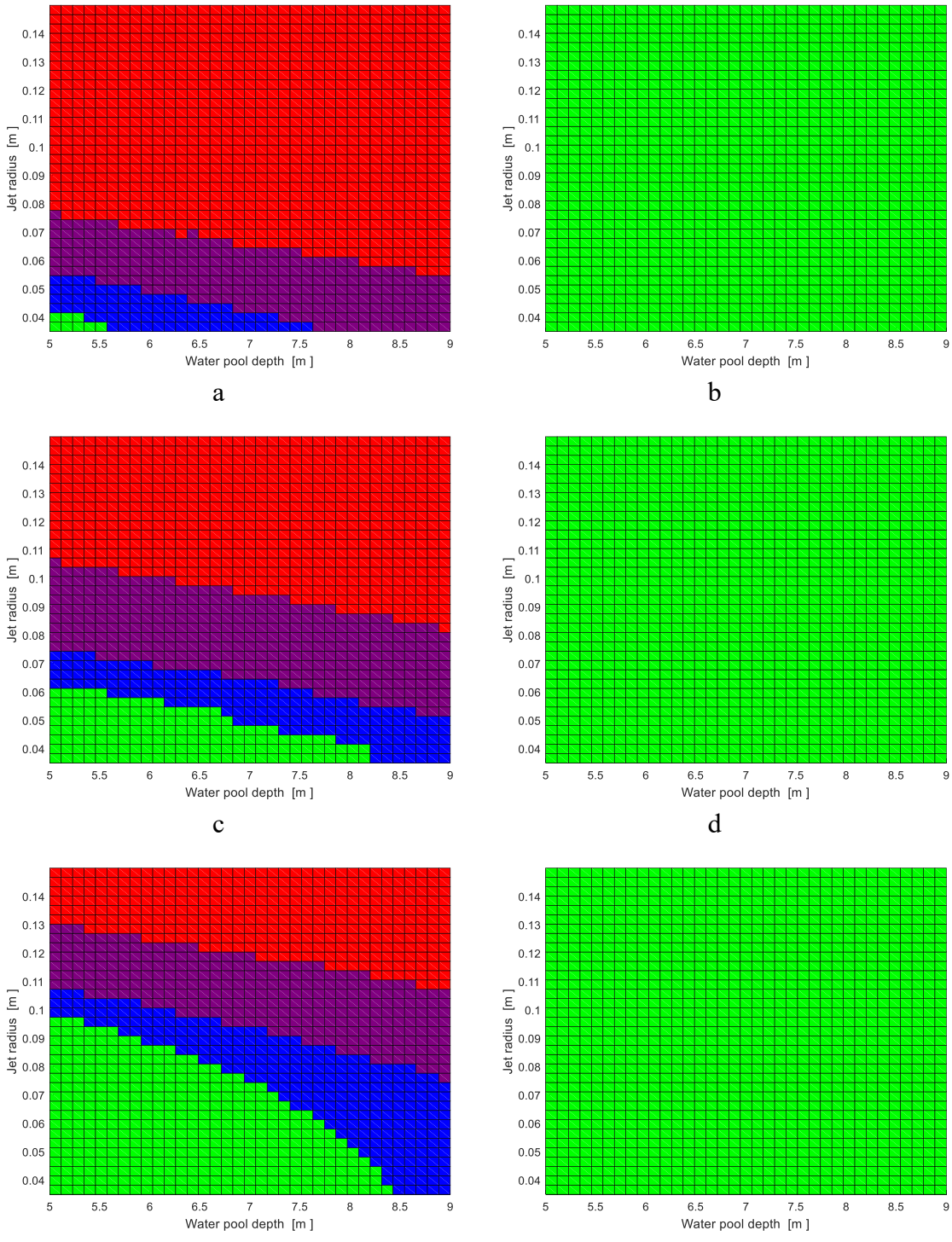

Figure 4.3: Failure domain maps in terms of water level and jet radius
(a and b – scenario of oxidic melt release for 6 kPa·s and 50 kPa·s fragility limit;
c and d – scenario of metallic melt release Case 01 for 6 kPa·s and 50 kPa·s fragility limit;
e and f – scenario of metallic melt release Case 02 for 6 kPa·s and 50 kPa·s fragility limit)

Comparison of Case 01 vs Case 02 (see Table 4.3), i.e. Figure 4.2c vs Figure 4.2d and Figure 4.3c vs Figure 4.3d, suggests as expected that with increase of melt superheat

failure domain increases. Current version of the TEXAS-V SM predicts larger failure domain for the oxidic melt than for the metallic one (compare Figure 4.2a vs Figure 4.2c and Figure 4.3a vs Figure 4.3c). It is instructive to note that there is no modelling of crust formation effect on the explosion energetics in TEXAS-V, and melt emissivity was not considered in development of the current SM (because it was identified as less important parameter in the preliminary sensitivity analysis [220]).

4.3 Results of Reverse Analysis for Debris Bed Coolability

4.3.1 Sensitivity Analysis for Debris Coolability and Spreading in the Pool

According to the general approach for reverse analysis in ROAAM+ framework, failure domain identification starts with model sensitivity analysis to identify the most influential parameters for both standalone and coupled through the framework models.

In this section we discuss sensitivity analysis for Debris Bed Coolability SM that has been carried out in order to evaluate the importance of the DECO SM input parameters and their ranges on the output. Figure 4.4 represents the results of sensitivity analysis using Morris method for the DECO SM output HF-DHF (MW/m^2) (the difference between heat flux and dryout heat flux) for the "Base Case" scenario and ranges (see Table 4-4). The results indicate the dominant effect of DPAR and porosity (particle diameter and porosity) together with tsub (water subcooling) on the results. Initial water subcooling affects time delay for onset of the debris bed spreading and thus height of the debris bed.

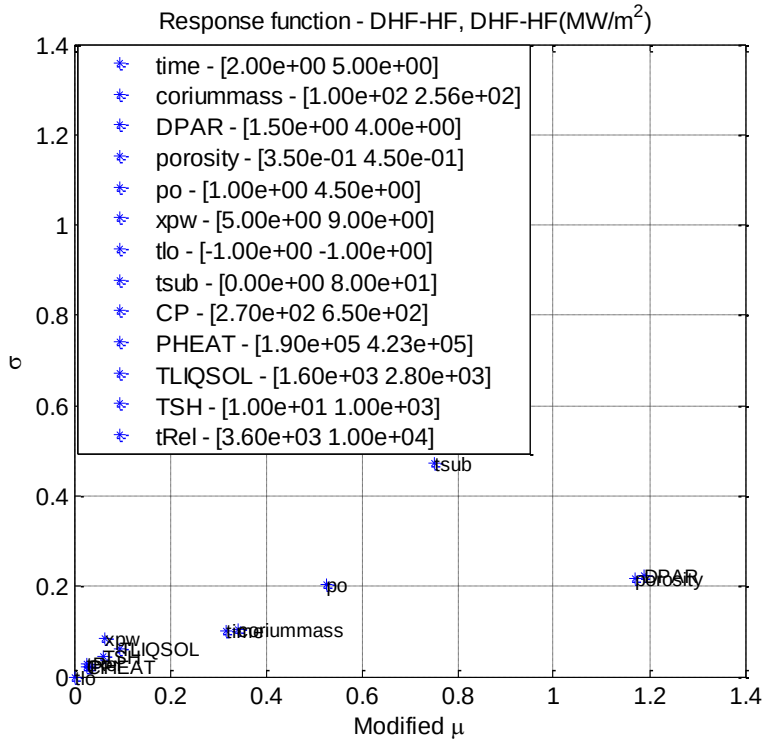

Figure 4.4. Morris diagram for Debris bed coolability input parameters (Base Case)

4.3.2 Failure Domain Analysis for Debris Coolability and Spreading in the Pool

Figure 4.5 presents the results of failure domain analysis for DECO SM. The figure illustrates the effect of the screening probability in the space of water subcooling and debris porosity. Note that only spreading in the pool is considered in this model currently.

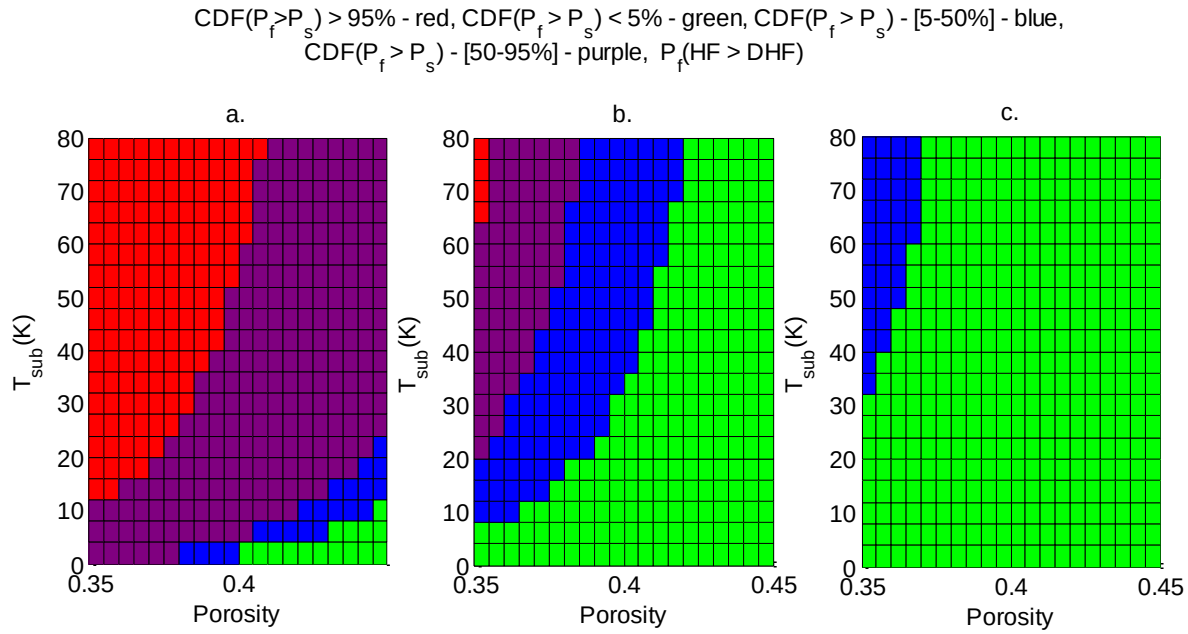

Figure 4.5. Failure domain analysis for DECO SM with different values of screening probability P_s, a. $P_s = 10^{-3}$; b. $P_s = 0.5$; c. $P_s = 0.99$

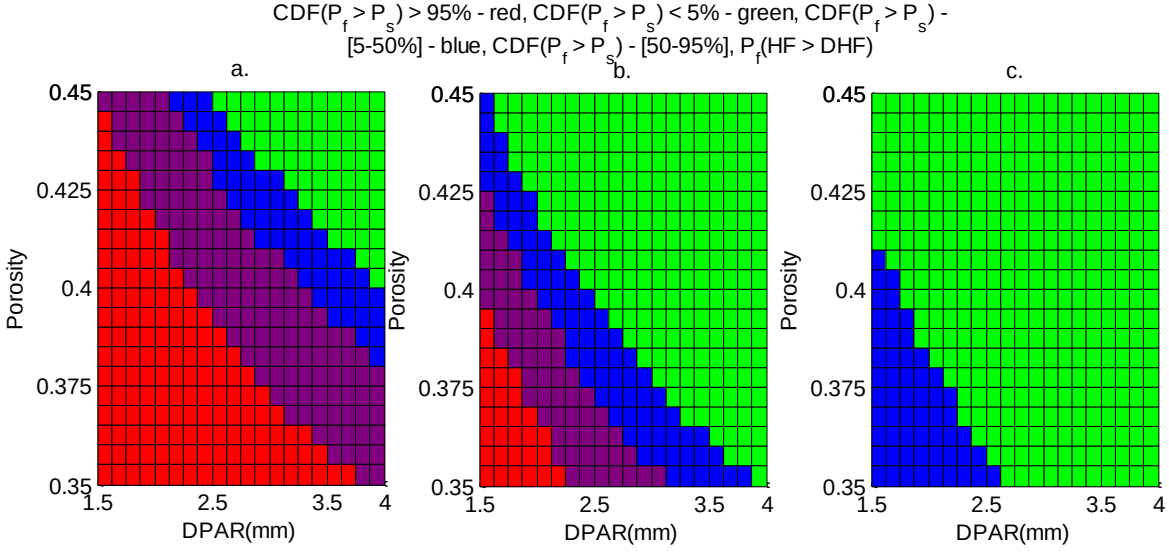

Figure 4.6. Failure domain analysis for DECO SM with different values of screening probability P_s, a. $P_s = 10^{-3}$; b. $P_s = 0.5$; c. $P_s = 0.99$

The Figure 4.5a can be interpreted as follows: the failure (HF>DHF) probability P_f does not exceed screening frequency $P_f \leq P_s = 10^{-3}$ only for scenarios high debris porosity (>40%) and low water pool subcooling (<5-10 K) for more than 95% possible combinations of distributions of uncertain parameters. In other words, green domain in

Figure 4.5a can be considered as “safe” where “possibility” of failure is extremely small. The necessity of failure is illustrated in Figure 4.5c. With small debris porosity (<38%) and high water subcooling (>30K) probability of failure exceed $P_s = 0.99$ in approximately 5-50% of possible combinations of the distributions of the uncertain parameters.

Figure 4.6 presents similar results but in the space of particle size and porosity. Formation of a non-coolable debris bed is of low possibility for porosity >0.4 and effective particle size >2.5 mm (Figure 4.6a). High necessity of failure is observed for smaller particles and porosity Figure 4.6b,c.

Table 4-4: DECO SM ranges for the “Base Case”

Name	Description	Range	Units
Time	Time after SCRAM	[2-5]	Hours
coriummass	Debris mass in LP	[100-256]	Tons
DPAR	Particle diameter	[1.5-4]	Mm
Porosity	Debris porosity	[0.35-0.45]	-
PO	System pressure	[1-4.5]	Bar
XPW	LDW water pool depth	[5-9]	M
Tsub	Water pool subcooling	[0-80]	K
CP	Fuel heat capacity	[270-650]	J/kg·K
PHEAT	Fuel latent heat	[1.9e5-4.23e5]	J/kg
TLIQSOL	Temperature of Liquidus\Solidus	[1600-2800]	K
TSH		[10-1000]	K
tRel	Duration of melt release	[3600-10000]	sec

Better knowledge about particle size and porosity would be the most effective means for reduction of the uncertainty in coolability. Further experimental studies can be carried out using corium simulant materials in DEFOR-S type experiments to assess the ranges of porosity for debris of prototypic morphology.

Water subcooling is a factor of severe accident scenario and its ranges can be reduced through modeling of different accident sequences. The effect of water subcooling on debris bed height is an epistemic uncertainty that can be reduced through

- further development of DCOSIM models and extensive validation and against PDS-P experiments;
- analysis of the accident sequneces and possible ranges of water subcooling.

Combining the modeling of particle spreading in the pool and particulate debris bed spreading after debris settling due to self-leveling phenomenon might be the most effective approach to reduction of the uncertainty in the assessment of the risks associated with porous debris bed coolability.

Among the other parameters only system pressure, mas of debris and time after SCRAM can noticeably affect the difference between decay heat flux and dryout heat flux. Uncertainty in mass of debris and time after SCRAM can be reduced through improved modeling of the melt release mode in MEM.

4.3.3 Reverse and Failure Domain Analysis using Combined SM on Debris Bed Coolability and Particulate Debris Spreading

Main results

The developed ANN-based SM of the coolability of debris bed with taken into account effect of bed self-leveling (particulate debris spreading) has been has been used to in reverse analysis to identify the failure domain. The input parameters and their varied ranges used in both, sensitivity study and FD identification, are provided in Table 4-5. The final results, namely the Morris diagram and identified FDs are shown respectively in Figure 4.4 and set of plots from Figure 4.8 till Figure 4.10.

There is an easily observable link between the Morris diagram and FD plots. Three most influencing input parameters identified from Morris diagram are (in the order of most influential first):

- Particle diameter (DPAR)
- Bed porosity (porosity)
- Initial bed heat-up rate (trat)

The failure domains are shown for any two combinations of the above listed parameters: porosity-DPAR (Figure 4.8); TRAT-DPAR (Figure 4.9) and TRAT-porosity (Figure 4.10). It is natural that highly porous debris bed composed of large particles should have higher probability to be coolable. Indeed, Figure 4.8 demonstrate this.

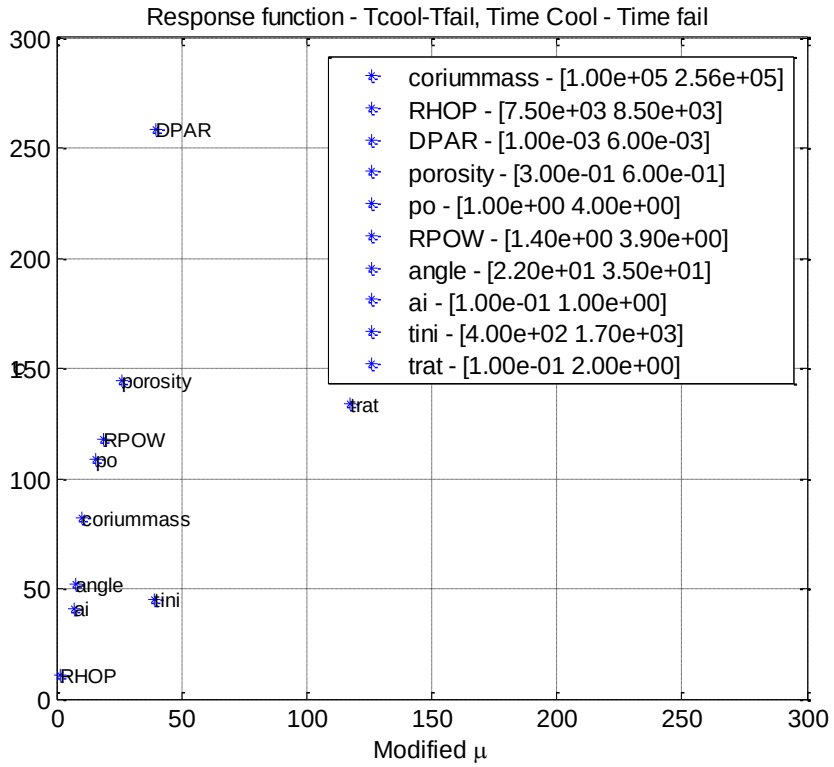

Figure 4.7. Morris diagram for coolability and self-leveling.

Table 4-5: SM ranges for the input parameters

	Name	Range		Description	Units
1	coriummass	1e5	2.5e5	Debris mass	Kg
2	RHOP	7500	8500	Fuel density	JKg/m3
3	DPAR	1e-3	6e-3	Particle diameter	m
4	porosity	0.3	0.6	Porosity	-
5	PO	1	4	LDW Pressure	bar
6	RPOW	1.4	3.9	Reactor Thermal Power	GW
7	angle	22	35	Critical angle or repose	degrees
8	ai	0.1	1.0	Initial angle factor	-
9	tini	400	1700	Initial temperature of settled particles	K
10	trat	0.1	2.0	Initial heat up rate	K

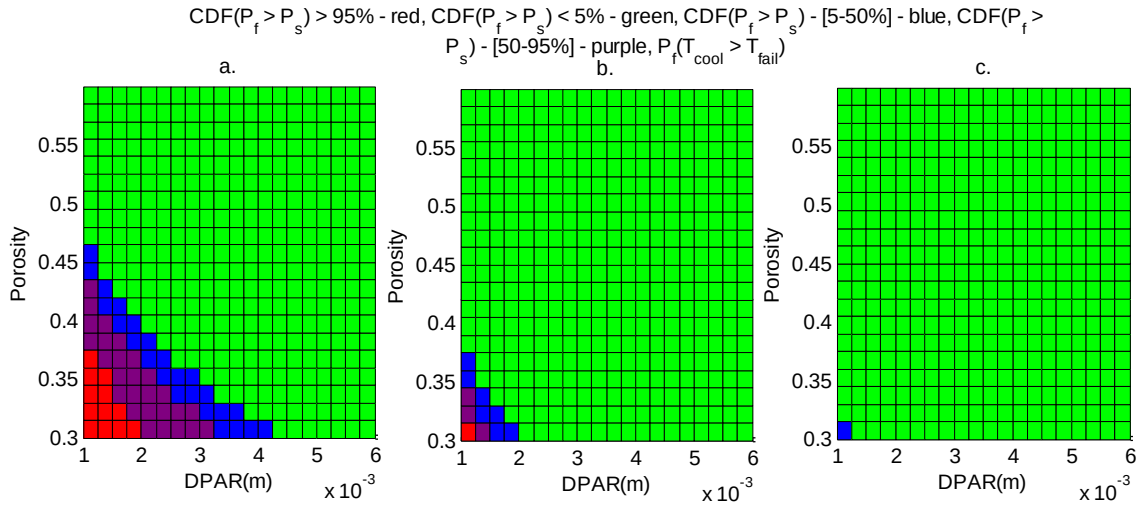

Figure 4.8. Failure domain analysis for PDS SM with different values of screening probability P_s, a. $P_s = 10^{-3}$; b. $P_s = 0.5$; c. $P_s = 0.99$

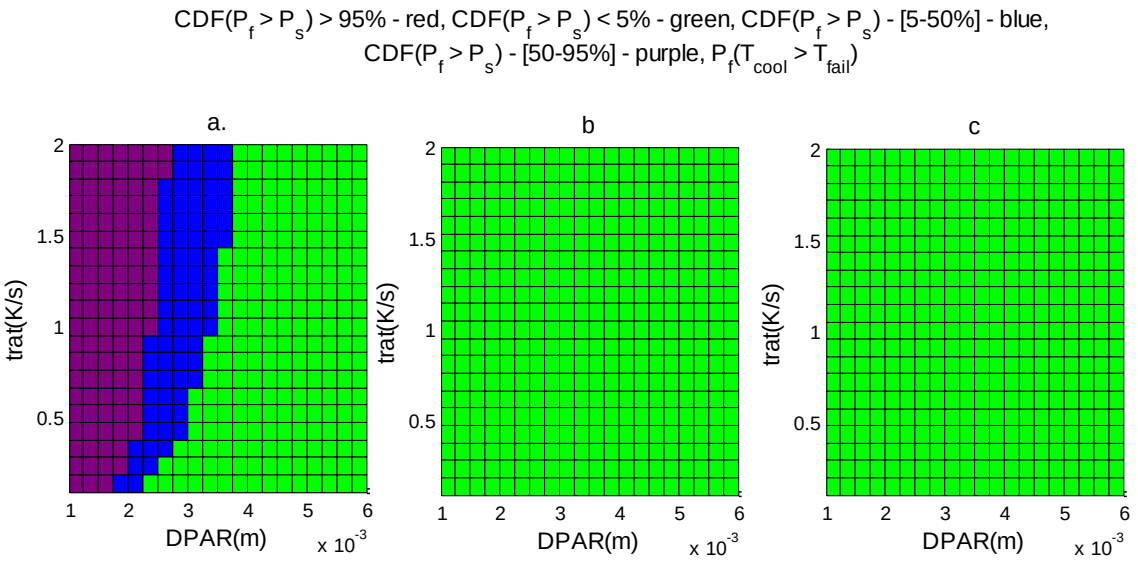

Figure 4.9. Failure domain analysis for PDS SM with different values of screening probability P_s, a. $P_s = 10^{-3}$; b. $P_s = 0.5$; c. $P_s = 0.99$

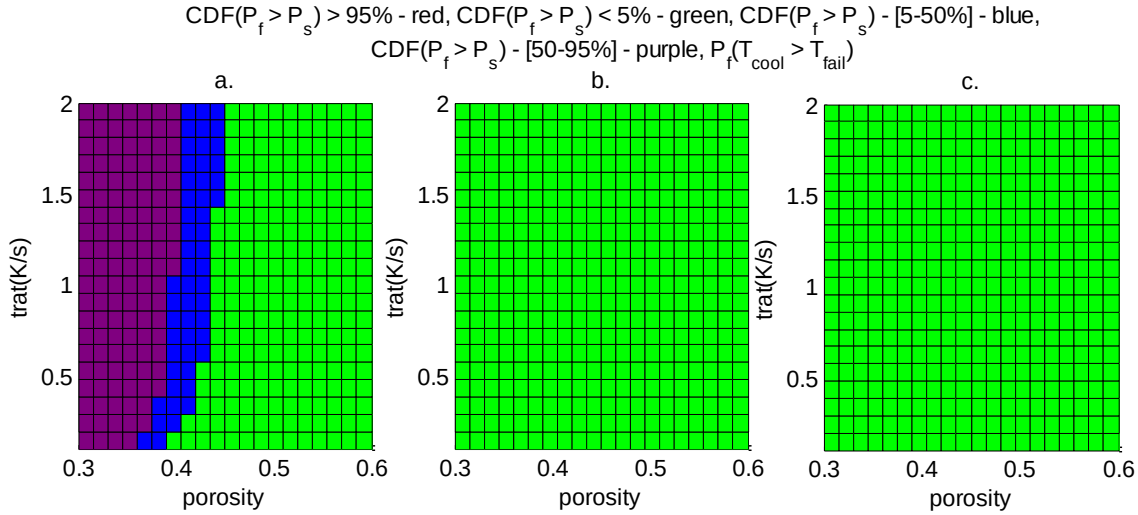

Figure 4.10. Failure domain analysis for PDS SM with different values of screening probability P_s, a. $P_s = 10^{-3}$; b. $P_s = 0.5$; c. $P_s = 0.99$

Effect of distribution selected for input PDF

With help of SM on combined coolability of the debris bed and self-leveling we have investigated the influence of different types of the distributions selected for PDFs of the input parameters. As an example, we demonstrate how typically used normal distribution (Figure 4.11a) can be different from another type, namely beta distribution (Figure 4.11b).

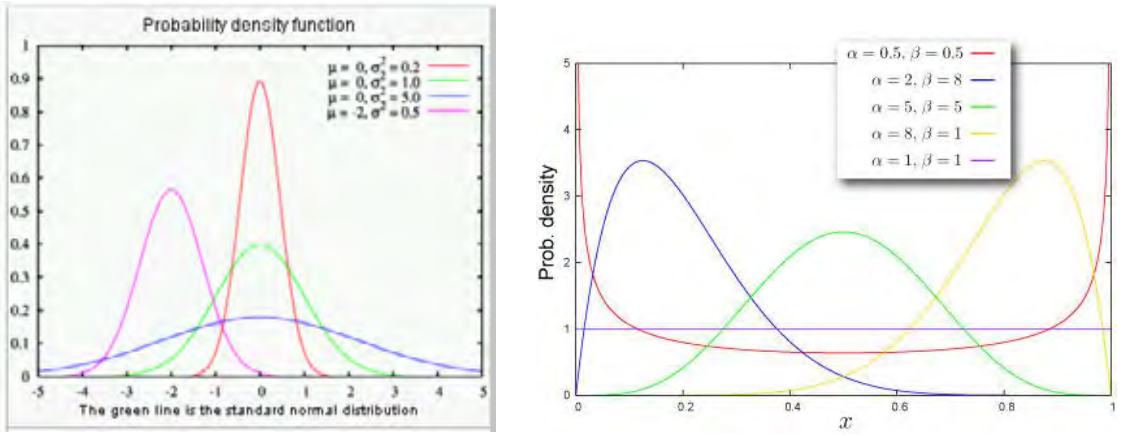

a) b)

Figure 4.11: Example of normal (a) and beta (b) distributions.

To quantify the influence of the distribution on the FD we have assumed and performed following steps:

- Consider the PDFs as source of uncertainty;
- Different families of the PDFs are determined by respective parameters;
- An independent sampling of those parameters is performed as any other input parameter;
- Two families of distributions are considered:
  - Truncated normal distribution characterized by mean μ and standard deviation σ
- Beta distribution characterized by two shape factors α and β

Table 4-6: Input and distribution parameters and their ranges.

Input parameter	Range	Uncertainty ranges for distribution parameters			
		Normal Distribution		Beta Distribution	
		Mean	Standard Deviation	Shape Parameter α	Shape Parameter β
Total Debris mass [tons]	10-250	10-250	28.9-250	0.01-100	0.01-100
Containment Pressure [Bar]	1-4	1-4	0.55-4	0.01-100	0.01-100
Initial angle factor [-]	0.1-1	0.1-1	0.12-1.0	0.01-100	0.01-100
Material density [kg/m^3]	7500-9000	7500-9000	1833-9000	0.01-100	0.01-100
Debris Bed Porosity [-]	0.3-0.6	0.3-0.6	0.1-0.6	0.01-100	0.01-100
Effective Particle diameter [mm]	1.0-6.0	1.0-6.0	0.77-6	0.01-100	0.01-100
Critical angle of repose at zero gas flow [degree]	22-35	22-35	6.3-35	0.01-100	0.01-100
Heat-up rate [K/s]	0.2; 1; 10 (no PDF for this parameter, fixed values are used)				

The nested Monte Carlo sampling method has been used to propagate the input and distribution uncertainties. The used ranges for both, input and distribution parameters are provided in Table 4-6. An equal probability of having any distribution parameter from the range was assumed.

The result of the Monte Carlo simulations are show in Figure 4.12, Figure 4.13 and Figure 4.14: Effect of the normal (a) versus beta (b) distribution types on failure probability for $\dot{T}_{rate}$=10 K/s.

corresponding to three fixed values of the bed heat-up rate (Table 4-6). Remarkably, as seen from these plots we conclude that:

- The selected family of the distributions has an apparent effect on the assessment of the failure probability;
- If a decision changes depending on selected family of the distributions and ranges of the parameters, it means that: additional information is necessary about those ranges and distributions in order to perform further safety analysis.

Further analysis on influence of the PDF distribution on resulting failure probabilities and FD in general is required.

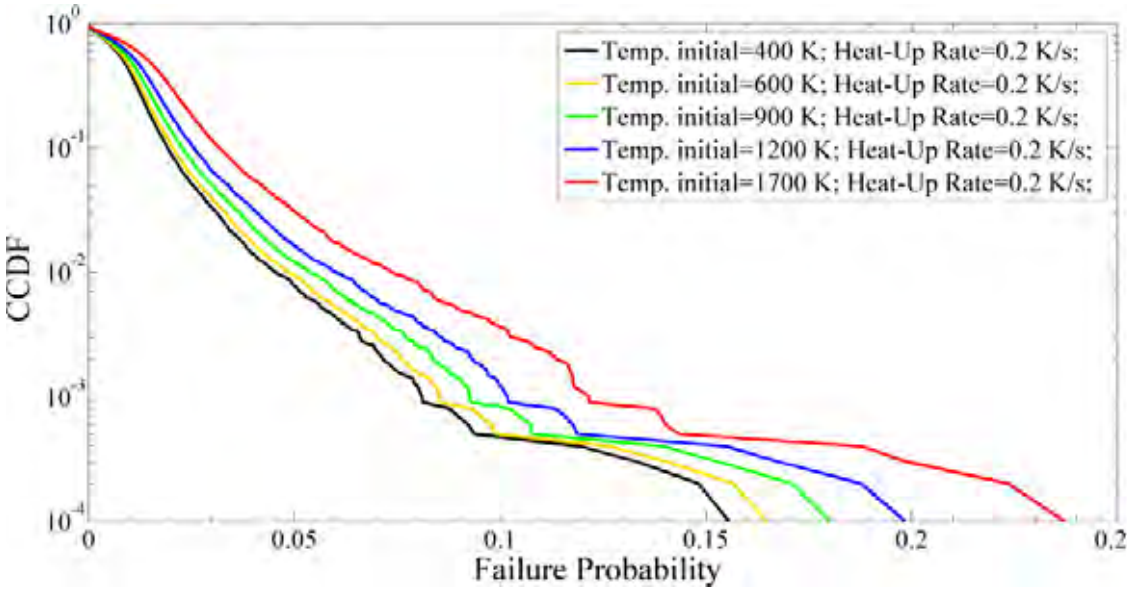

a) NORMAL

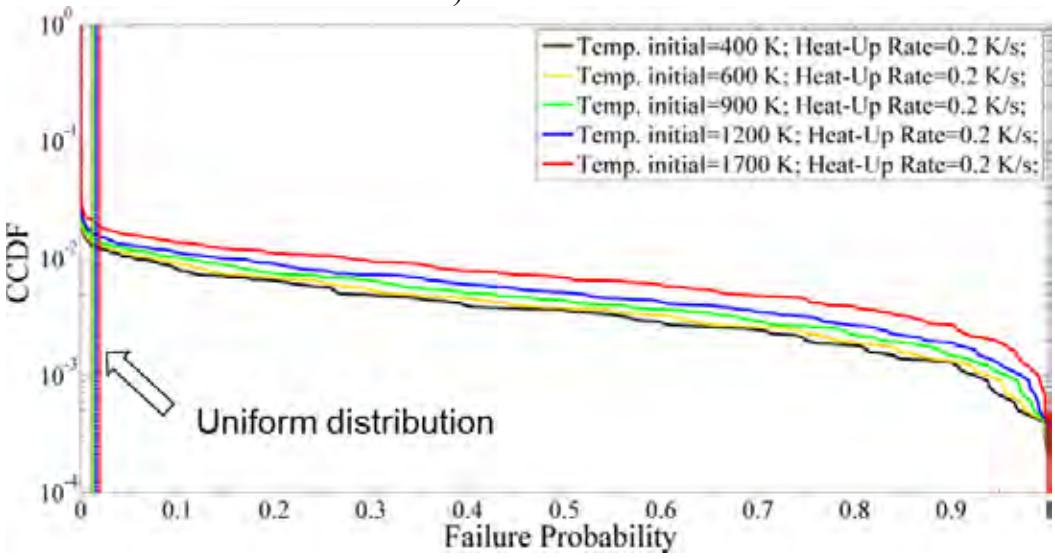

b) BETA

Figure 4.12: Effect of the normal (a) versus beta (b) distribution types on failure probability for $\dot{T}_{rate}$=0.2 K/s.

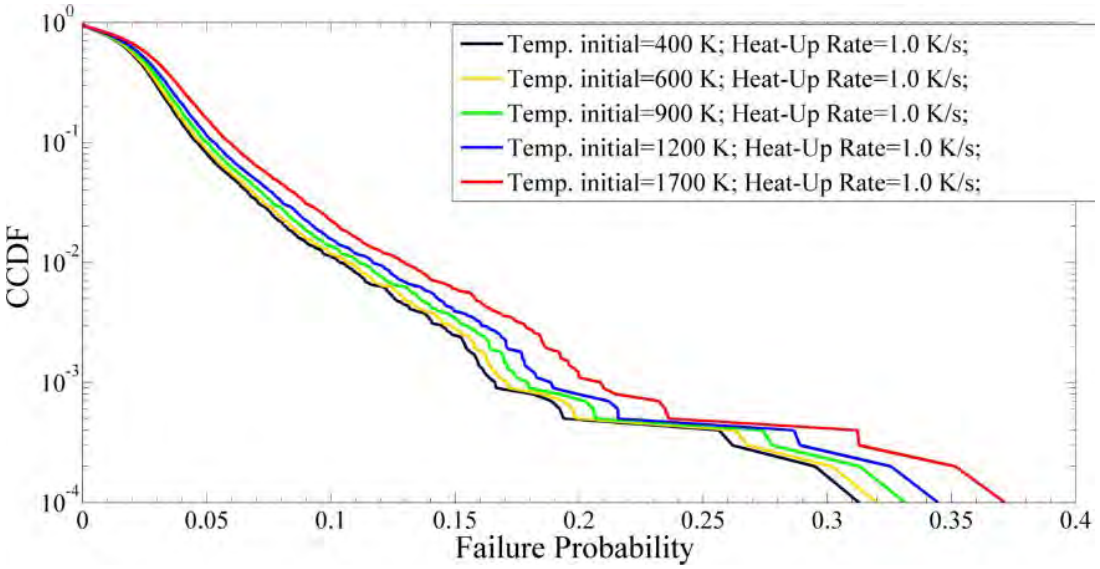

a) NORMAL

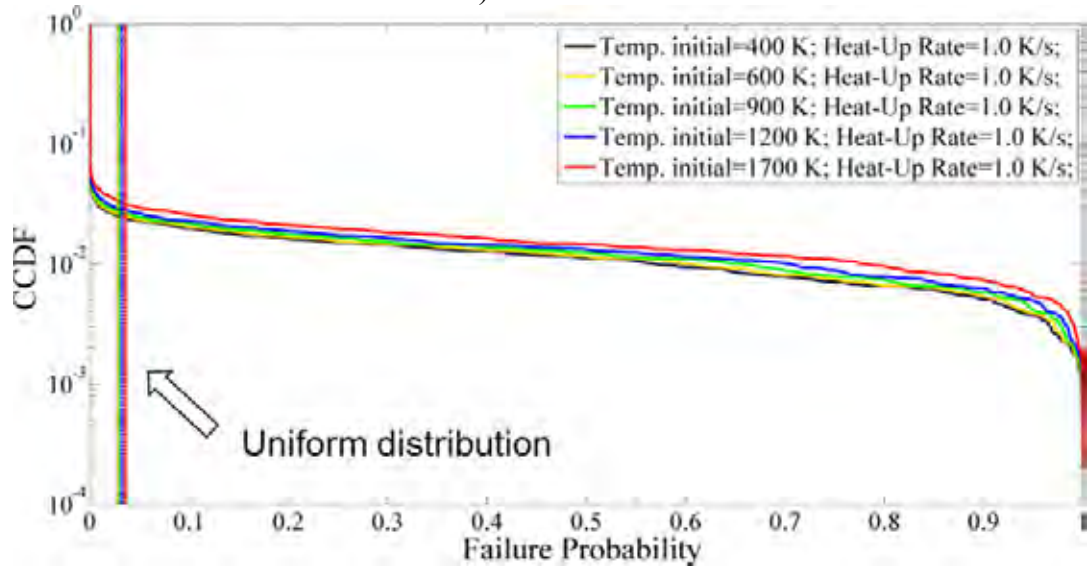

b) BETA

Figure 4.13: Effect of the normal (a) versus beta (b) distribution types on failure probability for $\dot{T}_{rate}$=1 K/s.

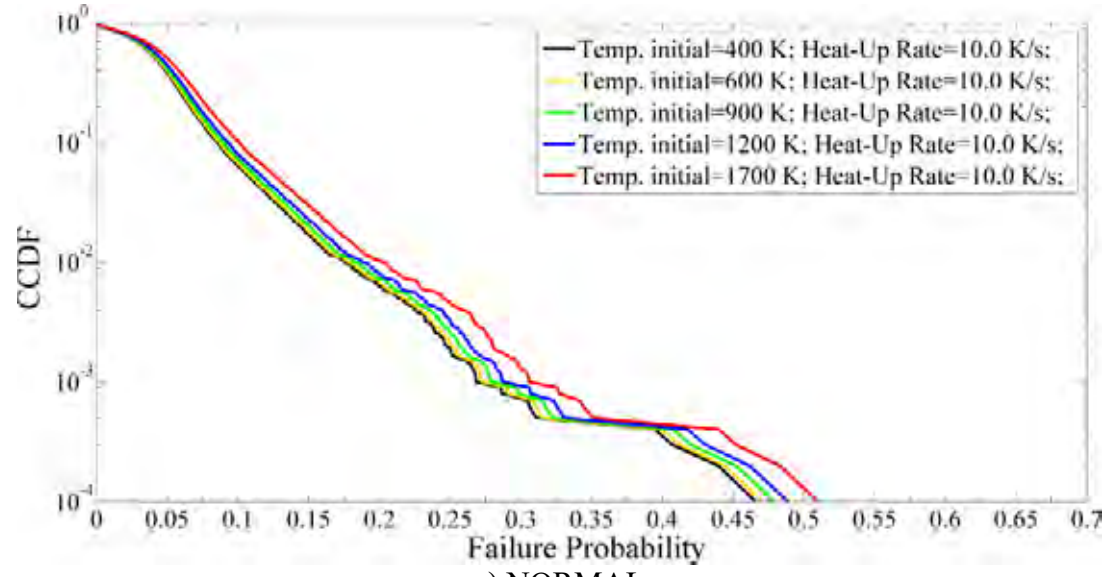

a) NORMAL

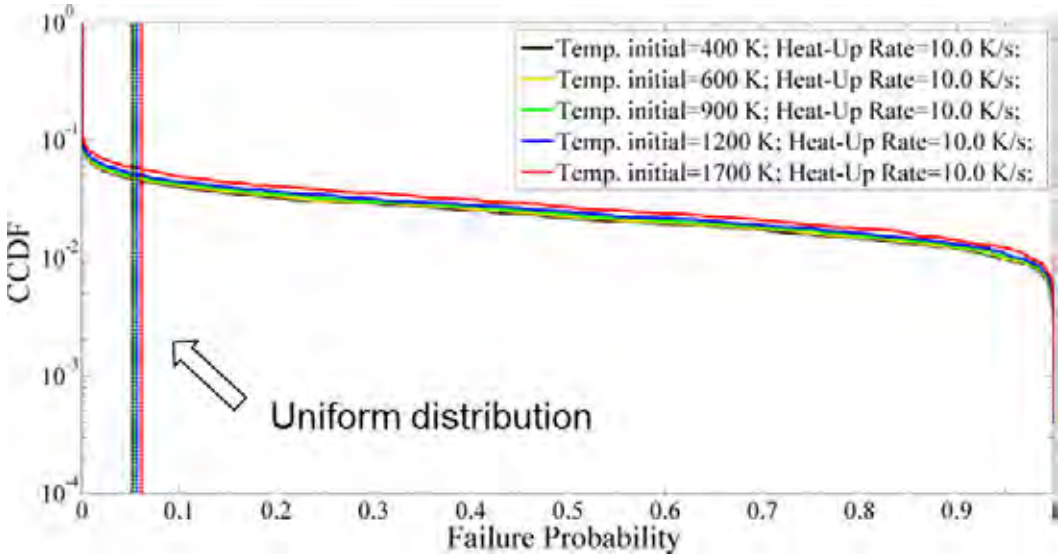

b) BETA

Figure 4.14: Effect of the normal (a) versus beta (b) distribution types on failure probability for $\dot{T}_{rate}$=10 K/s.

4.3.4 **Debris Agglomeration Failure Domain Analysis**

In order to understand better how influential factors affect the risks we employ failure domain approach. Failure domain is a domain in the space of the input parameters where probability of "failure" can exceed a certain limit (screening probability P_S). The failure can be considered, for instance, as an exceedance of safety important parameter over a critical threshold. It is instructive to note that failure probability can be calculated for a given set of probability distributions of the uncertain input parameters. However, the information about the distributions is rarely available. In this work we use second order probability analysis where uncertain distributions are also varied. As a result, a set of possible failure probability values are obtained and characterized by cumulative distribution function (CDF) of the failure probability (P_F).

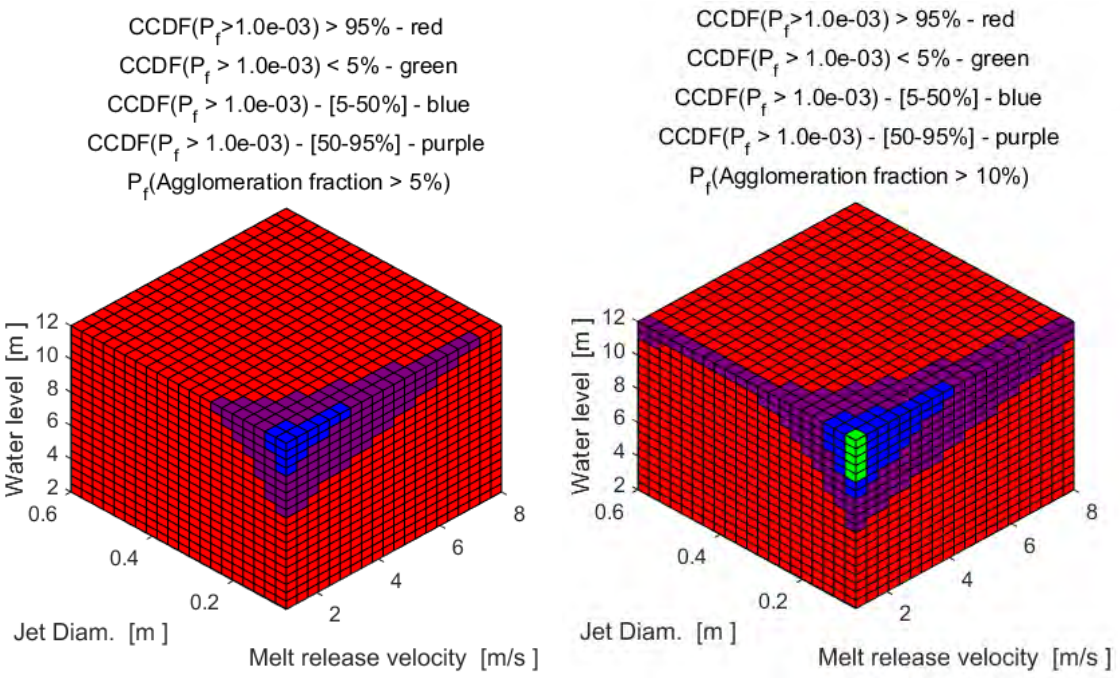

a) b)

Figure 4.15: Failure domain analysis for Debris Agglomeration SM (P_S=0.001) in terms of Jet Diameter (m), Melt release velocity(m/s) and LWD water level (m), with different values of debris agglomeration fraction threshold a) 5%; b) 10%.

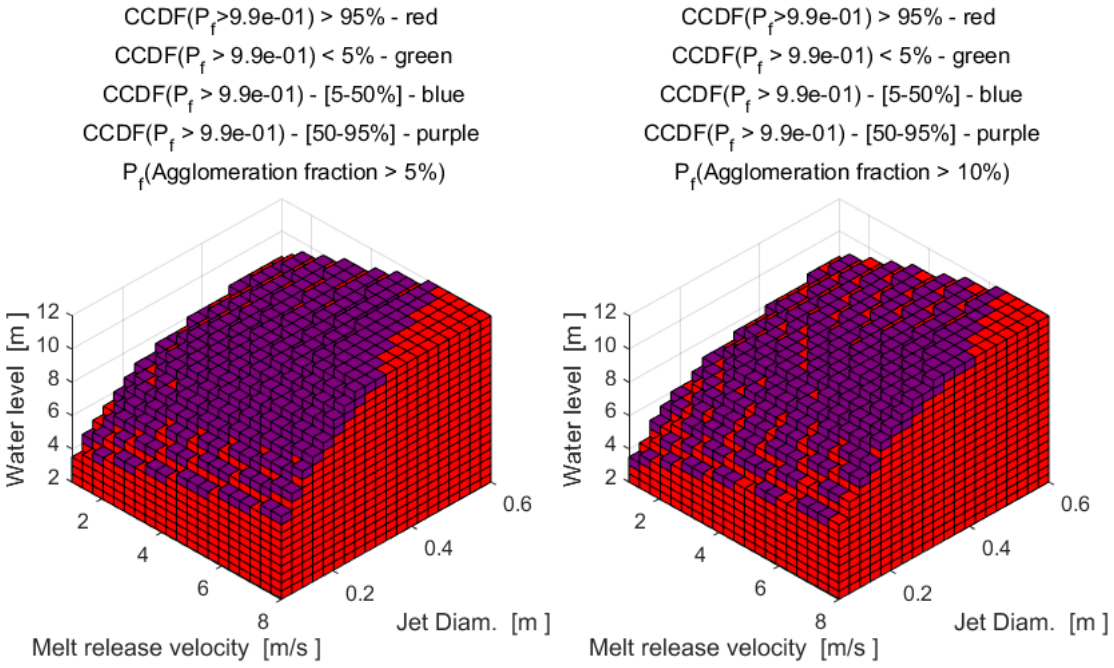

a) b)

Figure 4.16: Failure domain analysis for Debris Agglomeration SM (P_S=0.99) in terms of Jet Diameter (m), Melt release velocity(m/s) and LDW water level (m), with different values of debris agglomeration fraction threshold a) 5%; b) 10%. Only domain with $CDF(P_f > P_s) > 50\%$ are shown.

Results of failure domain analysis performed for Debris Agglomeration SM are presented in Figure 4.15 and Figure 4.16 . Different colors correspond to the different values of the $\boldsymbol{CDF(P_F)}$. The value of $\boldsymbol{CDF(P_F)}$ correspond to the percentile of possible combinations of the distributions of uncertain parameters that result in $\boldsymbol{P_F > P_s}$. Different safety thresholds (5 and 10%) were used for the fraction of agglomerated debris. In Figure 4.15 the results for screening probability $\boldsymbol{P_s = 10^{-3}}$ are presented. Apparently a green domain which correspond to $\boldsymbol{CDF(P_F > 10^{-3}) < 5\%}$ occupies only a small part that correspond to deep pool, small jet diameters and small velocities of melt release. Figure 4.16 show that the exceedance of the safety threshold for the fraction of agglomerates is practically imminent with $\boldsymbol{P_s = 0.99}$ in case of relatively shallow pools, large jets and large melt release velocities.

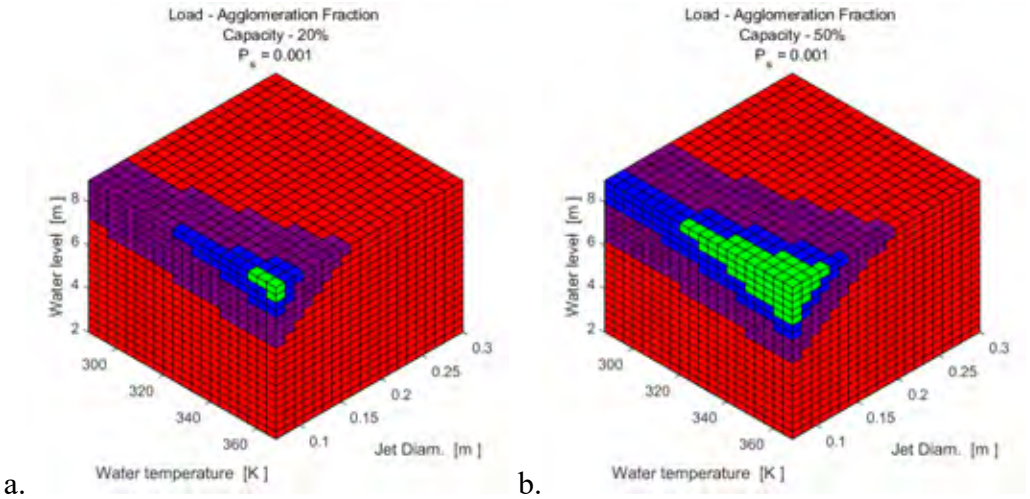

a. b.

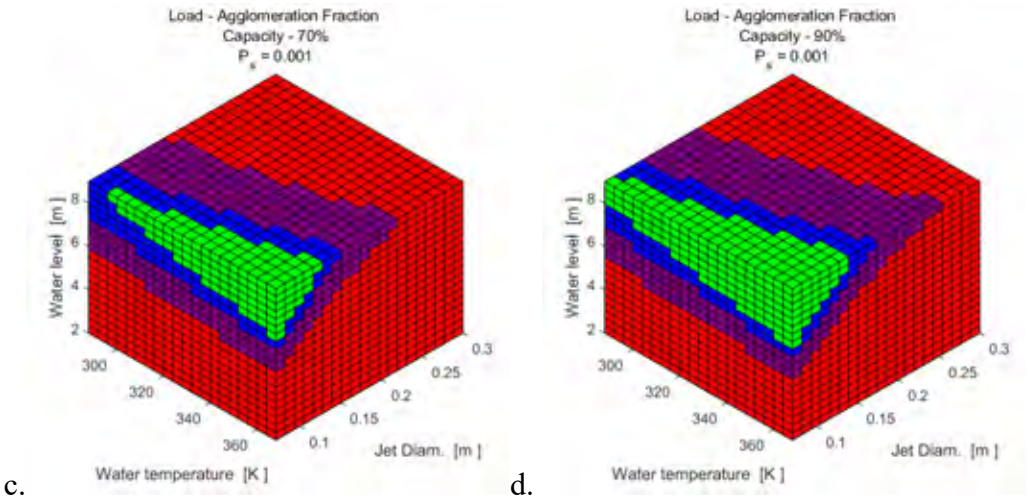

c. d.

Figure 4.17: Failure domain analysis for Debris Agglomeration SM (P_s=0.001) in terms of Jet Diameter (m), Melt release velocity(m/s) and LDW water level (m), with different values of debris agglomeration fraction threshold a) 20%; b) 50% c) 70%. d) 90%

Figure 4.17 illustrate failure domain analysis results for Debris Agglomeration as a function of Jet Diameter, LDW Pool Temperature and Pool depth. The results show that debris agglomeration is currently one of the major contributor to the uncertainty in debris bed coolability. Current model suggest that agglomeration can be avoided only in dripping mode of melt release (very small jet, deep pool). Yet, it is believed that there is significant degree of conservatism in current modeling of agglomeration, especially jet breakup length; Modeling of the effect of agglomeration on coolability (see results obtained with DECOSIM). Thus possible ways to reduce the uncertainty in prediction of coolability are:

- Significant reduction of the uncertainty in the melt release.
- Reduction of uncertainty in
  - Effect of jet breakup on agglomeration modeling
  - Coolability analysis.

4.4 Decision Support and Connection to PSA with ROAAM+ Results

Top layer of ROAAM+ framework for Nordic BWR is comprised of a set of coupled modular frameworks connecting initial plant damage states with respective containment failure modes. The results of ROAAM+ framework are presented as failure domain maps constructed in the space of the input/scenario parameters (input space) partitioned into a finite number of cells. Every cell is characterized by a unique combination of the input parameters ranges. The output of the SM is sampled in each cell (by varying deterministic and intangible parameters, see Chapter 2.5, Paragraphs 2.5.2-2.5.4). The framework compares loads against capacity and renders every computed case to a failure or success. The number of "fail" and "success" cases is counted in each cell, weighted by corresponding probability density functions of deterministic and intangible parameters and normalized to provide conditional failure probability which is compared to the screening probability. The cells where conditional failure probability exceed screening level are grouped into a "failure domain" indicating conditions at which the mitigation strategy fails.

Information about severe accident scenario s_i and its frequency f_i - is necessary input to ROAAM+ framework and it can be provided from the PSA-L1.

4.4.1 Decision Support

The aim of the ROAAM+ framework is to provide an assessment in support of the decision whether or not the risk associated with current SAM strategy is acceptable. The risk in each scenarios is presented as a triplet $R_i = \{s_i, f_i, pdf(P_{Fi})\}$, where scenario s_i has frequency f_i and uncertainty in the failure is characterized by distribution probability of failure probability $pdf(P_{Fi})$. Such approach keeps separation between frequencies of scenarios (s_i, f_i) that characterize statistical data about frequencies of failures of systems and components etc. that can be obtained from PSA-L1, and confidence in prediction of the phenomena determining containment failure $(pdf(P_{Fi}))$ that is obtained from the uncertainty analysis using deterministic models. As we will demonstrate, this separation is important for an adequate approach to interpretation of the risk and respective decision making process.

Scenario frequencies are the inputs to ROAAM+ framework provided from PSA L1 analysis results, i.e. frequencies of correspondent plant damage states (PDSs). Conditional containment failure probability (or probability distribution of conditional containment failure probability) for each scenario is a main outcome of ROAAM+ framework analysis. Figure 4.18a presents decision criteria as a function of accident scenario frequency (CDF) and Conditional Containment Failure Probability (CCFP) or Conditional Probability of Unacceptable Release (CPUR), and Figure 4.18b illustrates ROAAM+ results of $pdf(P_{Fi})$ as box and whiskers plots for scenario s_i, with frequency f_i). Based on the results it is possible to judge, whether or not current SAM strategy is effective for a given severe accident scenario s_i, and the likelihood that there are some combinations of modelling parameters (i.e. deterministic, intangible parameters and correspondent probability distributions, see Chapter 2.5, Paragraph 2.5.4) that can cause failure for the given scenario.

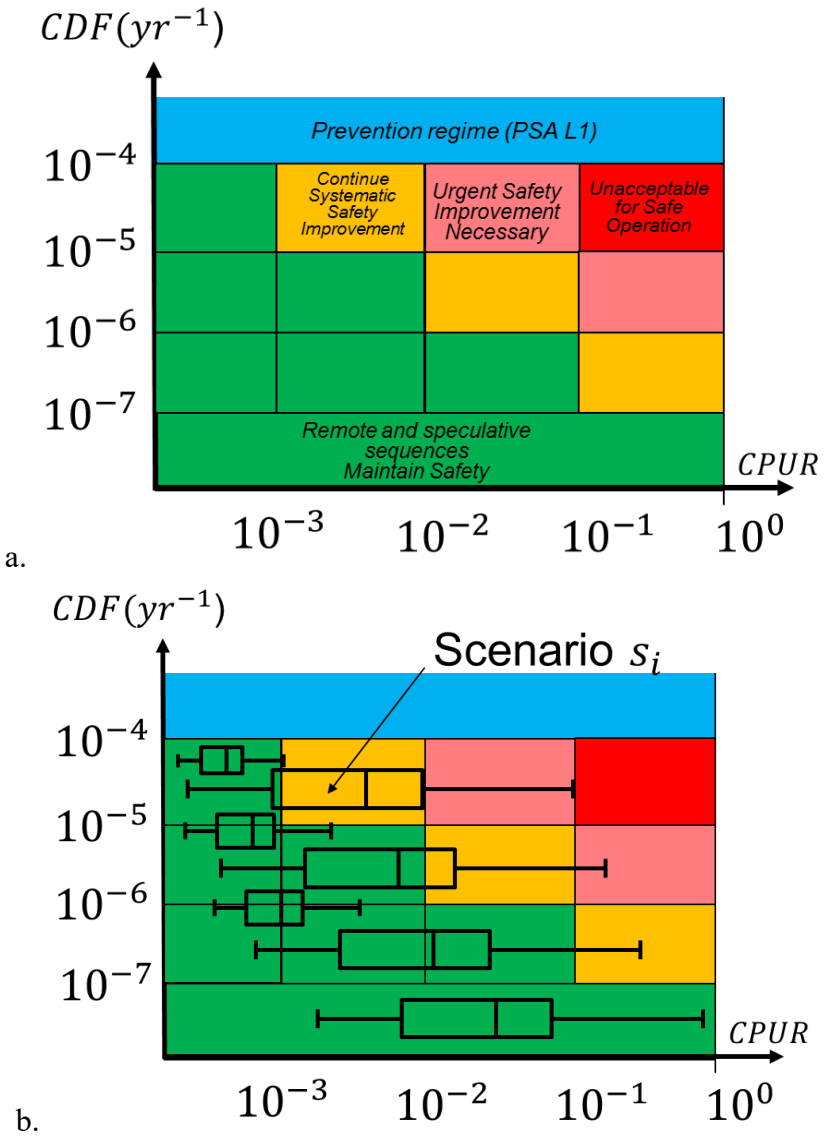

Figure 4.18. Decision support with ROAAM+

4.4.2 Improvement of Sequence Modelling with IDPSA Methodology

From the initial sequences in the PSA Level 1, all events that are leading to a certain PDS are then treated in the same manner in the continued sequence (however, dependencies are treated logically correct if the failure should affect systems in PSA Level 2). It is however obvious that it will be different scenarios from a deterministic stand point if there is an initial loss of offsite power and no start of the diesels, compared to a scenario where the diesels would stop after some hours.

The purpose with the improved integrated link between the PSA and deterministic analyses is hence to be able to judge if, for example, these scenarios need to be treated differently in the PSA context.

The approach chosen in this report was to identify some sequences from the PSA Level 1 and to use ROAAM+ framework to evaluate the progress of these sequences and correspondent conditional containment failure probability for different severe accident

scenario.

To illustrate an approach for improvement of sequence modelling in PSA L1 (L1+) let's assume the following failure domain maps obtained with ROAAM+ framework for ex-vessel steam explosion as a function of lower drywell water pool depth and release size (jet diameter), see Figure 4.19.

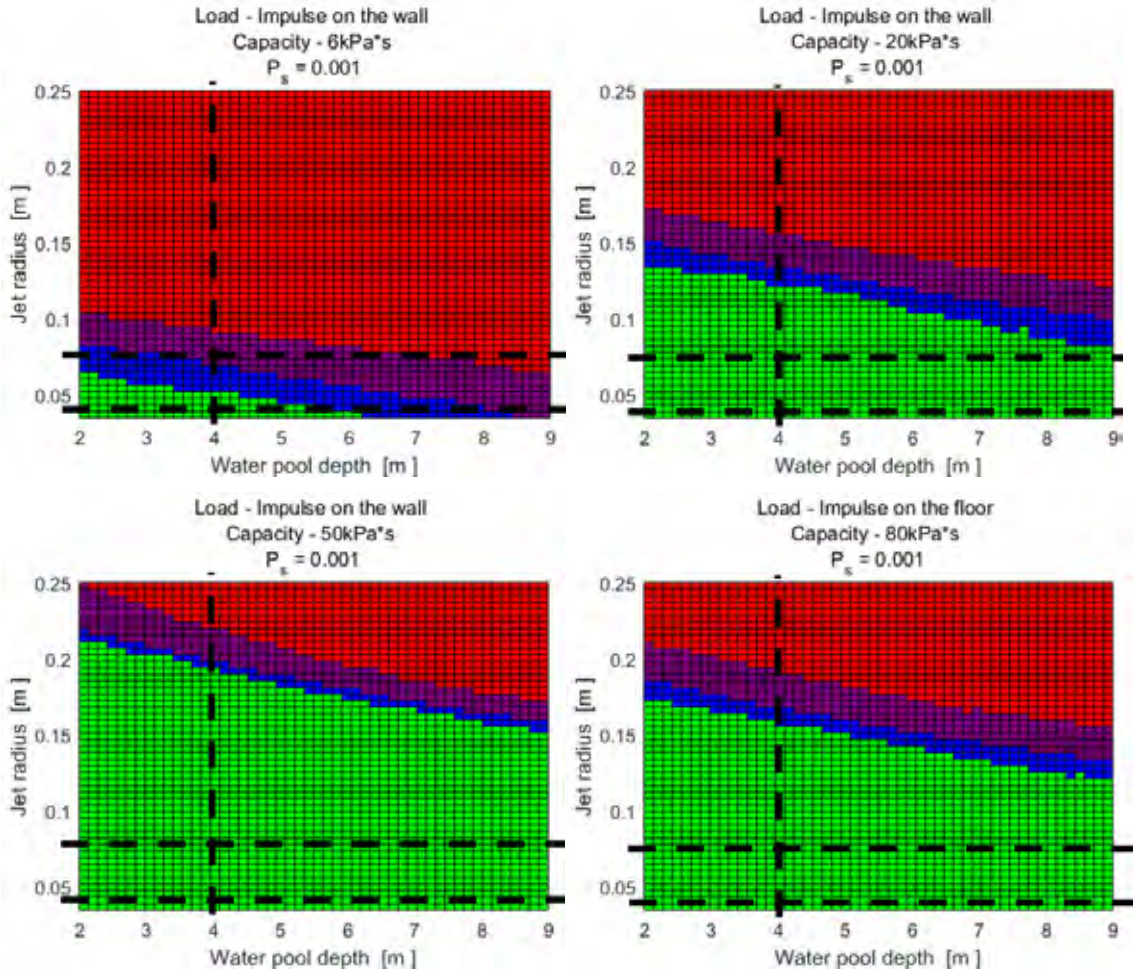

Figure 4.19. SEIM Failure Domain Map

Assuming the following:

- Lower Drywell Pool Depth:
  - "Deep" if pool depth > 4m
  - "Shallow" otherwise.
- Release Size (Jet diameter (Djet))
  - Djet <75.e-3m – Dripping Mode (corresponds to IGT failure)
  - 75.e-3m <= Djet <150.e-3m – Medium release (ablated IGT)
  - Djet >= 150.e-3m – CRGT failure + ablated CRGT.

The failure domain map can be represented by 6 modes:

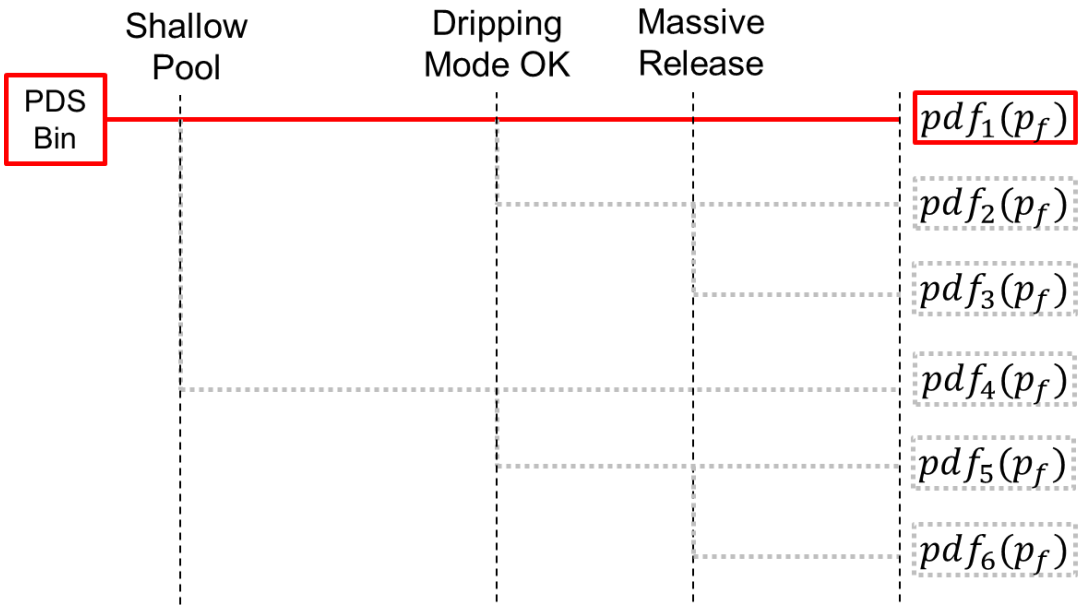

Figure 4.20. Containment Event Tree Example. Mode 1: Shallow Pool + Dripping Mode

In Mode 1 ("Shallow Pool" and "Dripping Mode"), based on ROAAM+ results (see Figure 4.19), maximum conditional containment failure probability is 0 for all fragility limits, meaning that whatever uncertainty is in modelling of ex-vessel steam explosion (SEIM, see paragraph 3.8), containment failure due to ex-vessel steam explosion is physically unreasonable, and SAM strategy is effective even with non-reinforced LDW hatch door.

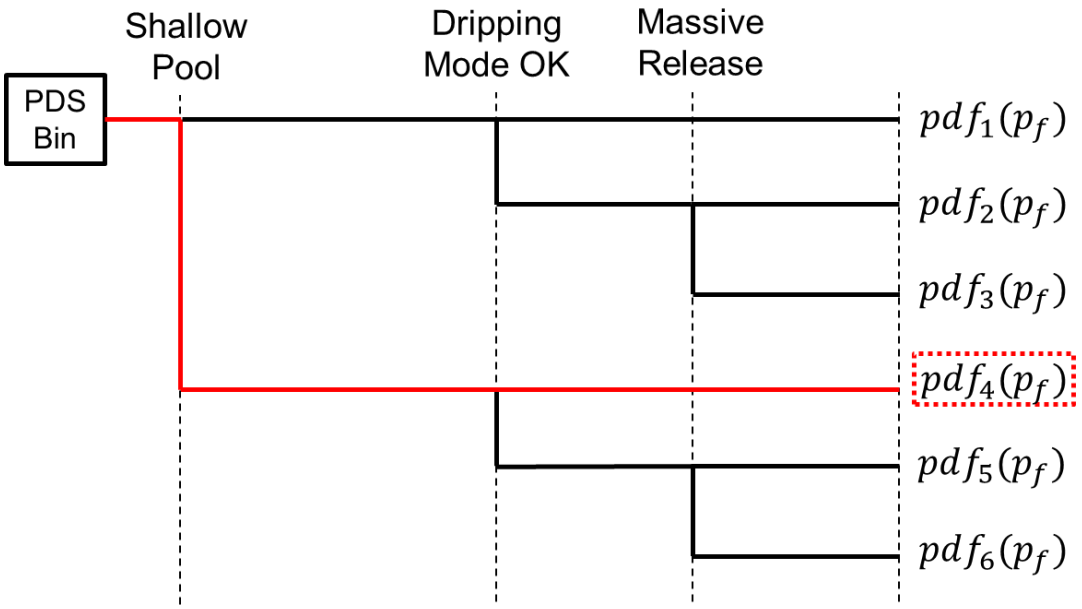

Figure 4.21. Containment Event Tree Example. Mode 4: Deep pool + Dripping Mode

On the other hand, in case of "deep pool" (i.e. LDW pool depth > 4m), probability of failure in case of non-reinforced door ranges from [0,0.729] (see Figure 4.22),

depending on water pool depth within this range and deterministic, intangible parameters used in modelling of ex-vessel steam explosion.

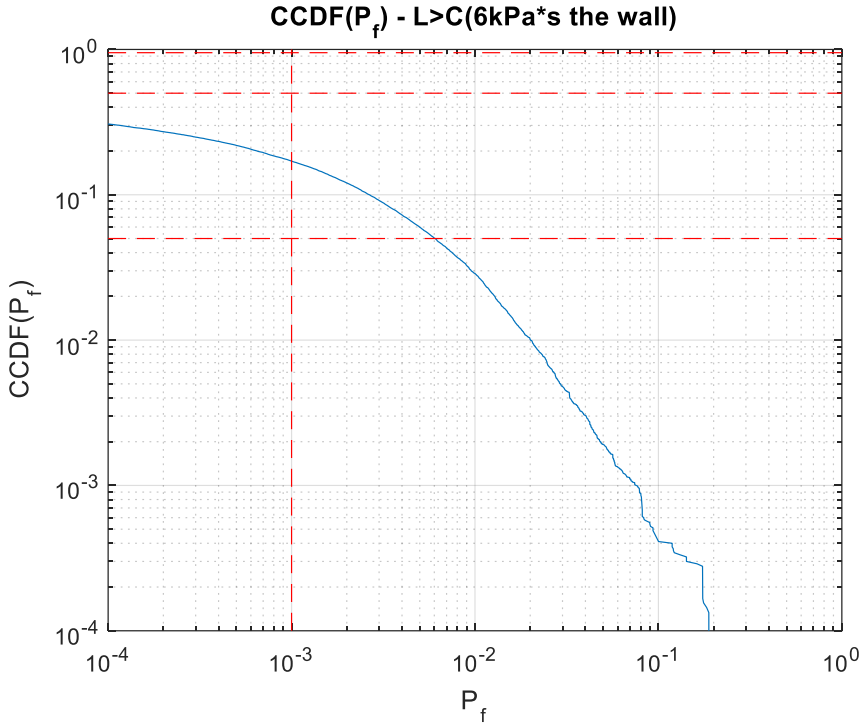

Figure 4.22. Complimentary Cumulative Distribution Function of Conditional Containment Failure Probability due to Ex-Vessel Steam Explosion with Non-reinforced hatch door in Mode 4.

Figure 4.23a,b show the CCDF of conditional containment failure probability due to ex-vessel steam explosion in case of medium release and shallow (Figure 4.23a)/deep (Figure 4.23b) pool. These results clearly indicate that there's significant difference in CCFP depending on the LDW water pool depth.

Presented results of ROAAM+ framework analysis clearly show that there are sequences that affect the phenomena that can occur, e.g. in presented example, depending on the water pool depth, the conditional containment failure probability due to ex-vessel steam explosion can change significantly and result in consequences of risk significance. Moreover, reverse analysis with ROAAM+ can provide insights regarding under what conditions each phenomenon is relevant. Thus, based on ROAAM+ results we can judge if these sequences need to be treated differently in PSA context, and result in refinement of plant damage states in PSA L1.

This example is studied further in section 5.3, where its results are integrated with the PSA model.

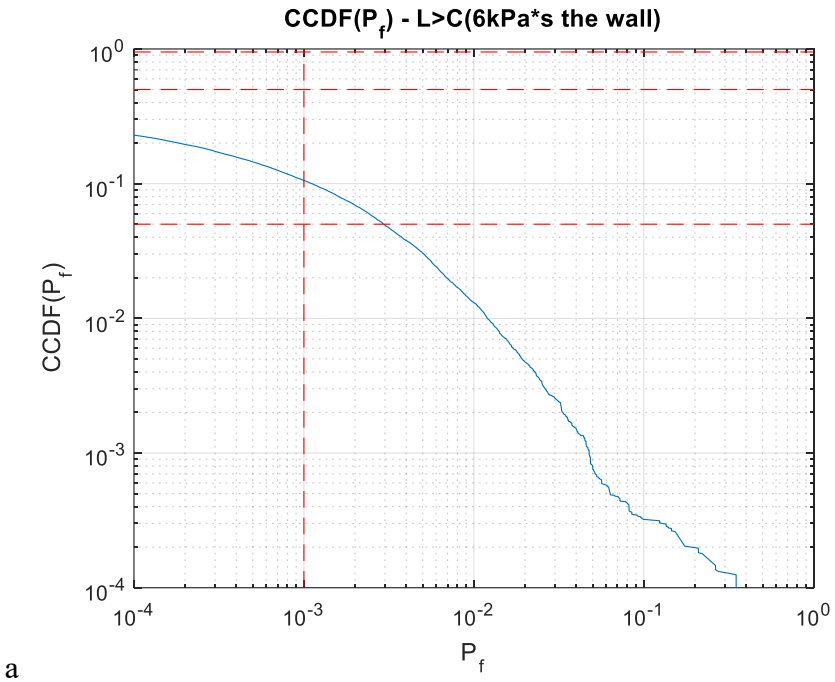

a

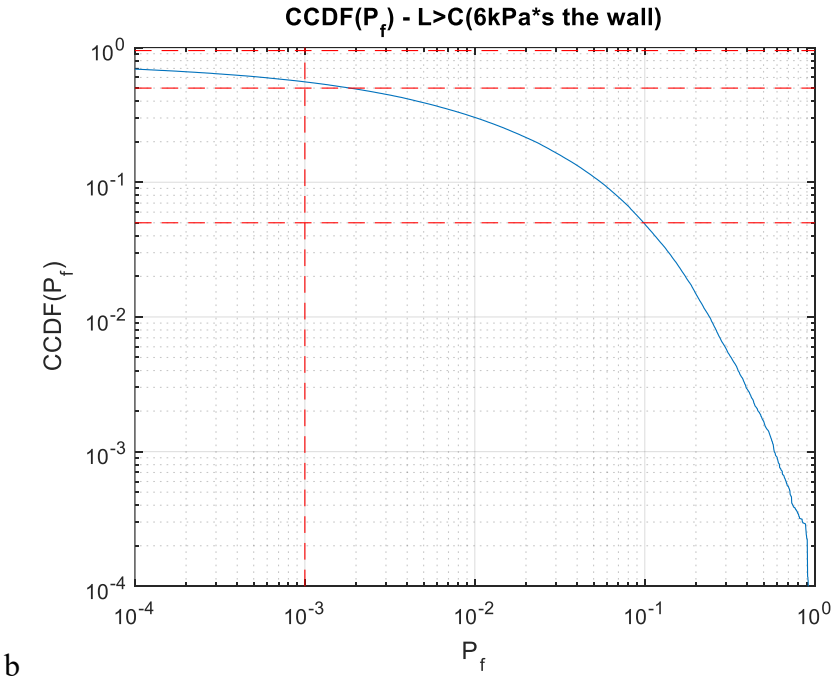

b

Figure 4.23. Complimentary Cumulative Distribution Function of Conditional Containment Failure Probability due to Ex-Vessel Steam Explosion with Non-reinforced hatch door in (a) Mode 3 (Shallow Pool and Medium Release) and (b) Mode 6 (Deep Pool and Medium Release).

Chapter 5. Improvements in PSA modelling to integrate dynamic features.

Section 5.1 provides a general introduction to a common approach for modelling of severe accident progression sequences in Probabilistic Safety Assessment (PSA). Section 5.2-5.4 discusses possible methodological enhancements of PSA using a dynamic approach as well as a feasibility study performed for a large scale PSA model, which continues the example discussed in section 4.4.2.

5.1 Sequence Modelling in PSA Level 2

5.1.1 Assumptions and Limitations in PSA

PSA is used to systematically identify, evaluate and rank the sequence of events that can lead to core damage and radioactive release to the environment. Identification and hence opportunities for improvement in risk dominant feature of the facility is one of the overall objectives. The analysis is probabilistic, i.e. it is based on probability and reliability calculations and the result is an estimate of the frequency of detected events.

Some key assumptions and limitations in PSA level 1 (L1) analysis are:

- Implemented deterministic analyses are correct.
- Blow-down paths and building structures can withstand emerging loads at rupture.
- Studied transient time is normally 1 day, i.e., objective function is required during this time (Level 1 analysis includes 20-24 hours from initiating event, sequences that have not led to the core overheating within this time are not considered as core damage sequences and excluded from Level 2 analysis).
- Aggravating manual interventions are not considered.
- Restricted modeling of manual interventions during transients (only when clear instructions are provided and there is sufficient time available).
- System requirements should be established either via thermal-hydraulic calculations or through references in the SAR.
- Timing within sequences is represented simplified (conservative).

5.1.2 Phases during severe accidents

The first phase of an accident is studied in PSA L1 and the result is a number of sequences ending with either success or core damage.

For those sequences ending with core damage the following accident progression is studied in PSA level 2 (L2). The accident progression is often divided in the following parts:

- **In-vessel** – Describes the heat up and meltdown of the core.
- **Vessel melt through**– Describes the phenomena occurring at vessel melt through.

- **Ex-vessel** – Describes the long term progression of the plant after melt through.

There are interesting phenomena to study with deterministic methods both in PSA L1 and in the different phases of PSA L2.

Core Damage States in PSA L1

The simplest form of core damage states in PSA L1 is to just differ between core damage and success. Normally the core damage states are separated into different categories with respect to the cause of the core damage. Possible reasons to core damage can be:

- HS1: Failure to shut down the reactor.
- HS2: Failure to make up water to the reactor.
- HS3: Loss of residual heat removal.
- HS4: Overpressure of the primary system.
- Overpressure of the containment.

Typically, loss of core cooling or failure of residual heat removal gives the major contributions to core damage, but this varies from plant to plant.

Failure to shut down the reactor normally gives a low contribution to the total core damage frequency. Reactivity control is a very complex process to model since an incomplete or delayed shutdown puts higher demands on the other functions such as higher demands for core cooling, increasing pressure in the primary system etc. It may therefore be interesting to study this in more detail since the core damage frequency due to failure of shutdown may be underestimated in the existing PSA studies.

Plant Damage States Classification in PSA L2

In PSA L1 for Nordic BWR reference plant design the core damage states are grouped into 4 categories: HS1 (ATWS), HS2 (Loss of core cooling), HS3 (Failure to remove decay heat) and HS4 (Primary system overpressure). The categories (HS1, HS2, and HS4) correspond to early core damage scenarios, HS3 – corresponds to late core damage.

In addressing ex-vessel behavior and consequences, the following physical phenomena can challenge containment integrity: direct containment heating (DCH), ex-vessel steam explosions (EVE) and ex-vessel debris coolability (DECO).

A quantitative perspective on these matters should be derived from the PSA L1. DCH scenario corresponds to high pressure (HP) accident scenario, steam explosion in the containment (EVE) corresponds to low pressure (LP) scenario and, finally, both consequences will lead to large amounts of core debris relocated to the lower drywell and it can challenge lower drywell floor and penetrations integrity, so the question of ex-vessel debris bed coolability is an all-pervasive issue.

Initial conditions and correspondent frequencies that will lead to different core degradation, in-vessel debris bed formation, vessel failure scenarios can be identified from PSA L1 data.

The core damage sequences, thus, can be grouped together based on the aforementioned challenges to the containment integrity as follows:

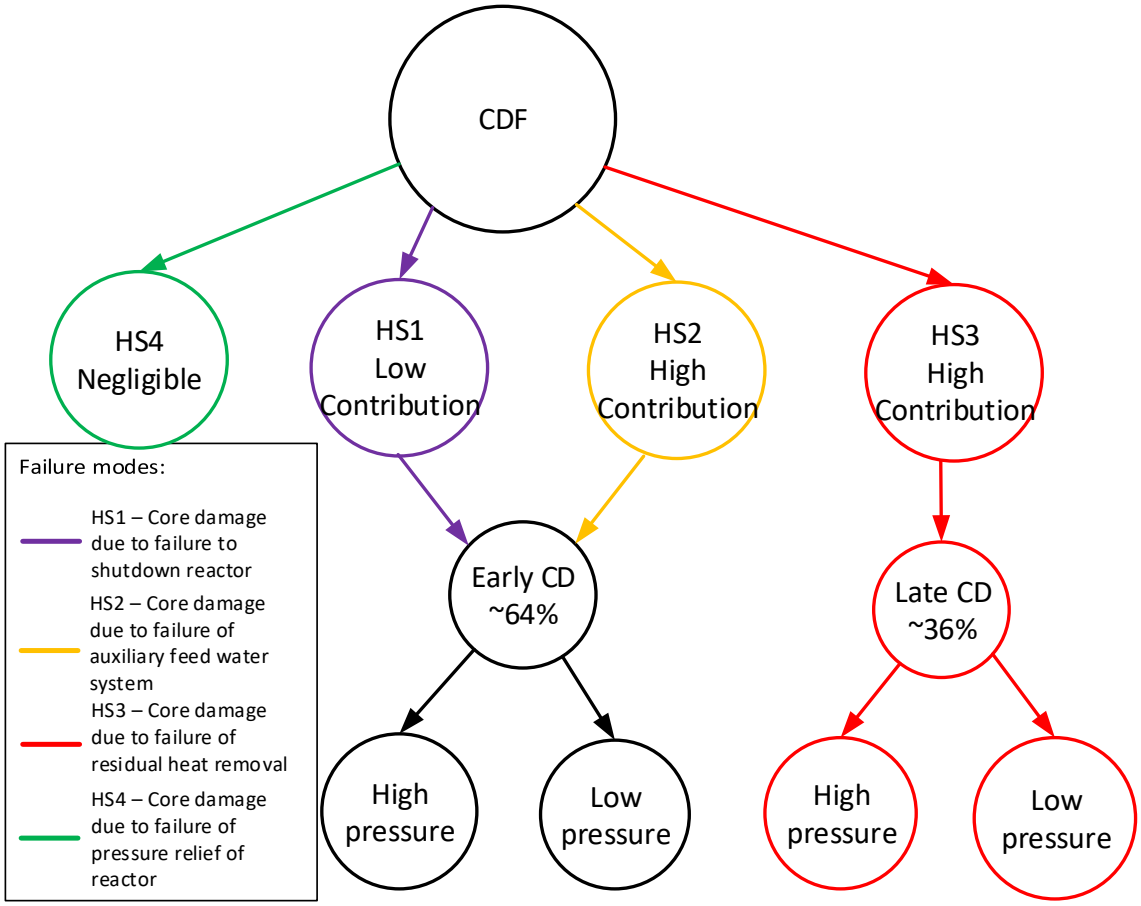

Figure 5.1. Core Damage States Classification

Level 2 PSA

In a standard PSA, the output of PSA Level 1 is typically core damage (possibly separated in a few sub-categories). These core damage sequences are then divided into a number of sub-categories based on attributes, which shall be representing the important features for the Level 2 progression.

The link between PSA L1 and L2 is the plant damage states. The plant damage states describe not only the core damage state but also the conditions in the primary system and the containment. There is normally around 20-40 Plant Damage States (PDS) defined in the interface between Level 1 and 2. This interface is therefore reasonably crude.

For the generic Nordic BWR studied there are 27 PDSs for power operation and low power operating modes. The attributes that are considered relevant to characterize the core melt for the continued process are:

- Core damage state (failure of shutdown, core cooling or residual heat removal).
- Initiating event (transient or LOCA).
- Time point of the core melt (early, late).
- Reactor pressure (low, high).
- Containment atmosphere (inert, air).

- Can cooling with containment spray system be taken into account? (failed, yes).
- Activated containment pressure relief, 361 (activated, not activated).
- Activated filtered release, 362 (activated, not yet activated, failed).
- Bypass of containment (bypass, intact).
- Warm suppression pool (warm if pool cooling fails, else cool).

The events that are represented in a PSA Level 2 are the events that change the conditions for retaining of releases within the RPV or within the containment. Hence, if the coolability in the RPV is different in different scenarios – then this is vital information. If the sequences are affecting the phenomena that can occur, then this is also vital information. For each of the PDS there is a containment event tree. The containment event tree (CET) defines the accident progression as analyzed in the PSA.

The accident progression sequences are influenced by physical phenomena. The types of phenomena that are usually accounted for in a PSA are:

- Re-criticality (in the core, in lower plenum, in containment).
- Hydrogen burn (deflagration and detonation).
- In-vessel steam explosion.
- Ex-vessel steam explosion.
- Direct containment heating.
- Rocket mode.
- Melt concrete interaction (basemat penetration).
- Steam generator tube rupture (only for PWR).

The effect of the phenomena can be:

- Containment rupture.
- Different type of bypass.
- Activation of filter.

The effect of the phenomena most focused on is containment rupture.

The sequences in the CET end at the release categories (RC), and there are normally around 15-40 of such. The RCs can be defined in different ways, for example release size or defined by type of sequence. The normal approach is to use "by type of sequence", because then only a limited amount of verifying deterministic calculations are considered to be required. For the "by type of sequence" approach the characterization is based on, for example;

- Release path (containment bypass, containment rupture, filtered release, leakage).
- Timing of release (early, late).
- Initiator (pipe rupture, transient).
- Sprinkling of containment established (yes/no).

5.2 Methodological enhancement – DSA and PSA integration

All possible failure combinations should be covered by the PSA and the PSA model therefore includes a large number of possible failures and possible severe accident progression sequences. Current PSA models are static and grouping of sequences (failure combinations that have similar effect) as well as simplified treatment of timing of failure combinations are needed.

Ideally, a risk analysis would at all point consider all challenges that can occur at that particular point in time. The process could be thought of like a dynamic event tree covering all possible failures (aleatory) and uncertainties associated with the lack of knowledge about system response (epistemic uncertainty). As much this is an appealing approach, the state space that would need to be analyzed to cover all possible scenarios and epistemic uncertainties is enormous and it will not be feasible to perform this analysis with a brute force approach.

A limited dynamic approach to PSA would give enhanced input about which scenarios that should be studied separately and also information about timing of events of importance. One important aim of a dynamic approach to PSA is to quantify and eventually reduce epistemic uncertainties. The deterministic analysis can provide important insights to which parameters that are of relevance and should be included in the definition of the sequences and the modelling of physical phenomena.

One major advantage with a dynamic approach to PSA is the possibility to address different types of parameters, dependencies and uncertainties that are not taken into account in a static PSA. As discussed in section 2.3 it is relevant to distinguish between different types of parameters influencing the severe accident progression:

- Scenario parameters: Parameters describing the aspects of systems response are noted.
- Physical parameters: Parameters describing well-posed physical problems or “causal relations”.
- Intangible parameters: Other aspects which are subject to inherently variable behavior.

The static PSA is built on choosing correct scenario parameters to describe the accident progression and typically uses a pre-set choice physical parameters in the underlying deterministic analysis. It is however difficult to handle both intangible parameters and physical parameters influencing more than one sequence of events and may for example influence more than one phenomena. The benefit of the dynamic approach within ROAAM+ framework is that this can address all of these three types of parameters.

As it will be practically impossible to consider all possible combinations, there is a need to find which of these parameters and in which combination (scenario, physical and intangible) that may have a large influence on the risk analysis.

The enhanced information from a dynamic approach can be used in the PSA in several ways. Examples of possible gains in the PSA using the information from a dynamic approach are:

- Improved sequence definitions when phenomena can be relevant (improved PDS definitions and the sequences in the containment event tree), see section 5.2.1. This corresponds to improvement in the definition of scenario parameters.

- Estimation of probabilities for phenomena, se section 5.2.2. This follows from improved definition of scenario parameters and also the improved understanding of how the physical and intangible parameters affect the phenomena.
- Improved knowledge of timing in sequences (see also bullet 1 above) which can be another base for improved realism in PSA quantification. Improvements in PSA quantification methods would for example enable repair and correctly consider mission time during the sequence. See section 5.2.3. This corresponds to better definition of scenario parameters.

It shall be mentioned that a dynamic approach to PSA is expected to be especially relevant regarding PSA-L2 since physical phenomena and grouping of events have higher influence on the analyzed scenarios. The improvement of dynamic behavior of especially timing in sequences may also be relevant for increased realism when PSA are developed to reach "safe state" – as the transient time studied will be long, and hence would call for better treatment of repair.

5.2.1 **Improved Sequence Definitions**

The binning of accident sequences from PSA level 1 into plant damage states as well as the modelling of accident progression scenarios in PSA level 2 are based on factors such as type of initiating event, time from initiating event and pressure in the reactor. These factors, scenario parameters and physical parameters, are normally based on a finite amount of analyses, where engineering judgements are necessary.

An IDPSA approach can provide valuable information regarding these scenario parameters and influence the definition of sequences in PSA, since the IDPSA approach is informed by significantly more calculations. Several key elements in the level 2 sequences and phenomena handling and their boundaries can be analyzed at each stage of the modelling of accident progression via for example a reverse analysis in the ROAAM+.

The scenario parameters can be considered in the PSA by improved definition of the attributes of the sequence from PSA L1. The definition of the scenario parameters should not stop at the definition of the plant state at onset of core damage, but reflect the plant state (with regard to system availability) for the complete sequence also including systems relevant for the containment event trees. This means a significant increase of plant damage states, compared to normal practice.

The analysis of the phenomena will then have all relevant information about scenario parameters, and the quantification of the phenomena can then focus on a correct and consistent quantification (considering the dependency between phenomenon and how the physical and intangible parameters affect them in the specific scenario). This is further discussed in section 4.4.2.

Example of improved sequence definition

One example that have been studied with reverse analysis in the ROAAM+ approach is how recovery of emergency cooling system (ECCS) and ADS should inform the scenario parameters (and therefore definition of plant damage states). These safety systems are, for some reason, assumed failed during PSA level 1 and a possibility of system recovery to avoid more severe consequences is modelled in PSA level 2. A

successful recovery early in the sequence would allow the core to be arrested in the reactor pressure vessel (RPV) and hence provide the best possibility to limit the releases.

To arrest the core in the RPV based on the assumption that coolability is possible given successful recovery of the ECCS and ADS. Low pressure scenarios with activated re-flooding can for example be considered successful if it is activated within three hours after core melt. This modelling is supported by a few MAAP analyses.

The human reliability analysis regarding recovery actions is based on the available time for the operator action. It can be noted that the dominating sequences for loss of feed water from PSA level 1 are due to loss of external power supply and failure of back-up power systems. The time for possibility of manual recovery of back-up power systems and the time for possibility of return of of-site power are therefore very important for the quantitative results.

The result of the reverse analysis using the ROAAM+ approach is graphically shown in the decision tree indicates the "safe" timespans, i.e. recovery of ECCS and ADS leads to coolability of the debris, and "failed" timespans, i.e. even with recovery there is a possibility that the debris may not be coolable. The reverse analysis using the ROAAM+ approach indicates that the current assumptions regarding available time for recovery needs to be updated, since the successful states in the IDPSA indicates that the systems needs to be activated earlier to ensure a successful cooling.

It can be noticed that the "safe" state in the decision tree is given based on a threshold. Safe means, in the ROAAM+ approach, that the conditional failure probability for debris coolability is lower than 1E-3, which indicates in the arbitrary scale of probability a "physically unreasonable" level of likelihood (see Section 2.3).

When likelihoods used in ROAAM+ are translated into PSA probabilities, the arbitrary scale of probability should be applied in reverse in order to achieve the same meaning between "physically unreasonable" level in ROAAM and screening frequency in PSA. For instance, it should be evaluated in a continued project if 1E-3 probability threshold in ROAAM+ should be translated into PSA as 1E-4 of conditional frequency. The reason is that a threshold should preferably be set so that the conditional probability would be insignificant with regard to the target value (frequency of <1E-7 for releases).

The target value for PSA Level 1 is often set as 1E-5. A conditional failure probability for level 2 less than 1E-4 would hence fulfil the condition to be insignificant (two orders of magnitude below the acceptable threshold). This means that all "safe" scenarios can be disregarded in the PSA if 1E-4 is used as a threshold value in the analysis. This is identified as a future update and development of the connection between reverse analysis and PSA.

The studied example provides a possibility to identify how the scenario parameter timing of the recoveries affects the possibility to obtain coolability. The results can be used to improve sequence definition in several ways:

- Give more accurate and refined definition of available times for different operating actions and thus provide a better basis material for the HRA.
- Identify the sequences where the debris may not be coolable after re-flooding.
- Provide failure probabilities for the identified sequences. Coolability may need to be modelled with a failure probability that is dependent on the timing of the sequence. Time dependent failure probabilities can be considered since the plant damage states are binned with time after initiating event as one factor. The binning of the plant damage states may therefore be updated with regards to the

findings from the deterministic analysis.

The dynamic approach used in this project has provided interesting information regarding scenario parameters that can be used to improve the sequence definitions and reduce the epistemic uncertainty. The inverse ROAAM+ approach has, in addition to the coolability, also provided very interesting results for the treatment of phenomena in the sequence following melt through. An example of how this information can be used to improve sequence definition is shown in the feasibility study, see section 5.3.

5.2.2 Estimation of Probabilities of Phenomena and Consequences

In addition to a better understanding of the sequences and their causes, it has to be recognized that we will neither have full understanding nor the possibility to represent all possible realistic situations in a risk analysis. Hence it will also be of vital importance that, in addition to a better representation of the sequences, we improve our ability to estimate the probability that a certain phenomenon with risk significant consequences can occur.

The analysis of physical phenomena requires extensive understanding of complex interactions and feedbacks between scenarios of accident progression and phenomenological processes. Physical phenomena are of high importance for the PSA level 2 results since they influence the severity of the consequences.

The analysis includes identification of relevant phenomena, identification of relevant sequences where phenomena can occur as well as estimating the probability of the phenomena. The available data for phenomena is often based on scarce data, which typically leads to conservative assumptions. Better support and basis material for the analysis of probabilities for phenomena, given conditions of scenario, would therefore increase the level of accuracy and credibility substantially.

The phenomena are often seen as independent in the PSA. The physical and intangible parameters influencing the phenomena are therefore not taken fully into account. A dynamic approach to PSA can therefore provide valuable insights influencing the modeling of phenomena.

The analysis with ROAAM+ provides insights regarding under what conditions each phenomenon is relevant. The backward analysis regarding steam explosion, for instance, provides information regarding at what conditions a steam explosion can give consequences of risk significance. The analysis provides a possibility to handle scenario, physical and intangible parameters and identify the parameters of high importance. The scenario parameters, see previous section, can be improved and the epistemic uncertainty can be reduced. There are however still epistemic uncertainty remaining through the physical parameters (which cannot be addressed by improved scenario definition) and the intangible parameters. The dynamic analysis should properly consider how the intangible and physical parameters affect the different phenomena. Since the phenomena share parameters, the phenomena are not independent and thereby it is not correct to estimate them separately.

An example of how a dynamic approach, considering both improvements in scenario parameters and also considering the most important dependencies in physical and intangible parameters, can influence the modelling of phenomena and the estimation of probabilities are shown in the feasibility study, see section 5.3.

5.2.3 **Improved Knowledge of Timing in Sequences**

From the PSA, cut set lists are produced (or rather minimal cut set lists). Improvements in timing in sequences could be implemented in different ways. Here we discuss two ways:

- Improved definition of scenario parameters including timing of systems.
- Improvements in mathematical models for inclusion of dynamic features into the cut set list calculation.

These two ways are discussed below.

Improved definition of scenario parameters including timing of systems

Let us assume that we have an MCS list. This list will include basic events representing phenomena (as well as component failures and human actions – but these are not of interest in this context). These phenomena are treated as individual events – and there is no information on timing. Now, let us assume that we have a decision tree describing the success and failure cases (the scenario parameters).

The combination of the MCS list, and the information in the decision tree could be merged. Conceptually, this could be done in an automated way, but currently the information is needed to inform the sequence definition – and allow for a refined set up of the sequence.

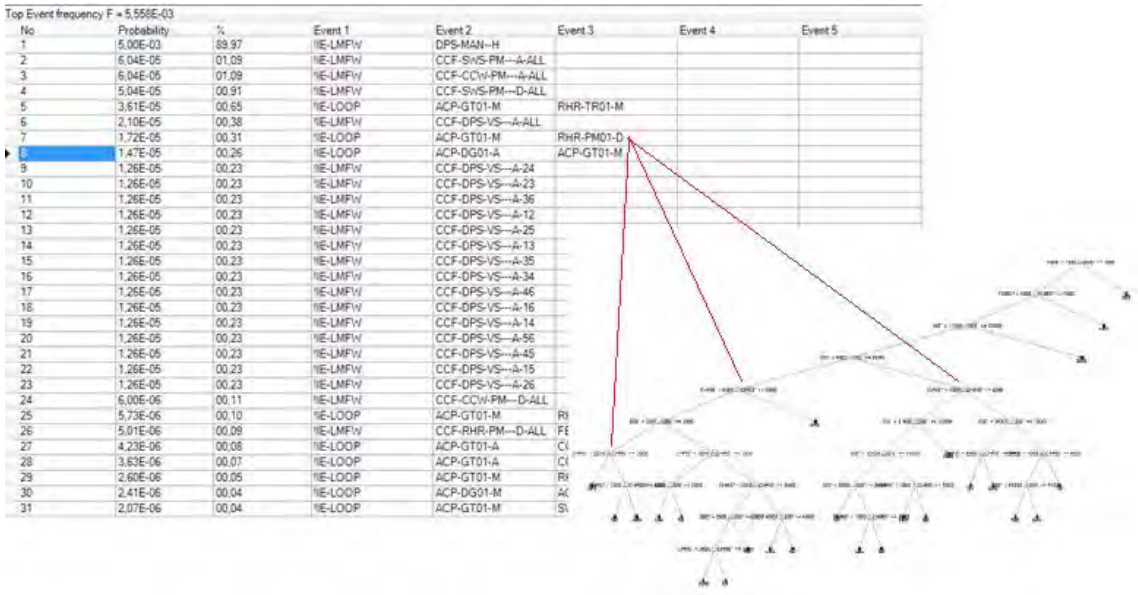

Figure 5.2. The conceptual idea of having the decision tree as input for the quantification of an MCS list. The figure is intended to illustrate that one event may have different failure probability in different cases.

In [2] an example is given, presenting a decision tree where the ROAAM+ approach is used to develop the timing information that should be considered when the failure domains for debris coolability (with regard to restart of ECCS and activation of ADS) in a high pressure core damage sequence is studied.

Improvements in mathematical models for inclusion of dynamic features into the cut set list calculation

Large PSA studies characterize failure combinations or failure scenarios leading to failures being analyzed in a static way. Timed dependencies between systems are either disregarded or approximated by discretization of time and convolution. The static character of PSA models offers no natural way of modelling repairs either.

Certain scenarios in Level 2 (and Level 3) analyses for nuclear power plants require longer time horizon, e.g., reaching a cooled and stable situation in a scenario with the core melt arrested in the reactor pressure vessel, The Fukushima accident gives analyses of longer scenarios additional importance.

As an example, probability of each individual pump system failing in operation grows with growing mission time for each pump. However, one does not need each pump to operate over the entire time horizon.

For very small systems, you could build Markov Chains to better represent timing. However, for the size of problem that PSA models of nuclear stations represent – it will not be feasible to build a model as a Markov Chain.

A recently developed formalism, Static and Dynamic FT, is presented in [234]. The method improves the calculation of large PSA models, using the cut set list and using Continuous Time Markov Chains (CTMCs) to include time into the calculation. The dependency between basic events is defined by triggers, see figure below.

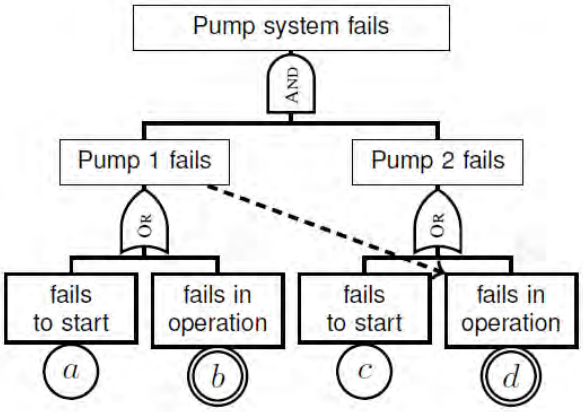

Figure 5.3. Pump 2 mission time event is dependent on a trigger – failure of pump 1. This allows for more realistic consideration of time in operation for pump 2.

The approach described in [234] develops a set of Markov Chains, using the MCS list and the information about triggers from the PSA model.

This way of including time into a dynamic calculation is not addressing exactly the same type of dynamic behavior as discussed in previous section – even though the approach definitively can be used to improve the accuracy in the frequency of the scenarios. The improvement in this algorithm is focusing on improved accuracy in the reliability calculation itself (and not the appropriate setup of the scenario parameter).

5.3 Example of a Dynamic Approach in a Large Scale PSA Model

The dynamic approach to PSA can, as described in section 5.2, be used to enhance the PSA in several aspects. A feasibility study is performed as an example of how a dynamic approach can be used in a large scale PSA. The feasibility study is aiming at studying, in a greater level of detail, the attributes that are of interest for the core relocation, melt through of the reactor pressure vessel (RPV) and the following effects on phenomena.

A generic PSA for Nordic BWR is uses as a reference case. In the reference model each phenomenon, for example steam explosion and debris bed coolability, is modelled with fixed probabilities independent of the accident progression sequence in which they are used. The reference case provides information to the deterministic analysis about which phenomena and parameters that are currently analyzed and used in the binning of sequences and consequences.

Two important phenomena at reactor vessel melt through are steam explosion and debris bed coolability. To be able to study how these phenomena are dependent of different parameters a dynamic approach is used. The parameters that may influence the phenomena are physical parameters such as pressure, temperature and water depth in different parts of the plant, scenario specific parameters such as size of the melt through as well as intangible parameters.

5.3.1 Dynamic Approach

In Chapter 4 the ROAAM+ framework has been used to study some phenomenon. The deterministic study has analyzed a large number of parameters and the analysis shows that the probabilities for the studied phenomena are highly dependent of the following parameters:

- The mass flow of core melt at reactor vessel melt through.
- The depth of the water pool under the reactor vessel.
- The temperature of the water pool.

The chosen parameters influence the probabilities of the phenomena which can be taken into account in the PSA. In this feasibility study a reference large scale PSA model is modified to consider the depth of the water pool and the mass flow of corium at vessel melt through.

The information from the deterministic analysis is used to improve the sequence definition and estimation of probabilities of phenomena creating an enhanced PSA model. The model is updated with regards to the containment event trees (CET) and scenario specific probabilities for the phenomena. The study aims at indicating the effect of taking the enhanced information about phenomena into account when calculating the large early release frequency for transients and CCI leading for these PDS.

The analysis is performed for a few selected specific the plant damage states (PDS). The selected PDS that are studied are named HS2-TH1 and HS2-TL4, se Chapter 5.3.2 for description.

5.3.2 Description of Reference Case PSA model

The reference case PSA model is a generic full scale PSA for Nordic BWR.

In the reference case PSA model the accident progression is modeled in a containment event tree, CET. In the CET there is no explicit modeling of phenomena. Instead there is a function event where all the phenomena are treated in a common fault tree.
The probability for steam explosion resulting in containment failure is:

- 1E-3 for low pressure melt through.
- 3E-3 for high pressure melt through.

These values are always applied even if the lower drywell (LDW) flooding system fails. The reason for this modeling is that no positive credit should be taken for system failures. Furthermore, there may be water enough for steam explosion but not enough to avoid melt through of the penetrations in the LDW floor. The probability for melt through of the penetrations in the LDW floor is:

- 1E-3 after successful LDW flooding.
- 1.0 after failure of the LDW flooding system.

The studied PDS in this feasibility study are:

- HS2-TH1 is a plant damage state where the initiating event is a transient or a CCI, core cooling has failed and the reactor vessel pressure is still high (the automatic depressurization system, ADS, has failed).
- HS2-TL4 is a plant damage state where the initiating event is a transient or a CCI, core cooling has failed and the reactor vessel pressure is low.

5.3.3 Description of Enhanced PSA Model

Containment Event Tree

The containment event trees for the plant damage states HS2-TH1 and HS2-TL4 are modified to consider the depth of the water pool in lower drywell (LDW) and the mass flow of corium at vessel melt through.

The water depth alternatives are:

- Deep water pool in LDW.
- Shallow water pool in LDW.
- No water in LDW.

The melt flow alternatives are:

- Dripping.
- Medium.
- Large.

For each combination of water depth and melt flow there is a unique probability for steam explosion and not coolable debris bed in LDW. This is explicitly modeled in the CET.

The water temperature in lower drywell is scenario specific and set to constant for the modelled plant damage states. This has therefore no influence on the improvement of sequence definitions in the CET.

Figure 5.4 shows the part of the CET influenced by the updated modelling. In the complete CET there are also function events and sequences for isolation, long term residual heat removal etc. As seen in Figure 5.4 there is one common function event for steam explosion and one common function event for coolability. For each sequence, however there is a unique basic event used for each phenomenon depending on the sequence (i.e. the combination of depth and melt flow).

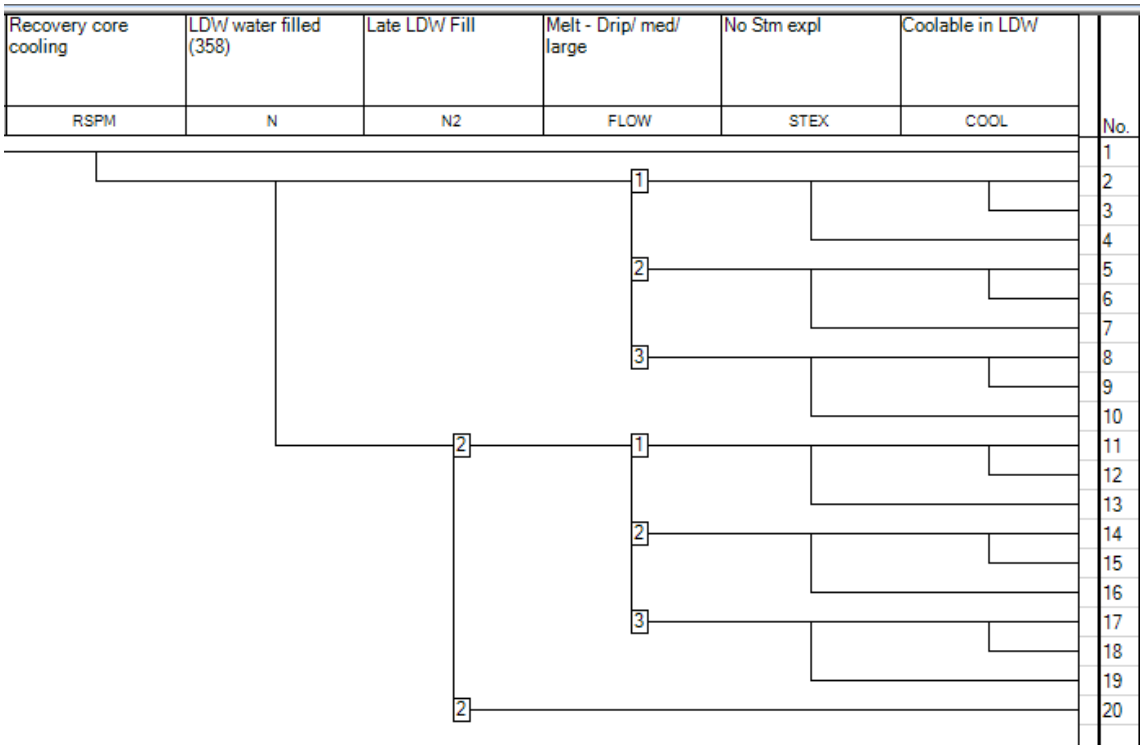

Figure 5.4. Containment Event Tree with explicit modeling of steam explosion and coolability

Deterministic input

The deterministic analysis described in section 4.4 yields probability distributions for steam explosion and coolability given a certain combination of temperature, water depth and melt flow.

The melt flow is expressed as the corresponding diameter of the melt jet. The parameters vary from:

- LDW water temperature 290 - 366 K, 20 different values
- LDW water depth 2,21 - 8,8 m, 20 different values
- Melt jet diameter 0,07575 - 0,2945 m, 20 different values

For each phenomenon there are 4 different sets of data as described above.
For steam explosion there are data for containment fragility of:

- 6 kPa*s
- 20 kPa*s
- 50 kPa*s
- 80 kPa*s

For debris bed coolability there are data for different fractions of agglomeration:

- 20% agglomeration.
- 50% agglomeration.
- 70% agglomeration.
- 90% agglomeration.

Assumptions and limitations

Temperature in LDW

The temperature is assumed to be 322 K for all cases. This is according to MAAP calculations of HS2-TH1 and HS2-TL4 sequences. It is also seen in the input data that the LDW water temperature has a small effect on the phenomena studied here.

Fragility

- For steam explosion the non-reinforced door (6 kPa*s) probabilities are used. This gives the highest probabilities for the steam explosion damage of the containment structures.
- For coolability the 90 % agglomeration probabilities are used. This gives the highest probabilities for non coolable debris bed.

Deep pool – 7.8 m

After successful automatic opening of the LDW flooding system it is assumed that the LDW water level will be 7.8 m at reactor vessel melt through. This is according to MAAP calculations of HS2-TH1 and HS2-TL4 sequences.

The probability for opening of LDW flooding is modelled in Risk Spectrum.

Shallow pool – 3.9 m

If automatic opening of LDW flooding fails it is assumed that the operators can manually take actions to fill the LDW. Possible actions are:

- Manual opening of LDW flooding.
- Manual start of the drywell spray system.
- Manual start of the independent spray system.

Successful manual start of LDW flooding is assumed to lead to shallow pool in LDW at reactor vessel melt through. The level for shallow pool is assumed to be 3.9 m. The probability for failure of manual flooding is assumed to be 0.1.

Failure of LDW flooding

If LDW flooding fails completely the following probabilities are assumed:

- Steam explosion 0.0.
- Debris bed not coolable 1.0.

Melt flow at reactor vessel melt through

The melt flow at reactor vessel melt through is divided in dripping, medium and large. The melt flow corresponds to the diameter of the melt jet:

- $d_{jet} < 0.075$ m Dripping flow.
- $0{,}075 < d_{jet} < 0.150$ m Medium Flow.
- $d_{jet} > 0.150$ m Large Flow.

In the deterministic input data there are probability distributions for steam explosion and coolability for 20 different melt flows varying from 0.07575 m to 0.2945 m. In this case

it is assumed that $d_{jet} = 0.7575$ gives dripping flow. (Otherwise there are no data for dripping flow.)

- Dripping flow Based on $d_{jet} = 0.7575$.
- Medium flow Based on 6 different d_{jet} between 0.08725 and 0.14475.
- Large flow Based on 13 different d_{jet} between 0.15625 and 0.29425.

At present there is no probability distribution for the different melt flow sizes so it is assumed that 1/3 of the cases will result in dripping flow, 1/3 in medium flow and 1/3 in large flow.

The probability distribution is set to uniform. For medium and large flow, the minimum values are set to 0.20 and maximum values are set to 0.46 which gives an average 0.33. The probability for dripping flow is $p_{drip} = 1 - p_{med} - p_{large}$.

Probabilities of phenomena

The probabilities for steam explosion and non-coolability is calculated as the average value of different melt flows in each size respectively, given the depth and the temperature described above. This results in the following probabilities for steam explosion and non coolable debris bed in LDW:

	Steam explosion	Not coolable
• Deep pool, dripping flow	0	3.61E-02
• Deep pool, medium flow	1.55E-02	2.83E-01
• Deep pool, large flow	6.36E-01	8.52E-01
• Shallow pool, dripping flow	0	1,0
• Shallow pool, medium flow	3.60E-04	1.0
• Shallow pool, large flow	3.78E-01	1.0

In the PSA model it is not the average values that are given, instead there are probability distributions for each of the phenomena given above.

Uncertainties of phenomena

In the deterministic analysis of the physical phenomena described in section 4.4 a set of simulations are performed depending on a number of parameters. The output of the analysis is probabilities for physical phenomena associated with an uncertainty distribution. The uncertainty distributions for the different phenomena are therefore not independent since the underlying calculations are based on variations of the same deterministic and intangible parameters. To be able to use this information correctly a non-standard interface, allowing use of externally developed simulation data, should be used in RiskSpectrum to enable the uncertainty distribution for the phenomena to be consistently treated. To be consistently treated the simulations should not use a Monte-Carlo approach on the probabilistic distributions for each phenomenon independently, but simulate on the deterministic and intangible parameters.

In the sample model used in this example, full consideration of the correlation between phenomena has not been considered – due to project constraints. The uncertainty data for the phenomena has been developed considering the deterministic parameter “melt flow”, but each phenomenon (given the type of melt through) has been represented as a probabilistic distribution in the PSA tool.

The following uncertainty distributions are used in the enhanced model:

- Steam explosion uses a discrete probability function with values according to ROAAM+ output data.
- Coolability uses a discrete probability function with values according to ROAAM+ output data.
- Distribution between dripping, medium and large melt flow
    - The probability distribution for medium and large release is uniform with a minimum of 0.16 and a maximum of 0.50.
    - The probability for dripping melt flow is 1-medium-large.
    - The distribution for dripping is therefore uniform from 0.0 to 0.68.

5.3.4 Analysis and Comparison between Reference Case Model and Enhanced Model

All transients and CCIs leading to the plant damage states HS2-TH1 and HS2-TL4 are analyzed for all analyzed level 2 release categories. Release categories leading to release frequencies over 0.1% of the core inventory of an 1800 MW BWR are grouped as non-acceptable.

The normalized result for non-acceptable release per type of initiating event is shown in Figure 2.1 and Table 5.1. The result for Loss of offsite power and non-acceptable release is set to 1.0 for the reference case and all the other results are divided by the same scaling factor.

The analysis shows that the non-acceptable release frequency is doubled in the enhanced model.

The release frequency related to the release category "*Penetration of the LDW floor (basemat melt through)*" is shown in Table 5.2. The frequency approximately increases with a factor of 42 due to the increased probability for non-coolable debris bed. Note that basemat melt through is not grouped as a non-acceptable release. If this release category would be included the frequency for non-acceptable release would increase much more.

The release frequency related to the release category "*Containment failure due to phenomena (always early and no DW spray is credited)*" is shown in Table 5.3. The frequency approximately increases with a factor of 4 due to the increased probability for steam explosion.

The release frequency related to the release category "*Filtered release, Early opening, No DW spray*" decreases to 50 % of the reference case.

The release frequency related to the remaining release categories changes only slightly between the reference model and the enhanced model.

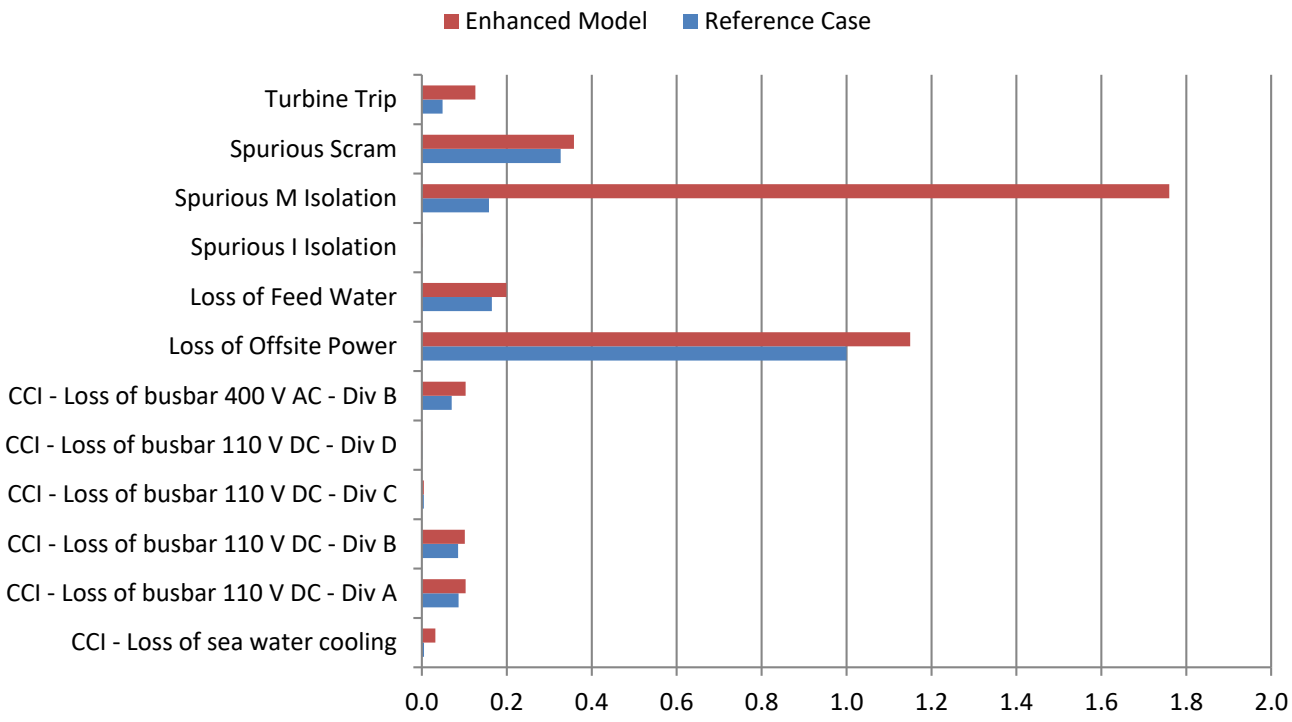

Figure 5.5. Comparison between the reference case and the modified model for non-acceptable release (normalized).

Table 5.1: Comparison between the reference case and the modified model for non-acceptable release (normalized)

Initiating event	**Reference Case**	**Enhanced Model**	**Difference**
CCI - Loss of sea water cooling	5,0E-03	3,2E-02	541%
CCI - Loss of busbar 110 V DC - Div A	8,7E-02	1,0E-01	19%
CCI - Loss of busbar 110 V DC - Div B	8,5E-02	1,0E-01	18%
CCI - Loss of busbar 110 V DC - Div C	4,7E-03	4,7E-03	0%
CCI - Loss of busbar 110 V DC - Div D	1,4E-03	1,2E-03	-16%
CCI - Loss of busbar 400 V AC - Div B	7,0E-02	1,0E-01	47%
Loss of Offsite Power	1,0E+00	1,2E+00	15%
Loss of Feed Water	1,7E-01	2,0E-01	21%
Spurious I Isolation	7,9E-04	1,7E-03	118%
Spurious M Isolation	1,6E-01	1,8E+00	1014%
Spurious Scram	3,3E-01	3,6E-01	9%
Turbine Trip	4,9E-02	1,3E-01	158%
Total result	**2,0E+00**	**3,9E+00**	**102%**

Table 5.2: Comparison between the reference case and the modified model for basemat melt through (normalized)

Initiating event	Reference Case	Enhanced Model	Difference
CCI - Loss of sea water cooling		2,6E-02	
CCI - Loss of busbar 110 V DC - Div A	2,6E-03	1,7E-02	540%
CCI - Loss of busbar 110 V DC - Div B		1,5E-02	
CCI - Loss of busbar 110 V DC - Div C	2,7E-03	2,2E-03	-18%
CCI - Loss of busbar 110 V DC - Div D			
CCI - Loss of busbar 400 V AC - Div B		3,0E-02	
Loss of Offsite Power		1,4E-01	
Loss of Feed Water	7,0E-05	2,4E-02	33661%
Spurious I Isolation	7,0E-05	6,8E-04	874%
Spurious M Isolation	3,0E-02	1,6E+00	5256%
Spurious Scram	5,5E-03	4,2E-02	656%
Turbine Trip	5,3E-03	8,4E-02	1489%
Total result	**4,6E-02**	**2,0E+00**	**4179%**

Table 5.3: Comparison between the reference case and the modified model for containment failure due to phenomena (normalized)

Initiating event	Reference Case	Enhanced Model	Difference
CCI - Loss of sea water cooling	4,8E-03	3,2E-02	561%
CCI - Loss of busbar 110 V DC - Div A	4,1E-03	2,1E-02	406%
CCI - Loss of busbar 110 V DC - Div B	1,8E-03	1,8E-02	873%
CCI - Loss of busbar 110 V DC - Div C	3,2E-03	3,2E-03	0%
CCI - Loss of busbar 110 V DC - Div D	2,4E-04		-100%
CCI - Loss of busbar 400 V AC - Div B	1,5E-03	3,4E-02	2240%
Loss of Offsite Power	2,7E-01	4,2E-01	56%
Loss of Feed Water	6,6E-04	3,5E-02	5180%
Spurious I Isolation	6,6E-04	1,7E-03	150%
Spurious M Isolation	1,6E-01	1,8E+00	1035%
Spurious Scram	5,6E-02	8,8E-02	56%
Turbine Trip	4,4E-02	1,2E-01	178%
Total result	**5,4E-01**	**2,5E+00**	**370%**

5.3.5 Uncertainty analysis

The performed uncertainty analysis reflects the uncertainties of the phenomena since no other uncertainty distributions are included in this example model.

The results of the uncertainty analysis for non-acceptable release is shown in Table 5.4. The results show that the uncertainty ranges from roughly half the point estimate frequency up to about 1.5 of the point estimate frequency. This is a reasonably narrow interval, which is positive – as the uncertainty is an important factor in PSA-L2. It could

be relevant to further study the cases where the uncertainty range is greater – to understand if the uncertainty can be reduced.

Table 5.4: Uncertainty analysis for non-acceptable release (All the median values are normalized.)

Initiating event	**5%**	**median**	**95%**
CCI - Loss of sea water cooling	56%	100%	158%
CCI - Loss of busbar 110 V DC - Div A	91%	100%	112%
CCI - Loss of busbar 110 V DC - Div B	91%	100%	112%
CCI - Loss of busbar 110 V DC - Div C	95%	100%	107%
CCI - Loss of busbar 110 V DC - Div D	100%	100%	100%
CCI - Loss of busbar 400 V AC - Div B	84%	100%	123%
Loss of Offsite Power	93%	100%	109%
Loss of Feed Water	91%	100%	112%
Spurious I Isolation	58%	100%	163%
Spurious M Isolation	54%	100%	161%
Spurious Scram	95%	100%	107%
Turbine Trip	66%	100%	147%

5.3.6 **Influence of Limitations in Enhanced PSA model**

There are a number of assumptions and limitations in the implementation in the enhance PSA model that influence the result. Some comments regarding the importance of different parameters and modeling aspects are:

- Melt jet diameter - dripping, medium, large: An assumed probability of 1/3 for each size is used in the analysis. This parameter is crucial for the results since steam explosion at dripping melt flow has a probability of zero. A more realistic modeling needs to take physical properties into account when determining the probabilities of the melt jet diameter.
- Failure criteria: The data from ROAAM+ for steam explosion and debris bed non-coolability are obtained according to different failure criteria. For both parameters the criteria yielding the highest phenomena probabilities were chosen. For steam explosion this is realistic since the doors are not yet reinforced. For debris bed non-coolability it is conservative since we assume that the agglomeration is 0.9. A more realistic assumption would have been to assume 70% for agglomeration fraction of 0.9 and above; 5% for 0.7-0.9; 7.5% for 0.5-0.7; and 17.5% for 0.2 and below.
- Water depth for deep/shallow pool: The water depth at “deep pool” is related to system functionality and can be calculated with MAAP or even with simple hand calculations. If the LDW flooding system works, there will always be about 8 m of water in LDW. The water depth for shallow pool is much more uncertain since this completely depends on the sequence. A more realistic modeling could take different water depth for shallow pool in different sequences.
- Water temp in LDW at vessel melt through: This parameter is not very uncertain. The temperature is assumed to be 322 K for all cases (This is

according to MAAP calculations of HS2-TH1 and HS2-TL4 sequences.) It is also seen in the data from ROAAM+ that the LDW water temperature has a small effect on the phenomena studied here.

There is a need to make the feasibility study more realistic regarding some of the related parameters discussed above. The quantitative results should therefore be seen as indicative.

5.4 Discussion Dynamic Approach to PSA

A dynamic approach to PSA can, as discussed in section 5.2 and shown in section 5.3, influence the analysis is several ways. The feasibility study has shown an example of a dynamic approach where the PSA is used as a basis to select important initiating events and sequences in the severe accident progression. These scenarios are then analyzed with a dynamic deterministic model yielding information about which parameters that are of high importance for the development of the accident progression. The results from the deterministic analysis are used in the PSA to improve sequence definition as well as improve the estimation of phenomena depending on the sequence and the varied parameters.

The dynamic approach used in the project requires extensive work regarding building the deterministic model. Once built, this model can however be modified to evaluate different initiating events and sequences. The changes in the enhanced PSA-model on the other hand are limited and easy to implement.

The integrated approach requires improvement in especially scenario definition, which practically leads to more plant damage states. The PDS should consider all necessary scenario parameters, that may affect the calculation of phenomena and hence consider also the system availability normally represented within CETs.

The implementation of the dynamic approach in the feasibility study in a large scale PSA model shows that the integration of the ROAAM+ results and the PSA model is not only feasible, but could potentially lead to a considerable change of the frequency for non-acceptable release. The results show that the parameters indicated by the dynamic approach as being of high importance to the results are indeed of high importance to the quantitative results. It also emphasizes the need to distinguish between different probabilities of phenomena depending on different scenario, physical and intangible parameters.

The integrated approach will also have the ability to give a more comprehensive estimation of the uncertainty compared to the standard approach. The uncertainty related to phenomena will consider the interdependency between phenomena (all the way back to relevant intangible and physical parameters, and of course scenario parameters).

Chapter 6. **Conclusions and Suggestions**

The results from the IDPSA show that an increased number of thermos-hydraulic calculations, performed according to an intelligent sampling algorithm, can improve the understanding of the sequences and therefore input to the PSA or to the deterministic safety analyses.

The forward and reverse analysis with the ROAAM+ approach has successfully been used in the project. The evaluation of the results shows that using the results leads to clear benefits for both deterministic as well as probabilistic analysis regarding quality and verification of severe accident progression scenarios.

IDPSA can for both deterministic analysis and PSA be used to refine and improve the analysis in several ways.

The initiating events included in deterministic safety analysis are traditionally divided into a limited number of event classes which have specified analysis assumptions and acceptance criteria. The sequences have to be known when performing the deterministic analysis and the parametric studies are normally limited to one or two parameters. The large strength using IDPSA is its possibility to analyze a large number of combinations of system functions and manual operations which has been shown successfully with ROAAM+ approach. If there are exceedance of the acceptance criteria for certain sequences the results show the excellence in using IDPSA to improve the understanding which conditions leads to the exceedance and also to provide basis for determining the probability of these sequences. By this the IDPSA results are excellent to use when there is a need for risk evaluation when for example the deterministic analysis shows that an analyzed sequence leads to exceedance of the acceptance criteria. It is in these cases possible to identify the conditions for the exceedance and thereby to either improve analysis or to make judgements if these conditions are acceptable. For sequences analyzed which involves manual operation or activation of non-safety systems the outcome of the IDPSA analysis is also important from an operational perspective as well as operator training to prevent those sequences which leads to exceedance of acceptance criteria.

IDPSA results can be used to refine and improve the PSA in several ways. One example is the analysis of recovery of core cooling, where IDPSA has provided usable information regarding the timing and possibility of core coolability (re-flooding). This information can be used as a basis material for the HRA, to re-define the binning of plant damage states as well as provide probabilities for failure of coolability.

Initially in the project the vision was to be able to continue the sequences from the core melting to study the impact on phenomena that could potentially challenge the containment. For each phenomenon the key factors of importance should be identified, for example timing of vessel melt through, pressure in vessel at melt through, pool depth, melt through mechanism etc. This would allow for an improved representation of phenomena, and also to represent the uncertainties in phenomena with their contributing factors.

The approach demonstrated in the report shows that a phenomenon is dependent on

three types of parameters; scenario, deterministic and intangible parameters. Scenario parameters represent information that are defined by the sequence. Such information can hence be refined by improved resolution of the scenario studied. Deterministic parameters are physical information about the process, which are not defined as a scenario parameter and can be characterized by a distribution. For intangible parameters the distribution cannot be obtained, while ranges of the intangible parameters can be conservatively assessed.

The refined information that may be developed can, and should, be used in the PSA. The scenario parameters give information about how the conditions should be specified to make it possible to study the phenomena in PSA level 2 in a relevant way. This could hence be compared to plant damage states. The scenario parameters may also need to contain information that are part of the containment event tree (such as for example pool depth under vessel at melt through - which is dependent on the successful initiation and operation of the systems used to fill the pool). This will require more plant damage states than traditionally included in PSA level 2, and they should not only consider the situation at vessel melt through.

The deterministic and intangible parameters are simultaneously affecting several phenomena and therefore a correct treatment of them is to analyze them together. This is especially relevant to perform uncertainty analysis in a correct way.

The analysis performed for the phenomena of steam explosion and coolability shows interesting results that have been further studied in a pilot study PSA model. The analysis performed for the phenomena provides insights regarding under which conditions each phenomenon should be modelled and therefore more specific scenarios have been represented in the pilot study PSA model. A simplified treatment of a deterministic parameter (melt flow) is also included in the pilot study PSA model. Altogether this study demonstrates that the results of the PSA may be significantly affected by the IDPSA approach.

The IDPSA approach has demonstrated that the vision, to develop the sequence from core melting, and to understand what are the important factors, is possible to meet. There are however still open issues to describe all phenomena to be considered in the form of scenario, deterministic and intangible parameters. One specific example is to study how the melt through mechanism (and thereby melt flow) is affected by scenario, deterministic and intangible parameters following core melt.

The new vision for an IDPSA would be to also be able to judge the size of release to environment, not only demonstrate the failure sequences of the containment.

Acknowledgement

The work is carried out with support of the MSWI-APRI-8, 9 projects at KTH.

NKS conveys its gratitude to all organizations and persons who by means of financial support or contributions in kind have made the work presented in this report possible.

Disclaimer

The views expressed in this document remain the responsibility of the author(s) and do not necessarily reflect those of NKS. In particular, neither NKS nor any other organization or body supporting NKS activities can be held responsible for the material presented in this report.

References

[1] VTT Research Report VTT-R-08589-12 Proceedings of the IDPSA-2012 Integrated Deterministic-Probabilistic Safety Analysis Workshop. November 2012.

[2] Kudinov P, Galushin S., Grishchenko D., Yakush S., Adolfsson Y., Ranlöf L., Bäckström O., Enerholm A., Krcal P., Tuvelid A., "Deterministic-Probabilistic Safety Analysis Methodology for Analysis of Core Degradation, Ex-vessel Steam Explosion and Debris Coolability", NKS-345 DPSA project, ISBN 978-87-7893-427-7. Jul 2015.

[3] M. Belhadj, M. Hassan, and T. Aldemir, *On the need for dynamic methodologies in risk and reliability studies.* Reliability Engineering and System Safety, 1992. **38**: p. pp.219-236.

[4] T. Aldemir, et al., *NUREG/CR- 6942, Dynamic Reliability Modeling of Digital Instrumentation and Control Systems for Nuclear Reactor Probabilistic Risk Assessments.* 2007b, US Nuclear Regulatory Commission, Washington, DC.

[5] C.D. Fletcher, and R.R. Schultz, *RELAP5/MOD3 User Guidelines. NUREG/CR-5535*. 1992, US Nuclear Regulatory Commission, Washington, DC.

[6] R.O. Gauntt, et al., *MELCOR Computer Code Manuals. NUREG/CR-6119/SAND 2005-5713*. 2005, US Nuclear Regulatory Commission, Washington, DC.

[7] A. Hakobyan, et al., *Dynamic generation of accident progression event trees.* Nuclear Engineering and Design, 2008. **238(12)**: p. 3457–3467.

[8] U. Catalyurek, et al., *Development of a code-agnostic computational infrastructure for the dynamic generation of accident progression event trees.* Reliability Engineering and System Safety, 2010. **95**: p. 278–304.

[9] T. Aldemir, *A survey of dynamic methodologies for probabilistic safety assessment of nuclear power plants.* Annals of Nuclear Energy, 2013. **52**: p. 113-124.

[10] M. Kloos, and J. Peschke, *MCDET Approach for Considering Epistemic and Aleatory Uncertainties in Accident Simulations*, in *The 9th International Topical Meeting on Nuclear Thermal-Hydraulics, Operation and Safety (NUTHOS-9)*. 2012: Kaohsiung, Taiwan.

[11] Y. Vorobyov and T.N. Dinh. *A Genetic Algorithm-Based Approach to Dynamic PRA Simulation*. in *ANS PSA 2008 Topical Meeting - Challenges to PSA during the nuclear renaissance*. 2008. Knoxville, Tennessee: American Nuclear Society, LaGrange Park, IL.

[12] Y.H. Chang, and A. Mosleh, *Dynamic PRA using ADS with RELAP5 code as its thermal hydraulic module.* PSAM 4. Springer-Verlag, New York, 1998: p. pp. 2468–2473.

[13] S. Guarro, A. Milici, and R. Mulvehill, *Extending the Dynamic Flowgraph Methodology (DFM) to Model Human Performance and Team Effects NUREGCR/6710*. 2001, US Nuclear Regulatory Commission, Washington, DC.

[14] T. Matsuoka, and M. Kobayashi, *GO-FLOW: a new reliability analysis methodology.* Nuclear Science and Engineering 1988. **98**: p. 64-78.

[15] T. Matsuoka, and M. Kobayashi, *An analysis of a dynamic system by the GO-FLOW methodology.* . In: Cacciabue, P.C., Papazoglou, I.A. (Eds.), Probabilisitic Safety Assessment and Management. Elsevier, New York, pp. 1436-1547, 1991.

[16] J.M. Izquierdo, et al., *Automatic generation of dynamic event trees: a tool for integrated safety assessment.* Reliability and Safety Assessment of Dynamic Process Systems, NATO ASI Series F, vol. 120. Springer-Verlag, Heidelberg, pp. 135–150., 1994.

[17] S.E. Yakush and P. Kudinov, "*A Model for Prediction of Maximum Post-Dryout Temperature in Decay-Heated Debris Bed*," Proceedings of the 2014 22nd International Conference on Nuclear Engineering, ICONE22, July 7-11, Prague, Czech Republic, ICONE22-31214, (2014).

[18] P. Kudinov, A. Karbojian, C.-T. Tran, W. Villanueva, "*Experimental Data on Fraction of Agglomerated Debris Obtained in the DEFOR-A Melt-Coolant Interaction Tests with High Melting Temperature Simulant Materials*," Nuclear Engineering and Design, 263, Pages 284-295, (2013).

[19] P. Kudinov and M.V. Davydov, "*Development and validation of conservative-mechanistic and best estimate approaches to quantifying mass fractions of agglomerated debris*," Nuclear Engineering and Design, 262, pp. 452-461, (2013).

[20] P. Kudinov and M. Davydov, "*Development of Surrogate Model for Prediction of Corium Debris Agglomeration*," In Proceedings of ICAPP-2014, Charlotte, USA, April 6-9, Paper 14366, (2014).

[21] S. Yakush and P. Kudinov, "*Simulation of Ex-Vessel Debris Bed Formation and Coolability in a LWR Severe Accident*," Proceedings of ISAMM-2009, Böttstein, Switzerland, October 26 - 28, (2009).

[22] T. Silvonen, *Steam explosion case study using IDPSA methodology.* VTT Research Report VTT-R-05974-13, 2013

[23] CEA/NERA, Working Group on Operating Experience; "Status of OECD/NEA Country Regulatory Responses to the Forsmark-1 Event of 25 July 2006 and NEA/CSNI DiDELSYS Task Group Report Recommendations" (2010)

[24] R.O. Gauntt, R.K.C., C.M. Erickson, R.G. Gido, R-D. Gasser, and M.F.Y. S.B. Rodriguez, S. Ashbaugh, M. Leonard, A. Hill, *MELCOR Computer Code Manuals Demonstration Problems* 2001, Sandia National Laboratories: U.S. Nuclear Regulatory Commission Washington, DC 20555-0001.

[25] Kudinov P., Galushin S., Yakush S., Villanueva W., Phung V.-A., Grishchenko D., Dinh N., "A Framework for Assessment of Severe Accident Management Effectiveness in Nordic BWR Plants," Probabilistic Safety Assessment and Management PSAM 12, June 22-27, 2014, Honolulu, Hawaii, Paper 154, 2014.

[26] P. Kudinov, S. Galushin, S. Raub, V.-P. Phung, K. Kööp, I. Karanta, T. Silvonen, Y. Adolfsson, O. Bäckström, A. Enerholm, P. Krcal, K. Sunnevik, "Feasibility Study for Connection Between IDPSA and conventional PSA Approach to Analysis of Nordic type BWR's" NKS-R DPSA, Report NKS-315, 65p., 2014.f

[27] T.G. Theofanous, "On Proper Formulation of Safety Goals and Assessment of Safety Margins for Rare and High-Consequence Hazards," Reliability Engineering and System Safety, 54, pp.243-257, 1996

[28] T.G. Theofanous and T.-N. Dinh, "Integration of multiphase Science and Technology with Risk management In Nuclear Power reactors: Application of the Risk-Oriented Accident Analysis Methodology to the Economic, Simplified

Boiling Water Reactor Design," Multiphase Science and Technology, V20(2), pp.81-211, 2008.

[29] Apostolakis G., Cunningham M., Lui C., Pangburn G., Reckley W., "A Proposed Risk Management Regulatory Framework," U.S. Nuclear Regulatory Commission, NUREG-2150, Washington, DC, April 2012.

[30] S. Kaplan and B. J. Garrick, "*On The Quantitative Definition of Risk*," Risk Analysis, 1: pp.11–27, (1981).

[31] Yakush S. and Kudinov P., "A Model for Prediction of Maximum Post-Dryout Temperature in Decay-Heated Debris Bed," Proceedings of the 2014 22nd International Conference on Nuclear Engineering, ICONE22, July 7-11, Prague, Czech Republic, ICONE22-31214. 2014.

[32] Kudinov, P., Karbojian, A., Tran, C.-T., and Villanueva, W., "The DEFOR-A Experiment on Fraction of Agglomerated Debris as a Function of Water Pool Depth," The 8th International Topical Meeting on Nuclear Thermal-Hydraulics, Operation and Safety (NUTHOS-8), Shanghai, China, October 10-14, N8P0296, 2010.

[33] Kudinov, P. and Davydov, M., "Development and Validation of the Approach to Prediction of Mass Fraction of Agglomerated Debris," The 8th International Topical Meeting on Nuclear Thermal-Hydraulics, Operation and Safety (NUTHOS-8), Shanghai, China, October 10-14, N8P0298, 2010

[34] Kudinov, P. and Davydov M., "Development of Surrogate Model for Prediction of Corium Debris Agglomeration," In Proceedings of ICAPP-2014, Charlotte, USA, April 6-9, Paper 14366, 2014.

[35] Yakush, S. and Kudinov, P., "Simulation of Ex-Vessel Debris Bed Formation and Coolability in a LWR Severe Accident," Proceedings of ISAMM-2009, Böttstein, Switzerland, October 26 - 28, 2009.

[36] Galushin, S. and Kudinov, P., "Scenario Grouping and Classification Methodology for Post Processing of Data Generated by Integrated Deterministic-Probabilistic Safety Analysis", Science and Technology of Nuclear Installations, Special Issue on Integrated Deterministic and Probabilistic Safety Analysis for Safety Assessment of Nuclear Power Plants" – In Press, June, 2015.

[37] Ilango and V. Mohan, A Survey of Grid Based Clustering Algorithms. International Journal of Engineering Science and Technology, (2010). Vol. 2(8).

[38] Jolliffe I. T., Principal Component Analysis. 2nd ed. (2002), New York, NY, USA: Springer.

[39] Maimon, O.Z. and L. Rokach, Data mining and knowledge discovery handbook. (2005), New York, Springer.

[40] Tuffery, S., Data Mining and Statistics for Decision Making. Wiley Series in Computational Statistics. (2011), Chichester, West Sussex ; Hoboken, NJ.: John Wiley & Sons, Ltd.

[41] L. Rokach and O. Maimon, Top-down induction of decision trees classifiers - a survey. IEEE Transactions of Systems, Man and Cybernetics, Part C, (2005). 35(4): p. 476-487.

[42] Mitchell, T.M., Machine Learning. McGraw-Hill series in computer science. (1997), New York: McGraw-Hill. xvii, 414 p

[43] K.P. Soman, S. Diwakar, and V. Ajay, Data Mining Theory and Practice. (2006), New Delhi: PHI Learning Pvt. Ltd.

[44] Bishop, Christopher M. (2006). *Pattern Recognition and Machine Learning*. Springer. p. vii.

[45] Han, H. Cheng, D. Xin, X. Yan, Frequent pattern mining: Current status and future directions. Data Mining and Knowledge Discovery, (2007), vol.15 (1) pp. 55–86

[46] Kudinov, P., Karbojian, A., Ma, W.M., Davydov, M., and Dinh, T.-N., "A Study of Ex-Vessel Debris Formation in a LWR Severe Accident", Proceedings of ICAPP 2007, Nice, France, May 13-18, 2007, Paper 7512.

[47] Lakehal D., "On the Modelling of Multiphase Turbulent Flows for Environmental and Hydrodynamic Applications," Int. J. Multiphase Flow, 28, pp. 823-863 (2002).

[48] Asmolov, V. V., Abalin, S. S., Merzliakov, A. V., Zagryazkin, V. N., Astakhova, Ye. V., Daragan, I. D., Daragan, V. D., D'yakov, Ye. K., Kotov, A. Yu., Maskaev, A. S., Rakitskaja, Ye. M., Repnikov, V. M., Vishnevsky, V. Yu., Volko, V. V., Popkov, A. G., Strizhov, V. F., "RASPLAV Final Report: Properties Studies: Methodology and Results," Kurchatov Institute, Moscow, 2000.

[49] Kudinov, P., Ma, W.M., Tran, C.-T., Hansson, R., Karbojian, A., and Dinh, T.-N. "Multiscale Phenomena of Severe Accident," NKS-R and NKS-B Joint Summary Seminar, Armémuseum, Stockholm, 26th - 27th March 2009.

[50] Kudinov, P. and Davydov, M., "Development and Validation of the Approach to Prediction of Mass Fraction of Agglomerated Debris," The 8th International Topical Meeting on Nuclear Thermal-Hydraulics, Operation and Safety (NUTHOS-8), Shanghai, China, October 10-14, N8P0298, 2010.

[51] Basso S., Konovalenko A. and Kudinov P., "Sensitivity and Uncertainty Analysis for Predication of Particulate Debris Bed Self-Leveling in Prototypic SA conditions", In Proceedings of ICAPP-2014, Charlotte NC, USA, April 6-9, paper 14329, 2014.

[52] Kudinov, P. and Davydov, M., "Development and Validation of the Approach to Prediction of Mass Fraction of Agglomerated Debris," The 8th International Topical Meeting on Nuclear Thermal-Hydraulics, Operation and Safety (NUTHOS-8), Shanghai, China, October 10-14, N8P0298, 2010.

[53] Wang, S.K., Blomquist, C.A., Spencer, B.W., McUmber, L.M., Schneider, Y.P., "Experimental Study of the Fragmentation and Quench Behavior of Corium Melts in Water, ANS Proceedings of the 25th National Heat Transfer Conference, HTC3, Houston, TX, 1988. pp. 120–153.

[54] Grishchenko D., Basso S., Kudinov P., "Development of TEXAS-V code surrogate model for assessment of steam explosion impact in Nordic BWR", NURETH-16, Chicago 2015, Paper 13937

[55] I. Lindholm, K. H. (1997). On Core Debris Behaviour in the Pressure Vessel Lower Head of Nordic Boiling Water Reactors. NKS.

[56] Nilsson, L. (2006). Development of an Input Model to MELCOR 1.8.5 for Oskarshamn 3 BWR. SKI Report 2007:05.

[57] R.O Gauntt, J. C. (2005). MELCOR Computer Code Manual Vol.2 Reference Manual Version 1.8.6. Albuquerque: Sandia National Laboratories.

[58] R.O Gauntt, J. C. (2005). MELCOR Computer Code Manuals Vol. 1 Primer and User's Guide Version 1.8.6 . Albuquerque : Sandia National Laboratories .

[59] Sunnevik, K. (2014). Comparison of MAAP and MELCOR and Evaluation of MELCOR as a deterministic tool within RASTEP.

[60] Helton, J.C., Johnson, J.D., Oberkampf, W.L., Sallaberry, C.J., "Representation of analysis results involving aleatory and epistemic uncertainty," International Journal of General Systems, Vol.39(6),pp.605-646, (2010).

[61] Liao, W.-K., Liu, Y., and Choudhary, A.. "A Grid-based Clustering Algorithm using Adaptive Mesh Refinement," In proceedings of the 7thWorkshop on Mining Scientific and Engineering Datasets, 2004.

[62] Adams, B.M., et al., Dakota, A Multilevel Parallel Object-Oriented Framework for Design Optimization, Parameter Estimation, Uncertainty Quantification, and

Sensitivity Analysis: Version 6.0 Reference Manual. 2014, Sandia National Laboratories. (2014).

[63] S. Galushin, W. Villanueva, D. Grishchenko, P. Kudinov, "Development of core relocation surrogate model for prediction of debris properties in lower plenum of a Nordic BWR", *NUTHOS-11: The 11th International Topical Meeting on Nuclear Reactor Thermal Hydraulics, Operation and Safety*, Gyeongju, Korea, October 9-13, (2016).

[64] S. Galushin, P. Kudinov, "Analysis of core degradation and relocation phenomena and scenarios in a Nordic-type BWR", *Nuclear Engineering and Design*, Volume **310**, Pages 125-141, ISSN 0029-5493, 15 December (2016).

[65] Villanueva W., Tran C.-T. and Kudinov P., "Coupled Thermo-Mechanical Creep Analysis for Boiling Water Reactor Pressure Vessel Lower Head" The 8th International Topical Meeting on Nuclear Thermal-Hydraulics, Operation and Safety (NUTHOS-8), Shanghai, China, October 10-14, N8P0248, 2010.

[66] Goronovski A., Villanueva W., Kudinov P., Tran C.-T. "Effect of Corium Non-Homogeneity on Nordic BWR Vessel Failure Mode and Timing," Proceedings of ICAPP 2015, May 03-06, Nice, France, Paper 15160, 2015.

[67] Goronovski, A., Villanueva, W., Tran, C.-T., and Kudinov, P., "The Effect of Internal Pressure and Debris Bed Thermal Properties on BWR Vessel Lower Head Failure and Timing," 15th International Topical Meeting on Nuclear Reactor Thermal Hydraulics, NURETH 15, May 12 to 17, 2013, Pisa, Italy, Paper 500.

[68] Randall Gauntt, Donald Kalinich, Jeff Cardoni, Jesse Phillips, Andrew Goldmann, Susan Pickering, Matthew Francis, Kevin Robb, Larry Ott, Dean Wang, Curtis Smith, Shawn St.Germain, David Schwieder, Cherie Phelan, "Fukushima Daiichi Accident Study", SAND2012-6173, Sandia Report, SNL, 2012.

[69] S. Galushin, P. Kudinov, "Comparison of MELCOR code versions predictions of the properties of relocated debris in lower plenum of Nordic BWR" *17th International Topical Meeting on Nuclear Reactor Thermal Hydraulics*, Xi'an, Shaanxi, China, Sept. 3-8, (2017)

[70] S. Galushin, P. Kudinov, "Effect of Severe Accident Scenario and Modeling Options in MELCOR on the Properties of Relocated Debris in Nordic BWR Lower Plenum" *17th International Topical Meeting on Nuclear Reactor Thermal Hydraulics*, Xi'an, Shaanxi, China, Sept. 3-8, (2017).

[71] L.L. Humphries, B.A. Beeny, F. Gelbard, D.L. Louie, J. Phillips, "MELCOR Computer Code Manuals", **Vol. 2**: Reference Manual Version 2.2.9541, SAND2017-0876 O, (2017).

[72] L.L. Humphries, B.A. Beeny, F. Gelbard, D.L. Louie, J. Phillips, "MELCOR Computer Code Manuals", **Vol. 1**: Primer and Users' Guide Version 2.2.9541, SAND2017-0455 O, (2017).

[73] Morris, M. D. (1991) "Factorial sampling plans for preliminary computational experiments. Technometrics", Vol **33**(2), 161–174. (1991).

[74] A. Saltelli, S. Tarantola, F. Campolongo and M. Ratto, "Sensitivity Analysis in Practice. A Guide to assessing scientific models". John Wiley & Sons Ltd, The Atrium, Southern Gate, Chichester, West Sussex PO19 8SQ, England. (2004).

[75] Imtiaz K. Madni, Evaluation of MELCOR improvements: Peach Bottom Station Blackout Analyses, BNL-NUREG-49201. (1994).

[76] A. Tuvelid, "Comparison of MELCOR and MAAP calculations of core relocation phenomena in Nordic BWR's" – Master Thesis, KTH, Stockholm, Sweden, (2016).

[77] Kyle Ross, Jesse Phillips, Randall O. Gauntt, Kenneth C. Wagner, MELCOR Best Practices as Applied in the State-of-the-Art Reactor Consequence Analyses (SOARCA) Project, NUREG/CR-7008, (2014).

[78] Müller, C. Review of Debris Bed Cooling in TMI-2 Accident. Garching: GRS Forschungsinstitute, (2006).
[79] Makoto Akinaga, Hirohide Oikawa, Ryoichi Hamazaki, Ken-ichi Sato, Takashu Uemura. Probablistic Evaluation of In-vessel retention capability applying phenomenological event tree. (2004).
[80] Magallon, D., "Characteristics of corium debris bed generated in large-scale fuel-coolant interaction experiments," Nuclear Engineering and Design, **236**, 2006, pp.1998–2009. (2006).
[81] Yakush, S.E., Kudinov, P., Villanueva, W., and Basso, S., "In-Vessel debris bed coolability and its influence on the vessel failure", In: *15th International Topical Meeting on Nuclear Reactor Thermal Hydraulics, NURETH 15*, May 12 to 17, Pisa, Italy, Paper 464.(2013).
[82] "Fukushima Daiichi Unit 1 Accident Progression Uncertainty Analysis and Implications for Decommissioning of Fukushima Reactors – Volume **I**", Sandia National Laboratories, SAND2016-0232, (2016).
[83] Yakush, S. and Kudinov, P., "Transient Phenomena of Ex-vessel Debris Bed Formation in a LWR Severe Accident," ANS Transactions, 2009, paper 210830.
[84] Tran, C. T., Kudinov P., and Dinh, T. N. "An approach to numerical simulation and analysis of molten corium coolability in a BWR lower head," XCFD4NRS Workshop, Grenoble, France, September 10-12, 2008.
[85] Villanueva, W., Tran, C.-T., Kudinov, P., "Coupled thermo-mechanical creep analysis for boiling water reactor pressure vessel lower head," Nuclear Engineering and Design, 249, 146-153. 2012.
[86] Karbojian, A., Ma, W., Kudinov, P., and Dinh, T.-N., "A Scoping Study of Debris Bed Formation in the DEFOR Test Facility", Nuclear Engineering and Design, 239, 2009, 1653-1659.
[87] Kudinov, P., Karbojian, A., Ma, W.M., and Dinh, T.-N., "An experimental study on debris formation with corium simulant materials," Proc. ICAPP'08, Anaheim, CA USA, June 8–12, 2008, paper 8390.
[88] Kudinov, P., Karbojian, A., Ma, W., and Dinh, T.-N. "The DEFOR-S Experimental Study of Debris Formation with Corium Simulant Materials," Nuclear Technology, 170(1), April 2010, pp. 219-230, 2010.
[89] Kudinov, P., Karbojian, A., and Tran, C.-T., "Experimental Investigation of Melt Debris Agglomeration with High Melting Temperature Simulant Materials," Proceedings of ISAMM-2009, Böttstein, Switzerland, October 26 - 28, 2009.
[90] Kudinov, P., Karbojian, A., Tran, C.-T., and Villanueva, W., "The DEFOR-A Experiment on Fraction of Agglomerated Debris as a Function of Water Pool Depth," The 8th International Topical Meeting on Nuclear Thermal-Hydraulics, Operation and Safety (NUTHOS-8), Shanghai, China, October 10-14, N8P0296, 2010.
[91] Kudinov P., Grishchenko D., Konovalenko A., Karbojian A., "Experimental Investigation of Debris Bed Agglomeration and Particle Size Distribution Using WO3-ZrO2 Melt," The 16th International Topical Meeting on Nuclear Reactor Thermal Hydraulics (NURETH-16), Chicago, IL, USA, August 30-September 4, paper 14220, 2015.
[92] Kudinov, P. and Davydov, M., "Development of Ex-Vessel Debris Agglomeration Mode Map for a LWR Severe Accident Conditions," Proceedings of the 17th International Conference on Nuclear Engineering, July 12-16, 2009, Brussels, Belgium, Paper ICONE17-75080.
[93] Kudinov, P. and Davydov, M., "Approach to Prediction of Melt Debris Agglomeration Modes in a LWR Severe Accident," Proceedings of ISAMM-2009, Böttstein, Switzerland, October 26 - 28, 2009.

[94] Dombrovsky, L.A., Davydov, M.V., Kudinov, P., "Thermal radiation modeling in numerical simulation of melt-coolant interaction," Comp. Therm. Sci. 1 (1) 2009, pp. 1-35. (2009).
[95] Kudinov, P. and Davydov, M., "Development and Validation of the Approach to Prediction of Mass Fraction of Agglomerated Debris," The 8th International Topical Meeting on Nuclear Thermal-Hydraulics, Operation and Safety (NUTHOS-8), Shanghai, China, October 10-14, N8P0298, 2010.
[96] Kudinov and Davydov M., "Prediction of Mass Fraction of Agglomerated Debris in a LWR Severe Accident," The 14th International Topical Meeting on Nuclear Reactor Thermal Hydraulics (NURETH-14), Toronto, Ontario, Canada, September 25-29, 2011.
[97] Kudinov P., Davydov M.V., "Development and validation of conservative-mechanistic and best estimate approaches to quantifying mass fractions of agglomerated debris," Nuclear Engineering and Design, 262, September 2013, pp. 452-461.
[98] Kudinov, P., Davydov, M., Pohlner G., Bürger M., Buck M., and Meignen R., "Validation of the FCI codes against DEFOR-A data on the mass fraction of agglomerated debris," 5th European Review Meeting on Severe Accident Research (ERMSAR-2012) Cologne (Germany), March 21-23, 2012.
[99] Yakush, S. and Kudinov, P., "Transient Phenomena of Ex-vessel Debris Bed Formation in a LWR Severe Accident," ANS Transactions, 2009, paper 210830.
[100] akush, S., Kudinov, P., and Dinh, T.-N., "Modeling of Two-Phase Natural Convection Flows in a Water Pool with a Decay-Heated Debris Bed," Proc. ICAPP'08, Anaheim, CA USA, June 8–12, paper 8409, 2008.
[101] Yakush, S., Kudinov, P., and Lubchenko, N., "Coolability of heat-releasing debris bed. Part 1: Sensitivity analysis and model calibration," Annals of Nuclear Energy, 52, February 2013, pp. 59-71, 2013.
[102] Theofanous, T. G., and Syri, S., "The Coolability Limits of a Reactor Pressure Vessel Lower Head," Nucl. Eng. Des. 169, 59–76, 1997.
[103] Bürger, M., Cho, S.H., Berg, E.V., Schatz, A., "Breakup of melt jets as pre-condition for premixing: Modeling and experimental verification," Nuclear Engineering and Design, Volume 155, Issues 1–2, 2 April 1995, Pages 215-251, 1995.
[104] Dinh, T.N., Bui V.A., Nourgaliev R.R., Green J.A., Sehgal B.R., "Experimental and analytical studies of melt jet-coolant interactions: a synthesis," Nuclear Engineering and Design, Volume 189, Issues 1–3, 11 May 1999, Pages 299-327, 1999.
[105] Epstein, M. and Fauske, H.K., "Applications of the Turbulent Entrainment Assumption to Immiscible Gas-Liquid and Liquid-Liquid Systems," Chemical Engineering Research and Design, Volume 79, Issue 4, May 2001, Pages 453-462, 2001.
[106] Takasuo, E., "Debris Coolability Simulations with Different Particle Materials and Comparisons to COOLOCE Experiments," VTT report VTT0R-00257-13 (2013).
[107] Saito, M., Sato, K., Furutani, A., Isosaki, M., Imahori, S., and Hattori, Y., "Melting Attack of Solid Plate by a High-Temperature Liquid Jet- Effect of Crust Formation," Nucl. Eng. Des. 121, 11–23. 1990.
[108] Sehgal, B.R. et al., Final report for the "Melt-Vessel Interaction (MVI)" project, SKI 00:53, 2000.

[109] SCDAP/RELAP5/MOD3.1 Code Manual, Volume IV: MATPRO -- A Library of Materials, Properties for Light-Water-Reactor Accident, Analysis. NUREG/CR-6150 EGG-2720, Vol. 4. (1993).
[110] Speranskaya, E.I., 1970. The Bi2O3-WO3 System. Inorganic Materials (Engl.Transl.), 6, pp.127–129
[111] Lipinski, R.J., "A one dimensional particle bed dryout model," ANS Trans. 38, pp, 386–387, 1981.
[112] Spencer, B.W., Gabor, J.D., Cassulo, J.C., "Effect of Boiling Regime on Melt Stream Breakup in Water." In: T.N. Veziroglu (Ed.), Particulate Phenomena and Multiphase Transport, vol. 3. Hemisphere. 1987.
[113] Karbojian, A., Ma, W.M., Kudinov, P., Davydov, M., Dinh, N., "A scoping study of debris formation in DEFOR experimental facility", 15th International Conference on Nuclear Engineering, Nagoya, Japan, April 22-26, 2007, Paper number ICON15-10620.
[114] Kudinov P., Grishchenko D., Karbojian A., Villanueva W., "Design and development of experiments for validation of debris remelting and interactions with structures," Accident Phenomena of Risk Importance (APRI-8), Report MEM1, Rev.2, January 10, 2015.
[115] Lucas A, Arnaldos J, Casal J, Puigjaner L, "Improved equation for the calculation of minimum fluidization velocity", Ind Eng Chem Process Des Dev, 25, 426-429 (1986).
[116] Spencer, B.W., Gabor, J.D., Cassulo, J.C., "Effect of Boiling Regime on Melt Stream Breakup in Water." In: T.N. Veziroglu (Ed.), Particulate Phenomena and Multiphase Transport, vol. 3. Hemisphere. 1987.
[117] Davydov, M.V., "Mathematical modeling of the process of interaction between high temperature melt and coolant in severe accident at NPP with water cooled reactor installation," PhD thesis: 05.14.03. 197p. (in Russian), 2010.
[118] Bürger M., Buck M., Schmidt W., and Widmann W., "Validation and Application of the WABE code: Investigations of Constitutive Laws and 2D effects on Debris Coolability," Nuclear Engineering and Design, Vol. 236, pp. 2164–2188, 2006.
[119] Dinh, T.-N. "Validation Data to Support Advanced Code Development", 15th International Topical Meeting on Nuclear Reactor Thermal Hydraulics, NURETH-14, paper 676, Pisa, Italy, May 2013.
[120] Ergün S., "Fluid Flow through Packed Columns," Chemical Engineering Progress, Vol. 48, 2, pp. 89-94 (1952).
[121] Yakush S. E., Lubchenko, N.T., and Kudinov P., "Surrogate Models for Debris Bed Dryout," 15th International Topical Meeting on Nuclear Reactor Thermal Hydraulics, NURETH 15, May 12 to 17, 2013, Pisa, Italy, Paper 278. 2013.
[122] Yakush, S., Kudinov, P., and Lubchenko, N., "Coolability of heat-releasing debris bed. Part 2: Uncertainty of dryout heat flux," Annals of Nuclear Energy, 52, February 2013, pp. 72-79, 2013.
[123] Torregrosa, C., Villanueva, W., Tran, C.-T., and Kudinov, P., "Coupled 3D Thermo-Mechanical Analysis of a Nordic BWR Vessel Failure and Timing," 15th International Topical Meeting on Nuclear Reactor Thermal Hydraulics, NURETH 15, May 12 to 17, Pisa, Italy, Paper 495. 2013.
[124] Magallon, D., Huhtiniemi, I., Hohmann, H., "Lessons Learnt from FARO/TERMOS Corium Melt Quenching Experiments," In: Proceedings of the OECD/CSNI Specialists Meeting on Fuel-Coolant Interactions, Tokai-Mura, Japan, NEA/CSNI/R(97)26, Part II, pp.431-446, 1997.
[125] Spencer, B.W., Wang K., Blomquist, C.A., McUmber, L.M., and Schneider, J.P., "Fragmentation and Quench Behaviour of Corium Melt Streams in Water," NUREG/CR-6133 ANL-93/32, Argonne National Laboratory. 1994.

[126] Kudinov, P., Karbojian, A., Tran, C.-T., Villanueva, W., "Experimental Data on Fraction of Agglomerated Debris Obtained in the DEFOR-A Melt-Coolant Interaction Tests with High Melting Temperature Simulant Materials," Nuclear Engineering and Design, 263, October 2013, Pages 284-295, 2013.

[127] Davydov, M.V., Melikhov, V.I., Melikhov, O.I., "Numerical Analysis of Multiphase Premixing of Steam Explosions," In: Proceedings of 3rd Int. Conf. Multiphase Flow (ICMF-98), 8-12 June, Lyon, France. 1998.

[128] Kudinov P., Galushin S., Yakush S., Villanueva W., Phung V.-A., Grishchenko D., Dinh N., "A Framework for Assessment of Severe Accident Management Effectiveness in Nordic BWR Plants," Probabilistic Safety Assessment and Management PSAM 12, June 22-27, 2014, Honolulu, Hawaii, Paper 154, 2014.

[129] Yakush, S. E., Lubchenko, N. T., and Kudinov, P., "Risk and Uncertainty Quantification in Debris Bed Coolability," 15th International Topical Meeting on Nuclear Reactor Thermal Hydraulics, NURETH 15, May 12 to 17, 2013, Pisa, Italy, Paper 283. 2013.

[130] Yakush S. E., Lubchenko, N.T., and Kudinov P., "Surrogate Models for Debris Bed Dryout," 15th International Topical Meeting on Nuclear Reactor Thermal Hydraulics, NURETH 15, May 12 to 17, 2013, Pisa, Italy, Paper 278. 2013.

[131] Grishchenko, D., Basso, S., Galushin, S., Kudinov P., "Development of TEXAS-V Code Surrogate Model for Assessment of Steam Explosion Impact in Nordic BWR," The 16th International Topical Meeting on Nuclear Reactor Thermal Hydraulics (NURETH-16), Chicago, IL, USA, August 30-September 4, paper 13937, 2015.

[132] Namiech J., Berthoud G., Coutris N., "Fragmentation of a molten corium jet falling into water," Nuclear Engineering and Design, Volume 229, Issues 2–3, April 2004, Pages 265-287, 2004.

[133] Matsuo E., Abe Y., Chitose K., Koyama K., Itoh K., "Study on jet breakup behavior at core disruptive accident for fast breeder reactor," Nuclear Engineering and Design, Volume 238, Issue 8, August 2008, Pages 1996-2004, 2008.

[134] Taylor, G.I., "The dispersion of jets of metals at low melting point in water." In: Batchelor, G.K. (Ed.), The Scientific Paper of Sir Geoffrey Ingram Taylor, vol. 3., Cambridge University Press, 559p., 1963.

[135] Saito, M., Sato, K., Imahori, S., "Experimental study on penetration behaviors of water jet into freon-11 and liquid nitrogen," In: Proceedings of 25th ANS National Heat Transfer Conference, Houston, U.S., Vol. 3, 1988, pp. 173–183, 1988.

[136] Schneider, J.P., Marciniak, M., Jones, B.G., "Breakup of Metal Jets Penetrating a Volatile Liquid," Proc. 5th International Topical Meeting on Reactor Thermal Hydraulics (NURETH-5), vol. 2. Salt Lake City, USA, pp. 437–449, 1992.

[137] Dombrovsky, L.A. and Dinh, T.-N. "The Effect of Thermal Radiation on the Solidification Dynamics of Metal Oxide Melt Droplets", Nuclear Engineering and Design, 236(6), pp. 1421–1429, 2008.

[138] Yakush, S., Lubchenko, N., and Kudinov, P., "Risk-Informed Approach to Debris Bed Coolability Issue," Proceedings of the 20th International Conference on Nuclear Engineering (ICONE-20), Anaheim, CA, USA, July 30 - August 3, Paper 55186, 2012.

[139] Takasuo, E., Kinnunen, T. Pankakoski, P.H., Holmström, S., "The COOLOCE particle bed coolability experiments with a conical geometry: Test series 6–7," Research Report VTT-R-07097-11. Espoo, 2011. 26 p.

[140] Kim E., J. H. Park, M. H. Kim and H. S. Park, "The influence of two-phase flow on pore clogging by fine particle settlement during ex-vessel debris bed formation in severe accident," in Proceedings of the 2014 22nd International Conference on Nuclear Engineering (ICONE22), Prague, Czech Republic, July 7-11, (2014).

[141] Yakush, S, Kudinov, P. “Effects of Water Pool Subcooling on the Debris Bed Spreading by Coolant Flow,” Proceedings of the 11th International Conference on Advanced Nuclear Power Plants (ICAPP 2011), Nice, France, May 2011, paper 11416, 14 p. 2011.

[142] Kudinov, P. and Dinh, T.-N., “An analytical study of mechanisms that govern debris packing in a LWR severe accident”, The 12th International Topical Meeting on Nuclear Reactor Thermal Hydraulics (NURETH-12), Sheraton Station Square, Pittsburgh, Pennsylvania, U.S.A. September 30-October 4, 2007. Paper 247.

[143] Shamsuzzaman M., B. Zhang, T. Horie, F. Fuke, T. Matsumoto, K. Morita, H. Tagami, T. Suzuki and Y. Tobita, "Numerical study on sedimentation behavior of solid particles used as simulant fuel debris," Journal of Nuclear Science and Technology, vol. 51, no. 5, pp. 681-699, (2014).

[144] Konovalenko, A., Basso, S., Karbojian, A., and Kudinov, P., “Experimental and Analytical Study of the Particulate Debris Bed Self-leveling,” Proceedings of The 9th International Topical Meeting on Nuclear Thermal-Hydraulics, Operation and Safety (NUTHOS-9), Kaohsiung, Taiwan, September 9-13, N9P0305, 2012.

[145] Basso S., Konovalenko A. and Kudinov P., “Development of scalable empirical closures for self-leveling of particulate debris bed”, In Proceedings of ICAPP-2014, Charlotte NC, USA, April 6-9, Paper 14330, 2014.

[146] Konovalenko A., Basso S., and Kudinov P. “Experiments and Characterization of the Two-Phase Flow Driven Particulate Debris Spreading in the Pool,” The 10th International Topical Meeting on Nuclear Thermal-Hydraulics, Operation and Safety (NUTHOS-10), Okinawa, Japan, December 14-18, 2014, Paper 1257, 2014.

[147] Alvarez D. and Amblard M., "Fuel leveling," Information Exchange Meeting on Post Accident Debris Cooling, Karlsruhe, July 28-30, (1982).

[148] Zhang N., Harada T., Hirahara D., Matsumoto T., Morita K., Fukuda K., Yamano H., Suzuki T. and Tobita Y., "Self-Leveling Onset Criteria in Debris Beds," J. Nuclear Science and Technology, vol. 47, p. 384, (2010).

[149] Zhang B., Harada T., Hirahara D., Matsumoto T., Morita K., Fukuda K., Yamano H., Suzuki T., Tobita Y. “Experimental investigation on self-leveling behavior in debris beds”, Nuclear Engineering and Design, 241(1), pp. 366-77, 2011.

[150] Cheng S., Tagami H., Yamano H., Suzuki T., Tobita Y., Zhang B., Matsumoto T. and Morita K., "Evaluation of debris bed self-leveling behavior: A simple empirical approach and its validations," Annals of Nuclear Energy, vol. 63, p. 188, (2014).

[151] Sudha A.J, Murthy S. S., Kumaresan M., Lydia G., Nashine B. K. and Chellapandi P., "Experimental analysis of heaping and self-levelling phenomena in core debris using lead spheres," Experimental Thermal and Fluid Science, vol. 68, pp. 239-246, 2015.

[152] Cheng, S., Yamano, H., Suzuki, T., Tobita, Y., Gonda, Y., Nakamura, Y., Zhang, B., Matsumoto, T., Morita, K., “An experimental investigation on self-leveling behavior of debris beds using gas-injection”, Experimental Thermal and Fluid Science, 48, 110-121, 2013.

[153] Konovalenko A., Basso S., Kudinov P., Yakush S. E., “Experimental Investigation of Particulate Debris Spreading in a Pool”, Nuclear Engineering and Design, Volume 297, pp208-219, 2016.

[154] Yang W.-C., “Handbook of Fluidization and Fluid-Particle Systems”, Taylor & Francis Group, ISBN 9780824702595, Chapter 26, p.712 , 2003.

[155] Cheng, S., Tanaka, Y., Gondai, Y., Kai, T., Zhang B., Matsumoto, T., Yamano, H., Suzuki, T., Tobita Y. “Experimental studies and empirical models for the

transient self-leveling behavior in debris bed", Journal of Nuclear Science and Technology, 48(10), pp. 1327-36, 2011.
[156] Kolev N., Multiphase Flow Dynamics, Vol. 2, Ch. 2, Springer, Berlin, Heidelberg, NY (2005).
[157] Eames, I., Gilbertson, M., "Aerated granular flow over a horizontal rigid surface", J. Fluid Mech. 424, 169-195, 2000.
[158] Robinson, D., Friedman, S., "Observations of the effects of particle shape and particle size distribution on avalanching of granular media", Physica A: Statistical Mechanics and its Applications, 311, 1, 97-110, 2002.
[159] Koide, K., Yasuda, T., Iwamoto, S., Fukuda, E.," Critical gas velocity required for complete suspension of solid particles in solid-suspended bubble columns". J. Chem. Eng. Jpn. 16 (1), 7–12, 1983.
[160] Koide, K., Horibe, K., Kawabata, H., Ito, S., "Critical gas velocity required for complete suspension of solid particles in solid-suspended bubble column with draught tube". J. Chem. Eng. Jpn. 17 (4), 368–374. 1984.
[161] Campolongo, F., J. Cariboni, and A. Saltelli, An effective screening design for sensitivity analysis of large models. Environmental Modelling & Software, 22, pp. 1509-1518, 2007.
[162] Howson, C., Urbach, P., "Scientific Reasoning the Bayesian Approach", 2nd edition Chicago, 52-55, (1997).
[163] Song, J., Kim, J., Hong, S., Min, B., Kim H., "The effect of corium composition and interaction vessel geometry on the prototypic steam explosion", Annals of Nuclear Energy, vol. 33, 1437-1451, (2006).
[164] Lindholm, I., Nilsson, L., Pekkarinen, E., Sjövall, H., "Coolability of degraded core under reflooding conditions in Nordic boiling water reactors", Nordic nuclear safety research, NKS-2(95), September, (1995).
[165] Kudinov P, Galushin S., Grishchenko D., Yakush S., Adolfsson Y., Ranlöf L., Bäckström O., Enerholm A., Krcal P., Tuvelid A., "Deterministic-Probabilistic Safety Analysis Methodology for Analysis of Core Degradation, Ex-vessel Steam Explosion and Debris Coolability", NKS-345, ISBN 978-87-7893-427-7. Jul 2015.
[166] Basso, S., Konovalenko, A., Kudinov, P., "Empirical Closures for Particulate Debris Bed Spreading induced by Gas-Liquid Flow", accepted for publication to Nuclear Engineering and Design, (2015).
[167] Yakush, S., Kudinov, P., and Dinh, T.-N., "Multiscale Simulations of Self-organization Phenomena in the Formation and Coolability of Corium Debris Bed," Proc. The 13th International Topical Meeting on Nuclear Reactor Thermal Hydraulics (NURETH-13), September 27-October 2, Kanazawa City, Ishikawa Prefecture, Japan, Paper N13P1143, 2009.
[168] Basso, S., Konovalenko, A., Kudinov, P., "Effectiveness Of The Debris Bed Self-Leveling Under Severe Accident Conditions", under review in Annals of Nuclear Energy Enquiry, ANUCENE-D-15-00512, (2015)
[169] Halton, J.H., Algorithm 247: Radical-inverse quasi-random point sequence. Commun. ACM, 1964. 7(12): p. 701-702.
[170] Inselberg, A. "Parallel Coordinates: Visual Multidimensional Geometry and Its Applications", Springer, (2009)
[171] Yakush S. E., Konovalenko A., Basso S., Kudinov P. "Effect of Particle Spreading on Coolability of Ex-Vessel Debris Bed," 16th International Topical Meeting on Nuclear Reactor Thermal Hydraulics (NURETH-16), Chicago, USA, August 30-September 4, 2015, paper NURETH-16-14112, 13p, 2015.
[172] Marsland, S., "Machine Learning: an algorithmic perspective", Chapman and Hall (2009).

[173] Samarasinghe, S., “Neural Networks for Applied Sciences and Engineering”, Taylor and Francis Group, (2007).
[174] Beale, M., Hagan, M., Demuth, H. “Neural Network Toolbox Version: 8.2.1, User’s Guide,” The Mathworks, Inc., (2014).
[175] Rahman, S., “Coolability of Corium Debris under Severe Accident Conditions in Light Water Reactors”, PhD thesis, Institute of Nuclear Technology and Energy Systems (IKE), University of Stuttgart, (2013).
[176] Pohlner, G., Buck, M., Rahman, S., “Modeling and validation basis of the JEMI code”,Institute of Nuclear Technology and Energy Systems, University of Stuttgart, IKE 2-161, (2013).
[177] Buck, M., Burger, M., Rahman, S., Pohlner, G.: “Validation of the MEWA Model for Quenching of a Severely Damaged Reactor Core,” Joint OECD/NEA EC/SARNET2 Workshop on In-Vessel Coolability, October 12 – 14, Paris, France, (2009).
[178] Hofmann, P., “Current knowledge on core degradation phenomena, a review”, Journal of Nuclear Materials 270 194-211, (1999).
[179] Breeding, R., Helton, J., Gorham, D., Harper, F., “Summary description of the methods used in the probabilistic risk assessments for NUREG-1150”, Nucl. Eng. Des. 135 (1) 1–27, (1992)
[180] Helton, J., Uncertainty and sensitivity analysis in the presence of stochastic and subjective uncertainty, J. Stat. Comput. Simulat. 57 (1–4) 3–76, (1997).
[181] Parry, G., Winter P. “Characterization and evaluation of uncertainty in probabilistic risk analysis. Nuclear Safety”, 28-42, (1981)
[182] Kallenberg, O., “Foundations of Modern Probability ”, ISBN 978-0-387-95313-7, New York, Springer, (2002).
[183] Dempster A. Upper and lower probabilities induced by a multivalued mapping. Annals of Mathematical Statistics 325-339, (1967).
[184] Shafer, G., “A mathematical theory of evidence”, Princeton, ISBN 9780691100425 , NJ: Princeton University Press, (1976).
[185] Dubois, D., Prade, H., “Possibility theory: qualitative and quantitative aspects” in Handbook of defeasible reasoning and uncertainty: Quantified Representation of Uncertainty and Imprecision Boston, MA: Kluwer Academic Publishers 168-226, (1998).
[186] Dubois D, Prade H: Possibility theory and its applications: a retrospective and prospective view. The 12th IEEE International Conference on Fuzzy Systems, FUZZ ‘03, 1:5-11, (2003)
[187] Moore, R., “Interval analysis”, Englewood Cliffs, NJ: Prentice Hall, (1966)
[188] Moore, R. Kearfott, R., Cloud, M., “Introduction to interval analysis”, Philadelphia, PA: Society for Industrial and Applied Mathematics, (2009).
[189] Apostolakis, G. E., “The concept of probability in safety assessments of technological systems”, Science, 250, 1359-1364, (1990).
[190] Dempster, A., “Upper and lower probability inferences based on a sample from a finite univariate population”, Biometrika, 54, 515–528, (1967).
[191] Rechard, R.P. “Historical relationship between performance assessment for radioactive waste disposal and other types of risk assessment”, Risk Analysis 19, 763–807, (1999).
[192] Rechard, R.P. “Historical background on performance assessment for the waste isolation pilot plant” Reliability Engineering and System Safety 69, 5–46, (2000).
[193] U.S. Nuclear Regulatory Commission. “Reactor safety study, an assessment of accident risks. Wash1400” Report NUREG-75/014.Washington, DC, (1975).

[194] Kaplan, S., "Formalisms for handling phenomenological uncertainties: the concepts of probability, frequency, variability, and probability of frequency", Nuclear Technology, 102, 137-142, (1992).
[195] National Academy of Science (NAS)/National Research Council (NRC) "Evaluation of quantification of margins and uncertainties for assessing and certifying the reliability of the nuclear stockpile", Washington, DC: National Academy Press, (2008).
[196] U.S. Nuclear Regulatory Commission "Probabilistic risk assessment and severe accident evaluation for new reactors", NUREG-0800 Rev 3, (2014).
[197] Helton, J., "Quantification of margins and uncertainties: Conceptual and computational basis", Reliability Engineering and System Safety, 96, 976-1013, (2011).
[198] Cullen, A., Frey, H., "Probabilistic techniques in exposure assessment: a handbook for dealing with variability and uncertainty in models and inputs", New York, NY: Plenum Press, (1999).
[199] Eldred, M., Swiler, L., Tang, T., "Mixed aleatory-epistemic uncertainty quantification with stochastic expansions and optimization-based interval estimation", Reliability Engineering and System Safety 96, 1092-1113, (2011).
[200] Helton, J., Breeding, R., "Calculation of reactor accident safety goals", Reliability Engineering and System Safety, 39, 129-158, (1993).
[201] Frid, W., et al., Severe Accident Research and Management in Nordic Countries: A Status Report, W. Frid, Editor. 2002.
[202] Chu, C.C. and D. Corradini, "A Dynamic Model for Droplet Fragmentation," Transactions of American Nuclear Society, 47p. 1984.
[203] Chu, C.C., "One dimensional transient fluid model for fuel-coolant interaction," university of Wisconsin-Madison. 1986.
[204] Chu, T. Y., Pilch, M. M., Bentz, J. H., Ludwigsen, J. S., Lu, W.Y. and Humphries, L. L., "Lower Head Failure Experiment and Analyses", NUREG/CR-5582, SAND98-2047, 1999.
[205] Chu, C.C., Sienicki, J.J., Spencer, B.W., Frid, W., Löwenhielm, G., "Ex-vessel melt-coolant interactions in deep water pool: studies and accident management for Swedish BWRs," Nuclear Engineering and Design, Volume 155, Issues 1–2, 2 April 1995, Pages 159-213.
[206] Corradini, M.L., et al., Users' manual for Texas-V: One dimensional transient fluid model for fuel-coolant interaction analysis. 2002, University of Wisconsin-Madison: Madison WI 53706.
[207] Tang, J., Modeling of the complete process of one-dimensional vapor explosions, University of Wisconsin-Madison, 1993.
[208] Kim, B.J., "Heat transfer and fluid flow aspect of small-scale single droplet fuel-coolant interaction," University of Wisconsin-Madison. 1985.
[209] Murphy, J., A Hydrogen Generation Model for TEXAS. 1992, University of Wisconsin.
[210] Meignen, R. Status of the Qualification Program of the Multiphase Flow Code MC3D in Proceedings of ICAPP '05. 2005. Seoul, KOREA, May 15-19, 2005.
[211] Grishchenko, D., et al., KROTOS KS-4 test data report 2011, CEA: France, Cadarache.
[212] Magallon, D., et al., OECD research programme on fuel-coolant interaction. Steam explosion resolution for nuclear applications - SERENA. 2007.
[213] Magallon, D., et al. Results of phase 1 of OECD programme SERENA on fuel-coolant interaction. in ERMSAR 2005. 2005. Aix-en-Provence.
[214] Magallon, D., SERENA Programme Reactor exercise: Synthesis of calculations. 20 p., 2012.

[215] Park, I.K., Kim D.H., and Song J.H. "Steam explosion module development for the MELCOR code using TEXAS-V," Journal of Korean Nuclear Society, 2003. 32(4): pp.286-298, 2003.
[216] Song, J.H., I.K. Park, and J.H. Kim, A coherent methodology for evalluation of a steam explosion load using TEXAS-V. Journal of Korean Nuclear Society, 2004. 36(6): p. 571-581.
[217] Chen, R.H., et al., Analysis of KROTOS Steam Explosion Experiments Using the Improved Fuel-Coolant–Interaction Code TEXAS-VI. Nuclear Science and Engineering, 2013. 174: p. 46-59.
[218] Moriyama, K., et al., Evaluation of Containment Failure Probability by Ex-Vessel Steam Explosion in Japanese LWR Plants. Journal of Nuclear Science and Technology, 2012. 43(7): p. 774-784.
[219] Moriyama, K. and H.S. Park, Probability distribution of ex-vessel steam explosion loads considering influences of water level and trigger timing. Nuclear Engineering and Design, 2015. 293: p. 292-303.
[220] Grishchenko D., Basso S., Kudinov P., and Bechta S. "Sensitivity Study of Steam Explosion Characteristics to Uncertain Input Parameters Using TEXAS-V Code," The 10th International Topical Meeting on Nuclear Thermal-Hydraulics, Operation and Safety (NUTHOS-10), Okinawa, Japan, December 14-18, 2014, Paper 1293, 2014.
[221] S.E. Yakush, W. Villanueva, S. Basso, P. Kudinov, "Simulation of In-Vessel Debris Bed Coolability and Remelting," *Proc. of the 10th International Topical Meeting on Nuclear Reactor Thermal-Hydraulics, Operation and Safety* (*NUTHOS-10*), Okinawa, Japan, paper NUTHOS10-1281 (2014).
[222] IAPWS, *The International Association for the Properties of Water and Steam*, http://www.iapws.org.
[223] V.X. Tung and V.K. Dhir, "A Hydrodynamic Model for Two-Phase Flow through Porous Media," *Int. J. Multiphase Flow*, **14**(1), pp. 47-65 (1988).
[224] W. Schmidt, "Interfacial Drag of Two-phase Flow in Porous Media," *Int. J. Multiphase Flow*, **33**, pp. 638-657 (2007).
[225] B. E. Launder, D. B. Spalding, *Mathematical Models of Turbulence*, Academic Press, London (1972).
[226] R. T. Lahey, Jr, D. A. Drew, "The Analysis of Two-Phase Flow and Heat Transfer Using a Multidimensional, Four Field, Two-Fluid Model," *Nuclear Engineering and Design*, **204**, pp. 29-44 (2001).
[227] S. E. Elghobashi, T. W. Abou-Arab, "A Two-equation Turbulence Model for Two-phase Flows," *Phys. Fluids*, **26**, pp. 931–937 (1982).
[228] M. Ishii, K. Mishima, "Two-Fluid Model and Hydrodynamic Constitutive Relations," *Nuclear Engineering and Design,* **82**, pp. 107-126 (1984).
[229] P. J. Oliveira, R. I. Issa, "Numerical Aspects of an Algorithm for the Eulerian Simulation of Two-phase Flows," *Int. J. Numer. Meth. Fluids*, **43**, pp. 1177–1198 (2003).
[230] S. E. Yakush, P. Kudinov, and T.-N. Dinh, "Multiscale Simulations of Self-organization in the Formation and Coolability of Corium Debris Bed", *Proceedings of the 13th International Topical Meeting on Nuclear Reactor Thermal-Hydraulics (NURETH13)*, Kanazawa City, Japan, October 2009, paper N13P1143, 13 pp. (2009).
[231] S. E. Yakush, A. Konovalenko, S. Basso, P. Kudinov, " Validation of DECOSIM Code Against Experiments on Particle Spreading by Two-Phase Flows in Water Pool", NUTHOS-11: The 11th International Topical Meeting on Nuclear Reactor Thermal Hydraulics, Operation and Safety, Gyeongju, Korea, October 9-13, 2016.

[232] S. E. Yakush, P. Kudinov, ”In-Vessel Debris Bed Coolability and Implications For Vessel Failure Mode”, NUTHOS-11: The 11th International Topical Meeting on Nuclear Reactor Thermal Hydraulics, Operation and Safety, Gyeongju, Korea, October 9-13, 2016.

[233] Tran, C. T., Kudinov, P., and Dinh, T. N., “An approach to numerical simulation and analysis of molten corium coolability in a BWR lower head,” Nuclear Engineering and Design, 240, 2010, 2148–2159.

[234] Butkova, Y., Bäckström, O., Hermanns, H, Krcal, P., Wang, W. "Dynamic Features in Large PSA Studies", ESREL 2016.

Bibliographic Data Sheet **NKS-395**

Title	Scenarios and Phenomena Affecting Risk of Containment Failure and Release Characteristics
Author(s)	Pavel Kudinov[1], Sergey Galushin[1], Dmitry Grishchenko[1], Sergey Yakush[1] Yvonne Adolfsson[2], Lisa Ranlöf[2], Ola Bäckström[2], Anders Enerholm[2]
Affiliation(s)	[1]Division of Nuclear Power Safety (NPS), Royal Institute of Technology (KTH); [2]Lloyd's Register Consulting – Energy AB
ISBN	978-87-7893-483-3
Date	August 2017
Project	NKS-R / SPARC
No. of pages	302
No. of tables	41
No. of illustrations	211
No. of references	234

Abstract
max. 2000 characters

The report summarizes results achieved within the project NKS-SPARC. The project is motivated by apparently high sensitivity of effectiveness of severe accident management (SAM) strategy in Nordic type BWR to the uncertainties in physical phenomena (deterministic) and accident scenarios (stochastic). We employ ROAAM+ approach in order to address both epistemic and aleatory sources of uncertainty in a consistent manner. The state of the art review of Integrated Deterministic Probabilistic Safety Analyses (IDPSA) is presented. The ROAAM+ framework addressing all stages of the accident progression from initial plant damage states, through core degradation and vessel failure, melt ejection mode to ex-vessel melt-coolant interactions and debris coolability, is discussed in detail along with implementation details of ROAAM+ framework itself. Main findings of the analysis of effectiveness of SAM strategy in Nordic BWRs using ROAAM+ framework and main results are presented using failure domain maps. A conceptual approach for combined use of Probabilistic Safety Assessment (PSA) and Integrated Probabilistic Deterministic Safety Assessment (IDPSA) is illustrated. Methodological enhancements of PSA analysis, based on PSA and DSA integration are proposed. The project outcome will allow the end users to enhance understanding, completeness and consistency of safety analysis dealing with risk analysis in: management of severe accident issues; improved reliability analysis modelling methods for level 2 PSA; presentation of results in level 2 PSA, and related risk criteria; handling of modelling uncertainties.

Key words

ROAAM+, IDPSA, PSA, DSA, BWR, Severe accident, MELCOR, core degradation, steam explosion, debris coolability.

Available on request from the NKS Secretariat, P.O.Box 49, DK-4000 Roskilde, Denmark.
Phone (+45) 4677 4041, e-mail nks@nks.org, www.nks.org